1994

PORE-LEVEL FLUID MIGRATION IN RESERVOIR SANDSTONES

MOSS, ADAM KEITH

PORE-LEVEL FLUID MIGRATION IN RESERVOIR SANDSTONES

by

ADAM KEITH MOSS

A thesis submitted to the University of Plymouth

in partial fulfilment for the degree of

DOCTOR OF PHILOSOPHY

Department of Environmental Sciences

Faculty of Science

In collaboration with

British Gas

Michael Road Research Station

London

July 1994

Pore Level Fluid Migration In Reservoir Sandstones

by

Adam Keith Moss

Abstract

The void space properties of a set of gas reservoir sandstone samples have been measured. The properties include porosity, absolute gas permeability, electrical resistivity formation factor and tortuosity. The mineralogy of each sandstone was determined by scanning electron microscopy and energy dispersive x-ray analysis. Mercury intrusion and extrusion data have been measured for most of the sandstone samples. A new procedure for measuring the degree and range of void size correlations within resin-filled sandstones has been developed. Image analysis of backscattered electron micrographs of these samples supplies void size and positional information. A "semi-variogram" study of void size and coordinate data ascertains the degree and range of void size correlation. Measurable correlation has been found in two sandstone samples, but was absent from four others.

Diffusion coefficients of methane, iso-butane and n-butane through dry sandstones have been measured using an adaptation of a non-steady state method, using a redesigned apparatus. A repeatability and error analysis of diffusion coefficient measurement has also been performed. A correlation between diffusion coefficients, absolute permeability, porosity and formation factor was detected for sandstones containing little clay. The diffusion coefficients measured for clay affected sandstones did not correlate with any petrophysical properties of these samples.

A computer model capable of simulating porous media has been previously developed. It consists of a 10x10x10 network of cubic pores and cylindrical throats, and simulates the mercury intrusion curve. The void size distribution is modified until both simulated and experimental curves closely match. New void size distribution input and curve fit algorithms have been developed to increase the speed and accuracy of the simulations and a new modelling procedure allows the modelling of samples with void size correlation. The model is capable of simulating porosity, permeability, tortuosity and mercury extrusion. Each of the reservoir sandstones has been modelled and their characteristic properties simulated. Successful simulations were obtained for all relatively clay-free reservoir sandstones. Clay affected sandstone simulations were less successful due to the high complexity of these samples.

A study into formation damage within reservoir sandstones was also undertaken. The effect of colloidal particulate void space penetration is measured and simulated.

List of Contents

Page

Copyright Statement i

Title Page ii

Abstract iii

List of Contents iv

List of Tables x

List of Figures xii

List of Plates xxii

Acknowledgements xxiii

Author's Declaration xxiv

Chapter 1 Introduction

1.1 Aim of the Research 1

1.2 Sandstones 1

1.3 Test Order 4

Chapter 2 Porosity and Permeability

2.1 Porosity Measurement 6

2.2 Permeability Measurement 8

2.2.1 The Klinkenburg Effect 9

2.3 The Samples 10

Chapter 3 Scanning Electron Microscopy

3.1 Introduction 15

3.2 Results 15

Chapter 7 Diffusion

7.1 Introduction 126

7.2 Theory 127

7.2.1 Relationship Between Diffusion and Tortuosity 132

7.3 The Apparatus 135

7.4 Regression Analysis To Find Lag Time 141

7.5 Results 142

7.5.1 Error Analysis 147

7.5.2 Analysis Of Variables Within Diffusion Measurements 152

7.6 Correlation Of Diffusion With Petrophysical Properties 155

7.6.1 Clay Affected Sandstones 157

Chapter 8 The Void Space Model

8.1 Other Void Space Models 159

8.1.1 Non-Wetting Phase Intrusion/Extrusion Simulations 160

8.1.2 Permeability Simulations 162

8.2 Description of the Model 165

8.2.1 The Construction of the Unit Cell 167

8.2.2 Mercury Intrusion Simulation 172

8.2.3 Convergence of Simulation onto Experimental Intrusion Data 176

8.2.4 The Simulation of Mercury Extrusion 181

8.2.5 Calculation of Absolute Permeability 183

8.2.5.1 Klinkenburg Correction 187

8.2.5.2 The Permeability Calculation 189

8.2.6 Tortuosity Simulation 190

8.2.7 Constructing Correlated Structures 190

8.2.7.1 Banded Structures 191

8.2.7.2 Unit Cells With Small or Large Pores

In Centre 194

8.2.8 Pore Block Simulation 194

Chapter 9 Modelling Results

9.1 Trends Within Simulations 195

9.1.1 Changing Connectivity Within A Random

Pore:Throat Network 195

9.1.2 Changing Throat Size Distribution Within A Random

Pore:Throat Network 198

9.1.3 Changing Degree Of Pore:Pore Correlation 201

9.2 First Attempts To Simulate Reservoir Sandstone

Void Space 202

9.3 Simulation Of Reservoir Sandstone Void Space Using

Truncated Mercury Intrusion Curves 207

9.3.1 Results 208

9.3.2 Summary 229

Chapter 10 Measurement and Simulation of Colloidal Flow Formation Damage in

Sandstones

10.1 Introduction 230

10.2 Formation Damage In Sandstone 231

Chapter 4 Formation Factor

4.1 Introduction 25

4.2 Tortuosity 28

4.3 Formation Factor and Tortuosity Measurement 32

4.3.1 Method 32

4.3.2 Results 34

Chapter 5 Mercury Porosimetry

5.1 Introduction 42

5.2 Structural Hysteresis 49

5.3 Contact Angle Hysteresis 51

5.4 Results 51

Chapter 6 Image Analysis

6.1 Introduction 72

6.1.1 Void Space Identification 72

6.1.2 Void Feature Measurements 77

6.2 Image Analysis on Fracture Surfaces 79

6.3 Image Analysis on Resin Filled Void Space 80

6.4 Void Size Distributions 83

6.5 Measurement of Void Size Correlation 94

6.6 Variogram Study 103

6.7 Geo-Eas 105

6.7.1 Results 105

6.8 Improved Curve Fit To Variogram 121

6.8.1 Results 123

6.9 Conclusions 123

10.3 Modelling Colloidal Flow 233

10.4 Outcrop Sandstones 235

10.4.1 Clean and Damaged Samples 235

10.5 Reservoir Sandstones 238

10.5.1 Clean and Damaged Samples 238

10.5.2 Formation Factor/Tortuosity Measurements 241

10.5.3 Mercury Porosimetry 241

10.6 Modelling Outcrop Sandstone Clean

and Damaged 250

10.7 Computer Modelling Of Reservoir Sandstones 251

10.8 Concluding Remarks 262

Chapter 11 Conclusions

11.1 Porosity 265

11.2 Permeability 265

11.3 Tortuosity 266

11.4 The Unit Cell and Mercury Porosimetry 266

11.5 Formation Damage 267

Glossary of Terms 268

List of Symbols 270

References 274

Appendix 1 Scanning Electron Microscopy . . . . . Ai

Appendix 2 Brine Composition . . . . . Av

Appendix 3 Mercury Porosimetry . . . . . Avi

Appendix 4 Geo-Eas Availibility and Usage . . . . . Ax

Appendix 5 Peak Area Against Time Plots . . . . . Axi

Appendix 6 Mercury Intrusion Curves From First Simulation Attempts . . . . . Axxix

Appendix 7 Truncated Mercury Intrusion and Extrusion Curves . . . . . Axliii

List of Tables

Chapter 2

TABLE 2.1: Porosity and Permeability Data. Bracketed values equal repeat experiments.

Chapter 3

TABLE 3.1: Mineral Characteristics Of Each Sample Group

Chapter 4

TABLE 4.1: Measured Data For Each Sandstone Plug.

Chapter 5

TABLE 5.1: Mercury Porosimetry Results.

Chapter 6

TABLE 6.1: Summary of Void Size Correlation Study Results.

Chapter 7

TABLE 7.1: Diffusion Coefficients for Reservoir Sandstones.

TABLE 7.2: Potential Factors Effecting Diffusion Coefficients.

Chapter 9

TABLE 9.1: Model Inputs To Simulate Reservoir Sandstone Void Space and Corresponding Outputs.

TABLE 9.2: Model Inputs and Outputs For Each Truncated Curve Fit Simulation

TABLE 9.3: Diffusion Coefficients Calculated From Median Modelled Tortuosities.

Chapter 10

TABLE 10.1: Parameters Measured For Clashach Outcrop Sandstone.

TABLE 10.2: Results of Formation Damage of Reservoir Sandstones.

TABLE 10.3: Analysis of formation damage in reservoir sandstone samples.

TABLE 10.4: Computer simulation of colloid induced formation damage.

List of Figures

Chapter 1

FIGURE 1.1: Scope of Pore-Cor Model.

FIGURE 1.2: Sandstone Test Order.

Chapter 2

FIGURE 2.1: Particle Packing Arrangements.

FIGURE 2.2: Permeability and Porosity Cross Plot.

Chapter 3

FIGURE 3.1: X-ray Spectra for Potassium Feldspar Grain in Plate 3.3.

FIGURE 3.2: X-ray Spectra for Illite/Smectite Clay in Plate 3.4.

FIGURE 3.3: X-ray Spectra for Kaolinite Clay in Plate 3.6.

FIGURE 3.4: X-ray Spectra for Illite Clay in Plate 3.7.

FIGURE 3.5: Permeability and Porosity Cross Plot with Mineralogy Grouping.

Chapter 4

FIGURE 4.1: Formation Factor Against Porosity Showing Cementation Exponent Range.

FIGURE 4.2: Core Conductivity Against Brine Conductivity.

FIGURE 4.3: A Schematic Porous Medium Showing a Tortuous Capillary Containing Brine of Resistivity R_w.

FIGURE 4.4: Apparatus Used to Measure Formation Factor.

FIGURE 4.5: Mean Formation Factor Against Porosity For Samples in Group 212.

FIGURE 4.6: Mean and Extremes of Formation Factor Range Against Porosity for Samples in Group 212.

FIGURE 4.7: Mean and Extremes of Formation Factor Range Against Porosity for Samples in Group 250.

FIGURE 4.8: Mean and Extremes of Formation Factor Range Against Porosity For Samples in Group 80.

FIGURE 4.9: Mean and Extremes of Formation Factor Range Against Porosity for Samples in Group 100.

FIGURE 5.1: Typical Mercury Intrusion/Extrusion Curves for Sandstone.

FIGURE 5.2: Family of Mercury Intrusion Curves With Varying Pore Geometrical Factors.

FIGURE 5.3: Two-Dimensional Void Space Arrangement.

FIGURE 5.4: Mercury Porosimetry Curves for Plug 212A.

FIGURE 5.5: Mercury Porosimetry Curves for Plug 212B.

FIGURE 5.6: Mercury Porosimetry Curves for Plug 212C.

FIGURE 5.7: Mercury Porosimetry Curves for Plug 212D.

FIGURE 5.8: Mercury Porosimetry Curves for Plug 212E.

FIGURE 5.9: Mercury Porosimetry Curves for Plug 250A.

FIGURE 5.10: Mercury Porosimetry Curves for Plug 250E.

FIGURE 5.11: Mercury Porosimetry Curves for Plug 250E Repeat Run.

FIGURE 5.12: Mercury Porosimetry Curves for Plug 490A.

FIGURE 5.13: Mercury Porosimetry Curves for Plug 490B.

FIGURE 5.14: Mercury Porosimetry Curves for Plug 490C.

FIGURE 5.15: Mercury Porosimetry Curves for Plug 490D.

FIGURE 5.16: Mercury Porosimetry Curves for Plug 490D Repeat Run.

FIGURE 5.17: Mercury Porosimetry Curves for Plug 490E.

FIGURE 5.18: Mercury Intrusion Curves For Sandstones Containing Pore Lining Clay or Clay as Discrete Particles.

FIGURE 5.19: Mercury Porosimetry Curves Showing Increased Extrusion After Overnight Exposure to Lowest Pressure Attainable.

Chapter 6

FIGURE 6.1: Grey Level Distribution of a Fracture Surface SEM Image.

FIGURE 6.2: Grey Level Distribution from a Backscattered SEM Image of Resin Filled Pore Space, Sample 212B. (Peak at 256 due to Scale Bar)

FIGURE 6.3: Void Size Distribution for Image Analysis of Sample 212B.

FIGURE 6.4: Void Size Distribution for Image Analysis of Sample 212E.

FIGURE 6.5: Cumulative Void Size Distributions for Different Feature Measurements on Sample 212B.

FIGURE 6.6: Cumulative Void Size Distributions for Different Feature Measurements on Sample 212E.

FIGURE 6.7: Comparison of Cumulative Void Size Distributions From Image Analysis With Mercury Intrusion Data for Sample 212B.

FIGURE 6.8: Comparison of Cumulative Void Size Distributions From Image Analysis With Mercury Intrusion Data for Sample 212E.

FIGURE 6.9: Comparison of Cumulative Void Size Distributions From Image Analysis With Mercury Intrusion Data for Sample 212A.

FIGURE 6.10: Comparison of Cumulative Void Size Distributions From Image Analysis With Mercury Intrusion Data for Sample 250A.

FIGURE 6.11: Comparison of Cumulative Void Size Distributions From Image Analysis With Mercury Intrusion Data for Sample 490D.

FIGURE 6.12: Comparison of Cumulative Void Size Distributions From Image Analysis With Mercury Intrusion Data for Sample 490E.

FIGURE 6.13: Difference in Log Diameter Between Largest Void and All Other Voids Against Distance From Largest Void for the Three Largest Voids Detected in Sintered Glass Image.

FIGURE 6.14: Difference in Log Diameter Between Largest Void and All Other Voids Against Distance From Largest Void for the Three Largest Voids Detected in Sample 212B.

FIGURE 6.15a: A Typical Semi-Variogram.

FIGURE 6.15b: A Semi-Variogram for an Anisotropic Sample.

FIGURE 6.16: Centre of Gravity Coordinate Plot for Detected Features Within the Sintered Glass System.

FIGURE 6.17: Semi-Variogram for Sintered Glass Data, *a* Equals the Zone of Influence.

FIGURE 6.18: Semi-Variogram for Sintered Glass Data, With Smoothed Curve and New Zone of Influence Value (*a*).

FIGURE 6.19: Semi-Variogram for Sintered Glass Data With "Noise" Features Removed.

FIGURE 6.20: Centre of Gravity Coordinate Plot for Detected Features Within a Multiple Banded Sintered Glass System, With "Noise" Features Removed.

FIGURE 6.21: Semi-Variogram for Multiple Banded Sintered Glass System, With "Noise" Features Removed.

FIGURE 6.22: Semi-Variogram for Multiple Banded Sintered Glass System, Including "Noise" Features, With Smooth Curve.

FIGURE 6.23: Centre of Gravity Coordinate Plot for Detected Features Within Reduced Multiple Banded Sintered Glass System, Including "Noise" Features.

FIGURE 6.24: Semi-Variogram for Sample 212B With Smooth Curve.

FIGURE 6.25: Semi-Variogram for Sample 212B Using Feature Breadth as the Variable.

FIGURE 6.26: Semi-Variogram for Sample Size with Smoothed Curve.

FIGURE 6.27: Semi-Variogram for Sample 212E Using Feature Breadth as the Variable.

FIGURE 6.28: Semi-Variogram for Sample 212B With Cubic Spline Fitted Curve.

FIGURE 6.29: Semi-Variogram for Sample 212E With Cubic Spline Fitted Curve.

Chapter 7

FIGURE 7.1: Principle Phases of Lag Time Diffusion Experiments.

FIGURE 7.2: Lag Time Plot.

FIGURE 7.3: Diffusive Flux Against Time.

FIGURE 7.4: Diffusion Apparatus.

FIGURE 7.5: Sample Cell Showing Gas-Tight Disc Operation.

FIGURE 7.6: Mini-Tab Regression Analysis.

FIGURE 7.7: Time Against Cumulative Peak Are Units.

FIGURE 7.8: Methane Diffusion Coefficient Ranges.

FIGURE 7.9: N-Butane Diffusion Coefficient Ranges.

FIGURE 7.10: Iso-Butane Diffusion Coefficient.

FIGURE 7.11a: Loadings for the Eleven Variables Identified in Table 7.2 for the First Three Modelling Factors.

FIGURE 7.11b: Residual Variance as an Increasing Number of Modelling Factors are Included in the Model.

FIGURE 7.12: Permeability and Formation Factor Against Iso-Butane Diffusion Coefficient, In Relatively Clay Free Sandstones.

Chapter 8

FIGURE 8.1: Model 3-D Unit Cell.

FIGURE 8.2a: Log Linear Throat Size Distribution With 1% of Every Throat Size.

FIGURE 8.2b: Log Linear Throat Size Distribution Skewed Towards The Large Throat Sizes.

FIGURE 8.2c: Log Linear Throat Size Distribution Skewed Towards The Small Throat Sizes.

FIGURE 8.3a: Pore-Throat Correlation For Berea Sandstone (From Wardlaw 1987).

FIGURE 8.3b: Pore-Throat Correlation For Indiana Limestone (From Wardlaw 1987).

FIGURE 8.4: Pore-Throat Correlation For Simulations With Varying Pore/Max. Throat Size.

FIGURE 8.5: Flow Diagram For Mercury Intrusion Curve.

FIGURE 8.6: Mercury Porosimetry Curves For Two Similar Samples Of Indiana Limestone; One Coated in Resin On All Sides Except One, the Other Sample Is Uncoated (From Wardlaw and Taylor 1976).

FIGURE 8.7: Mercury Extrusion Simulation Flow Diagram.

FIGURE 8.8: Model 3-D Unit Cell With Vertical Banding.

Chapter 9

FIGURE 9.1: Model 3-D Unit Cell Showing Mercury Breakthrough.

FIGURE 9.2: Simulated Mercury Intrusion Curve For Unit Cell In Figure 9.1, Showing Breakthrough Point.

FIGURE 9.3: Simulated Mercury Intrusion Curves For Networks With Varying Connectivity.

FIGURE 9.4: Relationship Between Permeability and Connectivity In Simulated Void Networks.

FIGURE 9.5: Simulated Mercury Intrusion Curves For Networks With Varying Connectivity.

FIGURE 9.6: Relation Between Permeability and Correlation In Simulated Void Networks.

FIGURE 9.7: Trends Identified Within Pore-Cor Void Space Model.

FIGURE 9.8: Truncated Experimental and Simulated Mercury Intrusion Curves for

Sample 212A.

FIGURE 9.9: Truncated Experimental and Simulated Mercury Intrusion Curves for Sample 212B.

FIGURE 9.10: Truncated Experimental and Simulated Mercury Intrusion Curves for Sample 212C.

FIGURE 9.11: Truncated Experimental and Simulated Mercury Intrusion Curves for Sample 212D.

FIGURE 9.12: Truncated Experimental and Simulated Mercury Intrusion Curves for Sample 212E.

FIGURE 9.13: Truncated Experimental and Simulated Mercury Intrusion Curves for Sample 250A.

FIGURE 9.14: Truncated Experimental and Simulated Mercury Intrusion Curves for Sample 250E.

FIGURE 9.15: Truncated Experimental and Simulated Mercury Intrusion Curves for Sample 250E. Repeat Run

FIGURE 9.16: Truncated Experimental and Simulated Mercury Intrusion Curves for Sample 490A.

FIGURE 9.17: Truncated Experimental and Simulated Mercury Intrusion Curves for Sample 490B.

FIGURE 9.18: Truncated Experimental and Simulated Mercury Intrusion Curves for Sample 490C.

FIGURE 9.19: Truncated Experimental and Simulated Mercury Intrusion Curves for Sample 490D.

FIGURE 9.20: Truncated Experimental and Simulated Mercury Intrusion Curves for Sample 490D. Repeat Run

FIGURE 9.21: Truncated Experimental and Simulated Mercury Intrusion Curves for Sample 490E.

FIGURE 9.22: Simulated and Measured Methane Diffusion Coefficient Ranges.

FIGURE 9.23: Simulated and Measured Iso-butane Diffusion Coefficient Ranges.

FIGURE 9.24: Simulated and Measured n-butane Diffusion Coefficient Ranges.

Chapter 10

FIGURE 10.1: Size Distribution of Particles in the Colloidal Chalk Suspension.

FIGURE 10.2: Mercury porosimetry curves for sample 81. _____ native intrusion, -- -- native extrusion, - - - colloid flooded intrusion, ... colloid flooded extrusion.

FIGURE 10.3: Mercury porosimetry curves for sample 82. _____ native intrusion, -- -- native extrusion, - - - colloid flooded intrusion, ... colloid flooded extrusion.

FIGURE 10.4: Mercury porosimetry curves for sample 98. _____ native intrusion, -- -- native extrusion, - - - colloid flooded intrusion, ... colloid flooded extrusion.

FIGURE 10.5: Mercury porosimetry curves for sample 107. _____ native intrusion, -- -- native extrusion, - - - colloid flooded intrusion, ... colloid flooded extrusion.

FIGURE 10.6: Mercury porosimetry curves for sample 108. _____ native intrusion, -- -- native extrusion, - - - colloid flooded intrusion, ... colloid flooded extrusion.

FIGURE 10.7: Mercury intrusion curves for Clashach sandstone: —— experimental, ----- optimum distribution.

FIGURE 10.8: Mercury intrusion curves for clean sample 81: —— experimental, ----- optimum distribution.

FIGURE 10.9: Mercury intrusion curves for colloid flooded sample 81, optimum distribution of clean sample 81 simulation with pore block of radius 7.3μm: —— experimental, ----- optimum distribution.

FIGURE 10.10: Mercury intrusion curves for colloid flooded sample 81: —— experimental, ----- optimum distribution.

FIGURE 10.11: Mercury intrusion curves for sample 82: —— experimental clean sample, -·-·- clean optimum distribution, ----- experimental colloid flooded sample, ····· colloid flooded optimum distribution.

FIGURE 10.12: Mercury intrusion curves for sample 98: —— experimental clean sample, -·-·- clean optimum distribution, ----- experimental colloid flooded sample, ····· colloid flooded optimum distribution.

FIGURE 10.13: Mercury intrusion curves for sample 107: —— experimental clean sample, -·-·- clean optimum distribution, ----- experimental colloid flooded sample, ····· colloid flooded optimum distribution.

FIGURE 10.14: Mercury intrusion curves for sample 108: —— experimental clean sample, -·-·- clean optimum distribution, ----- experimental colloid flooded sample, ····· optimum distribution for clean sample 108 simulation with a pore block of radius 6.5μm.

Appendix 1

FIGURE A1.1: Schematic Showing SEM/EDX System (from Welton 1984).

FIGURE A1.2: Interactions Between an Electron Beam and Sample.

FIGURE A1.3: Electron Transactions in an Atom.

Appendix 3

FIGURE A3.1: Mercury Injection Capillary Pressure Apparatus, a Modified Ruska 1059.

FIGURE A3.2: Pressure-Volume Calibration Data.

Appendix 5

FIGURE A5.1: Peak Area Against Time Plots for Clashach.

FIGURE A5.2: Peak Area Against Time Plots for Clashach.

FIGURE A5.3: Peak Area Against Time Plots for Sample 212A.

FIGURE A5.4: Peak Area Against Time Plots for Sample 212A.

FIGURE A5.5: Peak Area Against Time Plots for Sample 250A.

FIGURE A5.6: Peak Area Against Time Plots for Sample 250A.

FIGURE A5.7: Peak Area Against Time Plots for Sample 250E.

FIGURE A5.8: Peak Area Against Time Plots for Sample 250E.

FIGURE A5.9: Peak Area Against Time Plots for Sample 490A.

FIGURE A5.10: Peak Area Against Time Plots for Sample 490A.

FIGURE A5.11: Peak Area Against Time Plots for Sample 490B.

FIGURE A5.12: Peak Area Against Time Plots for Sample 490B.

FIGURE A5.13: Peak Area Against Time Plots for Sample 490C.

FIGURE A5.14: Peak Area Against Time Plots for Sample 490C.

FIGURE A5.15: Peak Area Against Time Plots for Sample 490D.

FIGURE A5.16: Peak Area Against Time Plots for Sample 490D.

FIGURE A5.17: Peak Area Against Time Plots for Sample 490E.

FIGURE A5.18: Peak Area Against Time Plots for Sample 490E.

Appendix 6

FIGURE A6.1: Experimental and Simulated Mercury Intrusion Curves for Sample 212A.

FIGURE A6.2: Experimental and Simulated Mercury Intrusion Curves for Sample 212B.

FIGURE A6.3: Experimental and Simulated Mercury Intrusion Curves for Sample 212C.

FIGURE A6.4: Experimental and Simulated Mercury Intrusion Curves for Sample 212D.

FIGURE A6.5: Experimental and Simulated Mercury Intrusion Curves for Sample 212E.

FIGURE A6.6: Experimental and Simulated Mercury Intrusion Curves for Sample 250A.

FIGURE A6.7: Experimental and Simulated Mercury Intrusion Curves for Sample 250E.

FIGURE A6.8: Experimental and Simulated Mercury Intrusion Curves for Sample 250E Repeat Run.

FIGURE A6.9: Experimental and Simulated Mercury Intrusion Curves for Sample 490A.

FIGURE A6.10: Experimental and Simulated Mercury Intrusion Curves for Sample 490B.

FIGURE A6.11: Experimental and Simulated Mercury Intrusion Curves for Sample 490C.

FIGURE A6.12: Experimental and Simulated Mercury Intrusion Curves for Sample 490D.

FIGURE A6.13: Experimental and Simulated Mercury Intrusion Curves for Sample 490D Repeat Run.

FIGURE A6.14: Experimental and Simulated Mercury Intrusion Curves for Sample 490E.

Appendix 7

FIGURE A7.1: Simulated Mercury Intrusion and Extrusion Curve for Truncated Curve Fit for Sample 212A.

FIGURE A7.2: Simulated Mercury Intrusion and Extrusion Curve for Truncated Curve Fit for Sample 212B.

FIGURE A7.3: Simulated Mercury Intrusion and Extrusion Curve for Truncated Curve Fit for Sample 212C.

FIGURE A7.4: Simulated Mercury Intrusion and Extrusion Curve for Truncated Curve Fit for Sample 212D.

FIGURE A7.5: Simulated Mercury Intrusion and Extrusion Curve for Truncated Curve Fit for Sample 212E.

FIGURE A7.6: Simulated Mercury Intrusion and Extrusion Curve for Truncated Curve Fit for Sample 250A.

FIGURE A7.7: Simulated Mercury Intrusion and Extrusion Curve for Truncated Curve Fit for Sample 250E.

FIGURE A7.8: Simulated Mercury Intrusion and Extrusion Curve for Truncated Curve Fit for Sample 250E Repeat Run.

FIGURE A7.9: Simulated Mercury Intrusion and Extrusion Curve for Truncated Curve Fit for Sample 490A.

FIGURE A7.10: Simulated Mercury Intrusion and Extrusion Curve for Truncated Curve Fit for Sample 490B.

FIGURE A7.11: Simulated Mercury Intrusion and Extrusion Curve for Truncated Curve Fit for Sample 490C.

FIGURE A7.12: Simulated Mercury Intrusion and Extrusion Curve for Truncated Curve Fit for Sample 490D.

FIGURE A7.13: Simulated Mercury Intrusion and Extrusion Curve for Truncated Curve Fit for Sample 490D Repeat Run.

FIGURE A7.14: Simulated Mercury Intrusion and Extrusion Curve for Truncated Curve Fit for Sample 490E.

List of Plates

Chapter 3

PLATE 3.1: SEM Photomicrograph of Plug 250B.

PLATE 3.2: SEM Photomicrograph of Plug 250B, Showing Quartz Overgrowth.

PLATE 3.3: SEM Photomicrograph of Diagenetized Potassium Feldspar Grain, Plug 250B.

PLATE 3.4: SEM Photomicrograph Authigenic Clay Within a Pore, Plug 250B.

PLATE 3.5: SEM Photomicrograph of an Unidentified Fine Particle, Plug 250B.

PLATE 3.6: SEM Photomicrograph of Clay Particles Within Plug 490A.

PLATE 3.7: SEM Photomicrograph Showing Hairy and Platey Illite Clay, Plug 490A.

Chapter 6

PLATE 6.1: Backscattered SEM Image of Sample 212B. The Image is 3.3mm Long.

PLATE 6.2: Backscattered SEM Image of Sample 212B With Grey Level Detect of 76 Shown in Red.

PLATE 6.3: Backscattered SEM Image of Sample 212B With Detect and Guard Frame Indicating Analysis Area. Individual Features Numbered.

PLATE 6.4: Backscattered SEM Image of Sample 212B With Detect and Segmentation.

PLATE 6.5: Backscattered SEM Image of Sample 212E. The Image is 2.28mm Long.

PLATE 6.6: Backscattered SEM Image of Sample 212E With Detect and Guard Frame Indicating Analysis Area. Individual Features Numbered.

PLATE 6.7: Backscattered SEM Image of Sample 212E With Detect and Segmentation.

PLATE 6.8: SEM Photo Micrograph of Sintered Glass Disc.

PLATE 6.9: SEM Photo Micrograph of Sintered Glass Discs With Grey Level Detect of 123 and Guard Frame.

Chapter 10

PLATE 10.1: Calcium Carbonate Particles Deposited With Clashach Pore Space.

Acknowledgements

I would like to take this opportunity to thank my supervisor, Dr Peter Matthews for his unfailing enthusiasm and support over the last three years. I am also grateful to my second supervisor, Dr Roy Lowry for his helpful discussions.

I would like to acknowledge the help given to me by Dr Joe Ali, Dr Harvey Haniff and all at the core store, British Gas, London Research Centre.

I would like to thank Dr Mike Spearing for allowing me to 'tinker' with his Pore-Cor Algorithm. Thanks and good luck to Cathy Ridgway for the continuing development of Pore-Cor. I would also like to thank Toby Mathews and Gareth Powell for assistance with the formation damage study. Richard Harris deserves recognition for his help in the image analysis study.

I am indebted to Brian Lakey and Dr Roy Moate for introducing me to the wonderful world of the electron microscope ! Thanks go to Brian and staff in technical services for cutting, mounting and grinding of sandstone samples.

I would like to thank Dr Dave Dowdell for creating such a harmonious atmosphere in the lab. I would like to voice my dissatisfaction with the players of Plymouth Argyle F.C. for hindering me in the latter stages of this project by failing to gain promotion this season !

And finally I would like to thank Mary, from the bottom of my heart, for typing up this project and just being there.

Author's Declaration

At no time during the registration for the degree of Doctor of Philosophy has the author been registered for any other University award.

This study was financed with the aid of a studentship from the Science and Engineering Research Council, and carried out in collaboration with British Gas, Gas Research Centre, Loughborough.

A programme of advanced study was undertaken, which included a petroleum exploration course on reservoir geology, supervised scanning electron microscope instruction and final year honours tutorials in hydrology.

Relevant scientific seminars and conferences were regularly attended at which work was often presented; external institutions were visited for consultation purposes, and several papers prepared for publication.

Publications (or presentation of other forms of creative work):

Network Calculation of Mercury Intrusion and Absolute Permeability in Sandstone and Other Porous Media by G.P.Matthews, A.K. Moss, M.C. Spearing and F. Voland, *Powder Technology*, 1993, **76**, 95-107.

The Measurement of Pores in an Irregular Surface by P. Russell, Dr D. Wright and A.K. Moss, *Quantimet News Review*, 1993, **8**, 4-5.

Measurement and Simulation of Colloidal Flow Formation Damage in Sandstone by T. Mathews, G.P. Mathews, A.K. Moss and G. Powell, *Society of Petroleum Engineers Formation Evaluation*, submitted for publication December 1993.

Presentations and Conferences Attended:

'19th General Assembly of the European Geophysical Society', Grenoble, April 1994, (attended).

'Computer Modelling of the Pore Structure and Permeability' by A.K.Moss, G.P. Matthews and C.J. Ridgway, British Organic Geochemical Society Meeting, July 1993 (oral presentation).

'Computer Modelling of the Pore Structure and Permeability of Outcrop and Reservoir Sandstones' by A.K. Moss and G.P. Matthews, Geofluids '93, Torquay, May 1993, (oral presentation).

'Mercury Porosimetry as a Probe of the Three-Dimensional Pore Network Within a Porous Solid' by G.P. Matthews, A.K. Moss and C.J. Ridgway, IUPAC Symposium on the Characterisation of Porous Solids, Marseille, May 1993, (poster presentation).

'Correlation and Prediction of the Pore-Level Properties of Sandstones' by G.P. Matthews and A.K.Moss, Computer Modelling Applications in Petroleum Exploration and Development, Aberdeen, April 1993 (co-author of oral presentation).

'The Modelling of the Pore-Level Properties of Sandstones, Applications for Pollutant Transport' by G.P.Matthews and A.K. Moss, Computer Science for Environmental Protection, Munich, December 1991, (poster presentation).

'The Modelling of the Pore-Level Properties of Sandstones' by G.P. Matthews, A.K. Moss and M.C. Spearing, Faraday Symposium No:26 Molecular Transport in Confined Regions and Membranes, Oxford, December 1990, (poster presentation).

External Contacts:

Dr Joe Ali, British Gas, Gas Research Centre, Ashby Road, Loughborough, Leicestershire, LE11 3QU.

Signed A.K. Moss

Date 4TH JULY 1994

CHAPTER 1

INTRODUCTION

1.1 Aim Of The Research

A computer model capable of simulating the void space within sandstones and other porous media has been developed by a previous research student at the University of Plymouth, Dr Michael Spearing. The program, which we call Pore Cor, had been applied to modelling clean homogeneous sandstones. The brief for this research project was to further develop the model to simulate the void space of sandstones from a gas reservoir. A number of parameters characteristic of the void space being modelled are needed to construct the simulated void network. These include a pore and throat size distribution, porosity, connectivity and degree of pore size correlation. Figure 1.1 shows the principal inputs and outputs of the model. The chapter number for a full description of each phenomenon is also given. The study involved the measurement of a large number of parameters, for clarity the theory for each is outlined individually in each chapter.

1.2 Sandstones

Sandstones are mixtures of mineral grains and rock fragments which are the result of disaggregation of rocks of all types. Rock disaggregation can be both chemical and physical, these processes operate selectively on different minerals within the original rock. Mineral and rock fragment detritus can be transported by a number of mechanisms, water and wind being the commonest transport mediums. Transport from source area to sedimentary basin can lead to differential abrasion, soft minerals decrease in size and become rounded. High silica content minerals such as quartz are resistant to transport abrasion, these hard minerals constitute a high proportion of sandstone content.

The size of detritus particles transported is a function of the transporting mediums

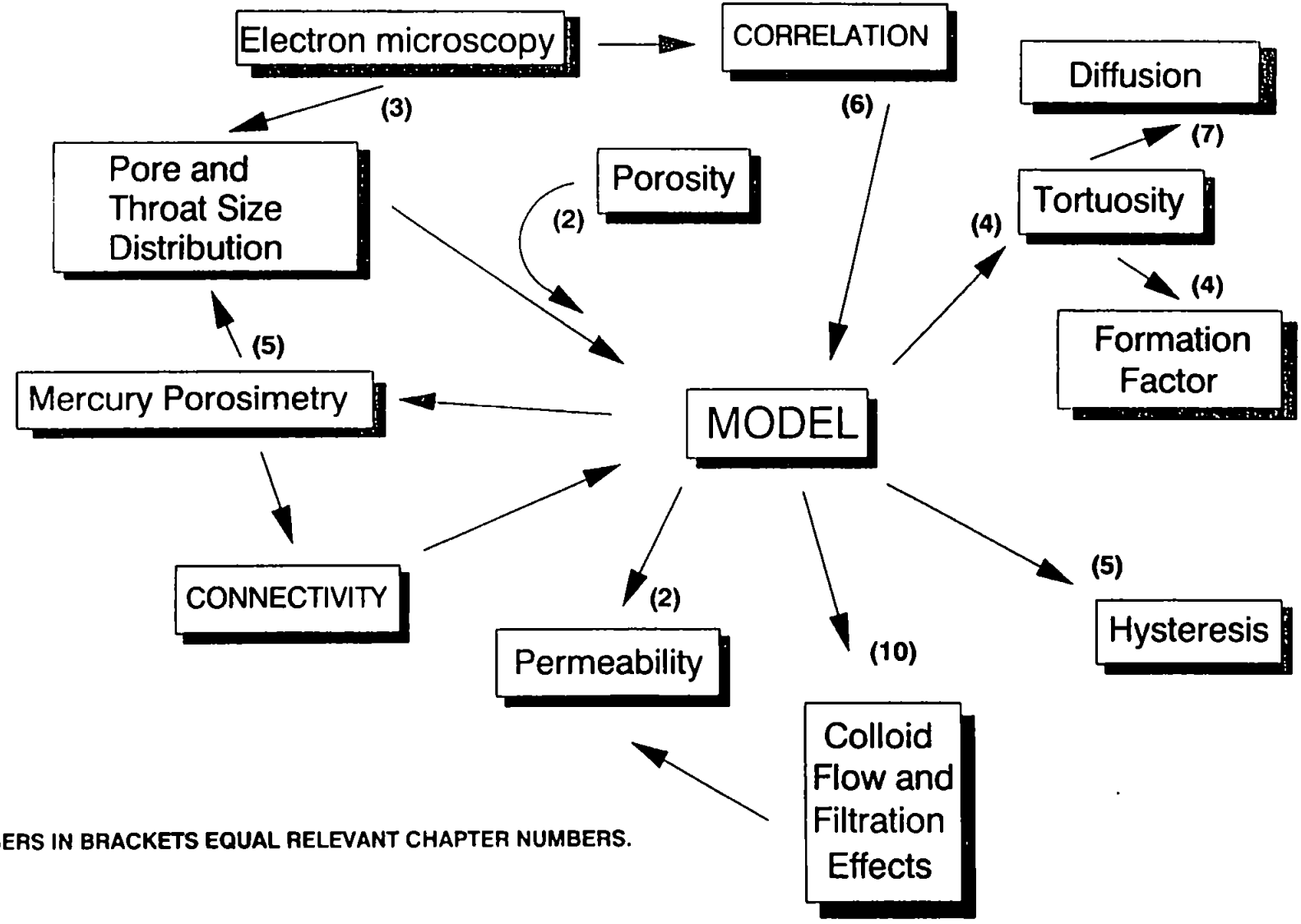

FIGURE 1.1: Scope of Pore-Cor Model

velocity. As the mediums velocity decreases smaller particles are deposited. Fluctuations in the transport mediums velocity causes differential deposition. Layers of particles of similar size are deposited at the same time, whilst different size particles may be deposited at a later date. Banding of similar size particles over a range of scales is common to all sandstone deposits. The classic sandstone depositional environment is an intertidal region, such as a beach. Within the turbulent wave region all small particles are held in suspension, as the wave velocity decreases smaller particles are deposited. Thus fine sand is deposited in the calm shallow water areas of the beach. The cycling tides mean the beach detritus is re-worked continually, but any major sea-level change can lead to the beach environment being preserved and sandstone units forming.

Sand grains usually form tangential contacts with their neighbours, thus forming an open three-dimensional void network. The void space between grains can be altered by stress, points of grain contact can experience pressure solution resulting in material redistribution and a decrease in void space. The introduction of clays and cementing materials also alters void space. Grain size, shape and surface features all effect the geometry of the void space and thus the fluid flow properties of the sandstone. The banding of similar size grains mentioned earlier leads to a variation in void sizes throughout a sandstone unit, generally the larger the grain size the larger the void size.

Hydrocarbon reservoir areas often contain large sandstone units. These sandstones can have hydrocarbon filling the void spaces or void space which is in contact with hydrocarbons. The geometry of hydrocarbon reservoir sandstone void space dictates the accessibility of any hydrocarbons present. Banded sandstones can contain areas of large voids which act as preferential flow channels during hydrocarbon extraction. Conversely a banded sandstone may contain an area of very small voids which could form a barrier to flow, hindering hydrocarbon extraction.

1.3 Test Order

This work was conducted on a set of fifteen sandstone plugs supplied by British Gas's London Research Station (LRS). These sandstones are from a gas reservoir area, the exact location is confidential. As we are only interested in the samples as examples of porous sandstone and not distinct stratigraphic units, this does not present a problem. Figure 1.2 shows the order of testing each sandstone sample. The terms basic and special core analysis are those used by core analysis laboratories which supply exploration geologists with data concerning a reservoir's hydrocarbon potential. The whole test scheme is extremely time consuming and requires samples of good condition. A model such as Pore-Cor could be used to predict elusive measurements such as diffusion coefficients or measurements unattainable in poorly consolidated samples such as permeability. A three dimensional void space model can also be applied to simulating particle invasion phenomena such as clay redistribution in reservoir rocks or general filtrate properties.

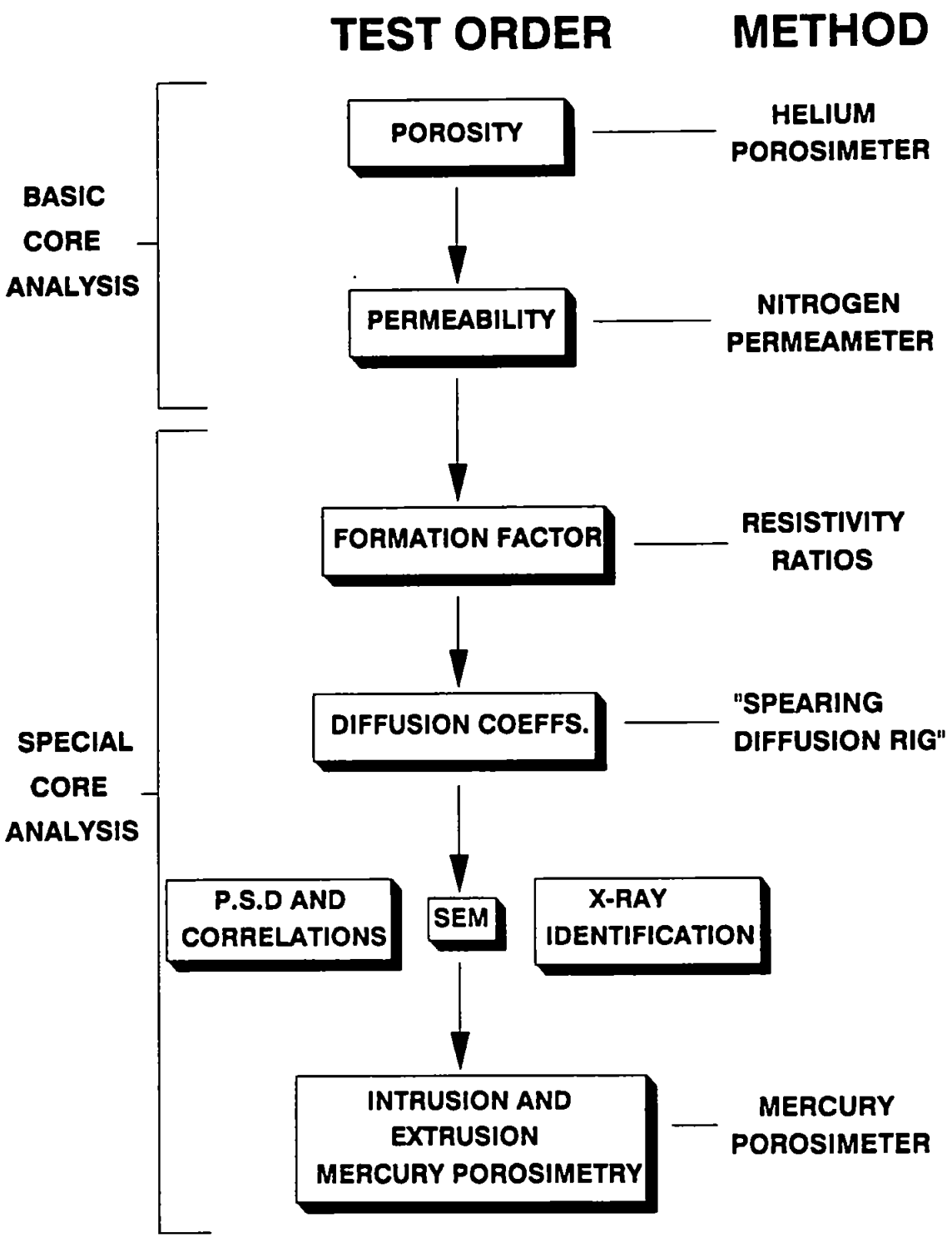

FIGURE 1.2: Sandstone Test Order.

CHAPTER 2

POROSITY AND PERMEABILITY

2.1 Porosity Measurement

The total porosity (Φ_T) of a porous solid is defined as the ratio of total pore volume to total sample volume:

$$\Phi_T = \frac{pore\ volume}{total\ volume} = \frac{total\ volume - solid\ volume}{total\ volume} \qquad (2.1)$$

The ratio of interconnected pore volume to total sample volume is termed the effective porosity. This is the pore space which contributes to fluid flow. Figure 2.1 shows the total porosity values obtained from different particle packing arrangements. Notice the large reduction in the porosity of the cubic packing system when a second smaller particle size is introduced. A sandstone contains particles of a range of different shapes and sizes so, porosities within the 10 - 25 % range, are common. One factor to be aware of when measuring porosities of randomly packed porous media is that any measured value is an average of an infinite number of composite porosities. Unlike the regular packed structures in Figure 2.1, if a random packed porous sample is cut up, different porosities will be measured for each part of the sample.

There are a number of methods used to measure total and effective porosity. These all involve the measurement of the sample volume, this is commonly done by measuring the volume of mercury the sample displaces. The mercury does not enter the pores at ambient pressures. Total porosity can be calculated from sample volume measurements before and after the destruction of the pore space by grinding. The analysis of a large number of thin sections can also supply a total porosity value.

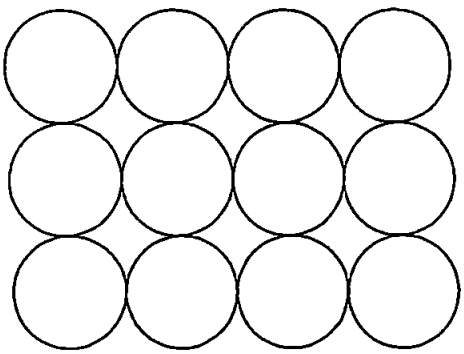

CUBIC PACKING
Φ = 47%

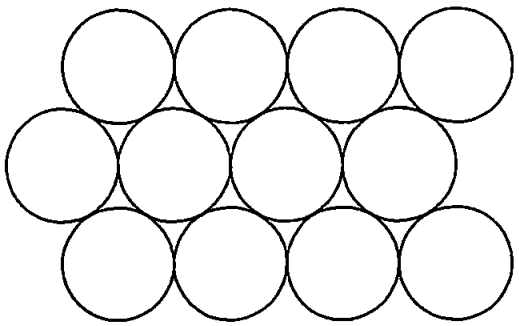

HEXAGONAL PACKING
Φ = 39%

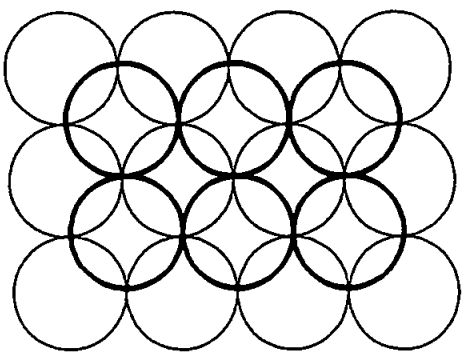

RHOMBOHEDRAL PACKING
Φ = 26%

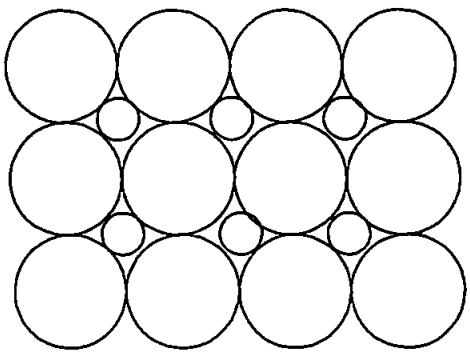

CUBIC PACKING WITH TWO DIFFERENT GRAIN SIZES
Φ = 13%

FIGURE 2.1: Particle Packing Arrangements.

Both these methods are obviously destructive and so not normally used in a core analysis regime. Filling the pore space with a gas or liquid is the most common method of measuring effective porosity. The filling of the pore space with helium is the method used by British Gas (LRS) to calculate effective porosity. A technique known as the gas expansion method utilises the ideal gas law (PV=nRT). The apparatus consists of two chambers A & B separated by a tap. At the start A is at a known pressure and B is evacuated, when the tap is opened a pressure equilibrium occurs. Knowing the volume of Chamber A and the resulting pressure, the volume of Chamber B can be calculated. By repeating the operation with the porous sample in Chamber B the solid volume can be measured. The ratio of solid volume over sample volume is the effective porosity. The gas expansion method of effective porosity measurement is prone to large experimental errors and the apparatus must be constantly recalibrated using solid blocks of known volume.

Another method of effective porosity measurement is to measure the volume of a liquid that can be forced into the pore space. A common liquid used is mercury, this non-wetting liquid is used in pore size distribution studies in a technique called mercury porosimetry (Chapter 5). During mercury porosimetry experiments the effective porosity is easily measured from the maximum volume of mercury intruded into the pore space.

2.2 Permeability Measurement

The ability of a rock to allow flow of a gas or fluid is defined as its permeability. The relationship between permeability (K), pressure gradient (dp/dx), sample cross sectional area (A) and viscosity of a flowing fluid (μ) at flow rate dv/dt is called Darcy's Law :

$$\frac{dv}{dt} = - \frac{AK}{\mu} \frac{dp}{dx} \qquad (2.2)$$

Darcy's Law assumes there is no reaction between the fluid/gas and rock and only one

component is flowing.

The unit of permeability most commonly used in the oil industry is the Darcy. A rock with a permeability of one Darcy allows a fluid of 1 cP viscosity to flow at $1cm^3/s$ when a pressure gradient of 1 atm/cm is applied across the sample with a face of $1cm^2$ surface area. Other common units for permeability are the perm and cm^2, 1 perm = $1cm^2$ = 10^8 Darcy. A perm is a very large unit. Sandstones have permeabilities within the range 10^{-7}-10^{-12} perm or 1 md - 10 Darcys (Monicard 1980). The permeability is a function of pore size and arrangement, generally the larger the pores, the larger the permeability. It is important to note that most porous media exhibit different permeabilities in different flow directions. Permeability of a sample is a combination of a large number of flow channels through the sample. Thus like porosity, the permeabilities of two halves of a sample are not the same as the whole except for extremely homogeneous samples.

2.2.1. The Klinkenburg Effect

The measurement of permeability at different pore pressures and using different fluids/gases gives different results. This is known as the Klinkenburg Effect and is caused by non-Darcy flow at the pore walls. In large diameter pores at atmospheric and high pressures, gas molecules collide with each other and rarely with the pore walls. At low pressure in small pores wall collisions are common and flow rate is increased. Thus for samples with small voids or large void samples tested at low pressure, the calculated permeability is erroneous. The Klinkenburg Equation defines the measured permeability (K_a) as the sum of the true permeability (K_∞) and a "collision/slip" term (b) :

$$K_a = K_\infty \left(1 + \frac{b}{P_m}\right) \qquad (2.3)$$

P_m is the Average Pressure

The "slip" term, is proportional to the collision diameter (λ) of the gas molecules :

$$b = \frac{4c\lambda P_m}{r} \qquad (2.4)$$

c = 1

r = pore radius

The true permeability (K_∞), effectively the liquid permeability, can be found by plotting measured permeability against the inverse of average pore pressure. The intercept at the permeability axis being the true permeability. McPhee and Arthur (1991) outline in detail the measurement of true permeability and "slip terms". Morrison and Duggan (1991) formulated equations for flow rates which would produce a maximum of a 1% non-Darcy slip flow during gas permeability measurements, within 1" diameter Morecambe Bay sandstone plugs.

British Gas (LRS) use an E.P.E. nitrogen permeameter to measure gas permeability. Samples are held in a "Hassler Sample Holder", which holds the plug tight in an inflatable sleeve. Nitrogen is flowed through the sample with the downstream side of the plug at either atmospheric or elevated pressure. Upstream and downstream pressures are measured by pressure transducers, flow rate is also measured. The whole apparatus is interfaced to a p.c for quick data acquisition. The nitrogen permeameter is run at conditions in which slip flow is negligible.

2.3 The Samples

The sandstone plugs from British Gas (LRS) were supplied with depth, porosity and gas permeability data. The fifteen sandstone plugs are grouped into three sets according to original depth. Sandstones 212A - 212E are from a depth of approximately 927m all within 25cm or each other. The quoted porosity and gas permeability being 20.4% and 2200md respectively. Sandstone plugs 250A-250E are from about 13 m deeper than the

212 sandstones. The group's porosity is 20.1% and gas permeability 685md. Plugs 490A - 490E are quoted as having porosities and permeabilities very much lower than the previous two sandstone groups, 15.1% and 83 md respectively. The 490 sandstones are from a far greater depth than the other sandstones (approx. 1017m). It was later discovered that the porosity and gas permeability data supplied by British Gas (LRS) was derived from measuring the porosity and gas permeability of one plug in close proximity to those in each of three groups, and assuming all sandstones in the group would have the same values. The assumption that sandstone plugs up to 30cm apart will have the same porosities and gas permeabilities is wrong. These properties can change greatly over a few centimetres. Table 2.1 shows porosities and gas permeabilities measured for each plug. Note that plug 212B was located only 5cm from 212A but has a gas porosity 1.7 times greater and a gas permeability 28 times larger. This highlights the importance of measuring all parameters for each individual plug and not assuming neighbouring samples are identical.

Table 2.1 does not contain porosity and gas permeability data for five of the plugs supplied. These five samples were mounted in epoxy resin, for diffusion coefficient (see Chapter 7) before the data from British Gas (LRS) was invalidated. The gas porosities and gas permeabilities of these five plugs could not be measured because they broke into irregular shapes when extracted from the resin. Samples must be cylindrical for accurate gas permeability measurements.

Comparing the porosities measured by filling pore space with either helium or mercury reveals the unsurprising conclusion that gas porosities are nearly always higher. The highest pressure applied to the invading mercury was 120atm this corresponds to a smallest invaded pore of 0.12μm diameter, calculated from the Washburn Equation, (see Chapter 5). Helium can fill pores significantly smaller that 0.12μm, thus the porosity measurement by gas is larger. Image analysis yields porosity from back scattered electron

PLUG NO.	DEPTH/m	$POROSITY_{GAS}$ /%	$POROSITY_{Hg}$ /%	$POROSITY_{IMAGE\ ANALYSIS}$ /%	PERMEABILITY/MD
212A	926.85	12.30	8.70	12.10	50.47
212B	926.90	20.80	16.80	20.60	1413.58
212C	927.00	24.40	21.50	-----	3161.56
212D	927.06	13.70	11.50	-----	335.05
212E	927.09	22.00	18.70	22.30	1427.77
250A	939.74	22.40	23.50	23.00	1208.49
250E	939.96	21.10	20.00 (21.20)	-----	693.52
490A	1017.12	13.20	10.43	-----	-----
490B	1017.19	15.70	14.10	-----	27.06
490C	1017.27	23.20	20.30	-----	-----
490D	1017.36	14.10	14.50 (13.20)	14.10	10.71
490E	1017.44	15.90	13.80	15.50	16.53

TABLE 2.1: Porosity and Permeability Data. Bracketed Values Equal Repeat Experiments.

microscopy images of the resin filled pore space. The results agree well with the gas porosity values but the technique is subjective because the operator has to decide what parts of the image are pore space and what solid, image analysis is discussed in depth in Chapter 6.

Gas permeability measurements range from 10.71md to 3161.56md. There is a general trend that high porosity samples have large permeabilities. Figure 2.2 shows a plot of log permeability against porosity for the ten samples. Regression analysis produced a positive slope with an R-squared line fit of 0.696. A better line fit is obtained of the regression analysis is restricted to plugs from the same group. For the 212 group of plugs R-squared equals 0.890 and for the 490 group of samples R-squared equals 0.622. This type of cross plot is used by hydrocarbon geologists for predicting permeability from down hole porosity measurements.

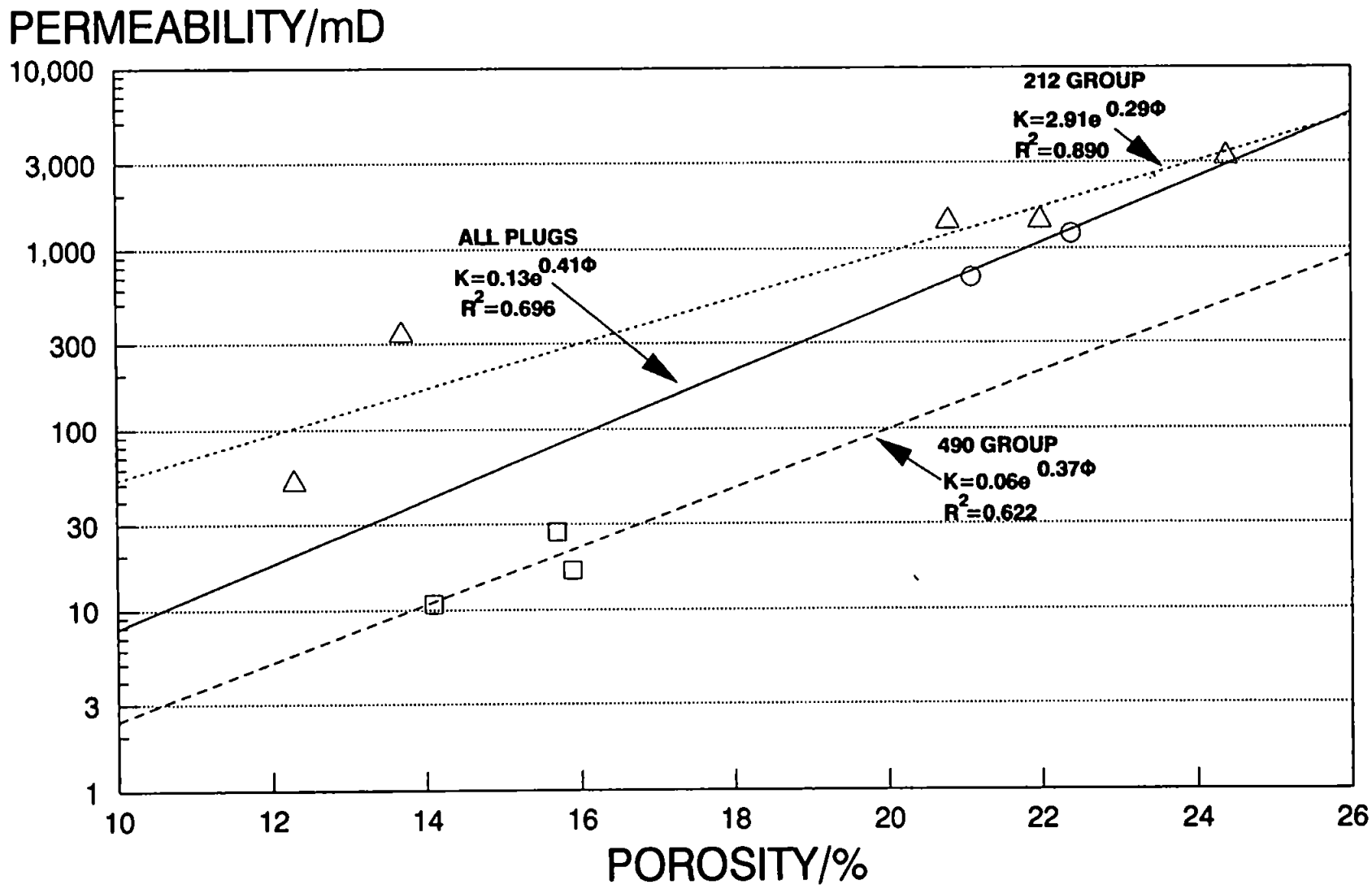

FIGURE 2.2: Permeability and Porosity Cross Plot.

CHAPTER 3

SCANNING ELECTRON MICROSCOPY

3.1 Introduction

The scanning electron microscope (S.E.M.) has become an invaluable tool in the analysis of reservoir rocks. High magnification images with a great depth of field are easily obtainable from small amounts of sample material. Appendix 1 outlines the theory and instrumentation used in S.E.M. The concepts involved in the analytical technique of energy dispersive x-ray analysis (E.D.X.) are also covered. The analysis of the reservoir sandstones was performed on a Jeol 6100 S.E.M. E.D.X analysis has been applied to selected sample areas.

A slice approximately 3mm thick is cut off the end of each sandstone plug. The slice is broken to form fresh fracture surfaces for analysis. The small "chips" of sample are mounted on metal stubs using graphite paste. The S.E.M. sample is coated in gold to a thickness of 10nm to allow electrical conduction and so avoid image distortion due to charge build up. The working voltage of the S.E.M. is 20 KV.

3.2 Results

Plate 3.1 shows a typical image obtained from a relatively clean high porosity/permeability gas reservoir sandstone. This image is of plug 250B, grain size ranges from about 300μm downwards. Grain contacts show some deformation and grain surfaces have a sparse covering of fine material. Plug 250B contains the occasional authigenic quartz overgrowth, Plate 3.2. These euhedral growths are common at grain contacts and a pressure solution origin has been proposed (Pittman 1972). The action of heat and pressure can cause the break up of other mineral grains. Plate 3.3 shows a broken-up or diagenetized potassium feldspar grain. The mineral was identified by its x-ray spectra, Figure 3.1. Energy dispersive x-ray analysis is semi-quantitative and so the

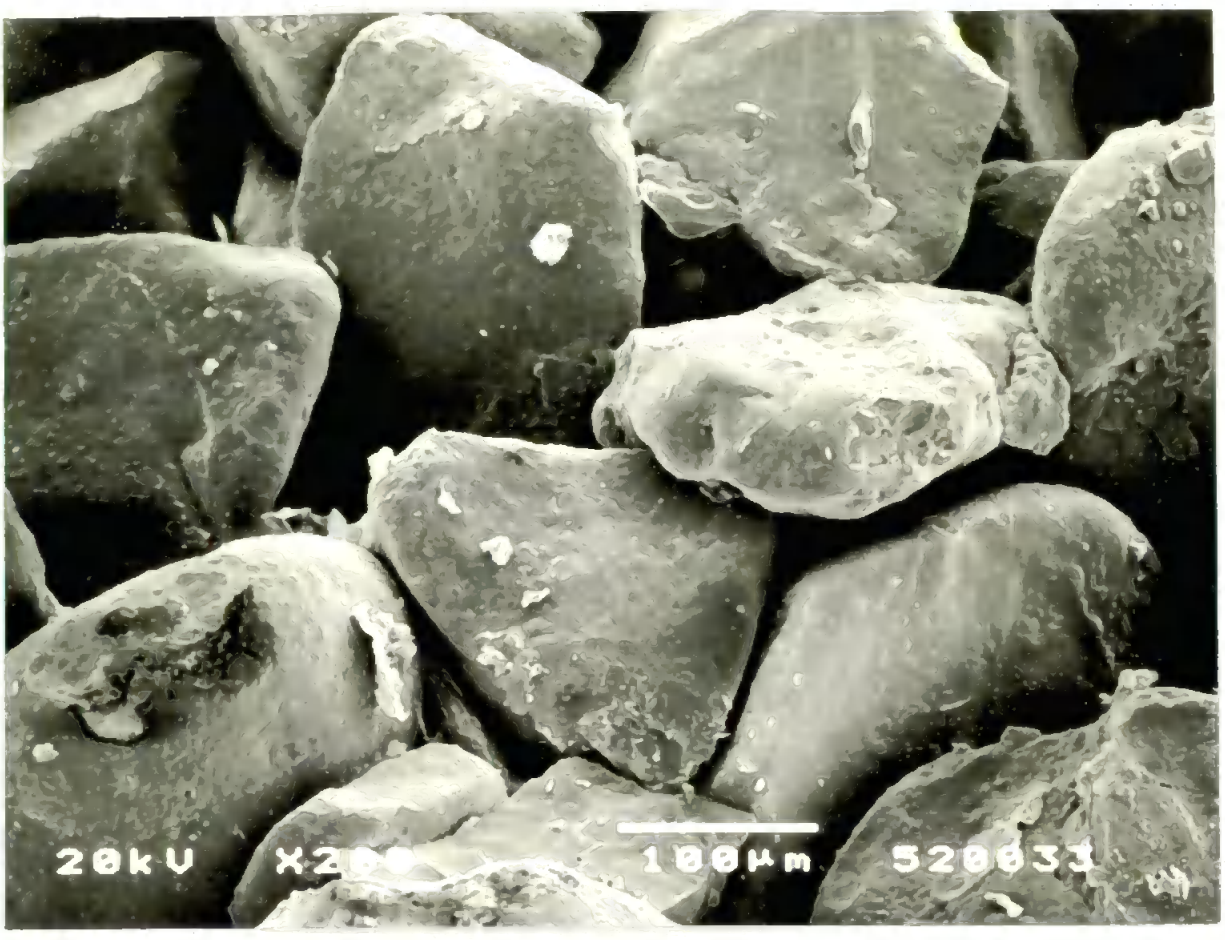

PLATE 3.1: SEM Photomicrograph of Plug 250B.

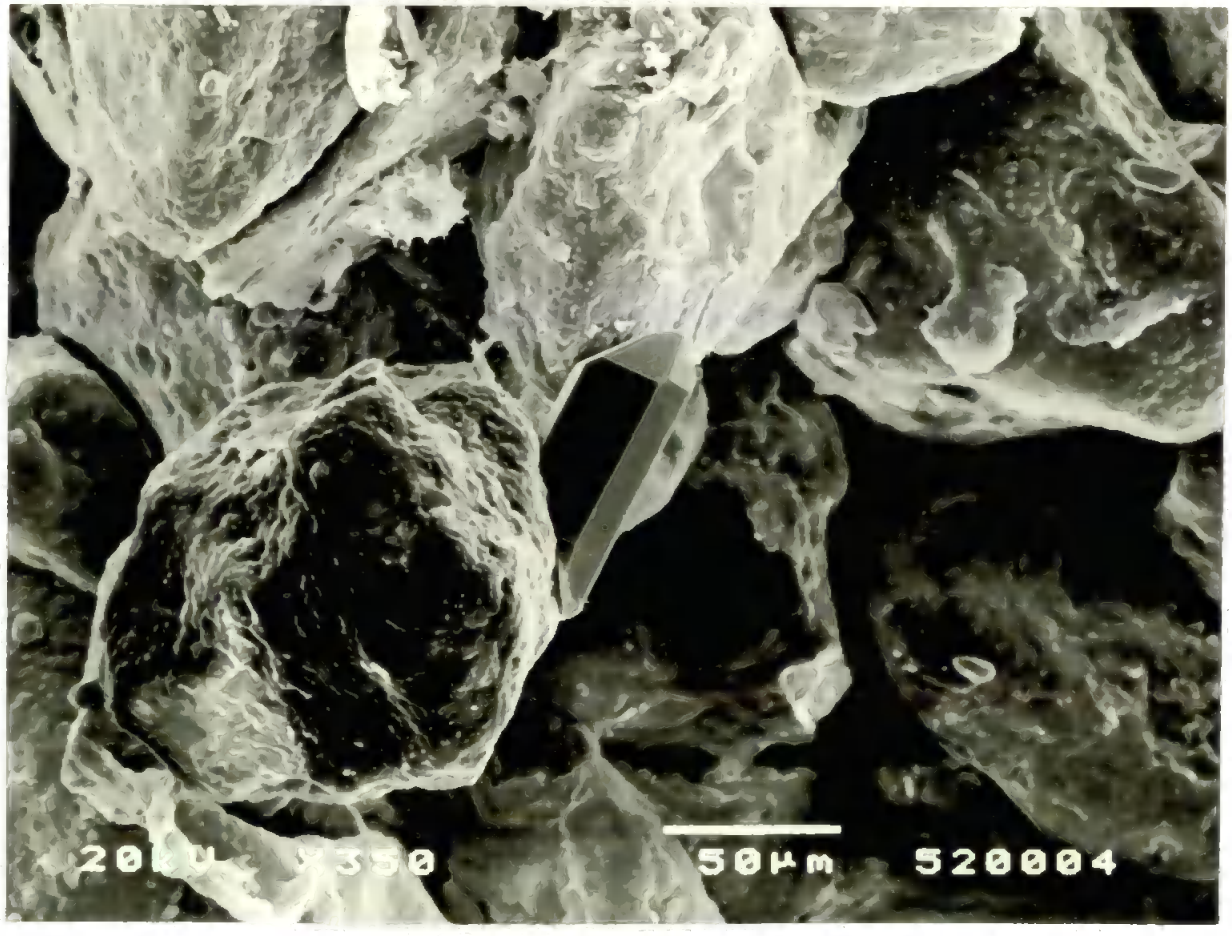

PLATE 3.2: SEM Photomicrograph of Plug 250B, Showing Quartz Overgrowth.

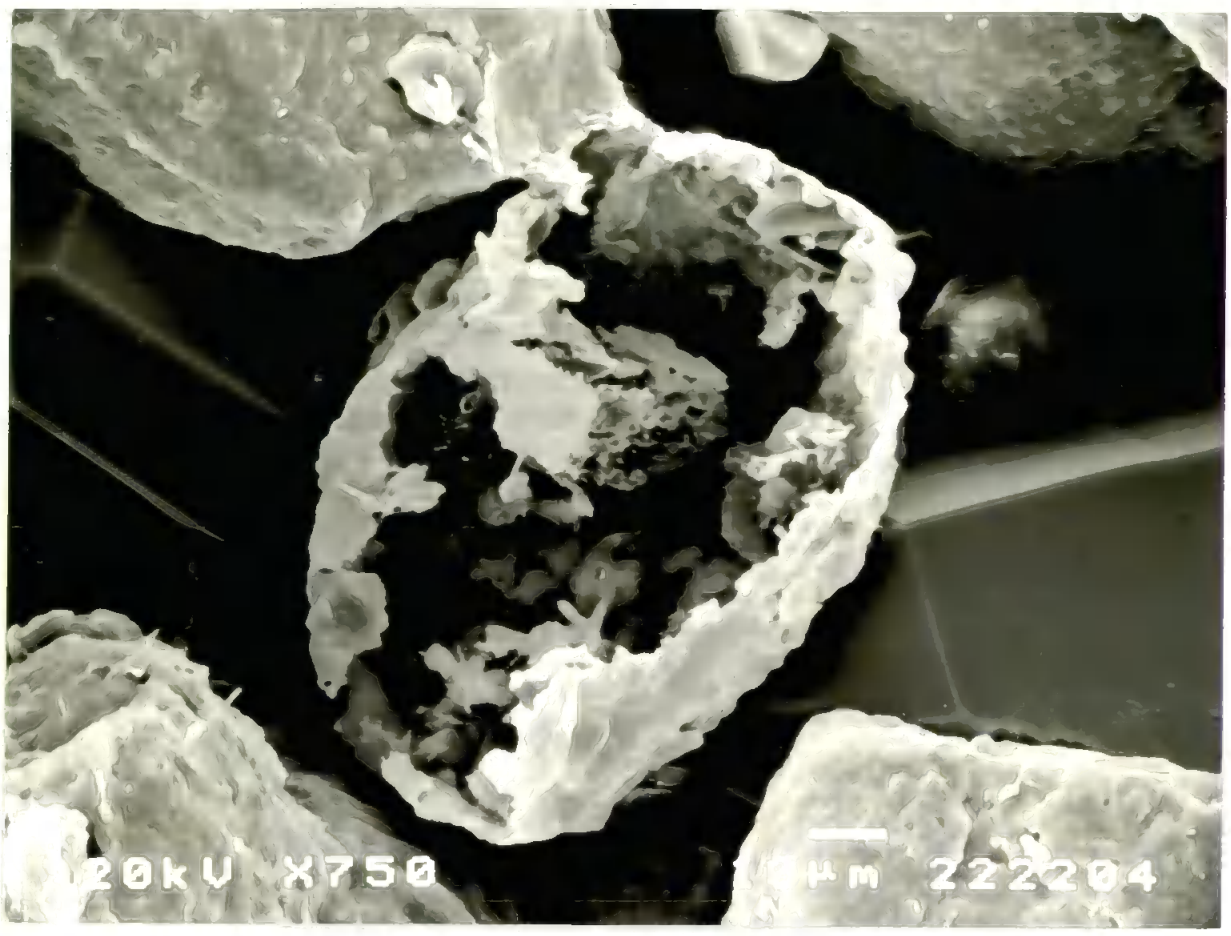

PLATE 3.3: SEM Photomicrograph of Diagenetized Potassium Feldspar Grain, Plug 250B.

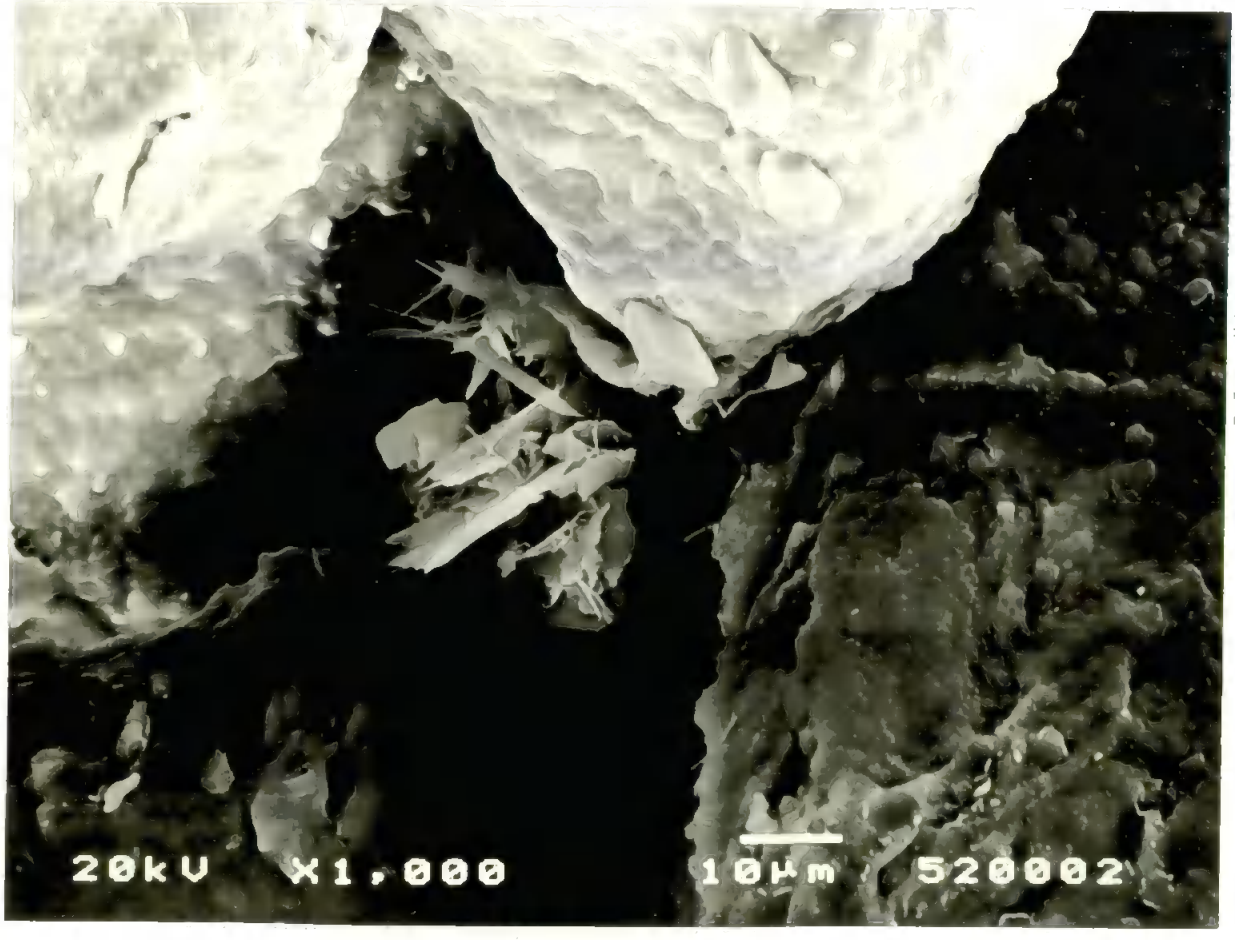

PLATE 3.4: SEM Photomicrograph Authigenic Clay Within a Pore, Plug 250B.

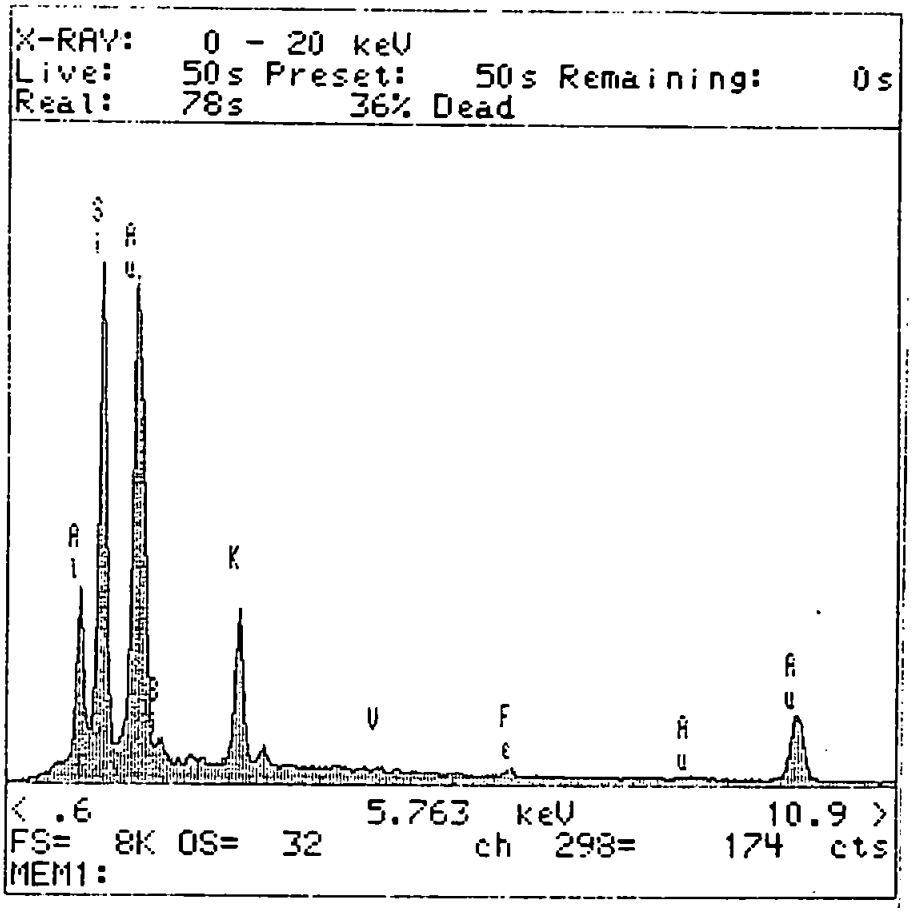

FIGURE 3.1: X-ray Spectra for Potassium Feldspar Grain in Plate 3.3.

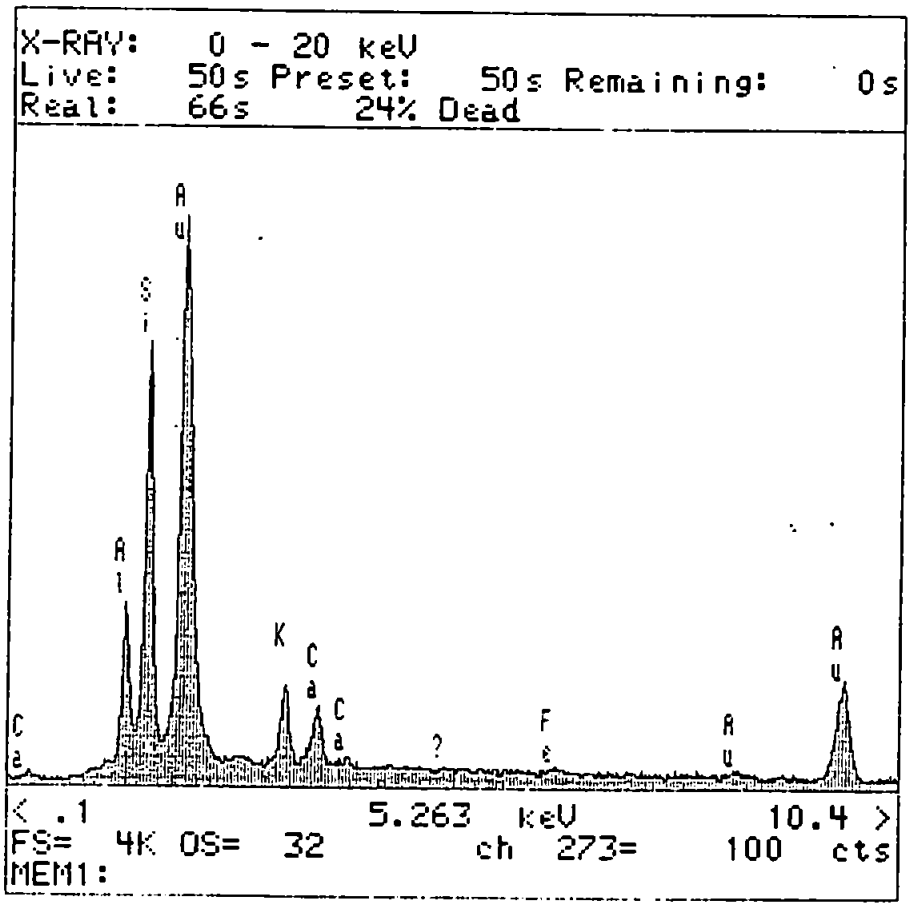

FIGURE 3.2: X-ray Spectra for Illite/Smectite Clay in Plate 3.4.

ratios of peak heights in Figure 3.1 are related to the elemental ratios in the mineral formula. The spectra in Figure 3.1 has aluminium and potassium peaks of equal height and a silicon peak approximately three times in height. This corresponds with the composition of potassium feldspar Al K Si_3O_8 (The large gold peak in Figure 3.1 is due to the gold coating on the sample). Feldspars form clay minerals upon diagenesis. The fine grained material inside the feldspar grain in Plate 3.3 may be authigenic clay materials. Note the quartz overgrowth in the bottom right of Plate 3.3 has partially enveloped the detrital grain below it. A cluster of authigenic clay is shown in Plate 3.4. This clay has a crystal structure common to illite and obviously formed after deposition because it fills the pore space and has a delicate crystal morphology (Wilson & Pittman 1977). Figure 3.2 shows the x-ray spectra for this clay. A clay of illite/smectite mixed layer clay mineralogy can be deduced from this spectra. This clay cluster is an isolated feature and the occurrence of clays within sample 250B is rare. The surface of grains within sample 250B are sparsely covered in fine grained material. Plate 3.5 shows a high magnification image of one of these fine particles. This beautiful mineral contains silicon, aluminium and calcium but remains unidentifiable. The morphology and distribution of minerals found in sample 250B is similar to that found in all samples from groups 212 and 250. The exception being sample 212A which has an area of partially cemented grains.

S.E.M. analysis of sample 490A showed a very different mineral assemblage. The grains of this sample are coated in clay particles, Plate 3.6. Two types of clays are identifiable, kaolinite in its characteristic stacked plates formation and grain coating Illite. Figure 3.3 shows the x-ray spectra from one of the kaolinite stacks, the dominant elements are aluminium and silicon. Kaolinite particles usually have a pseudohexagonal morphology. The examples in Plate 3.6 have broken edges probably caused by sample cleaning. Illite clays coat the grains in a more random fashion. A close inspection of the illite particles shows the presence of "hairy" illite, Plate 3.7. These laths are a common morphological

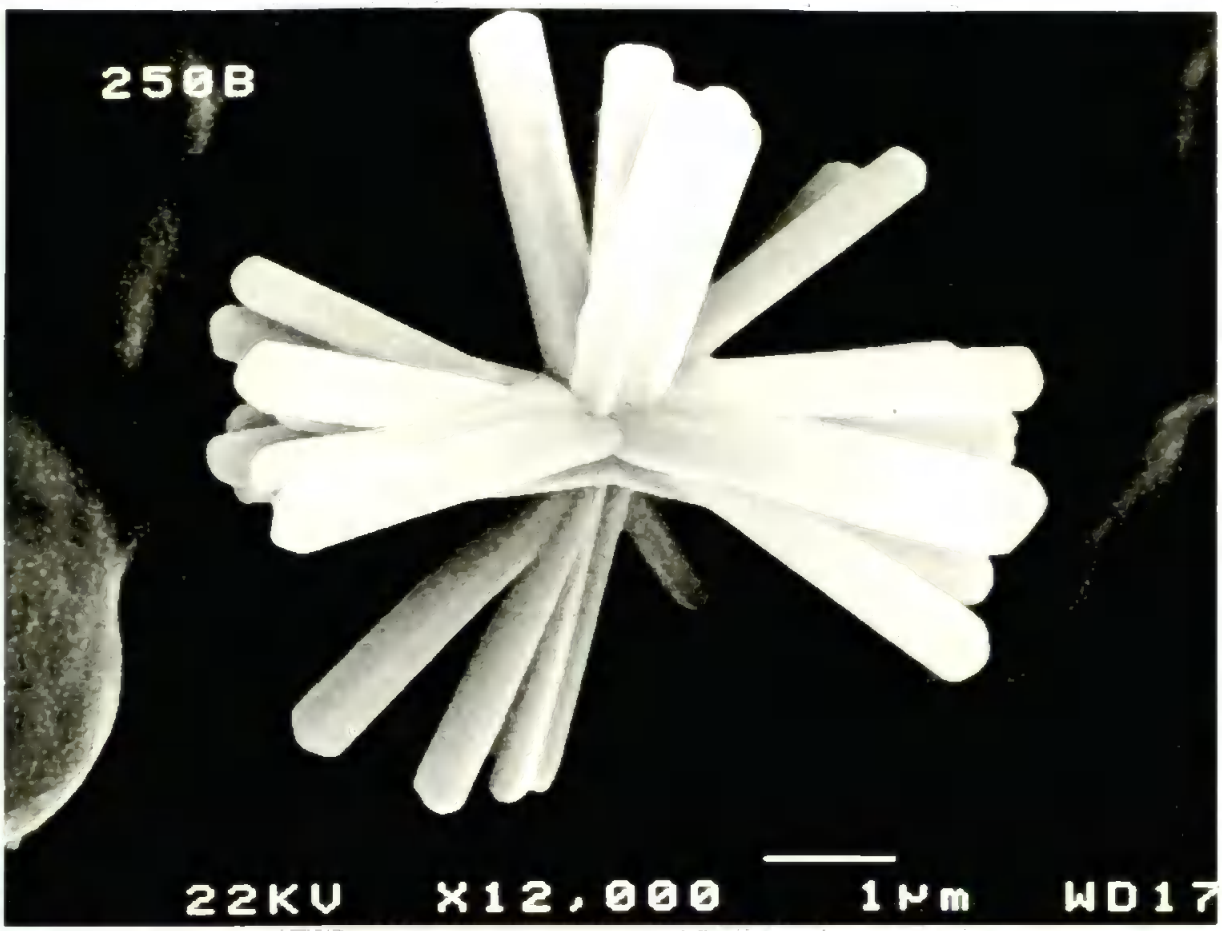

PLATE 3.5: SEM Photomicrograph of an Unidentified Fine Particle, Plug 250B.

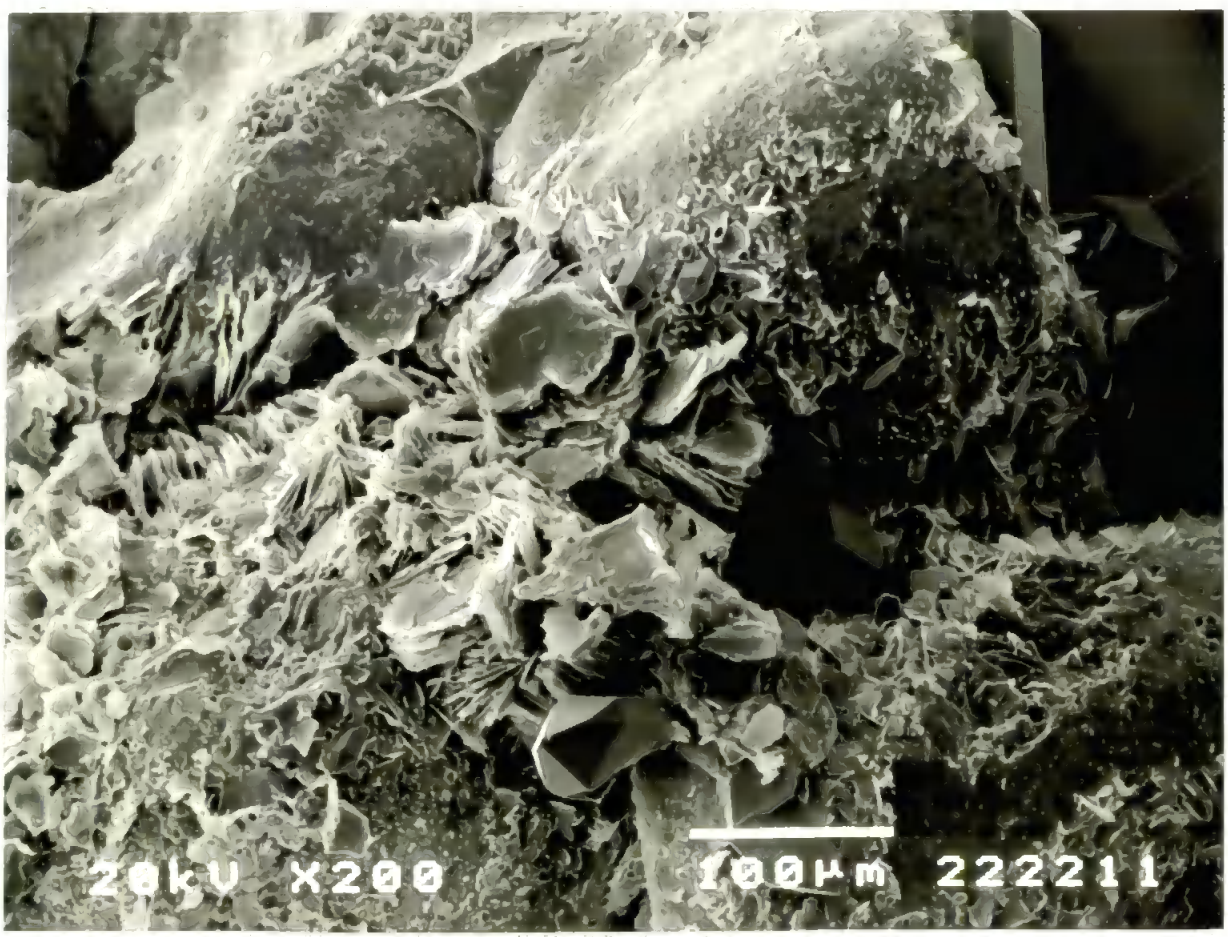

PLATE 3.6: SEM Photomicrograph of Clay Particles Within Plug 490A.

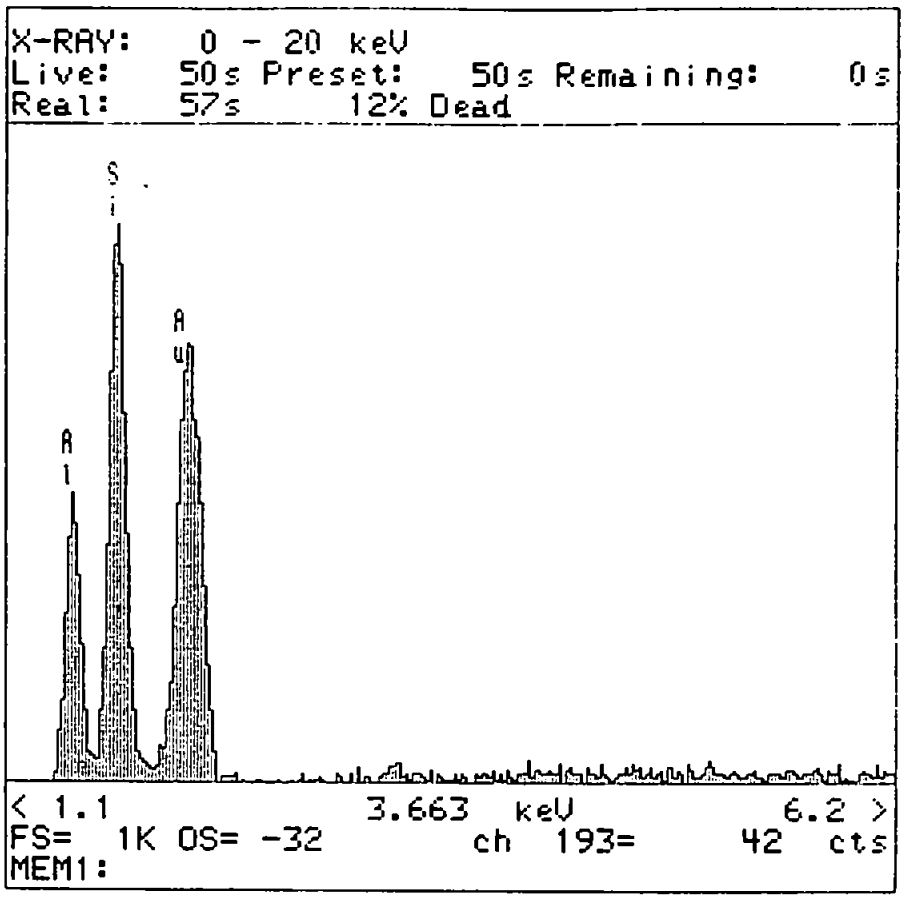

FIGURE 3.3: X-ray Spectra for Kaolinite Clay in Plate 3.6.

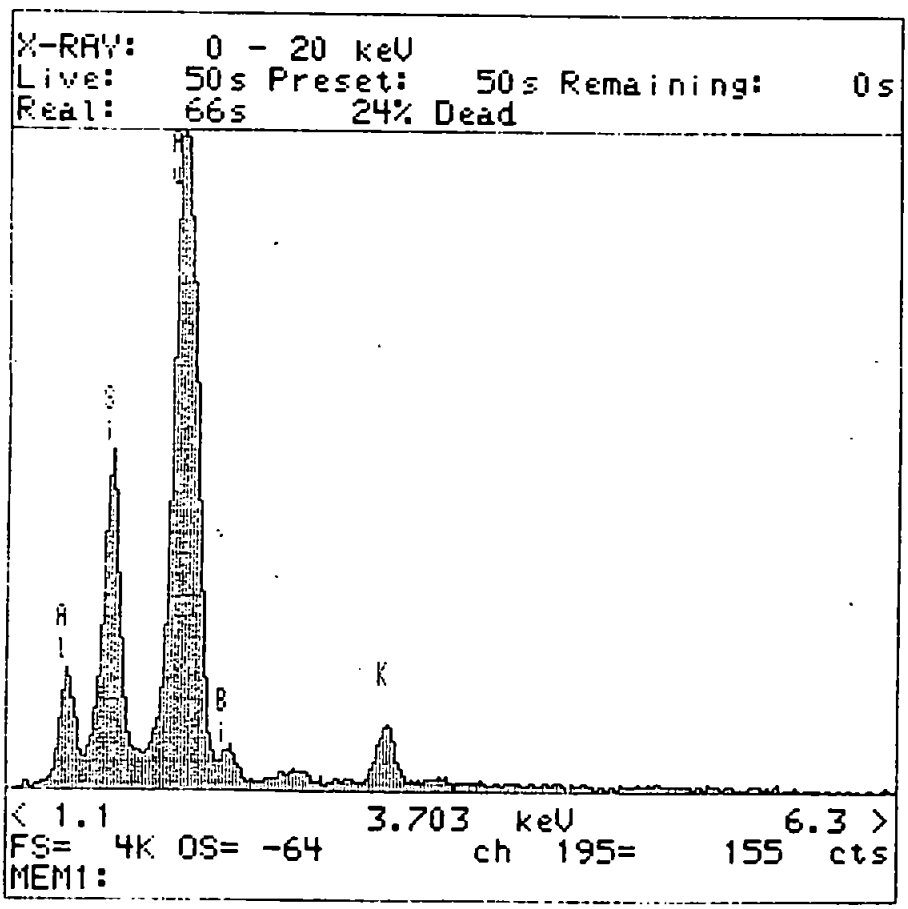

FIGURE 3.4: X-ray Spectra for Illite Clay in Plate 3.7.

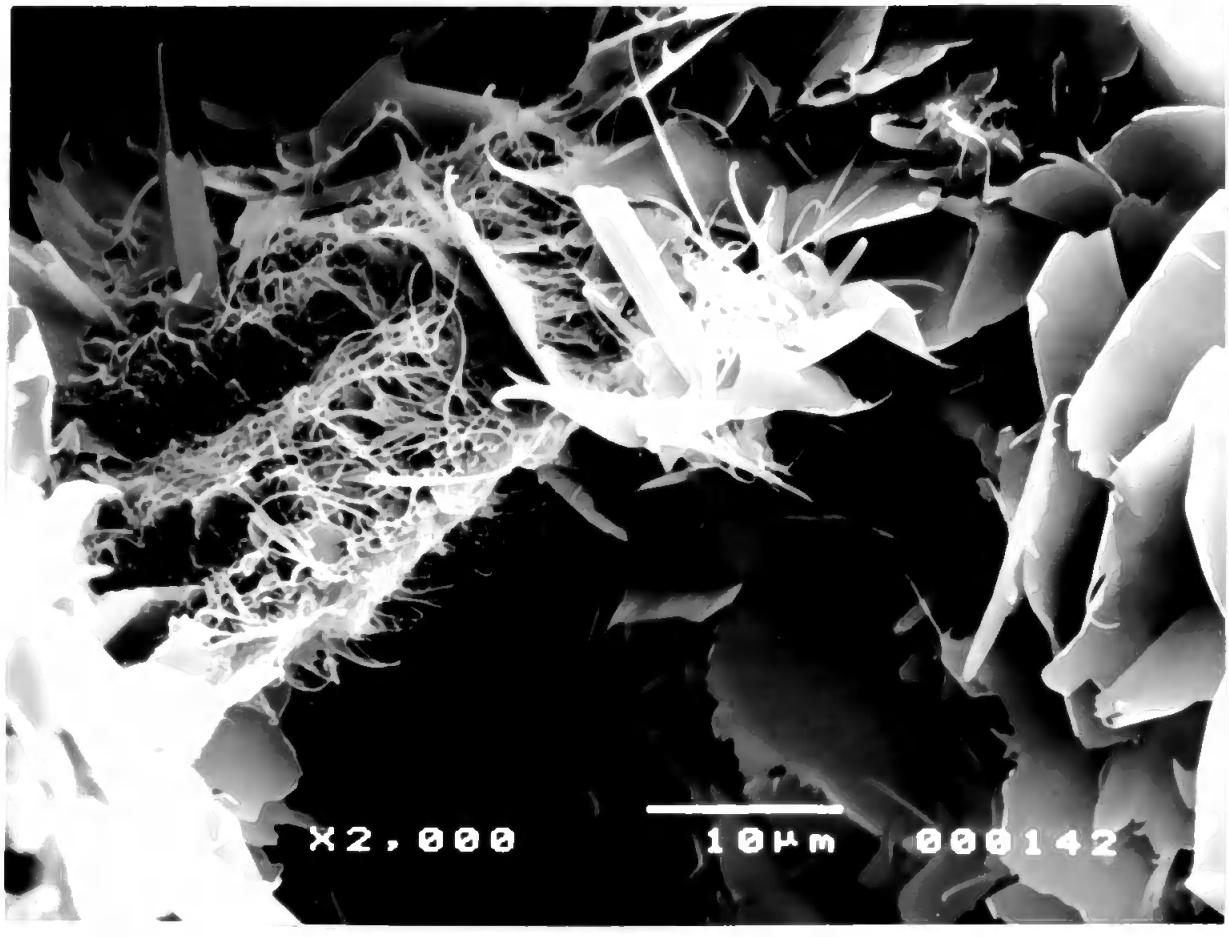

PLATE 3.7: SEM Photomicrograph Showing Hairy and Platey Illite Clay, Plug 490A.

form of illite (Guven et al 1980). The x-ray spectra for the illite indicated aluminium, silicon and potassium as major elements, Figure 3.4.

Nearly all the sandstone samples have been analyzed by S.E.M. and it is possible to group the samples according to their mineralogy:

SAMPLE NO.	MINERALOGY
212A	PREDOMINANTLY QUARTZ, AREA OF CEMENTED GRAINS, CLAY FREE
212B-212E	PREDOMINANTLY QUARTZ, ALMOST CLAY FREE.
250A-250E	PREDOMINANTLY QUARTZ, ALMOST CLAY FREE.
490A-490E	QUARTZ WITH ILLITE AND KAOLINITE CLAY COATING

TABLE 3.1: Mineral Characteristics Of Each Sample Group

There is a correlation between clay content and porosity and permeability data, Figure 3.5. Clay particles block pore space reducing porosity and restricting flow causing low permeabilities. The presence of clay minerals within gas reservoir sandstones has been cited as causing problems during hydrocarbon extraction from these areas (Macchi et al 1990).

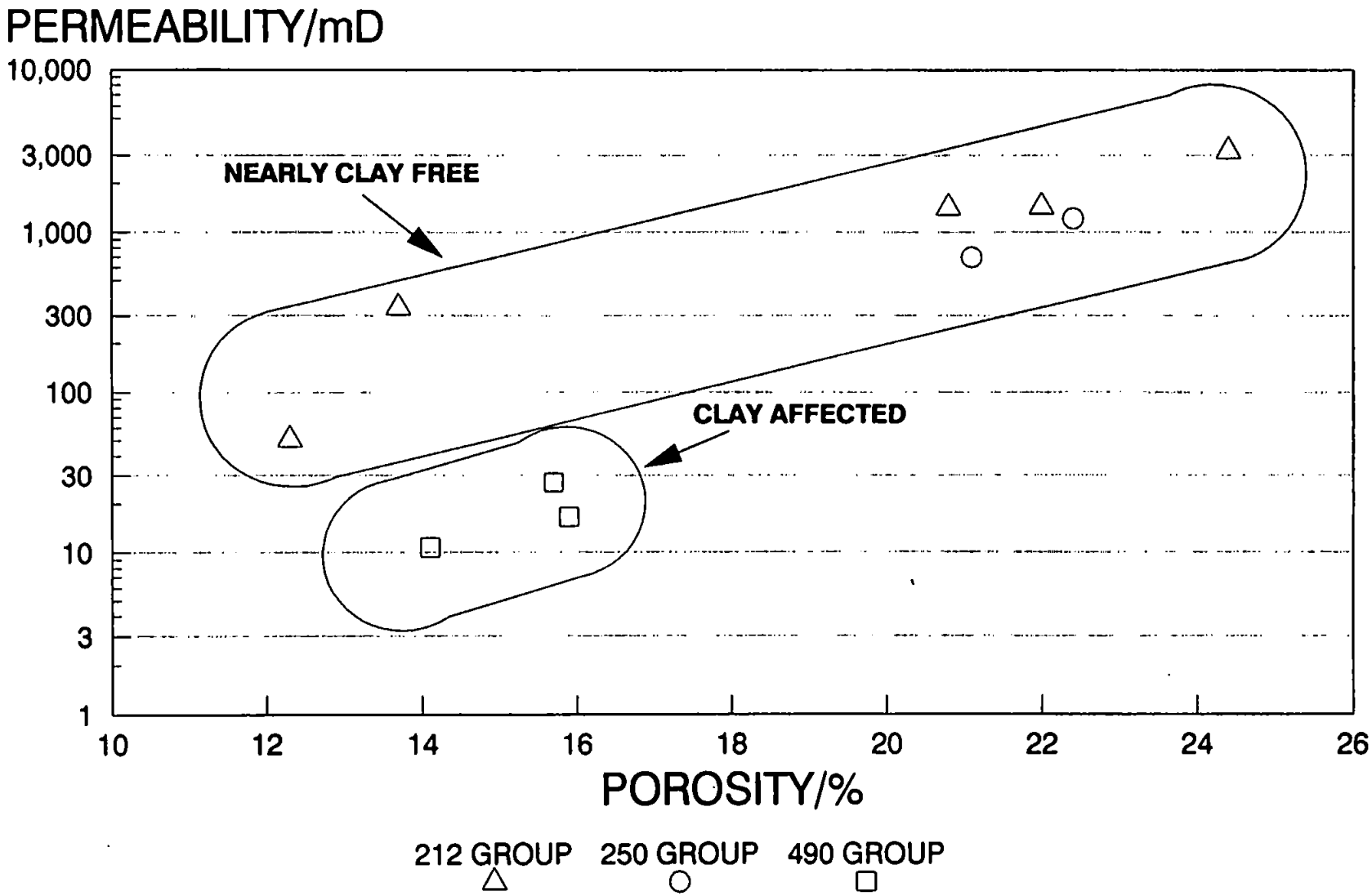

FIGURE 3.5: Permeability and Porosity Cross Plot with Mineralogy Grouping.

CHAPTER 4

FORMATION FACTOR

4.1 Introduction

The measurement of the electrical resistivity of a brine filled rock plug is a common test within a special core analysis regime. The ratio of electrical resistivity of the brine filled pore space (R_0) and the electrical resistivity of the pure brine of the same dimensions as the sample (R_w) is approximately constant. This relationship was first noted by Archie (1942) and he named the constant the "formation factor" (F):

$$F = \frac{R_o}{R_w} \tag{4.1}$$

Archie also found a correlation between the formation factor and the sample porosity (Φ):

$$F = \frac{a}{\Phi^m} \tag{4.2}$$

The constant, a, has value of approximately 1, m is called the cementation exponent. A graph of the log formation factor against log porosity will yield a line with gradient m and porosity-axis intercept a. Theoretically the line should intercept the porosity axis at 100%, since a porosity of 100% means that no solid is present and thus the formation factor is unity. In reality this intercept is not always at 100%. The gradient m, the cementation exponent, is related to the consolidation character of a group of samples. A cementation exponent of 2.2 indicates highly cemented grains and a value of 1.3 an unconsolidated sample, Figure 4.1. The cementation exponent is strictly related to formation factor and not measurable by any other method. The grouping of the exponent values in Figure 4.1 is obtained from correlating visual appearance of many samples with

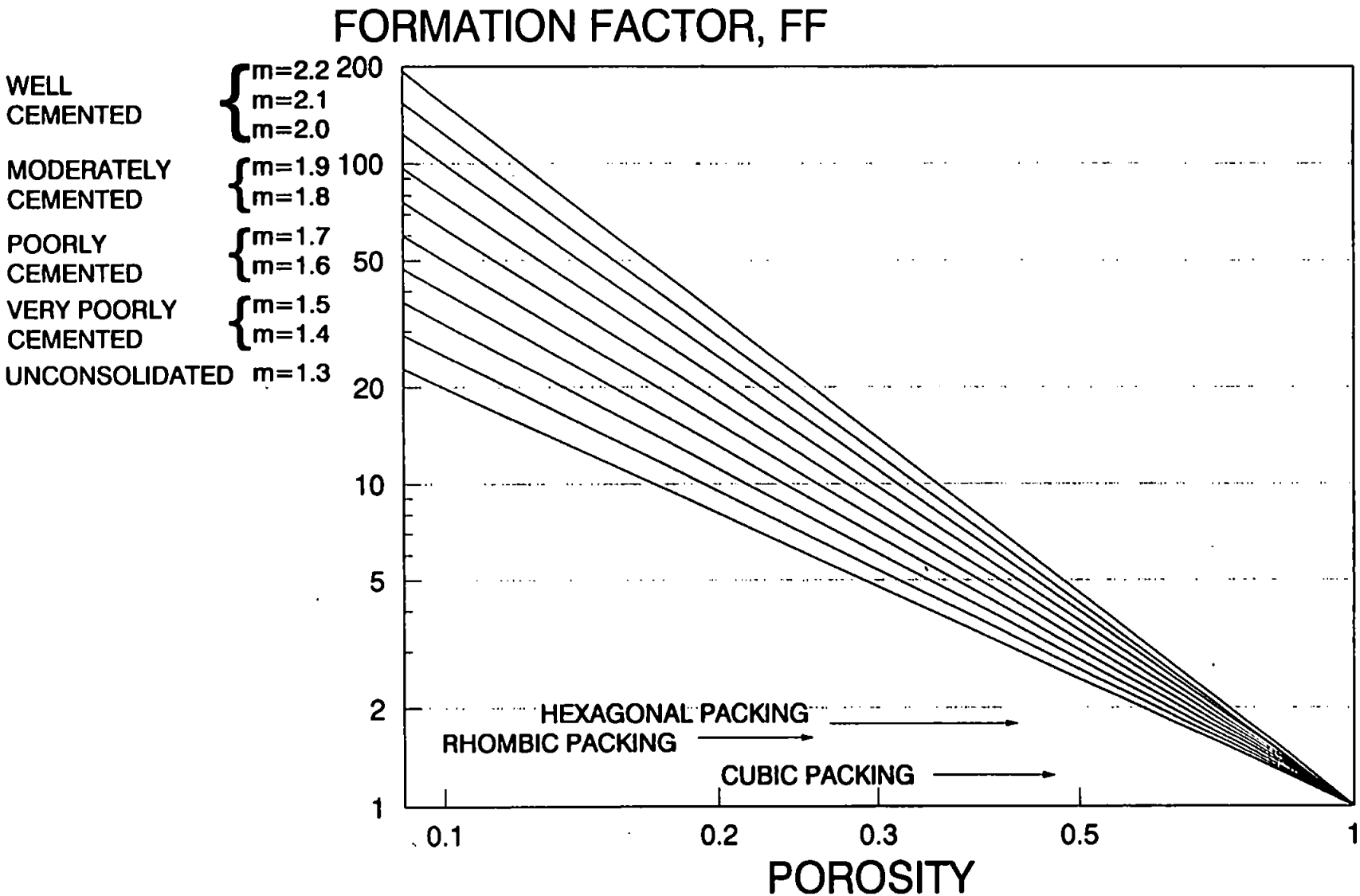

FIGURE 4.1: Formation Factor Against Porosity Showing Cementation Exponant Range.

measured cementation exponent values. Note the points obtained from hexagonal, rhombic and cubic packed structures are all below those obtained for real reservoir samples.

Archie (1942) formulated an expression for the resistivity of a partially saturated sample.

$$\frac{R_t}{R_0} = \frac{1}{S_w^{\,n}} \tag{4.3}$$

R_t is the resistivity of the partially brine filled sample at saturation S_w. R_0 is the resistivity of the sample at 100% saturation, n is called the saturation exponent. The saturation exponent is approximately 2 and Archer and Wall (1986) quoted a value of 2.27 for a suite of Berea sandstones. Equation 4.3 is extensively used during petroleum and gas exploration to estimate the amount of non-conducting oil/gas within the pore space.

All the above equations rely on the assumption that the rock matrix is non-conducting, ie the only conducting medium is the brine within the pore space. For sandstones containing no clays or metallic minerals (Pyrite etc) the above assumption holds. For shaly sandstones with high clay content the measured resistivity of the brine filled sample is lowered by the presence of conductive water/ion layers on the clay surfaces. Thus sandstones with high clay content will have lower formation factors, which may lead to a low estimate of cementation characteristics, or an underestimate of the water saturation within a potential reservoir if Equation 4.3 is employed, (Keelan and McGinley 1979).

Within sandstones the amounts of metallic minerals such as pyrite found is low, the most common conducting minerals are clays. The conductivity of the clays depends on the brine salinity and the clay cation exchange capacity (C.E.C). A high C.E.C. means many ions are present at the clay surface, producing a high conductivity and a low formation factor.

Waxman and Smits (1968) proposed a method for assessing the contribution of clay conductance to the measured formation factor. By measuring core conductivity at different brine strengths, a plot of core conductivity (C_s) against brine conductivity (C_w) yields an x-axis intercept equal to the clay conductivity C_e effect, see Figure 4.2. The Waxman-Smits approach was used by Keelan and McGinley (1979) to obtain formation factors independent of clay conductivity (F^*).

4.2 Tortuosity

The tortuosity (T) of a porous sample is the ratio of the distance through the pore network (L_e) and the length of the sample (L), see Figure 4.3

$$T = \frac{L_e}{L} \tag{4.4}$$

Obviously tortuosity has a lower limit of one ie a straight path through the sample. The movement of a diffusing gas molecule or ion within the pore space will be tortuous and it has long been recognised that a study of these processes can elucidate the tortuosity. Cornell and Katz (1953) related tortuosity to formation factor and porosity :

$$T^2 = F\Phi \tag{4.5}$$

The equation was also used by Chen (1973) in a study of sandstone tortuosities measured by both resistivity and gas diffusion methods. Referring to Figure 4.3, the porosity (Φ) is defined as the fractional void of the sample. If A is the cross-sectional area of the sample and X is the fraction of A made up of void space, such that *XA* is the sum of areas of all surface pores, then the total pore volume is $XA.L_e$. As the volume of the sample of length L normal to the plane of the cross-section is A.L, porosity is :

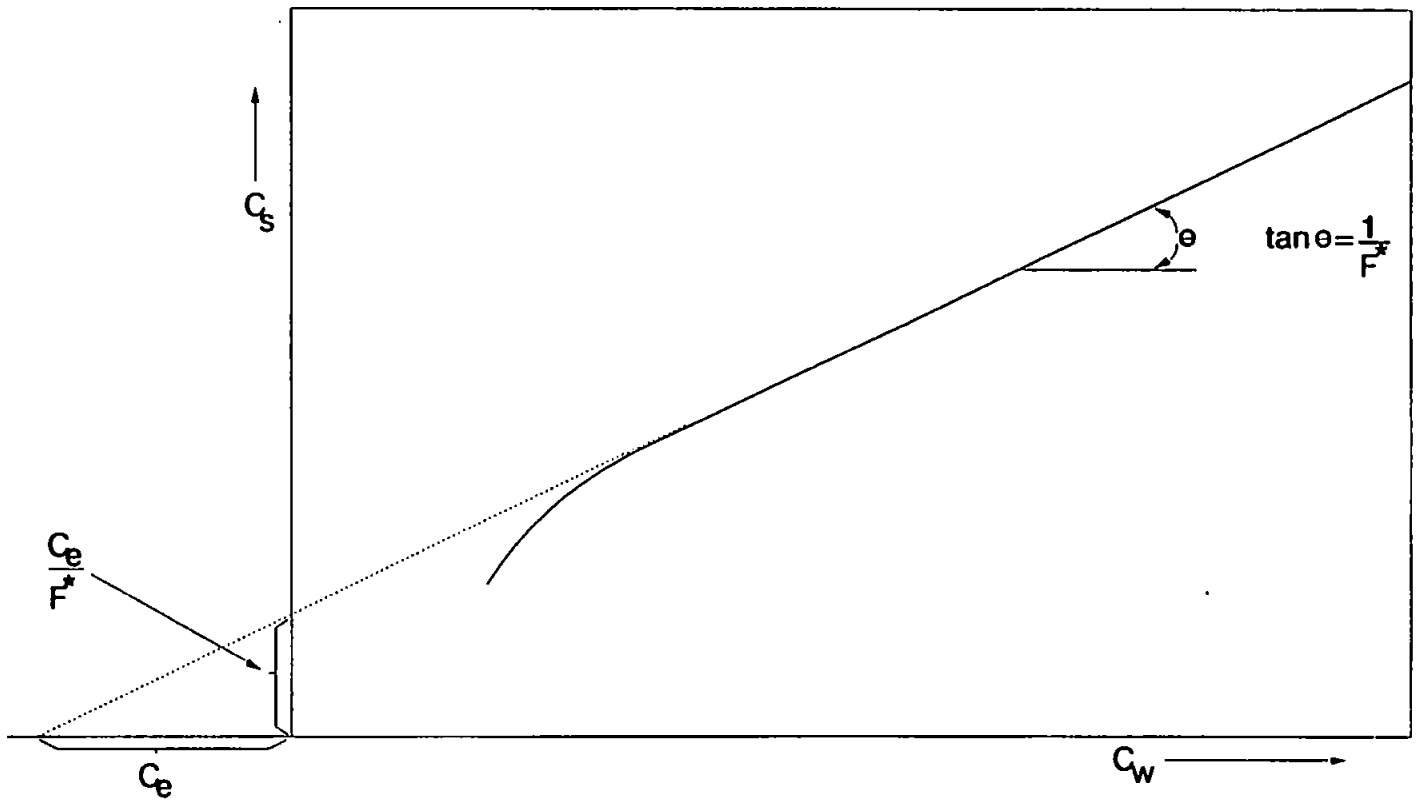

FIGURE 4.2: Core Conductivity Against Brine Conductivity (After Waxman and Smits, 1968).

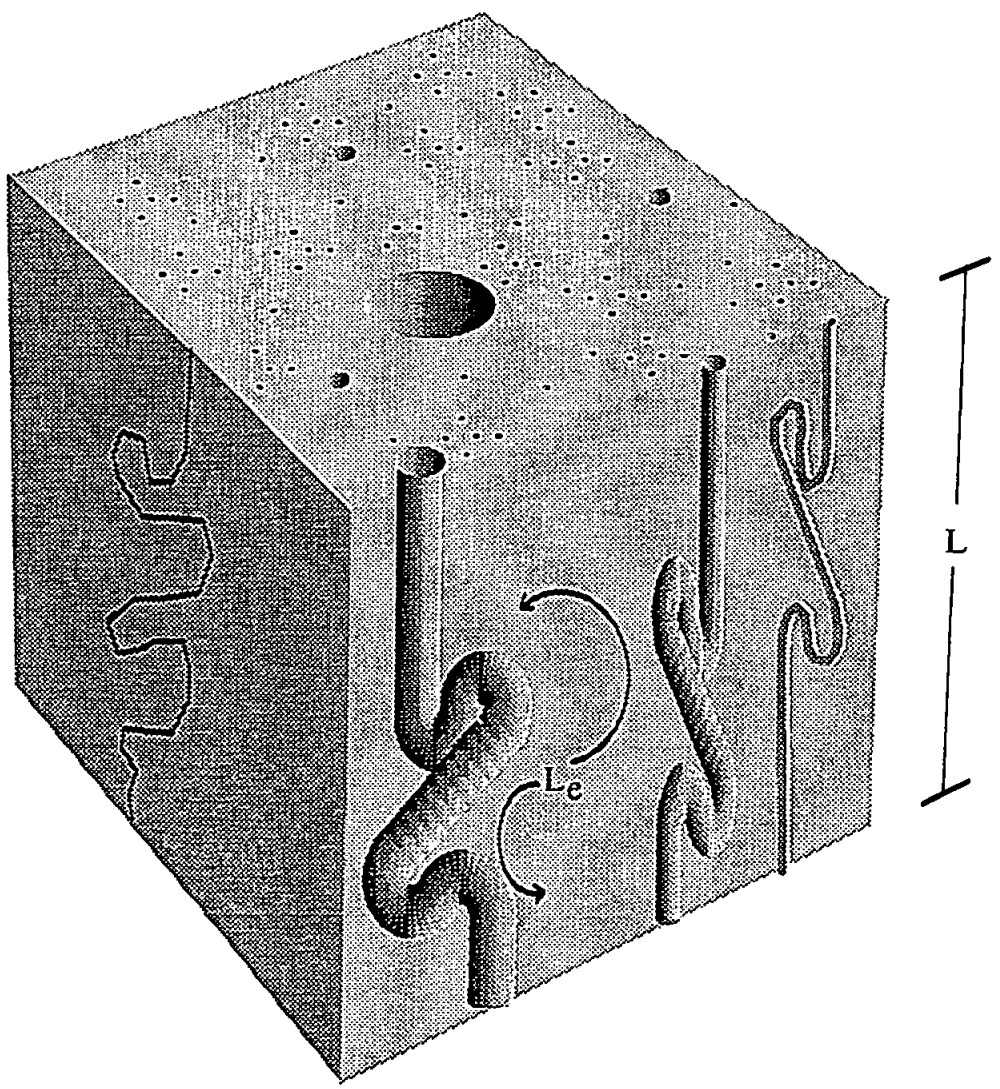

FIGURE 4.3: A Schematic Porous Medium Showing a Tortuous Capillary containing Brine of resistivity R_w. Cross Sectional Area=A.

$$\Phi = \frac{XAL_e}{AL} = \frac{XL_e}{L} \tag{4.6}$$

The resistance of the brine filled pore space is :

$$R_1 = \frac{R_w L_e}{XA} \tag{4.7}$$

The resistance of the brine of the same dimensions as the sample :

$$R_2 = \frac{R_w L}{A} \tag{4.8}$$

Therefore:

$$F = \frac{R_1}{R_2} = \frac{R_w L_e}{XA} \cdot \frac{A}{R_w L} = \frac{L_e}{XL} \tag{4.9}$$

Using Equation 4.6 to eliminate X:

$$F = (\frac{L_e}{L})^2 \frac{1}{\Phi} \tag{4.10}$$

Equation 4.10 is equivalent to Equation 4.5 and Equation 4.5 has also been substantiated by Tye (1982). Wyllie and Rose (1950) proposed a different equation relating to tortuosity and formation factor :

$$T = (F\Phi)^2 \tag{4.11}$$

Here they define $T = (L_e/L)^2$ and during the derivation they use the product ΦA as the cross-sectional void area, which is incorrect. The porosity Φ is an average for the whole sample and not the open void area in a plane normal to the measurement direction, as is required in the derivation. The correct term is XA as used in our earlier derivation of

Equation 4.10. Suman and Ruth (1993) noted this discrepancy and introduced areosity (ξ) as the open void area associated with local flow direction. They stated that :

$$T = F\xi \tag{4.12}$$

The concept of areosity is valid but practically it is impossible to measure its value.

4.3 Formation Factor And Tortuosity Measurement

4.3.1. Method

The dry sandstone plug of known porosity and bulk volume is weighed and saturated with brine solution using the vacuum saturation technique. This involves placing the plug in a desiccator with a side-arm connection to a vacuum pump. The plug is evacuated for two hours. The vacuum is then broken by running in the brine via a funnel with a tap attached to the top of the desiccator. If the saturated plug is weighed and the brine density is known the percentage saturation can be calculated :

$$\%SATURATION = \frac{SATURATED\ MASS - DRY\ MASS}{BULK\ VOLUME\ .\ \Phi\ .\ BRINE\ DENSITY} X\ 100 \tag{4.13}$$

Any plug with a percentage saturation not in the upper 90% region will have an abnormally high resistivity and thus large errors in formation factor measurement will be incurred.

The saturated samples are left for 24 hours for ionic equilibrium to establish between rock and brine (ie 24 hours). The brine solution is prepared to match the real down hole water from the area in which the samples were obtained (Appendix 2). After the equilibration period, excess brine is removed from the surface of the sample and it is carefully loaded into a rig similar to that shown schematically in Figure 4.4. The resistivity is measured.

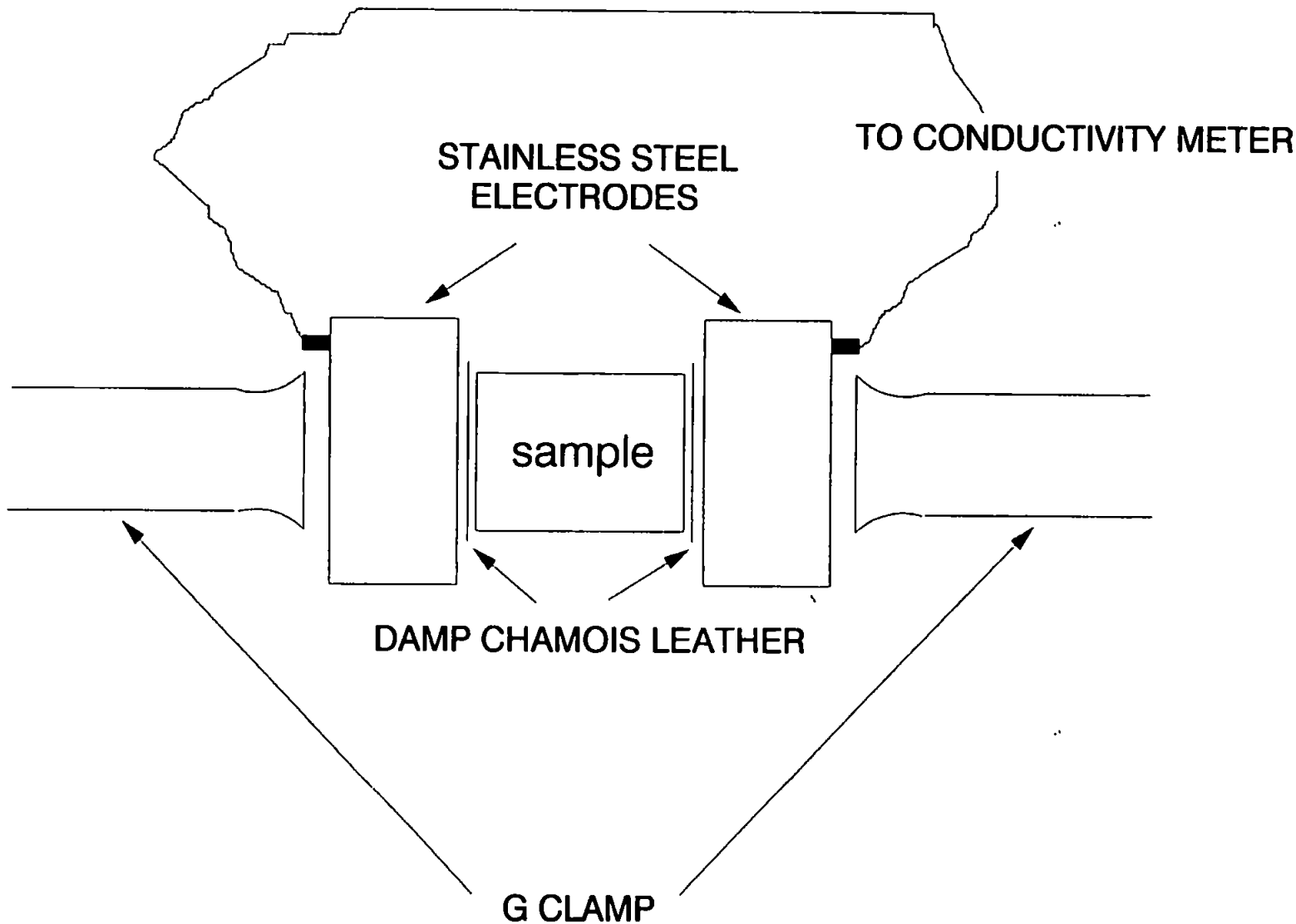

FIGURE 4.4: Apparatus Used to Measure Formation Factor.

Measurements are repeated twice daily until the calculated formation factor is consistent to within 2-5% over at least three measurements. The measurement of the formation factor is a very "user unfriendly" test.

An excess brine film on the surface of the sample causes surface conductants and a lowering of the tortuosity. The excess brine must be removed by dabbing on a tissue, which can cause errors if brine is sucked out of the sample. A full explanation of errors in resistivity measurements are to be found in Worthington (1975).

4.3.2. Results

The formation factors and tortuosities of thirteen of the reservoir sandstones have been measured, Table 4.1. Samples 81 through to 108 are reservoir sandstones used in a formation damage study, see Chapter 10. The formation factors quoted in Table 4.1 are all calculated ignoring the effect of clay conductivity. To apply the Waxman-Smits correction, the cation exchange capacity of each sample must be measured, which is very time consuming. The most clay affected sample 490E has a high formation factor. A trend of low permeability, low porosity samples having high formation factors is observed. Therefore the suppression of formation factor by clay conductivity is not acute.

Equation 4.2 has been applied to each group of sandstones from the same bedding horizon within the reservoir. All samples with the prefix 212 are from the same lithological horizon so plotting log formation factor against log porosity yield a gradient equal to the cementation exponent, Figure 4.5. Different cementation exponents are obtained if the regression line is forced through the unity porosity point ie a = 1 in Equation 4.2. A cementation exponent of 1.765 for forced regression and 1.741 for free regression (a = 1.05) was measured. Using Figure 4.1 these cementation exponent values correspond to a poorly to moderately cemented group of sandstones. Figure 4.6 shows the cementation exponents obtained when the extremes of the measured formation factor range are used.

PLUG GROUP	PLUG NO.	PERM/mD	POROSITY/%	FORMATION FACTOR	TORTUOSITY	TORTUOSITY RANGE/+_ %	CEMENTATION EXPONENT RANGE
212	212A	50.47	12.30	42.05	2.27	+2.6/-2.3	1.733 - 1.795
	212B	1413.58	20.80	14.76	1.75	+3.8/-3.7	
	212C	3161.56	24.40	13.71	1.83	+4.8/-5.2	
	212D	335.05	13.70	32.86	2.12	+3.8/-3.7	
	212E	1427.77	22.00	13.92	1.75	+2.5/-2.6	
250	250A	1208.49	22.40	16.21	1.91	+2.3/-2.8	1.830 - 1.878
	250E	693.52	21.10	17.74	1.94	+1.0/-1.5	
490	490E	16.53	15.90	51.12	2.85	+4.9/-5.1	N/A
80's	81	421.47	14.00	28.96	2.01	+6.0/-6.3	1.656 - 1.762
	82	34.47	11.10	43.11	2.19	+4.6/-5.0	
90's	98	213.62	16.20	20.00	1.80	+1.7/-1.7	N/A
100's	107	218.14	12.1	49.04	2.44	+3.2/-3.6	1.787 - 1.864
	108	29.17	9.50	72.12	2.62	+4.9/-5.2	

TABLE 4.1: Measured Data For Each Sandstone Plug. Formation Factors Equal Mean of Measured Range.

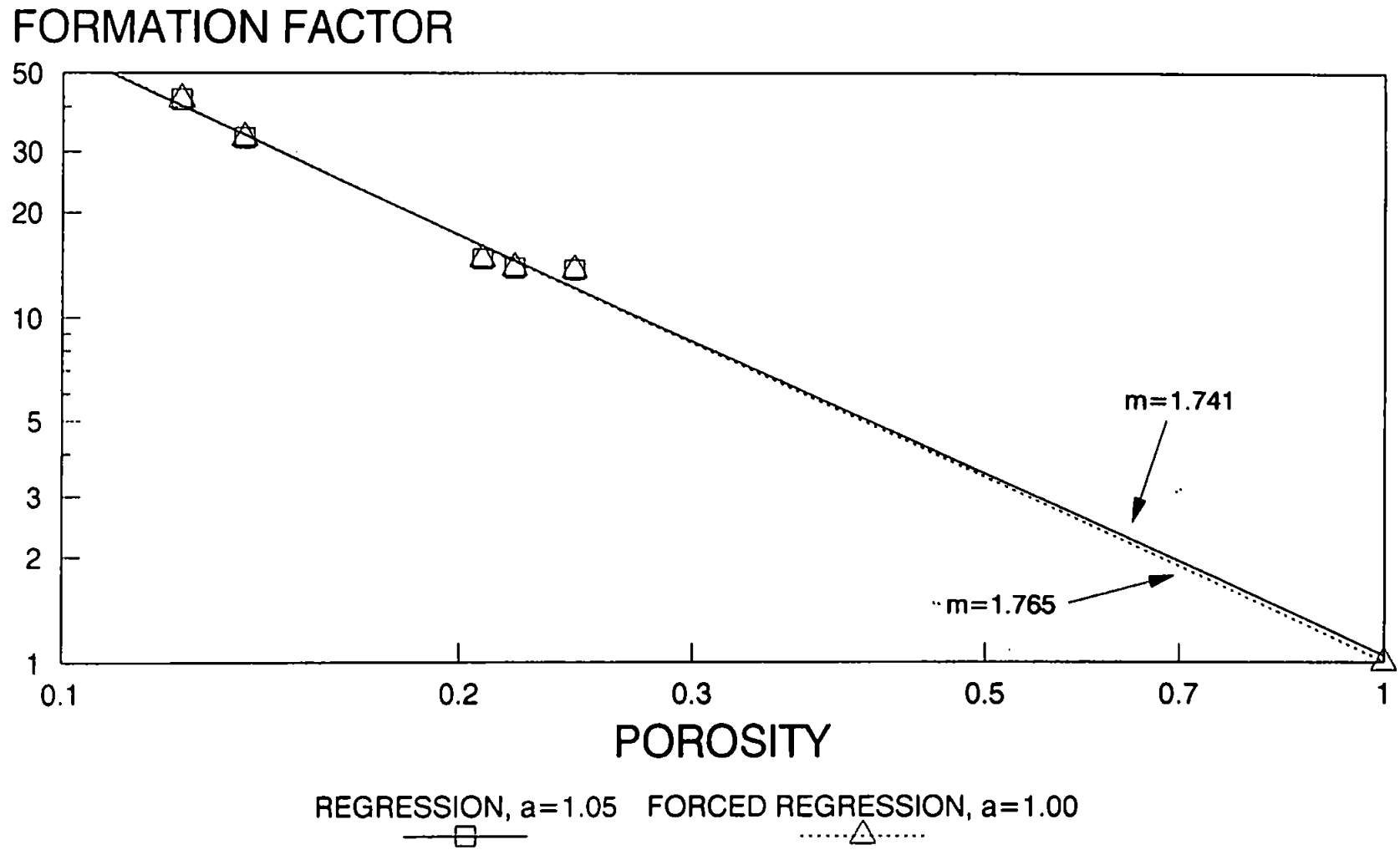

FIGURE 4.5: Mean Formation Factor Against Porosity For Samples in Group 212.

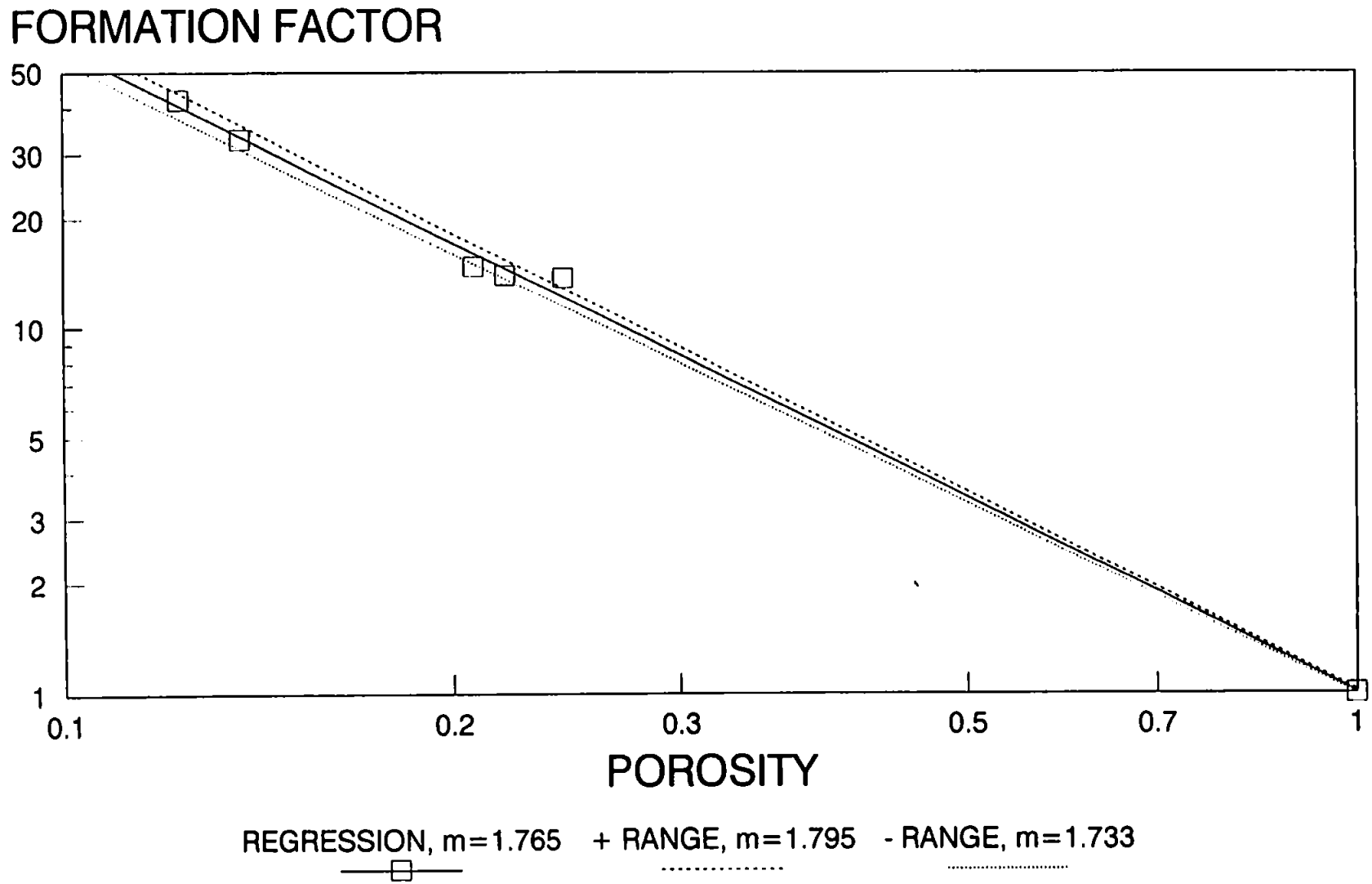

FIGURE 4.6: Mean and Extremes of Formation Factor Range Against Porosity for Samples in Group 212. Mean Cementation Exponent equals 1.765.

The resulting cementation exponents are still within the poorly to moderately cemented grouping. This result matches physical appearance because all samples within Group 212 are quite friable.

Group 250 consists of only two samples. To obtain a regression line the unity porosity value is used as a third point, Figure 4.7. The cementation exponent for group 250 is 1.855, indicating moderately cemented sandstones. The 80's group of sandstones had a cementation exponent of 1.712 (poorly cemented), Figure 4.8. The 100's group of samples were moderately cemented with an exponent of 1.828, Figure 4.9. Samples 490E and 98 are single samples. The formation factors of similar samples have not been measured, and therefore their cementation exponents cannot be calculated.

Tortuosities are calculated using Equation 4.5. Measured tortuosities roughly correlate with permeability, in that high permeability samples have a low tortuosity, see Table 4.1.

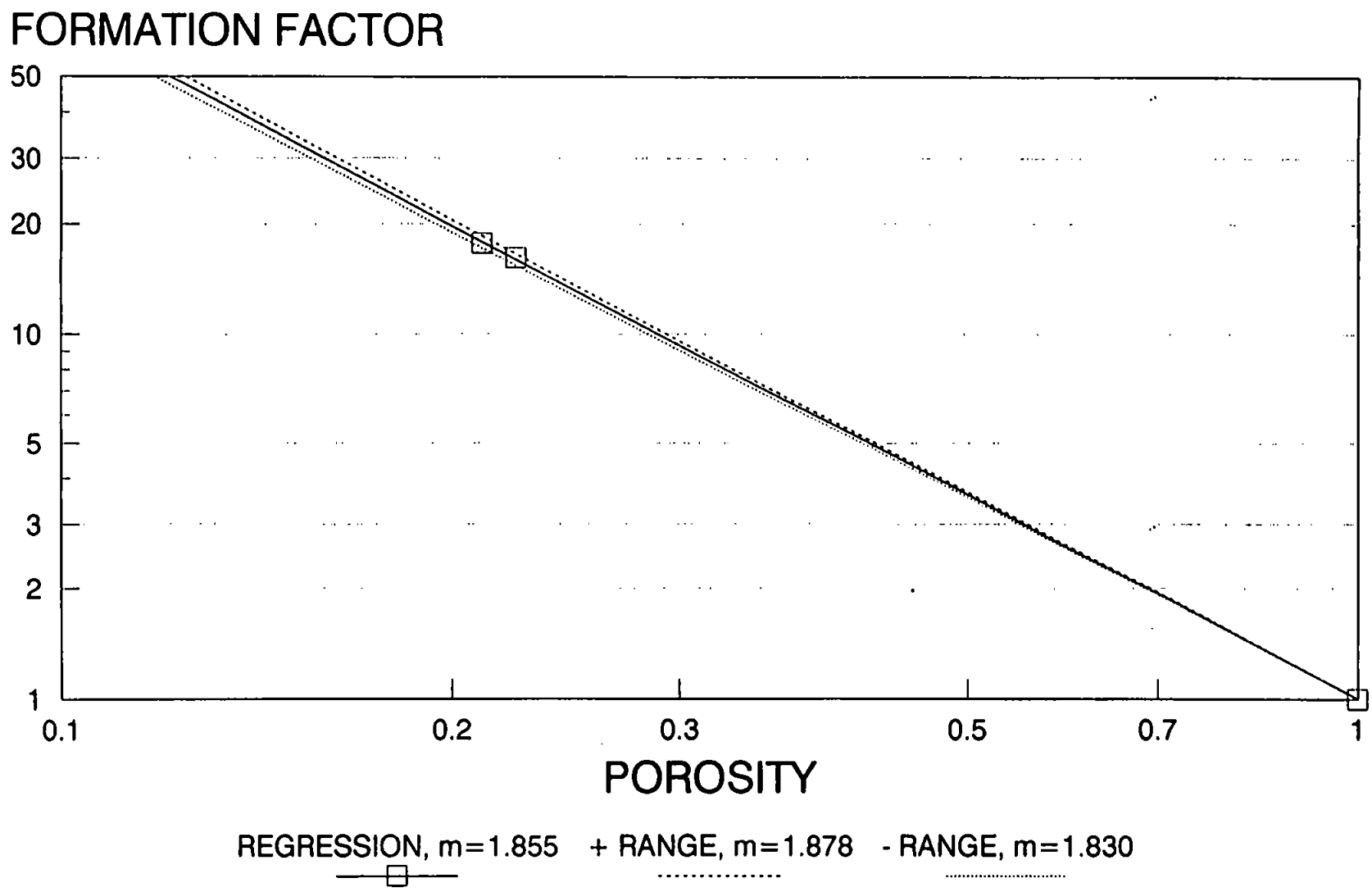

FIGURE 4.7: Mean and Extremes of Formation Factor Range Against Porosity for Samples in Group 250. Mean Cementation Exponent Equals 1.855.

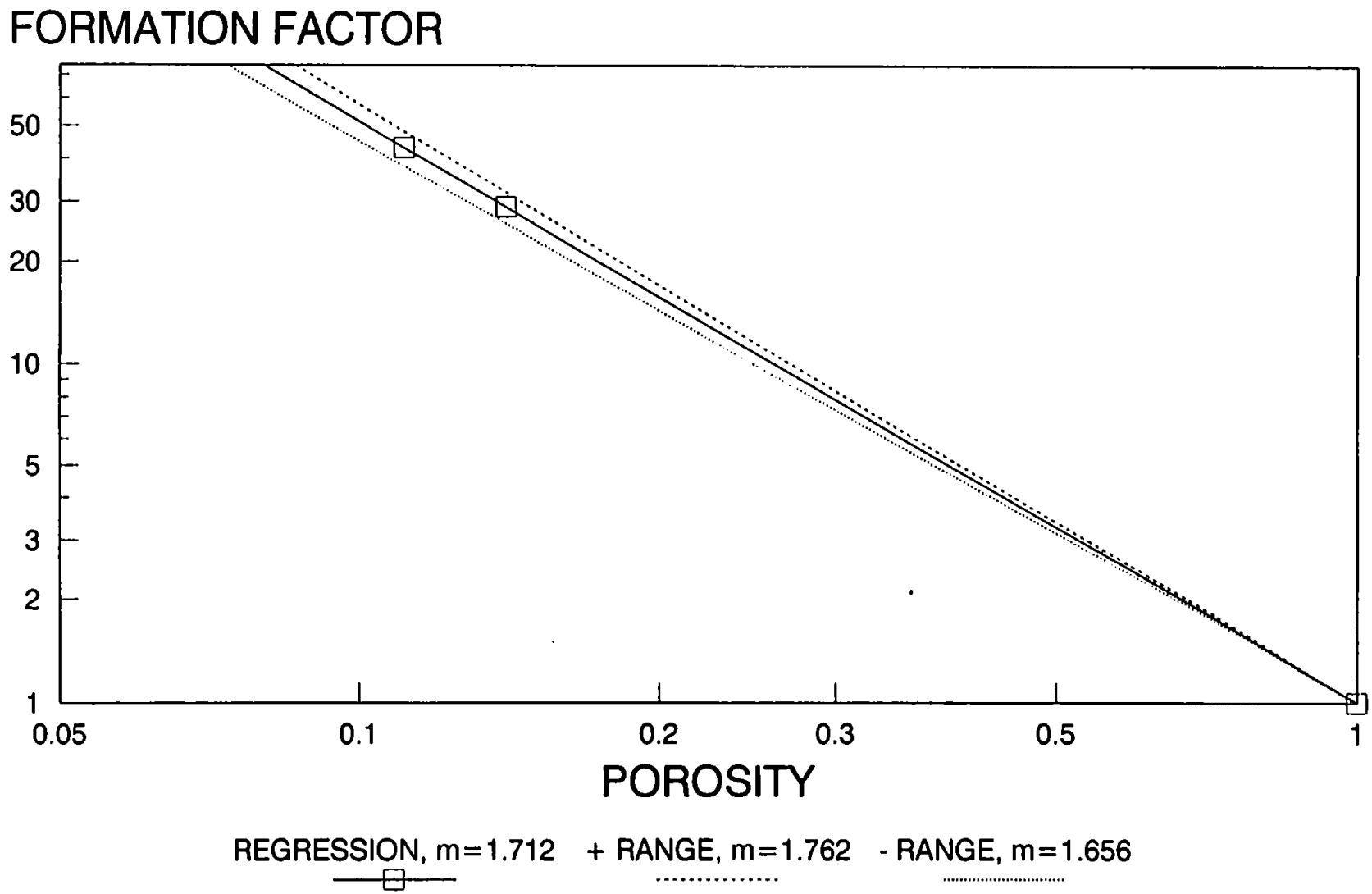

FIGURE 4.8: Mean and Extremes of Formation Factor Range Against Porosity For Samples in Group 80. Mean Cementation Exponent (m) equals 1.712.

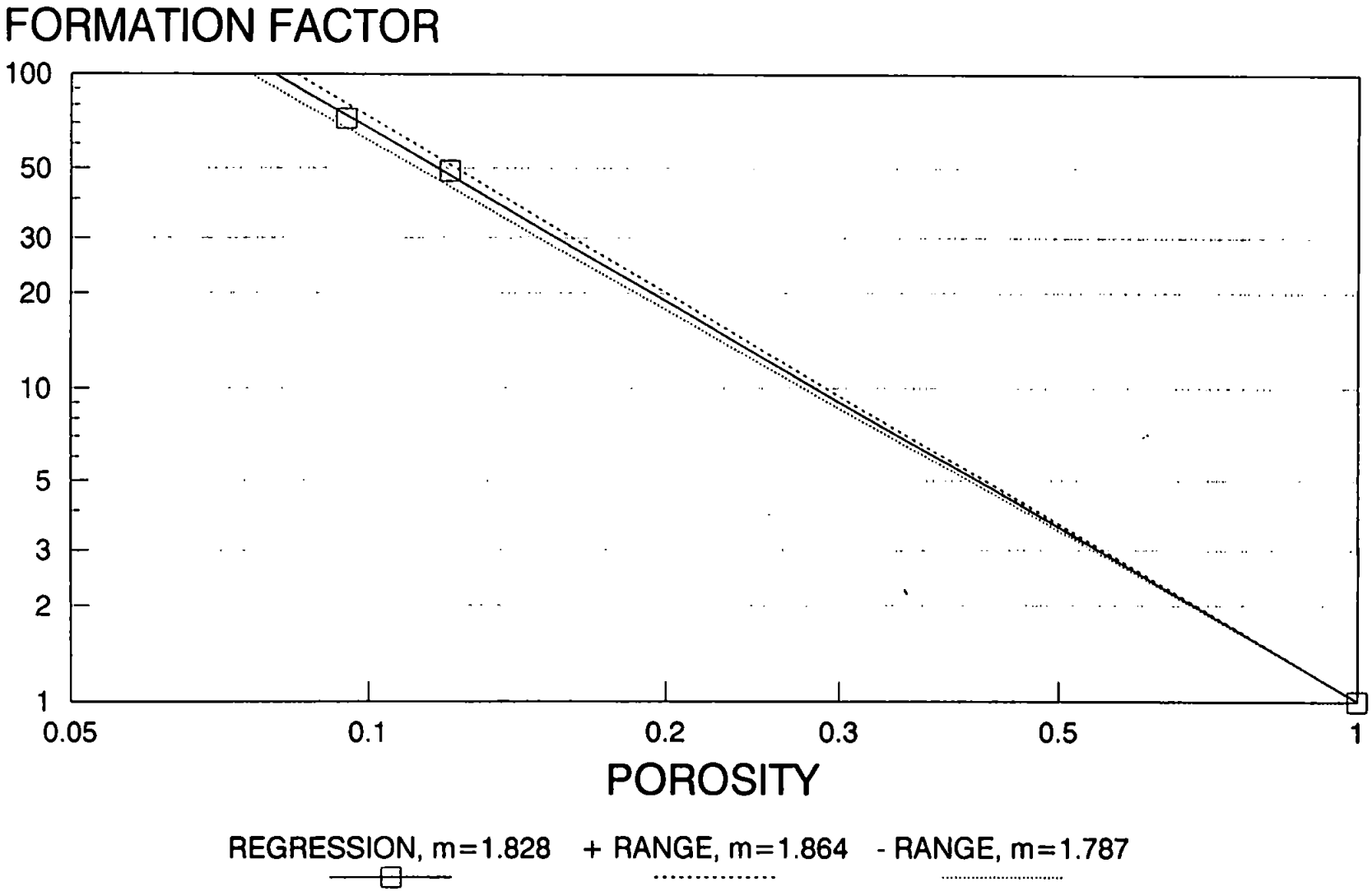

FIGURE 4.9: Mean and Extremes of Formation Factor Range Against Porosity for Samples in Group 100. Mean Cementation Exponent (m) equals 1.828.

CHAPTER 5

MERCURY POROSIMETRY

5.1 Introduction

Mercury porosimetry is probably the most commonly used technique for porous media investigation. Mercury is non-wetting to most surfaces. A pressure must be applied for it to penetrate pore space. The smaller the pores in the pore network, the higher the pressure needed to facilitate penetration.

Although the basis of mercury porosimetry was formulated in the 1940s (Ritter & Drake 1945), much controversy still surrounds interpretation of mercury porosimetry data. If a pore/throat shaft is of an idealised cylindrical shape of radius, r, the pressure P_c, applied to the mercury to cause penetration is defined by the Washburn Equation :

$$P_c = -\frac{2\sigma\cos\theta}{r} \qquad (5.1)$$

where σ = surface tension of mercury, and θ is the contact angle of mercury on the sandstone. The Washburn Equation is a simple adaption of the Young-Laplace Equation which is a general equation of capillarity.

The Washburn Equation is used to obtain pore/throat size distributions in the majority of studies, even though most natural pores are not cylindrical. Many workers have mentioned the inadequacies of the Washburn Equation. Cedeci (1980), demonstrated that if the Washburn Equation is applied to divergent conical shaped pores, there is an overestimation of the pore size. It was also postulated that mercury will penetrate low angle divergent conical shaped pores without the application of any positive pressure on the mercury. Thus the volume of small, low angle conical pores will be assigned to the larger pore region of the calculated size distribution.

In an analysis of the shape of graphs of volume of intruded mercury against applied

pressure, Shiveley (1991) calculated the dominant pore shapes within silica gel and precipitated sulphur pore networks. The theory would not be applicable to pore networks of varying pore shapes. From SEM observations, reservoir sandstones do not contain regular pore shapes, so the application of Shiveley's theory is limited only to ideal pore systems.

Dullien and Batra (1970) mention the use of 'equivalent pore radii'. This is the radius of a straight cylindrical capillary that would give rise to the same capillary pressure as the measured value. The idea of equivalent pore radii was dismissed by Van Brakel (1981) because for complicated pore shape, the relationship between P_c and $\cos\theta$ is not linear.

Use of the Washburn Equation requires values for contact angle and surface tension. The most commonly used values for contact angle of mercury on sandstones are 140° for the intrusion of mercury and 130° for the extrusion. In reality values ranging from 112° to 180° have been measured (Van Brakel 1981).

The best method of measuring contact angle is debatable. The most common method involves measuring the contact angle of a small drop of mercury on a surface similar in composition to the porous sample; thus a glass or silica surface would be used for sandstones. This method must take account of surface roughness, since most reservoir sandstones do not have smooth pores. In general surface roughness increases contact angle. Good and Mikhail (1981) maintained that for most pore systems with rough surfaces contact angle approaches 180°. The Washburn Equation assumes a constant value for contact angle throughout intrusion, which is almost certainly a mistaken assumption. It has been shown that contact angle changes with different solid surfaces and different absorbed species on these surfaces. Mouscou and Lub (1981) obtained shifts in calculated pore size distributions when cyclohexane was adsorbed onto the surface of a homogeneous γ-alumina porous structure. A shift in pore size distributions was also measured when the γ-alumina

was coated with molybdate ions. Both shifts can be attributed to the changes in the contact angle. The effect of sorbates can be minimised by outgassing samples. Most sandstones consist of many minerals of varying polar strengths, so change in contact angle as mercury moves over each different mineral would not be unexpected. The contact angle has also been reported by Kloubek 1981 and Good and Mikhail 1981, as changing with pore radius, albeit only in micropores ie. pores of diameters below 2 x 10^{-4}µm; this is called the Tolman Effect.

As mentioned earlier there is a general trend of a drop in contact angle when comparing intrusion of mercury with extrusion - this is termed contact angle hysteresis. This difference has been attributed to slight wetting of the sample by the mercury. Smithwick (1986) tested this theory by performing multiple mercury intrusion/extrusion cycles and found virtually no change in contact angle between the first and second intrusions; thus any wetting by mercury does not explain contact angle hysteresis. Smithwick postulated that contact angle hysteresis was due to irreversible energy losses occurring when the three-phase boundary (mercury, vapour, rock) moves. This energy loss is analogous to heat formation by frictional forces.

The surface tension of the mercury within the pore space is also non-constant. Surface tension can change due to mercury impurities and adsorbates from the sample surface. These two effects can be minimized if instrument grade mercury is used, and samples are sufficiently outgassed (Good and Mikhail 1981). The Tolman effect also alters surface tension as well as contact angle, but again this effect only occurs within micropores. It will have little effect on pore size distributions within sandstones, whose pores of interest are predominantly within the macropore region ie. pores with diameters greater than 2 x 10^{-2}µm. The recommended value for surface tension of mercury within sandstone pores is 485 Dyn/cm or 0.48 nm^{-1} (Good and Mikhail 1981), which is the value we have used in all future calculations.

The commonest method of obtaining a pore size distribution from mercury porosimetry data involves calculating the first derivative of the intrusion curve. As mentioned earlier a pore/throat can only be penetrated if a high enough pressure is applied to the mercury. If the sample contains large pores shielded by small pores/throats the large pores will only be filled after a pressure sufficient to penetrate the smallest pores/throats is reached. Thus the volume of the large pores is attributed to the small pores within the pore size distribution. Some workers have tried to statistically correct for this "shielding effect" (Connor and Horowitz, 1988).

Another common misinterpretation of mercury primary intrusion data is due to the assigning of the pore diameter corresponding to the point of inflection as the most frequent or characteristic pore size of the sample. In fact, this size is neither the most common nor the average pore size. As is shown later from computer modelling, the pore size corresponding to the point of inflection is better defined as the "threshold pore size". This is in line with percolation theory in which the percolation threshold corresponds to the point at which a continuous path of mercury forms through the sample. Katz and Thompson (1987) found the point of inflection to correspond with break-through of mercury through the sample. In our computer simulations of mercury intrusion, the point of inflection always occurs just when a continuous path of mercury spans the sample ie. at break-through (Matthews et al 1993). Most sandstones produce a sigmoidal shape primary intrusion curve when percentage pore space occupied by mercury is plotted on a linear scale and pore entry diameter on a log scale, Figure 5.1. The point of inflection of the sigmoidal curve is dependent on the arrangement of pores in the network as mentioned above. The shape of the curve is also dependent on the spatial pore arrangement. Neasham (1977) compared mercury intrusion data with scanning electron micrographs of each sample. He found that samples with little clay distributed in isolated areas has steep mercury intrusion curves. Mercury had also intruded nearly all available pore space at the

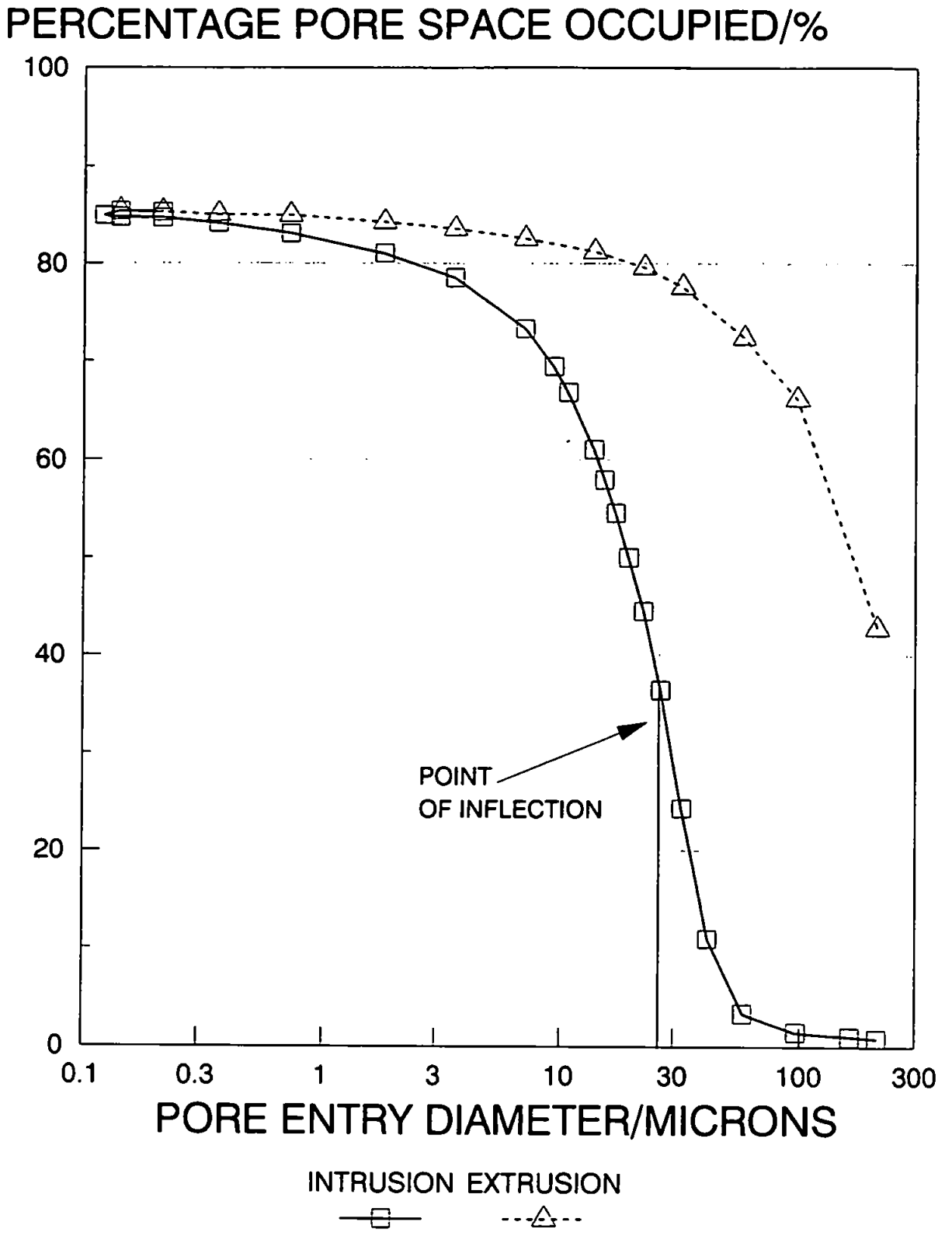

FIGURE 5.1: Typical Mercury Intrusion/Extrusion Curves for Sandstone.

maximum applied pressure. Samples with pore lining clay had shallower intrusion curves and a smaller maximum intruded volume. Pore-bridging clay reduces the pore volume accessible to mercury still further and causes very shallow intrusion curves. Thomeer (1960) noticed that plotting mercury intrusion data on a log-log axis produced a near hyperbolic curve. The equation for such a hyperbola can be written:

$$\frac{(V_b)_{Pc}}{(V_b)_{P\infty}} = e^{-G/(Log P_c/P_d)} \qquad (2)$$

Where $(V_b)_{pc}$ = Fractional bulk volume occupied by mercury at pressure P_c.

$(V_b)_{p\infty}$ = Fractional bulk volume occupied at infinite pressure.

P_c = Mercury capillary pressure.

P_d = Extrapolated mercury displacement pressure.

G = Geometrical parameter.

The geometrical parameter (G) defines the shape of the hyperbola. The geometrical parameter can range from 0 to 10. The "steep" intrusion curves have a low geometrical parameter value, Figure 5.2. Neasham (1977) applied Thomeer's intrusion curve theory to his clay affected samples. Sandstones with a discrete particle clay distribution had G values of 0.05 to 0.15. Sandstones with pore-lining clays had larger values from 0.25 to 0.8. The Washburn Equation can be used to convert P_c and P_d to the pore diameter equivalents, pore diameter (D_c) and extrapolated displacement diameter (D_d).

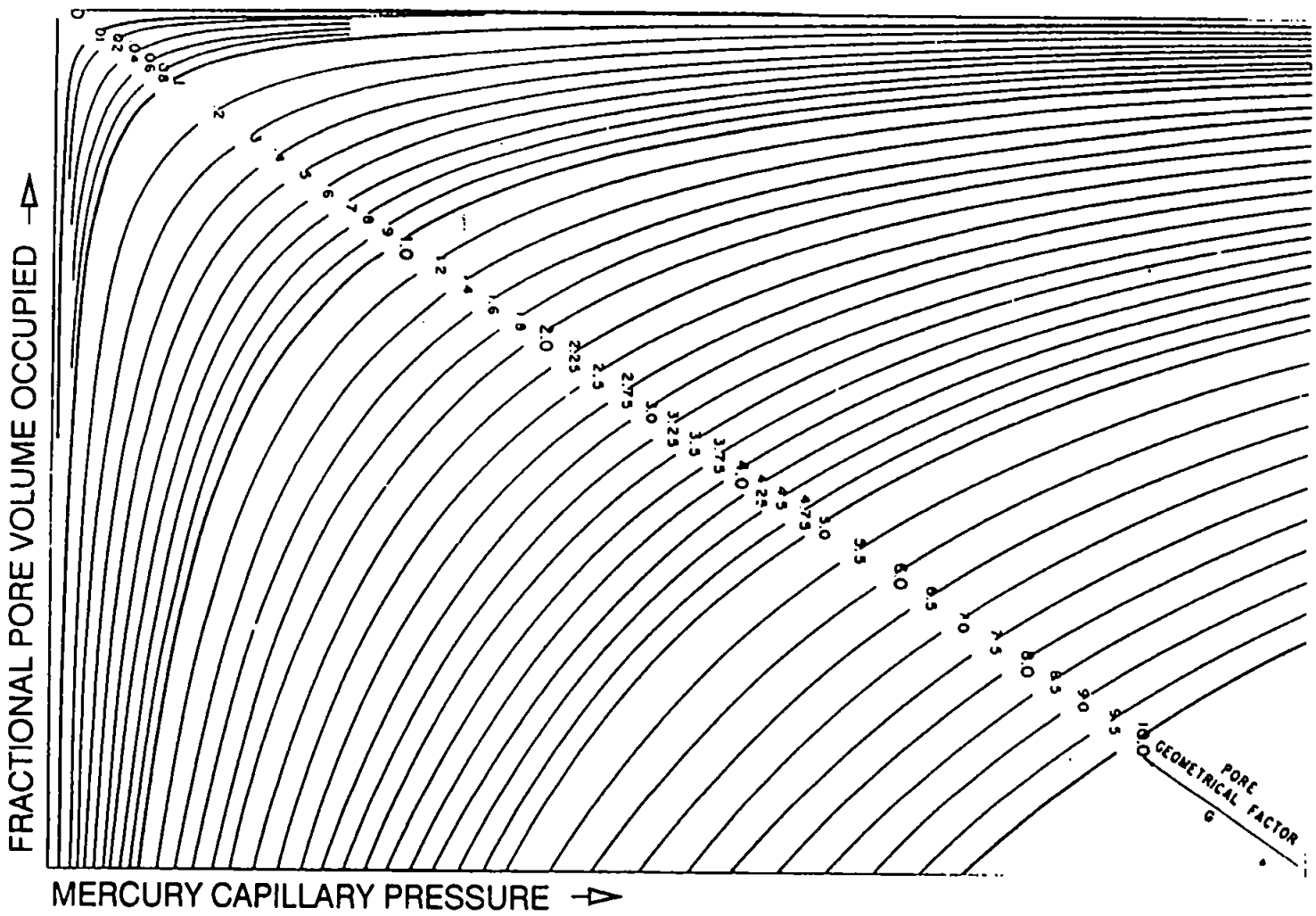

FIGURE 5.2: Family of Mercury Intrusion Curves With Varying Pore Geometrical Factors.

5.2 Structural Hysteresis

During mercury intrusion the size of the throats connected to a particular pore, determines at which pressure mercury will penetrate that pore. As the pressure applied to the mercury is decreased, mercury starts to leave the pore network and compressed residual air enters the pores. The removal of mercury from the pores is termed mercury extrusion. Application of the Washburn Equation to the mercury extrusion data, shows that only the smallest pores empty at high pressures. A pore network containing small pores shielded by large pores, will only completely empty of mercury when a low pressure corresponding to the large pore sizes is reached. Thus the mercury extrusion curve is different to the primary intrusion curve, a phenomenon known as Structural hysteresis.

Structural hysteresis can be demonstrated in the pore network of Figure 5.3. During mercury intrusion Pore B of the internal pores would fill first, then D and then A & C at about the same pressure. When the whole pore network is full and pressure is decreased, the first pore to empty is B. The retreating mercury meniscus will next move through D and then C. Pore A will remain full of mercury until a low enough pressure is reached. However by this time all other pores/throats will have emptied and the path of mercury to the surface will "snap-off" at pore A, leaving a residual amount of mercury trapped in the network. Thus not only is the sequence of pore filling different to that of pore emptying, but also residual mercury trapping can occur within large pores at "snap-off" sites. Wardlaw & McKeller (1981) observed the withdrawal of mercury from a glass micromodel and found that trapping increases as pore to throat size ratio increases. Snap-off of the mercury occurs at large pore/small throat junctions. Samples with areas of large pores and connecting large throats ie banded samples will produce low mercury residuals (Tsakiroglou 1991).

Dead end pores are also thought to be sites for mercury trapping (Vavra 1990).

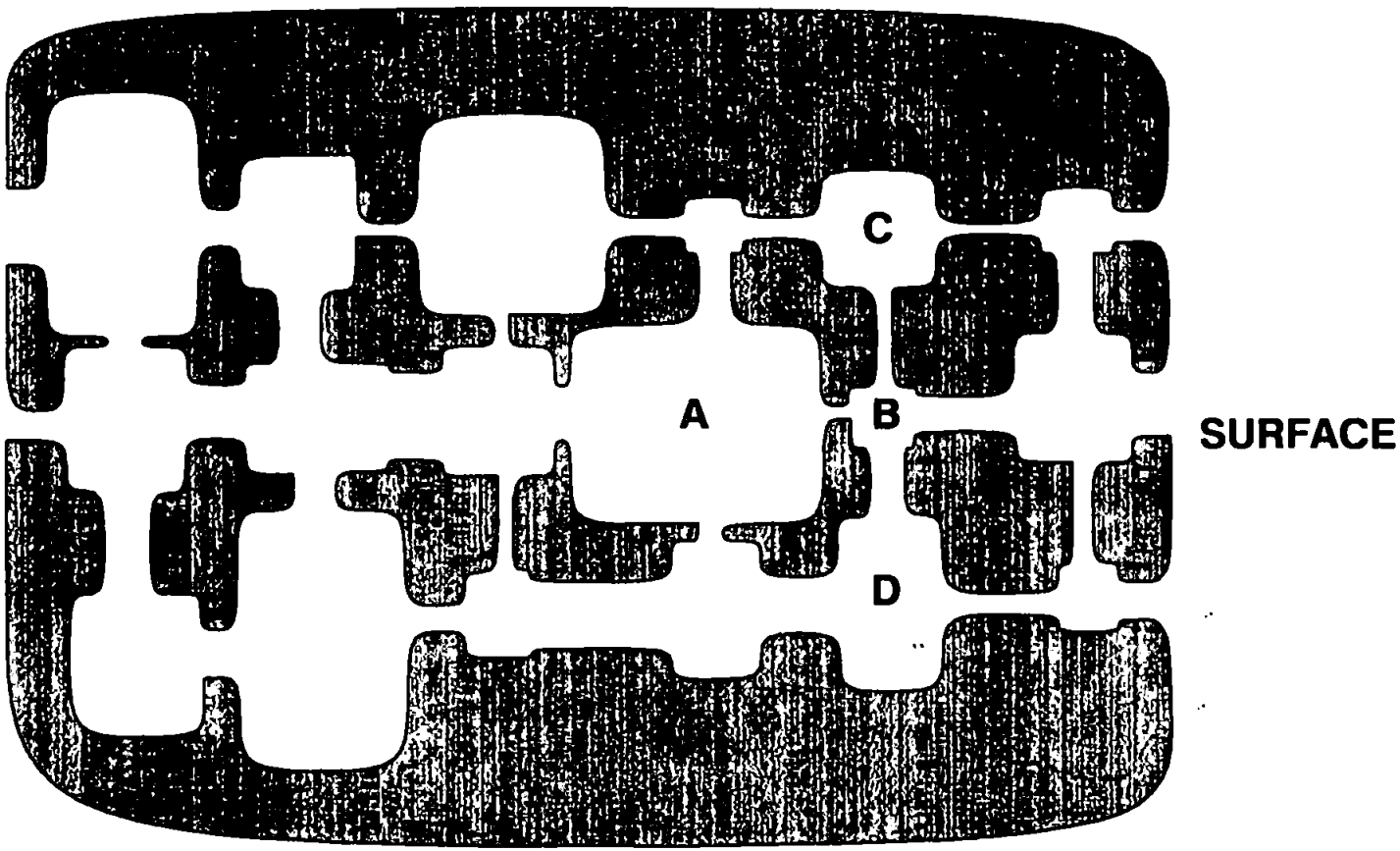

FIGURE 5.3: Two-Dimensional Void Space Arrangement.

Dead end pores only have one entrance. The wetting phase cannot re-enter the pore, assuming there is no throat surface flow of the wetting phase. Thus a large number of dead-end pores within the pore network will lead to significant mercury trapping.

5.3 Contact Angle Hysteresis

The contact angle of the mercury meniscus with the pore will decrease when an intruding mercury front becomes an extruding front. As mentioned earlier, the most commonly used contact angles are 140° for intrusion and 130° for extrusion. The change in contact angle is termed contact angle hysteresis. When applied to the Washburn Equation, the change causes the extrusion curve to be shifted towards the smaller pore region. The ambiguity of precise contact angle values during intrusion and extrusion means that the exact magnitude of any contact angle hysteresis is unknown.

The combined effects of structural and contact angle hysteresis within mercury porosimetry are phenomena closely related to the void space arrangement within the pore network. Wardlaw & Cassan (1979) postulated that the volume of mercury trapped after complete mercury extrusion, is proportional to residual oil volumes after water flooding within an oil reservoir. This theory was recently reiterated by Vavra et al (1992). They stated differences between injection and extrusion curves can provide information on recovery efficiency.

5.4 Results

Twelve samples from the reservoir sandstone plugs supplied by British Gas were analyzed on a Ruska 1059 mercury porosimeter - Figures 5.4 - 5.17.

Appendix 3 shows the apparatus diagram, experimental procedure and calibration curves. The apparatus must be calibrated to remove the effect of mercury and line compression with pressurisation.

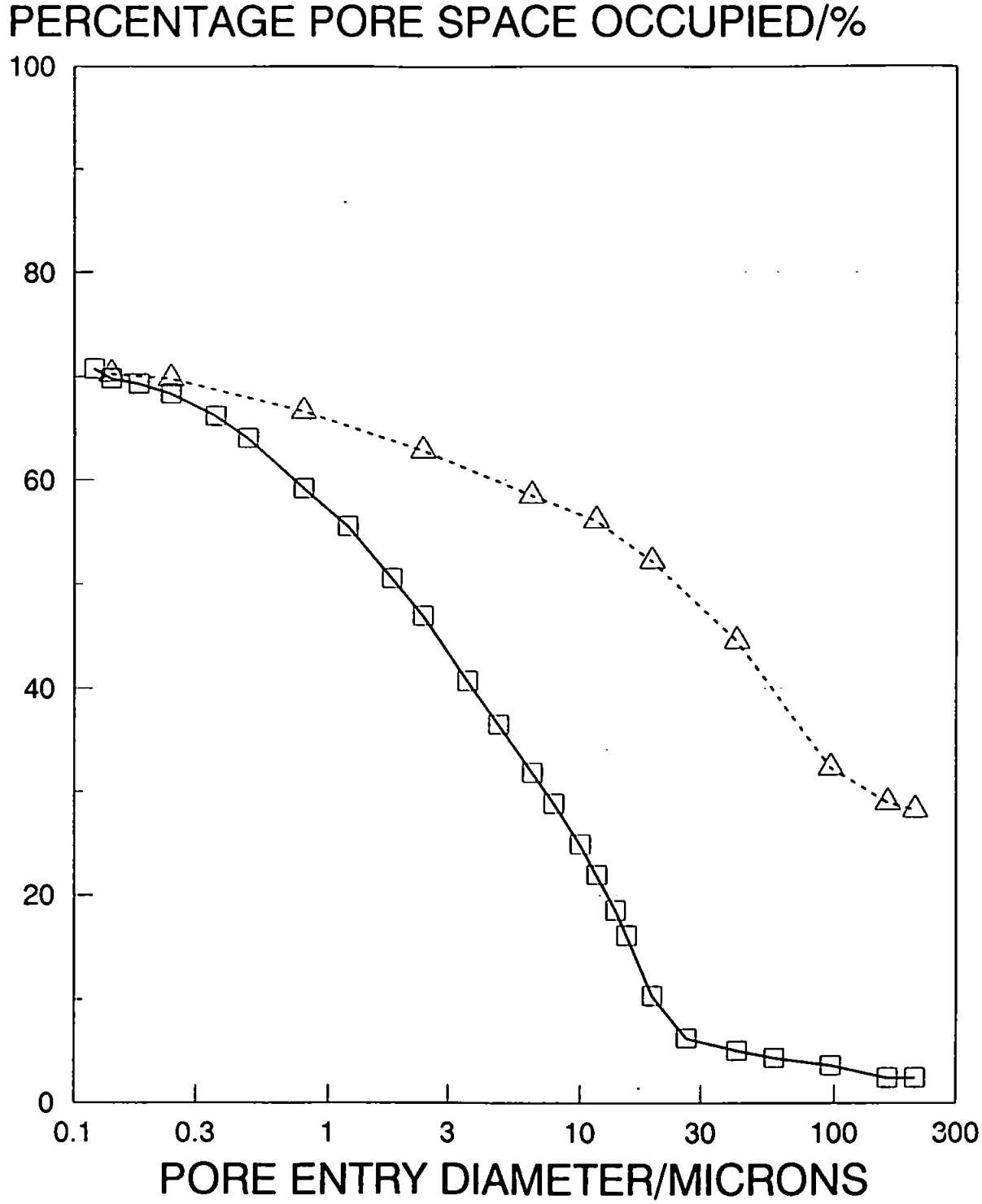

FIGURE 5.4: Mercury Porosimetry Curves for Plug 212A.

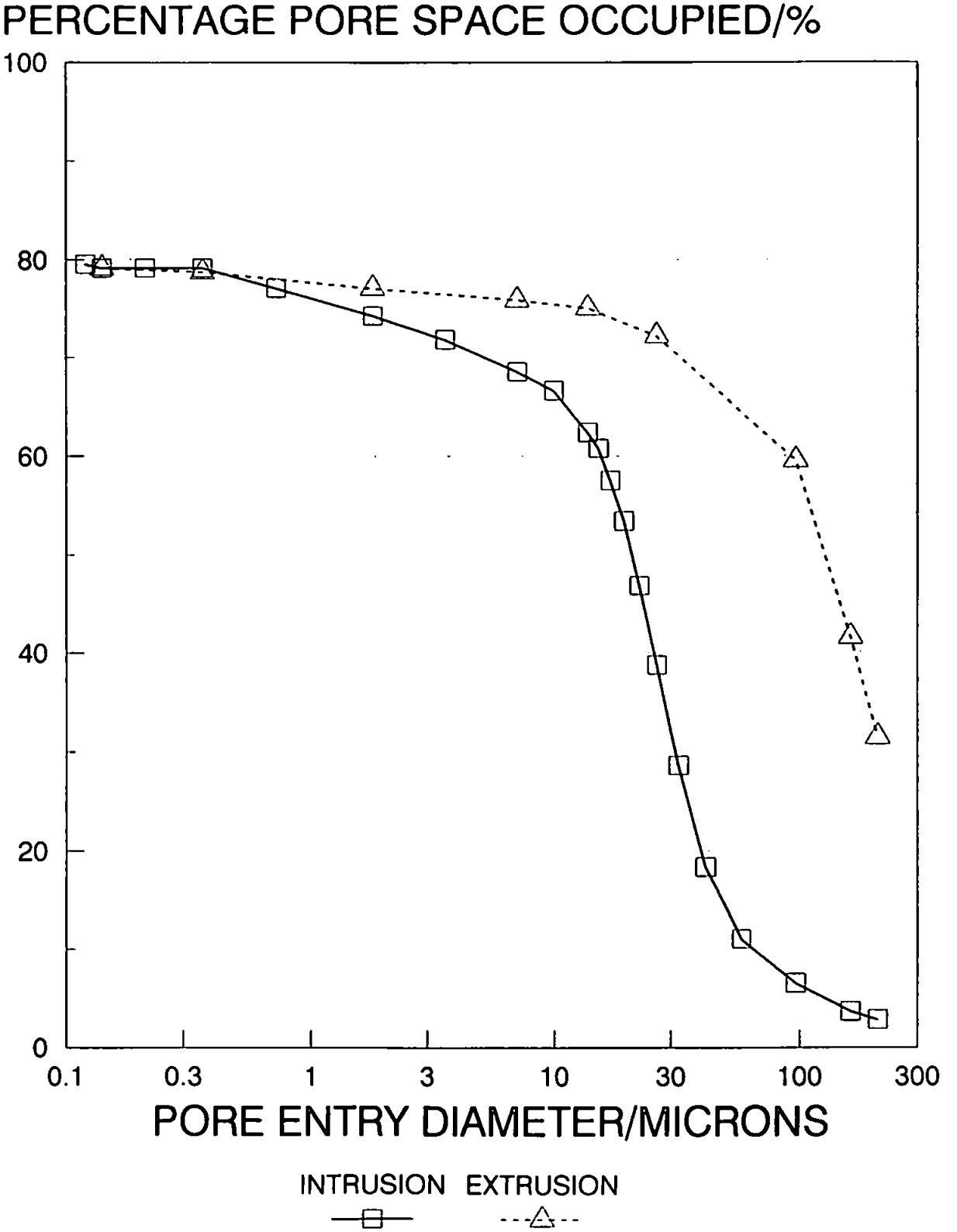

FIGURE 5.5: Mercury Porosimetry Curves for Plug 212B.

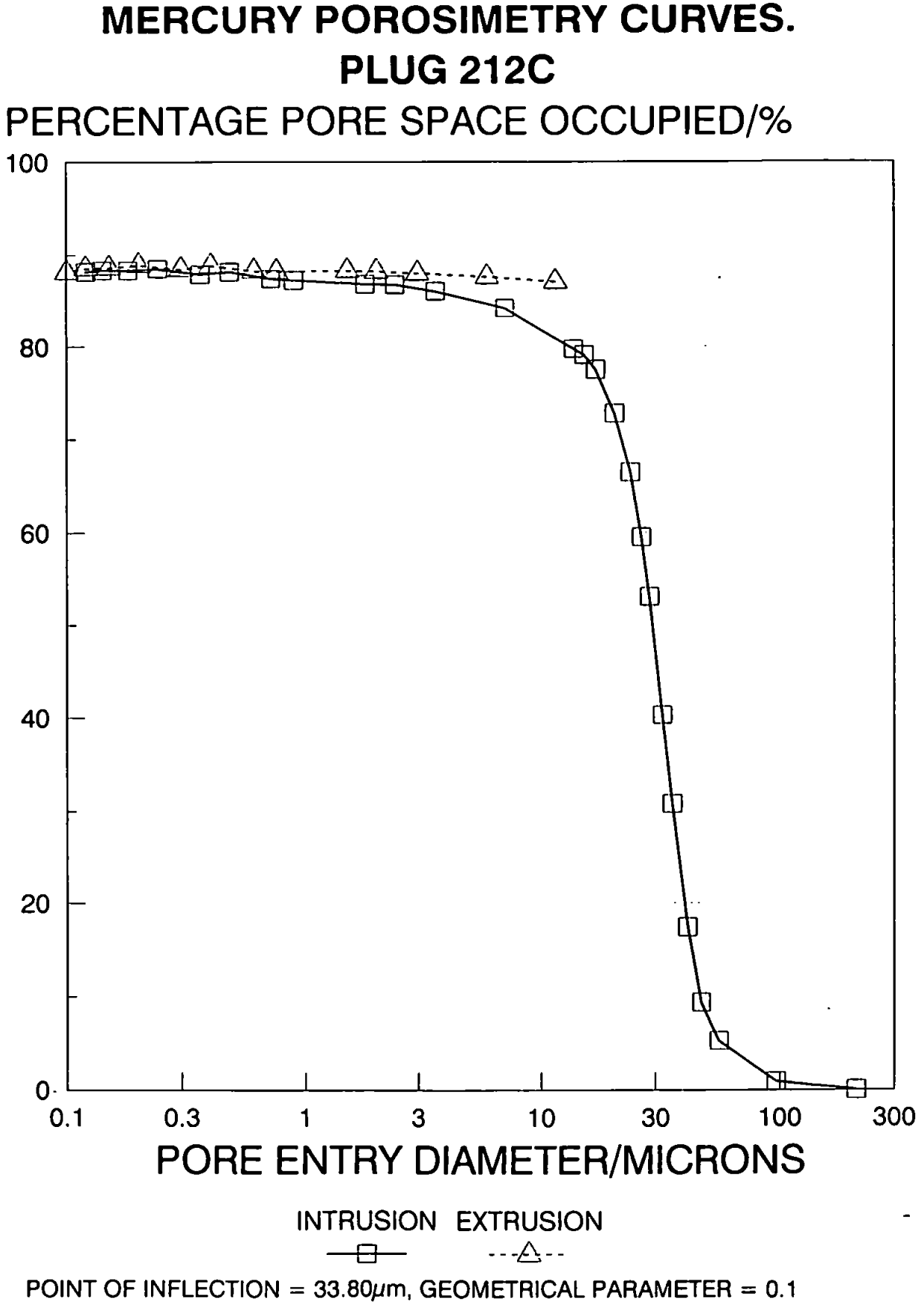

FIGURE 5.6: Mercury Porosimetry Curves for Plug 212C.

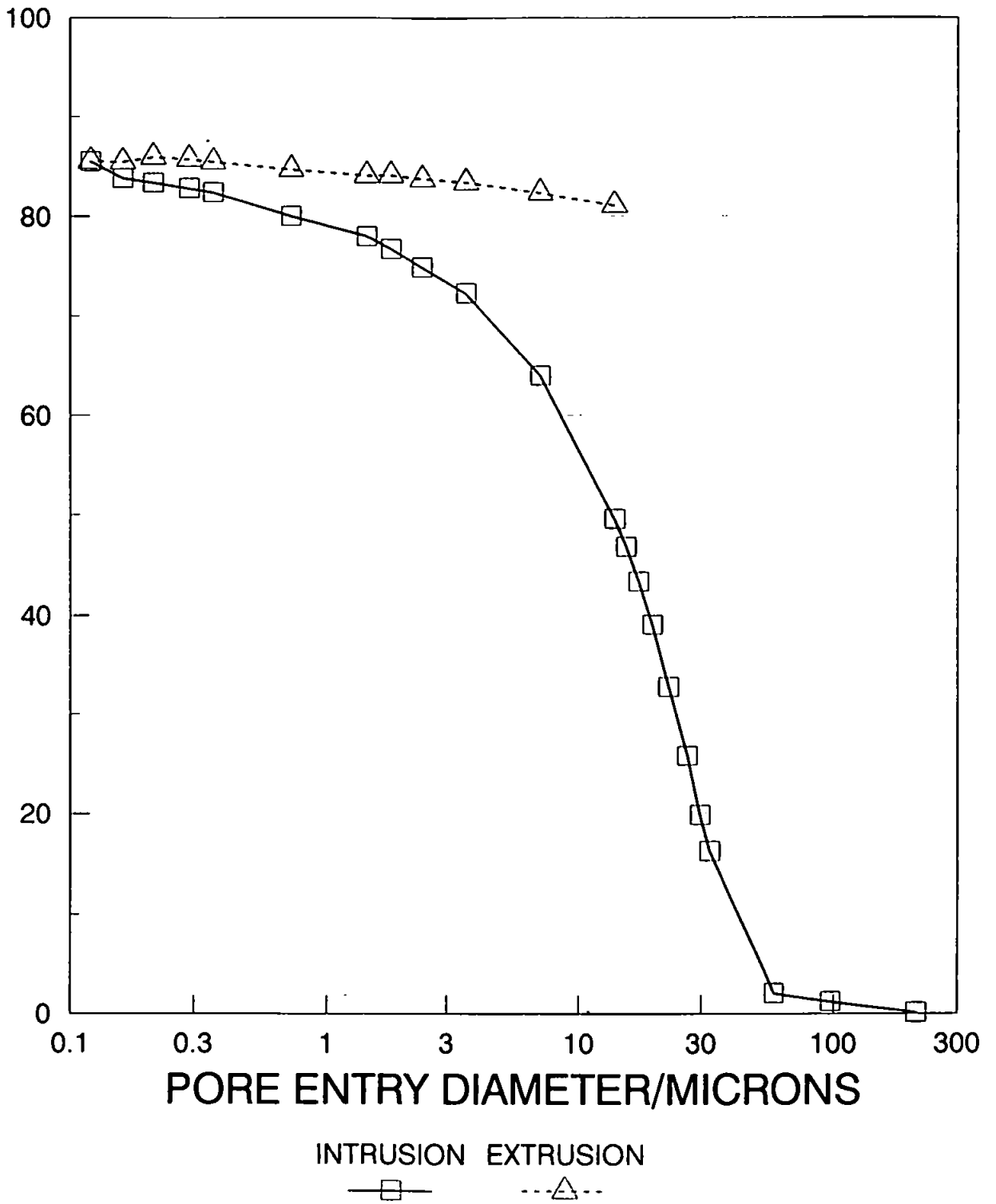

FIGURE 5.7: Mercury Porosimetry Curves for Plug 212D.

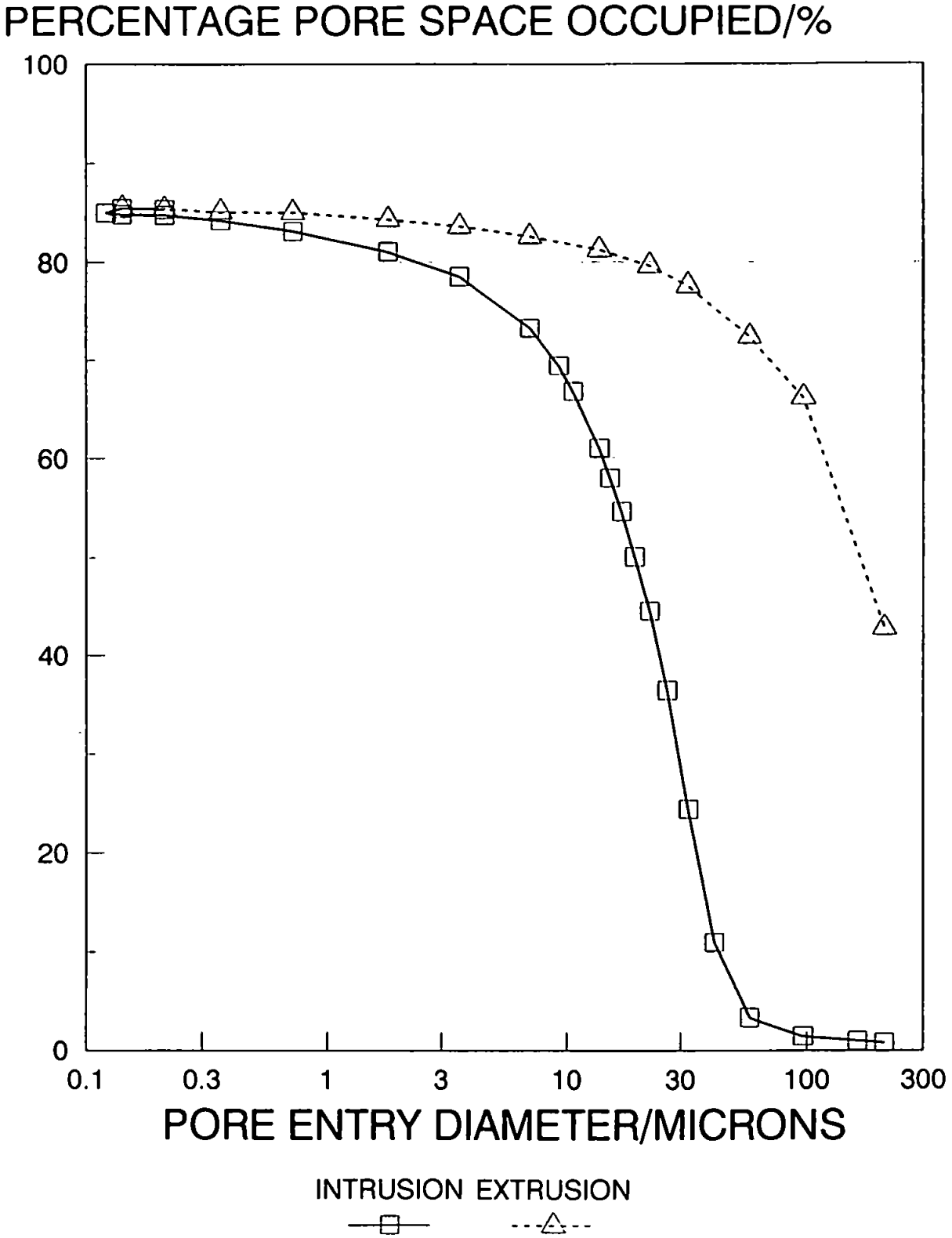

FIGURE 5.8: Mercury Porosimetry Curves for Plug 212E.

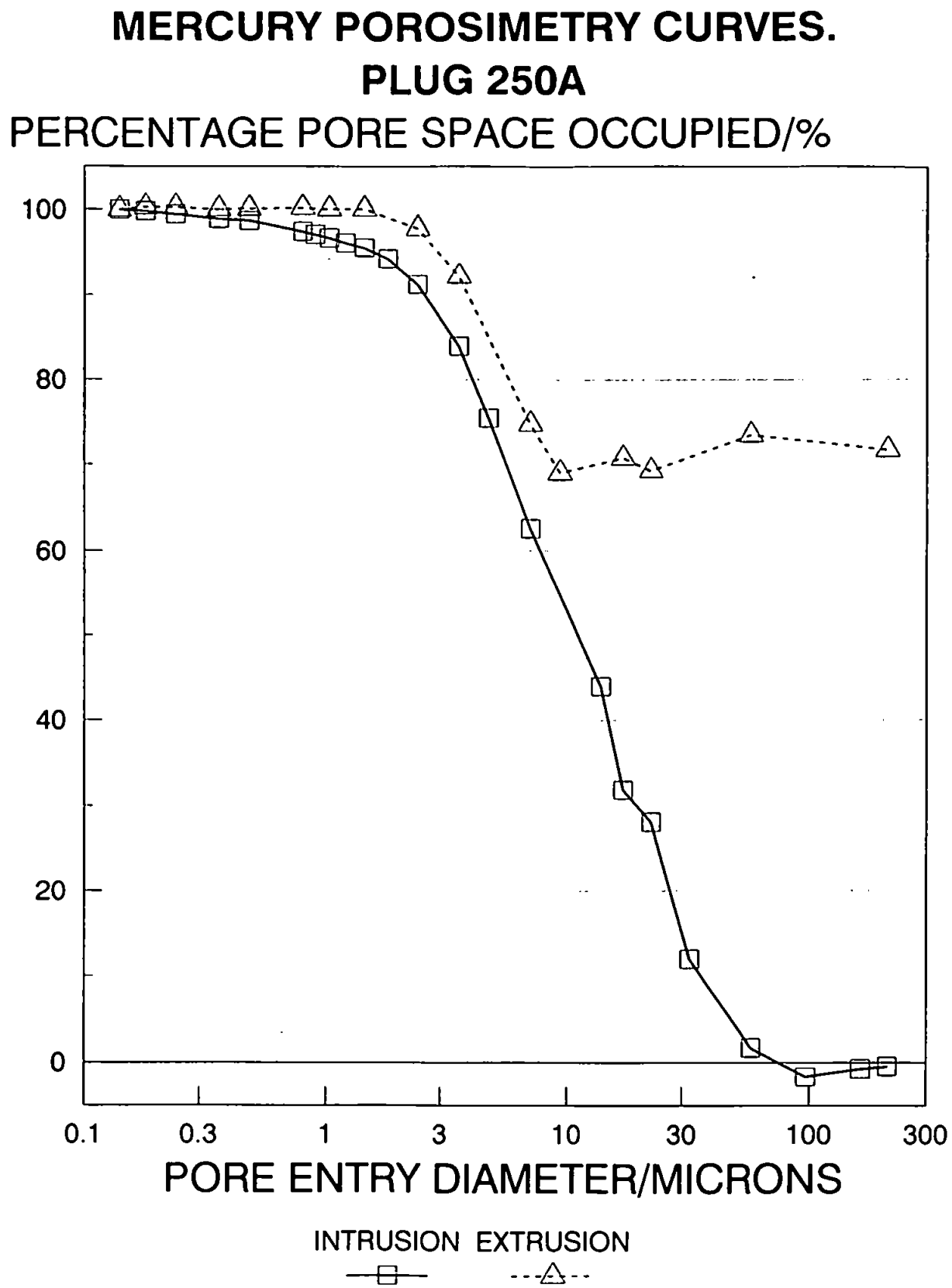

FIGURE 5.9: Mercury Porosimetry Curves for Plug 250A.

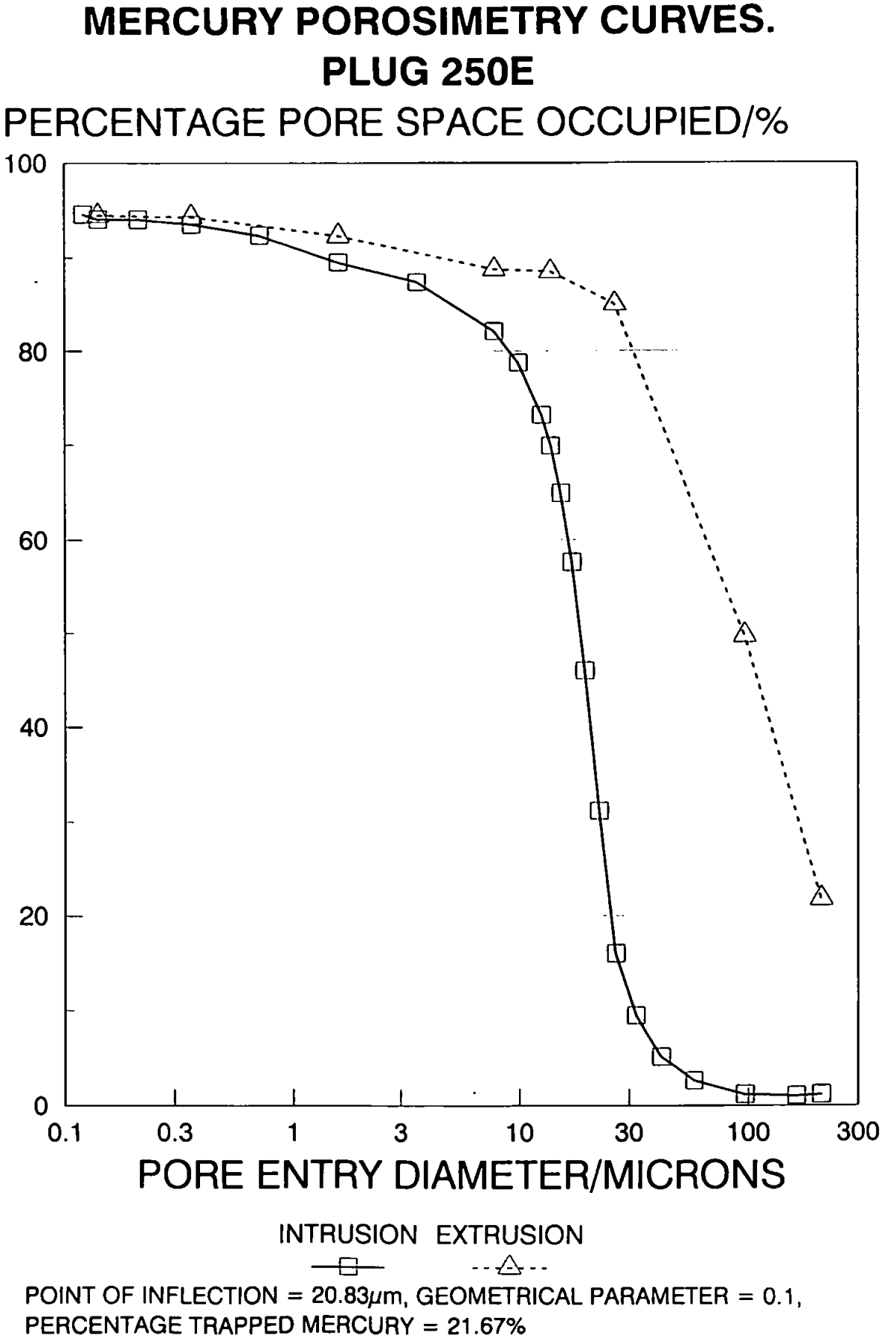

FIGURE 5.10: Mercury Porosimetry Curves for Plug 250E.

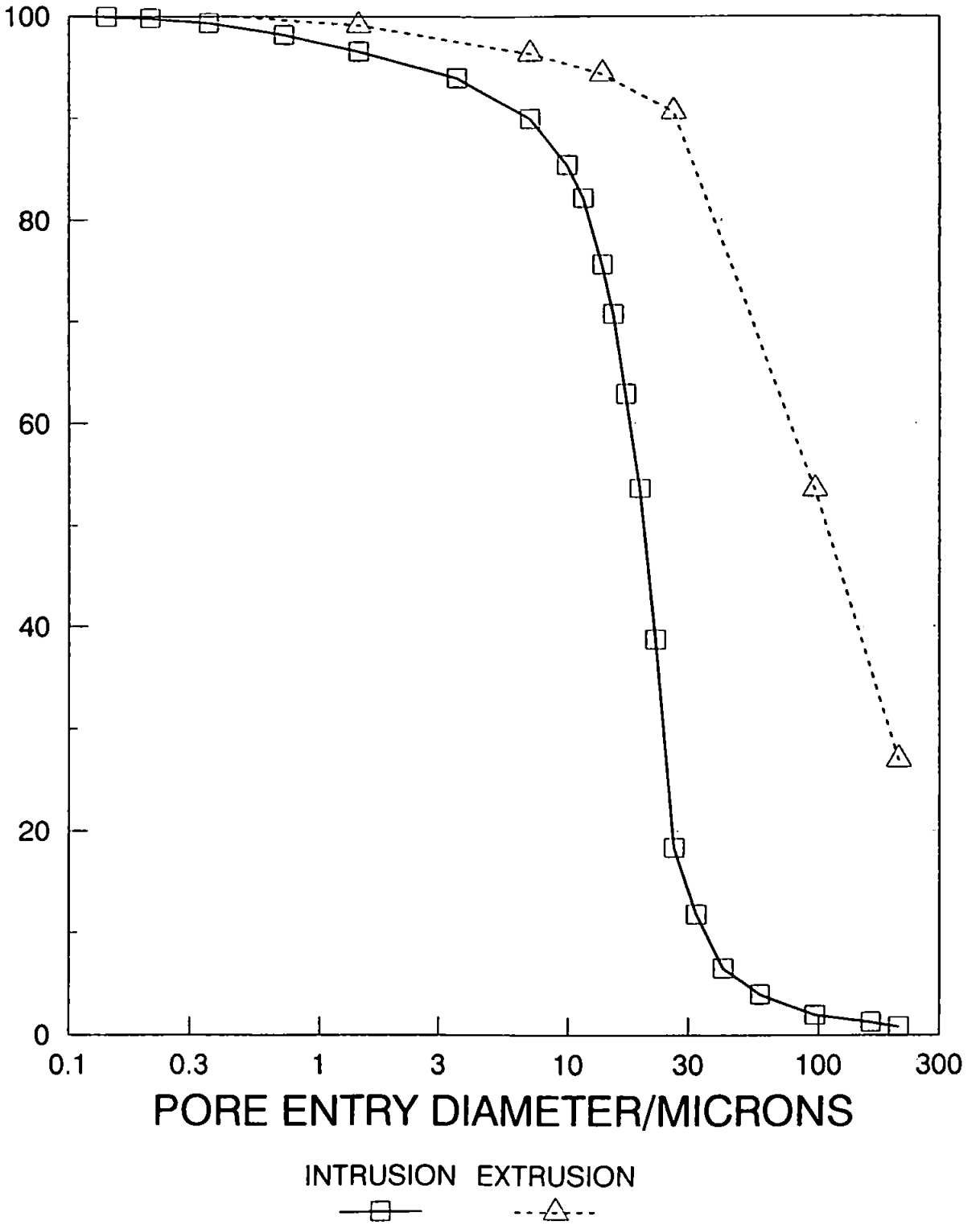

FIGURE 5.11: Mercury Porosimetry Curves for Plug 250E Repeat Run.

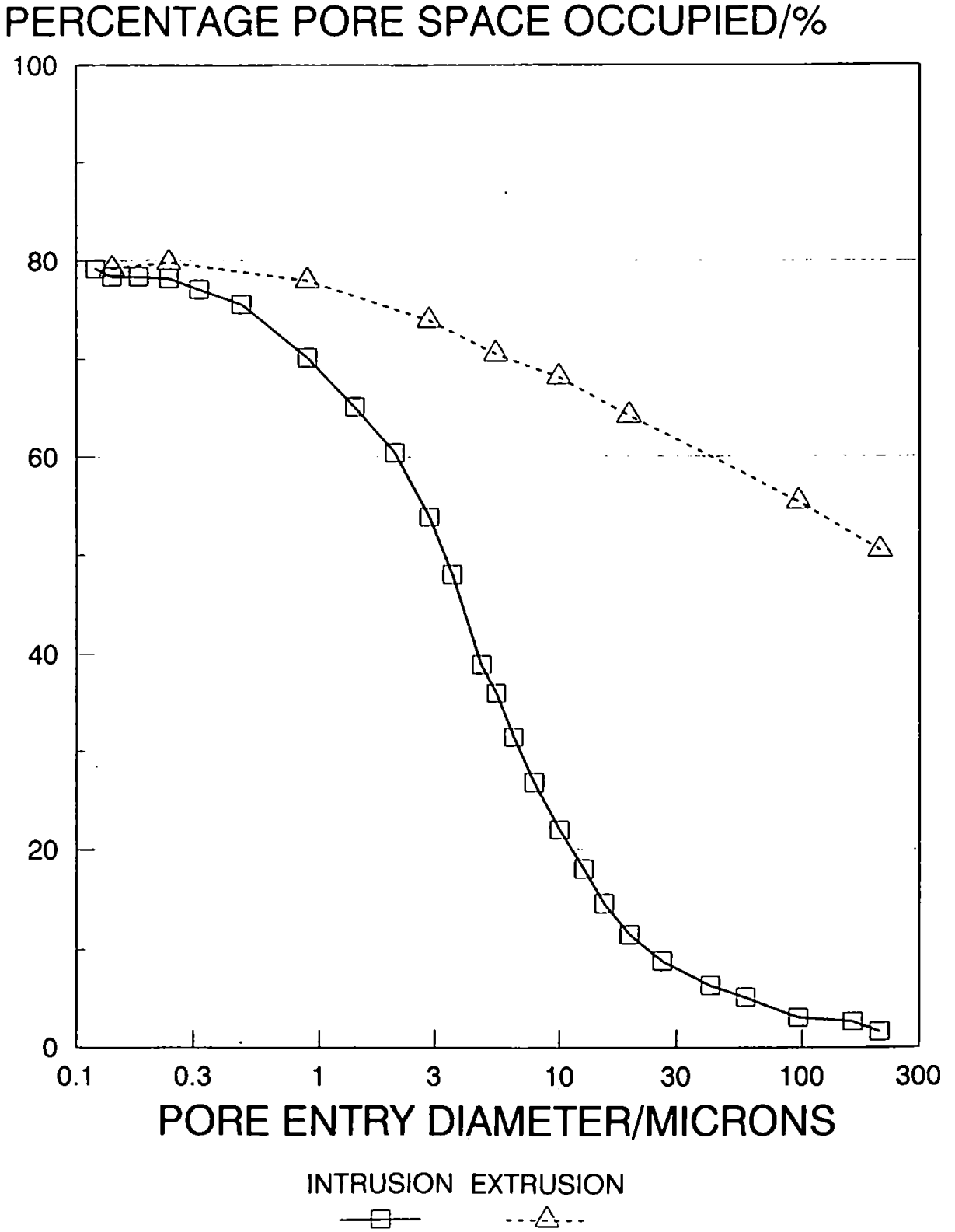

FIGURE 5.12: Mercury Porosimetry Curves for Plug 490A.

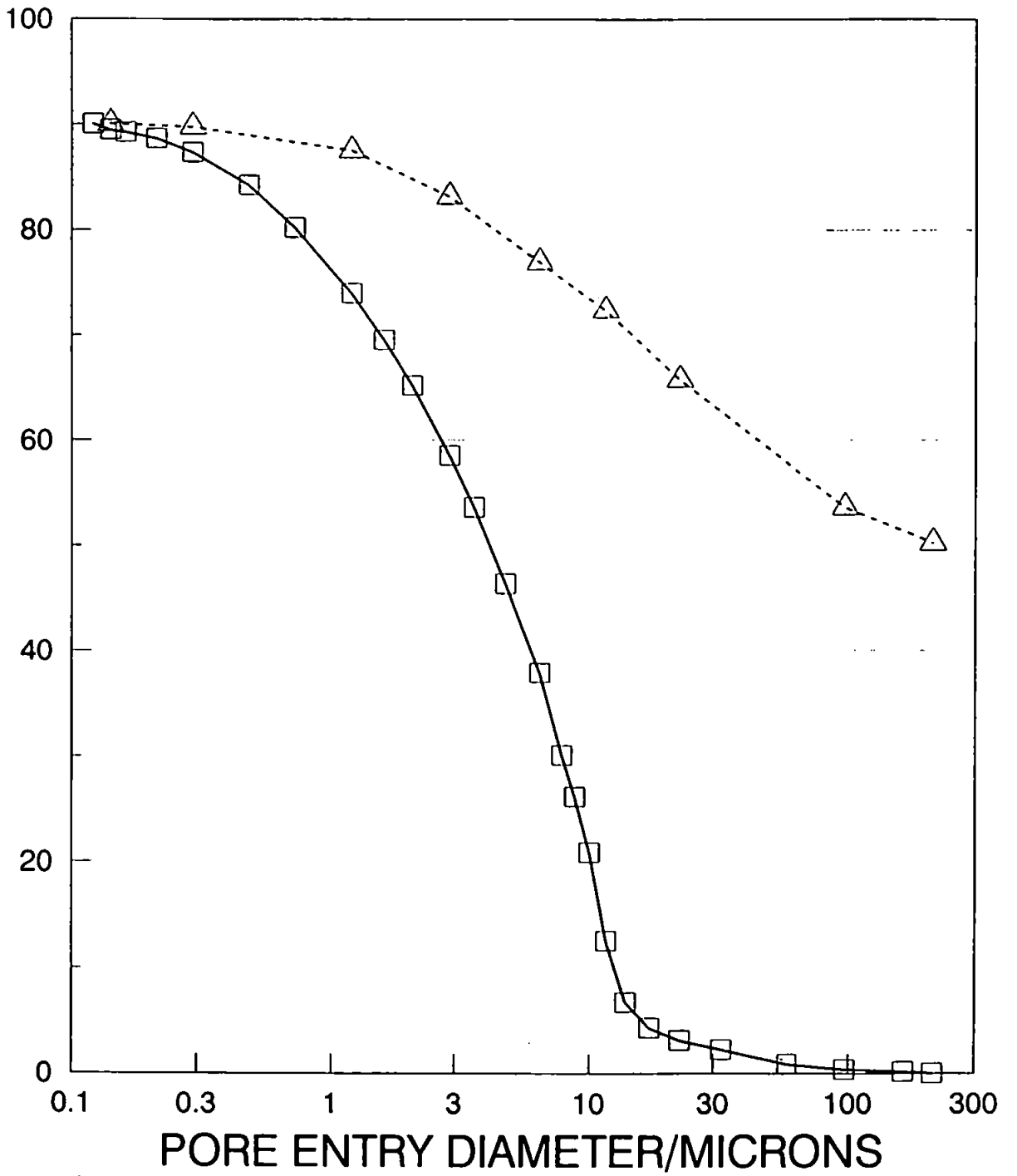

FIGURE 5.13: Mercury Porosimetry Curves for Plug 490B.

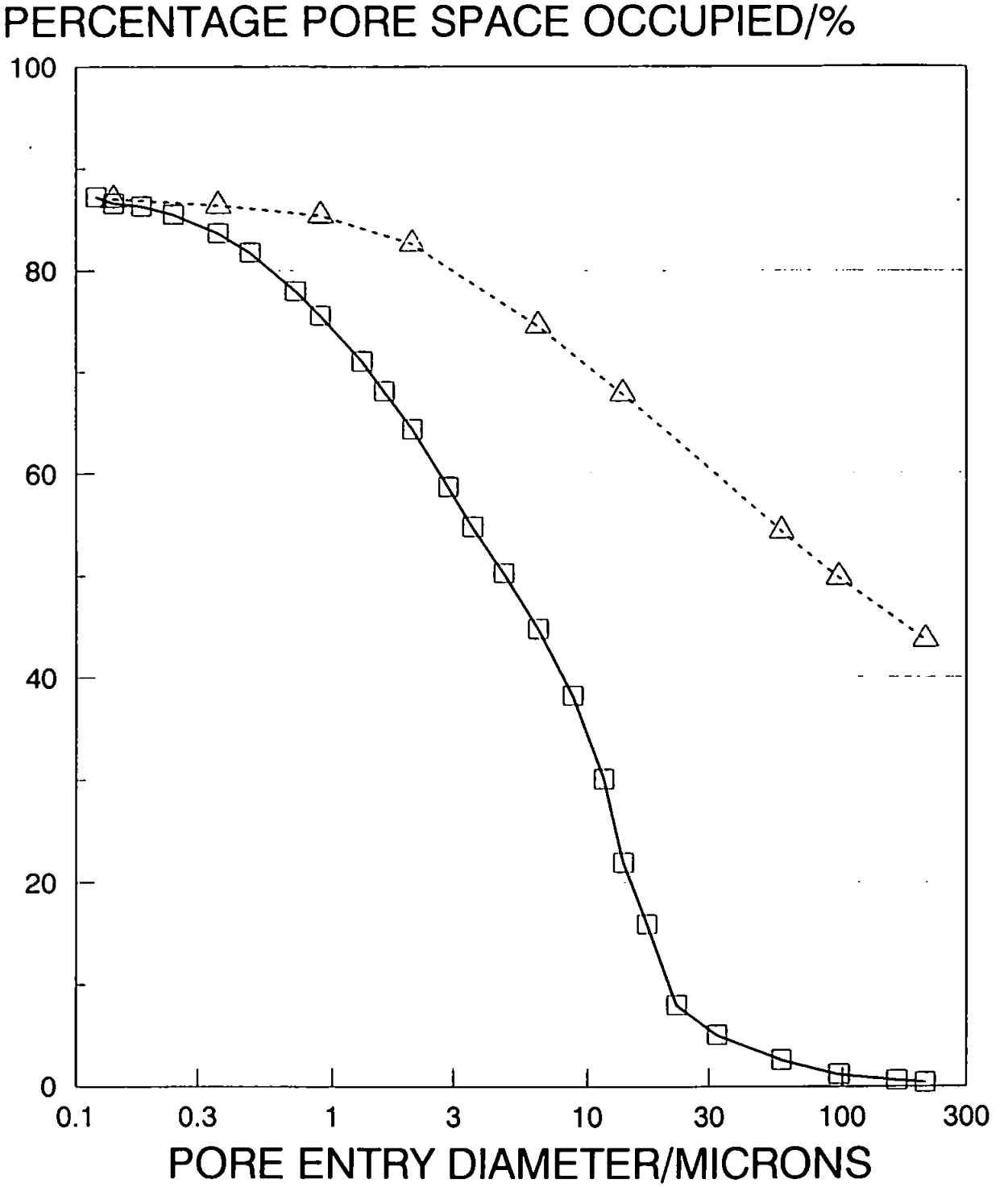

FIGURE 5.14: Mercury Porosimetry Curves for Plug 490C.

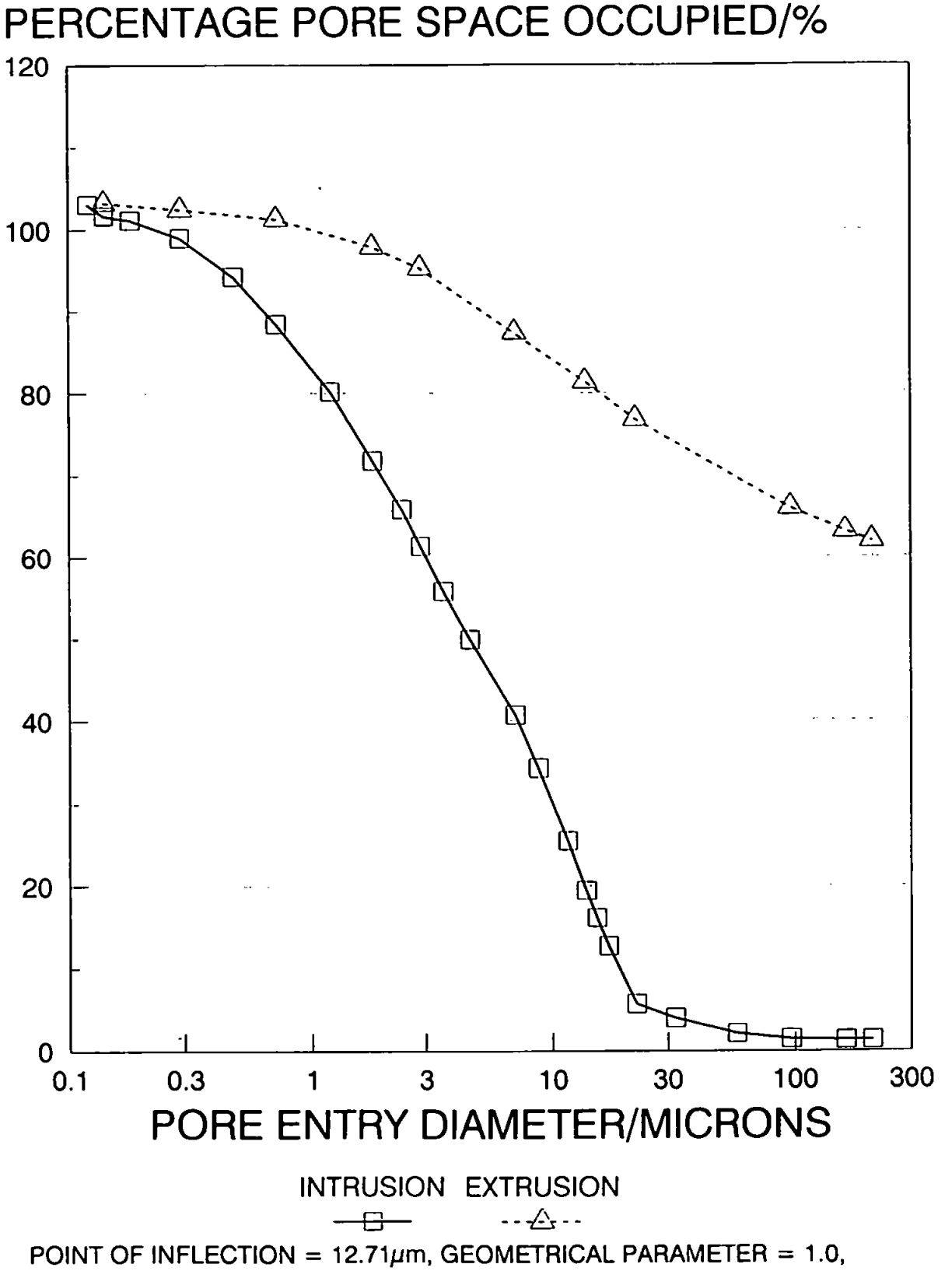

FIGURE 5.15: Mercury Porosimetry Curves for Plug 490D.

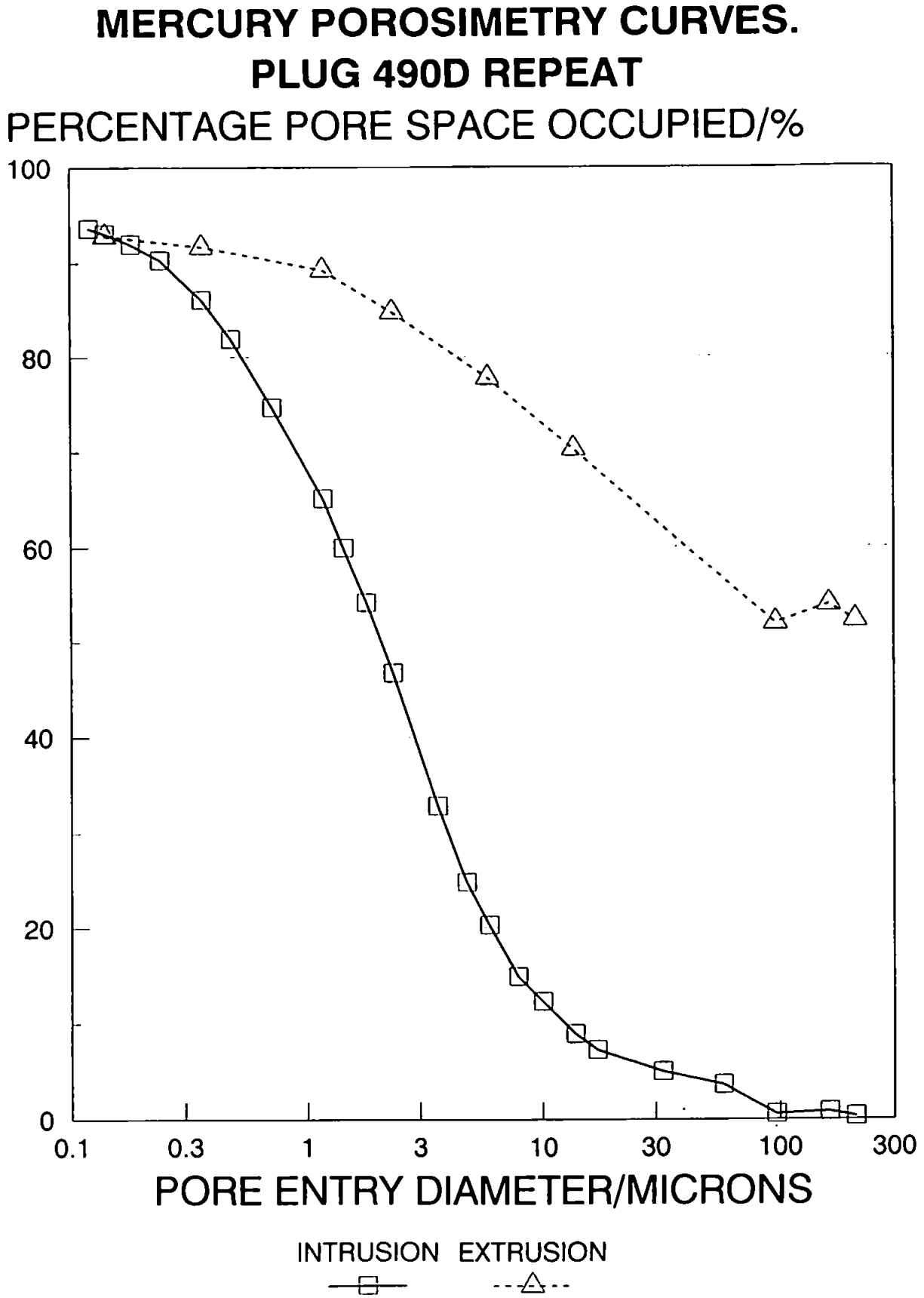

FIGURE 5.16: Mercury Porosimetry Curves for Plug 490D Repeat Run.

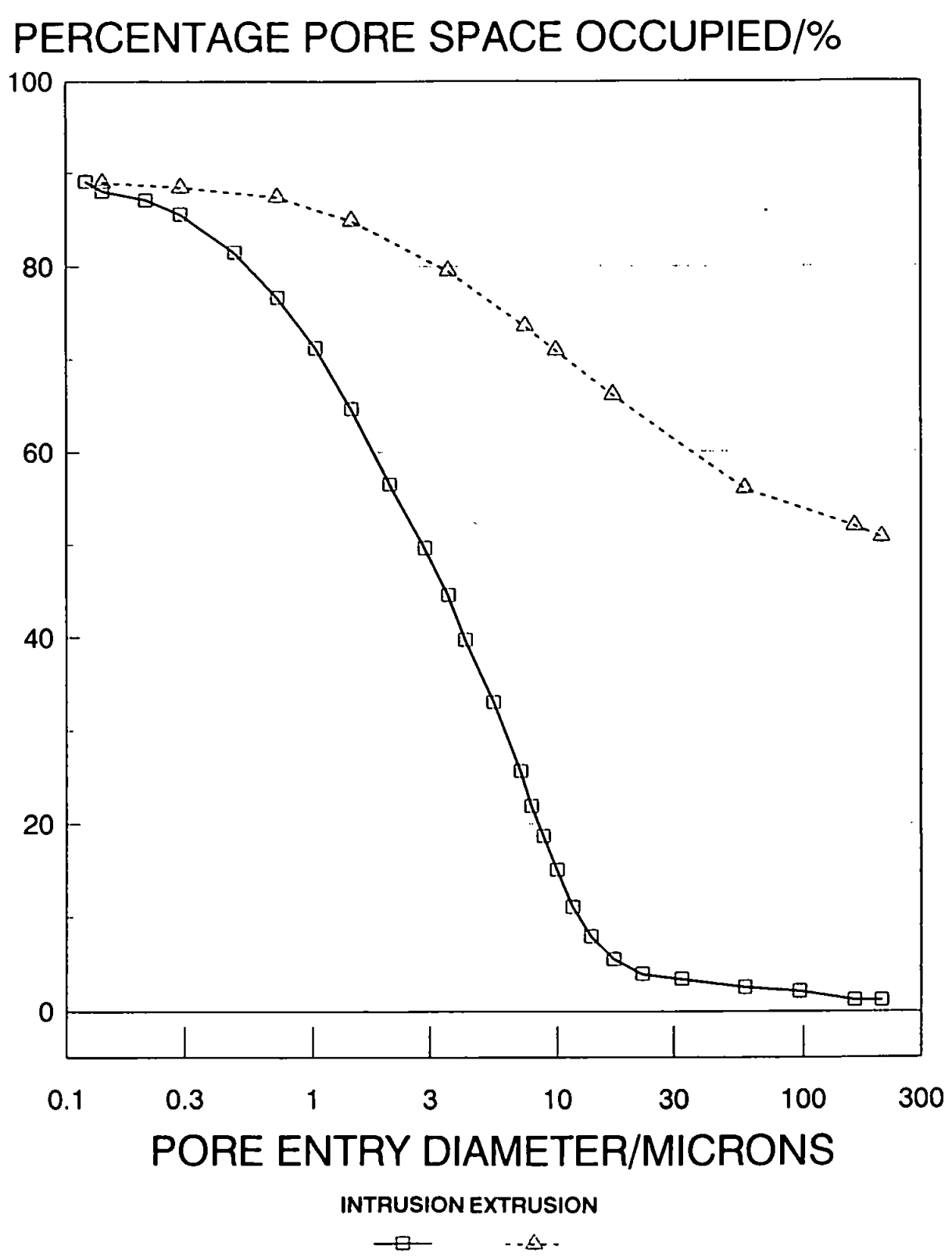

FIGURE 5.17: Mercury Porosimetry Curves for Plug 490E.

Mercury intrusion data for all samples produced the sigmoidal shape curve when percentage pore space occupied by mercury on a linear scale is plotted against pore entry diameter on a log scale. The point of inflection for each intrusion curve can be measured, Table 5.1. Samples within groups 212 and 250 were found, by scanning electron microscopy, to be relatively clay free. Points of inflection for these two groups of sandstones range from 15.44 to 33.80μm. Group 490 sandstones contain a large amount of pore lining clay, points of inflection for this group are lower that those of the clean sandstones; ie 2.95 to 12.7μm. There is a correlation between permeability and point of inflection in mercury intrusion curves. Generally higher permeability samples have higher points of inflection. It is to be expected that a sample with predominantly large pores will have a high permeability. The same sample will have a low pressure mercury break through point or percolation threshold. As mentioned earlier, mercury breakthrough and percolation threshold correspond to the intrusion curve point of inflection. Conversely clay affected sandstones have a majority of small pores and therefore low permeabilities and low points of inflection.

The geometrical parameter (G) has been calculated for each mercury intrusion curve, Table 5.1. The parameter was measured using the graphical method outlined in Thomeer (1960). This involves overlaying the experimental intrusion curve on Figure 5.2 and matching the experimental curve with the similar shaped curve from the family of curves. The relatively clay free sandstones in groups 212 and 250 have low geometrical parameters, which indicate steep mercury intrusion curves. Sample 212A has a geometrical parameter of 2.0; the shallowness of the intrusion curve for this sample is due to a high percentage of cemented pore space as highlighted in Table 3.1, Chapter 3. The clay affected samples, group 490, all have high geometrical parameters, ranging from 0.5 to 1.6. The shallower mercury intrusion curves in the clay affected sandstones are due to such factors as wide pore size distributions and low pore connectivity. The geometrical

SAMPLE NO.	PERMEABILITY/mD	POINT OF INFLECTION/μm	GEOMETRICAL PARAMETER	EXTRAPOLATED DISPLACEMENT DIAMETER/D_bμm	TRAPPED MERCURY/%
212A	50.47	17.30	2.0	34.33	28.15
212B	1413.58	29.30	0.2	39.18	31.86
212C	3161.56	33.80	0.1	47.66	____
212D	335.05	28.09	0.4	51.60	____
212E	1427.77	29.30	0.3	44.79	42.77
250A	1208.49	15.44	0.8	36.04	74.66
250E	693.52	20.83	0.1	23.79	21.67
250E REPEAT	693.52	24.34	0.1	25.53	26.94
490A	____	4.17	1.0	20.06	50.46
490B	27.06	10.80	0.5	19.01	50.24
490C	____	12.71	0.6	30.79	43.63
490D	10.71	12.71	1.0	26.22	61.92
490D REPEAT	10.71	2.95	1.6	24.85	52.22
490E	16.53	7.46	1.4	19.90	50.67

TABLE 5.1: Mercury porosimetry Results.

parameter does not correlate directly with other petro-physical properties of sandstones but it is a useful parameter to quantify the shapes of mercury intrusion curves. Figure 5.18 shows eight mercury intrusion curves plotted on the same axis. The effect of sandstone lithology on a mercury intrusion curve shape can clearly be seen. The intrusion curve shallowing effect caused by the presence of pore lining clay is in line with the findings of Neasham (1977).

Figures 5.4 to 5.17 show both intrusion and extrusion data for each sample. Extrusion data down to the lowest pressure attainable on the porosimeter used were obtained for all samples except 212C and 212D. For these two samples extrusion was stopped at atmospheric pressure (approx. 1 atm.), because at the time of their analysis the monitoring of mercury withdrawal in the vacuum region was not thought possible on the Ruska porosimeter. The percentages of mercury trapped within the pore space at the lowest attainable pressure are listed in Table 5.1. Clay free samples generally have lower percentages of trapped mercury than clay affected samples. The one exception is sample 250A, Figure 5.9. No further mercury is extruded from the pore space below atmospheric pressure. Wardlaw et al (1987) measured zero extrusion below atmospheric pressure for a sample of Indiana limestone. The extrusion data for sample 250A should not therefore be dismissed as inaccurate, just unusual for a sandstone.

The amount of mercury trapped within the pore space is related to the number of large pore/small throat connections and dead end pores within the pore network. The shape of the mercury intrusion curve depends on factors such as pore size distribution/throat size ratios and connectivity. The shallower the intrusion curve, the flatter the pore size distribution, higher the pore/throat size ratio and lower the connectivity. Thus there should be a correlation between the geometrical parameter and percentage residual mercury. Samples 212B, 212E, 250E and 250E repeat, all show such a correlation. The higher the geometrical parameter, the higher the percentage of mercury trapped.

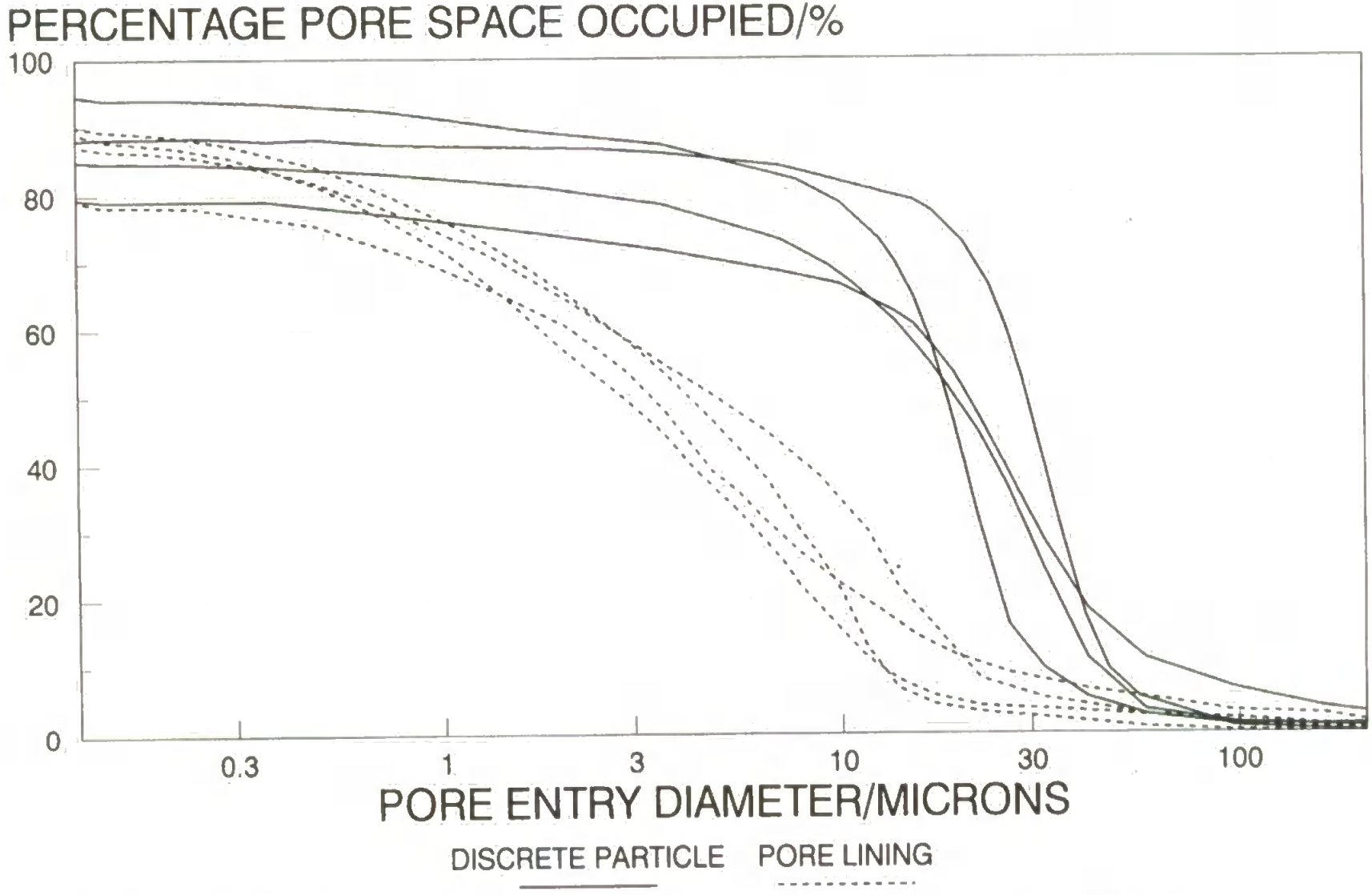

FIGURE 5.18: Mercury Intrusion Curves For Sandstones Containing Pore Lining Clay or Clay as Discrete Particles.

Sample 212A should be reviewed in isolation because it is highly cemented and has different lithology than the other clay free sandstones.

The presence of clay within the pore space adversely affects the extrusion of mercury. Group 490 sandstones generally have higher percentages of trapped mercury than the clay free sandstones. The rough surface caused by pore-lining clay will cause alteration of the extruding mercury contact angle. Work is done by the mercury whilst extruding over the clay surface. Smithwick (1986) postulated that energy losses due to friction occur during extrusion. Such energy losses will reduce the extrusion potential of the mercury.

Redistribution of clays during mercury intrusion can cause high mercury trapping percentages (Churcher et al 1990). Clay particles may move through the pore space at the head of the intruding mercury. These clays can mechanically block pores thus hindering the extruding mercury.

All extrusion data displayed in Figures 5.4 to 5.17 were collected in single day sessions. In a few cases the samples were left at the lowest pressure overnight, Figure 5.19. The two examples in Figure 5.19 show small "loops" at the end of the extrusion curves; this is due to a slight pressure rise overnight. The lowest pressure was reattained thus forming the loop. The continued extrusion of mercury overnight would indicate that perhaps equilibrium was not reached during extrusion the previous day. The results of overnight extrusion are probably spurious. To explain the results, the system needs to be calibrated at low pressure overnight. This is an area for future work.

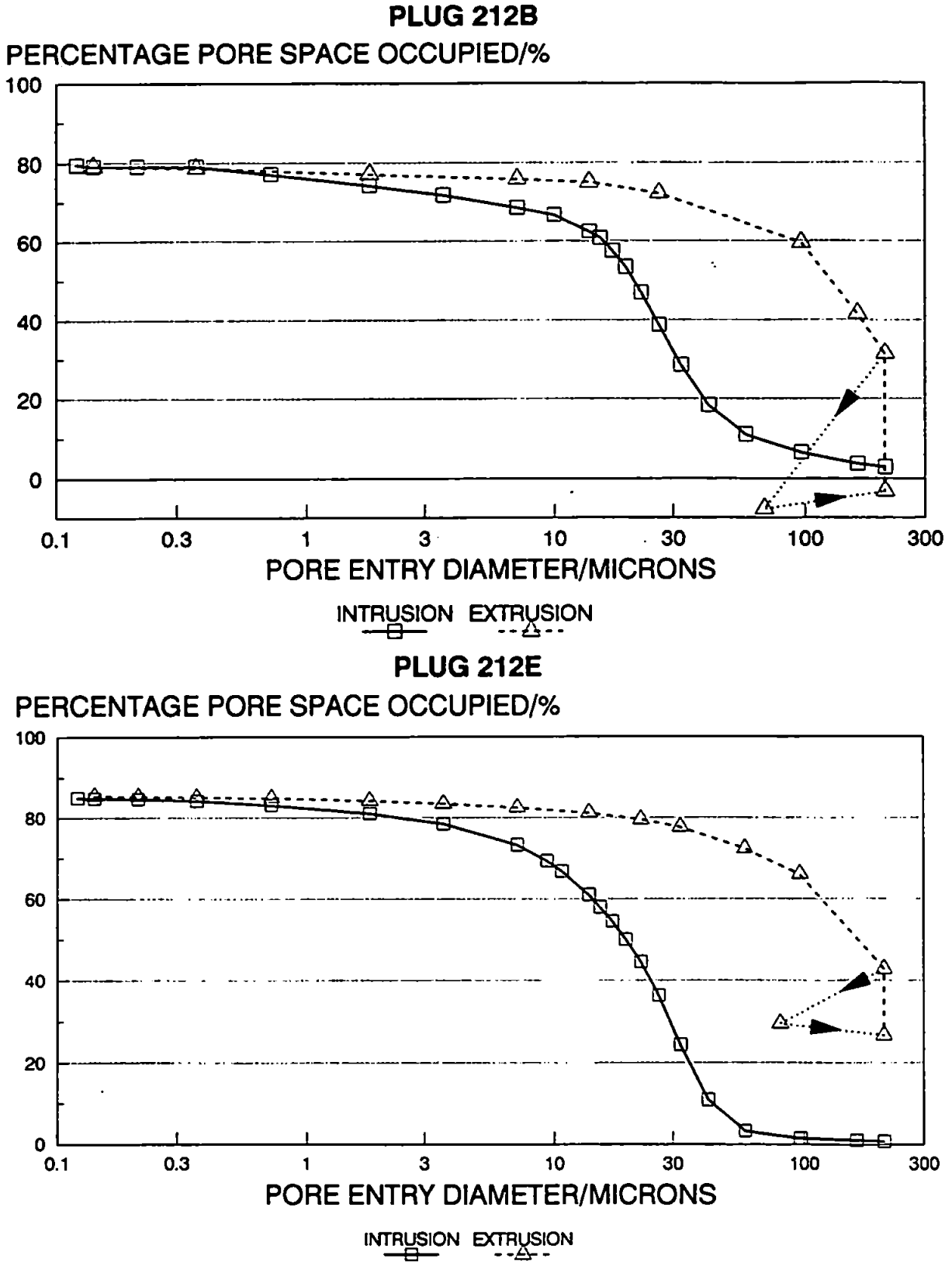

FIGURE 5.19: Mercury Porosimetry Curves Showing Increased Extrusion After Overnight Exposure to Lowest Pressure Attainable.

CHAPTER 6

IMAGE ANALYSIS

6.1 Introduction

The visual inspection of a sample is the oldest form of analysis. Optical and electron microscopes facilitate the inspection of features undistinguishable to the naked eye. "What is discreet at one scale is composite at a larger scale" - M L Thompson (1992). Computer manipulation of images started in the seventies. The introduction of fast, cheap computers has lead to image analysis being applied to a wide range of materials, ranging from sandstones soils and textiles, to biological specimens and components in nuclear reactors.

An image analysis system consists of three main computer controlled components. An image-acquisition component converts the features of the sample into a digital image which is stored in an electronic memory. In our studies, the image-acquisition component was an electron microscope under low magnification, although a high magnification optical microscope connected to a video camera could also have been used. The second component is an image processor which can manipulate and measure features within the image. Finally an image display component presents both image and calculated data in either VDU or printed form.

The advent of powerful computers has meant that intricate image manipulations and complex measurements are attainable in seconds. This advance has meant image analyzers are often used as "black box instruments", without proper regard to process and procedure.

6.1.1 Void Space Identification

The most important part of an image analysis scheme is sample preparation. The sample must be processed to preserve and highlight the features of interest. This study

involved pore size measurement, and therefore pore space had to be emphasised. The most common method of pore space enhancement involves resin impregnation of the sample. Epoxy resin is pressurised and forced into the pore space, the resin hardens and the sample is cut and polished. The polished face can be observed by backscatter electron microscopy which highlights the low molecular mass resin as dark areas (see Appendix 1). Some resins fluoresce naturally when illuminated (autofluorescence), whereas others fluoresce when stained (Bouabid et al 1992). Some workers have used Wood's metal to impregnate pore space. Wood's metal is an alloy with a low melting point of 70°C. In the liquid state, Wood's metal has a similar surface tension and contact angle to mercury, and thus Wood's metal porosimetry produces similar intrusion curves to mercury porosimetry (Dullien and Dhawen 1975). Once Wood's metal has intruded throats of a desired size calculated by the Washburn equation, the alloy is frozen. Cutting and polishing the sample facilitates inspection of the intruded pores.

The above methods of resin or alloy impregnation, followed by the cutting and polishing of the sample, produce two dimensional images from a three dimensional sample. Any measurements of the two dimensional image will only be representative of the three dimensional sample if the sample if isotropic (Thompson et al 1992). Anisotropic and inhomogeneous samples are best analyzed by taking multiple slices through the sample, a technique known as serial sectioning. A recent sandstone study by Lymberopoulos and Payatakes (1992) involved analyses of thirty serial sections approximately 7.5μm apart. From the images of the section an average three dimensional connectivity and pore:throat size correlation factor was calculated. A similar study on Berea sandstone has been performed by Lin and Cohen (1982). Serial section analysis is the most informative method for investigation of anisotropic/inhomogeneous porous media. However, the accurate mapping of clean sandstone samples would require accurately located serial sections about 0.1μm apart, and for reservoir sandstones with clay inclusions, the spacing

would need to be 0.01μm or less. At a spacing of 7.5μm, intervening layers have to be interpolated using a series of assumptions, and it is difficult to make a reliable estimate of connectivity we have therefore restricted this study to single plane image analyses. With studious selection, such analyses can provide images which reveal the data we require, namely pore size distributions and void space size correlation factors.

Obviously an image should represent the features of interest within a sample, and therefore care must be taken in selecting investigation areas and magnifications. When using a single plane through a sample to calculate a pore size distribution, the image area should include all pore sizes of interest. Samples with wide pore size distributions are difficult to analyse completely within one image. Unfortunately there is no easy way of integrating image analysis results from different scales (Thompson et al 1992).

A typical image-acquisition component within the image analyzer produces a digitized black and white image of a sample, made up of pixels of a range of 256 grey levels. Grey level 0 being black and 256 being white. As mentioned earlier, to facilitate easy feature detection there should be a large contrast between features of interest and the remaining image. Pore space impregnation produces easily detectable pore voids. When comparing many SEM images, brightness and contrast levels should be kept constant. This will produce images in which pore space is always of a certain grey level and below, thus avoiding any ambiguity about pore space recognition. The grey level below and at which, a pixel is detected is called the "threshold grey level". The selection of the threshold grey level is outlined by Gong and Newton (1992) in a study of fabric pore size distributions. Figures 6.1 and 6.2 show grey level distributions for images of a fracture surface under normal SEM mode and resin filled pore space using backscatter SEM, respectively. The threshold grey level is easier to deduce in the backscattered electron image because the pore space grey level peaks at about 64, a threshold level of about 76 would detect most of the image pore space. The grey level distribution for the SEM image of the fracture surface shows that pore space and grains have similar grey levels within this

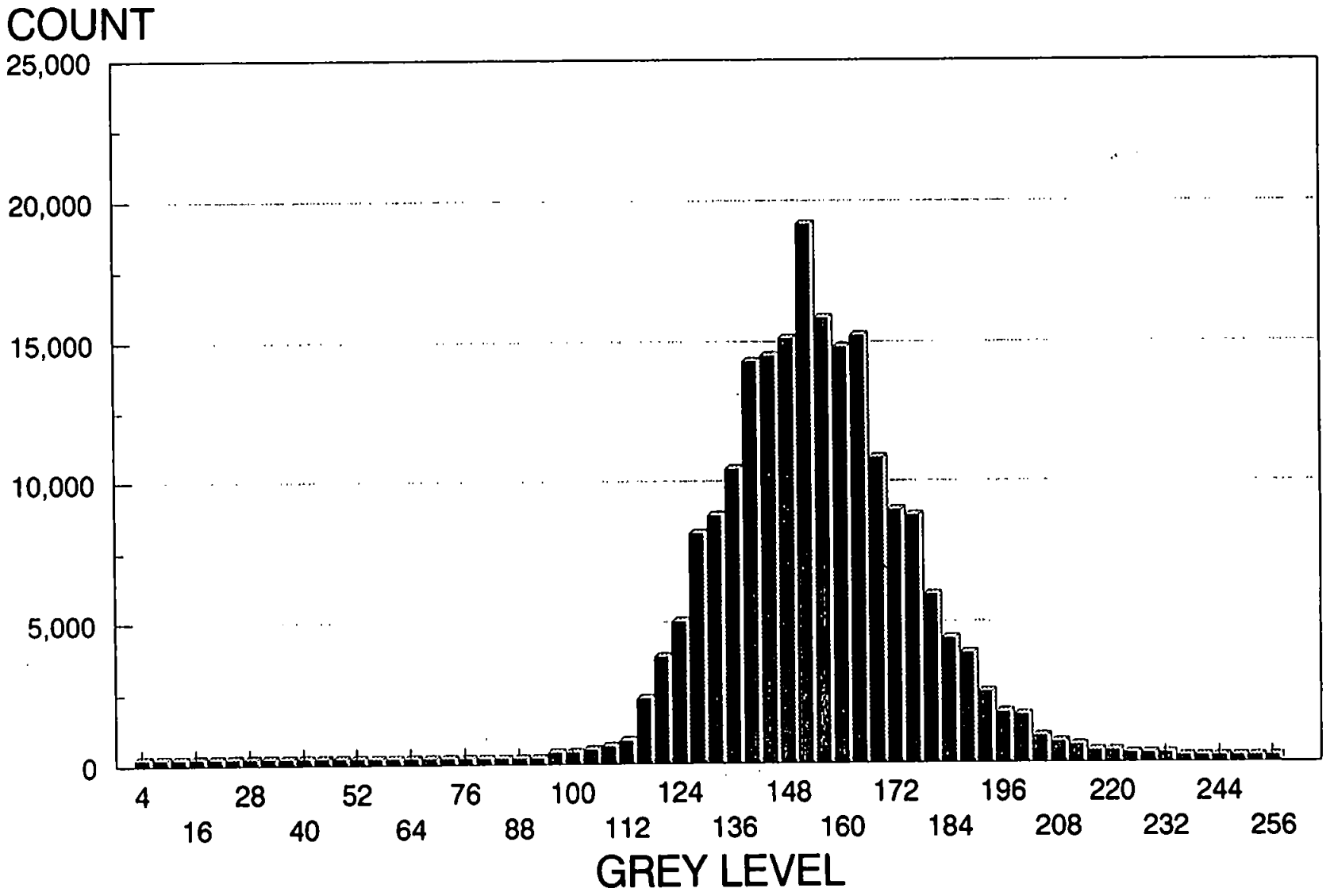

FIGURE 6.1: Grey Level Distribution of a Fracture Surface SEM Image.

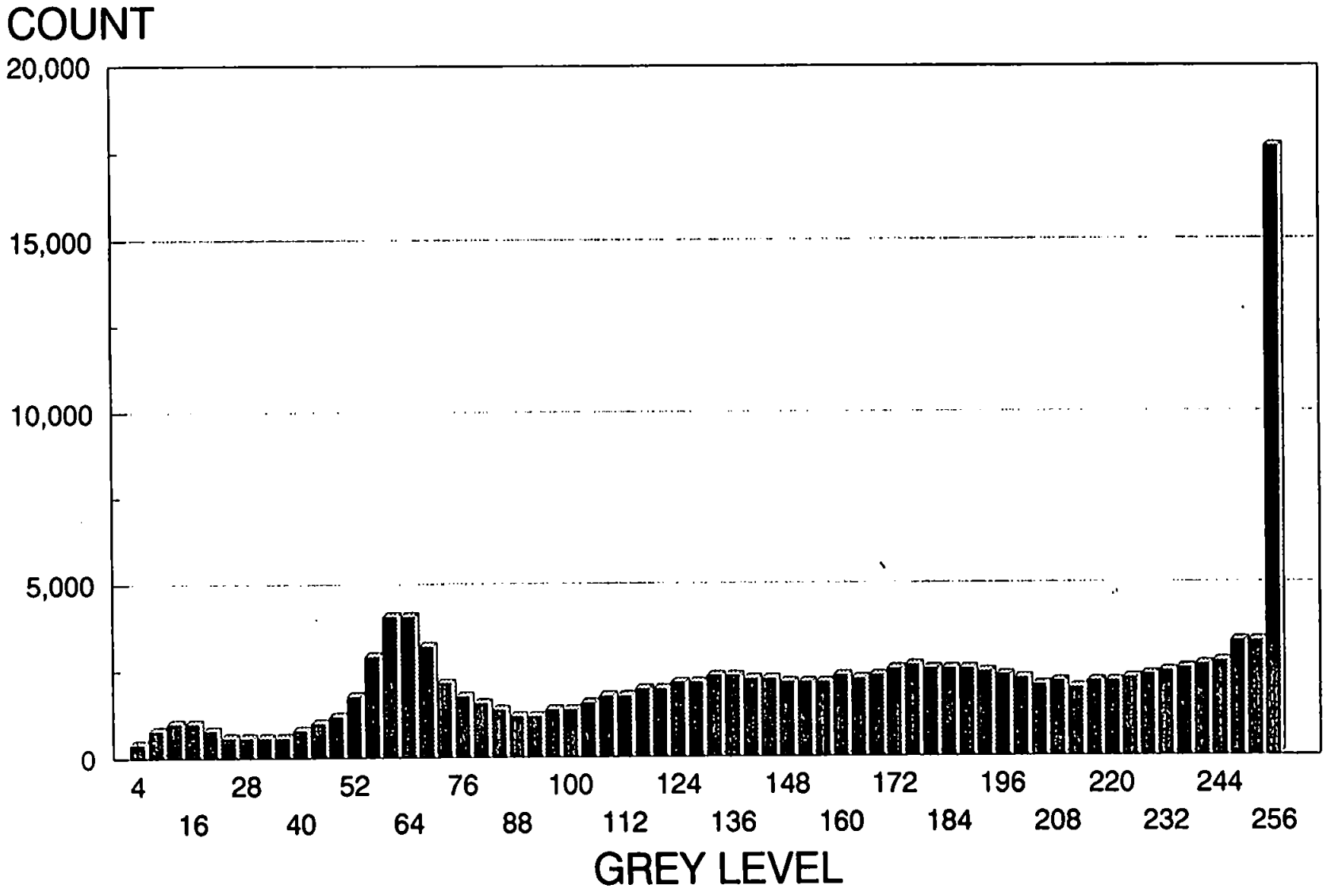

FIGURE 6.2: Grey Level Distribution from a Backscattered SEM Image of Resin Filled Pore Space, Sample 212B. (Peak at 256 due to Scale Bar)

type of image.

Threshold grey level allocation is the first step in the image processing scheme. There are numerous procedures which can be applied to the image after threshold grey level detection, including erosion, dilation and smoothing. These image processing steps are collectively known as a image analysis protocol. Any image analysis protocol should produce a final image in which pore space is easily identifiable but an accurate representation of the original grey level image (Thompson et al 1992). Any protocol should also include identification of edge features when measuring pore size distributions from two dimensional images. Any measurement on features cut by the edge of the image will erroneously effect the pore size distribution. To remove this effect, an inner frame is defined within the image and only pores whose bottom right-hand pixel are within the frame are included in the analysis. Measurement of porosity and pore size distributions are attainable if edge features are removed. Lymberopoulos and Payatakes (1992) found that the image boundary can cause problems when calculating three dimensional connectivity. Upon completion of the image analysis protocol, pore space should be easily recognisable. Each pore/throat is represented by a two dimensional shape.

6.1.2 Void Feature Measurements

In image analysis differentiation between pores and throats is difficult therefore the universal term "void" is used to describe any space between solid particles within the sandstone sample. A "void feature" is the two-dimensional expression of a void after sectioning. When comparing image analysis with other void space investigative techniques, such as mercury porosimetry, measurements should be comparable to each other. Best et al (1985) compared mercury intrusion curves with image analysis data for graphite nuclear moderators. They found that image analysis void measurements produced a void size distribution with a higher percentage of large voids than that obtained from mercury intrusion data. This is due to mercury intrusion being controlled by small voids connecting

the larger voids; thus for an effective comparison only void entry diameters should be measured. Bouabid et al (1992) reiterated Best's conclusions when using image analysis to measure soil void size distributions. Bouabid et al stated that the smallest chord length of a feature is most representative of effective capillary diameter. For complicated feature shapes, as are detected within sandstones, the minimum chord will always be one or two pixel lengths. This is because a complex shape will have "nooks and crannies" in which very small chord lengths will be measured. A more practical feature measurement which is still representative of capillary diameter is minimum feret at feature centre of gravity, also known as breadth. If we assume that breadth of a void feature is analogous to capillary diameter or pore entry diameter in mercury porosimetry, we are assuming all void entrances are perpendicular to the image plane. This assumption is not as great as that of Bouadid et al who would calculate a very low capillary diameter distribution by the minimum chord method on complex feature shapes.

Ruzyla (1986) considered the maximum feret diameter to be a measure of void diameter, a feret being the spacing between parallel tangents to a void feature in a given direction. Dullien and Dhawan (1975) defined void diameter as the mean of maximum feret intercept with the feature taken in many directions. Their study, on sandstone samples, compared void size distributions obtained from mercury porosimetry and Wood's metal impregnation/sectioning.

A slice through a three dimensional array of voids produces void features with irregular shapes. A void feature maybe an expression of a number of different size and shaped voids. A revealing form of image analysis on such images is called segmentation. A feature is eroded, as the feature gets smaller it breaks up into its principal shape components. Complete erosion will reduce each principal shape component to its centre of gravity. Each shape can be built back until it is nearly the fully connected original feature. If the reconstruction is stopped one pixel width before reconnection, the resulting features can be said to represent each interconnected void, without appreciable area loss.

The many different measurements used to quantify void size distributions using image analysis highlight the problems involved in using two dimensional images to quantify three dimensional pore space.

Image analysis has been applied to a number of the gas reservoir sandstones used throughout this study. Primarily to measure the degree of void size correlation within each sample. The void size correlation investigation described below compares results obtained from two different measurements on each detected void feature. The breadth at the void centre of gravity of every feature is measured, this being analogous to the capillary diameter of the void as described earlier. The area of every detected feature is also measured, the square root of this value being defined as the void diameter. This definition of void diameter assumes void features approximate square shapes. This is obviously an over simplification but the measurement does allow an easily calculated void diameter, which is of use in void size comparison studies such as the void size correlation investigation. The void size data obtained can also be used to calculate void size distributions. The void size distributions for a number of sandstones have been calculated using feature breadth and square root of feature area as the void size measurements, both before and after a segmentation process.

6.2 Image Analysis on Fracture Surfaces

An initial attempt to measure void size correlations involved analysis of images from an SEM study of fractured sample surfaces. Fracture surfaces were initially used because they are quick to prepare and allow EDX analysis of the relatively undisturbed surface. The major disadvantage of using SEM images of irregular surfaces for quantitative image analysis, is due to the shadowing around each exposed artifact. The shadows are impossible to differentiate from the dark areas caused by the voids.

To overcome this three images were obtained from the same area of the specimen. The images differ only in their orientation to the SEM detector. The second and third

images being created by rotating the sample clockwise through 90° and 180° respectively from the original position. The three images are digitized and stored in a TIFF format, a format compatible with most image analyzers. Each image is made up of 256 grey levels, 0 being black and 256 white. Image analysis is performed on a Cambridge Quantimet 570 instrument. A computer program has been written on the Quantimet 570 to allow analysis of the three images.

The three images are imported into the Quantimet 570. The second and third images are rotated anti-clockwise by 90°and 180° degrees respectively. A one pixel marker is placed on all three images at an easily identifiable point. The centre of gravity for the three created markers is recorded. The differences between the three x and y coordinates are then used to move the rotated grey images to a comparable position of the first. All three images are then detected for voids and shadows, ie. a threshold grey level is set. The resulting binary planes are 'superimposed' so that when any feature is detected in all three planes the resulting feature is kept. To prevent loss of features due to the original markers not being coincident a build is done back into the original detection of image one. As these features occur in all three images they can not be shadows but deep seated pores.

The procedure described above successfully removed the detected area caused by shadowing but the resulting detected voids are only those deep within the rough fracture surface. An analysis of correlations between these would give erroneous results because only pores dominant at depth would be analyzed. Unfortunately this novel procedure is unable to supply suitable images for a void size correlation study. The technique does illustrate the power of image analyzers and may find an application in other studies involving rough surfaces.

6.3 Image Analysis on Resin Filled Void Space

Due to the failure of the fracture surface rotation procedure, the traditional method

of resin filling the void space has been used. This allows the acquisition of images suitable for pore size correlation analysis. Fragments of six sandstones have been resin impregnated, the analysis of two of these samples 212B and 212E is outlined in detail.

Sample 212B was strongly banded in appearance, had a porosity of 21.2% and a permeability of 1410.5md. Sample 212E was less strongly banded with a porosity of 22.0% and permeability of 1427.8md.

The void space of each sample was pressure saturated with epoxy resin (Araldite). After resin curing, the samples were cut perpendicular to any banding, and cut surface ground using carborundum paste. After grinding, the surface was checked for any un-filled pores using an optical microscope. Any sample with unimpregnated void space is resaturated in resin and reground.

Images of each sample were collected on a Joel 6100 scanning electron microscope (SEM) with backscattered electron detector. Samples were carbon coated to facilitate conductance when operating the SEM. The resin filled void space appeared black when observed in backscatter mode. Images were set with a high contrast so that the dark void space is easily detectable. Backscatter SEM images can be collected as polaroids or digitized. Digitization produces an image (TIFF Extension) which is superior to polaroid images. Image analysis was performed on the Quantimet 570 instrument. Figure 6.2 shows the grey level distribution for a backscattered SEM image of 212B with resin filled void space. The backscatter distribution shows a peak at about grey level 64, due to the dark resin filled voids. Thus, as mentioned previously, a threshold grey level of 76 would detect most of the image void space.

The backscattered SEM image of sample 212B is shown in Plate 6.1; magnification is x33 and the image is 3.3mm long. Plate 6.2 shows the image of 212B with all pixels of grey level 76 and below detected in red. As mentioned earlier, edge features can give erroneous void size distributions, and therefore a guard frame is placed in the centre of the

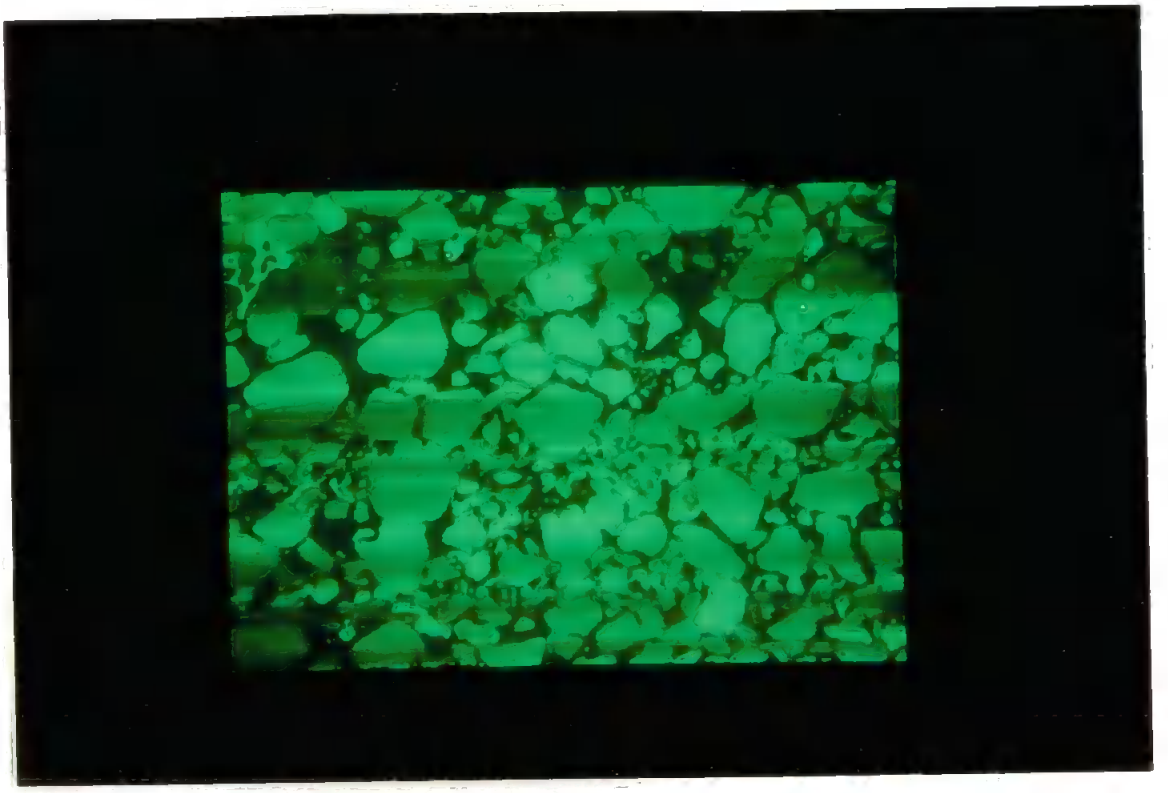

PLATE 6.1: Backscattered SEM Image of Sample 212B. The Image is 3.3mm Long.

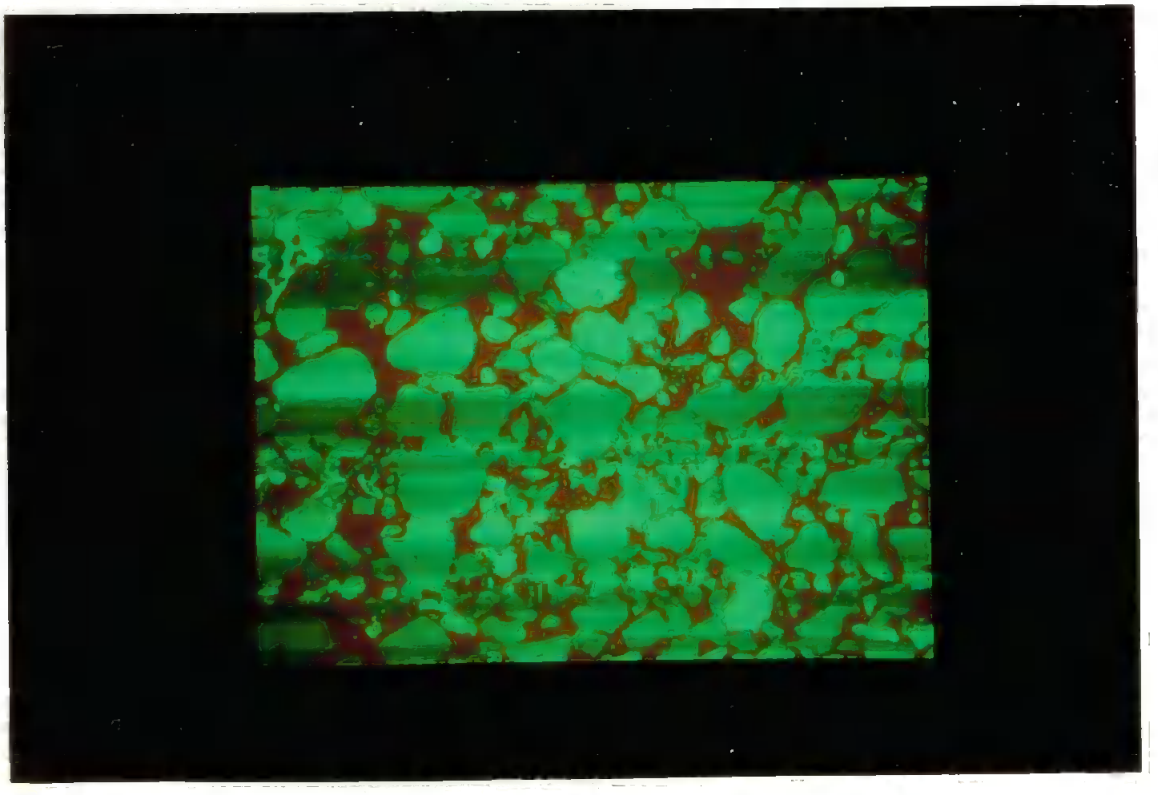

PLATE 6.2: Backscattered SEM Image of Sample 212B With Grey Level Detect of 76 Shown in Red.

image. Only features whose top right hand pixel is contained within the guard frame are counted. Experimentation with the guard frame size produces a detect area in which no feature is cut by the image edge, Plate 6.3. Each feature can be numbered for easy identification, as shown. Before any feature measurement can be executed the image analyzer must be calibrated, using an image scale bar which does not appear in Plates 6.1 to 6.3. The 212B image was calibrated to 6.536μm per pixel. After calibration, it is possible to make absolute measurements of many features such as area, length, breadth and distance between centres of gravity of two features. The results can be output as hard copy or as a data file. Plate 6.4 shows the segmentation process applied to sample 212B; the detected area is the same as Plate 6.3. Comparison of Plates 6.3 and 6.4 shows that complicated pore features have been split into features more recognisable as an idealized interconnecting void network.

The same image analysis procedure was also applied to sample 212E. Plate 6.5 shows the backscattered SEM image of sample 212E at a magnification of x50, the image being 2.28mm long with a calibration of 4.545μm per pixel. Detected area and feature numbers are shown in Plate 6.6 and detection after segmentation in Plate 6.7.

6.4 Void Size Distributions

Data from the images of samples 212B and 212E can be analyzed to calculate void size distributions. Figures 6.3 and 6.4 are void size distributions for the images of samples 212B and 212E respectively. The features are grouped into 20 size ranges, indicated by the discontinuities in graph lines. The vertical axis is the number of features in a particular size range divided by the total number, expressed as a percentage.

Figure 6.3 shows that void breadth in sample 212B ranges from 13μm to 778μm. Sample 212E has a void breadth range of 4.545 - 359 μm, Figure 6.4. The smallest size

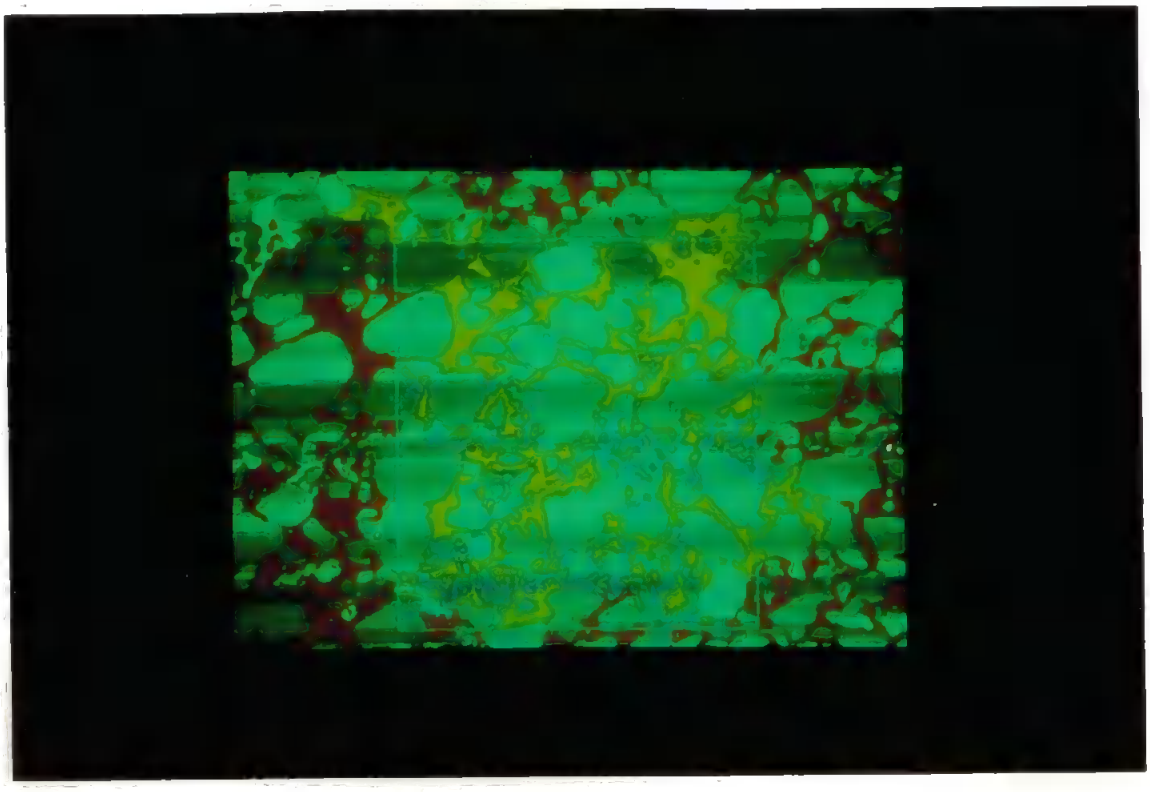

PLATE 6.3: Backscattered SEM Image of Sample 212B With Detect and Guard Frame Indicating Analysis Area. Individual Features Numbered.

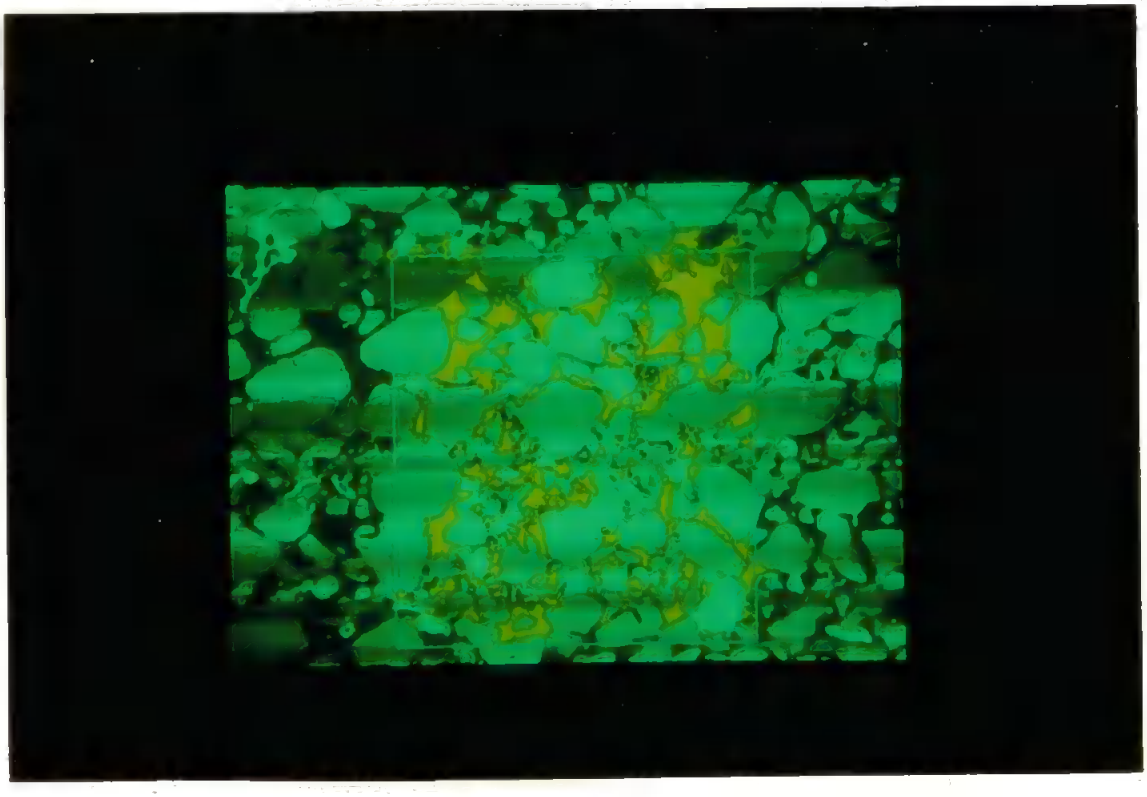

PLATE 6.4: Backscattered SEM Image of Sample 212B With Detect and Segmentation.

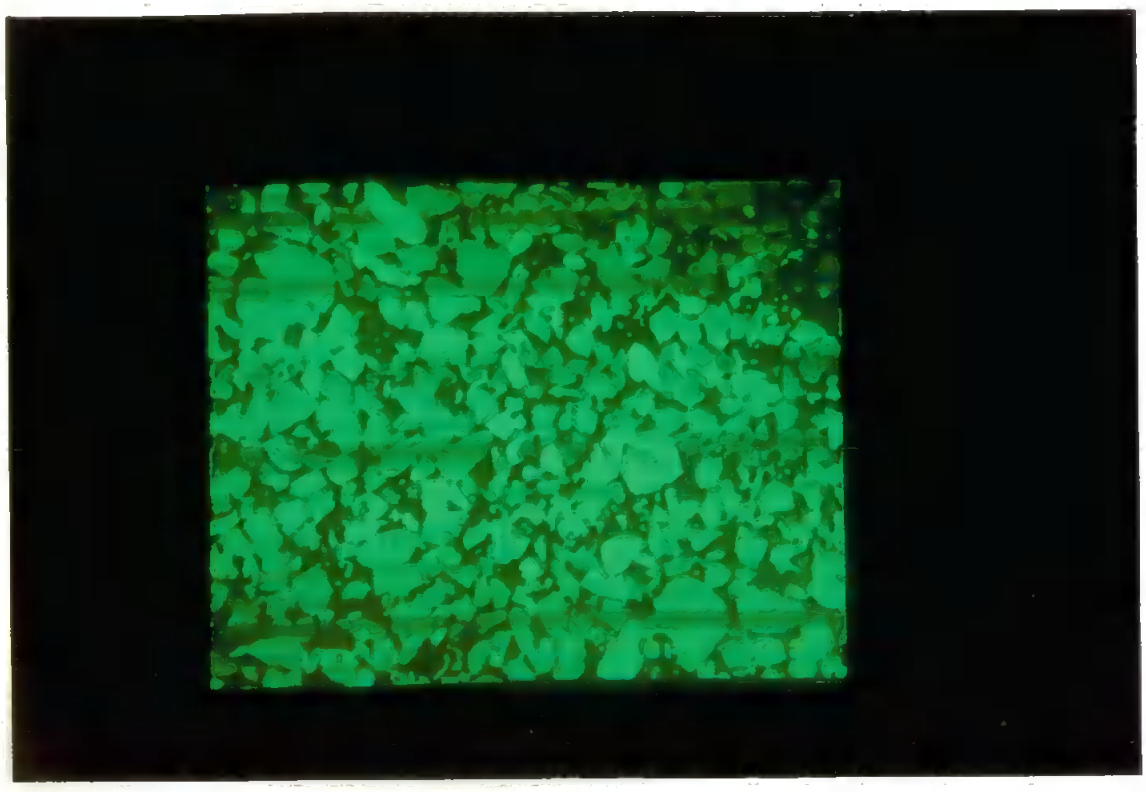

PLATE 6.5: Backscattered SEM Image of Sample 212E. The Image is 2.28mm Long.

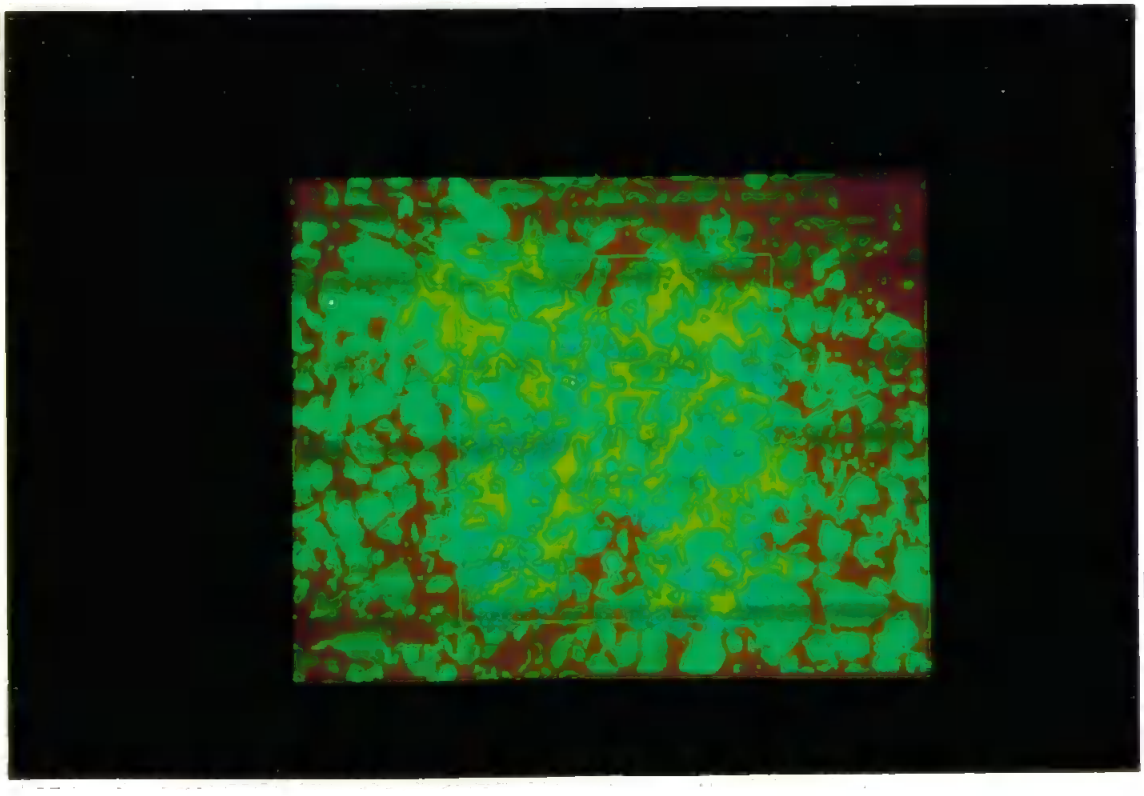

Plate 6.6: Backscattered SEM Image of Sample 212E With Detect and Guard Frame Indicating Analysis Area. Individual Features Numbered.

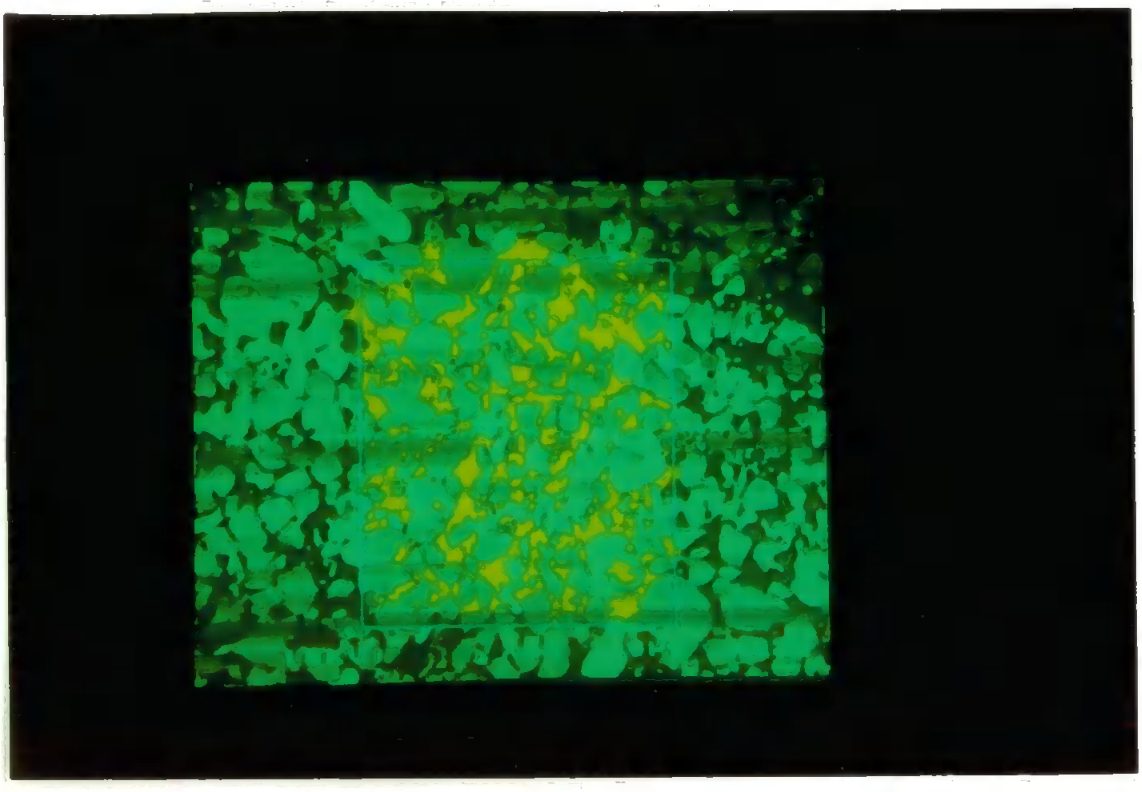

PLATE 6.7: Backscattered SEM Image of Sample 212E With Detect and Segmentation.

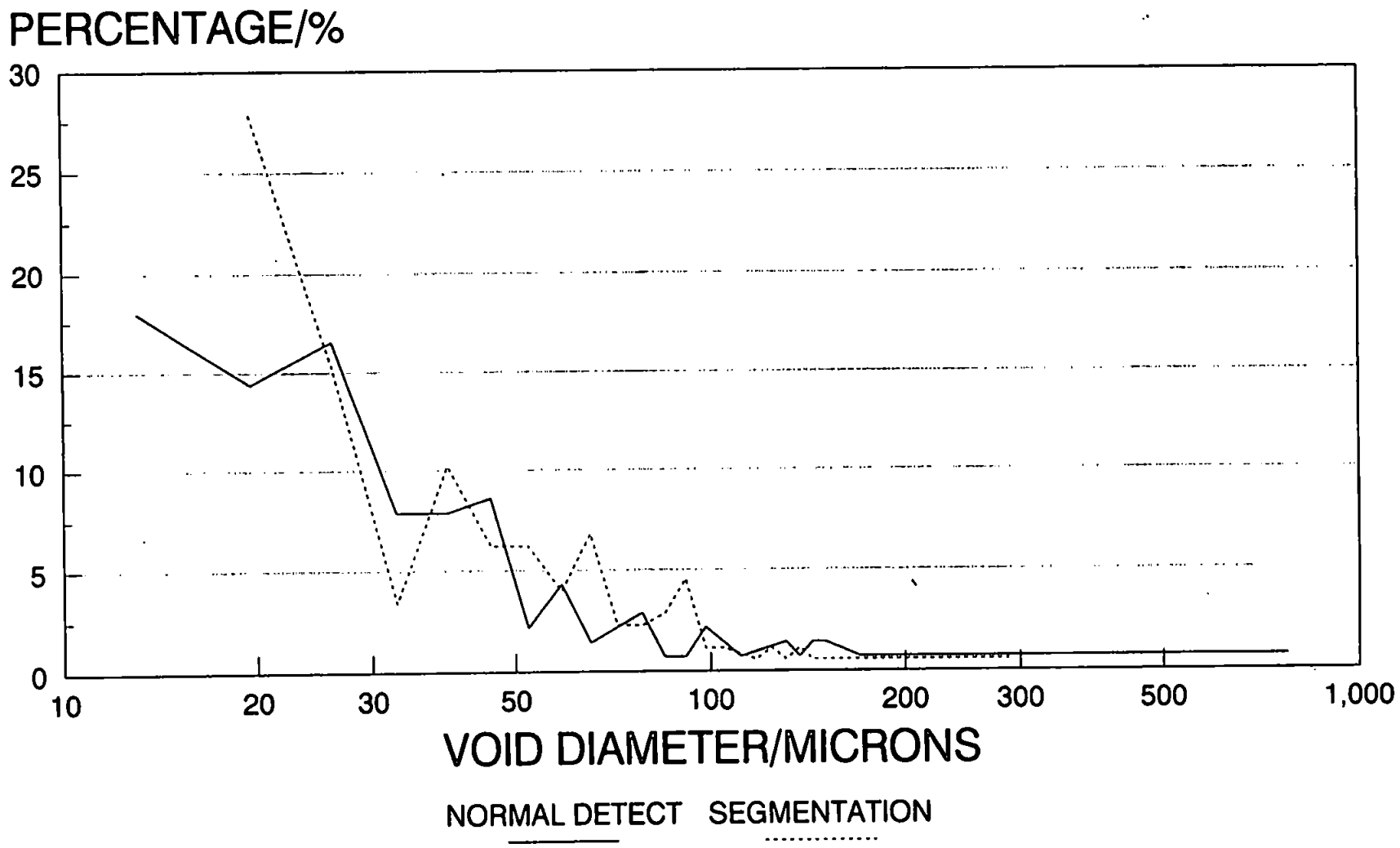

FIGURE 6.3: Void Size Distribution for Image Analysis of Sample 212B.

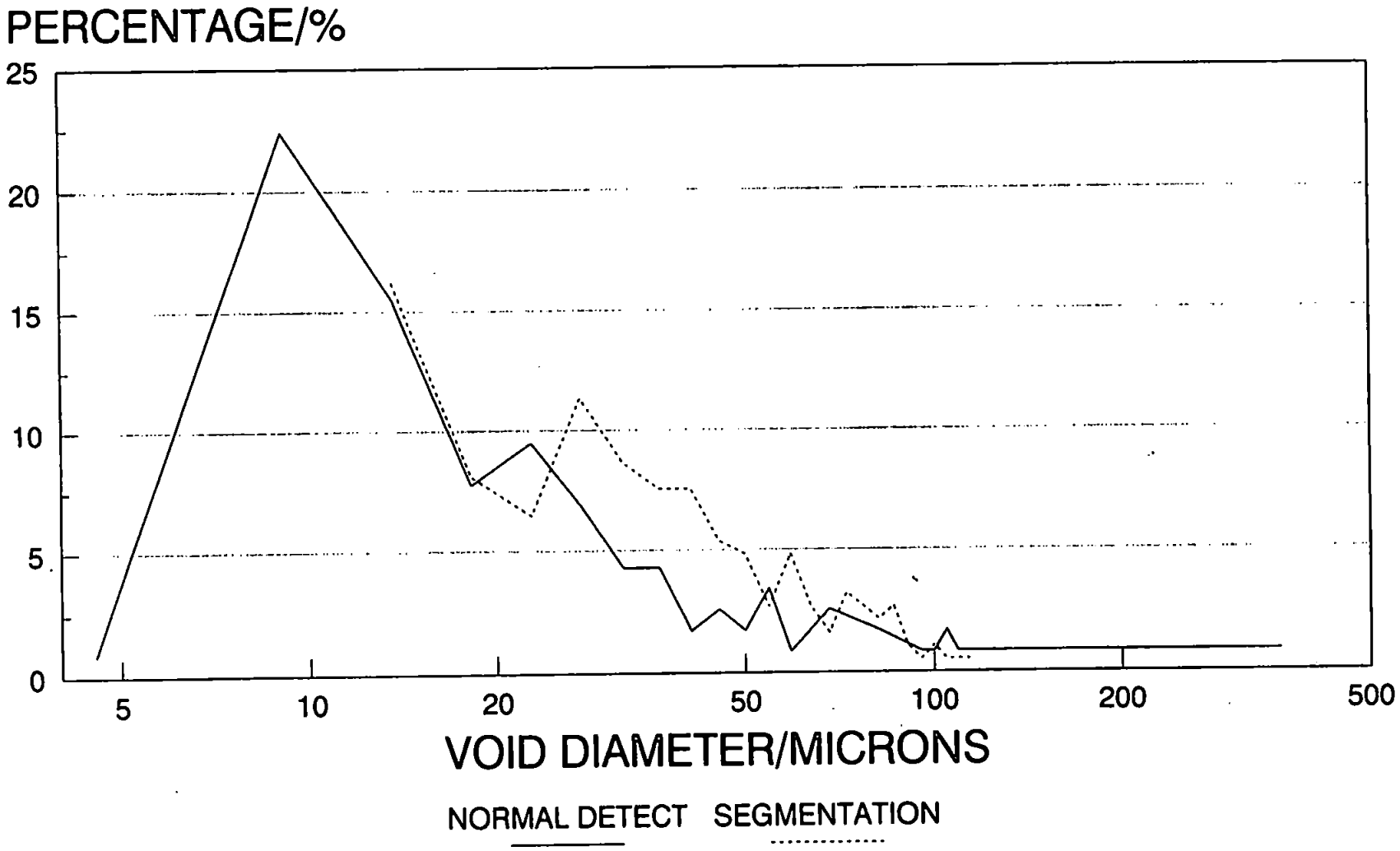

FIGURE 6.4: Void Size Distribution for Image Analysis of Sample 212E.

of any void space distribution derived from image analysis is dependent on the magnification of the image. A feature has to be at least one pixel in size and thus the pixel calibration defines the smallest feature size possible. Figure 6.3 shows that the smallest void detected in sample 212B had a breadth of 13μm, ie. two pixels wide. Sample 212E contained voids of 4.5μm breadth, ie. one pixel wide. Obviously smaller voids could only be detected if the images were of higher magnification, but then the observation area becomes smaller and unrepresentative of the whole sample. Both samples have void distributions skewed towards the smaller sizes and very few features above 100μm.

Void size distribution data can be plotted as cumulative void area against void diameter. Figure 6.5 shows such distributions for a range of feature measurements on sample 212B. An obvious effect of segmentation is to increase the percentage of the smallest voids. The cumulative void size distributions for sample 212E are shown in Figure 6.6. Comparing the segmentation distributions for both samples it can be seen sample 212B has a more open void space. Approximately 65% of sample 212B is made up of voids 100μm and below, whereas nearly 100% of sample 212E's void space is within this size range.

Figures 6.7 and 6.8 show void space distributions obtained from both segmented and normal detect images, compared with the mercury intrusion curves for samples 212B and 212E. Void entry diameter in image analysis is take as the breadth of void feature at the centre of gravity as described above. Image analysis distributions are all overestimated compared to mercury intrusion distributions, in line with the findings of Best et al (1985). For both samples the segmentation distribution is a closer fit to the mercury intrusion distribution than the normal detect distributions. This is because segmentation splits the complex void feature shapes into their principal component shapes, these being more representative of the void network than the complex void shapes. The discrepancy between the segmentation distributions and the mercury intrusion distributions is due to the

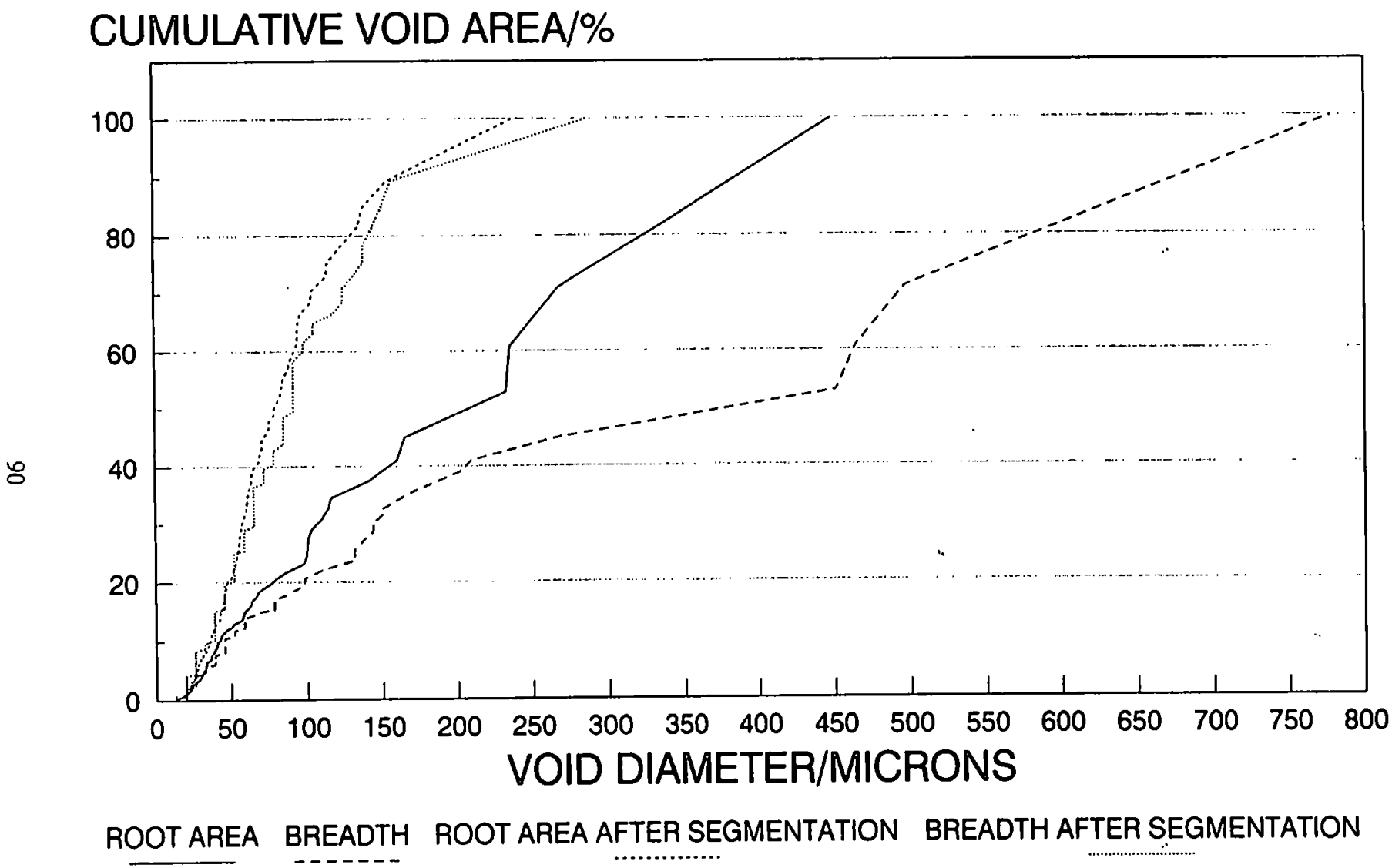

FIGURE 6.5: Cumulative Void Size Distributions for Different Feature Measurements on Sample 212B.

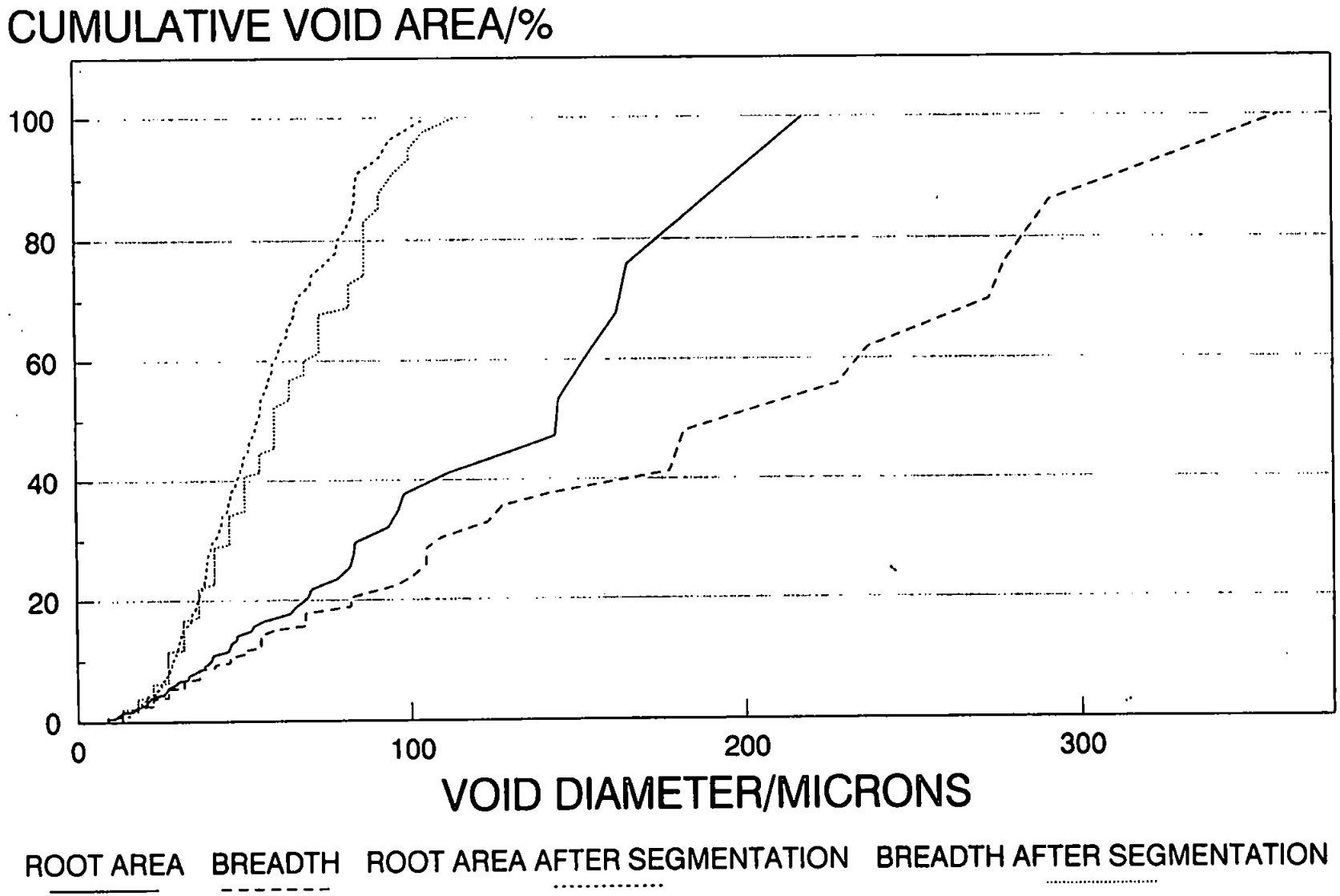

FIGURE 6.6: Cumulative Void Size Distributions for Different Feature Measurements on Sample 212E.

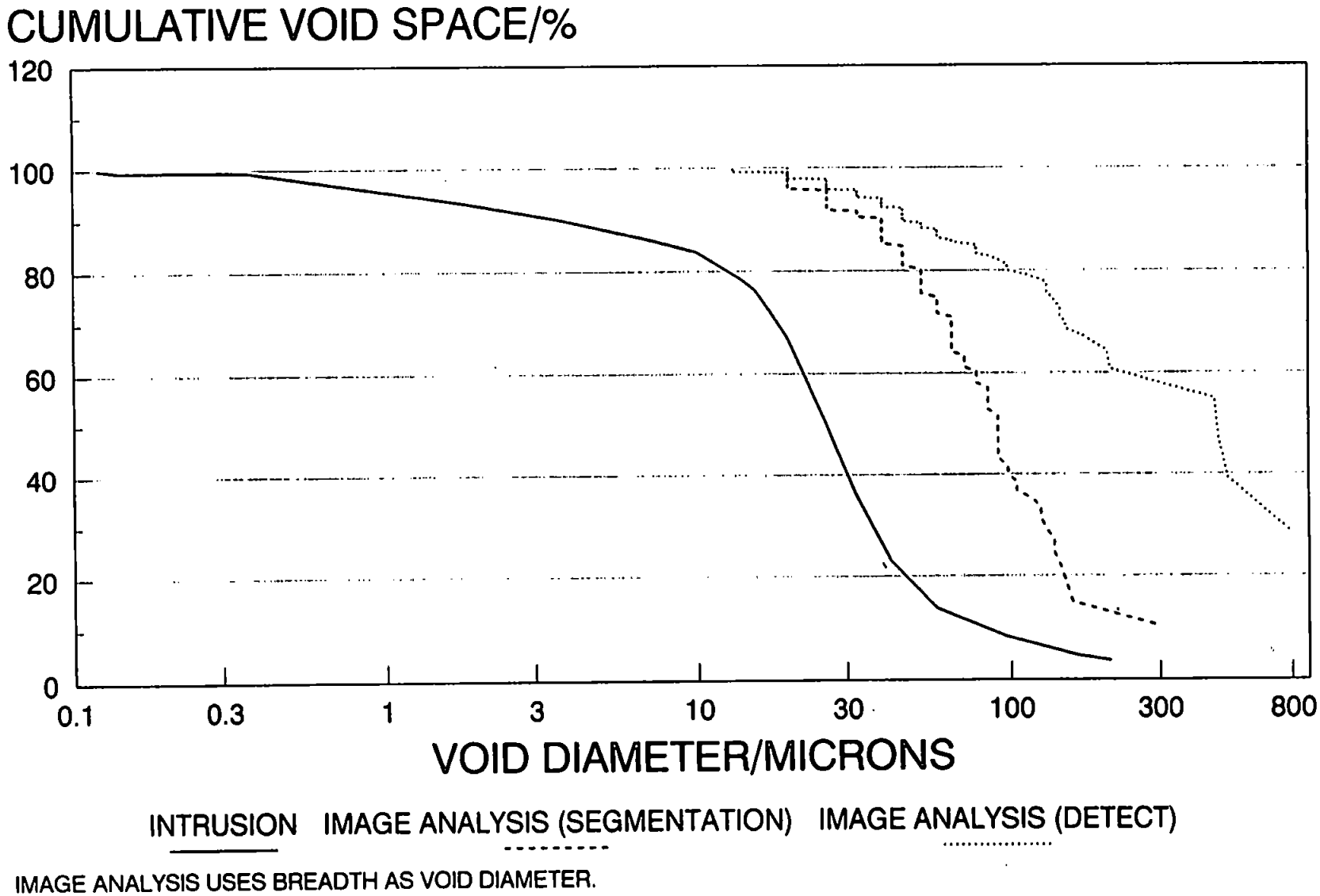

FIGURE 6.7: Comparison of Cumulative Void Size Distributions From Image Analysis With Mercury Intrusion Data for Sample 212B.

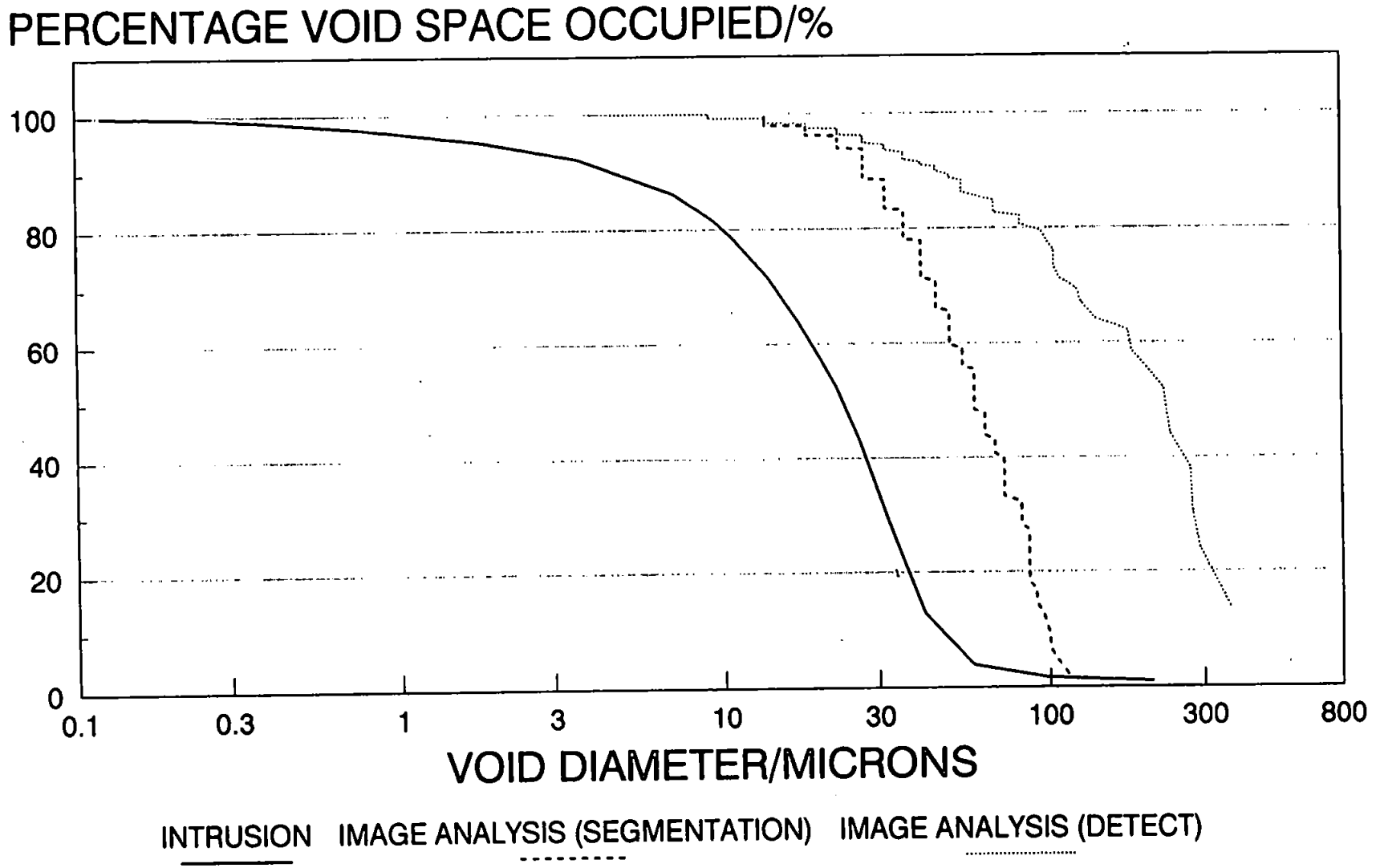

FIGURE 6.8: Comparison of Cumulative Void Size Distributions From Image Analysis With Mercury Intrusion Data for Sample 212E.

shielding effect of the void network during mercury intrusion. The shielding effect is described in detail in Chapter 5. Mercury cannot penetrate a large pore until a high enough pressure is reached to penetrate the smaller pore entrance (throat). Thus this shielding effect shifts the mercury intrusion void size distribution to the smaller void sizes. The difference between the segmentation and intrusion distributions is a measure of this shielding effect. Figures 6.9 to 6.12 show the void size distributions for samples 212A, 250A 490D and 490E. Unfortunately the segmentation process was not applied to these images.

6.5 Measurement of Void Size Correlation

Porous media investigators usually measure the media's void size distribution and co-ordination number and decline to investigate void size correlation. The importance of void size correlation on the transport properties of porous media has long been known. Tsakiroglou and Payatakes (1991) demonstrated that simulated mercury intrusion curves had a less pronounced point of inflection within pore-pore and pore-throat correlated models. Ioannidis and Chatzis (1993) obtained similar results in a correlated void space model used to simulate oil-water drainage capillary pressure curves for sandstones.

The need to measure void size correlation factors for effective modelling is obvious but such studies are rare. Wardlaw et al (1987) measured pore:throat size correlations of Berea sandstone and Indiana limestone using Wood's metal porosimetry coupled with image analysis. Pore-throat size correlation was high within the limestone but the sandstone had a weak correlation. Lymberopoulos and Payatakes (1992) found weak pore-pore correlation within a sandstone, but significant pore-throat correlation during a serial section analysis. The Wardlaw investigation involved tedious pore counting methods to

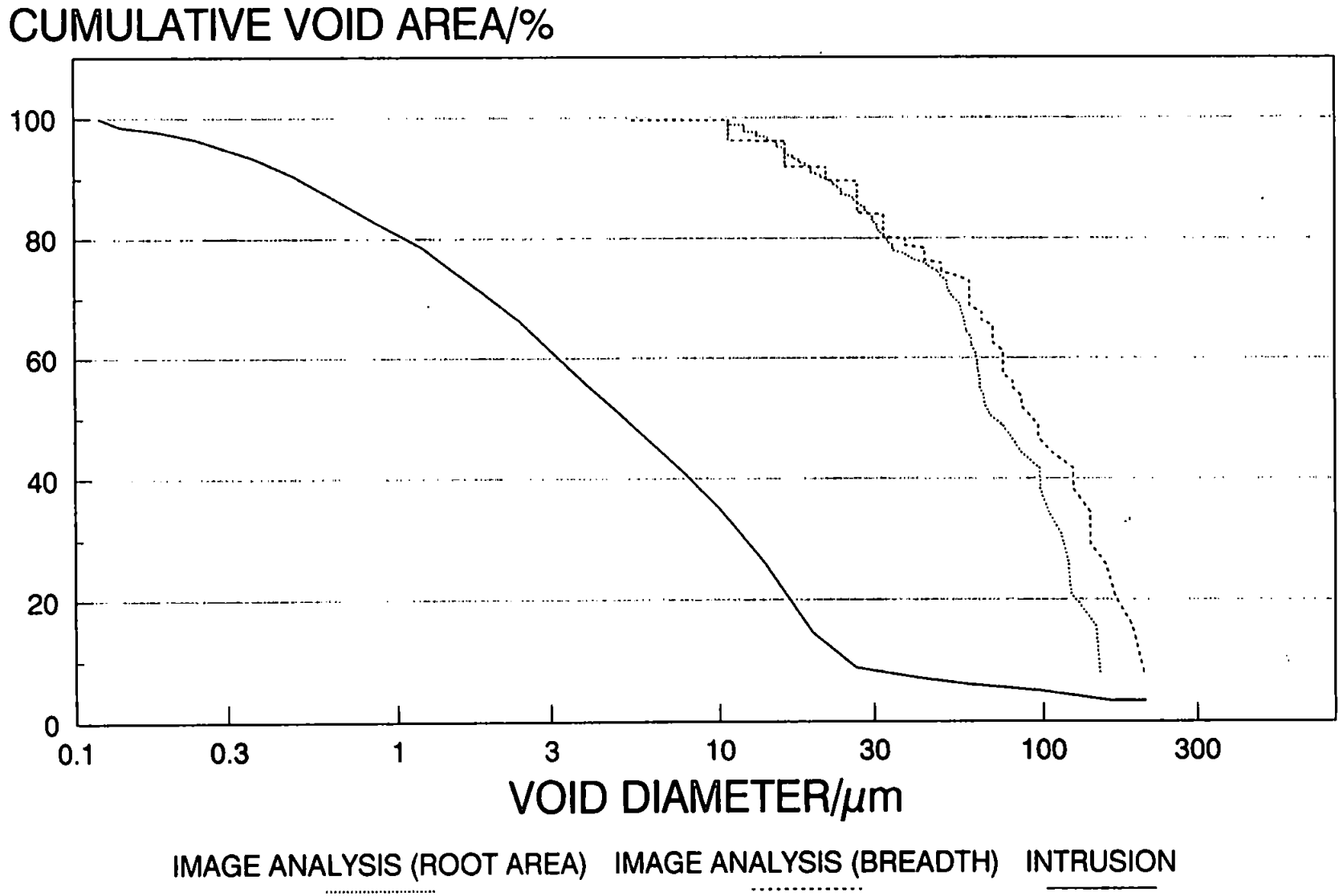

FIGURE 6.9: Comparison of Cumulative Void Size Distributions From Image Analysis With Mercury Intrusion Data for Sample 212A.

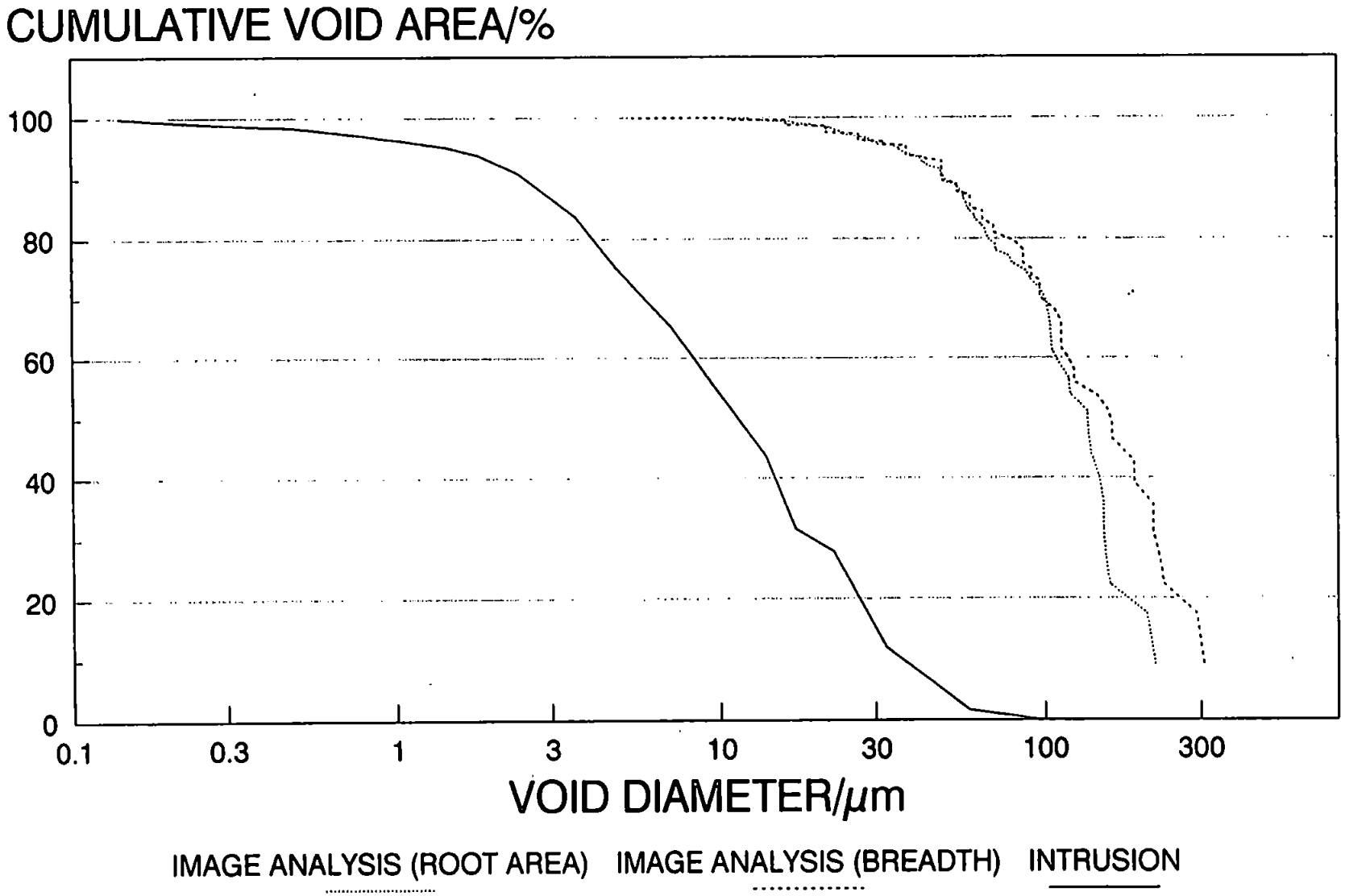

FIGURE 6.10: Comparison of Cumulative Void Size Distributions From Image Analysis With Mercury Intrusion Data for Sample 250A.

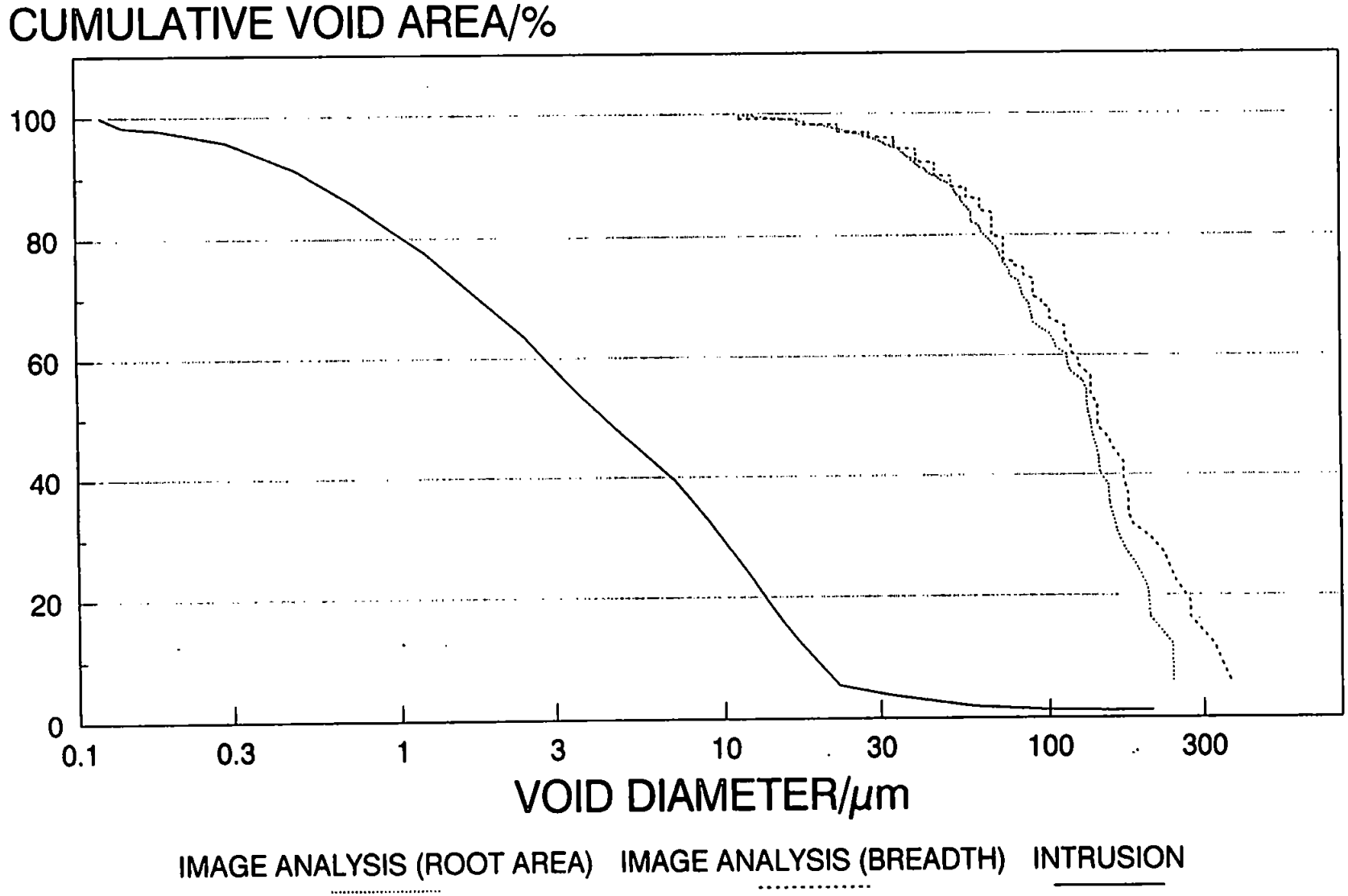

FIGURE 6.11: Comparison of Cumulative Void Size Distributions From Image Analysis With Mercury Intrusion Data for Sample 490D.

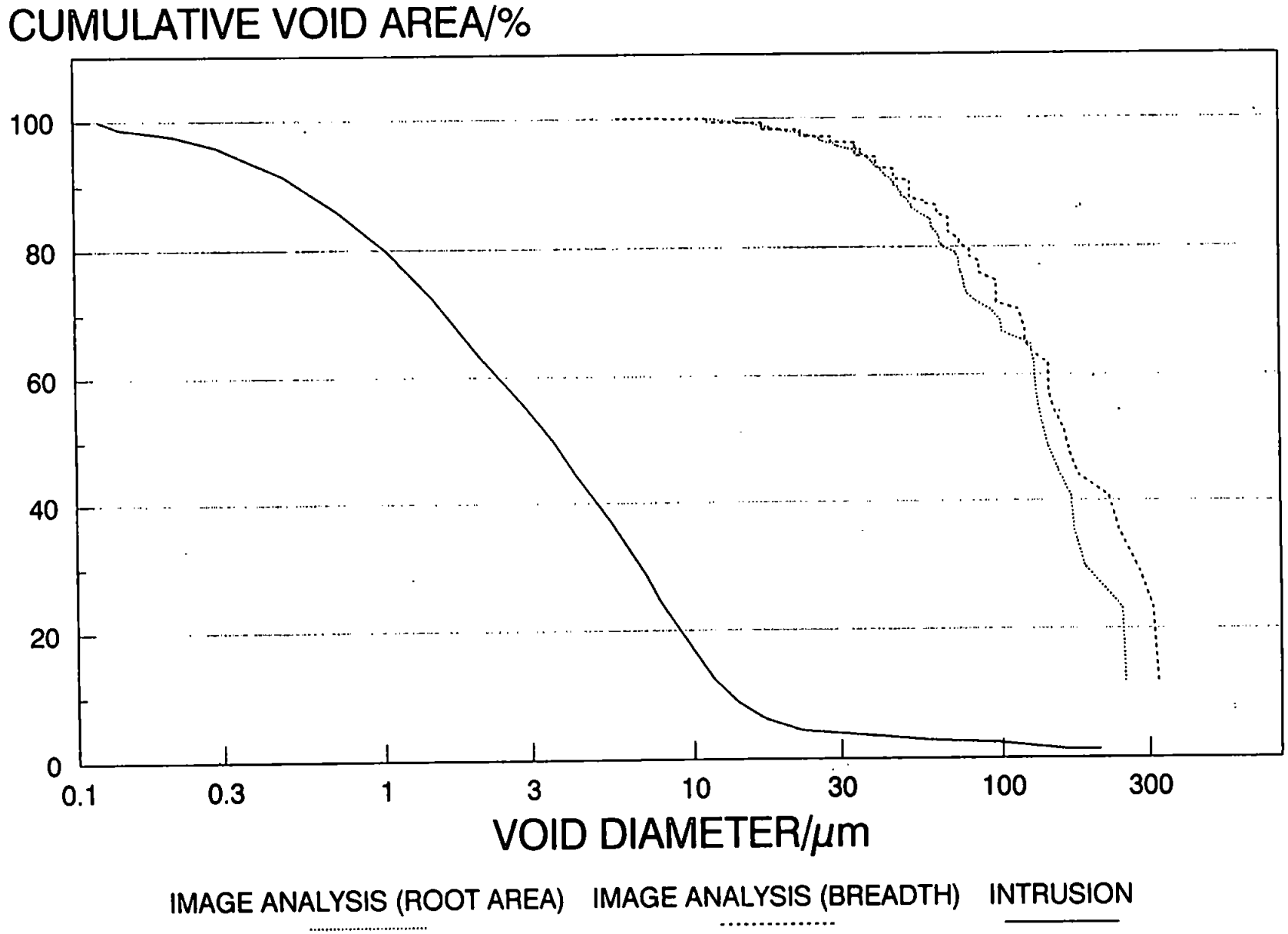

FIGURE 6.12: Comparison of Cumulative Void Size Distributions From Image Analysis With Mercury Intrusion Data for Sample 490E.

calculate the correlations. Lymberopoulos and Payatakes devised an original program for pore and throat recognition and measurement. Both the above methods are time consuming in application or development so we have followed an alternative approach to void space correlation measurement. To test the void size correlation measurement method, an ideal highly correlated porous media was developed. This correlated system consisted of two sintered glass discs of different pore size ranges. The coarse disc had a pore size range of 100-160μm and the fine disc had a 16-40μm pore size range. These discs were stuck together and ground flat using silicon carbide paste. An image of the discs is obtained by scanning electron microscopy (Plate 6.8) and this image processed by image analysis (Plate 6.9). The threshold grey level on Plate 6.9 was 123 and the calibration was 6.579μm per pixel. The area and centre of gravity of each detected pore feature was saved as a data file for future analysis. As in the void size distribution measurement, the square root of the void feature area is taken as the void diameter. Figure 6.13 shows a graph of difference in the log of diameter between a large void feature and all other features, for the three largest features. The regression analysis indicates a slight correlation, $R^2 = 0.164$ to 0.327. The above analysis was applied to the ten largest void features, a similar scatter of points as Figure 6.13 was obtained. The clustering of points in the upper right hand corner of Figure 6.13 indicates that most small void features are a long way from the biggest void features. The wide scatter in Figure 6.13 highlights the problem of using two-dimensional sections of three-dimensional porous media.

Although an area of a porous structure may contain all large voids, when sectioned only small expressions of these voids may be cut by the section plane. Within the large pore region of the sintered glass image, small pores are found. These small expressions of large pores adversely effect the correlation measurements.

Applying the above analysis to the resin filled sample 212B (Plate 6.3), no correlation was found, Figure 6.14. Although the image has distinct areas of large and

PLATE 6.8: SEM Photo Micrograph of Sintered Glass Disc.

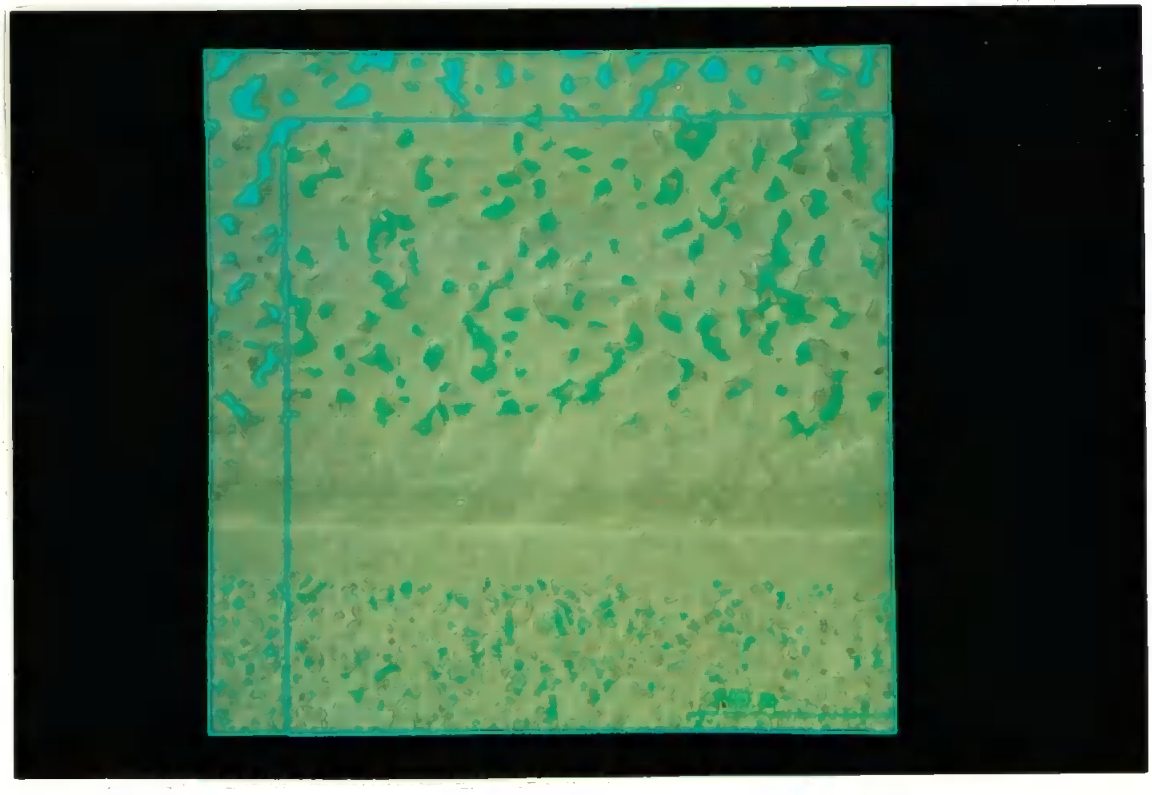

PLATE 6.9: SEM Photo Micrograph of Sintered Glass Discs With Grey Level Detect of 123 and Guard Frame.

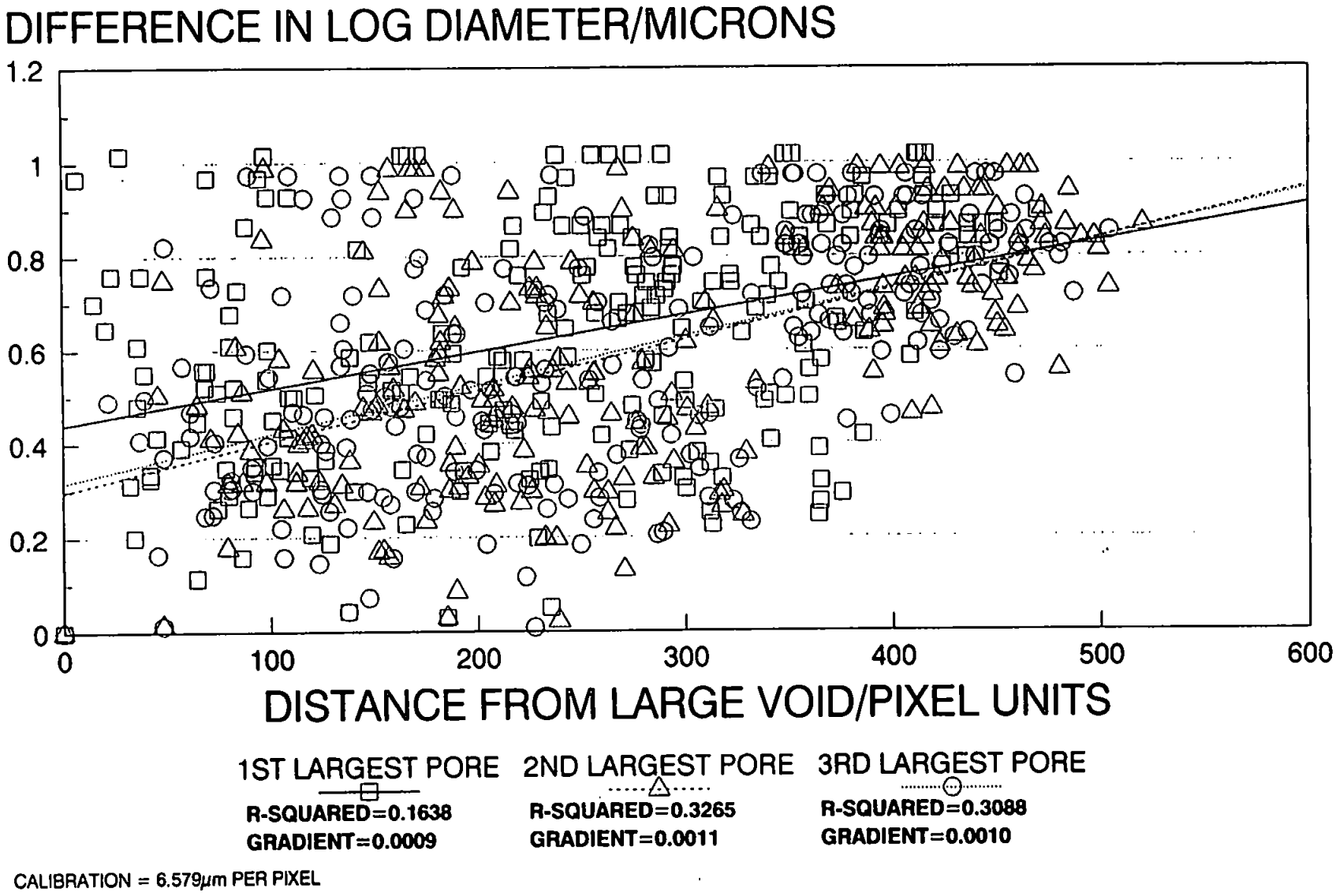

FIGURE 6.13: Difference in Log Diameter Between Largest Void and All Other Voids Against Distance From Largest Void for the Three Largest Voids Detected in Sintered Glass Image.

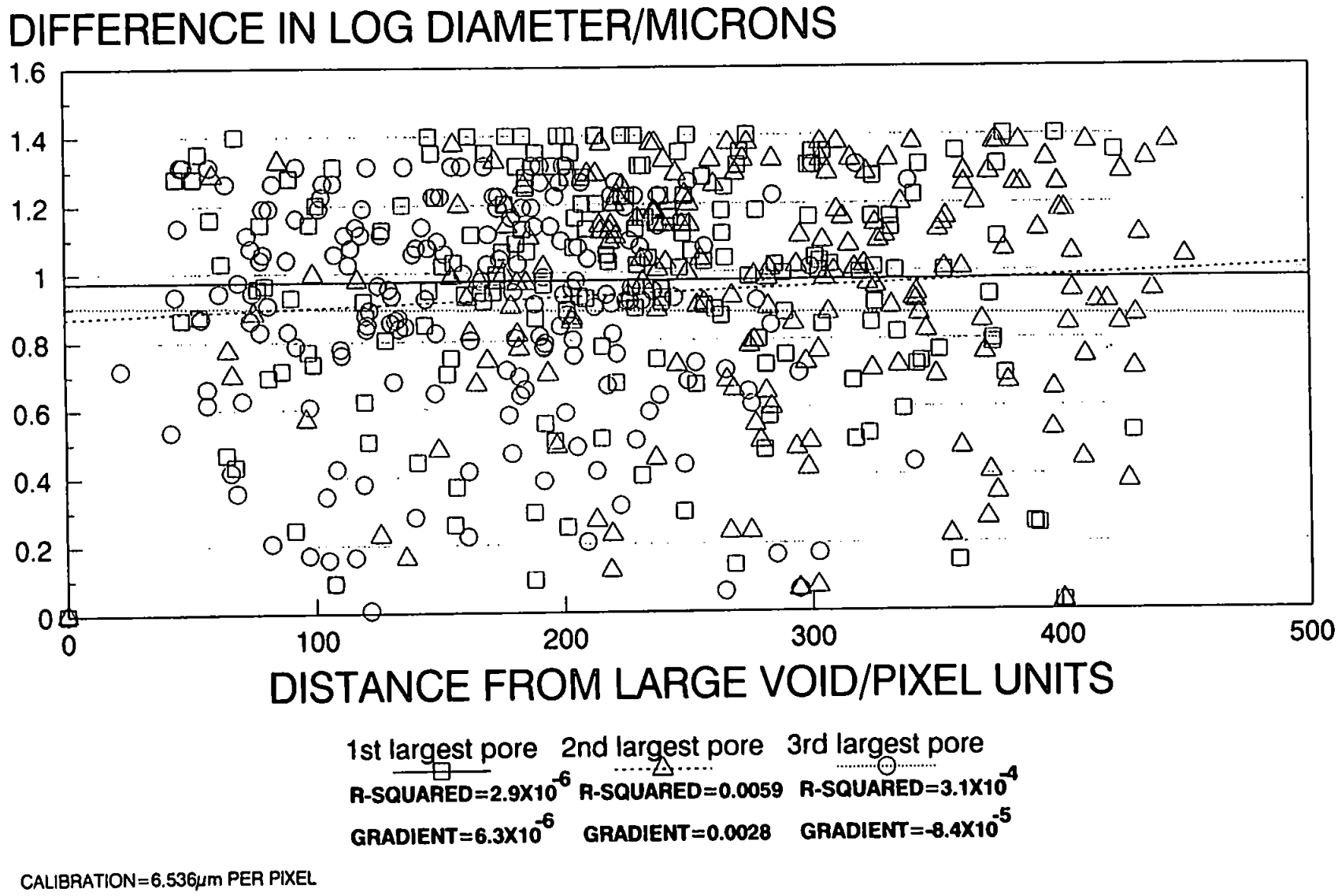

FIGURE 6.14: Difference in Log Diameter Between Largest Void and All Other Voids Against Distance From Largest Void for the Three Largest Voids Detected in Sample 212B.

small voids Figure 6.14 is very scattered, $R^2 = 2.9 \times 10^{-6}$ to 5.9×10^{-3} and no void size correlation is measurable. This result is mirrored in the analysis of the ten largest void features.

The above analysis detected no correlation in the obviously correlated banded sandstone (212B) and only partial detected correlation in the highly correlated glass model structure. An alternative correlation measurement technique was therefore developed.

6.6 Variogram Study

The variogram is a commonly used tool for the analysis of spatial variability. Consider two points x_i and x_i+h separated by a vector h. At these two points a property has been measured, eg feature area, the values of this property equals $Z(x_i)$ and $Z(x_i+h)$ respectively. The variability between these two values is given by the variogram function $2\gamma(h)$.

$$2\gamma(h) = \frac{1}{N(h)} \sum_{i=1}^{N(h)} [\, Z(x_i) - Z\,(x_i + h)\,]^2 \qquad (6.1)$$

Gamma (γ) is termed the semi-variance or estimate (Journel and Huijbregts 1978). Therefore the estimate is half the average of the squared differences. The variogram is usually expressed as a plot of semi-variance against distance between points or vector, h. Figure 6.15a shows that the variogram can become constant beyond a given distance, a_i. The upper limit of semi-variance is called the sill. The term sill originates from ore exploration, an area in which variogram studies are extensively applied. The occurrence of the sill corresponds to a region where semi-variance is no longer a function of direction and distance. The distance at which this occurs is called the Range, a_i. The distance up to the Range is commonly called the Zone of Influence. The variogram can often be linear, ie the sill is never attained Figure 6.15b. A linear variogram often denotes a change in the

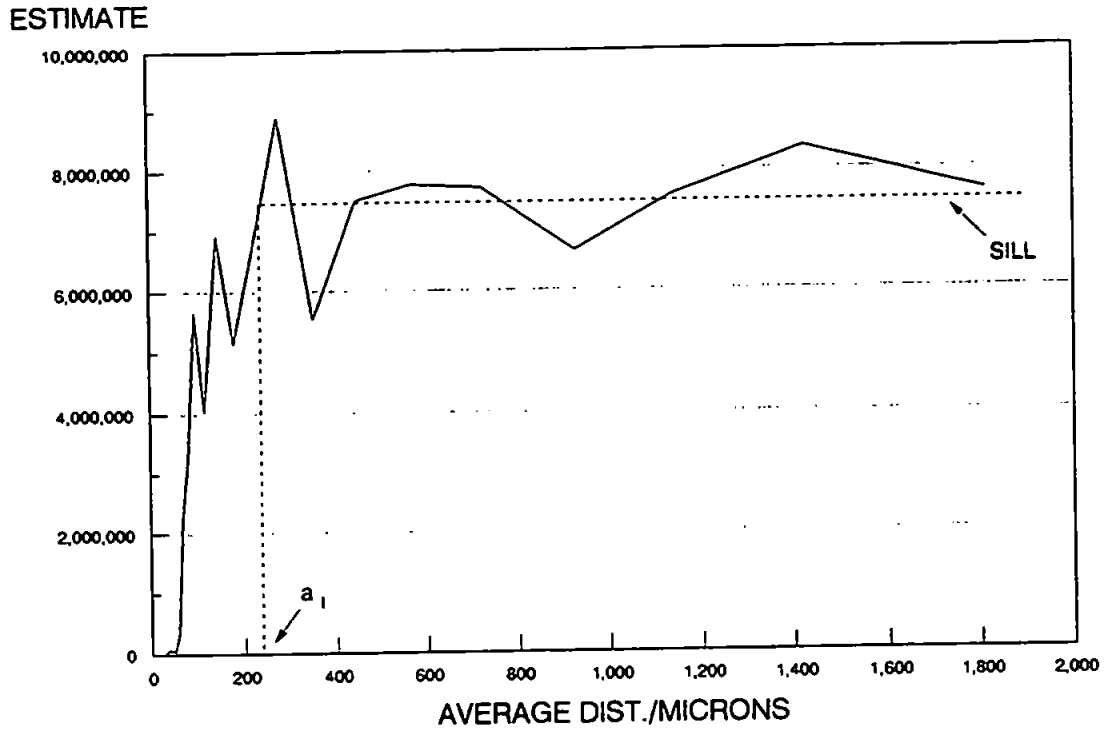

FIGURE 6.15a: A Typical Semi-Variogram.

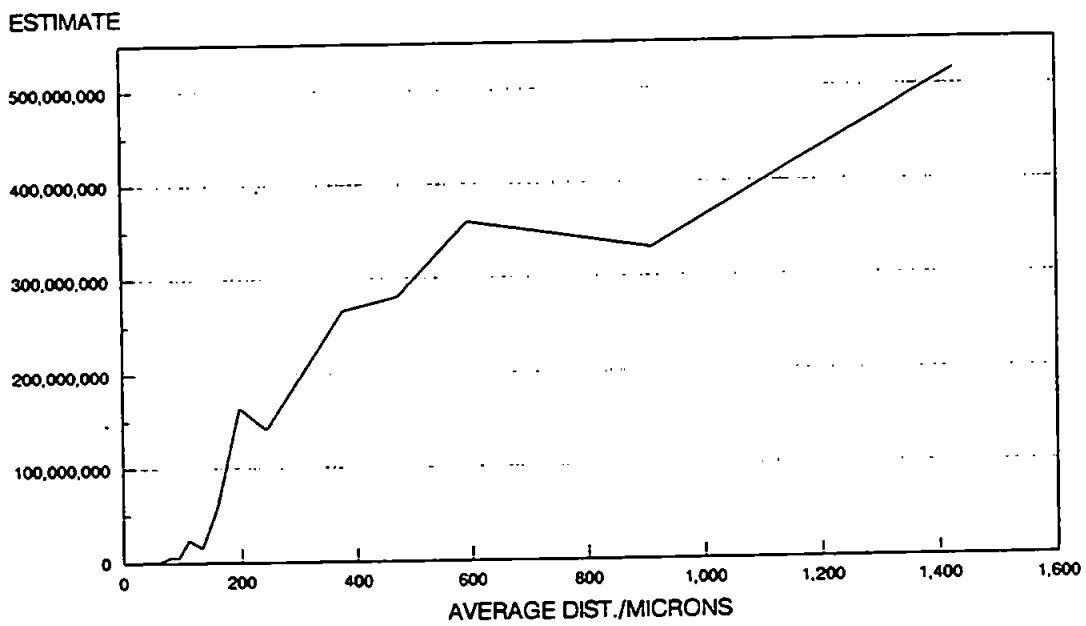

FIGURE 6.15b: A Semi-Variogram for an Anisotropic Sample.

general mean and semi-variance with distance ie anisotropy.

6.7 Geo-Eas

The variogram study on the data from the sandstone images was performed using a computer program called Geo-Eas. This program was developed for ore exploration studies but is within the public domain. The software availability and usage is outline in Appendix 4.

6.7.1 Results

Geo-Eas has been applied to the image analysis data obtained from the highly correlated sintered glass system, Plate 6.9. Figure 6.16 is a pixel co-ordinate plot of each void feature's centre of gravity. The semi-variogram for this data set using void area as the variable is shown in Figure 6.17. The semi-variogram shows that the Zone of Influence (a_i), is only 38.4 pixel units. The centre of gravity co-ordinate plot in Figure 6.16 shows a distinct gap of approximately 100 pixel units between the small and large void regions. A semi-variogram of this highly correlated system should have a Zone of Influence measurement of about 100 pixel units. The discrepancy in the Zone of Influence measurement is due to small voids within the large void region, as mentioned earlier, these are artifacts of large voids caused by the two-dimensional sectioning of the void network. Figure 6.18 shows a fitted curve through the glass variogram. This idealised variogram yields a Zone of Influence which approaches the expected result ie, 94 pixel units.

The small voids within the large void region can be removed creating an extremely high correlated glass model system. We have removed the "noise" caused by two-dimensional sectioning. Whilst ignoring data within real sandstone images would be foolish, the glass model system can be viewed as a training system which can be used to produce different variograms. Thus variograms produced by real void networks should be easily diagnosed.

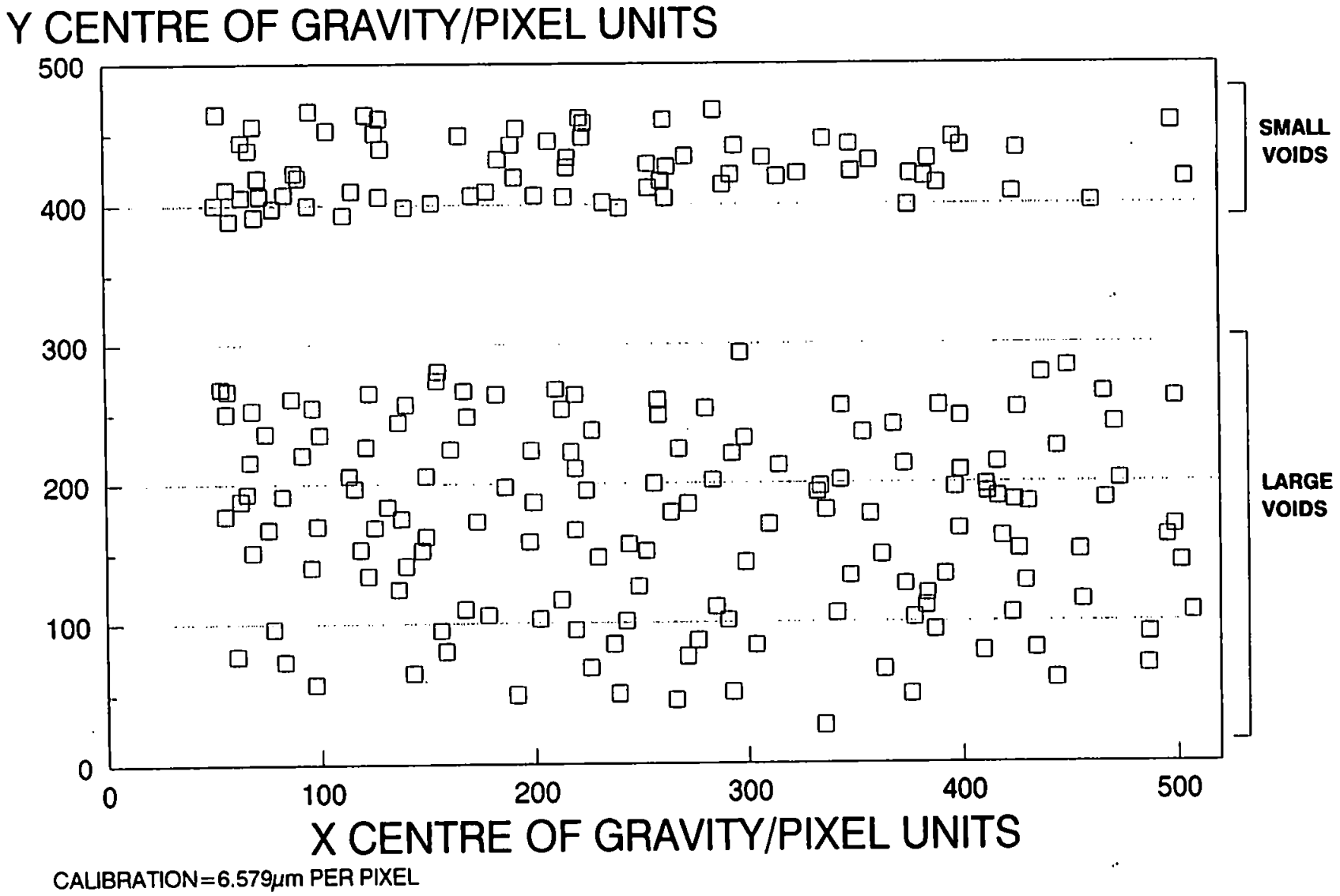

FIGURE 6.16: Centre of Gravity Coordinate Plot for Detected Features Within the Sintered Glass System.

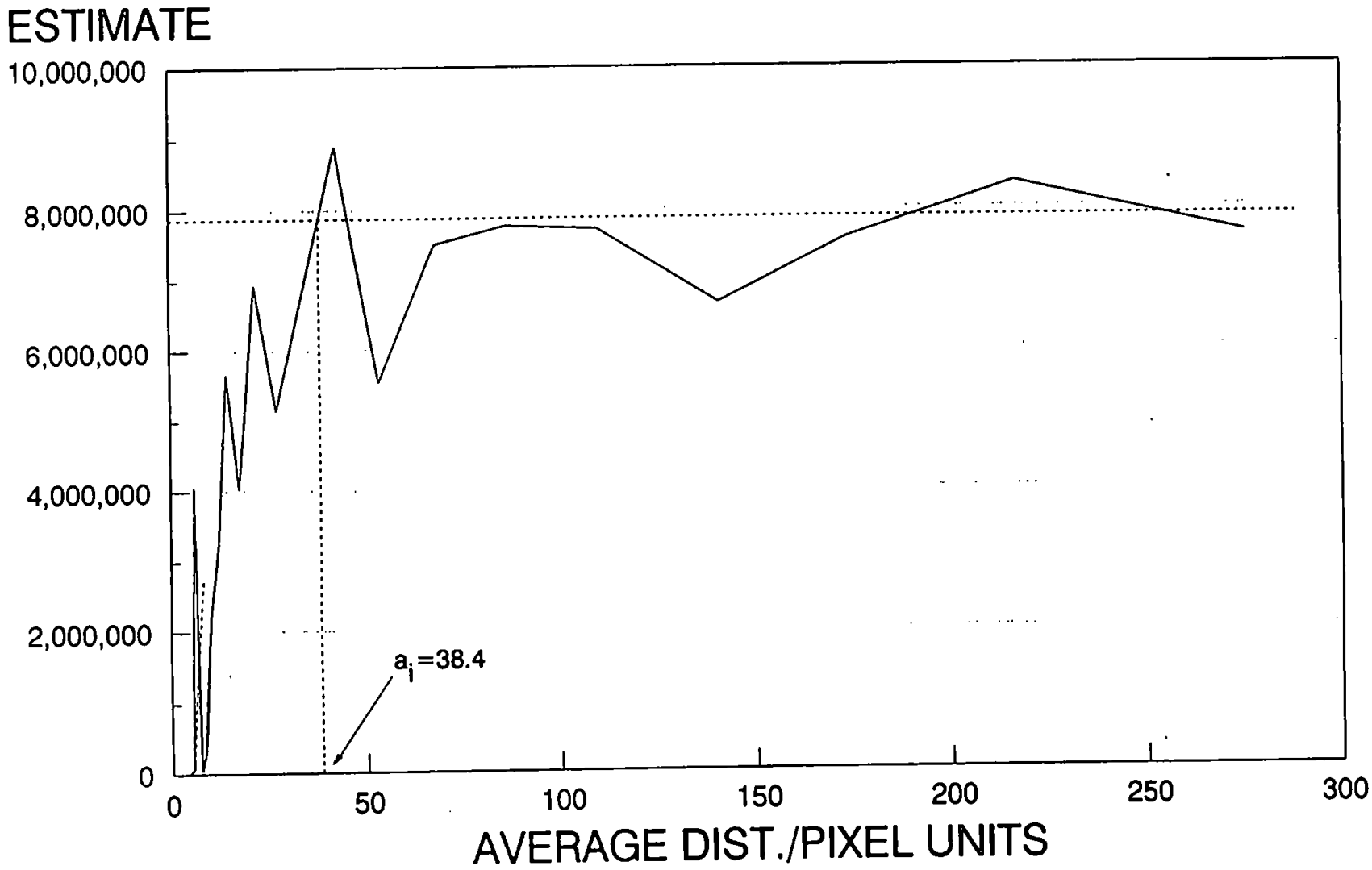

FIGURE 6.17: Semi-Variogram for Sintered Glass Data, a_i Equals the Zone of Influence.

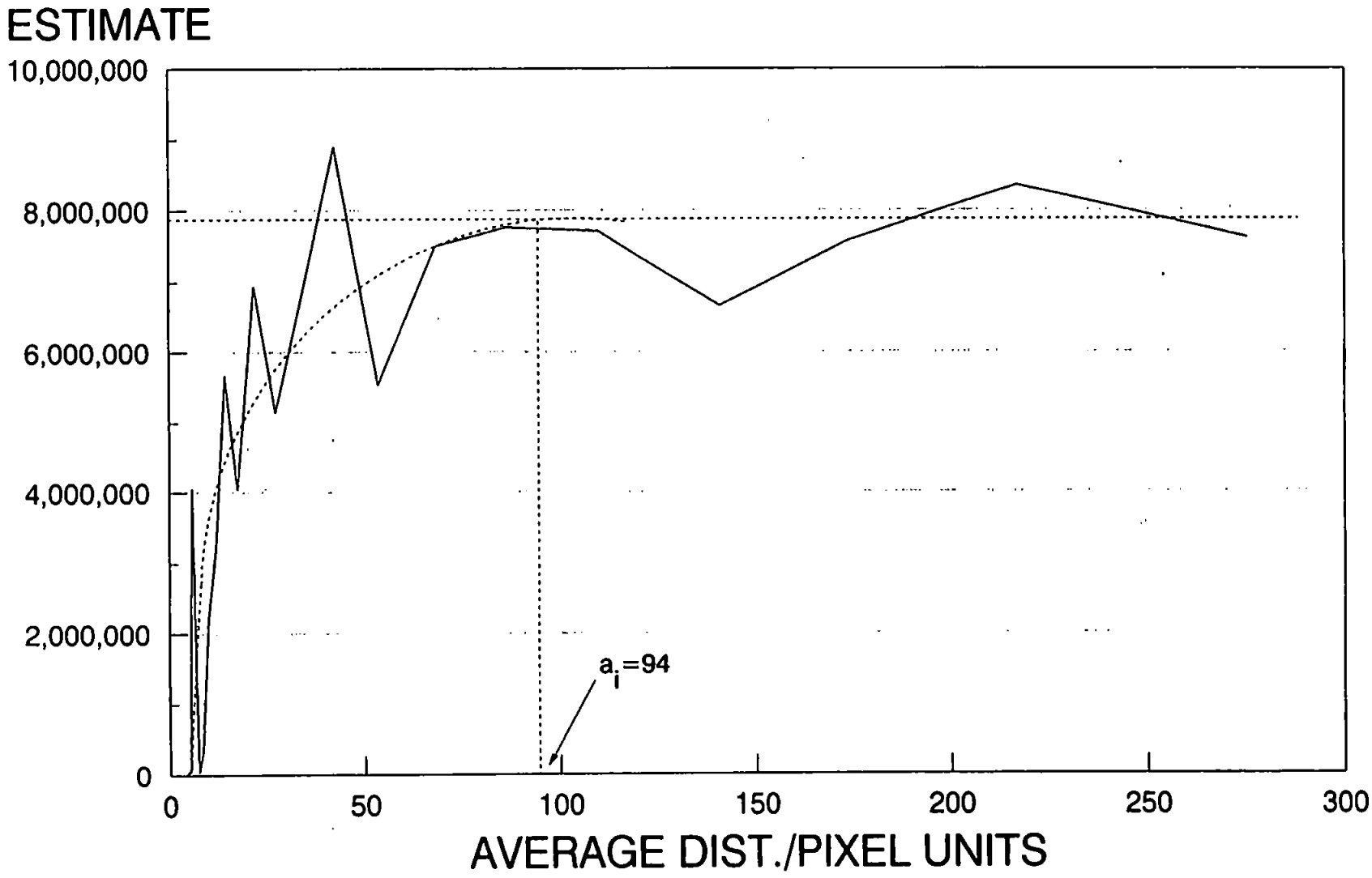

FIGURE 6.18: Semi-Variogram for Sintered Glass Data, With Smoothed Curve and New Zone of Influence value (a_i).

The variogram of the very highly correlated glass system without "noise" indicates little variance within each specific void region, Figure 6.19. Variance increases once the investigation distance is greater than the 100 pixel unit gap.

By joining two sets of data from the sintered glass model, a correlated multiple banded structure can be fabricated. Figure 6.20 shows such a structure containing two large void bands and two small void bands. All "noise" features have been removed as described earlier. The semi-variogram for this structure is of the expected shape, Figure 6.21. Variance reaches a maximum at about 175 pixel units (a_1); this is approximately the distance between the mid-points of a void band and its contrasting neighbour. The semi-variogram has a variance minimum at approximately 280 pixel units (a_2), this is the distance between mid-points of like void bands. At distances greater than a_2, variance increases as voids within the second contrasting void bands are included in the variance calculation. Unfortunately, the maximum analysis distance in Figure 6.21 is only 327 pixel units; this distance corresponds to the data processing limit of the Geo-Eas program. The variance trend is still discernible without the full data set being analyzed.

The semi-variogram in Figure 6.22 is for the multiple banded glass model including the "noise" void features. The pixel co-ordinate plot for centres of gravity of each void within the multiple banded glass model is shown in Figure 6.23. Notice that the glass model has been reduced to approximately 100 x 100 pixel units. The number of void features has been reduced so that the data processing limit of Geo-Eas is not exceeded. In Figure 6.22 the number of void pairs at each distance used to calculate the estimate are given beside each point. The semi-variogram for the multiple banded glass model with "noise" shows distinct maxima and minima, despite the presence of many local maxima and minima. A smoothed best fit line has been drawn; this highlights the distinct maxima and minima. The first variance maximum is at 22 pixel units, 22 units corresponds to approximately the distance between mid-points of adjacent contrasting void bands, see

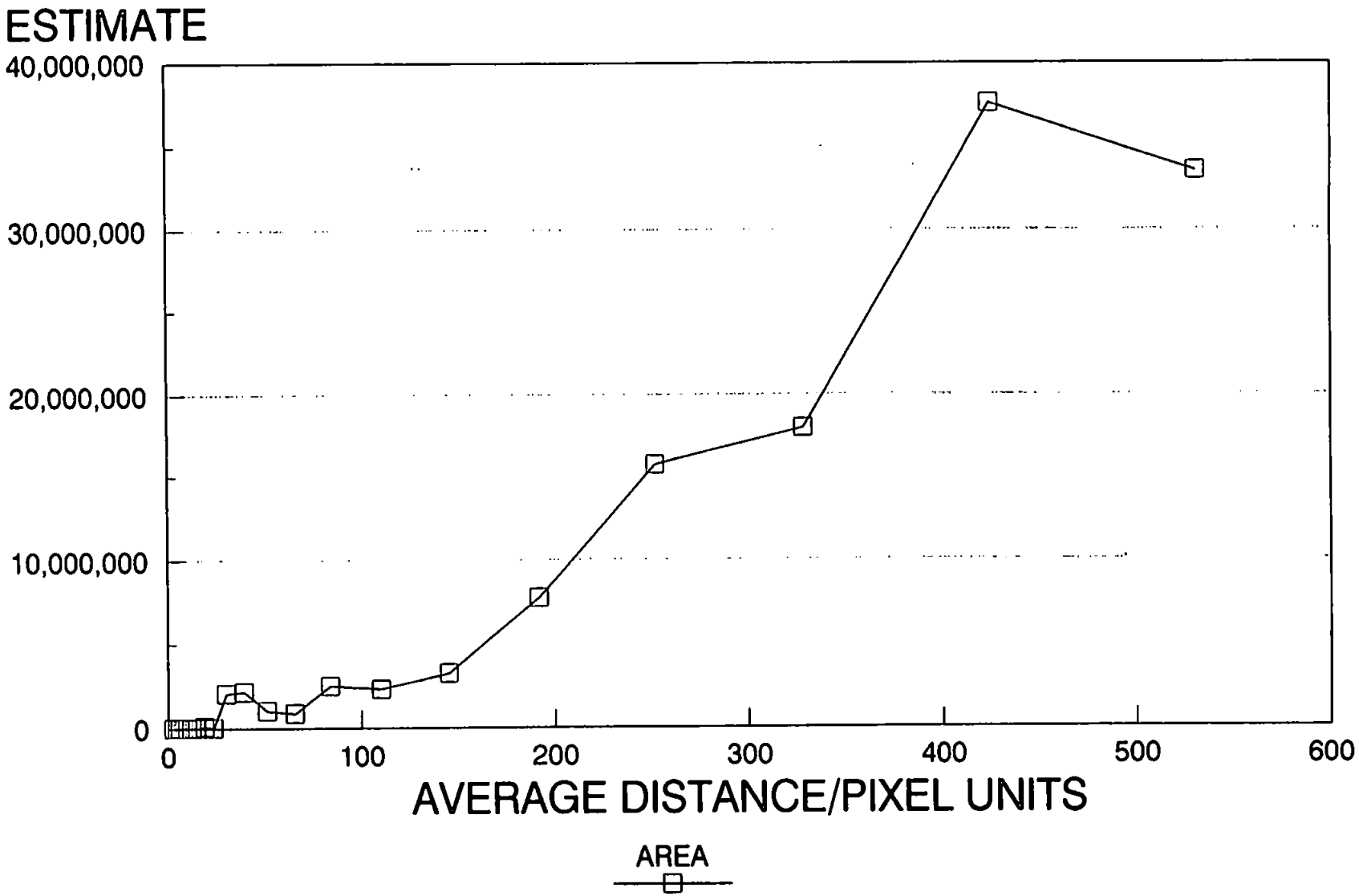

FIGURE 6.19: Semi-Variogram for Sintered Glass Data With "Noise" Features Removed.

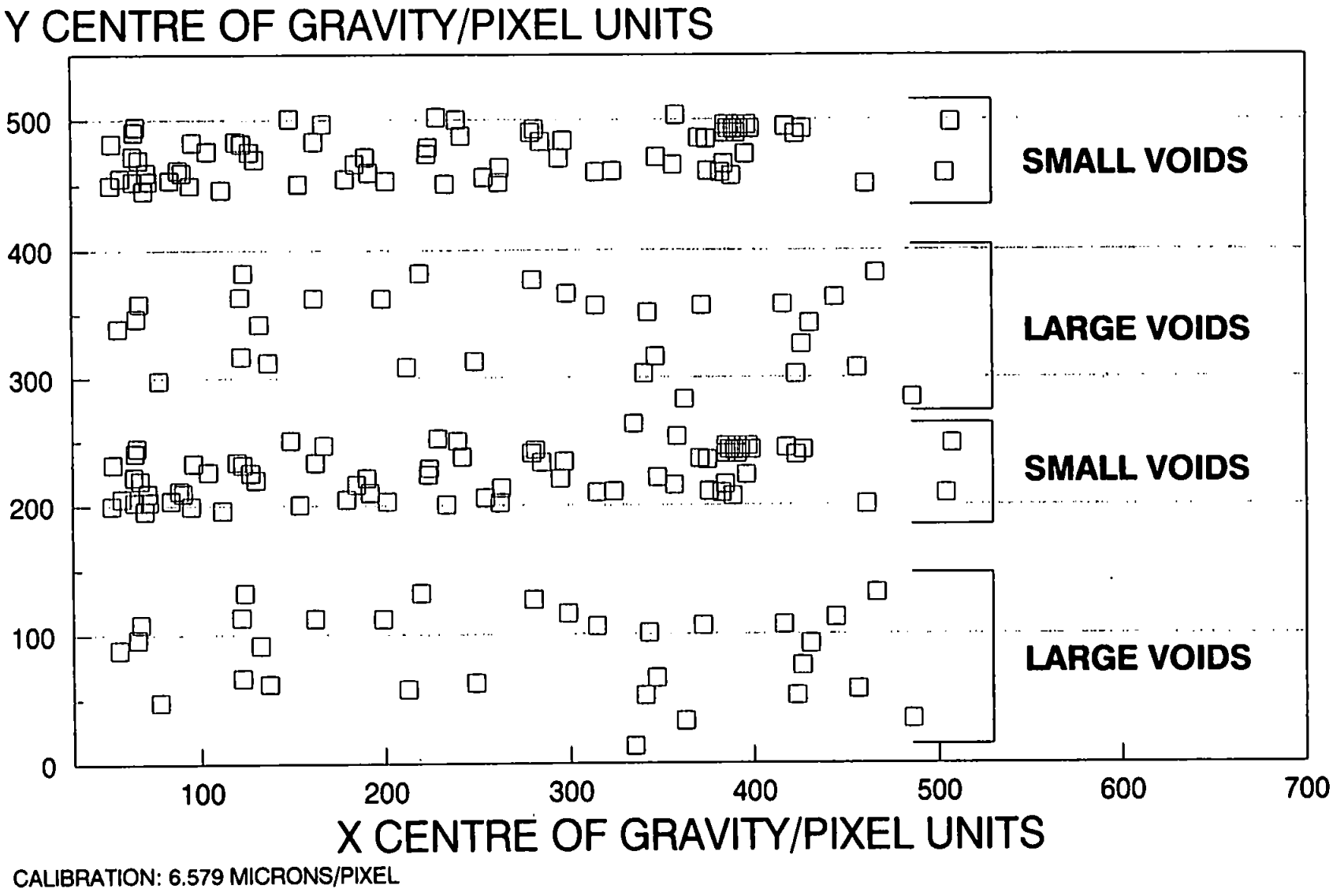

FIGURE 6.20: Centre of Gravity Coordinate Plot for Detected Features Within a Multiple Banded Sintered Glass System, With "noise" Features Removed.

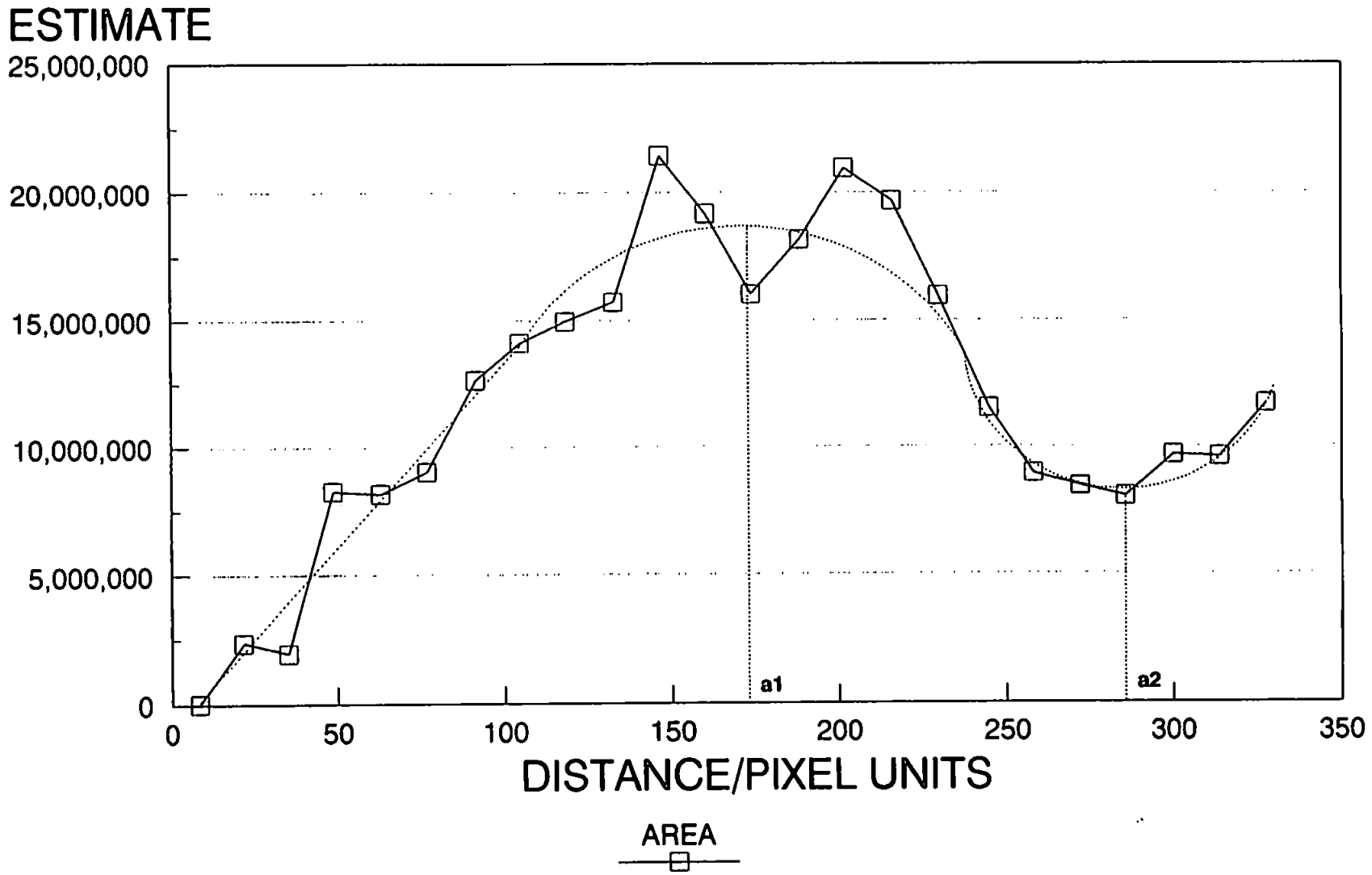

FIGURE 6.21: Semi-Variogram for Multiple Banded Sintered Glass System, With "Noise" Features Removed.

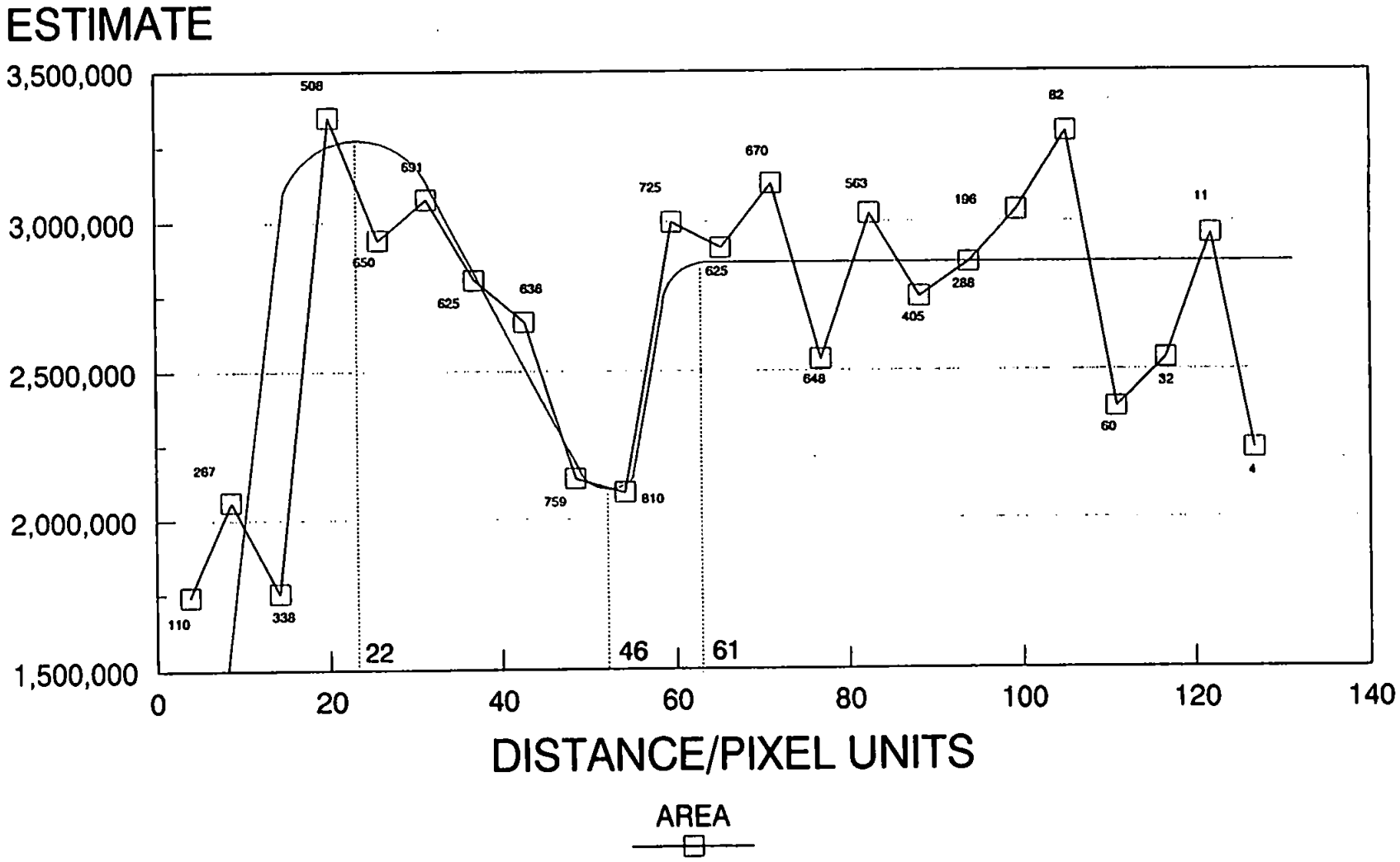

FIGURE 6.22: Semi-Variogram for Multiple Banded Sintered Glass System, Including "noise" Features, With Smooth Curve.

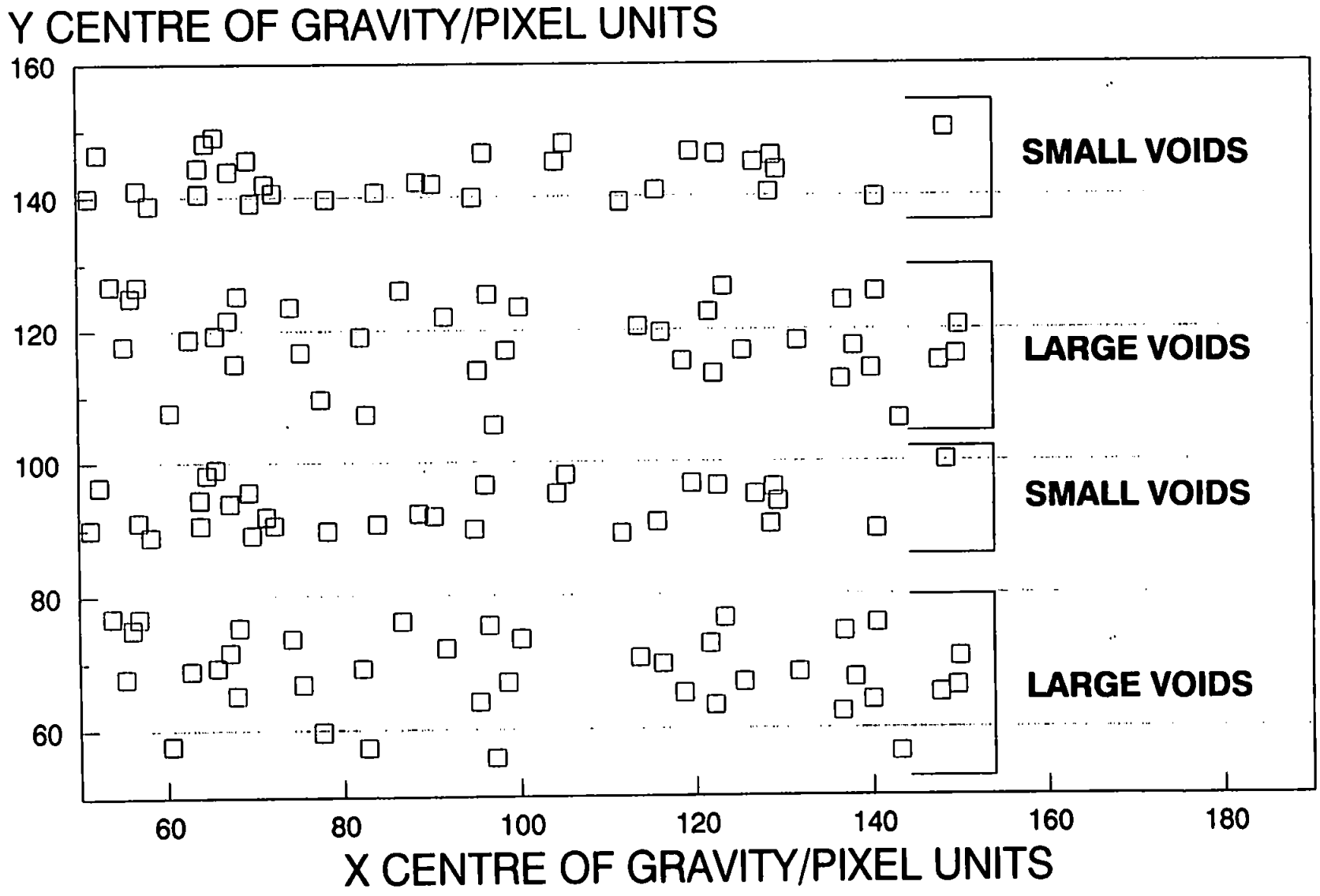

FIGURE 6.23: Centre of Gravity Coordinate Plot for Detected Features Within Reduced Multiple Banded Sintered Glass System, Including "Noise" Features.

Figure 6.23. The minima at 46 pixel units indicates the presence of like void bands with mid-points approximately this distance apart. The second maxima at 61 pixel units is indicative of the occurrence of a second contrasting void band. The semi-variogram has thus successfully measured the spatial relationships between void space within a synthetic correlated structure. However the void space within reservoir sandstones is of far greater complexity that of the sintered glass model, and any correlation present is therefore harder to measure.

The Geo-Eas program has been applied to the analysis data obtained from the back scatter electron microscopy images of the reservoir sandstones, 212B & 212E, Plates 6.3 & 6.6 respectively. The semi-variogram for sample 212B is shown in Figure 6.24. The image analysis data used to generate this semi-variogram are the same data used in the root area size distribution of Figures 6.5. The semi-variogram for sample 212B has a maxima at 718μm a minima at 1031μm and a second maxima at 1367μm. The second minima at 2109μm is only due to a few void pairs whilst not being a significant proportion of the investigation area; these voids may be part of another void band which extends beyond the measure zone. Plate 6.3 shows the image analysis investigation area for sample 212B. The top of the measure area contains a band of large voids; below this is a cluster of smaller voids. Plate 6.3 includes feature identification numbers, the small void banding is highlighted by the clustering of these numbers. Below the small void band is another large void band and below that another small void band. Thus the investigation area in sample 212B (Plate 6.3) contains a double set of large and small void bands over a distance of 1.78mm. The values of maxima and minima distances do correspond to approximately the distances between the mid-points of each like or unlike void band.

Applying the variogram study to the breadth of each feature for the 212B data set produces a semi-variogram of very similar form to that obtained when area is the variable, Figure 6.25. For sample 212B the area and breadth of a void are related. This relationship

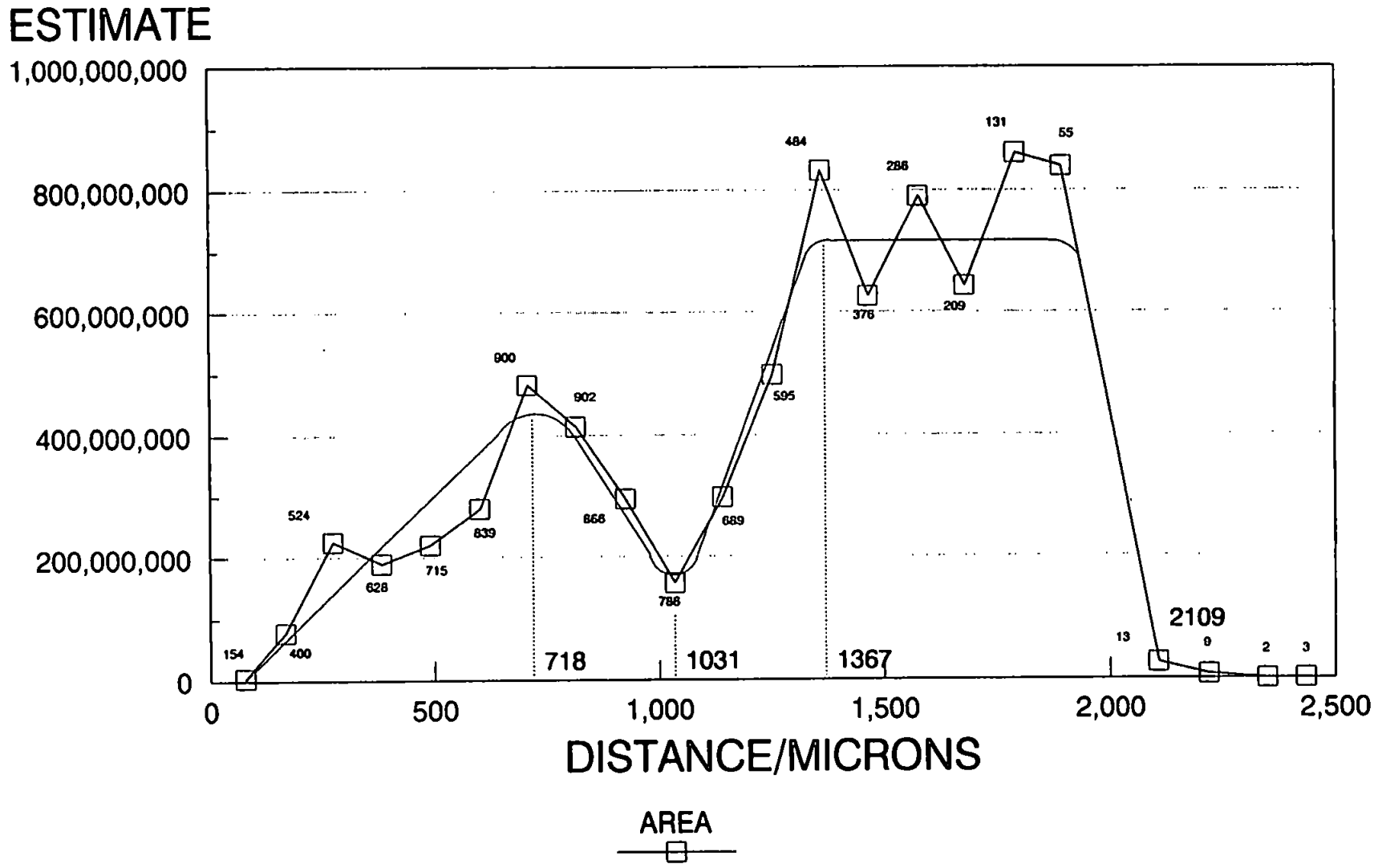

FIGURE 6.24: Semi-Variogram for Sample 212B With Smooth Curve.

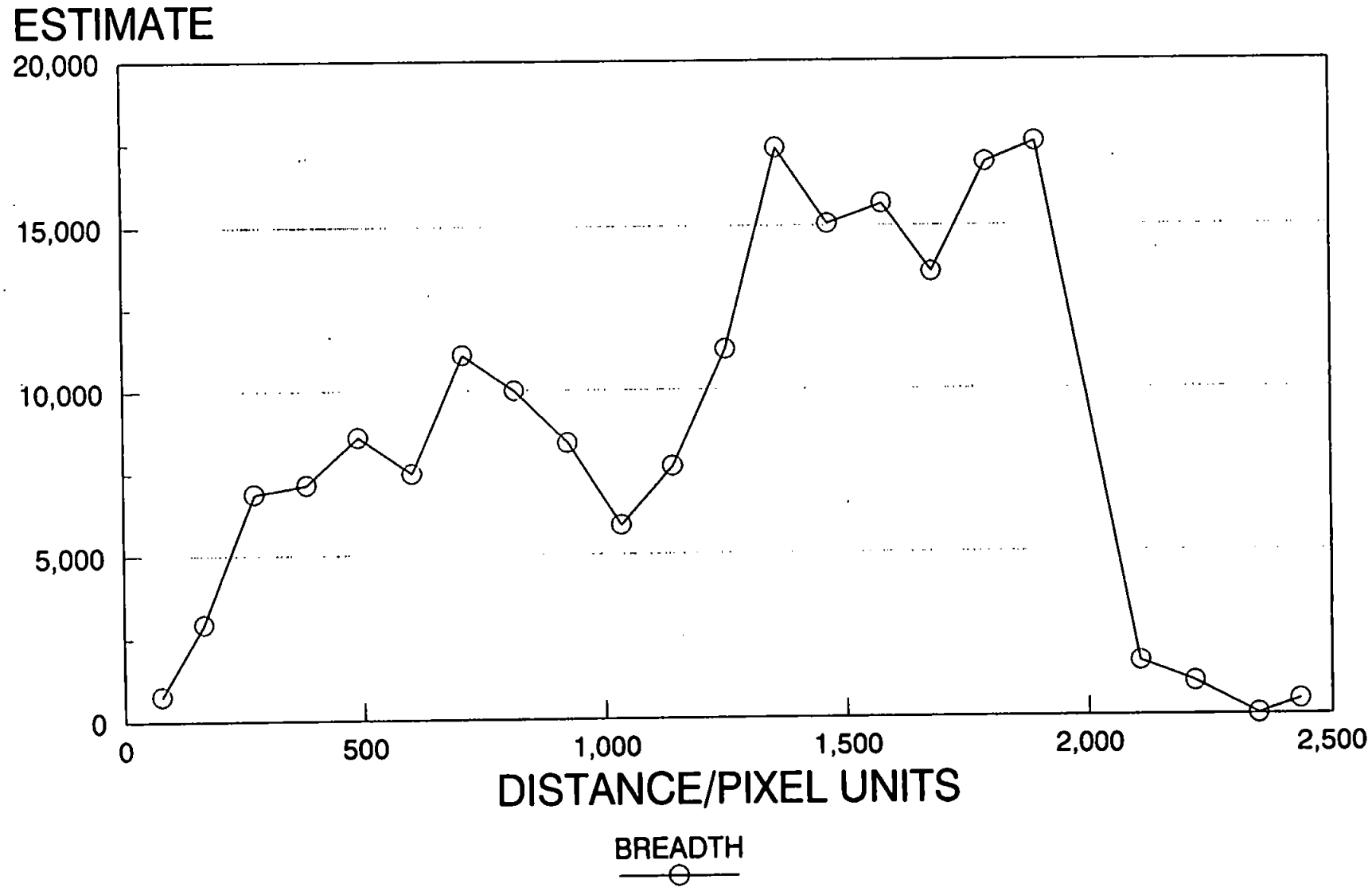

FIGURE 6.25: Semi-Variogram for Sample 212B Using Feature Breadth as the Variable.

indicates relatively simple void cross section geometries.

Figure 6.26 shows the semi-variogram for the image analysis data output from sample 212E .(Plate 6.6). The semi-variogram increases to a plateau, although after attaining this plateau estimate increases slightly. The peak at approximately 170μm is a noise peak. This shape semi-variogram indicates either a random void arrangement or a simple coupling of a small and large void band. Close inspection of Plate 6.6 shows that the latter is true, a region of large voids are situated at the top of the investigation area and smaller voids below. The semi-variogram for the breadth of void features, Figure 6.27 , again has a similar form as that for area within sample 212E. At first glance it would appear that sample 212B has more correlated void space than 212E, but a comparison of correlation over the same size area indicates a similar degree of correlation.The investigation area of Sample 212B is 1.78mm x 1.78mm, and within this area a double set of large and small void bands are detectable. Sample 212E had an investigation area of 1.077 x 1.077mm and a single set of large and small bands was detected. If the samples are compared over the same distance a similar degree of correlation is obtained.

The Geo-eas analysis has been applied to four other reservoir sandstone samples, samples 212A, 250A, 490D and 490E. No void size correlation has been detected in these samples. Table 6.1 summarizes the correlation investigation results:

SAMPLE NO.	DEGREE OF CORRELATION
212A	NON DETECTED
212B	TWO SETS OF LARGE AND SMALL VOID BANDS OVER 1.78mm
212E	ONE SET OF LARGE AND SMALL VOID BANDS OVER 1.08mm
250A	NON DETECTED
490D	NON DETECTED
490E	NON DETECTED

TABLE 6.1: Summary of Void Size Correlation Study Results.

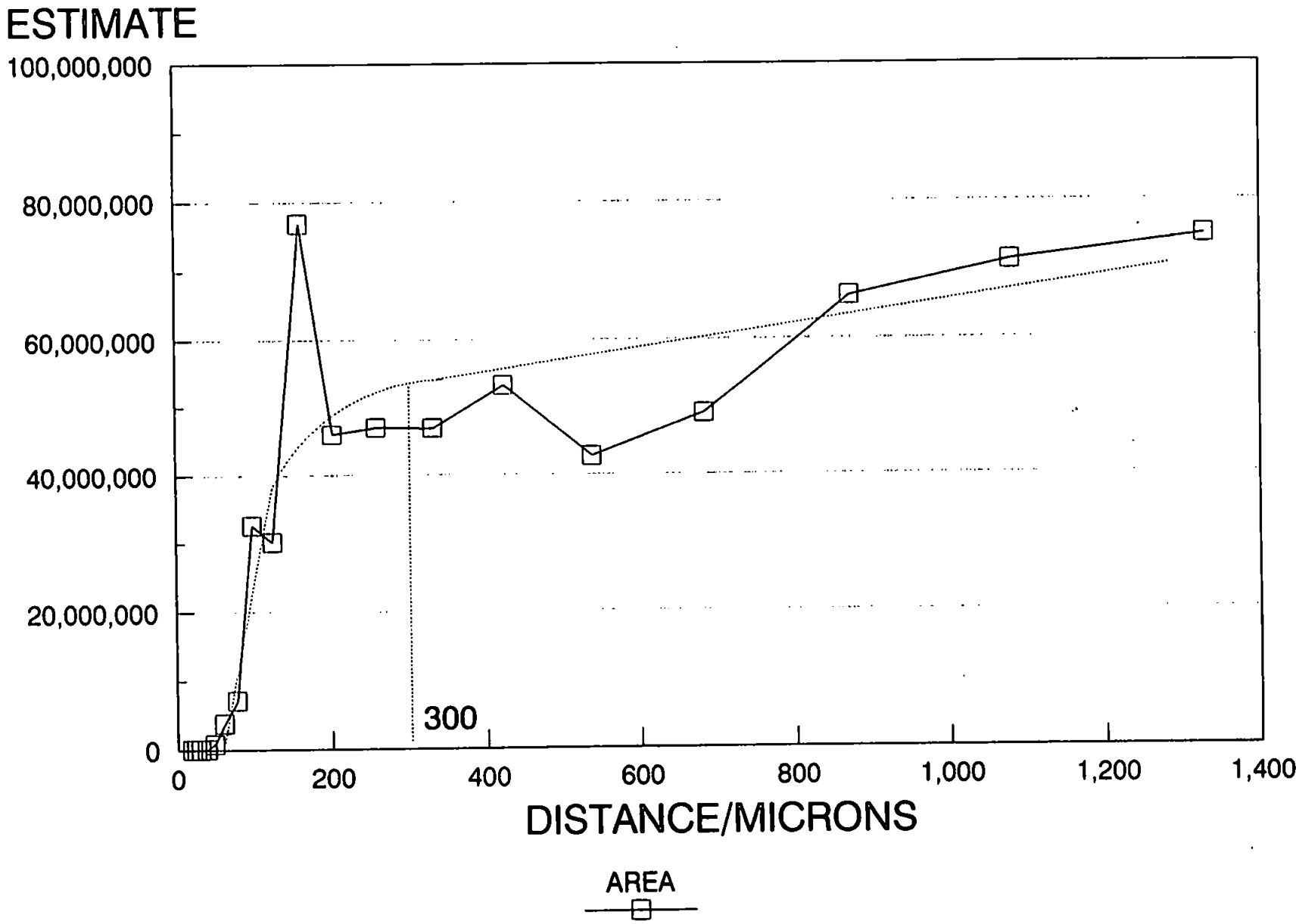

FIGURE 6.26: Semi-Variogram for Sample Size with Smoothed Curve.

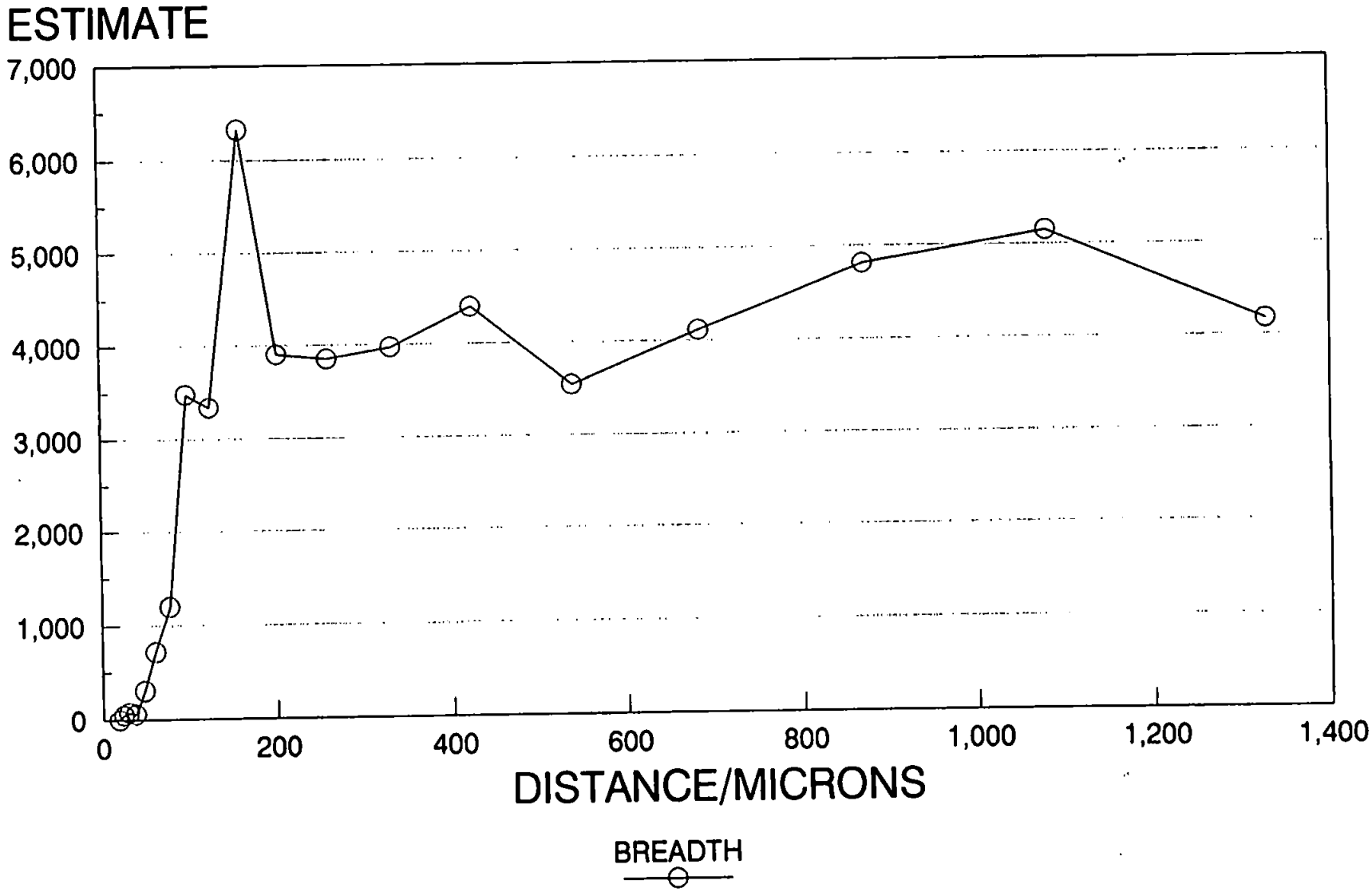

FIGURE 6.27: Semi-Variogram for Sample 212E Using Feature Breadth as the Variable.

6.8 Improved Curve Fit To Variogram

It is clear from the preceding discussion that the conclusions concerning the degree of pore size correlation within a sample depend critically on the shape of the variogram curve. The manual fit to the data points, used above, is made difficult by the fact that the variogram points are scattered and are generated by widely differing numbers of void pairs, so that the statistical weighting W of the points varies typically from 1 to around a thousand. Moreover, the statistical weighting tends to be greatest in the middle of the h (abscissa) range, with very low values as $h \rightarrow 0$ and $h \rightarrow_{max}$. This precludes standard fitting procedures, such as polynomial fits, since these become unstable in the high and low h regions, which are nevertheless important in determining correlation within the sample. Thus to achieve a stable and reliable curve fit, one needs to make some careful assumptions about the variogram, while remembering that its overall shape cannot be pre-determined. The assumptions are as follows:

(i) the minimum investigation distance is limited by the fact that the digitised image is in the form of pixels, which typically correspond to an absolute size of around 5 microns. Because of this resolution cut-off, it is reasonable to assume that the variogram and its first derivative should both tend to zero as the vector h tends to zero.

(ii) We assume that we have chosen the magnification level such that the largest h values are greater than the correlation distances h of interest, i.e. those distances corresponding to features which affect fluid migration characteristics on a plug scale. It then follows that the variogram will tend to a constant value, and its first derivative to zero, as h becomes large.

(iii) As h increases, the radius of investigation increases, and so do the chances of features being masked by other property values Z. Hence the flexibility of the

variogram curve decreases as $\sqrt{h}$.

These three conditions are independent of the fractal nature of the sample, which is masked by the resolution lower limit, and the investigation area upper limit. Obviously the resolution could easily be improved by increasing the magnification, but this might then invalidate assumption (ii) above.

A best fit cubic spline algorithm (NAG library E02BAF) is capable of taking into account both the statistical weights and the three characteristics listed. The latter are input as follows:

(i) two $\gamma = 0$ points are added to the experimental data at $h = 0$ and $h = -h_1$, where h_1 is the first experimental value of h.

(ii) two points are added to the experimental data at $h = 2h_n - h_{n-1}$ and $h = 3h_n - 2hn-1$, where n is the number of experimental points, with the asymptotic mean value of γ at high h given by :

$$\langle\gamma\rangle_{h=h_{max}} = \frac{\sum_{j=n}^{j=n-k} (W_n \cdot \gamma(n))}{\sum_{j=n}^{j=n-k} W_n} \qquad (6.2)$$

The number of points $(n-k+1)$ used to calculate the asymptotic mean value is on the basis of the statistical weights of the highest h values, is the maximum possible provided that:

$$\sum_{j=n}^{j=n-k-1} W_j < W_{n-k-1} < \sum_{j=n}^{j=n-k} W_j \qquad (6.3)$$

(iii) 7 intermediate knots κ are specified for the cubic spline, the knots being those points at which the cubic curves join with continuous value, and with continuous first and second derivative. The knots are spaced such that:

$$\sqrt{\kappa_l} = l.\left(\frac{\sqrt{h_{max}}}{7}\right) \tag{6.4}$$

6.8.1 Results

Figures 6.28 and 6.29 show the cubic spline curve fit procedure applied to the semi-variograms of samples 212B and 212E respectively. The curves are similar to those obtained by a manual fit. The maxima and minima for each curve are approximately the same as those measured in Figures 6.24 and 6.26. The cubic spline fit eliminates the degree of ambiguity associated with the manual fit procedure.

6.9 Conclusions

A new method has been developed for measuring the degree of void size correlation within resin filled sectioned sandstone samples. The procedure has been tested against an artificially correlated void network, consisting of two sintered glass discs of different grade. The Geo-eas program calculated the distance between different void bands within this test system, the results being consistent with distances measured manually. The Geo-eas program has also been applied to image analysis data from the more complex void networks found in sandstones. Void size correlation has been found in two sandstones and homogeneous void space detected in four other samples. The correlation information can be used in the Pore-cor void space model to facilitate an accurate simulation of sandstone void networks. At the moment the information obtained in the correlation study can only be used as an indication of degree of correlation to use in the model. Future work will involve calibrating the model by applying the correlation procedure to images from model networks with varying void size correlation.

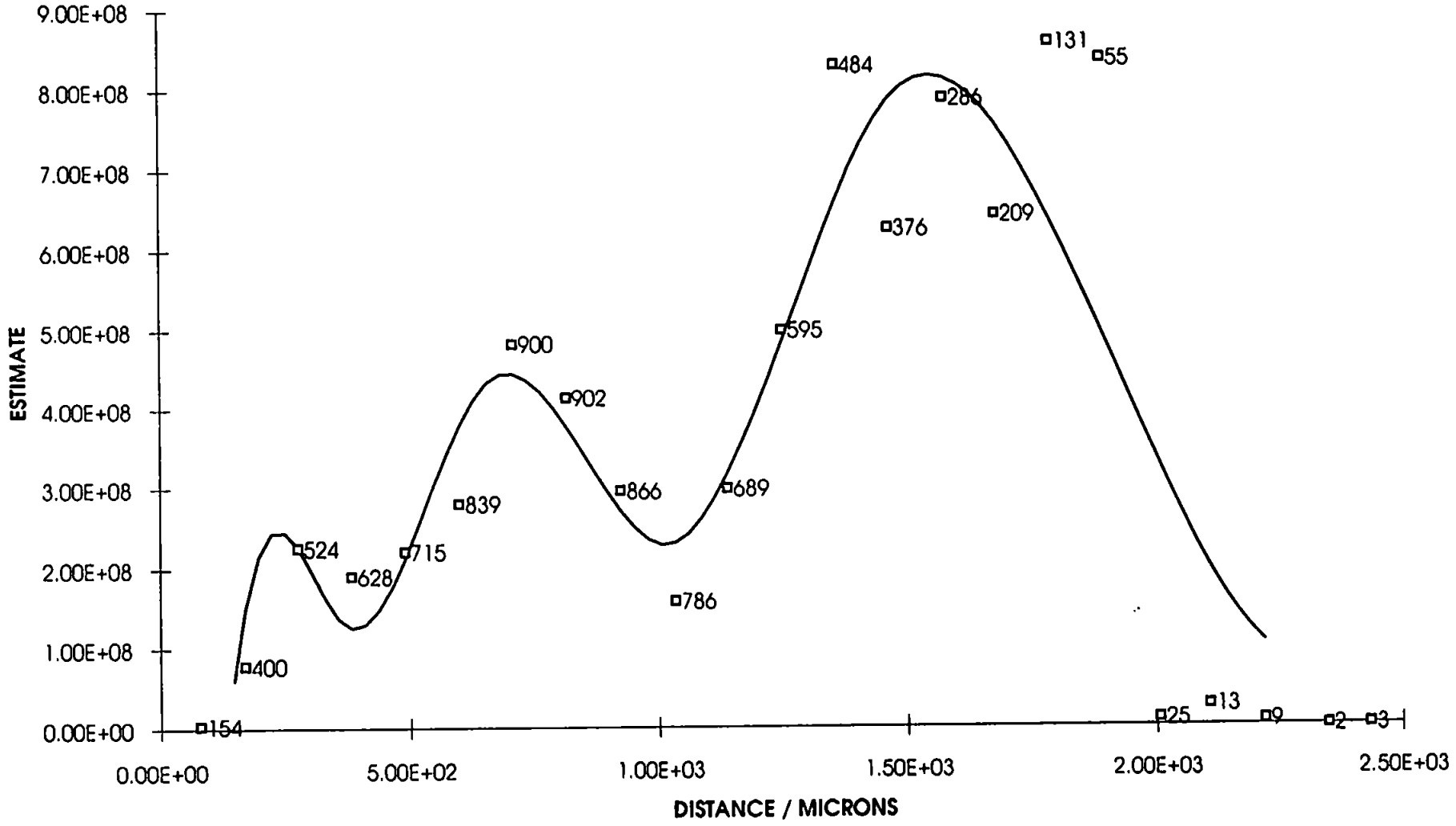

FIGURE 6.28: Semi-Variogram for Sample 212B With Cubic Spline Fitted Curve.

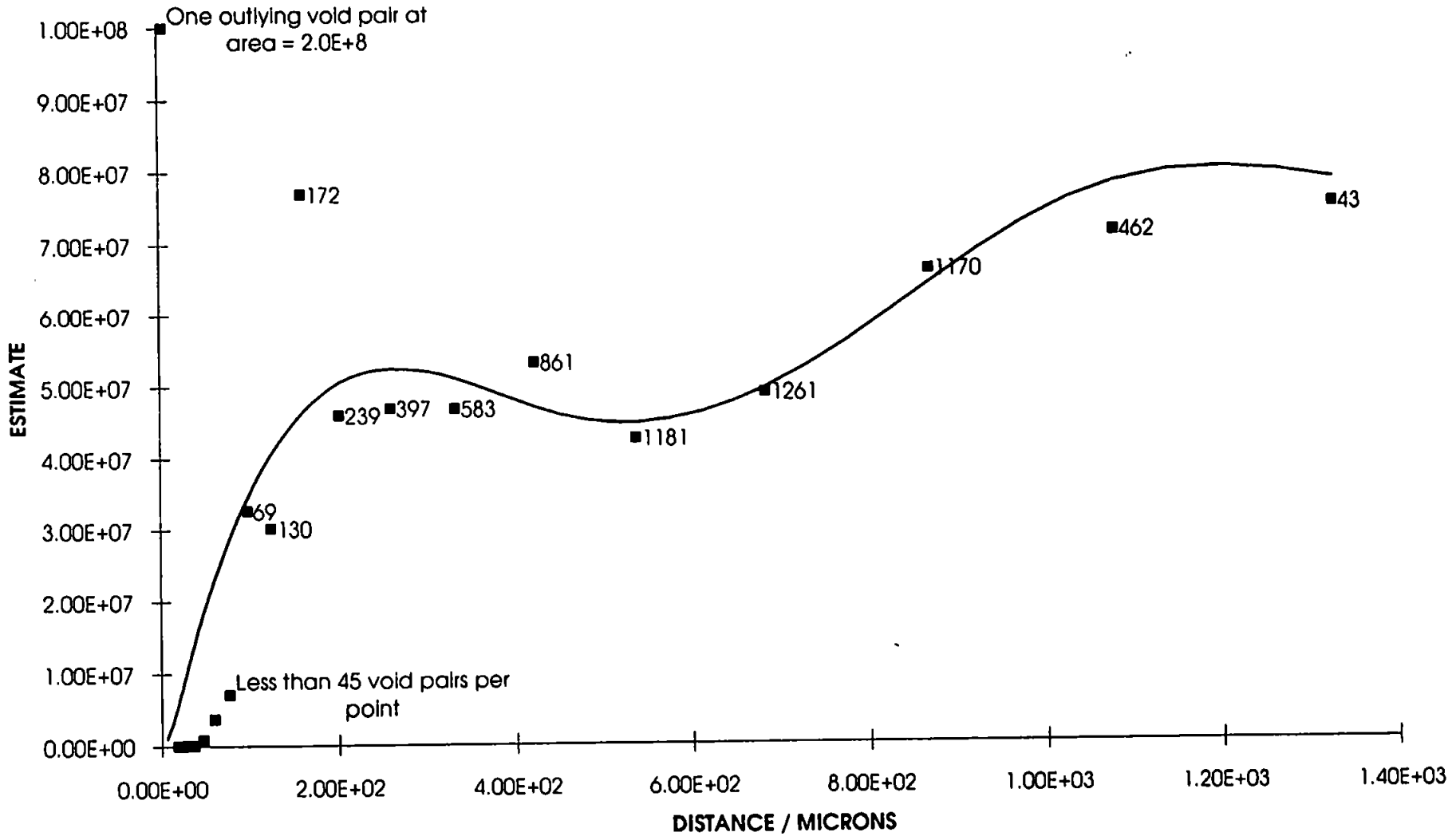

FIGURE 6.29: Semi-Variogram for Sample 212E With Cubic Spline Fitted Curve.

CHAPTER 7

DIFFUSION

7.1 Introduction

The redistribution of hydrocarbons in subsurface rocks can be facilitated by different migratory mechanisms including viscous/bulk flow, solution and gaseous diffusion. This migration can be divided into two stages; primary migration denoting the transport from fine grained source rock to adjacent more permeable beds and secondary migration which is the movement of the hydrocarbons within these reservoir rocks.

Diffusion has long been argued as a principal mode of hydrocarbon redistribution in subsurface rocks. Molecular diffusion involves the statistical movement (Brownian motion) of molecules, unlike viscous flow which is driven by pressure gradients (Krooss 1987). Often migration is a combination of viscous and diffusive fluxes. Thorstenson and Pollock (1989) stated that very small pressure gradients can produce viscous fluxes that are of the same order or overwhelm diffusion phenomena.

The potential for large scale diffusive migration was noted by Leythaeuser et al (1982). In the Harlingen gas field, Holland, it is estimated that $1x10^9$ m^3 of methane have been lost due to diffusion through the cap rock over a period of 4.5 million years. Leythaeuser and co-workers analyzed core samples from Spitsbergen Island at a depth of 80m. The distribution of hydrocarbons throughout this whole length and across a lithological siltstone/sandstone boundary, were measured. Both siltstone and sandstone had acted as a source rock early in the areas history. Both contained type III kerogen. The light hydrocarbons were later removed from the lower sandstone unit. This produced a sink into which hydrocarbons from the siltstone could diffuse. This work proved that molecular diffusion is an important transport mechanism in primary migration.

The diffusion of hydrocarbons can be within many different phases; gas, water, oil

or within the kerogen geopolymer. Mineral and organic phase surfaces can also provide interfaces for diffusive processes (Krooss 1987). The complex nature of diffusive processes within subsurface rocks was noted by Thomas (1989), who pointed out the danger of applying the classical diffusion laws to multi-phase systems.

Much work has been done on the measurement of diffusion coefficients within saturated rocks (Krooss 1986, 1987). The majority of subsurface rocks contain pore waters, but diffusion in the unsaturated zone can be important in any prediction of diffusive losses from potential reservoirs. Chen (1973) measured the methane diffusion coefficients for a set of dry sandstones with permeabilities ranging from 7 to 336 md. Results indicated a correlation of diffusion with permeability, porosity and formation factor. However no information has been published on the repeatability and errors associated with diffusion coefficient measurements. In this study we measure the diffusion coefficients of methane, iso-butane and n-butane within nine dry sandstone samples. Repeated measurements were performed and a detailed analysis of factors affecting diffusion undertaken.

7.2 Theory

The theory for the experimental measurement of diffusion coefficients in sandstones is adapted from the non-steady state method used by Daynes (1920). This method was originally used to measure diffusion through rubber membranes and was applied to sedimentary rocks by Krooss (1986). The technique monitors the build-up of a steady state of diffusive flux within the sample. Figure 7.1 shows the concentration profiles throughout the sample during steady state attainment.

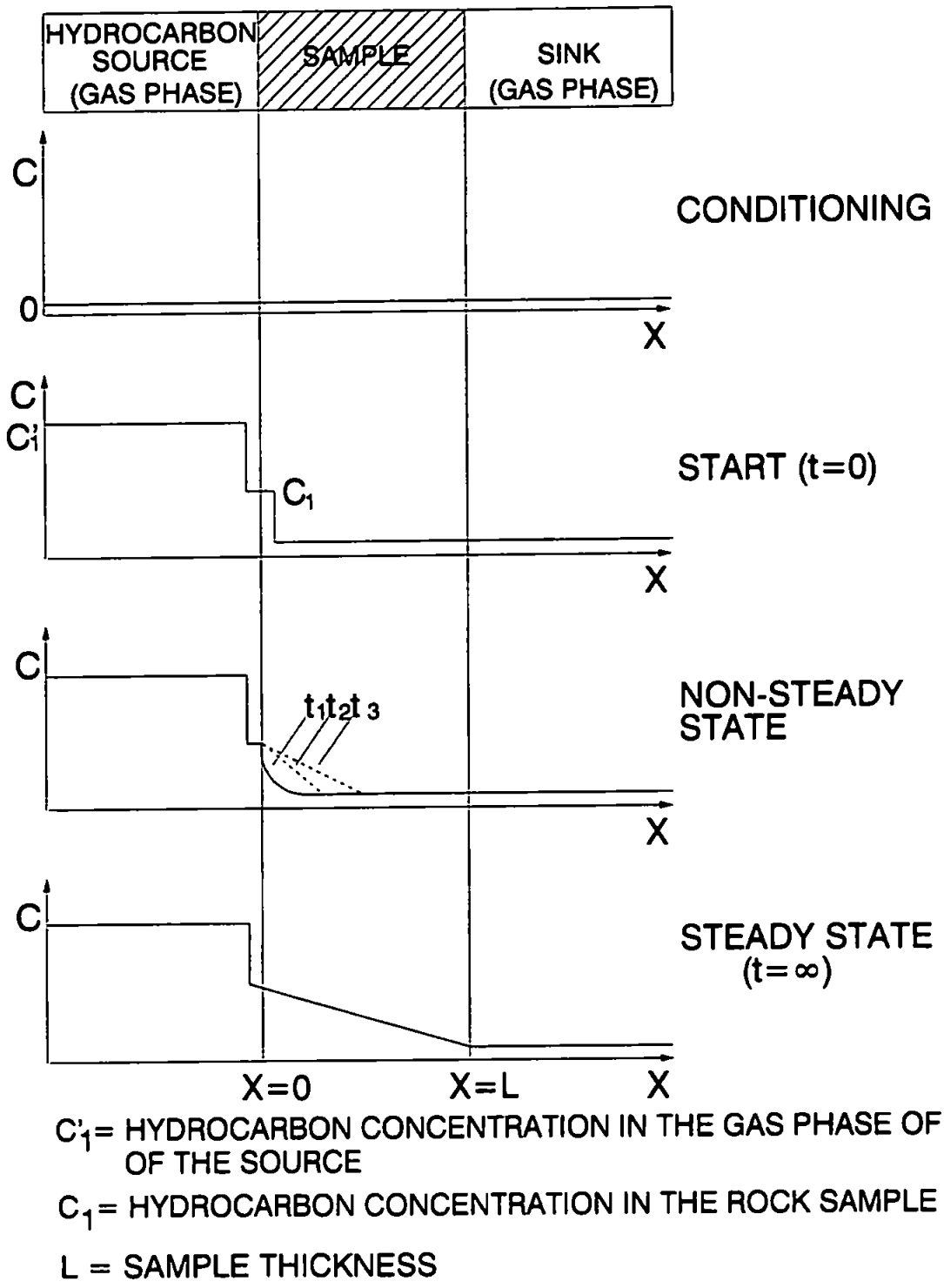

FIGURE 7.1: Principal Phases of Lag Time Diffusion Experiments

Fick's First and Second Laws give a mathematical description of diffusion in isotropic substances. Fick's First Law states that:

$$J = -D \frac{\partial C}{\partial X} \tag{7.1}$$

J is the gas flux per unit area of the section, flux being the rate of mass transfer of the diffusing gas, C is the concentration of the diffusing substance, X the space co-ordinate normal to the section and D is the diffusion coefficient. Fick's Second Law is:

$$\frac{\partial C}{\partial t} = D \frac{\partial^2 C}{\partial X^2} \tag{7.2}$$

If C_1 and C_2 are concentrations at distances x = 0 and x = l respectively, t is time, then we define boundary conditions, $C = C_1$ at $x = 0$ $t > 0$

$C = C_2$ at $x = l$ $t > 0$

and initial conditions $C = F(x)$ $0 < x > l$ $t = 0$

Crank (1975) mathematically describes the concentration change during the build up to the steady state condition. If face x = 0 is kept at a constant concentration C_1, and the other face x = l at C_2 and the sample is at an initial uniform concentration C_o then :

$$C = C_1 + (C_2 - C_1)\frac{x}{l} + \frac{2}{\pi}\sum_{n=1}^{\infty} \frac{C_2 \cos n\pi - C_1}{n} \sin \frac{n\pi x}{l} \exp(-D n^2 \pi^2 t / l^2) + \frac{4C_0}{\pi}\sum_{m=0}^{\infty} \frac{1}{2m+1} \sin \frac{(2m+1)\pi x}{l} \exp\{-D(2m+1)^2 \pi^2 t / l^2\} \tag{7.3}$$

Where n and m = 1,2,3...

A common experimental arrangement is that C_o and C_2 are zero, ie the sample is initially at zero concentration and the "sink" face of the sample is maintained at effectively zero concentration. Therefore Equation 7.3 reduces to :

$$C = C_1\left(1 - \frac{x}{l} - \frac{2}{\pi}\sum_{n=1}^{\infty}\frac{1}{n}\sin\frac{(n\pi x)}{l}\exp(-Dn^2\pi^2 t/l^2)\right) \qquad (7.4)$$

The rate at which the hydrocarbons emerge from unit area of sink side is given by, $-D(dC/dx)_{x=l}$ which is in effect Fick's first law of diffusive flux,

$$J = -D\frac{\partial C}{\partial X}$$

therefore,

$$\frac{\partial C}{\partial x} = C_1\left(\frac{-1}{l} - 2\sum_{1}^{\infty}\frac{1}{l}\cos\left(\frac{n\pi x}{l}\right)\exp(-Dn^2\pi^2 t/l^2)\right)$$

substitute for x = l

$$\frac{\partial C}{\partial x_{x=l}} = C_1\left(\frac{-1}{l} - 2\sum_{1}^{\infty}\frac{1}{l}\cos\left(\frac{n\pi l}{l}\right)\exp(-Dn^2\pi^2 t/l^2)\right)$$

$$-D\frac{\partial C}{\partial x_{x=l}} = DC_1\left(\frac{1}{l} + 2\sum_{1}^{\infty}\frac{1}{l}\cos n\pi\exp(-Dn^2\pi^2 t/l^2)\right)$$

The total amount of diffused gas, Q(t) is obtained by integrating with respect to t,

$$Q(t) = -D\int_0^t \frac{\partial C}{\partial x_{x=l}}dt = DC_1\left(\frac{t}{l} + 2\sum_{1}^{\infty}\frac{1}{l}\cos n\pi.\frac{-l^2}{Dn^2\pi^2}\exp(-Dn^2\pi^2 t/l^2)\right) + Constant$$

$$Q(t) = DC_1\left(\frac{t}{l} - \frac{2l}{D\pi^2}\sum_1^{\infty} \frac{\cos n\pi}{n^2} \exp\left(-Dn^2\pi^2\, t/l^2\right)\right) + Constant$$

At t = 0, Q(t) = 0 and substituting $(\cos n\pi)/n^2 = (-1)^n/n^2$ then,

$$0 = \frac{-2lDC_1}{D\pi^2} \sum_1^{\infty} \frac{(-1)^n}{n^2} + Constant$$

Therefore,

$$Constant = \frac{2lDC_1}{D\pi^2} \sum_1^{\infty} \frac{(-1)^n}{n^2}$$

and thus:

$$Q(t) = DC_1\left[\frac{t}{l} + \frac{2l}{D\pi^2} \sum_1^{\infty} \frac{(-1)^n}{n^2} \left(1 - \exp(-Dn^2\pi^2 t/l^2)\right)\right]$$

$$but \sum_1^{\infty} \frac{(-1)^n}{n^2} \; is\ equivalent\ to \; \frac{-\pi^2}{12} \; (a\ geometric\ series)$$

therefore,

$$Q(t) = DC_1\left[\frac{t}{l} + \frac{2l}{D\pi^2} \cdot \frac{-\pi^2}{12} \left(1 - \exp(-Dn^2\pi^2 t/l^2)\right)\right]$$

which, as $t \rightarrow \infty$ approaches the line

$$Q(t) = DC_1\left[\frac{t}{l} - \frac{l}{6D}\right] \qquad (7.5)$$

This represents a straight line graph and has an intercept on the t axis when Q(t) = 0 where

$$t_o = \frac{l^2}{6D} \tag{7.6}$$

t_0 is the period a plane of diffusate would take to transverse the sample and is called the lag time. Thus from a measurement of lag time and length, the sample thickness, the diffusion coefficient may be calculated. An example of such lag time plot is shown in Figure 7.2. On plotting the diffusive flux against time the attainment of the steady state is easily observed, Figure 7.3. The lag time does not correspond to the time at which the steady state is first attained. The dotted line, Figure 7.3, shows the flux verse time profile for such an ideal system. The amount of gas diffusing through the sample should not affect the lag-time. Figure 7.3 shows the situation in which two different steady states are achieved but the time to attain each is constant. Such a case is presented later for diffusion through reservoir sandstone samples.

7.2.1 Relationship Between Diffusion and Tortuosity

The path a diffusing species takes through a porous medium is dependant on the arrangement of voids and the connectivity of the void network. Van Brakel formulated an equation relating diffusion coefficients with tortuosity (T), porosity (Φ) and bulk diffusion coefficient of the gas into nitrogen (D_{12}):

$$D = \frac{D_{12}\Phi}{T^2} \tag{7.7}$$

The bulk diffusion coefficients for the three gases studied into nitrogen, were given the following values by Wackeham and Slater (1973):-

D_{12} methane = 0.243 cm^2/s

D_{12} iso-butane = 0.107 cm^2/s

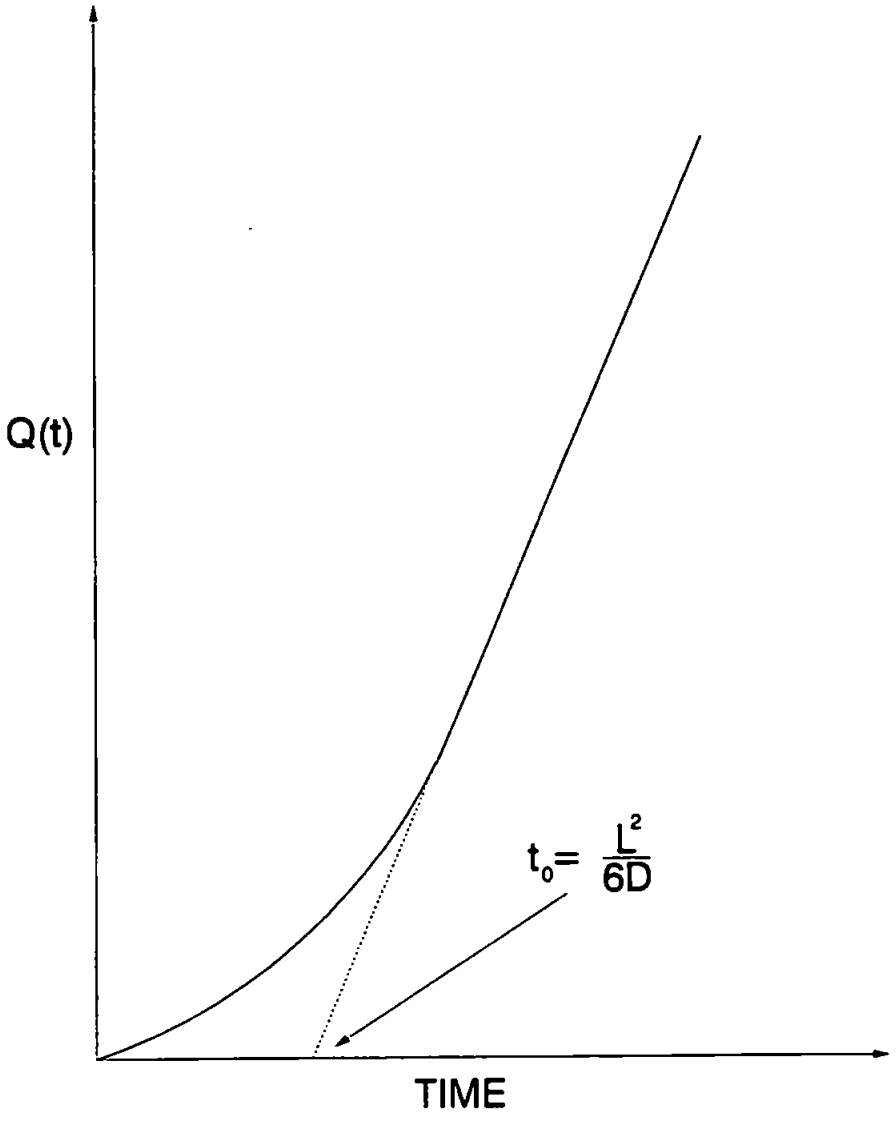

FIGURE 7.2: Lag Time Plot

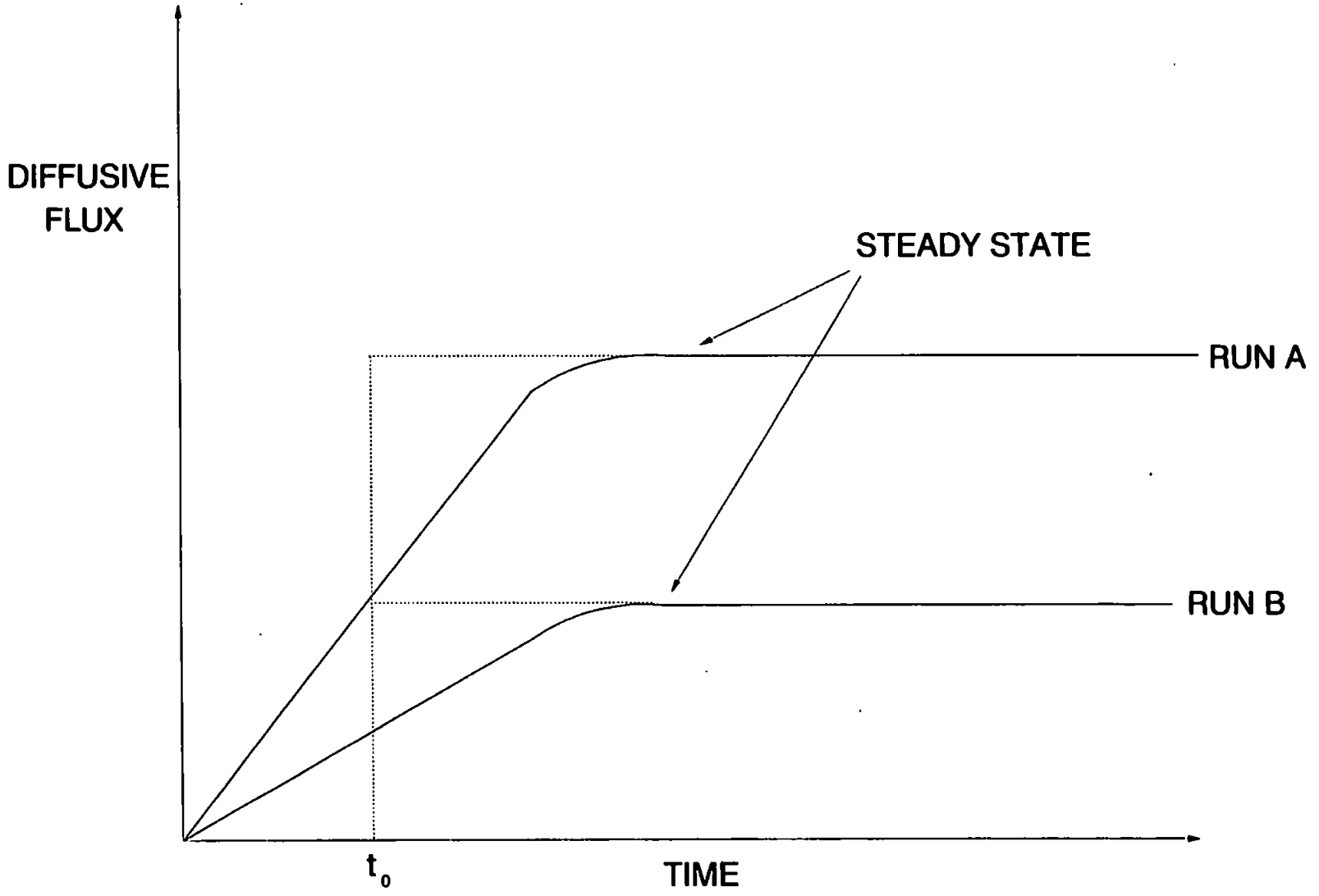

FIGURE 7.3: Diffusive Flux Against Time

D_{12} n-butane = 0.106 cm^2/s

Equation 7.7 is used later to calculate diffusion coefficients from simulated tortuosity values. A comparison of simulated and measured diffusion coefficients is made.

7.3 The Apparatus

The apparatus used to measure diffusion coefficients is adapted from a design by Krooss (1986). Changes to the Krooss' design that Dr Spearing initiated were due to the inability of Krooss' cold trap to collect the diffusing gases. The apparatus used in this study was initially constructed by Dr M.C. Spearing, to which gas-tight discs and other modifications were made, as described below. The Spearing diffusion apparatus is shown in Figure 7.4.

The principal components of the apparatus are a gas diffusive source, the sample cell, gas collection and analytical system. The source of the diffusing gases are two gas cylinders, one containing methane and the other a 50:50 mixture of n-butane and iso-butane. The flow rate from each cylinder is controlled by the cylinder regulators and in-line needle valves. Bubble flowmeters are used to measure total flow rate and that from each cylinder. All flow lines are made of 1.8mm internal diameter brass tubing, all fittings are Swagelok or captive seal.

The sandstone samples must be mounted in brass rings to allow a gas-tight fit within the sample cell. The mounting medium is an epoxy resin. A resin to hardener ratio of 2:1 was found to be the best composition. The epoxy resin is allowed to cure for approximately two hours before setting the sample in the brass ring. Curing before application produces a high viscosity resin which is unlikely to penetrate deep within the sandstone pore space. After complete resin hardening the brass and resin are ground smooth on one face by a lathe.

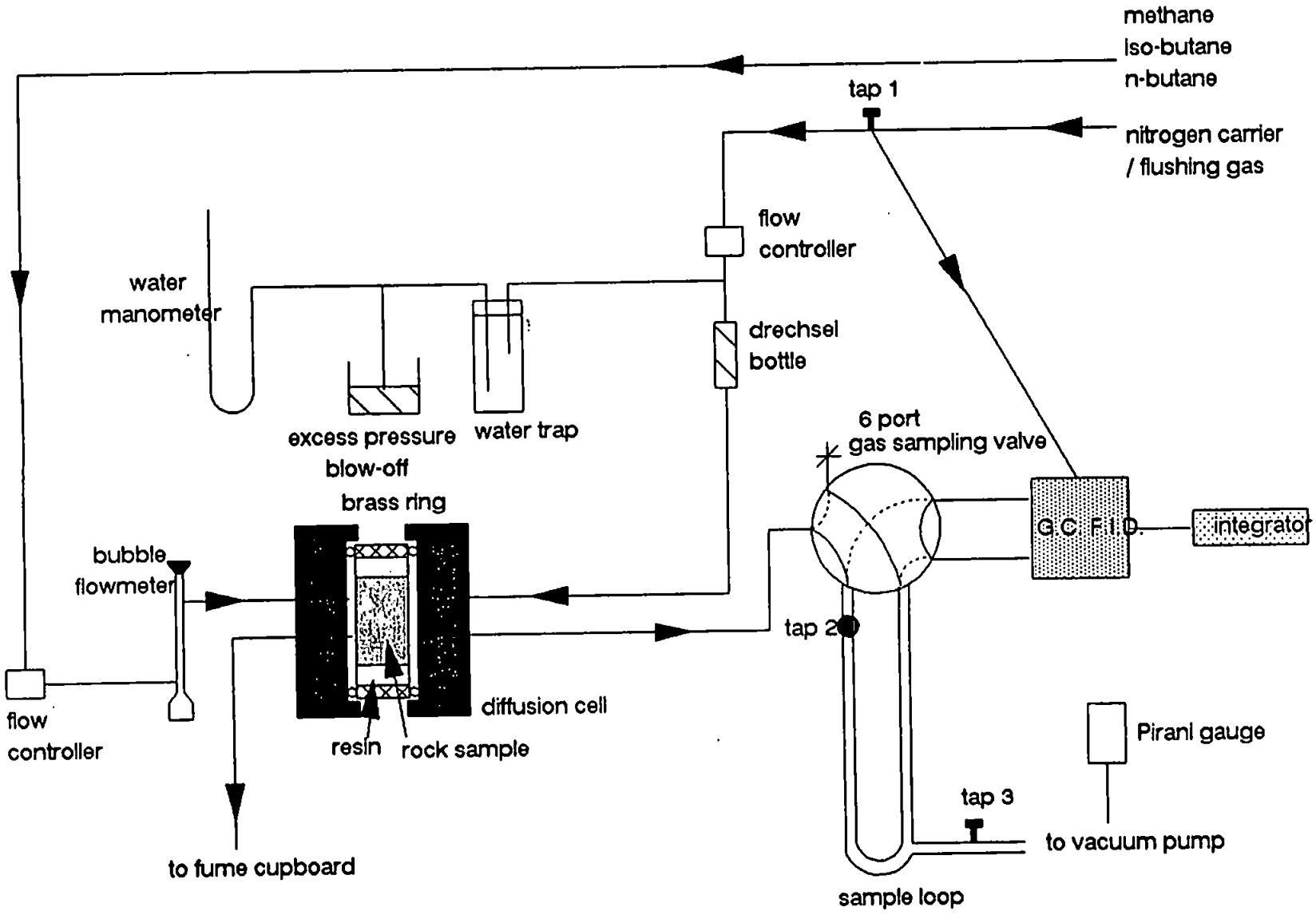

FIGURE 7.4: Diffusion Apparatus

The sample cell consists of two stainless steel plates. The mounted sample sits in a recess cut in the steel discs, the brass ring fits tight against rubber o-rings set in each steel disc which forms a gas tight seal. A gas tight disc can be positioned over the face of the sample which stops diffusion into the sample before the source cavity is full of diffusate, Figure 7.5. A full explanation of the gas tight disc operation is given on pages 139-140. The source and sink volumes are 7.2 cm^3 and 8.5 cm^3 respectively. The source side of the sample cell has an inlet of diameter 3mm and an outlet diameter of 6mm. The large outlet diameter is to reduce pressure build up on the source side. The volume of the sink has been optimized to allow negligible concentration build-up, thus satisfying the criteria that $C_2 = O$ in equation 7.4, but not excessively large, so as to maintain short sampling periods.

The gas collection system consists of a sample loop of 1.8mm internal diameter brass tubing connected to the sink side of the sample cell and the analytical system, a gas chromatograph (G.C.), via a 6-port gas sampling valve. The sample loop has a volume of 18.2 cm^3. This volume is large enough to accommodate all the gases flushed from the sink side of the sample cell, whilst not being too large and causing a large pressure drop upon transfer to the G.C.. Tap 2 is a needle valve and allows fine control over the transfer of gas into the sample loop. Tap 3 is an on-off valve used to control evacuation of the sample loop. To maintain a zero pressure gradient across the sample during sink flushing, a nitrogen blow-off and water manometer are connected to this side of the sample cell. Upon sink flushing nitrogen is directed from the G.C. into the sink via Tap 1. The nitrogen flow rate is high within the G.C.; a flow controller reduces this flow for flushing purposes.

The analytical system is a Pye 104 Gas Chromatograph with a flame ionisation detector. The G.C. column which gave the best separation of the three alkanes contained Porapak P, which is a porous cross linked polymer bead packing. The G.C. signal is processed by an integrator.

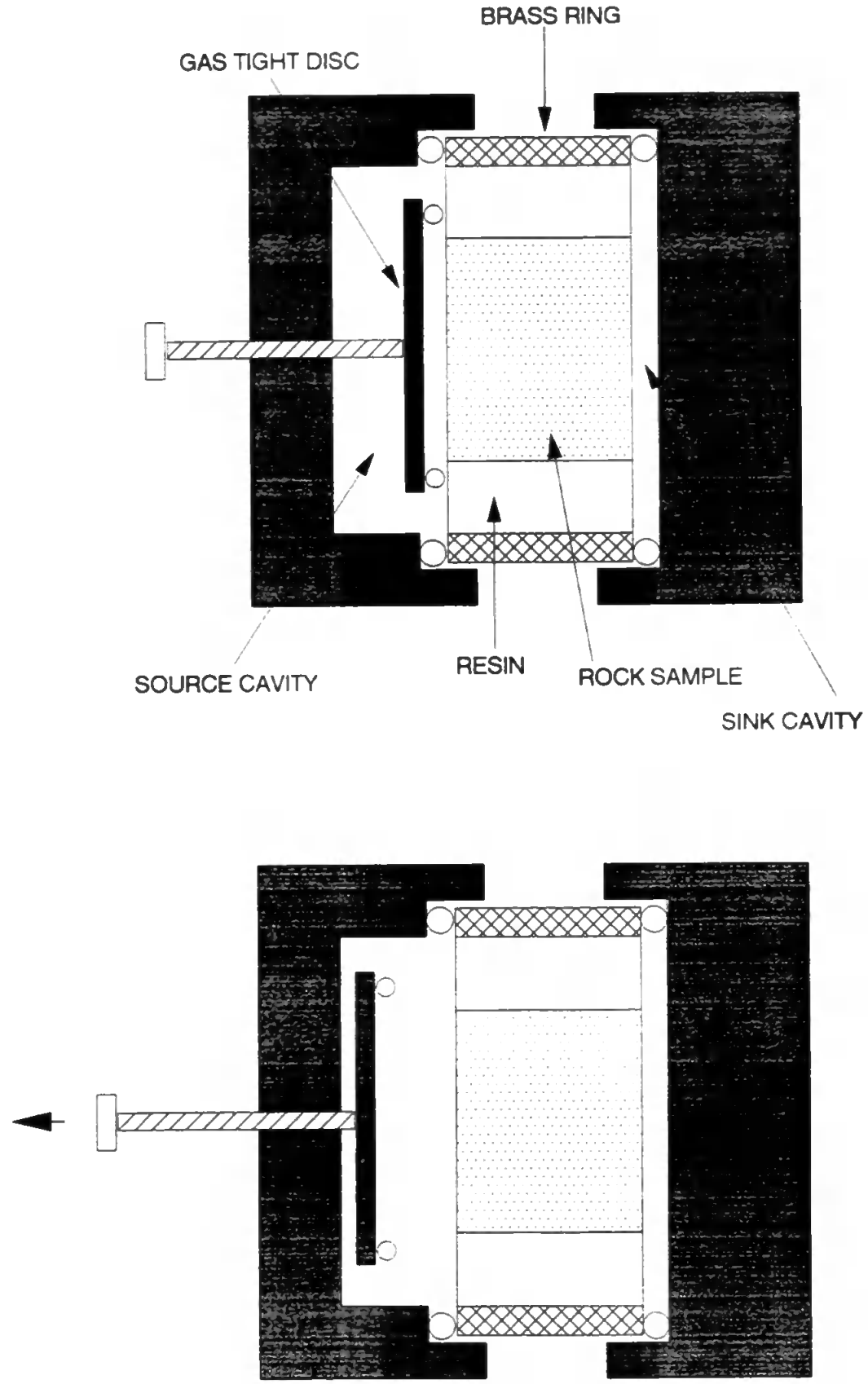

FIGURE 7.5: Sample Cell Showing Gas-Tight Disc Operation

Experimental Procedure

1) The G.C. is turned on, the flame is lit and the oven left to equilibrate. The G.C. settings are as follows :

Attenuation	10×10^2
Oven Temperature	82°C
Nitrogen Carrier Gas Flow Rate	75 ml/min.
Detector Temperature	150°C
Flame Ionisation Detector Air Flow Rate	300 ml/min.
Flame Ionisation Detector Hydrogen Flow Rate	44 ml/min.

The integrator is set up as follows :

Attenuation	1 - 4
Peak Width	0.05 - 0.16
Threshold	0.0
Area Reject	-2

Equilibration of the G.C. is usually accomplished overnight. When running many samples it was found best to leave the G.C. on constantly.

2) A few hours before an experiment the hydrocarbon flow rates are set at a cumulative rate of 0.2 ml/min.. Equilibrium of hydrocarbon flow is very difficult to obtain but once reached can be maintained easily. Thus when running many experiments it is best to leave the hydrocarbons in constant flow mode. When not entering the sample cell hydrocarbons are piped into the fume cupboard.

3) The mounted sandstone is secured in the sample cell and the gas tight disc screwed down over the source face of the rock.

4) The mixture of hydrocarbons are introduced to the source side of the sample cell. The time the hydrocarbon flow line is connected should be noted. At a combined flow rate

of 0.2 ml/min., the source cavity will take 36 minutes to fill.

5) During filling of the source cavity the sample loop is evacuated up to Tap 2. A vacuum of 0.05 Torr can be achieved if the system is totally leak free.

6) When the source cavity is full the gas tight disc is screwed away from the sample face, a stop watch is started at this point.

7) The flushing sequence is started after the disc is withdrawn to check that no alkanes entered the rock during source cavity filling. Tap 3 is closed and Tap 2 is opened carefully until the water manometer rises slightly. Tap 1 is switched to direct the nitrogen from the G.C. into the sink side of the sample cell. Tap 2 is slowly opened further, keeping the water manometer level. When the sample loop is full, excess nitrogen will bubble through the blow-off. Tap 1 is immediately returned to its original position, to direct nitrogen through the G.C.. The gas sampling valve is switched from the "fill" position to the "inject" position, thus flushing the contents of the sample loop into the G.C. The integrator is started. Transfer of the sample loop contents to the G.C. takes about one minute. After this time Tap 2 is closed and the sampling valve returned to the "fill" position. Tap 3 can now be opened to re-evacuate the sample loop.

8) The flushing sequence is repeated every 6½ minutes until the peak areas for each hydrocarbon are constant for at least four consecutive intervals.

The experiment is then stopped, the cumulative peak areas of each hydrocarbon calculated and each flushing time noted.

The flushing sequence is extremely difficult to perform without inducing large pressure differences across the sample. During some experiments a hexane manometer was placed across the sample cell to monitor pressure differences. With practice the manometer could be kept level during each flushing. The experimental procedure is the same as that outlined in Spearing (1991), apart from the magnitude of the combined flow rate used, and the covering of the rock face with the gas tight disc during source cavity filling. Spearing

recommended a combined hydrocarbon flow rate of 1.5 ml/min. At this flow rate the hexane manometer across the sample indicated 0.5mm of hexane pressure difference for a 99.74md sandstone sample. Applying Darcy's Law to this system such a pressure difference across this sample produce viscous fluxes of the same order as the diffusion results quoted by Spearing (1991). Thus the combined hydrocarbon rate has been reduced to 0.2 ml/min.. No pressure difference was detected at this flow rate, either by hexane manometer or differential pressure transmitter. The new low hydrocarbon flow rate causes a long source cavity filling time (36 minutes). The gas tight disc allows complete filling of the source cavity before any hydrocarbons enter the rock. The Spearing method had a large error associated with the exact starting time of the experiment. Even at a flow rate of 1.5 ml/min., the source cavity takes 4.8 minutes to fill, thus the exact time diffusion commences is unknown. The source cavity concentration is not constant thus the criteria for Equation 7.4 are not fulfilled. The gas tight disc eliminates all these errors and uncertainties.

7.4 Regression Analysis to Find Lag Time (t_o)

The lag time (t_o) can be calculated by plotting the cumulative peak height, from the G.C. integrator, for each gas against time and finding the straight line intercept when cumulative peak height equals zero, as in Figure 7.2. The lag time can be obtained in an accurate manner by carrying out a regression analysis of the data using a computer statistics package. The Minitab statistical package has been used in this study. The cumulative peak areas and time data are input into the computer except for the first few points where the steady-state diffusive flux has not been reached. The regression calculation calculates the equation of the best fit straight line. As new points at lower sampling times are added the curve deviates from the straight line. The deviation from the straight line is expressed as an error value, E_n with D_n associated degrees of freedom.

If

$$\frac{E_n - E_{n-1}/D_{n-1}}{E_{n-1}/D_{n-1}} > 4 \qquad (7.8)$$

then the current data point deviates from the straight line. For a reasonable number of points on the straight line, the critical value of 4 for the ratio above corresponds to a 5% significance level. The equation of the straight line before the unacceptable deviation occurred is used to obtain the lag-time. Using equation 7.8 the diffusion coefficient can be calculated.

Figure 7.6 shows an example of successive regressions as performed on the Minitab package. In this example time is plotted against cumulative peak area, so lag time is equal to the y-axis intercept. Applying Equation 7.8 to the error data a ratio of 1 is obtained. Assuming that the next data point deviates then in this example lag time is 4.17 minutes.

7.5 Results

The diffusion coefficients of the three hydrocarbons, methane, iso-butane and n-butane, have been measured in one sample of Clashach outcrop sandstone and eight reservoir sandstone samples. Spearing (1991) extensively studied diffusion within samples of Clashach outcrop sandstone, and this sandstone is almost 100% quartz and contains very little fine material. Such a clean void structure contrasts greatly with that of the reservoir sandstones. If the degree of complexity of the void space affects diffusion then this may be indicated in the diffusion coefficients measured.

The operation of the diffusion apparatus was extremely difficult. Many runs had to be aborted because the hydrocarbon flow rate fluctuated or a large pressure difference was induced across the sample during sink flushing. Appendix 5 shows the peak area against time plots for at least five successful runs for each sample. The peak area against time plots show the build up to a steady-state flux for each gas. Occasionally methane attains a steady state before the second sink flushing time (ie 6.5 minutes), so in these

```
MTB > PRINT C1 C2
```

C1=TIME, C2=CUMULATIVE PEAK AREA.

ROW	C1	C2
1	0.0	*
2	6.5	*
3	13.0	*
4	19.5	*
5	26.0	5035944
6	32.5	6478144
7	39.0	7985744
8	45.5	9470944
9	52.0	11000644
10	58.5	12540544

DATA SET

```
MTB > REGRESS C1 1 C2

The regression equation is
C1 = 4.38 +0.000004 C2

6 cases used 4 cases contain missing values

Predictor       Coef        Stdev    t-ratio       p
Constant      4.3835       0.2072      21.15   0.000
C2        0.00000433   0.00000002     190.43   0.000

s = 0.1428      R-sq = 100.0%    R-sq(adj) = 100.0%

Analysis of Variance
```

D_{n-1}

```
SOURCE       DF        SS         MS          F       p
Regression    1    739.29     739.29   36264.27   0.000
Error         4      0.08       0.02
Total         5    739.37
```

E_{n-1}

```
MTB > LET C2(4)=3563844
MTB > REGRESS C1 1 C2

The regression equation is
C1 = 4.17 +0.000004 C2

7 cases used 3 cases contain missing values

Predictor       Coef        Stdev    t-ratio       p
Constant      4.1678       0.1751      23.80   0.000
C2        0.00000435   0.00000002     212.34   0.000

s = 0.1620      R-sq = 100.0%    R-sq(adj) = 100.0%

Analysis of Variance
```

D_n

```
SOURCE       DF        SS         MS          F       p
Regression    1    1182.9     1182.9   45087.70   0.000
Error         5       0.1        0.0
Total         6    1183.0
```

E_n

APPLYING EQUATION 7: $$\frac{E_n - E_{n-1} / D_n - D_{n-1}}{E_{n-1} / D_{n-1}} = \frac{0.1-0.08/5-4}{0.08/4} = 1$$

FIGURE 7.6: Mini-Tab Regression Analysis

cases the lag time cannot be calculated. The methane diffusion in high porosity/permeability sandstones is difficult to measure with this apparatus for short sample lengths due to short lag times. Thus for high porosity/permeability rocks the longest sample length obtainable is recommended.

The flame ionisation detector within the G.C. measures the number of carbon radicals produced when each hydrocarbon is ionised. Thus the peak area response for unit volumes of iso-butane and n-butane will be four times that for the same volume of methane. The experimental peak area against time plots show that iso-butane always attains a higher peak area plateau, ie steady state, than n-butane. The butane source cylinder contains a 50:50 mixture of iso and n-butanes, and so the difference in the steady state peak areas must be due to subsequent change in the butane ratio. The butane mixture is not very volatile at room temperature. Iso-butane has the lowest boiling point, so fractionation of the mixture as it leaves the cylinder is a distinct possibility. The flame ionisation detector is very sensitive; a small increase in the amount of gas diffusing through the sample will produce a large increase in peak area. Diffusion is related to the time taken to reach the steady state, not the steady state peak area. The independence of diffusion and steady state peak area are discussed later in more depth.

The regression analysis using the Minitab statistical package produced excellent line fits. In all experiments, the best fit line to the data, including the last data point to satisfy equation 7.8 had an R-square regression fit of 1.000. The excellence of the fitted line means that the lag time intercepts had low variances. One standard deviation from the lag time intercepts produced diffusion coefficients which never exceeded ± 7% of the coefficient calculated from the regression analysis value. In many experiments the lag time intercept had a standard deviation of zero.

The diffusion coefficients measured during successive runs on the same samples were found to have a wide range. Extreme results from these ranges were analyzed by a

Q-test. A few extreme values were discarded with 90% confidence. Table 7.1 shows the remaining range of diffusion coefficients for each sandstone sample: the mean values are shown in brackets. The range of values for each sample still appear quite large. The narrow range of methane diffusion coefficients is due to the small number of successful runs for this gas as explained earlier. The wide range of diffusion coefficients measured for each sandstone sample prompted an analysis of errors associated with the technique.

SAMPLE NO.	METHANE DIFFUSION COEF. RANGE/cm^2s^{-1} $X10^{-3}$	ISO-BUTANE DIFFUSION COEF. RANGE/cm^2s^{-1} $X10^{-3}$	n-BUTANE DIFFUSION COEF. RANGE/cm^2s^{-1} $X10^{-3}$
CLASHACH	1.460-10.250 (5.415)	4.330-9.660 (6.978)	4.930-7.290 (6.325)
212A	_____	2.204-5.853 (4.328)	1.784-5.049 (3.565)
250A	_____	4.774-18.568 (10.901)	2.700-8.319 (5.260)
250E	_____	6.808-8.587 (7.687)	1.967-6.032 (4.033)
490A	1.375-1.496 (1.435)	1.309-17.490 (7.274)	1.321-9.797 (5.071)
490B	1.330-2.447 (1.888)	1.010-12.765 (5.107)	1.671-11.562 (4.618)
490C	4.524	3.067-23.570 (12.477)	2.918-16.310 (9.559)
490D	8.279-11.678 (9.978)	3.289-9.262 (5.465)	2.701-7.325 (4.508)
490E	5.053-6.851 (5.952)	1.213-4.396 (2.982)	1.185-3.960 (2.660)

EXTREME RESULTS EXCLUDED FROM RANGES WITH 90% CONFIDENCE.
BRACKETED VALUES ARE THE MEAN OF ACCEPTED RESULTS.

TABLE 7.1: Diffusion Coefficients for Reservoir Sandstones.

7.5.1. Error Analysis

The formation for viscous fluxes within the sample has already been cited as a major source of error within diffusion coefficient measurement. The combined alkane flow rate into the source cavity had been reduced to 0.2 ml/min. At this flow rate, no pressure difference is detected across the sample cell. The possibility of viscous fluxes still exists even at this reduced flow rate. If viscous fluxes predominated, the lag times and diffusion coefficients will be proportional to the peak area once the steady state is established. Figure 7.7 shows two examples of samples which have given the same lag time for runs with very different peak areas at steady state. The top graph of Figure 7.7 is for iso-butane during runs 6 and 10 in sample 250A. The peak area at the steady state for run 10 is approximately four times that of run 6 but the lag times are almost the same. The bottom graph of Figure 7.7 shows a similar result for n-butane in sample 250E. Diffusion is independent of steady-state peak area and so viscous flux did not dominate during these experiments. Figure 7.7 also shows that the capacity of the sample for diffusing increased quantities of hydrocarbon has not been exceeded during these experiments. Ambiguity about the start time of diffusion has been eliminated by the addition of the gas-tight disc within the source cavity. The start of hydrocarbon diffusion is known to within ± 2 seconds.

Error within the measurement of sampling time could introduce significant error in the lag time calculation. The sink cavity is flushed with nitrogen periodically, usually every 6.5 minutes however the exact time of flushing is unknown. The sink volume also takes a finite time to empty when flushed. These effects produce a flushing time error of ± 0.25 minutes. The effect of this error on the diffusion coefficients can be great, especially if low lag times are measured.

Figures 7.8 to 7.10 show the measured diffusion coefficient ranges with the effect of the identified errors. As mentioned earlier the ranges for methane are narrower because

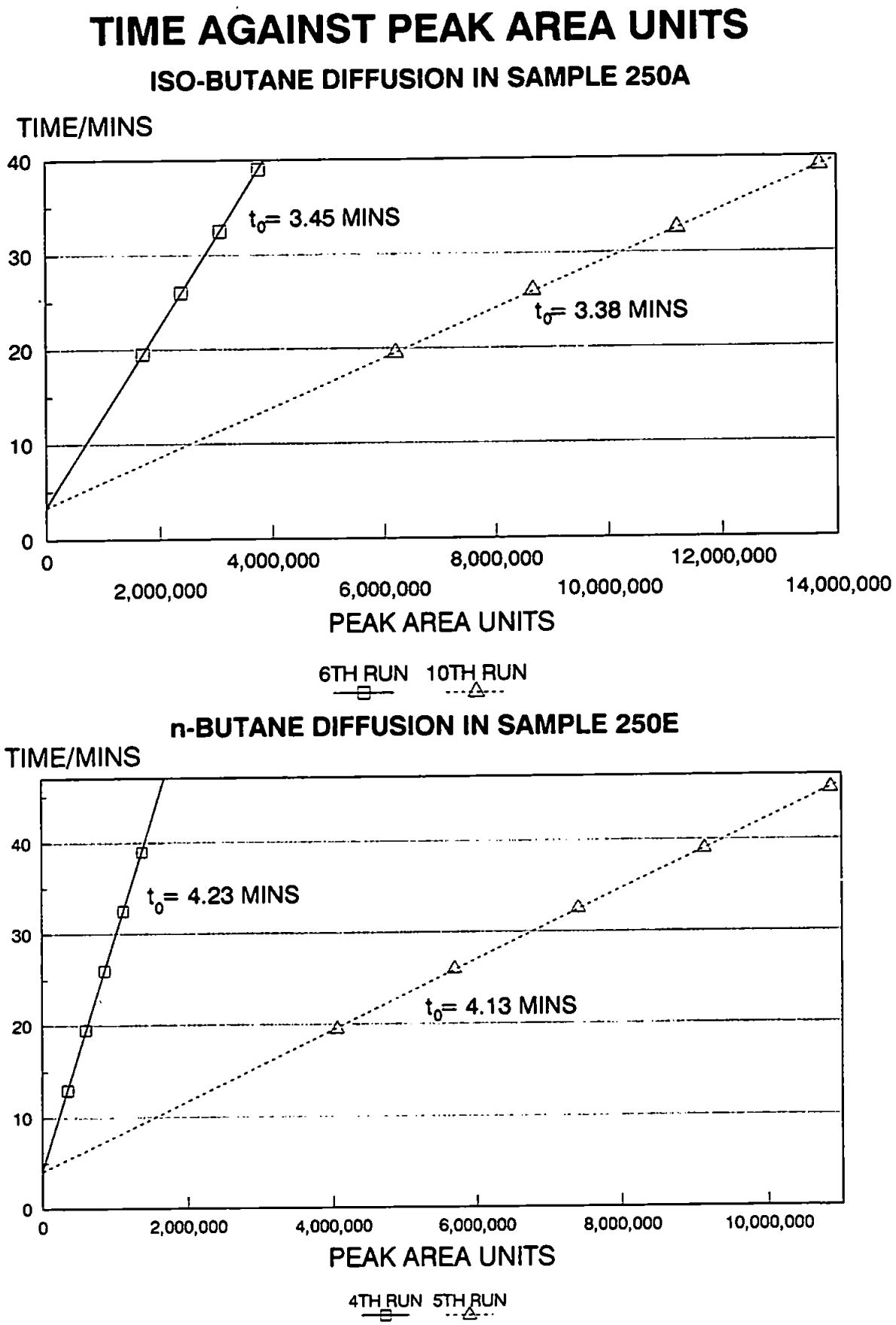

FIGURE 7.7: Time Against Cumulative Peak Are Units

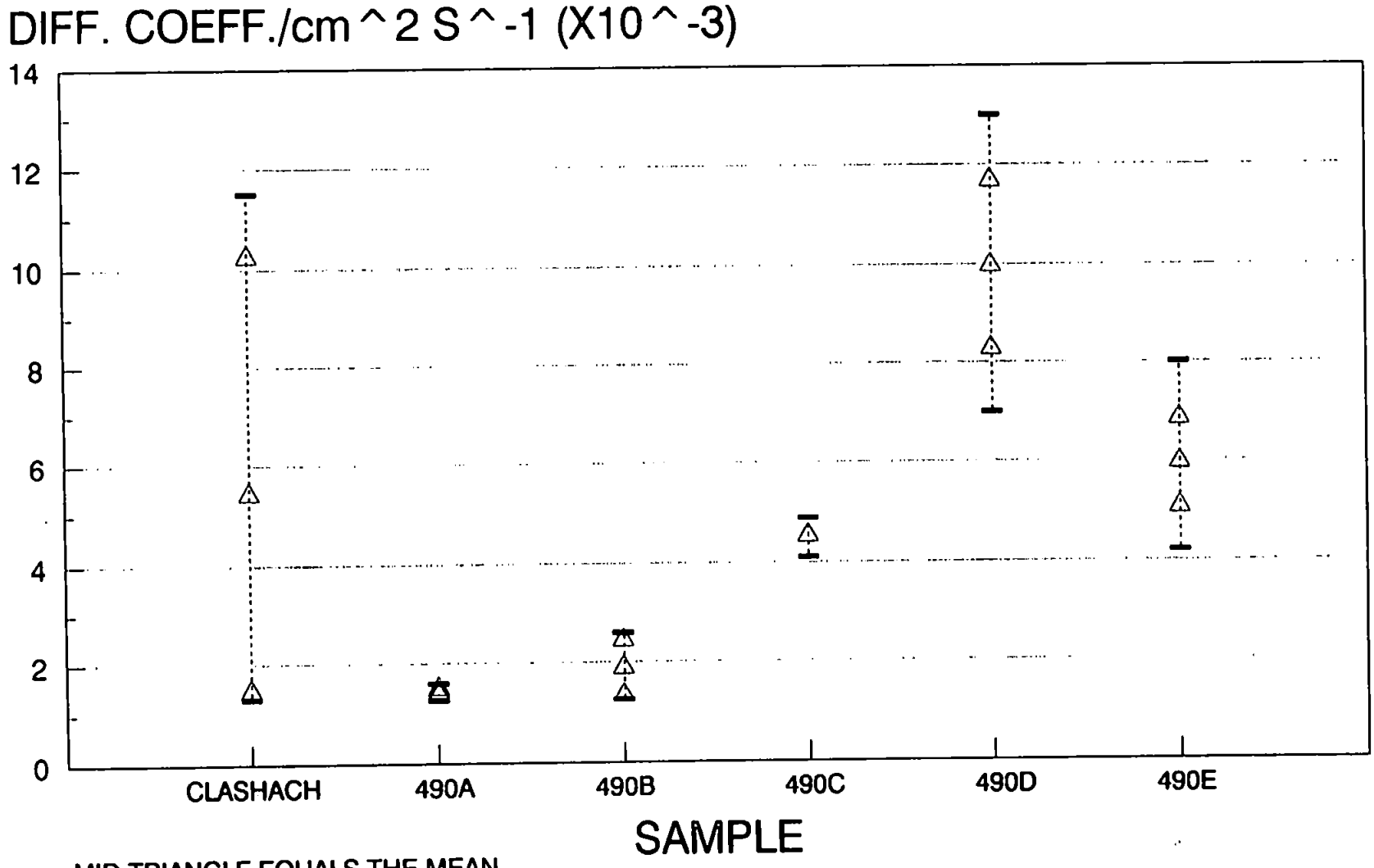

FIGURE 7.8: Methane Diffusion Coefficient Ranges

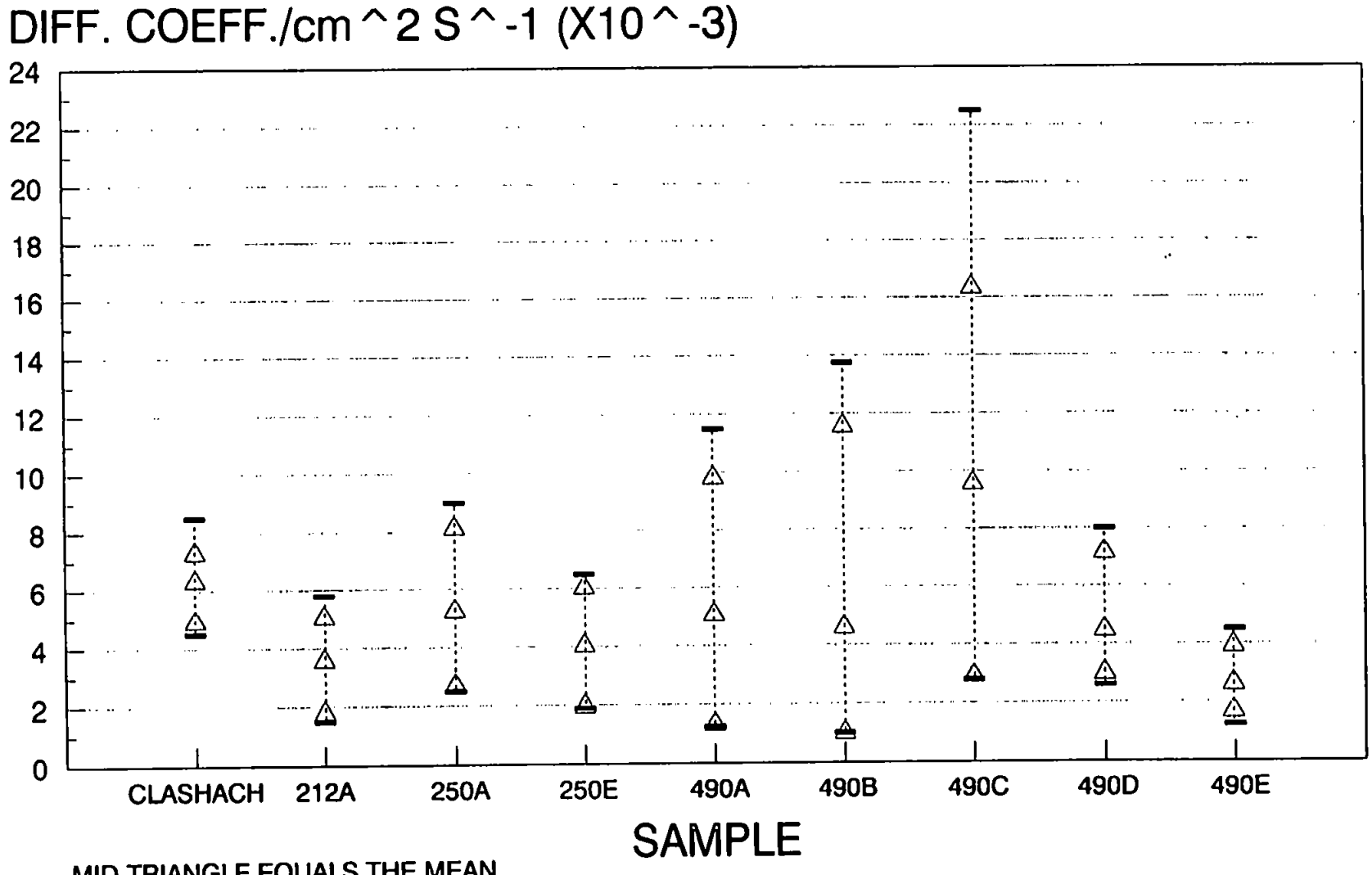

FIGURE 7.9: N-Butane Diffusion Coefficient Ranges

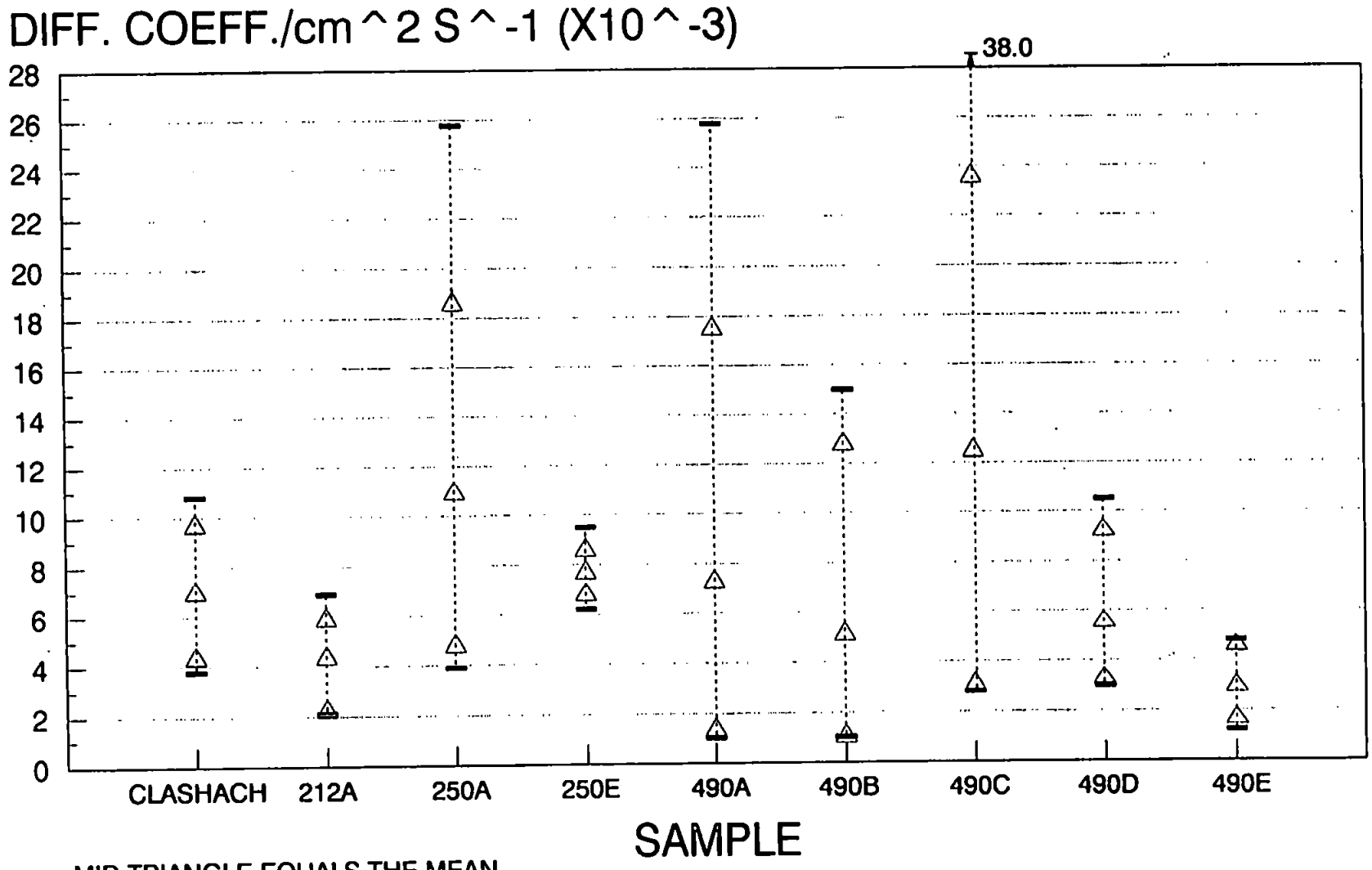

FIGURE 7.10: Iso-Butane Diffusion Coefficient

only a few successful runs were performed. The effect of the flushing time error on large diffusion coefficients is reflected in the larger ranges of the iso-butane coefficients compared with the ranges for n-butane.

7.5.2 Analysis of Variables within Diffusion Measurements

The error associated with the flushing time can explain part of the diffusion coefficient range. In an attempt to identify any other factors which may affect diffusion coefficient measurement, a multivariate data analysis computer package called Unscrambler has been applied to the data. Eleven factors which may affect the diffusion measurements have been calculated. Table 7.2 outlines each factor and its range.

Multivariate data analysis is used to find a mathematical relation between two data sets, x and y. The x data set contains the values of the eleven variables during each run. The y data set contains all the calculated diffusion coefficients including those later removed during the Q-test. The Unscrambler program can produce a calibration model to explain the variance in the y-data set ie. in the diffusion coefficients. The calibration model can then be used to predict unknown y-values from new measured x-values. Unscrambler uses a partial least squares regression to form the model. The calibration model relates the variance in the x-data to the variables in the y-data through a set of components or model factors. The first factor explains the most dominant variance, the largest fraction of the total data set variance. The second factor handles the next-largest fraction of variance. Figure 7.11a shows the relationship between the variables and the first three model factors. The loadings on the y-axis indicate which variables are dominant within each factor. Positive and negative loading carry equal weight. The first factor within the model uses permeability, porosity and the percentages of each alkane detect at zero time as its dominant variables. The correlation of porosities and permeabilities with diffusion is to be expected and this is discussed later.

KEY TO FIG7.11a	FACTOR	DEFINITION	RANGE
A	PERMEABILITY/mD	ABSOLUTE GAS PERMEABILITY OF SAMPLE, AS DEFINED IN CHAPTER 2.	CONSTANT FOR EACH SAMPLE. 10.74-1208.49 mD BETWEEN SAMPLES
B	POROSITY/%	GAS POROSITY, AS DEFINED IN CHAPTER 2.	CONSTANT FOR EACH SAMPLE. 12.3-23.2% BETWEEN SAMPLES
F	COMBINED ALKANE FLOW RATE/ml/min	COMBINED FLOW RATE OF THE THREE ALKANES, MEASURED ON BUBBLE METER.	0.154-0.273 ml/min
H	METHANE FLOW RATE/ml/min	METHANE FLOW RATE, MEASURED ON BUBBLE METER.	0.047-0.178 ml/min
J	ISO-BUTANE FLOW RATE/ml/min	ISO-BUTANE FLOW RATE, CALCULATED BY MULTIPLYING BUBBLE METER READING BY RATIO OF IS0 AND n-BUTANE STEADY STATE PEAK HEIGHTS.	0.016-0.090 ml/min
I	n-BUTANE FLOW RATE/ml/min	n-BUTANE FLOW RATE, CALCULATED BY MULTIPLYING BUBBLE METER READING BY RATIO OF IS0 AND n-BUTANE STEADY STATE PEAK AREA.	0.003-0.060 ml/min
G	DAYS BETWEEN RUNS	NUMBER OF DAYS BETWEEN SUCCESSIVE RUNS.	7-335
C	PERCENTAGE OF METHANE STEADY STATE AT EXPT. START	METHANE PEAK AREA AT FIRST SINK FLUSHING (T=0) AS A PERCENTAGE OF FINAL STEADY STATE PEAK AREA.	0.0-20.0%
D	PERCENTAGE OF ISO-BUTANE STEADY STATE AT EXPT. START	ISO-BUTANE PEAK AREA AT FIRST SINK FLUSHING (T=0) AS A PERCENTAGE OF FINAL STEADY STATE PEAK AREA.	0.0-2.8%
E	PERCENTAGE OF n-BUTANE STEADY STATE AT EXPT. START	n-BUTANE PEAK AREA AT FIRST SINK FLUSHING (T=0) AS A PERCENTAGE OF FINAL STEADY STATE PEAK AREA.	0.0-3.1%
K	METHANE:ISO-BUTANE RATIO	RATIO OF METHANE AND ISO-BUTANE STEADY STATE PEAK AREA.	0.166-2.737

TABLE 7.2: Potential Factors Affecting Diffusion Coefficients.

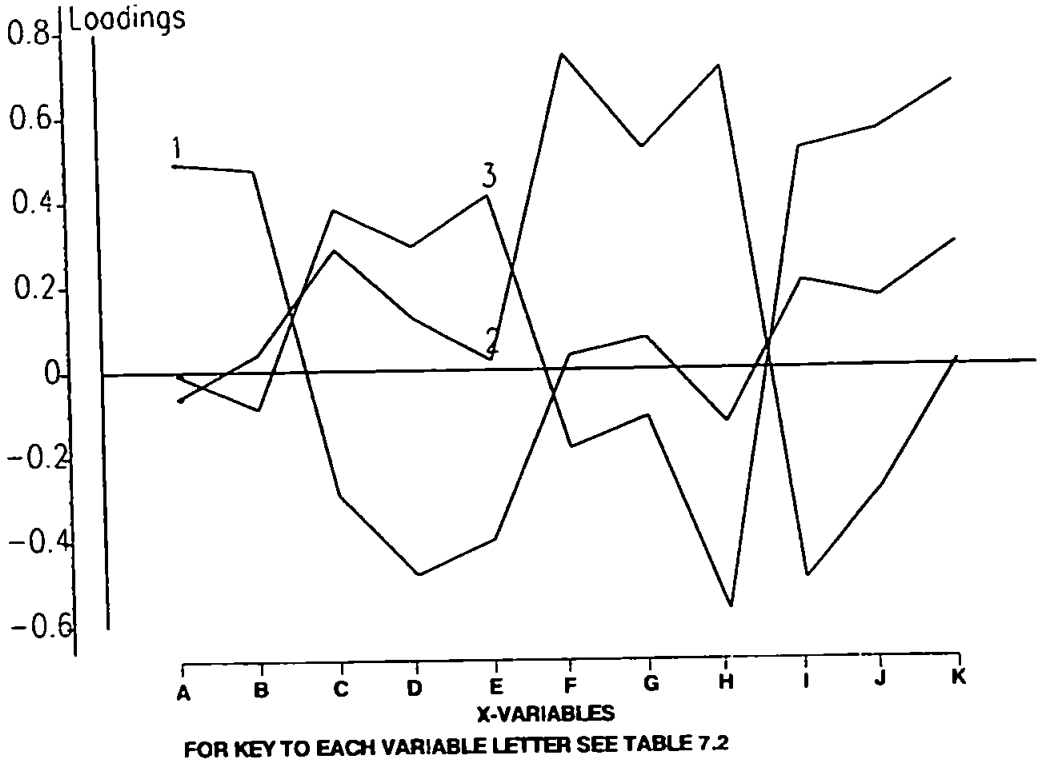

FIGURE 7.11a: Loadings for the Eleven Variables Identified in Table 7.2 for the First Three Modelling Factors

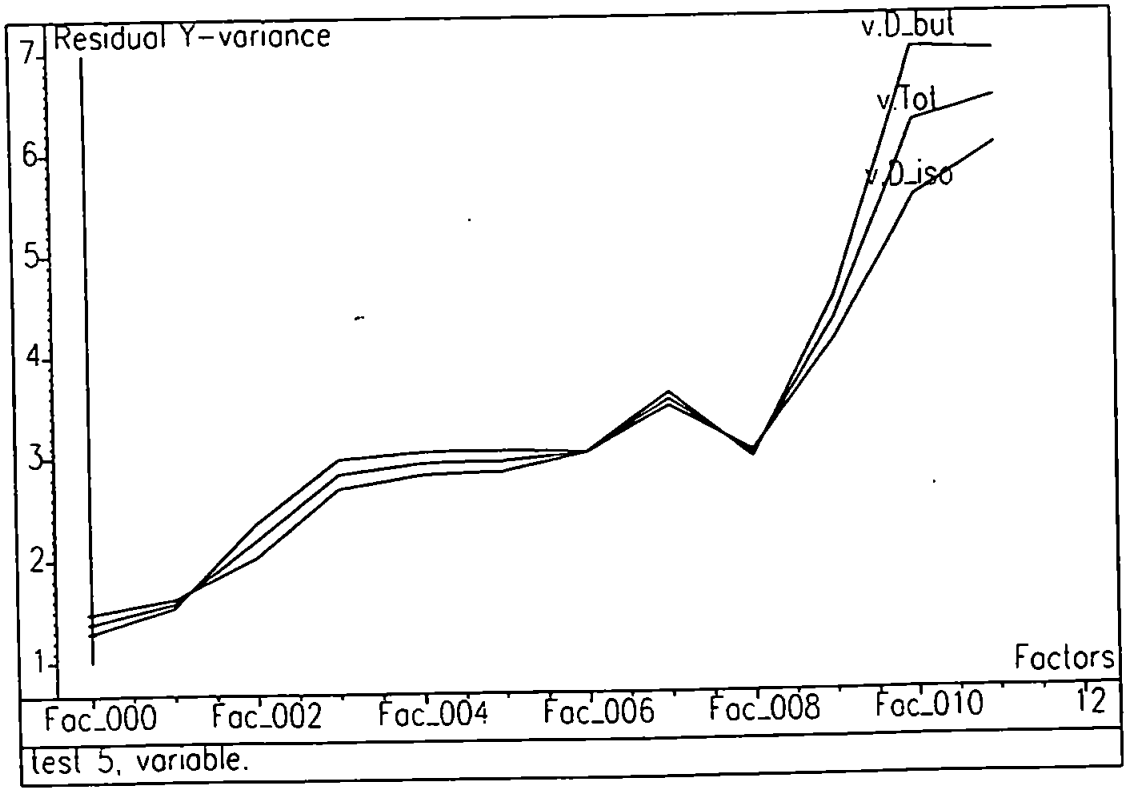

FIGURE 7.11b: Residual Variance as an Increasing Number of Modelling Factors are Included in the Model

The relation between diffusion coefficients and percentage of each alkane at zero time is also obvious. If the gas tight disc leaks during source cavity filling, then the diffusion coefficient measured will be anomalously high. These extreme results were removed later by the Q-test. Unscrambler has proved that it is wise to reject these extreme results. The second and third model factors represent less dominant components of variance. The combined and individual alkane flow rates have high loadings within the second model factor and days between successive runs also had high loading.

A test of the calibration model is its ability to explain the variance in the diffusion coefficient data set. Figure 7.11b demonstrates the amount of variance left as the number of factors within the model is increased. The ideal model will attain a local residual variance minimum at a given number of model factors. The residual variance increases with addition of each model factor. This indicates that the calibration model is unable to explain the variance in the diffusion coefficient range. There is a slight correlation between porosity, permeability and diffusion. The remaining variance within the diffusion coefficient data set is not related to any of the variables identified. The unexplained variance maybe due to an amount of natural randomness within diffusion processes.

7.6 Correlation of Diffusion with Petrophysical Properties

The mean values of the iso-butane diffusion coefficients for all the relatively clean sandstones correlate well with permeability and formation factor. The clean sandstone samples are clashach, 212A, 250A and 250E. The regression analysis of the data is shown in Figure 7.12. The permeability correlation produced an R-squared value of 0.93 for the four samples. The formation factors correlate less precisely with diffusion coefficient. The porosity of each sample also correlates with mean iso-butane diffusion coefficient, although not as well as permeability and formation factor. The intercept of the best fit line with the 100% porosity point should be equal to the bulk diffusion coefficient of iso-butane in air.

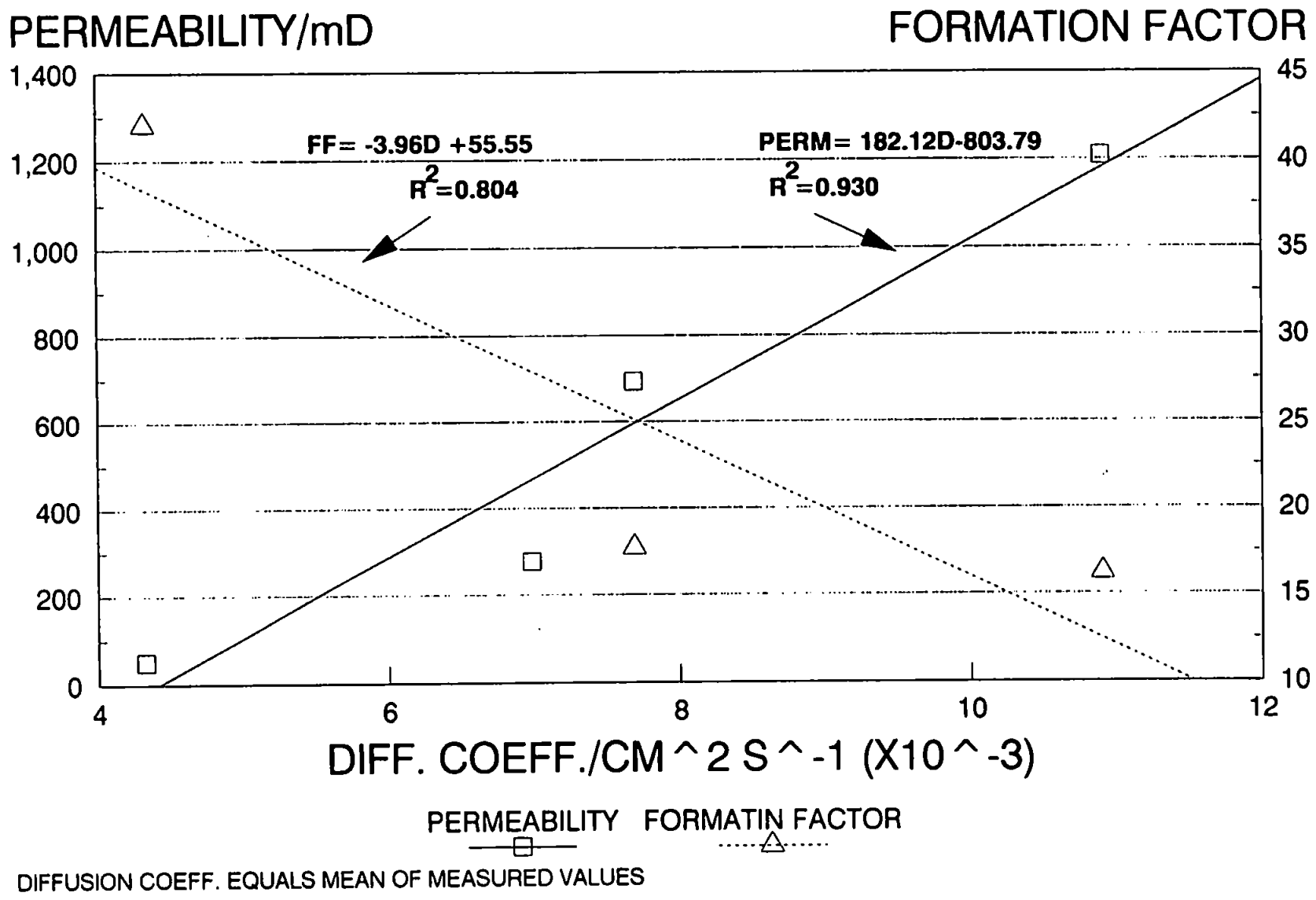

FIGURE 7.12: Permeability and Formation Factor Against Iso-Butane Diffusion Coefficient, in Relatively Clay Free Sandstones

The calculated 100% porosity intercept is 0.056716 cm^2/s. The is approximately half the value of 0.106 cm^2/s quoted by Spearing (1991). This result is interesting but the regression line has a low R-squared fit coefficient 0.6115. One standard deviation from the regression line produces an 8% variation in the 100% porosity intercept. A good correlation between the n-butane diffusion coefficients and other petrophysical properties of the samples was not found. The small number of clean sandstones used in this study means any correlation is hard to detect. If a large number of clean sandstones were analyzed, perhaps a better correlation would be found.

7.6.1. Clay Affected Sandstones

The five clay affected sandstones produced no correlation between any measured variable and diffusion coefficients. Spearing (1991) reported that a sample containing a high percentage of clay would be liable to alkane adsorption on the clay surface. The effect of alkane adsorption within the pore network is cited by Spearing as causing a low diffusion coefficient measurement on the first run, all subsequent runs giving higher coefficients. The same conclusions cannot be drawn from these data. Four samples had a successful first run and on no occasion did these runs give the lowest diffusion coefficient within the range. Spearing based his conclusions on one successful first run for each sample so his data are very limited.

One effect which was noticed during successive runs was that if a sample was tested on consecutive days, a large coefficient was measured for the second run. This is due to the sample containing alkane remnants during the second run. Samples must be alkane free at the start of the experiment to satisfy Equation 7.4, any residual alkanes will cause a reduction in lag time. For this reason, samples were left at least seven days between runs. After this time no correlation with diffusion coefficient and the period between runs was found.

Absence of a correlation between diffusion and any petrophysical property within clay affected sandstones points to a number of subtle effects involving the clays and diffusing alkanes. The adsorption and release of alkanes from the clay surface would be dependant on the type and distribution of clay within the pore space. Variation in diffusion coefficients measured in clay affected samples with similar porosity and permeability may be due to small differences in clay morphology and location. A detailed study of clay distribution within pore space and its effect on diffusion is needed to quantify these effects.

Clays within the pore space can have a more direct effect on successive diffusion coefficient measurements due to their brittle nature. During the long period in which the samples were tested (4 months to 1 year), clays could have become redistributed due to mechanical dislocation. A fine clay particle may move if the sample is handled roughly and pathways for diffusive flux become blocked. This phenomenon is common when fluids permeate the pore-space. It is termed formation damage and is discussed in detail in Chapter 10. The effects of preferential adsorption and clay migration could combine to cause a wide range of measured diffusion coefficients for the clay affected sandstones.

CHAPTER 8

THE VOID SPACE MODEL

8.1 Other Void Space Models

Before detailing the void space model and calculation, it is interesting to compare our network with other networks used to simulate pore space phenomena. A comprehensive survey of work up to 1975 has been given by Van Brakel (1975). He discusses models ranging from simple bundles of straight, equal radius capillary tubes, through to three-dimensional interconnecting networks. Van Brakel recommends that work be done on networks of interconnecting tubes in which the volume and geometry of the network and its junctions are explicitly specified. This is the course undertaken in this study. Van Brakel raised some interesting points about the nomenclature used by porous media investigators. He cited the use of the terms pore size and pore size distribution as hindering progress, stating that real pore space has a continuous complicated structure and pores do not have a finite length. The idea of a pore size distribution could be thought of as meaningless to real porous media. However, if the void space is characterised by such techniques as measuring sphere or cube sizes which fill a void, then terms like pore and pore size distribution are meaningful even in real void space. Void space models use simple three-dimensional shapes to represent the pores and throats in porous media, so that within a void space model the terms pores and throats are valid. Within this study any voids with smaller connecting voids is defined as a 'pore' the smaller connecting voids being defined as 'throats'. The modeller must be careful only to use these terms in the modelling context.

The three-dimensional shapes used to represent pore space within models are as numerous as the methods for measuring feature size within image analysis, Chapter 6. In

the next section we describe many different network simulators used to model intrusion/extrusion of a non-wetting phase and absolute permeability.

8.1.1 Non-Wetting Phase Intrusion/Extrusion Simulations

Garboczi (1991) demonstrated mathematically that a range of pores and throats of different shapes and sizes could be successfully represented by a random network of interconnecting elliptical cylinders. The elliptical cylinders can range from circular cylinders (semi-minor axes equal) through to cracks (one semi-minor axis = 0). Yanuka *et al* (1986) have also used different void shapes in the form of a three-dimensional network of intersecting ellipsoids for their simulation of percolation processes.

Lenormand and coworkers (1988, 1989) have used 100 x 100 x 1 and 25 x 25 x 1 networks of spherical pores and cylindrical throats to simulate two-phase displacement effects, namely capillary fingering, viscous fingering and stable displacements. They link the displacement effects to a statistical percolation model. The different behaviour is expressed in terms of a 'phase diagram' plotted using axes log M and log C_n , where M is the viscosity ratio (= viscosity of injected fluid / viscosity of static fluid) and the capillary number C_n is the ratio of viscous forces to capillary forces, given by

$$C_n = \frac{\mu \, dV/dt}{A \, \sigma} \qquad (8.1)$$

where μ is the viscosity of the fluid, dV/dt is the volume flow rate normal to a plane of an area A, and σ is the interfacial tension. Our method of simulating mercury porosimetry corresponds to an invasion percolation calculation in the invasion percolation region of the Lenormand phase diagram, which occurs at low C_n and high M.

Blunt and King (1990, 1991) generate 2-D and 3-D networks of up to 80,000 pores of equal volume, with individual pore coordination numbers in the range 3 to 12, and overall connectivity of 6. The throat sizes are uncorrelated and form a uniform, linear

distribution. The invasion percolation and unstable viscous flood regimes are modelled.

Tetrahedral pores were irregularly arranged and used to model mercury intrusion and extrusion by Mason and Mellor (1991). Mason and Mellor used a Haine's in-sphere approximation to calculate the mercury meniscus curvature. The centre co-ordinates of the pores were the same as those measured for a random packing of 3,367 equal spheres by Finney (1970). These same co-ordinates were used by Bryant and Cade (1992) as the starting co-ordinates of pores within a model to monitor permeability, porosity and mercury intrusion point of inflection, with increasing cementation and compaction. Mason and Mellor and Bryant and Cade maintained that a spatial correlation existed within the supposed random pore arrangement. Bryant and Cade used this as evidence for spatial correlation within all granular porous media. The detected spatial correlation may only be a function of the original packing used in the model and not indicative of all pore networks.

Chatzis and Dullien (1985) used 33 x 33 x 1 and 18 x 18 x 12 networks formed from angular capillary tubes with angular bulges to represent pores. The network was expressed as a regular network with pore-throat correlation, and a mathematical percolation performed. The network was then transformed to a pore volume network, and fitted to experiment. There was good fit around the points of inflection of the mercury intrusion curves of a range of sandstones, as would be expected because the curves were scaled by means of their break-through point pressures, but above about 70% pore volume the theoretical curves differed by up to 8%.

Conner and Horowitz (1988) developed a 10 x 10 x 10 matrix, all pores having the same volume, and throats having zero volume. Mercury intrusion curves were calculated using the Washburn/Laplace equation. Throat size distributions are often assumed to be the derivatives of mercury intrusion curves, and they corrected these derivatives using a distortion and structural factor. The necessary but arbitrary choice of a connectivity of 6

in their simulation was found to be very limiting.

Tsakiroglou and Payatakes have used 20x20x20 and 30x30x2 networks (1990, 1991) for the simulation of mercury intrusion and extrusion curves. They used an invasion percolation algorithm effectively the same as in this work, but also included resistance effects due to pore shape. The simulations showed that pore-throat correlation and to a greater extent pore-throat and pore-pore correlations, shallowed the mercury intrusion curve and reduced residual mercury trapping.

Day *et al* (1991) used a cubic lattice with random pore size allocation from a log-normal distribution to simulate mercury intrusion and extrusion. The lowering of connectivity increased residual mercury trapping. Two mechanisms for mercury trapping were simulated. The first, a purely structural hysteresis type extrusion, produced very little mercury trapping even at low connectivities. The second mechanism assumed that two mercury menisci did not coalesce when a pore is filled from two different connections. The meeting point of the two menisci acts as a seed for mercury extrusion. This approach to simulating mercury extrusion leads to increased trapping. Similar conclusions have been reached by Park and Ihm (1990) using percolation theory to model intrusion and extrusion with or without mercury menisci coalescence.

8.1.2 Permeability Simulations

A long standing problem in the study of porous media has been the question of how to calculate the permeability of a solid from a knowledge of the geometry of the void space within it.

Early attempts to calculate permeability from a combination of characteristic parameters were reviewed by Scheidegger (1974). The simplest method is to assume that flow is occurring through a bundle of straight capillaries.

Permeability has dimensions of length^2 , and dimensional considerations lead to the

definition of a hydraulic radius ϕ/S, related to the square root of permeability. ϕ is the effective porosity and S the total externally accessible surface area per unit volume of the solid. Extension of this dimensional approach by Kozeny (Scheidegger, 1974) to what he refers to as a *virtual stream tube* led to an equation:

$$k = c_k \phi^3 / S^2 \qquad (8.2)$$

where c_k is the Kozeny constant which varies from 0.5 for a virtual stream tube of circular cross-section, to 0.66 for a strip cross-section tube. In practice the consideration of a virtual stream tube, though more rigorous and generalised than the straight capillary model, adds little further insight.

If equation 8.2 is corrected for tortuosity T, one obtains

$$k = c_k \phi^3 / (T S^2) \qquad (8.3)$$

However, the concept of tortuosity is alien to the Kozeny virtual stream tube approach, which by its very nature does not invoke detail of the structure of the medium. T in equation 8.3 is thus ill-defined.

Koplik *et al* (1984) uses the "effective medium" approach to calculate permeability. The pore network of a sample of Massilon sandstone had previously been characterized by serial section image analysis. In their calculation of the permeability of the sandstone, they set up a "ball and stick" network of pores and throats. However, the geometry of the pores does not enter the calculation because the pressure drop across each pore is assumed to be zero - only pressure drops across the throats are considered. Simulated permeabilities were about a tenth of the measured values. The small sample used for the image analysis and the width between sections is cited by the authors as the reason for the model's failings. The effect of averaging the effective capacities of each throat within the effective medium and then averaging the pressure gradient along each throat also has a detrimental

effect on the simulated permeability.

A further relationship for the permeability has recently been given by Katz and Thompson (1986, 1987), based on a consideration of the dimensionality of characteristic parameters, and the sensitivity of permeability to threshold values of these parameters. They obtain

$$k = \frac{1}{226}\frac{d_b^2}{F} \qquad (8.4)$$

d_b is the characteristic throat diameter at the 'break through point' on the mercury intrusion curve. As mentioned in Chapter 5, the 'break through point' corresponds to the percolation threshold, the pressure (or diameter), at which a continuous mercury path spans the rock. Our model shows this to occur at the point of inflection of the mercury intrusion curve. The Katz and Thompson approach to modelling permeability is quoted as predicting permeabilities to within a factor of two from the measured value. Obviously the model is dependent on the assumptions used in the Washburn Equation. The 1/226 factor is derived from assumptions about the relationships between pore length and pore diameter, Garboczi (1991). The Katz and Thompson model is also only able to simulate permeabilities. A pore space model should ideally simulate different pore space phenomena so that the complicated relationships between these pore space properties can be elucidated.

The permeabilities and formation factor of homogeneous isotropic Fontainbleau sandstone has been modelled by Adler (1990, 1992). Two-dimensional thin section images of the sandstone were used to characterize each sample's porosity and correlation function, and this function was then applied to the model. Formation factor was always overestimated whilst permeability was always underestimated by as much as a factor of 5. Adler appears to compare his simulated formation factors with those measured on real sandstones by another worker in 1964 ! Fontainbleau sandstone is in fact very homogeneous so it is unlikely Adler's samples varied significantly from those studied in the 1960s.

Ioannidis and Chatzis (1993) compare the results of their three-dimensional pore space model with experimental data from many sources. The mercury intrusion curves, porosity, permeability and formation factors for each sandstone are quoted as having been measured by different workers during three different studies. Thus the measured porosity for one sandstone lithology is measured on a different sample from that used in the permeability measurements. To compare the results of a pore space simulation with such data is meaningless. The true test of any void space model is its ability to simulate the pore space of a sample and its characteristic properties which are unique to that specific pore arrangement.

8.2 Description of the model

The network model which we call PORE-COR (Pore-level Correlator) has three main characteristics: (i) it has a real geometry, (ii) the same network with precisely the same geometry is used to model a wide range of properties, and (iii) no property-independent fitting parameters are invoked, and thus the model can be applied to any porous medium.

The first characteristic, the model's real pore space geometry, is evident from Figure 8.1. This is the diagram for the model's three-dimensional unit cell. Each unit cell contains 1000 nodes on a regular 10 x 10 x 10 matrix. The nodes are positioned using Cartesian coordinates x,y,z. If the sample is isotropic, the allocation of these axes is arbitrary. The void volume in the unit cell comprises up to 1000 cubic pores centred on the nodes. The origin of the axes is at the corner of the unit cell adjacent to the first node. For clarity in the figure, the axis origin is displaced to the left, i.e. negative y, and only the outer layers of pores are shown, numbered as indicated. Connected to each pore are up to six cylindrical throats along the line of the arcs in the positive and negative x,y and z directions. The arguments for using different shapes to model pore space are numerous

FIGURE 8.1: Model 3-D Unit Cell

as mentioned earlier. However, the use of cylindrical throats allows easy application of the model to mercury intrusion studies. The choice of cubic pores is mainly due to the simplicity of modelling these shaped pores. The construction and intricacies of the model unit cell are outlined later.

The second feature, the wide range of properties which have been modelled with the same network, is detailed in the box diagram, Figure 1.1. The third feature of the modelling is that no property-independent fitting parameters are invoked. We do use fitting parameters, namely the skew of the throat size distribution and the connectivity, and both parameters can be optimised manually or automatically. However, the parameters are actual properties of the sample, and can be checked as having realistic values. We do not need to use any entirely arbitrary, property-independent fitting parameters to fit the simulation to experiment. In methods where this is necessary, the applicability of the model is dramatically reduced, because one does not know whether the fitting parameters are general ones, or whether they apply only to the particular sample or samples under consideration.

8.2.1 The Construction of the Unit Cell

Initially a throat size distribution is entered into the model. This consists of 100 throat diameters and the percentage of each size within the throat distribution. Every value of throat size distribution had to be input into the model developed by Spearing (1991), a lengthy process. A new mode of throat size distribution has therefore been developed. The throat sizes are now distributed linearly between the maximum and minimum sizes with the hundred throat sizes spread evenly over a logarithmic axis. We term this type of distribution a log-linear distribution. Figure 8.2a shows the log-linear distribution for a flat throat size distribution of 1% of every throat size. The log-linear distribution can be tilted to increase the proportion of large throats, Figure 8.2b, or increase the proportion of small

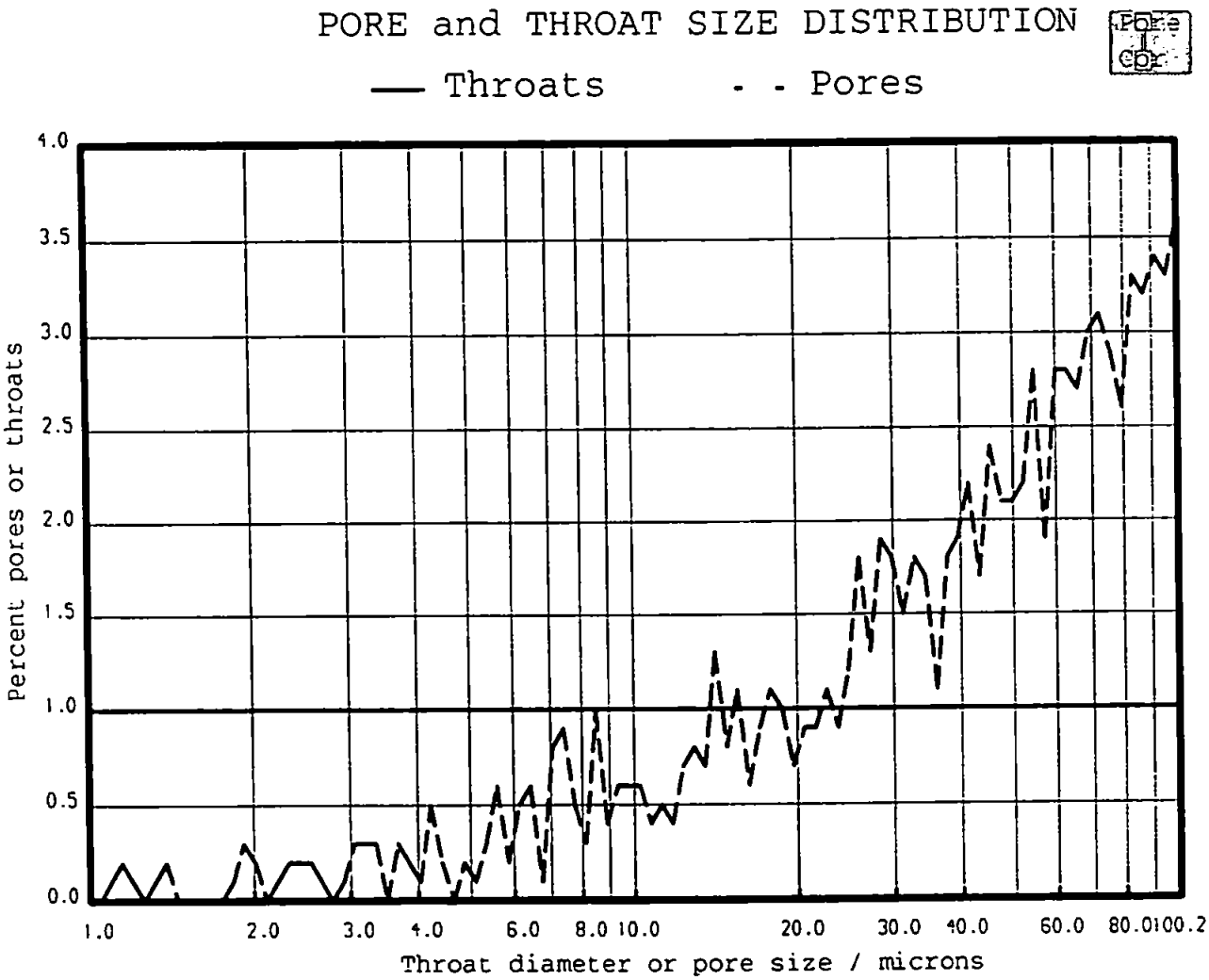

FIGURE 8.2a: Log Linear Throat Size Distribution With 1% of Every Throat Size.

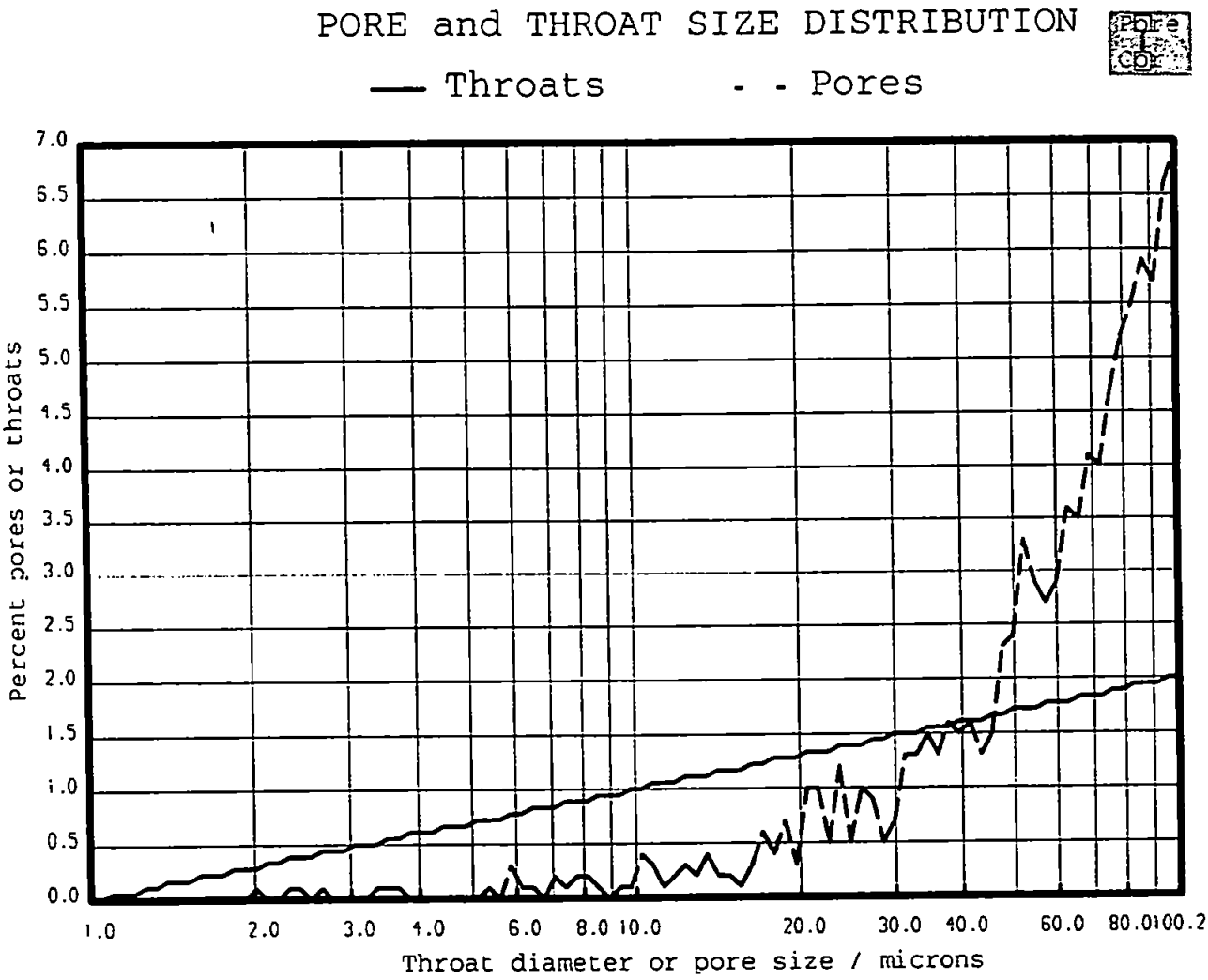

FIGURE 8.2b: Log Linear Throat Size Distribution Skewed Towards The Large Throat Sizes.

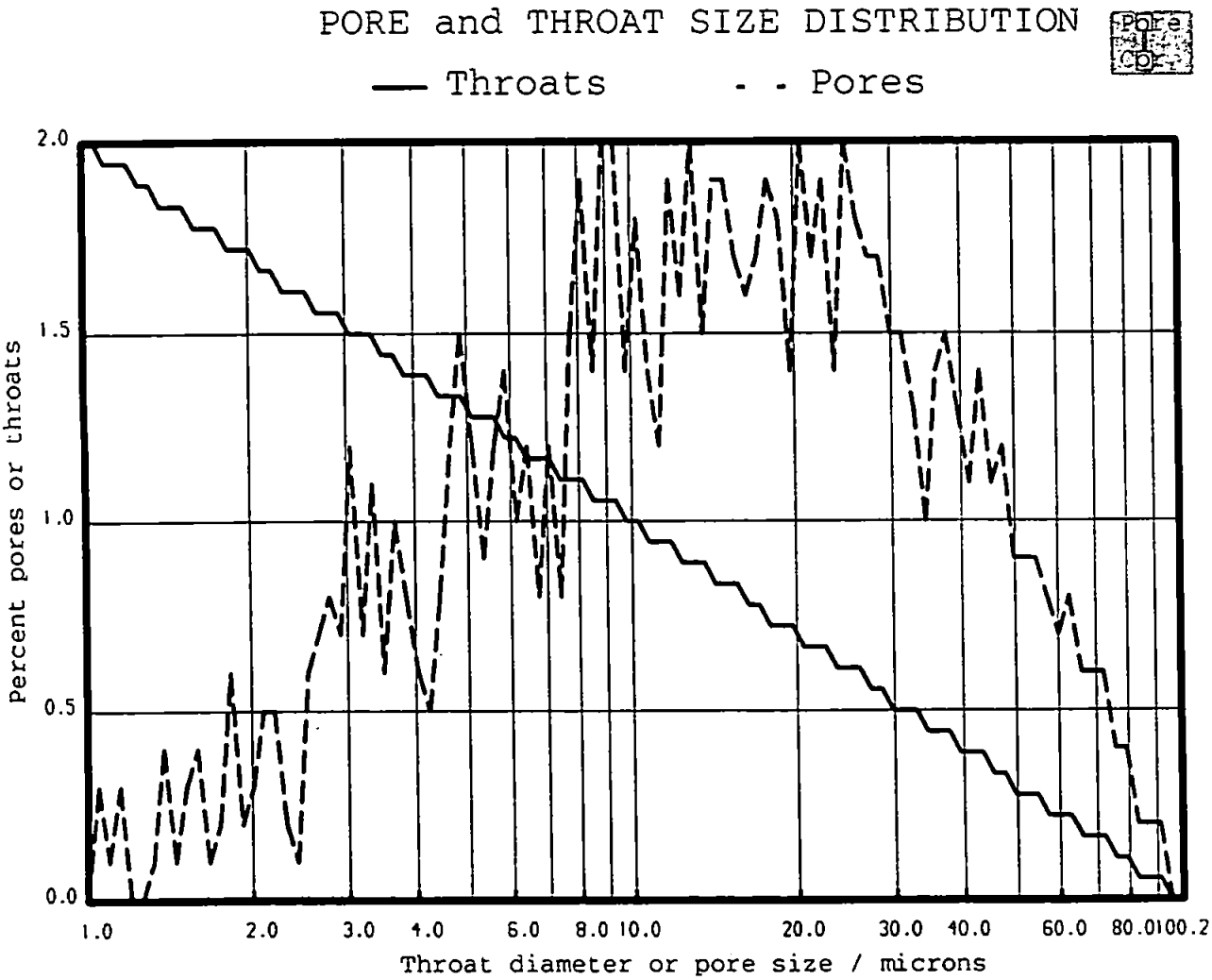

FIGURE 8.2c: Log Linear Throat Size Distribution Skewed Towards The Small Throat Sizes.

throats, Figure 8.2c. This type of throat size distribution input allows a wide range of void structures to be modelled and facilitates easy distribution input. The model requires simply the minimum and maximum throat sizes and the percentage of the smallest throats, termed the percentage skew, and the resulting throat distribution is calculated and input. The percentage skew values for the throat size distributions in Figures 8.2 a-c are 1%, 0% and 2% respectively. The pore size distributions in Figures 8.2 a-c will be explained later. The initial estimate of the throat size distribution is obtained from electron microscopy or the mercury intrusion curve. The throat size distribution is optimised by fitting the simulated mercury intrusion curve to the experimental curve; this optimization is outlined in detail later. The average number of throats connected to each pore can be set between 0 and 6. The number of throats connected to a specific pore we term the co-ordination number, while the average over the whole network is called the connectivity. The connectivity of porous media is exceptionally difficult to measure. Lin and Cohen (1982) measured an average co-ordination number of 2.9 from serial section analysis of Berea sandstone. Average co-ordination numbers of between 2.8 and 3.5 have been quoted in sandstone studies by Yanuka et al (1986) and Koplik et al (1984). The choice of connectivity within the model has a pronounced effect on simulated permeability, tortuosity and mercury intrusion. The model connectivity affects the breakthrough point and shape of the simulated mercury intrusion curve, and thus the value used will dictate the success of the fit between the simulated and experimental intrusion curves.

The throats are distributed randomly amongst the total of 300 positions within the unit cell which correspond to the arcs between each node. For throat allocation the cell effectively repeats infinitely in the x, y and z directions. This means that throats protruding from the outer faces of the unit cell are the same as those entering the opposite face. This joining of unit cells allows conservation of mass during the mercury intrusion and permeability simulations.

The pores centre on the 100 nodes within the unit cell. The pores are distributed randomly within the unit cell, the only allocation criterion being that each pore must be connected to at least one throat of the same diameter. The ratio of pore size to that of the largest throat entering it is called the pore size to maximum throat size ratio. The justification for this degree of pore:throat correlation is based on work by Wardlaw et al (1987). Figures 8.3a and 8.3b show Wardlaw's pore-throat correlation graphs for Wood's metal/image analyzer studies of Berea sandstone and Indiana limestone respectively. The pore-throat correlation criterion stated above is used to obtain the simulated pore:throat correlation graph shown in Figure 8.4. The spread of points in Figure 8.4 when the pore size to maximum throat size ratio is 1 closely resembles that for Berea obtained by Wardlaw (Figure 8.3a). The model is capable of simulating limestone type void space by altering the pore size to maximum throat size ratio from 1 to 5, Figure 8.4.

Once all pores and throats are allocated within the network the unit cell is expanded or contracted to simulate the experimental porosity. The distance between nodes is constant throughout the unit cell. This "pore-row spacing" term is not an arbitrary fitting parameter because the distance between nodes has a direct effect on the permeability simulation. The lower limit of the pore-row spacing is dependant on the size of the largest adjacent pores, thus avoiding pore overlap. The model unit cell is now complete and can be used to simulate a wide range of pore space phenomena.

8.2.2. Mercury Intrusion Simulation

The model reproduces the mercury intrusion curve by following the procedure in the flow diagram shown in Figure 8.5. The mercury is non-wetting, The wetting phase is air/mercury vapour at very low pressure. Figure 8.5 shows that the mercury first penetrates the top layer of the unit cell via the largest throat. The simulation of mercury intrusion is in terms of a percolation of non-wetting phase from the top layer and through the whole network. Penetration of mercury from only the top face of the unit cell allows the

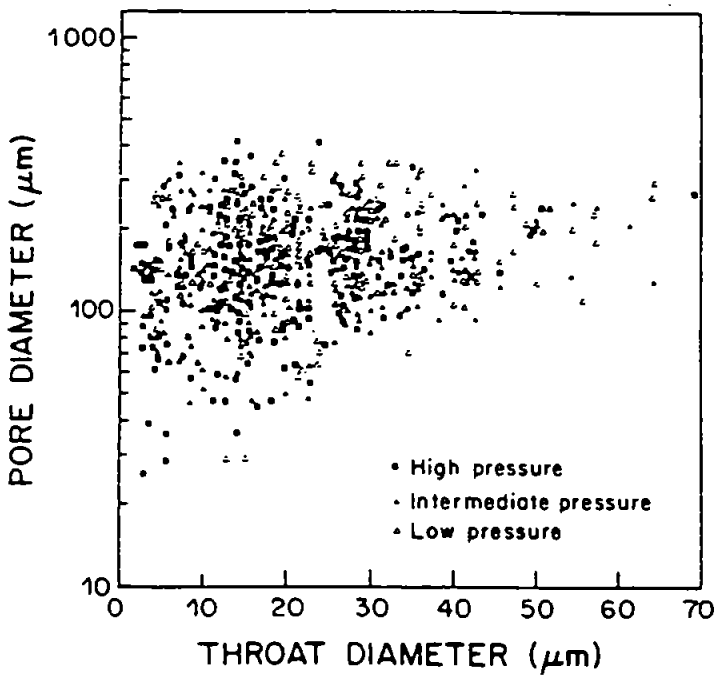

FIGURE 8.3a: Pore-Throat Correlation For Berea Sandstone (From Wardlaw 1987)

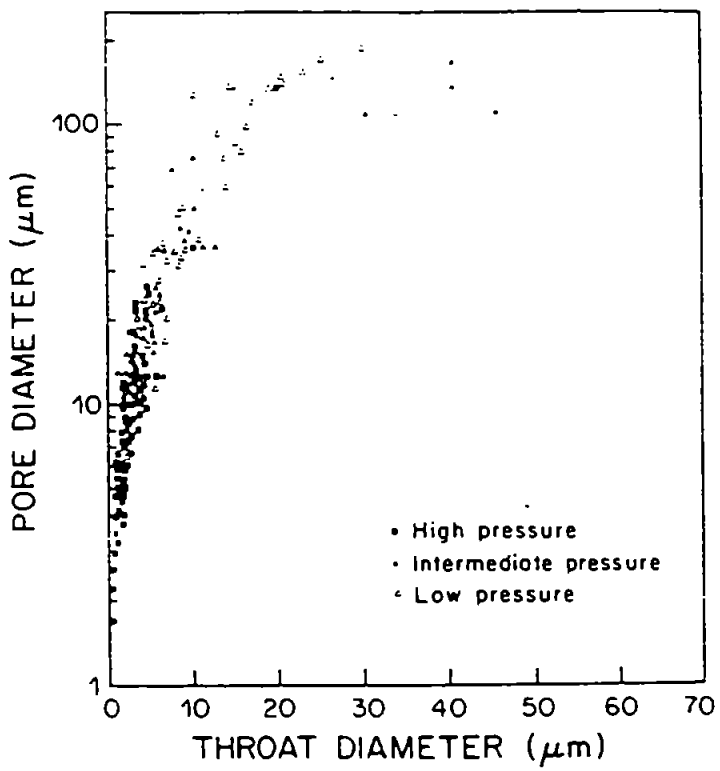

FIGURE 8.3b: Pore-Throat Correlation For Indiana Limestone (From Wardlaw 1987)

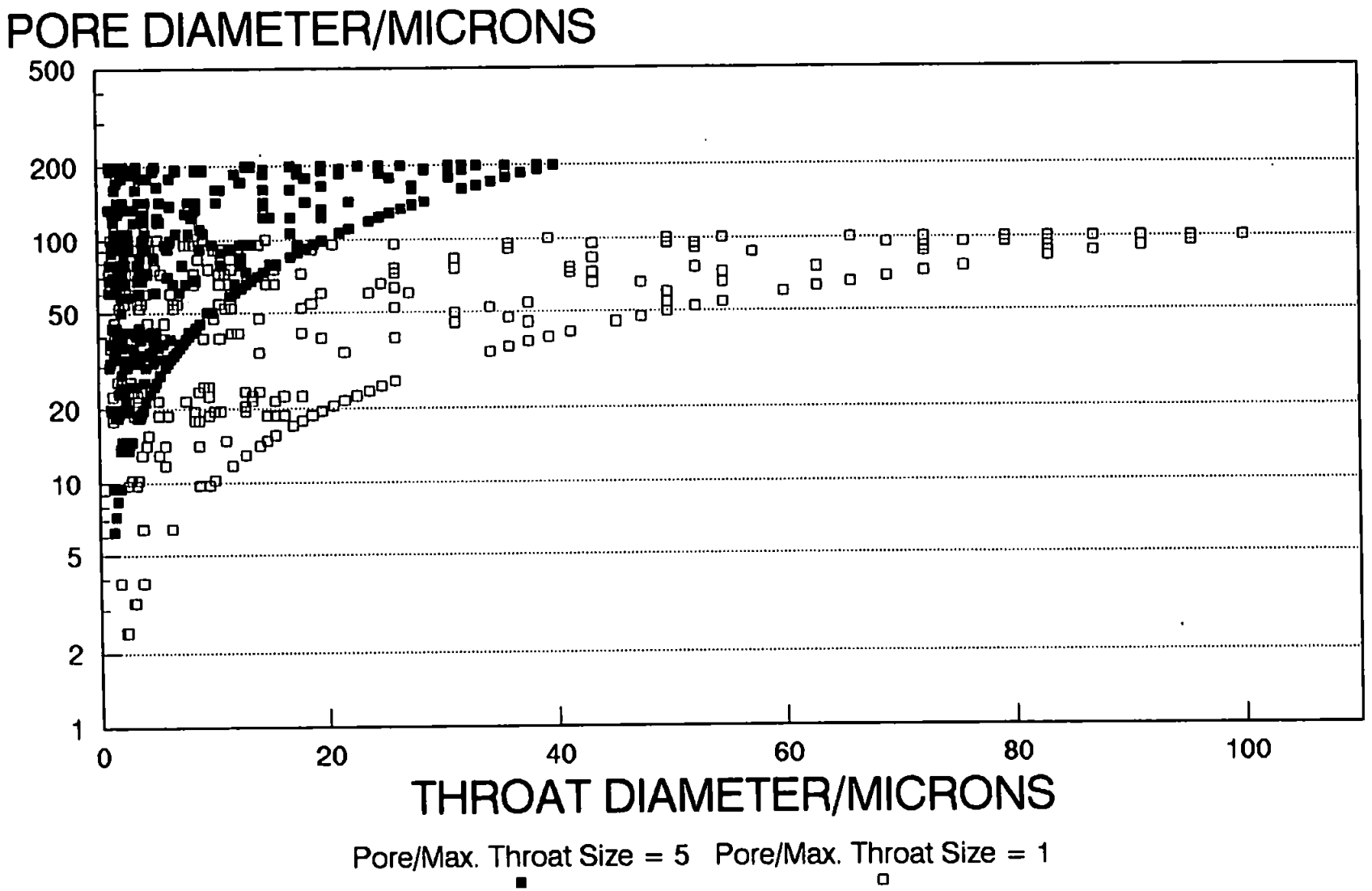

FIGURE 8.4: Pore-Throat Correlation For Simulations With Varying Pore/Max. Throat Size.

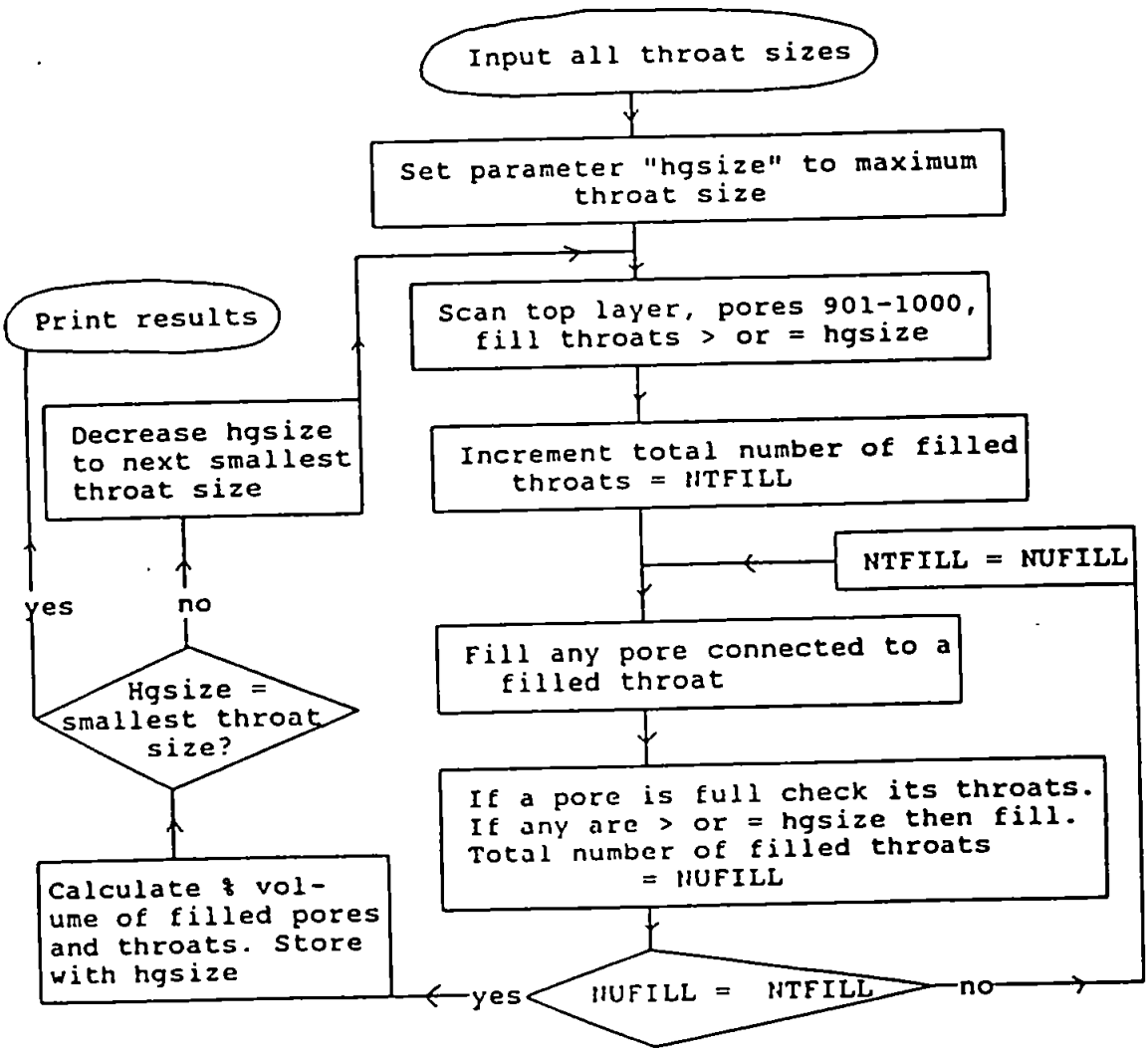

FIGURE 8.5: Flow Diagram For Mercury Intrusion Curve, (After Spearing 1991).

simulation to model intrusion into a sample of effectively infinite dimensions. Boundary pores and throats will thus not affect the form of the mercury intrusion curve.

The filling of the model is controlled by the throat size corresponding to the current capillary pressure as described by the Washburn Equation. A contact angle of 140° and a surface tension of 0.48 N/m are used within the Washburn Equation. Once the critical capillary pressure for a throat is reached both it and its connecting pore are filled. Mercury fills the whole pore space instantly in a piston-like motion. As a pore throat system fills with non-wetting phase, the wetting phase will empty. If wetting phase exits via one side of the unit cell it will re-enter at the opposite side. This is due to the unit cell infinitely repeating in the x and y directions. Wetting phase can only exit the model at the bottom face. During the mercury intrusion simulation, the network has inlet and outlet faces and the four other faces maintain the flow in the model. Although the simulation is of intrusion into a sample of infinite dimensions the percentage of void space occupied with mercury is calculated using the void dimensions of one unit cell.

The reason for simulating the mercury intrusion curve is to check that the throat size distribution input into the model is correct. If the point of inflection and shape of the simulated intrusion curve reproduces that of the experimental curve, then this gives confidence that the correct throat size distribution has been input. The simulation of a sandstone's void space is thus a mapping of the mercury intrusion curve onto the model network. Obviously this mapping is dependant on the assumptions within the Washburn Equation, as discussed in Chapter 5. Nevertheless the network produced gives an insight into the nature of the porous solid.

8.2.3. Convergence Of Simulation Onto Experimental Intrusion Data

Spearing adopted a 'trial and error' method of fitting simulated mercury intrusion curves to the experimental curve. This involved adjusting the throat size distribution and

connectivity until a good fit was achieved. This process was extremely laborious due to the need to input the one hundred throat sizes and respective frequencies individually. Thus few samples were successfully simulated by Spearing (1991). The log-linear throat size distribution was developed to allow quick input of a wide range of distributions. Time needed to successfully fit simulated with experimental curves was drastically reduced. The criteria for a successful fit are a close matching of points of inflection and the 'knee and shoulder' of the curves. The 'knee' corresponds to the low capillary pressure/large throat diameter region in which small pressure increases start to produce large intrusion volumes. Conversely the curve 'shoulder' is the region at a capillary pressure higher than the point of inflection, at which intrusion volumes decrease for a given pressure increase. Some mercury intrusion investigators have postulated that the low capillary pressure area of the intrusion curve, including the curve knee, is sensitive to the distribution of surface pores and sample size (Wardlaw and Taylor 1976). Figure 8.6 shows the mercury intrusion/extrusion curves obtained by Wardlaw and Taylor for two nearly identical limestone samples. One sample is coated with epoxy resin on all sides except one, and the other sample left uncoated. The coated sample has a reduced number of surface pores and illustrates the shape curves obtained for an effectively infinite sample size. Ioannidis and Chatzis (1993) only used the portion of the intrusion curve at capillary pressures above the point of inflection, when comparing experiments with their intrusion simulations. The magnitude of sample size and surface pore effects on the low capillary pressure region of the intrusion curve are unknown, but it would be sensible to fit experimental and simulated curves with a heavier bias towards the area at pressures corresponding to the point of inflection and above.

The fitting of simulated and experimental intrusion curves by visual inspection can

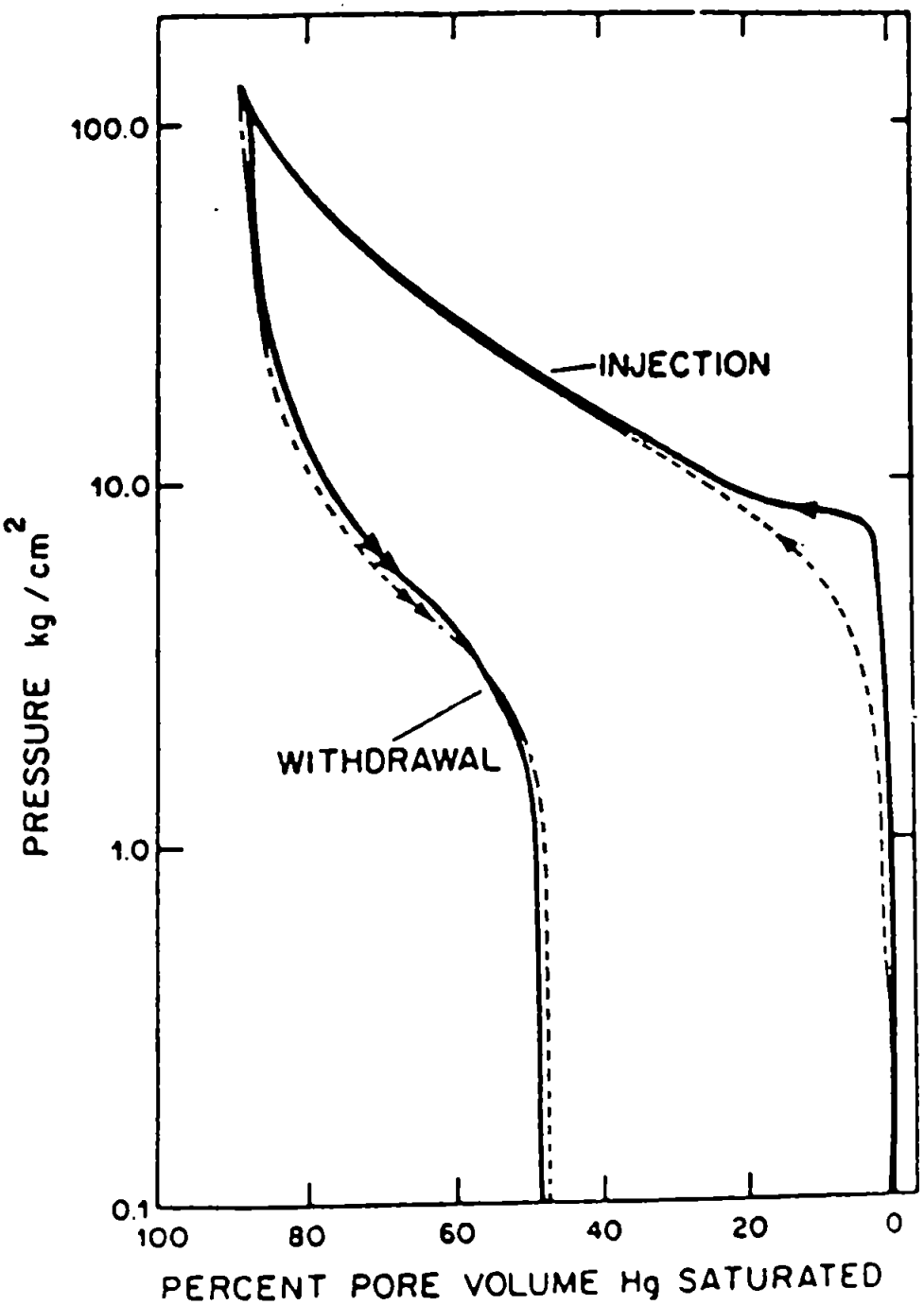

—— Coated Sample
------- Uncoated Sample

FIGURE 8.6: Mercury Porosimetry Curves For Two Similar Samples Of Indiana Limestone; One Coated in Resin On All Sides Except One, the Other Sample Is Uncoated (From Wardlaw and Taylor 1976).

be laborious and requires an experienced Pore-Cor operator. A less subjective method of curve fitting procedure was required. Three different automatic curve convergence procedures have been programmed into the model by C Ridgway, currently a research student at the university. The model now outputs the values of throat size distribution skew and connectivity which give the best fit simulated intrusion curve.

The first method developed to fit the intrusion curves involved arbitrarily fixing the connectivity at 3.5 and varying the skew to find the best fit at the 50% pore volume point. The point of inflection of intrusion curves is usually close to the 50% pore volume point, thus its selection as a fitting point. This curve fitting procedure is simple because only one parameter is varied but the fixed connectivity means it has limited applications.

An improved fit between simulation and experiment can be made by varying both skew and connectivity and comparing the curves at many positions, not just the 50% pore volume point. When comparing a number of simulations with experiment the deviation between curves must be measured at a consistent evenly spaced group of points on the pore volume axis. Unfortunately experimental data are not usually evenly spaced in this way. Experimental data points are used whenever possible but points are removed or interpolated if the pore volume spacing exceeds set limits. The limits are set at half and twice the spacing on the pore volume axis compared to what the spacing would be if the experimental data were evenly spaced:

$$\frac{V_{tot}}{2n} < |V_i - V_{i-1}| > \frac{2V_{tot}}{n}$$

where V_{tot} is the maximum intruded volume and n is the total number of experimental data points. The data point selection and interpolation algorithm produces a set of comparison points which are used for every simulation of a given experimental curve. The difference

in simulated and experimental throat diameter at each pore volume point are used to find the best fit. The deviation between curves can be expressed either linearly or logarithmically.

Total deviation can be expressed as Δ_{log} or Δ_{lin} where

$$\Delta_{log} = \frac{\sum_{i=1}^{n} (\log d_{exp(vi)} - \log d_{simu(vi)})^2}{n} \qquad (8.6)$$

and

$$\Delta_{lin} = \frac{\sum_{i=1}^{n} (d_{exp(vi)} - d_{simu(vi)})^2}{n} \qquad (8.7)$$

where $d_{exp(vi)}$ is the experimentally measured throat diameter at pore volume point v_i, and $d_{simu(vi)}$ is the simulated throat diameter at the same pore volume point v_i. We call the minimisation of Δ_{lin} with change in skew and connectivity the linear method of curve fitting, and the minimisation of Δ_{log} the log method.

Both linear and log methods use the 50% pore volume method to find the central skew value for the range analyzed. All skews ± 0.7% from this value are simulated at intervals of 0.1% while, connectivities between 2.6 and 4.0 are used in both linear and log curve fit methods.

The linear method gives more weighting to fitting the curves at the low capillary pressure/large throat diameter region. The fact that this area of the intrusion curve is

affected by surface pores and sample size is a disadvantage. The log method gives equal weight to deviations on the whole curve, and is thus the most applicable method.

8.2.4. The Simulation Of Mercury Extrusion

The extrusion of mercury from pore space, after complete intrusion, is dependent on the size and arrangement of the larger voids within the sample. The effect of pore:throat size ratio on mercury extrusion was discussed in Chapter 5. The difference in mercury contact angle between the intruding and extruding meniscus is also cited as cause of the hysteresis common to mercury intrusion/extrusion curves. A simulation of mercury extrusion will thus utilize the model pore size distributions optimized during the mercury intrusion curve fitting procedure. The main criterion for a pore to empty is that there should be a continuous unbroken path of mercury from it to the surface. The bottom layer is the only face at which mercury can leave the unit cell. The network repeats infinitely in the x and y directions, so any mercury leaving the unit cell by a side face will re-appear on the opposite face. Figure 8.8 shows a flow diagram which outlines the procedures within the extrusion algorithm.

The 'conditions' for a pore to empty referred to in Figure 8.8 are as follows. The pressure corresponding to the pore diameter by the Washburn Equation must be low enough for the pore to empty. Emptying still depends on the following further conditions:

i) The pore has a continuous unbroken path of mercury to the sink ie. bottom layer.

ii) The pore/throat size ratio must not exceed a critical value. At high pore/throat size ratios 'snap off' can occur. If the pore size/throat size ratio of a specific pore-throat pair exceeds five then snap off of the mercury thread occurs at that pore-throat junction.

These conditions within the extrusion algorithm produce extrusion curves with residual mercury trapping. The critical pore/throat size ratio which causes snap off ie.5 is from observations of mercury snap-off in a glass micromodel (Wardlaw and McKeller 1981).

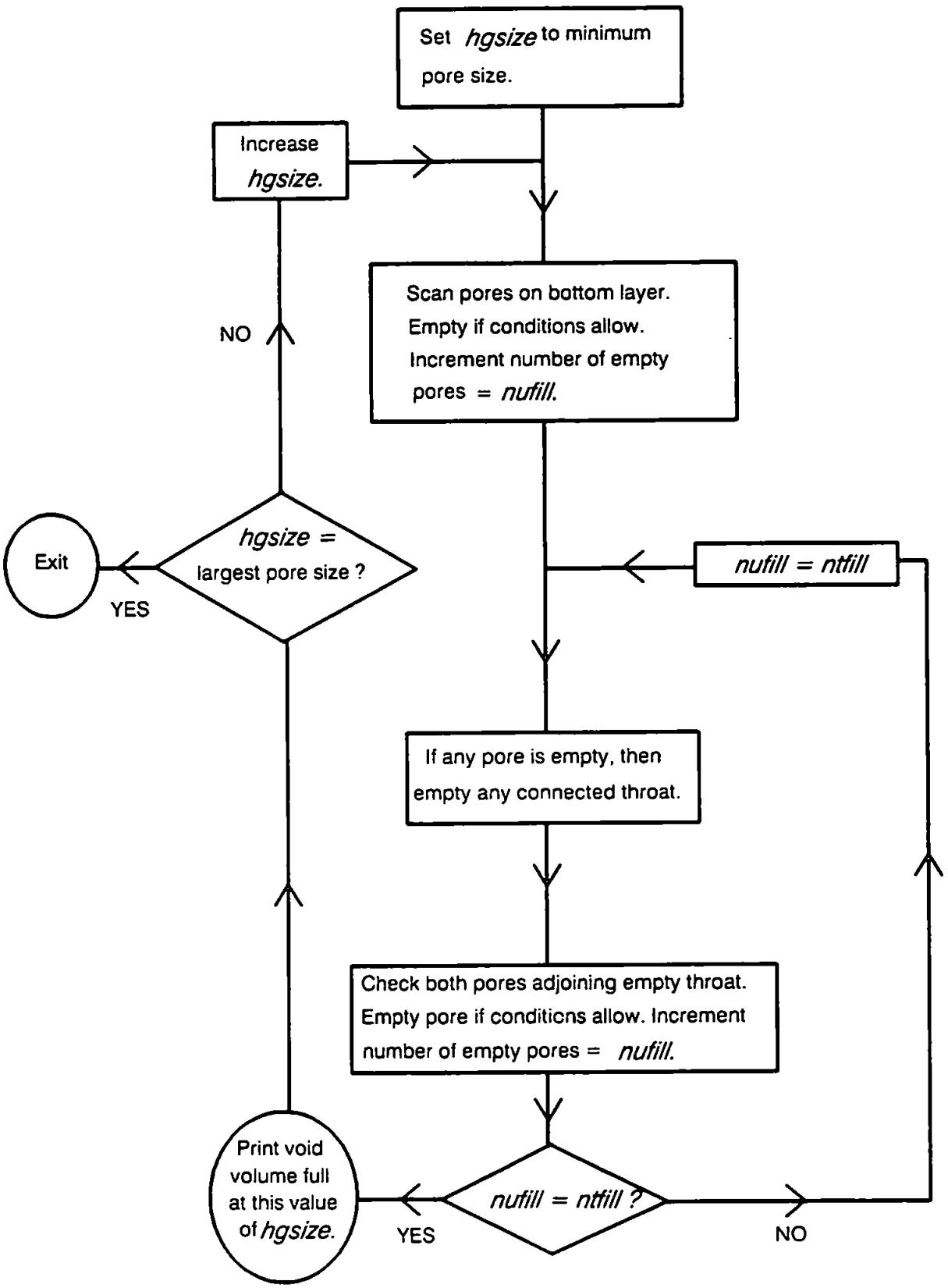

FIGURE 8.7: Mercury Extrusion Simulation Flow Diagram

Contact angle hysteresis is also modelled. A mercury extrusion contact angle of 130° is usually used. Mercury surface tension is kept constant for both intrusion and extrusion (0.48 nm^{-1}).

The movement of mercury in and out of the pores and throats is assumed to be piston-like and complete. No fractional filling or emptying is modelled.

8.2.5 Calculation Of Absolute Permeability

An incompressible fluid flowing through a tube takes up a parabolic velocity profile, with maximum flow rate down the centre of the tube. If the flow at the walls is assumed to be zero, integration over the velocity profile yields the Poiseuille equation:

$$\left(\frac{dV}{dt}\right)_{tube} = -\frac{\pi r_{tube}^4 \delta P_{tube}}{8 \mu l_{tube}} \qquad (8.8)$$

$(dV/dt)_{tube}$ is the volume flow rate, r_{tube} the radius of the tube and $\delta P_{tube} / l_{tube}$ is the pressure gradient across the tube. Poiseuillian flow has been shown to occur for oil displacement in capillaries down to 4μm in diameter (Templeton 1954). The Klinkenberg correction for slip flow is described later.

We now assume that Poiseuillian flow occurs across the whole cell in the -z direction, i.e. from the top to the bottom face of the unit cell. Then

$$\left(\frac{dV}{dt}\right)_{cell:-z} = -\frac{\pi}{8\mu} \Omega(r_{tubes:z}^4)_{cell} \frac{\delta P_{cell}}{l_{cell}} \qquad (8.9)$$

Ω is an averaging operator over the whole unit cell operating on the fourth power of the individual radii $r_{tube:z}$ of all tubes lying parallel to the z axis. It is defined such that Equation 8.9 is satisfied, and generates a term which is related to the effective Poiseuillian

capacity of the cell for flow in the -z direction. Since at this stage of the calculation, all the tube lengths $l_{tube;z}$ are identical and $l_{tube;z} = l_{cell}/10$, we can include these lengths in the averaging function, so that

$$\left(\frac{dV}{dt}\right)_{cell;-z} = -\frac{\pi}{8\mu}\,\Omega\left(\frac{r^4_{tubes;z}}{l_{tubes;z}}\right)_{cell}\delta P \qquad (8.10)$$

However, the unit cell is not a series of consecutive tubes of length l_{tube}, but a three-dimensional inter-connecting network. We do not allow flow in the +z direction, but do allow flow in the ±x and ±y directions. Thus we assume that

$$\left(\frac{dV}{dt}\right)_{cell;\pm x,\pm y,-z} = -\frac{\pi}{8\mu}\,\Omega_{\pm x,\pm y,-z}\left(\frac{r^4_{tubes;x,y,z}}{l_{tubes;x,y,z}}\right)_{cell}\delta P_{cell} \qquad (8.11)$$

or, simplifying the notation,

$$\left(\frac{dV}{dt}\right)_{cell} = -\frac{\pi}{8\mu}\,\Omega\left(\frac{r^4_{tubes}}{l_{tubes}}\right)_{cell}\delta P_{cell} \qquad (8.12)$$

where Ω is now operating on the dimensions of all the tubes.

Comparing Equation 8.12 with the Darcy Equation (Equation 2.2), it follows that

$$k = \frac{\pi}{8}\,\Omega\left(\frac{r^4_{tube}}{l_{tube}}\right)_{cell}\frac{l_{cell}}{A_{cell}} \qquad (8.13)$$

A network analysis approach to this problem supplies the term $\Omega(r^4_{tubes}/l_{tubes})$ as the maximal flow capacity through the network of pores and throats. There is an overall conservation of flow, so that the entire volume of fluid entering the top of the unit cell emerges at the bottom, with no build up through the network. However, the unit cell infinitely repeats in all horizontal (x and y) directions, and fluid can pass out sideways

from one unit cell to the next. Conservation is maintained by an identical volume flowing in at the opposite face of the cell. The value obtained as the maximal flow is an average of the capacity values over only the channels found to carry flow.

To model the flow, the network analysis program must be supplied with the flow capacity of each pore-throat-pore connection in the network, which we refer to as an arc. The nodes, which are connected to each other by arcs, are positioned at the centre of each pore. Thus an arc consists of 3 components: a throat and half of each adjoining pore.

The flow through a cylindrical throat is given by Poiseuille's equation (8.8). For the flow in a cubic pore of size Cu from the centre to the edge (i.e. a distance of Cu/2), the equivalent equation for flow through a square tube is required. This can be derived (Schlicting 1979) as

$$\frac{dV}{dt} = -\frac{4}{57}\frac{Cu^3\delta P}{\mu} \qquad (8.14)$$

Since the volume of incompressible fluid is conserved throughout the system, the volume of fluid flowing through each of the three components of the arc must be constant, but the time taken for this volume of fluid to flow through each component varies. Thus the overall flow time through the arc δt_{arc} per unit volume of fluid δV can be calculated by adding the individual flow times per unit volume:

$$\frac{\delta t_{arc}}{\delta V} = \frac{\delta t_{pore\,1}}{\delta V} + \frac{\delta t_{throat}}{\delta V} + \frac{\delta t_{pore\,2}}{\delta V} \qquad (8.15)$$

Thus the volume flow rate through the arc is

$$\frac{dV}{dt_{arc}} = \frac{\delta V}{\delta t_{arc}} = \frac{1}{\frac{\delta t_{pore\,1}}{\delta V} + \frac{\delta t_{throat}}{\delta V} + \frac{\delta t_{pore\,2}}{\delta V}}$$

$$\approx -\frac{\delta P}{\mu}\left[\frac{1}{\frac{57}{4Cu_1^3} + \frac{8h}{\pi r^4} + \frac{57}{4Cu_2^3}}\right] \qquad (8.16)$$

where Cu_1 and Cu_2 are the lengths of the sides of the cubic pores 1 and 2, and h the length of the throat connecting the two pores. The approximation indicated above arises from ignoring the discontinuities between the square and circular cross-sections of the fluid channel. On applying the Poiseuille Equation (8.8) to each arc, and rearranging:

$$\frac{r_{arc}^4}{l_{arc}} = -\frac{(dV/dt)_{arc}}{[\delta P\,\pi/8\mu]}$$

$$= \frac{8}{\pi}\left[\frac{1}{\frac{57}{4Cu_1^3} + \frac{8h}{\pi r^4} + \frac{57}{4Cu_2^3}}\right] \qquad (8.17)$$

The diameters of the throats in the network are always smaller than, or equal to, the width of the pores which they enter. Thus the throats cause the major restrictions in flow. Inspection of Equation (8.17) correctly reveals that the flow due to a pore-throat-pore arc is greater than the flow of an extended throat of the same overall length as the arc. Thus the greater effective capacities of the arcs over simple throat systems cause a greater flow through the medium, and a greater calculated permeability. Such a refinement is only possible in a fully geometric pore space network such as that presented here.

8.2.5.1. Klinkenburg Correction

The Klinkenburg Effect is an increase of the observed flow over the flow predicted from the Poiseuille or Darcy Equations, and is significant when the mean free path between collisions in the fluid is of the same order of magnitude as the diameter of the channel it is flowing through. It occurs because the velocity of the fluid at the walls of the channel is not zero as is assumed in case of Poiseuillian (laminar) flow. Only gases will exhibit significant slip flow in sandstones, because the mean free path for liquids is very small compared to the throat and pore sizes.

The Knudsen number, K_n, is indicative of the flow regime occurring in a channel:

$$K_n = \gamma/d \qquad (8.18)$$

where γ is the mean free path and d is the channel diameter. K_n is about 10^{-5} for laminar (Poiseuillian) flow, 10^{-3} for slip/laminar flow and 10^{-1} for slip flow.

The measured permeability with which we compare our simulation is a gas permeability which has been measured at optimum conditions, so slip flow becomes negligible. The capacity equation (8.17) derived for the simulation is for an incompressible fluid with no slip correction, and the permeability of the void space simulation is therefore independent of pressure. It is of interest to add a slip correction term to Equation 8.17 to assess the importance of the slip corrections in the simulation, and to infer its importance in experimental measurements. For this purpose we assume that the fluid is nitrogen, and approximate this to a perfect gas of molecule. The mean free path may then be calculated from simple kinetic theory:

$$\gamma = 1/(\sqrt{2}\ \pi N \varsigma^2) \qquad (8.19)$$

N is the number density of the gas (the number of molecules per unit volume), which for a perfect gas at 300K and 1 atm. pressure is 2.446×10^{25} m^{-3} . ς is the collision diameter

of the molecule, the value for nitrogen being 363 x 10^{-12} m. Thus the mean free path γ is 6.98 x 10^{-8} m. Then from Equation 8.18, the Knudsen number K_n for air in a 200 μm throat is approximately 3.49 x 10^{-4}, indicating laminar flow. In 50 μm and 2 μm throats K_n is 1.39 x 10^{-3} and 3.49 x 10^{-2} , indicating some slip flow and significant slip flow respectively.

A correction for slip has been applied by Dawe (1973) to capillary flow gas viscometers (Matthews 1986). For laminar flow with slip, the Poiseuille equation becomes

$$\left(\frac{dV}{dt}\right) = -\frac{\pi r^4 \delta P}{8 \mu l}\left[1 + \frac{s\gamma}{r}\right] \qquad (8.20)$$

for an incompressible fluid where s is a constant which may vary with temperature, capillary and molecular species and r is the radius of the tube; this equation is analogous to the Klinkenburg Equation in Chapter 2. Also

$$s\gamma = 4\mu/\varepsilon \qquad (8.21)$$

where the ratio μ/ε is the coefficient of slip, and ε is the coefficient of external friction. Rigorous calculations show that $\mu/\varepsilon \approx 1.1\ \gamma$, and thus from Equation 8.20, it follows that $s \approx 4.4$. Inspection of Equation 8.20 shows that the effect of slip is negligible when r is large compared to γ.

The percentage additional flow caused by the slip flow of nitrogen, relative to laminar flow of the gas through the same throat, may now be calculated from Equation 8.20. We find that for a 22μm diameter throat there is a 2.9% relative increase in flow, and for a 2 μm diameter throat, there is a 32% relative increase. The conductance of a porous medium is dominated by larger throats because the absolute flow rates are very different - a factor of 10^4 greater for the 22 μm throat than for the 2 μm throat. Thus the overall slip effect will be nearer 2.9% than 32%. The corrections would become increasingly significant in 'tighter' samples in which the pores and throats were smaller.

When this slip correction is added to the capacity term, Equation 8.17 becomes:

$$\frac{r_{arc}^4}{l_{arc}} =$$

$$\frac{8}{\pi}\left[\frac{1}{\frac{57}{4Cu_1^2(Cu_1 + 8.8\gamma)} + \frac{8h}{\pi r^3(r + 4.4\gamma)} + \frac{57}{4Cu_2^2(Cu_2 + 8.8\gamma)}}\right] \tag{8.22}$$

Equation (8.13) finally becomes

$$k = \frac{\pi}{8}\Omega\left(\frac{r_{arc}^4}{l_{arc}}\right)_{cell}\frac{l_{cell}}{A_{cell}} \tag{8.23}$$

8.2.5.2. The Permeability Calculation

Flow is allowed downwards or sideways in the unit cell, but not upwards. Therefore from the node at the centre of each pore extend 5 arcs - four horizontal and one downward - representing the 5 possible outward flows from the node. There are a total of 1000 nodes at the centre of the 1000 pores, and thus 5000 arcs. These include the 100 arcs extending downwards from the bottom layer of pores, which all join to a common 'super sink' node. In addition there are 100 arcs giving the flow capacity from the 'super source' node above the top surface, through the top layer of throats, into the top layer of nodes. The 5100 capacities r^4_{arc}/l_{arc}, calculated according to Equation 8.22, provide a complete description of the network to the Operational Research network analysis algorithm. This algorithm is the 'Dinic' routine which uses a variant of the revised primal simplex algorithm that exploits the network structure to reduce mathematical solution time. The algorithm calculates the maximum possible flow through each arc, allowing for shielding by neighbouring arcs of low capacity, and then calculates a single capacity term $\Omega(r^4_{arc}/l_{arc})_{cell}$. The permeability of the medium is then calculated from Equation 8.23.

8.2.6 Tortuosity Simulation

The tortuosity of a porous medium is defined as the ratio of actual path length taken through the medium to length of straight path through the medium. The application of this ratio to movement of charge within pore space has been discussed in Chapter 4.

The tortuosity has been simulated via a weighted random walk. A hypothetical particle is allowed to move through the model network starting at the top face. The particle randomly chooses its route but at each node the direction choice is weighted by a r^2/l type term where r is the throat radius and l is the length of the pore/throat system. The r^2/l takes into account the dimensions of the pore/throat system and not just the throats.

The particle movement can be in the ±x, ±y and -z directions; no backtracking towards the top face is allowed. This criterion simulates an electrical potential or concentration gradient across the unit cell. The particle is also not allowed to oscillate between groups of large pores, thus avoiding large tortuosity simulations.

Networks with low connectivities can contain pores with no exit, except by backtracking. In these cases the particle is allowed to return to its previous node and continue in a different direction. The distance from top to bottom face travelled by the particle is stored and the tortuosity calculated. One hundred particle walks are performed. The model outputs the median, first quartile and third quartile of the tortuosity distribution. The first and third quartiles being the values at 25% and 75% along tortuosity range respectively. The mean is not quoted because of its unreliability as a statistic to describe such distributions.

8.2.7. Constructing Correlated Structures

In the previous discussion all throats have been distributed randomly within the unit cell. A small number of sandstones are homogeneous over large distances and a random pore or throat arrangement gives a good representation of the void space; Clashach is an

example of such a sandstone. Conversely a large number of sandstones are inhomogeneous, banding being the commonest form of observed variance. Banded sandstones are a function of their depositional environment. Sand particles are transported by water or wind. The size of particle transported is a function of water or wind velocity. Thus a variation in deposited particles occurs with a fluctuation in transport medium velocity.

Within simple packing geometries an arrangement of large particles produces large voids/interstices. For sandstones unaffected by cement or authigenic clay this correlation between large grains forming large voids should also be true. A large number of our reservoir sandstones were visibly banded and a degree of pore size correlation had been detected by image analysis, it was decided to simulate void space with pore:pore correlation as well as the pore:throat correlation already incorporated in the model. The correlation algorithm was written by C. Ridgway.

8.2.7.1 Banded Structures

Figure 8.8 shows a unit cell with vertical bands of large and small pores. Vertical bands are modelled because permeabilities of banded sandstones are always measured perpendicular to the banding.

To construct this banded network the whole unit cell is split into ten vertical layers. The total number of throats is determined by the initial throat size distribution and connectivity input. The whole throat size range is split into ten equal groups and every throat assigned to a group depending on size. The first group will contain the smallest throats and the tenth group, the largest. For a totally correlated network all throats from the first group are placed in the first vertical layer of unit cell and similarly the second group of throats in the second layer etc. The tenth group which contains the largest throats will thus be positioned in the tenth vertical layer furthest from the smallest throat layer. The criterion that every pore must have at least one throat of the same diameter entering it is still invoked, so all large pores are positioned in the vertical layer containing all the

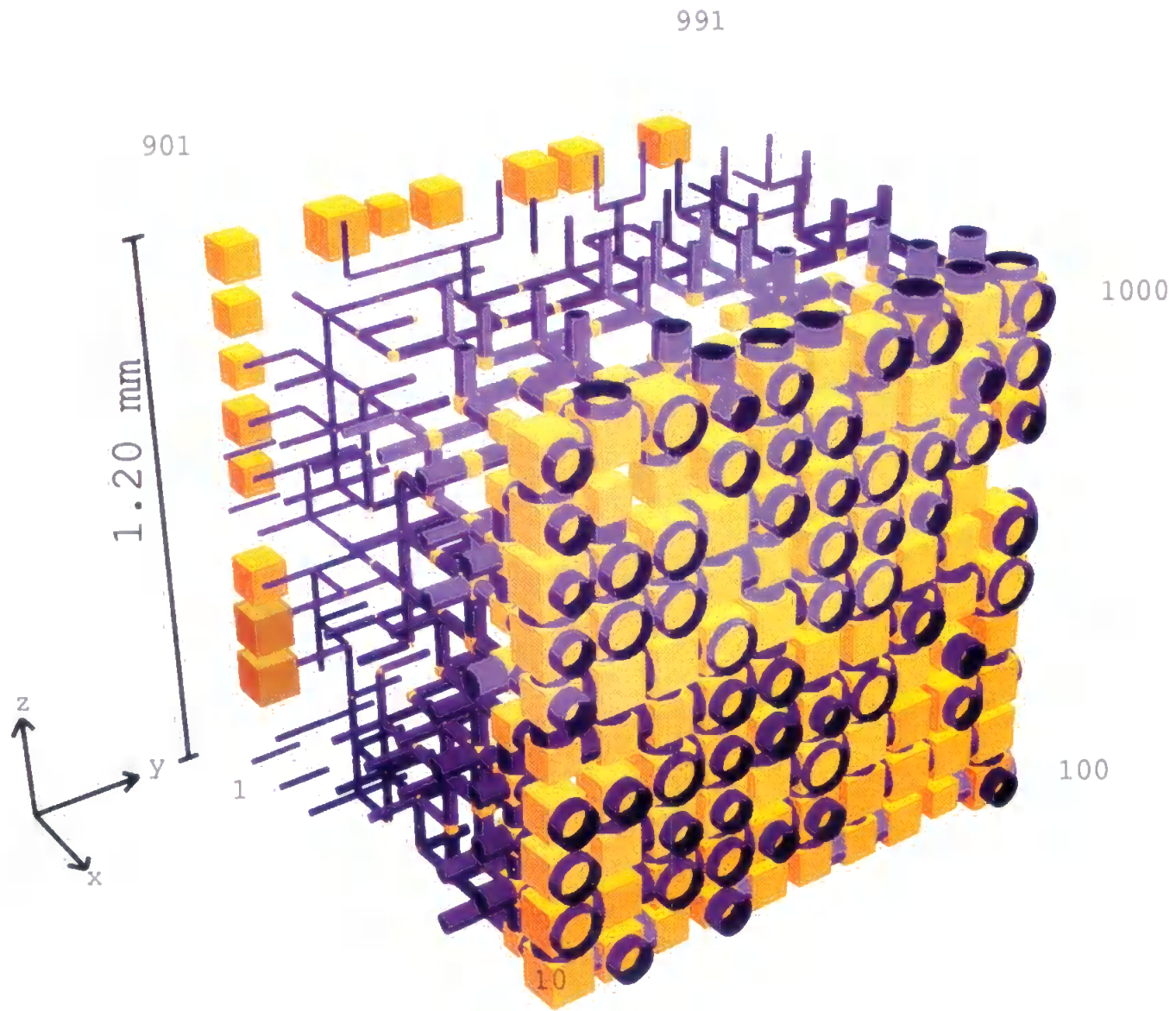

FIGURE 8.8: Model 3-D Unit Cell With Vertical Banding.

large throats. The same is true of all the small pores and a totally correlated unit cell is formed. The unit cell repeats in all directions. Therefore the vertical layer with large throats will join the small throats on the adjacent unit cell. A layer of large pores are constructed in the first layer of smallest throats to maintain the continuity of the network.

The above describes the construction of a totally correlated banded unit cell. Six different levels of correlation have been programmed. The correlation increments in steps of 0.2 from 0, a random network, to 1, the totally correlated unit cell. The lower levels of correlation are achieved by allowing throats from each group to be positioned in an increasing number of the vertical layers, until at a correlation of zero, a throat cell can reside anywhere in the unit cell. The table below summarizes the correlation level and the number of vertical layers a throat is free to position itself:

Correlation Level	No. of Accessible Layers
0.0	10
0.2	9
0.4	7
0.6	5
0.8	3
1.0	1

At a correlation level of 0.8 a throat can reside in the vertical layer it would have, if totally correlated, plus one other layer either side, making a total of three accessible layers. A correlation level of 0.6 allows five potential vertical layers for residence the one if totally correlated and two either side etc. Due to the repeatability of the unit cell, a throat assigned to one of the edge vertical layer in the totally correlated network, can at lower levels of correlation be positioned in vertical layers on the opposite side of the unit cell. This corresponds to a throat being positioned in the adjoining unit cell.

8.2.7.2. Unit Cells With Small Or Large Pores In Centre

An algorithm has been written to construct a unit cell with all the small pores and throats or all the large pores and throats in the centre (Matthews et al 1994). This type of simulation is not applicable to the void structures observed within sandstones. This simulation is useful to describe void space within soils. Grouping of like pores found in 'ped' structures, are a common constituent of soils.

8.2.8 Pore Block Simulation

The simple pore blocking action of a colloid within the pore network can be simulated using Pore-cor. Once the pores and throats have been positioned within the simulated unit cell, all pores and throats of a specified size or less are removed from the network. The blocking of all pores and throats of a specified size or less, assumes all these pores or throats are accessible to the simulated colloid, a reasonable assumption if blocking only the smallest pores and throats. The effect of pore blocking on the simulated model parameters can be monitored. The pore block simulation has been used to simulate formation damage within reservoir sandstones, this study is discussed in Chapter 10.

CHAPTER 9

MODELLING RESULTS

9.1 Trends Within Simulations

Before describing the results obtained from the simulations of reservoir sandstone void space, some of the model's properties are identified. An interesting application of both the mercury intrusion and three dimensional unit cell visualization is that the specific location of mercury with the unit cell can be observed. The mercury intrusion can be halted at any point throughout the simulation and the position of the mercury front noted within the unit cell. Figure 9.1 shows the point at which mercury has just broken through the unit cell. The corresponding position on the simulated mercury intrusion curve is indicated in Figure 9.2. As predicted by Katz and Thompson (1986), the breakthrough point/percolation threshold occurs at the point of inflection on the mercury intrusion curve. The next sections describe the effect of changing the connectivity, throat size distribution skew and degree of correlation within the unit cell on simulated mercury intrusion/extrusion, permeability and tortuosity.

9.1.1 Changing Connectivity Within A Random Pore:Throat Network

The connectivity of the unit cell obviously affects the percolation and flow properties. A reduction in connectivity will cause a reduction in mercury intrusion curve point of inflection and permeability. Figure 9.3 shows the simulated mercury intrusion curves for the same pore and throat size distribution and random throat allocation, with varying connectivities. The point of inflection is reduced to a lower throat diameter as connectivity is lowered. The curves also shallow as connectivity falls. Both these effects are due to the reduction in routes through the unit cell. As connectivity falls, the mercury

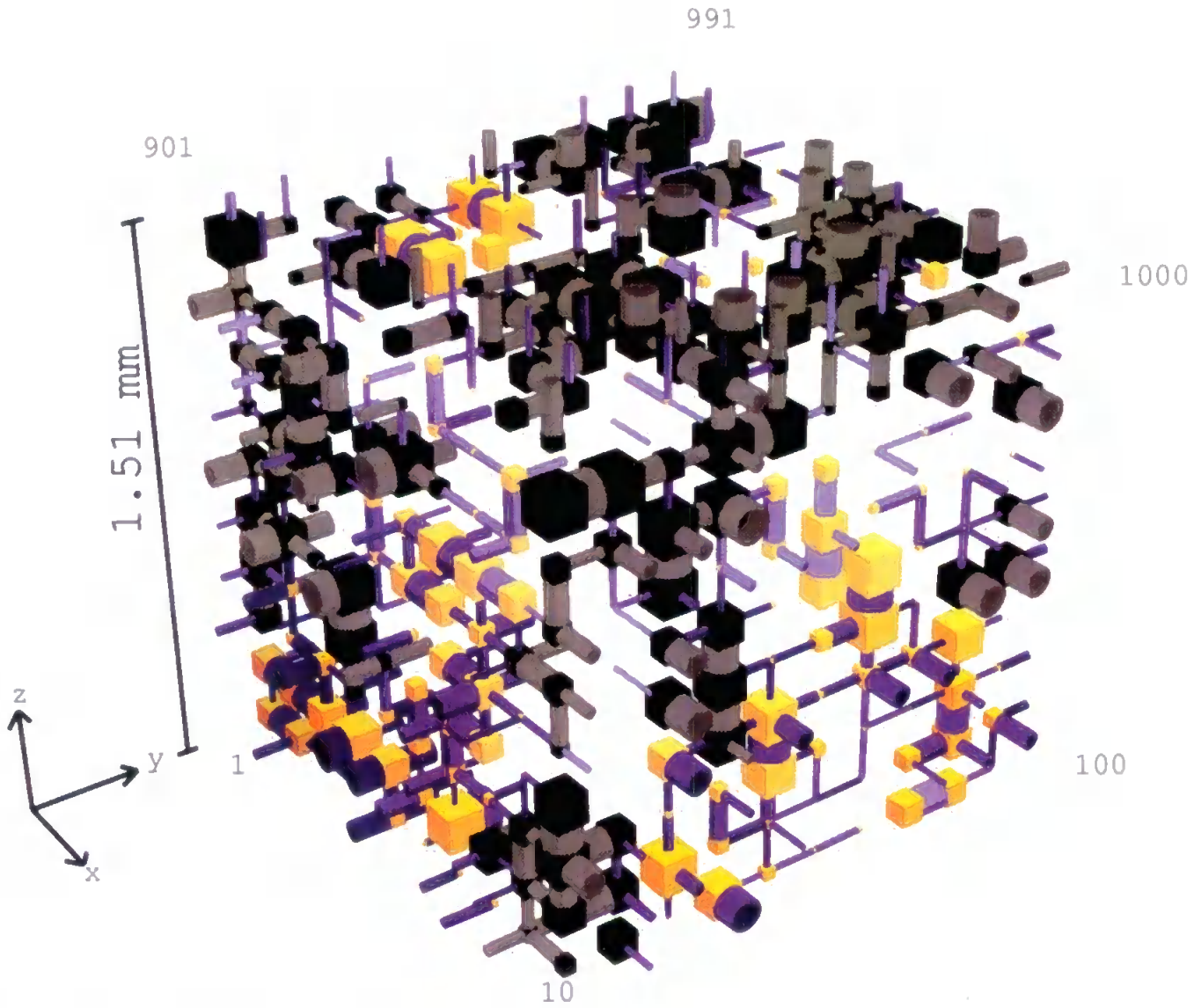

FIGURE 9.1: Model 3-D Unit Cell Showing Mercury Breakthrough.

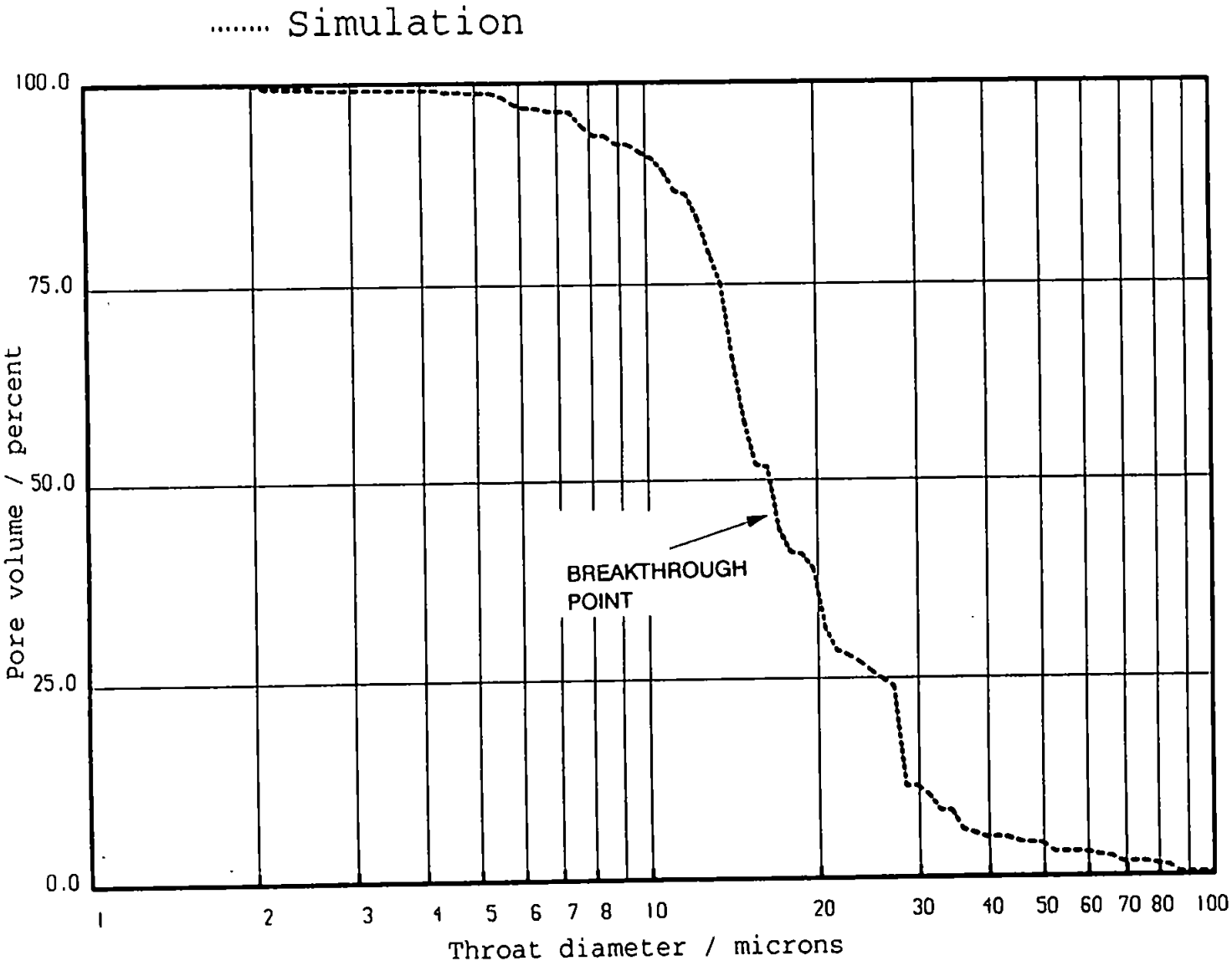

FIGURE 9.2: Simulated Mercury Intrusion Curve For Unit Cell In Figure 9.1, Showing Breakthrough Point.

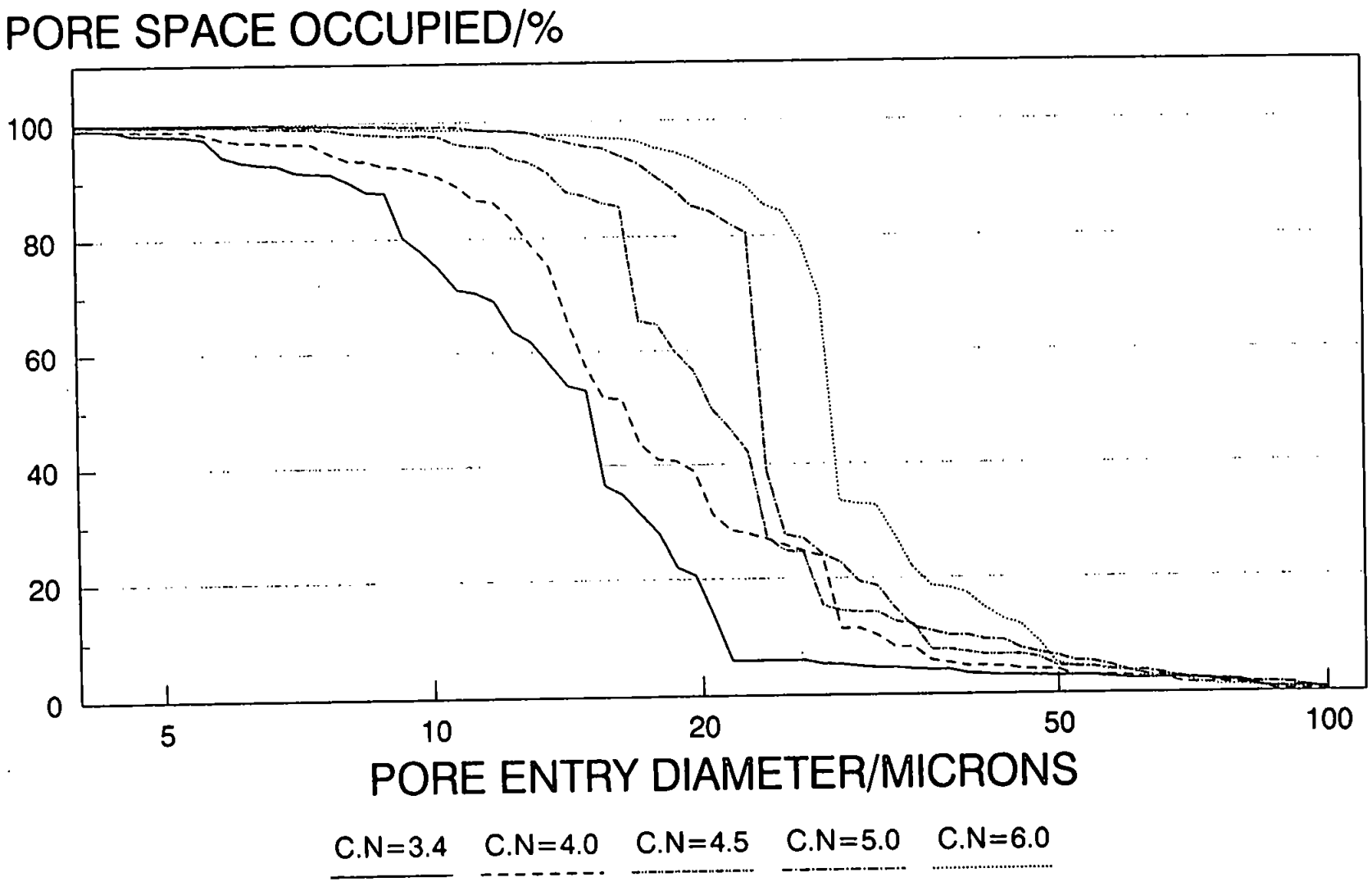

FIGURE 9.3: Simulated Mercury Intrusion Curves For Networks With Varying Connectivity.

follows a more tortuous route to achieve break-through, thus causing a fall in point of inflection and a shallowing of the curves. An attempt was made to quantify the shape of the simulated intrusion curves by measuring their geometrical parameter. Such an analysis is impossible for the simulated curves due to their rough nature, the rough intrusion curves being caused by the size of the unit cell. Intrusion into a unit cell of finite dimensions is "step wise" because each void represents a significant volume within the whole.

A reduction in connectivity will also increase the amount of mercury trapped within the void space after complete pressure reduction. A unit cell with a connectivity of four has a mercury residual of 50%, whereas the same pore:throat size distribution with a connectivity of 3.1 has a mercury residual of 58%. Again reduced accessibility causes this trend.

Permeability is significantly affected by a reduction in connectivity. With a connectivity of 3 and the pore and throat size distribution used in Figure 9.3, a permeability of 0.461 md is simulated. Reducing the connectivity to 2 causes a permeability reduction of 98% to 0.006md. Figure 9.4 shows the extent of permeability reduction with connectivity reduction. Note there is no path through the cell below a connectivity of 2. Such drastic permeability reductions are common during oil production from reservoirs due to pore plugging and cementation. These processes are collectively called formation damage, a phenomenon discussed later.

Tortuosity of the unit cell rises with decrease in connectivity. A unit cell of connectivity 3 has a median tortuosity of 2.7 (1st quartile = 2.2, 3rd quartile = 3.5). A connectivity of 2.5 produces a median tortuosity of 3 (1st quartile = 2.8, 3rd quartile = 5.4). Thus median tortuosity has risen and the range moved towards high values. The trend of increase in tortuosity with connectivity reduction is quite scattered.

9.1.2 Changing Throat Size Distribution Within A Random Pore:Throat Network

The throat size distribution input into the model also affects the mercury

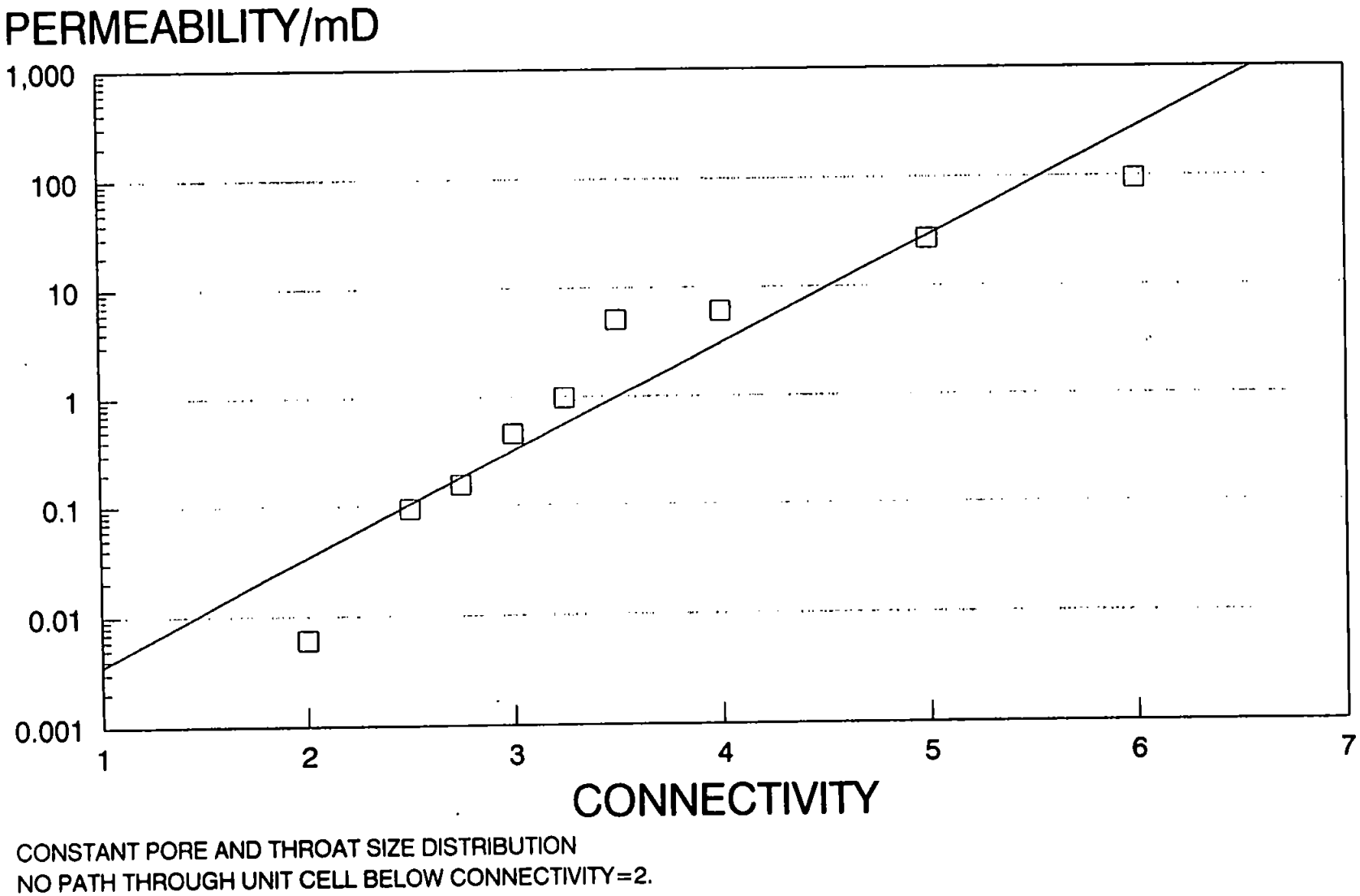

FIGURE 9.4: Relationship Between Permeability and Connectivity In Simulated Void Networks.

intrusion/extrusion, permeability and tortuosity simulations. Obviously increasing the throat size distribution skew percentage will increase the number of small throats in the network and cause the reduction in the point of inflection. A corresponding lowering of permeability and an increase in tortuosity will also occur if the number of small pores increases within the unit cell. A combination of varied connectivity and throat size distribution skew allow a wide range of mercury intrusion curves to be simulated.

The extrusion of mercury from the unit cell is also affected by the pore:throat size distribution. The extrusion of mercury is controlled by pore size and the trapping of mercury dependent on the pore/throat size ratio, as discussed in Chapter 5. For a random unit cell the percentage of mercury trapped rises as the number of small throats within the network increases. This is due to an increase in the number of large pores connected to small throats, thus increasing possibility of mercury snap-off and trapping.

9.1.3. Changing Degree Of Pore:Pore Correlation

The above discussion involved simulated void space networks with no pore:pore correlation and only a small degree of pore:throat correlation. The introduction of pore:pore correlation has a marked effect on the simulated mercury intrusion/extrusion curves, permeability and tortuosity.

Increasing pore:pore size correlation, with the same pore throat size distribution, causes an increase in point of inflection diameter on the simulated mercury intrusion curve, Figure 9.5. Increased pore:pore size correlation also leads to an increased pore:throat size correlation. In unit cells of high correlation, mercury breakthrough occurs at a larger throat diameter because of this pore and throat clustering. As correlation is reduced, breakthrough diameters decrease and intrusion curves become shallower, as seen in Figure 9.5. The grouping of large pores and throats allows efficient extrusion and low percentages of

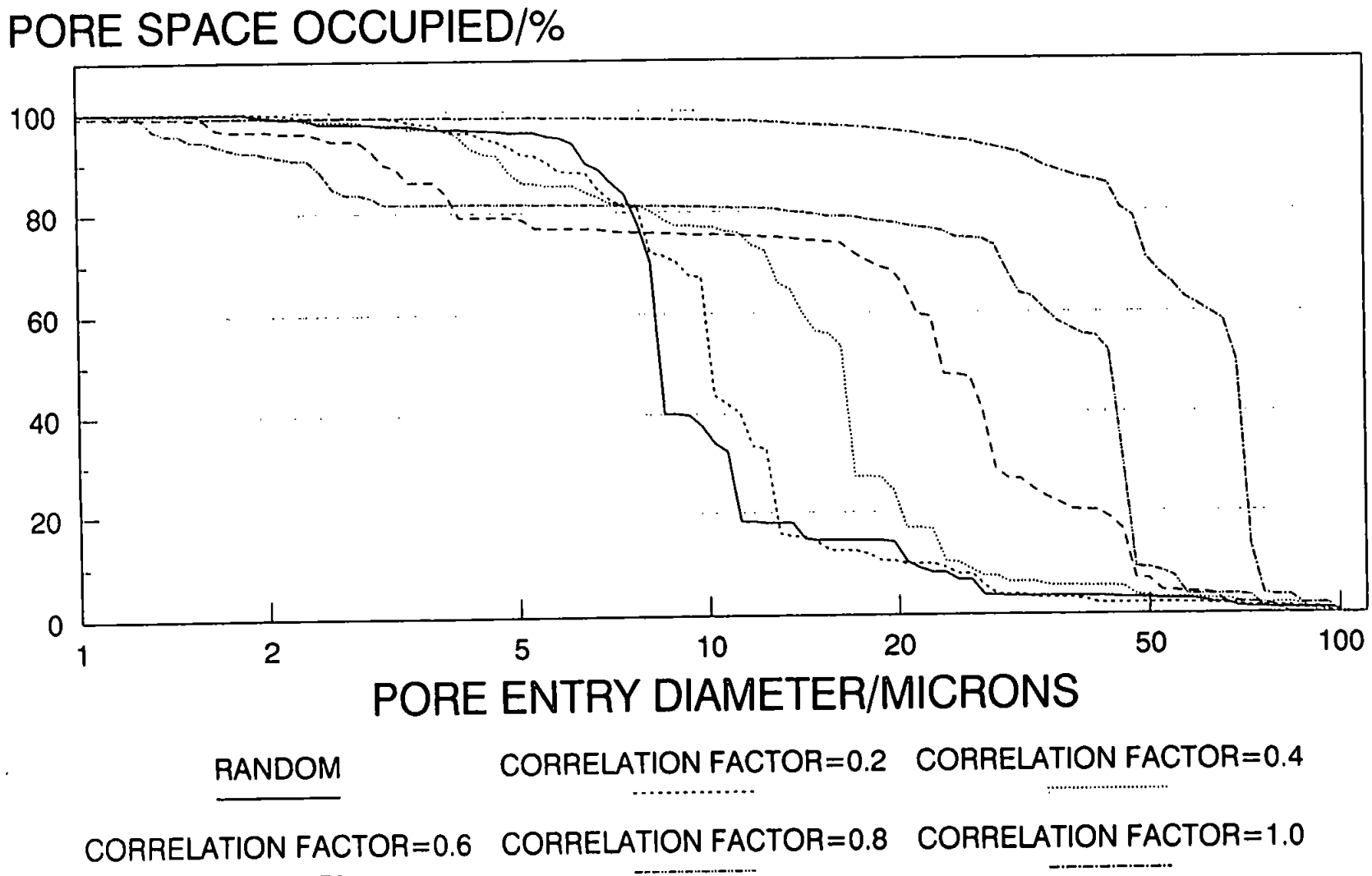

FIGURE 9.5: Simulated Mercury Intrusion Curves For Networks With Varying Correlation.

trapping mercury. Permeability is greatly increased by introducing correlation into the network. Figure 9.6 illustrates the effect of correlation on simulated permeability for the same pore:throat size distribution and connectivity. In this example the permeability is 5000 times larger within the fully correlated network. Increasing correlation produced a decrease in tortuosity.

The correlated networks will follow the same trends identified for random unit cells for variations in connectivity and pore throat size distributions. Figure 9.7 summarizes the trends identified with variation of connectivity, throat size distribution and correlation.

9.2 First Attempts To Simulate Reservoir Sandstone Void Space

Table 9.1 shows the parameters input into the model and the corresponding simulation output for every sample analyzed by mercury porosimetry. A log method of mercury intrusion curve convergence is used to obtain the optimised pore throat size distribution and connectivity. The curve fitting procedure has been applied to the whole throat diameter range measured during mercury intrusion. The pore and throat diameters in the unit cells range from 0.12 to 207.16μm.

The degree of pore:pore correlation has been estimated from the visual inspection of samples. Image analysis data for the samples analyzed are also used. Image analysis/variogram procedure is able to supply information about the degree of correlation in sandstones, but as yet the data obtained have not been utilised within the Pore-Cor model. The correlation factors used in Table 9.1 are somewhat subjective but the relative level of banding in each sample is estimable. The simulated and experimental mercury intrusion curves are shown in Appendix 6. All mercury intrusion curves are normalized to 100% occupied pore volume. Porosity of those simulation with a random pore:throat

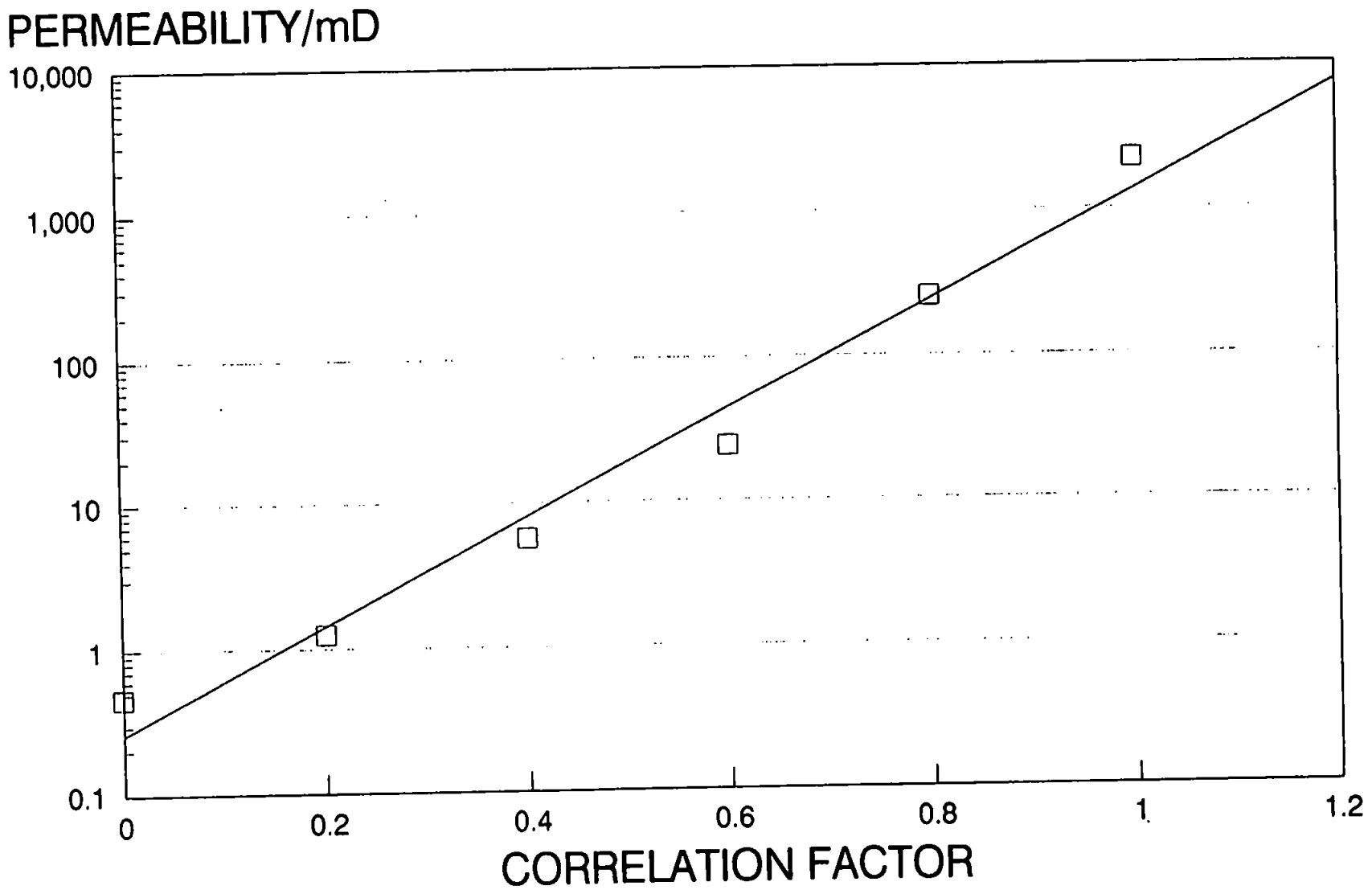

FIGURE 9.6: Relation Between Permeability and Correlation In Simulated Void Networks.

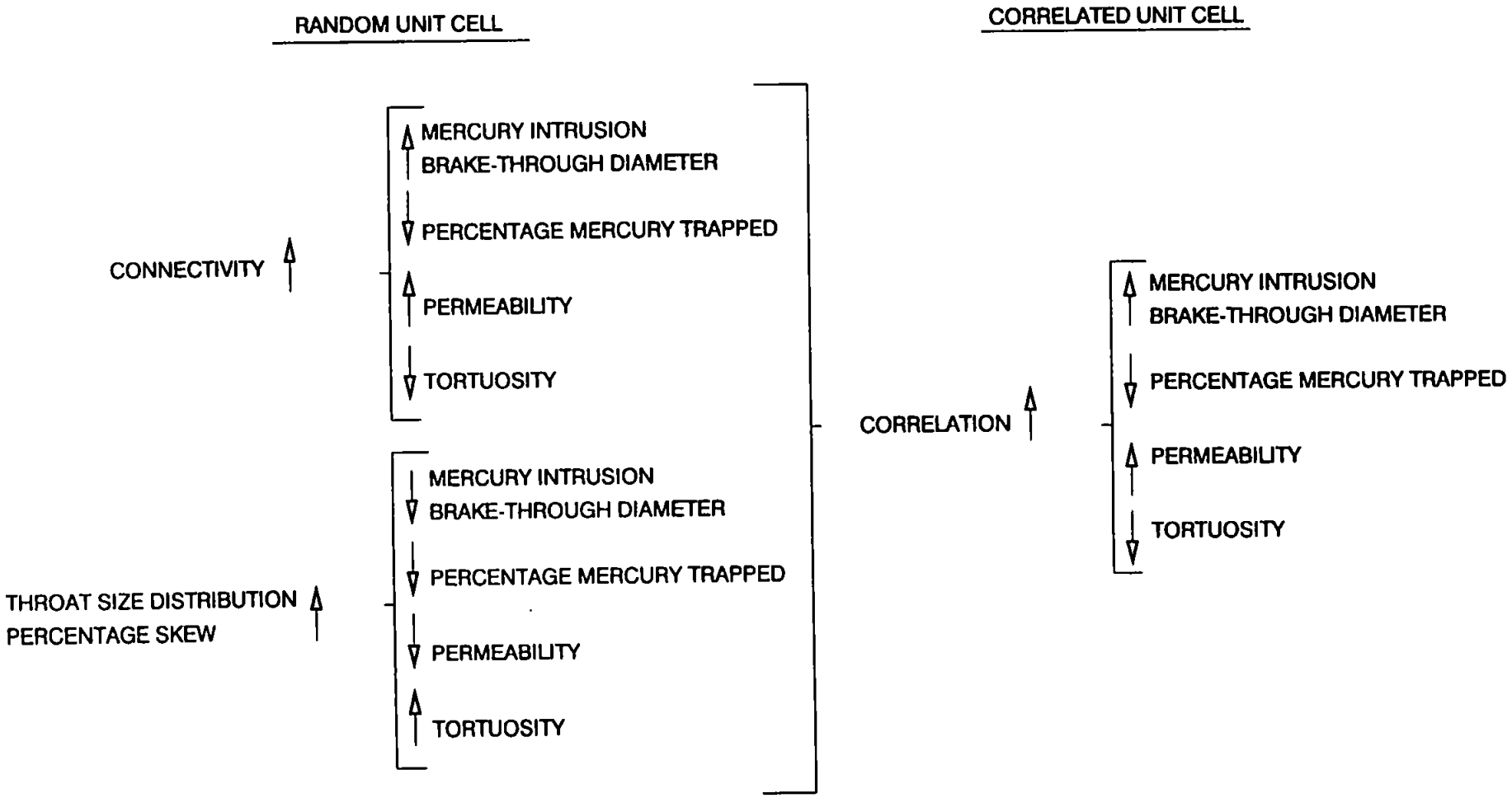

FIGURE 9.7: Trends Identified Within Pore-Cor Void Space Model

			INPUT						OUTPUT			
SAMPLE NO.	EXPT. PERME-ABILITY/mD	EXPT. TORTUOSITY	MIN. THROAT DIAMETER/μm	MAX. THROAT DIAMETER/μm	PERCENTAGE SKEW/%	CONNE-CTIVITY	CORRELATION FACTOR	POROSITY	PERMEAB-ILITY/mD	MEAN TORTUOSITY	FIRST QUARTILE	THIRD QUARTILE
212A	50.47	2.27	0.12	207.16	0.645	2.6	0.00	12.30	____	____	____	____
212B	1413.58	1.75	0.12	207.16	1.597	3.7	0.80	8.30	5.430	2.40	2.00	2.70
212C	3161.56	1.83	0.10	207.16	1.625	3.9	0.80	8.30	11.800	2.60	2.30	3.30
212D	335.05	2.12	0.10	207.10	1.613	3.9	0.60	8.80	0.596	3.20	3.00	3.50
212E	1427.77	1.75	0.12	207.16	1.734	3.5	0.80	6.20	3.940	2.40	2.00	3.60
250A	1208.49	1.91	0.14	207.16	1.735	3.8	0.60	6.80	0.232	____	____	____
250E	693.52	1.94	0.12	207.16	1.791	3.5	0.80	5.30	2.410	2.80	2.20	3.40
250E REPEAT	693.52	1.94	0.12	207.16	1.778	3.5	0.80	5.50	2.470	2.40	1.80	3.40
490A	____	___	0.12	207.16	0.687	2.7	0.00	13.20	0.002	____	____	____
490B	27.06	___	0.12	207.16	0.756	2.6	0.00	15.70	____	____	____	____
490C	____	___	0.12	207.16	0.595	2.6	0.00	17.90	0.002	____	____	____
490D	10.71	___	0.12	207.16	0.719	2.6	0.00	14.10	____	____	____	____
490D REPEAT	10.71	___	0.12	207.16	1.093	2.6	0.00	12.50	____	____	____	____
490E	16.53	2.85	0.12	207.16	0.883	2.6	0.00	14.90	____	____	____	____

TABLE 9.1: Model Inputs To Simulate Reservoir Sandstone Void Space and Corresponding Outputs.

allocation matches the experimental values exactly in many cases. Simulations with a high degree of pore:pore correlation have porosities below experimental values. For these simulations the pore:throat size distributions are skewed towards smaller values. The highest porosity obtainable for a given unit cell is dependent on the size of the largest pores. The porosities quoted for the correlated simulations are the values obtained at the minimum pore row spacing possible.

The permeability algorithm calculates permeabilities of 1×10^{-3}md and above. Any network with a permeability below this value is said to have no path through the unit cell. Simulations with a random pore network have extremely low simulated permeabilities, in most cases zero flow is attained. Whilst all sandstones of homogeneous appearance had lower permeabilities than the banded samples the model has exaggerated this trend. Mercury intrusion curves for homogeneous sandstones are usually shallower than those of banded sandstones. To fit simulated intrusion curves to shallow experimental curves a low connectivity is used, which causes the low permeabilities. Correlated simulations have a higher connectivity, but as mentioned earlier, the pore:throat size distributions are skewed towards the smallest sizes, thus simulated permeability is significantly below the measured values. Tortuosities of the networks are all higher than the corresponding measured values. In some cases no path was found through the unit cell.

9.3 Simulation Of Reservoir Sandstone Void Space Using Truncated Mercury Intrusion Curves

Fitting the whole experimental intrusion curve causes an overestimation of the large pore frequency. In real sandstones the large pores measured during mercury intrusion are predominantly surface pores. The model does not include surface pore effects but still include these large voids throughout the whole network. The overestimate of the frequency

of large pores and throats limits the success of the porosity, permeability and tortuosity simulations described above.

The best method of obtaining mercury intrusion data without the effects on surface void space is to coat the sample in resin on all sides except one, as performed by Wardlaw and Taylor (1976). This procedure is impossible for the samples used in this study as all the material was used in the mercury intrusion experiments. An alternative approach is to remove the knee of the measured intrusion curves and extrapolate the line from the point of inflection to the throat diameter axis. The intrusion curve in this form is an approximation of that obtained if a sample of infinite size was analyzed. The truncated intrusion curves for the reservoir sandstones have a maximum throat diameter ranging from 10 to 60μm. Image analysis has shown that some samples do contain voids larger than this, but these are rare. In terms of properties such as porosity, permeability, tortuosity and mercury intrusion, these few large pores play only a small part. The following results show that a truncated mercury intrusion curve facilitates a good simulation of the reservoir sandstone void space.

9.3.1 Results

Table 9.2 details the model input and output for each truncated curve fit simulation. The minimum throat size still matches that measured from mercury intrusion data. The correlation factors for each sample are the same as used in the first simulations. The log fit procedure has been used to obtain the optimized throat size distribution skew and connectivity. The simulated and experimental mercury intrusion curves for every sample are shown in Figures 9.8 to 9.21. Simulated mercury intrusion curves closely match experimental curves for the correlated simulations.

The shallow intrusion curves of the homogeneous sandstones were not so successfully

			INPUT						OUTPUT			
SAMPLE NO.	EXPT. PERME-ABILITY	EXPT. TORTUOSITY	MIN. THROAT DIAMETER/μm	MAX. THROAT DIAMETER/μm	PERCENTAGE SKEW/%	CONNE-CTIVITY	CORRELATION FACTOR	POROSITY	PERMEAB-ILITY/mD	MEAN TORTUOSITY	FIRST QUARTILE	THIRD QUARTILE
212A	50.47	2.27	0.12	30.00	0.464	2.80	0.00	12.30	0.10	3.30	3.10	3.70
212B	1413.58	1.75	0.12	60.00	0.185	2.90	0.80	20.00	559.00	2.30	1.70	2.70
212C	3161.56	1.83	0.10	45.00	0.291	4.00	0.80	24.40	1030.00	2.20	1.90	2.50
212D	335.05	2.12	0.10	42.00	0.258	3.60	0.60	13.70	86.20	2.30	2.00	2.70
212E	1427.77	1.75	0.12	50.00	0.106	2.90	0.80	22.00	521.00	2.40	1.70	3.30
250A	1208.49	1.91	0.14	50.00	0.351	2.70	0.60	22.40	44.60	NO PATH	—	—
250E	693.52	1.94	0.12	30.00	0.286	3.80	0.80	21.10	506.00	2.10	1.80	2.60
250E REPEAT	693.52	1.94	0.12	30.00	0.166	3.50	0.80	21.10	327.00	2.10	1.70	2.50
490A	—	—	0.12	17.00	0.000	2.70	0.00	13.20	0.21	2.80	2.20	3.20
490B	27.06	—	0.12	15.00	0.215	2.80	0.00	15.70	0.28	2.60	2.40	3.10
490C	—	—	0.12	28.00	0.153	2.70	0.00	23.20	0.24	3.10	2.30	3.30
490D	10.71	—	0.12	24.00	0.293	2.70	0.00	14.10	0.07	2.80	2.10	3.30
490D REPEAT	10.71	—	0.12	10.00	0.419	2.80	0.00	14.10	0.11	2.90	2.50	3.40
490E	16.53	2.85	0.12	16.00	0.088	2.70	0.00	15.90	0.18	3.00	2.70	3.50

TABLE 9.2: Model Inputs and Outputs For Each Truncated Curve Fit Simulation

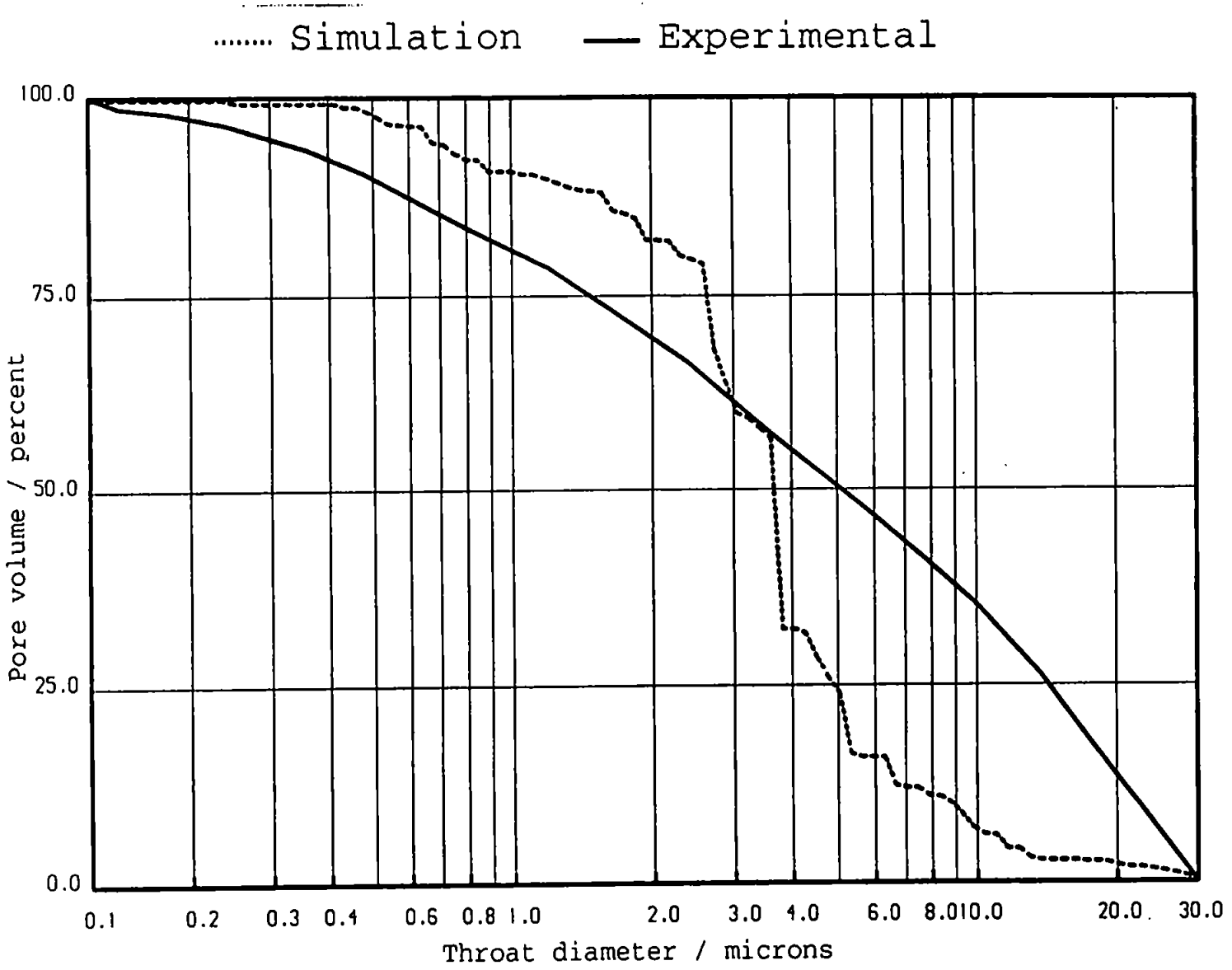

FIGURE 9.8: Truncated Experimental and Simulated Mercury Intrusion Curves for Sample 212A

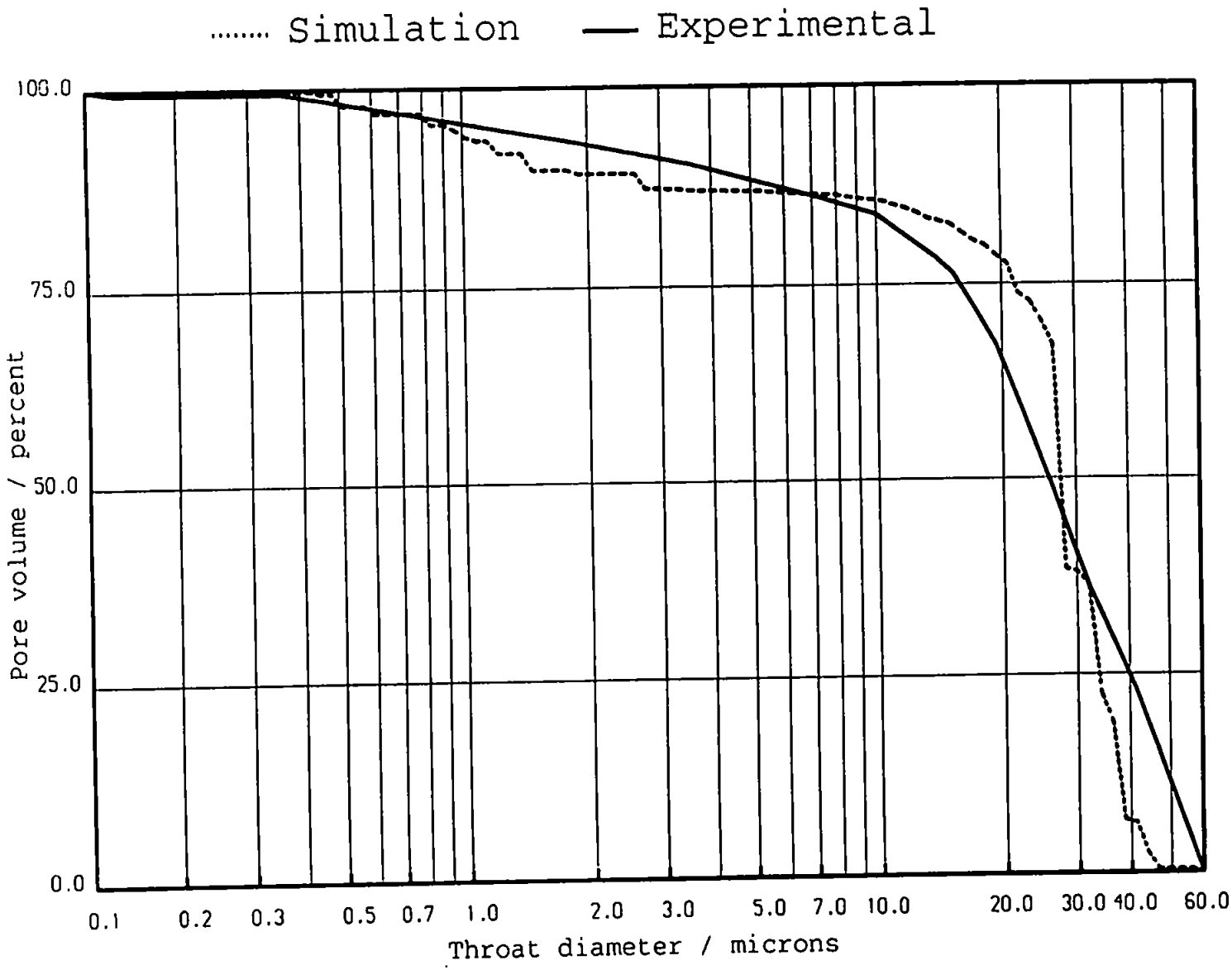

FIGURE 9.9: Truncated Experimental and Simulated Mercury Intrusion Curves for Sample 212B

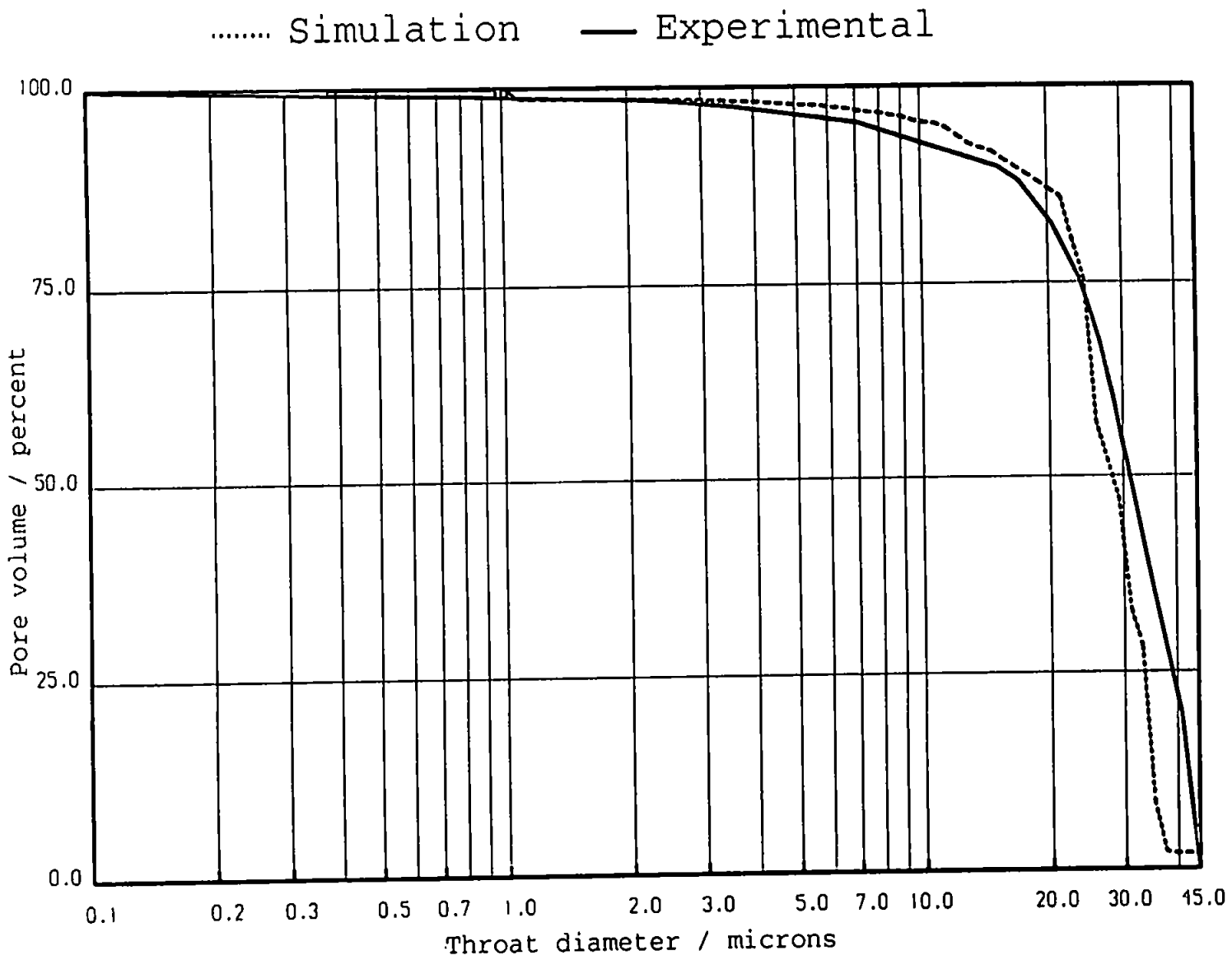

FIGURE 9.10: Truncated Experimental and Simulated Mercury Intrusion Curves for Sample 212C

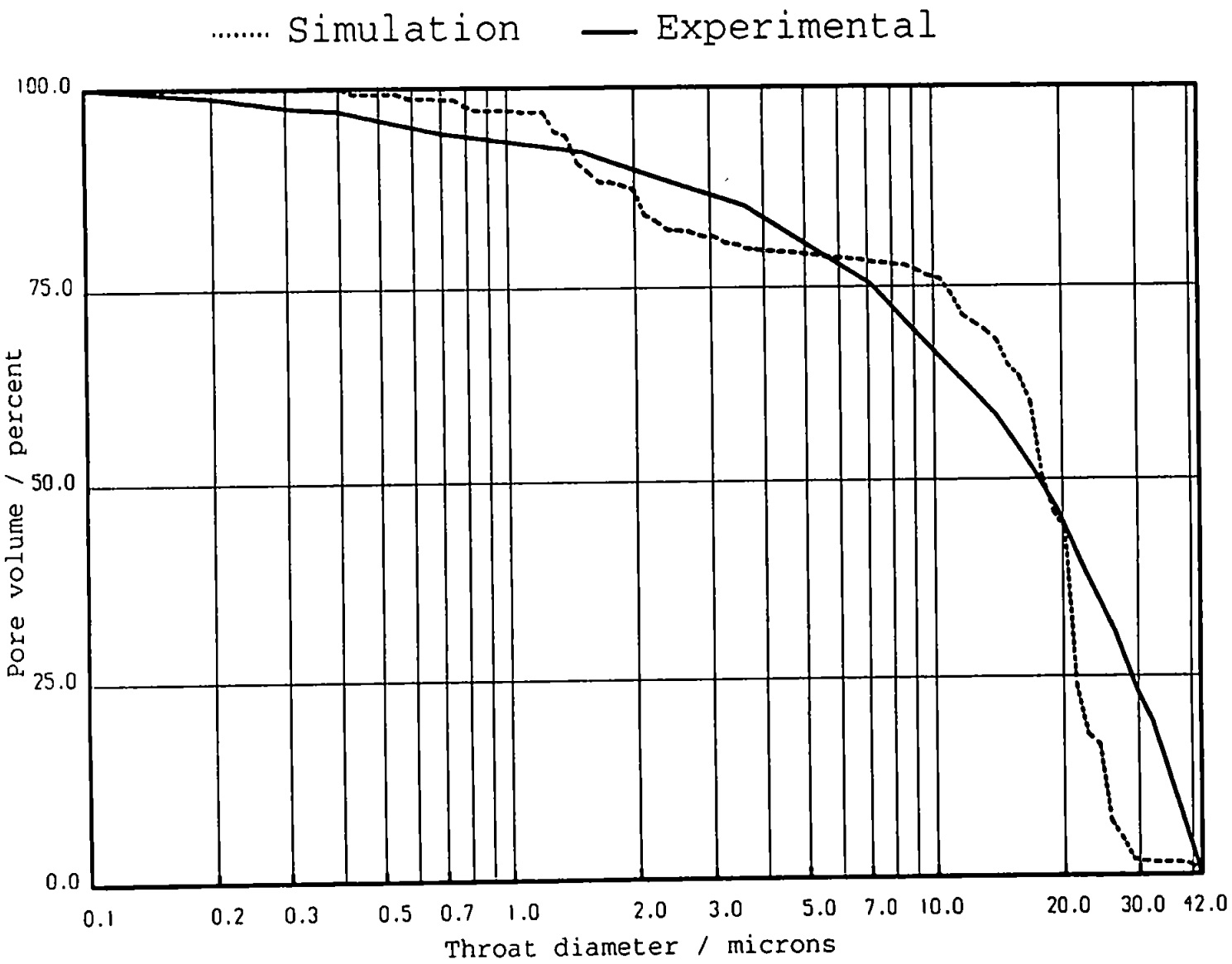

FIGURE 9.11: Truncated Experimental and Simulated Mercury Intrusion Curves for Sample 212D

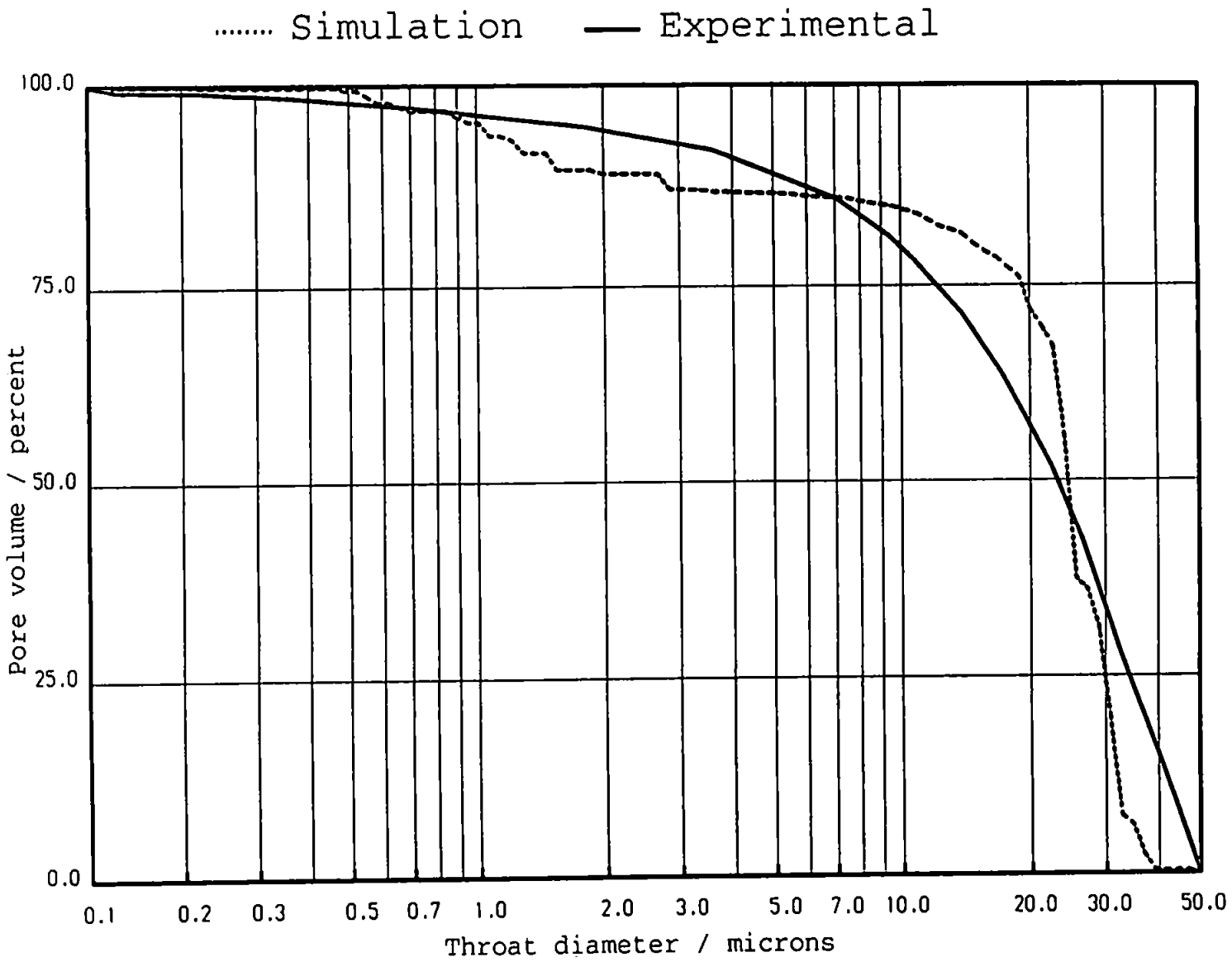

FIGURE 9.12: Truncated Experimental and Simulated Mercury Intrusion Curves for Sample 212E

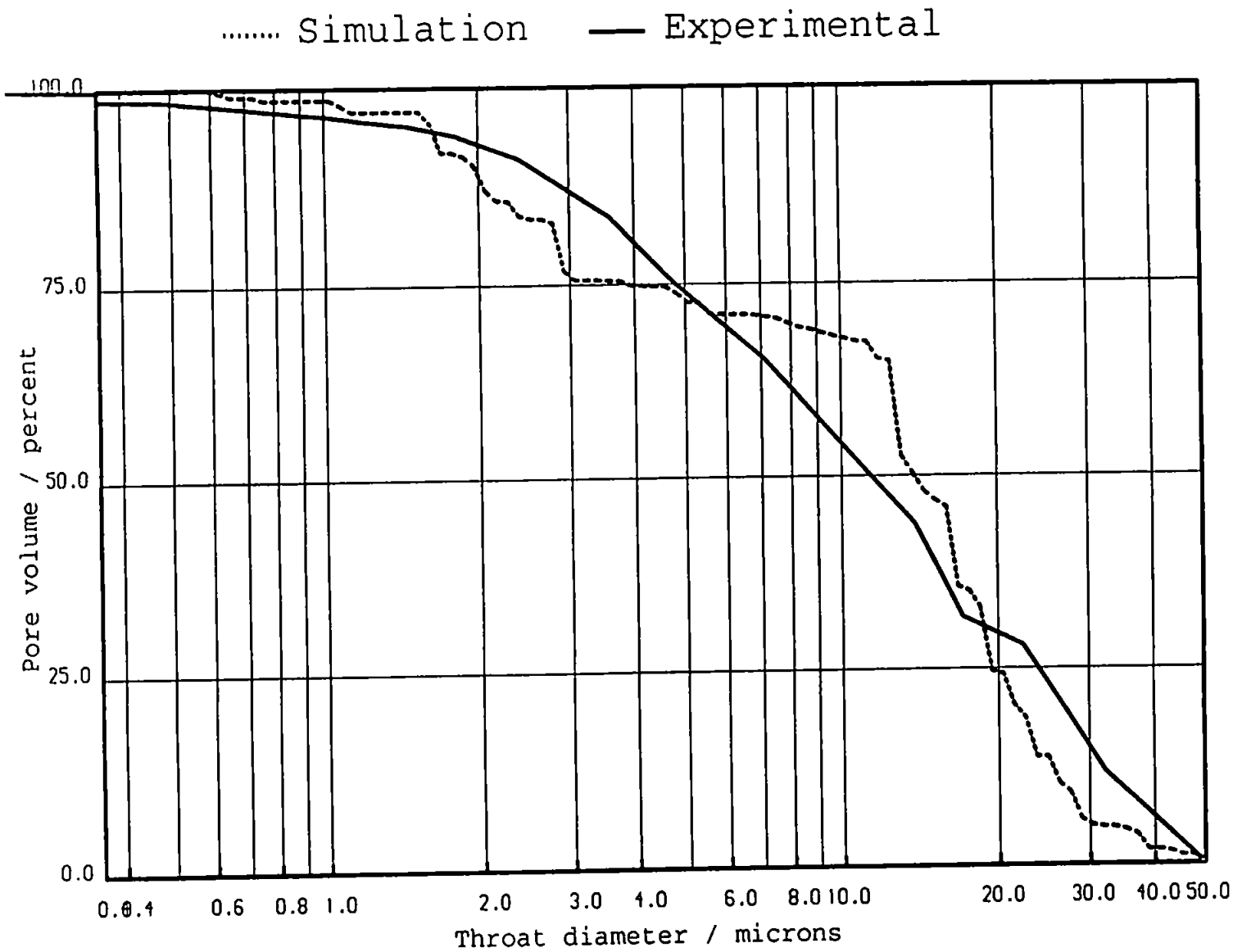

FIGURE 9.13: Truncated Experimental and Simulated Mercury Intrusion Curves for Sample 250A

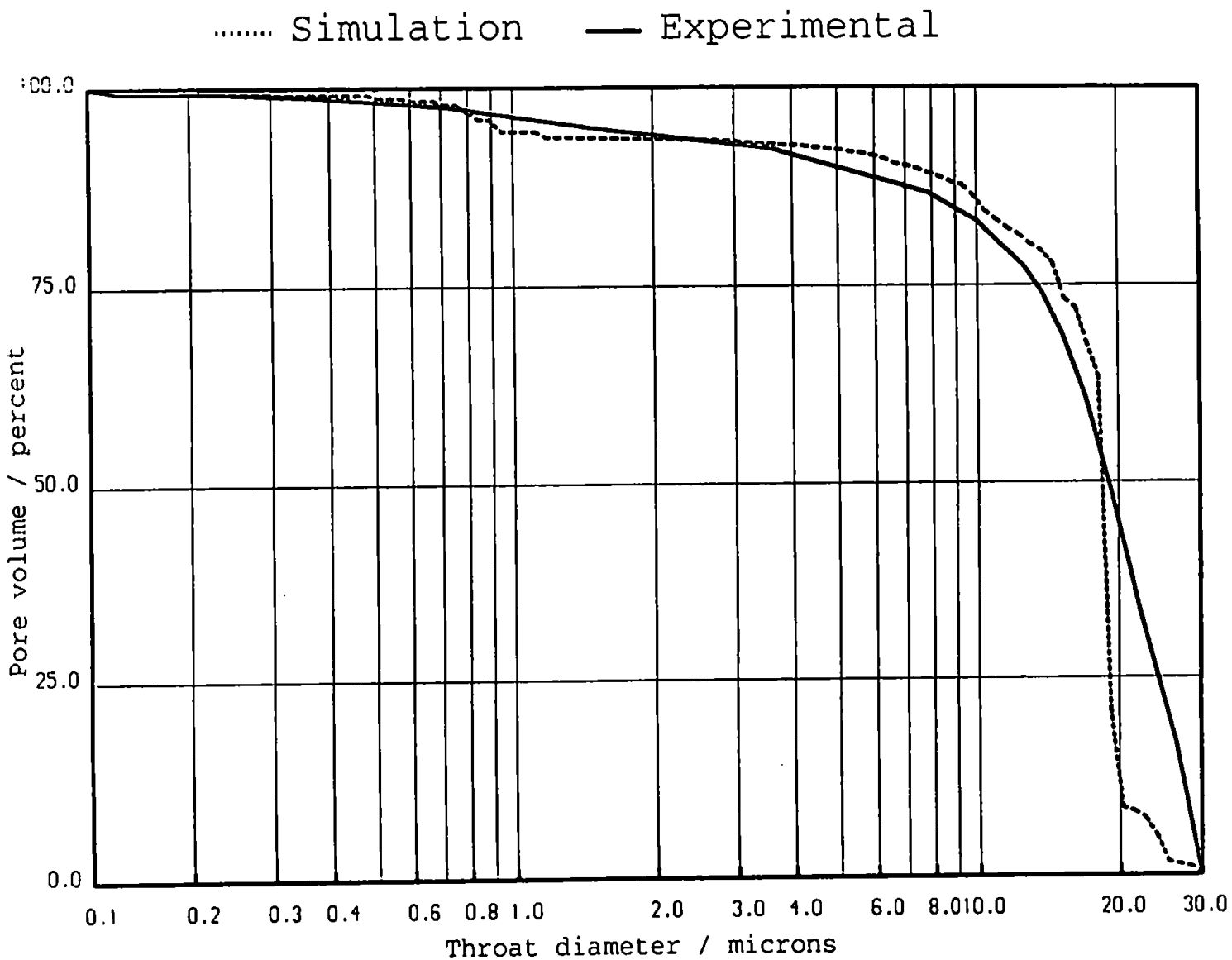

FIGURE 9.14: Truncated Experimental and Simulated Mercury Intrusion Curves for Sample 250E

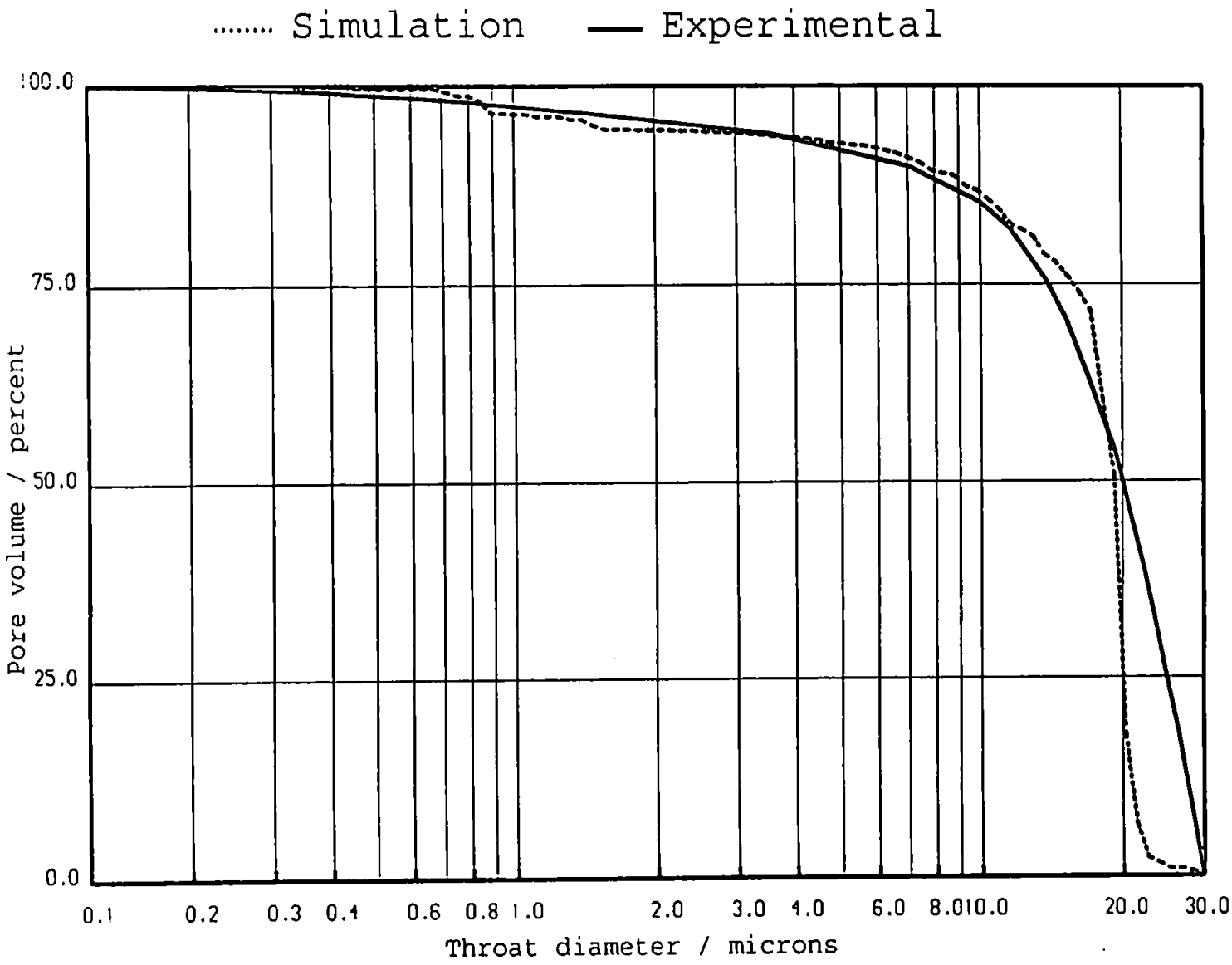

FIGURE 9.15: Truncated Experimental and Simulated Mercury Intrusion Curves for Sample 250E Repeat Run

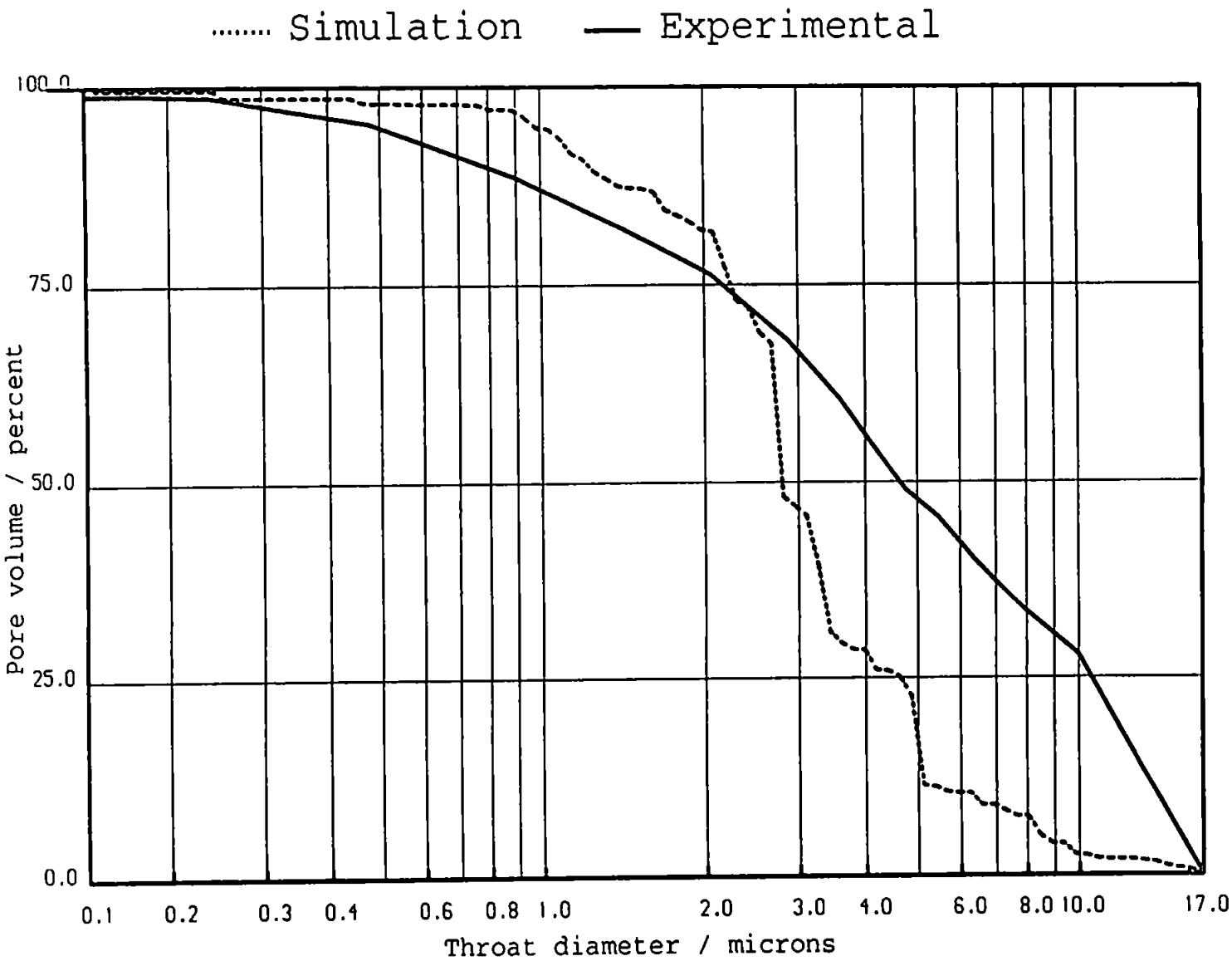

FIGURE 9.16: Truncated Experimental and Simulated Mercury Intrusion Curves for Sample 490A

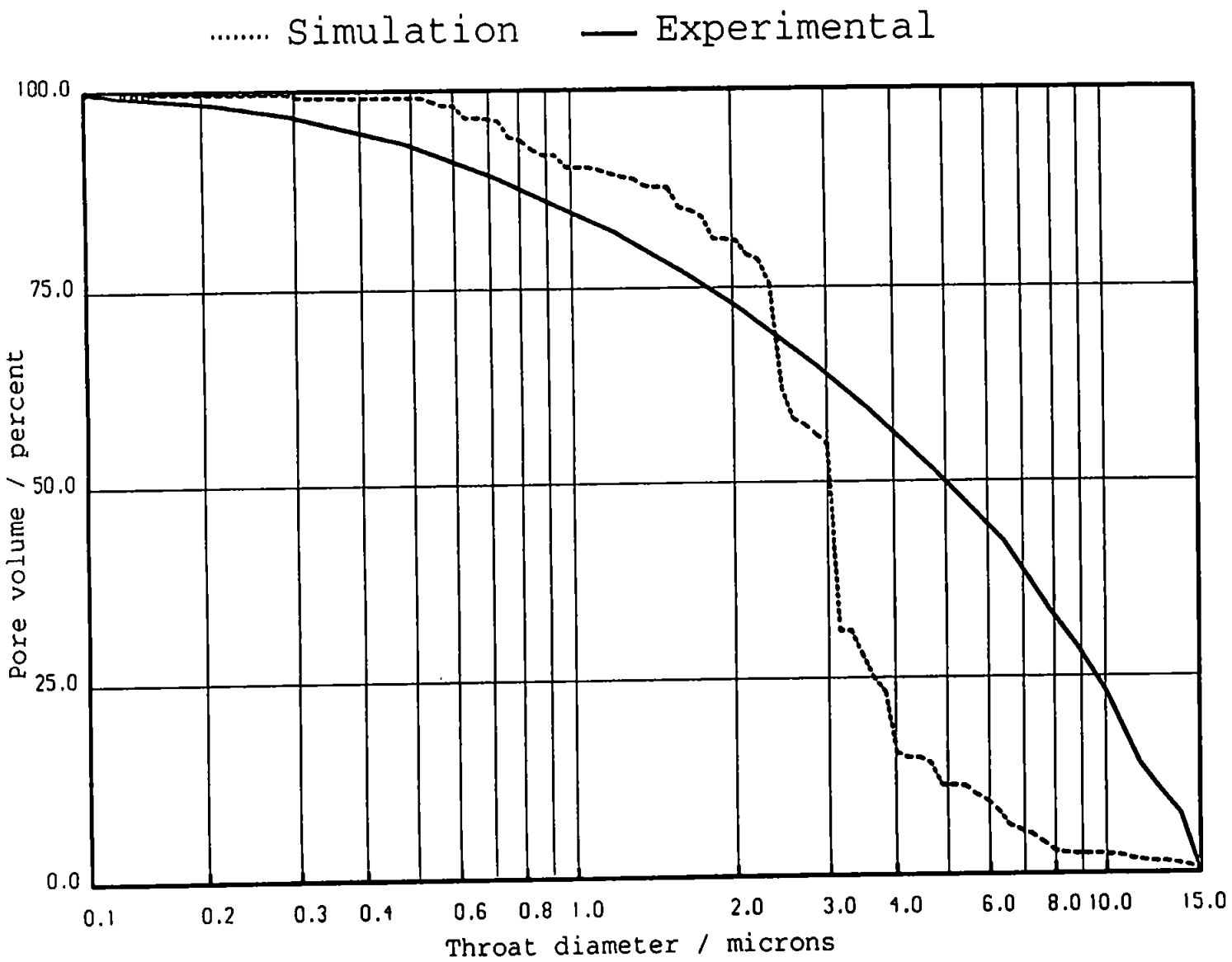

FIGURE 9.17: Truncated Experimental and Simulated Mercury Intrusion Curves for Sample 490B

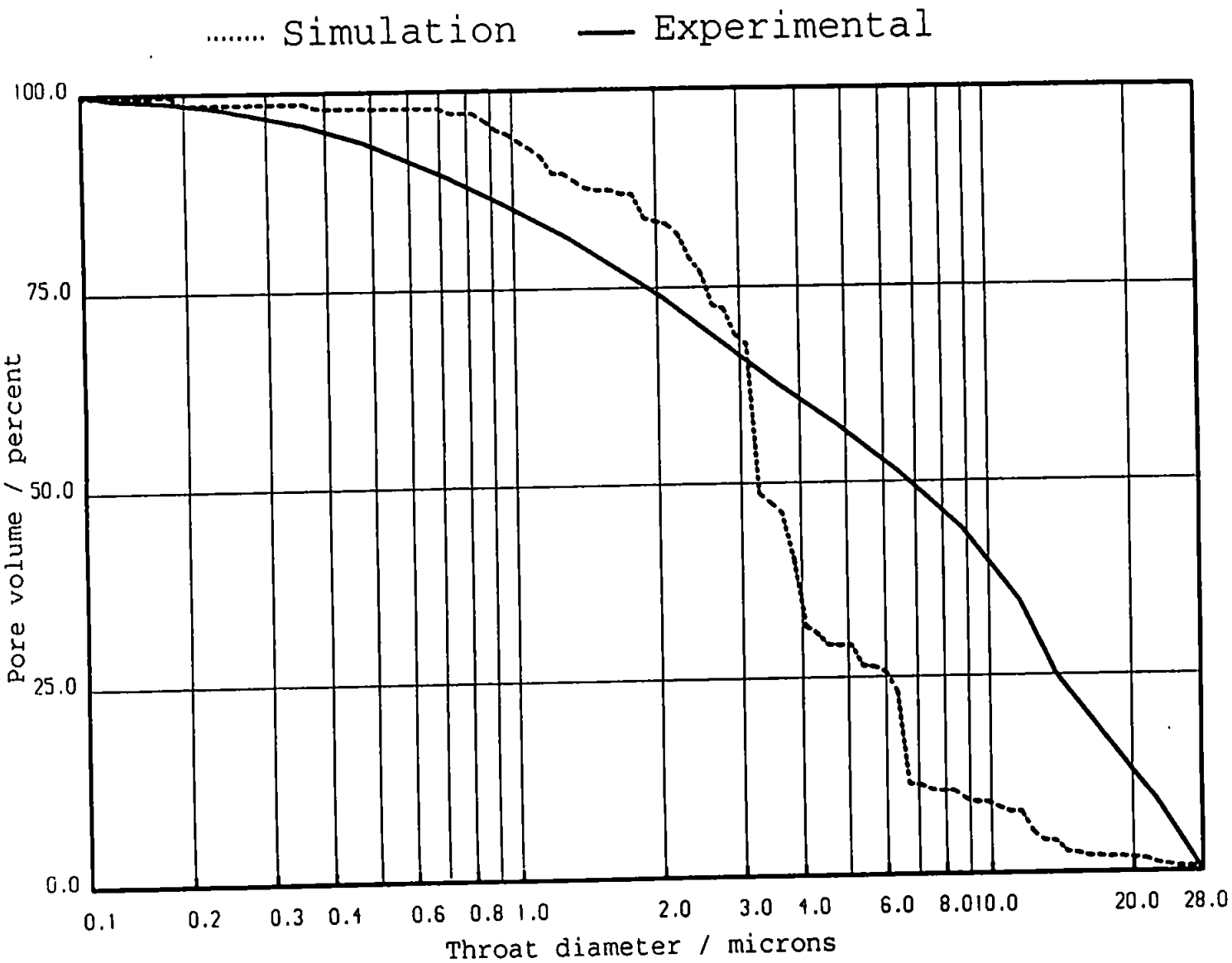

FIGURE 9.18: Truncated Experimental and Simulated Mercury Intrusion Curves for Sample 490C

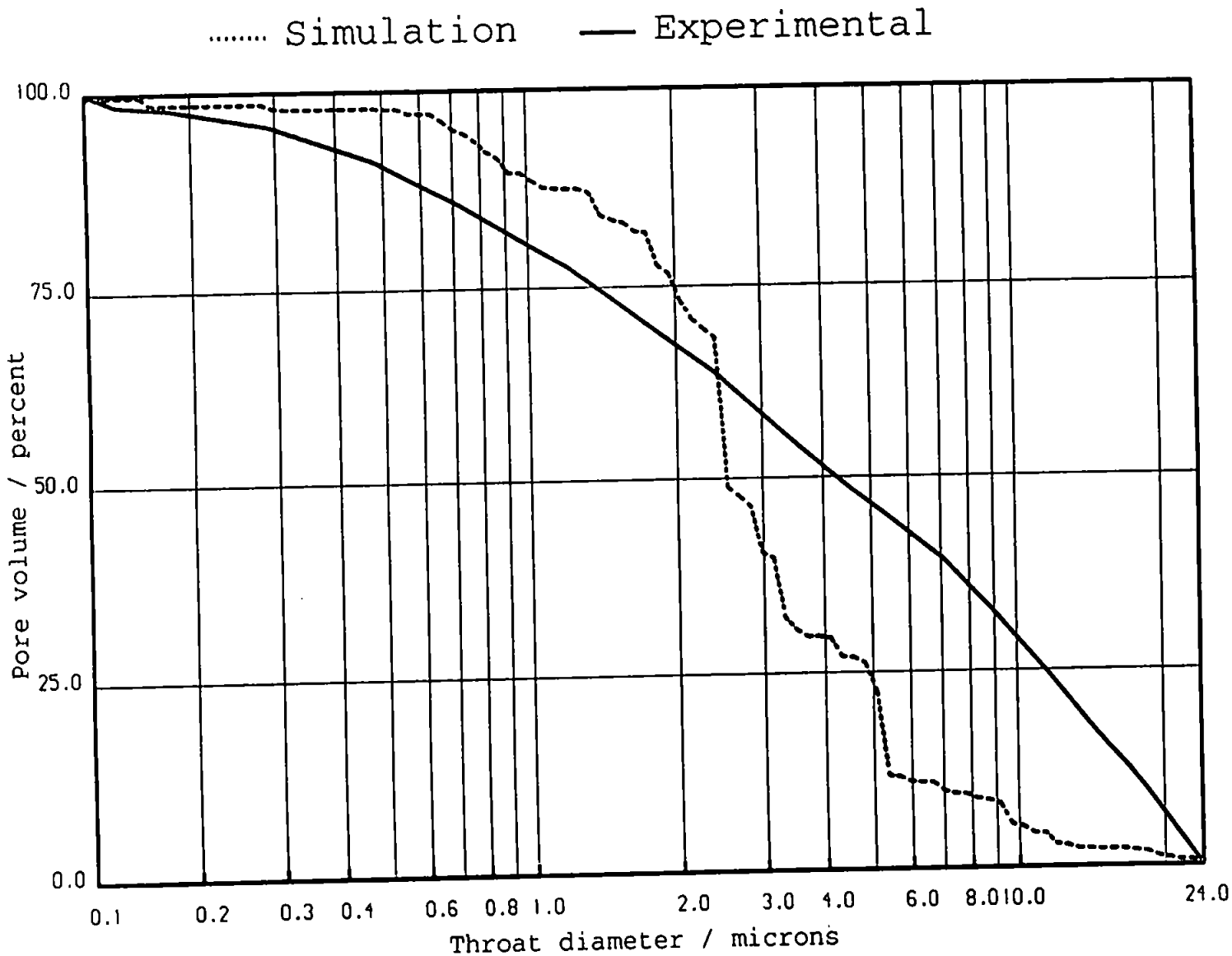

FIGURE 9.19: Truncated Experimental and Simulated Mercury Intrusion Curves for Sample 490D

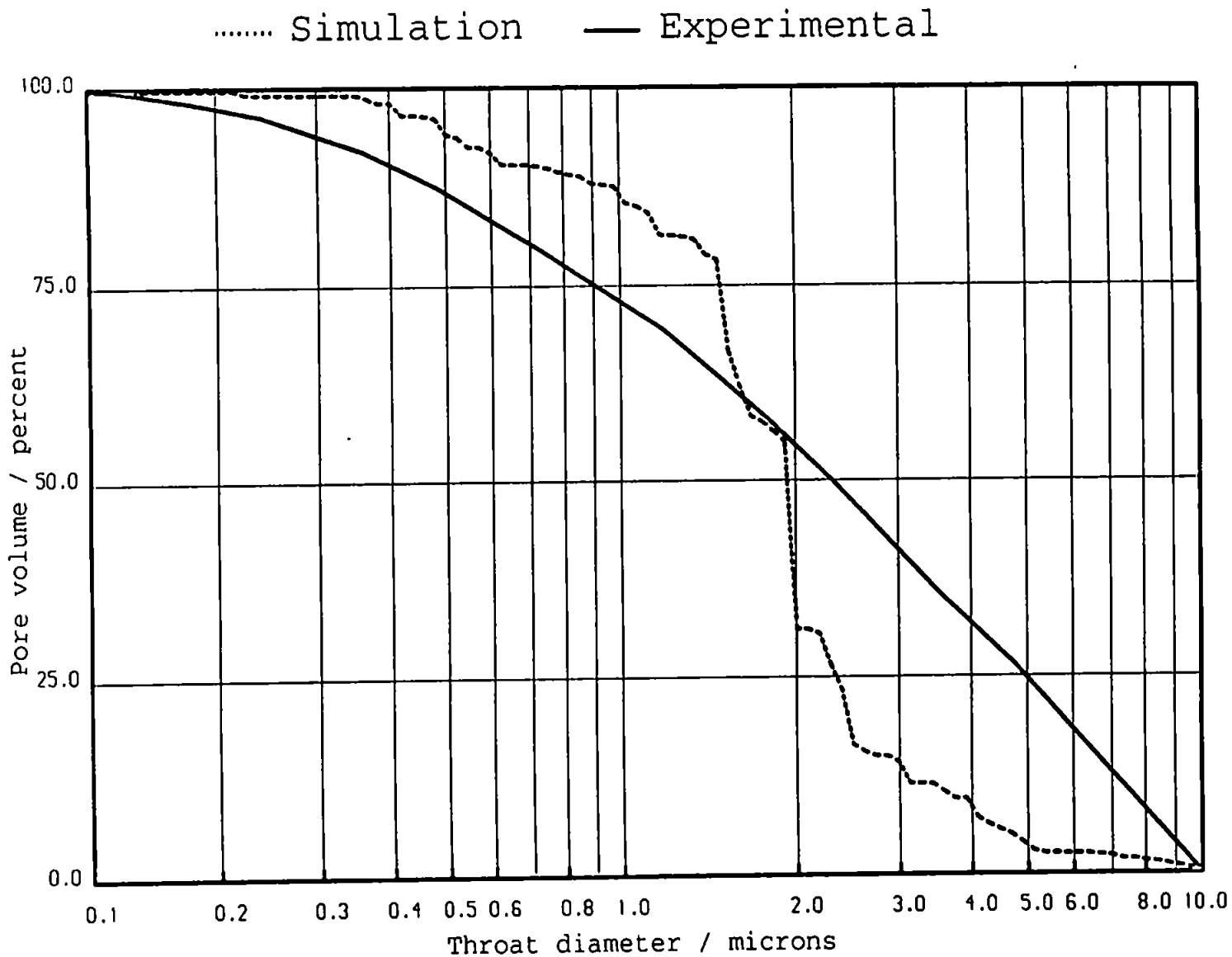

FIGURE 9.20: Truncated Experimental and Simulated Mercury Intrusion Curves for Sample 490D Repeat Run

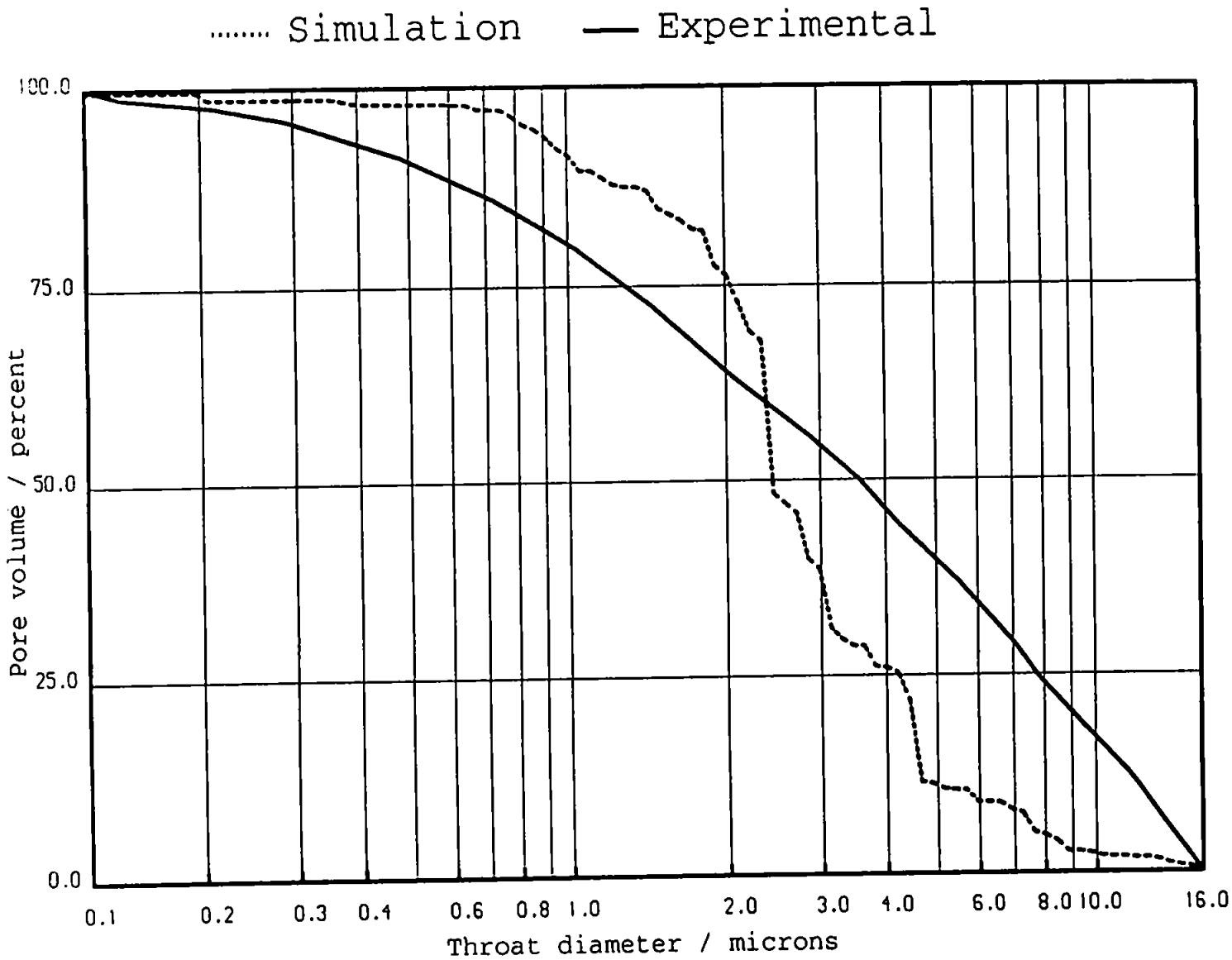

FIGURE 9.21: Truncated Experimental and Simulated Mercury Intrusion Curves for Sample 490E

simulated. All random simulations had connectivities from 2.7 to 2.8. These low connectivities produced the shallowest simulated curves attainable. Porosities of the simulations matched the experimental values in most cases.

The permeability of the correlated unit cells is very close to the measured data. The simulation of the Sample 250E produced a permeability only 30% smaller than the experimental value. Most other correlated networks have permeabilities a factor of three or four below the measured value. The exception is Sample 250A which although banded has a shallow intrusion curve the subsequent low connectivity within the model causes the low simulated permeability. Low connectivity in all random simulations leads to the very low permeabilities obtained for these samples. The tortuosity simulation follows the same trend as the permeability simulation. Correlated unit cells have lower median tortuosities than random simulations. Sample 250A is the exception again because no path was found through the unit cell, an unusual result due to this network having a permeability higher than some of the random unit cells that allowed tortuosity simulation. The median tortuosity is higher than the measured values (see Table 4.1) in all simulations. The values within the first quartile of the simulated tortuosity range coincide closer with the experimental values than the median of the range. Simulated diffusion coefficients for methane, iso-butane and n-butane using Equation 7.7. have been calculated. Table 9.3 shows the simulated diffusion coefficients calculated using the median tortuosity for each sample.

SAMPLE NO.	$D_{METHANE}/cm_2S^{-1}$ $X10^{-3}$	$D_{ISO\text{-}BUTANE}/cm_2S^{-1}$ $X10^{-3}$	$D_{n\text{-}BUTANE}/cm_2S^{-1}$ $X10^{-3}$
212A	2.745	1.209	1.197
212B	9.555	4.207	4.168
212C	12.250	5.394	5.344
212D	6.293	2.771	2.745
212E	9.281	4.087	4.049
250A	-----	-----	-----
250E	11.627	5.120	5.072
250E REPEAT	11.627	5.120	5.072
490A	4.091	1.802	1.785
490B	5.644	2.485	2.462
490C	5.866	2.583	2.559
490D	4.370	1.924	1.906
490D REPEAT	4.074	1.794	1.777
490E	4.293	1.890	1.873

TABLE 9.3: Diffusion Coefficients Calculated From Median Modelled Tortuosities.

Figures 9.22 to 9.24 summarize the simulated diffusion data comparing values calculated using the median, first quartile and third quartile tortuosities with experimental data. In most cases simulated diffusion coefficients are below the mean experimental values, but Figures 9.22 and 9.24 do show some overlap between simulation and experiment. Samples 490A to 490C are the exceptions to this trend, their simulated diffusion coefficient ranges for methane all higher than the experimental ranges. This would appear to conflict with the earlier statement that simulated tortuosities are too high. Any further reduction of these samples' simulated tortuosities would enhance the difference between simulated and experimental diffusion coefficients for methane. The conclusion must be that the experimental methane diffusion coefficients measured for 490A to 490C must be too low.

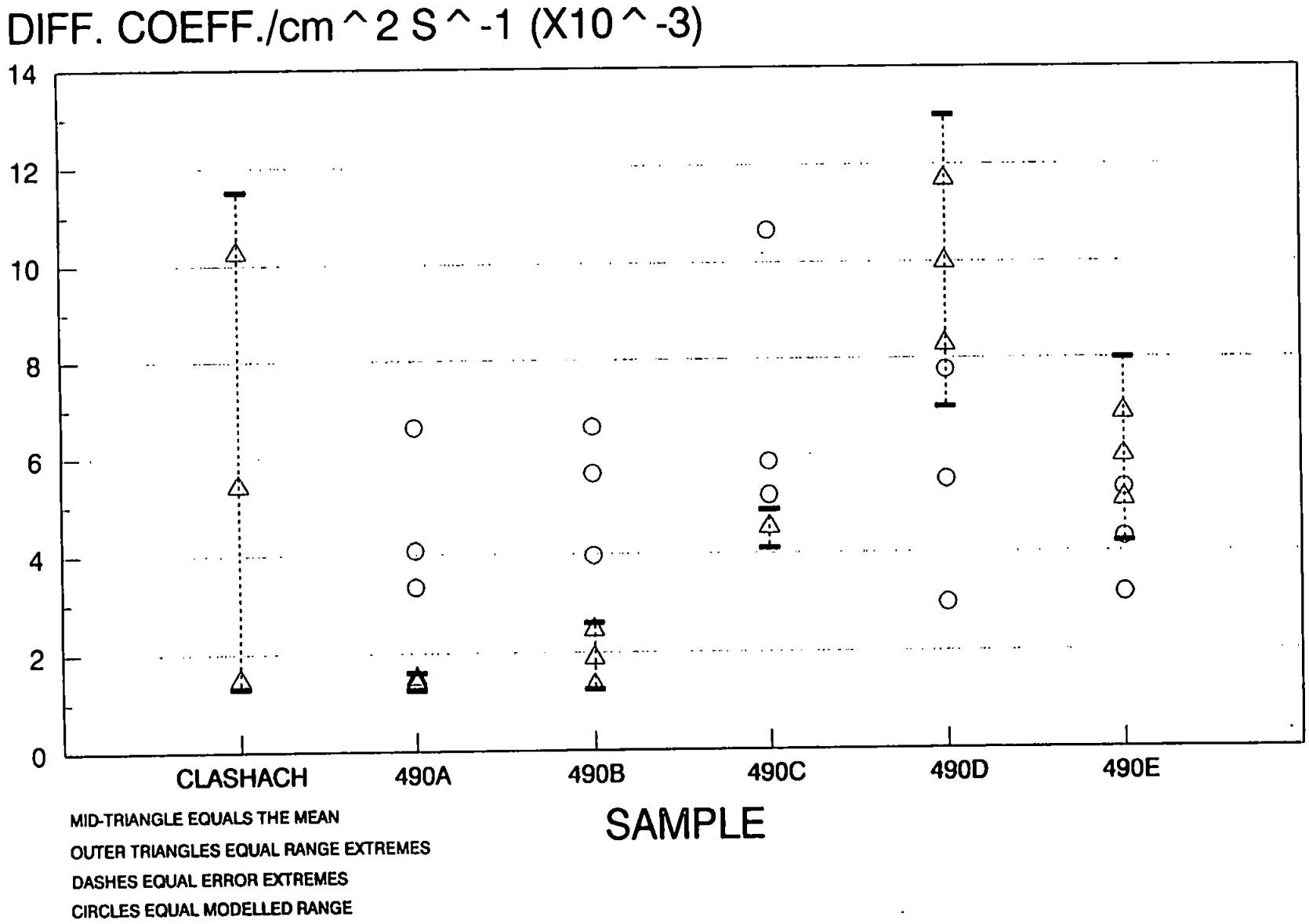

FIGURE 9.22: Simulated and Measured Methane Diffusion Coefficient Ranges.

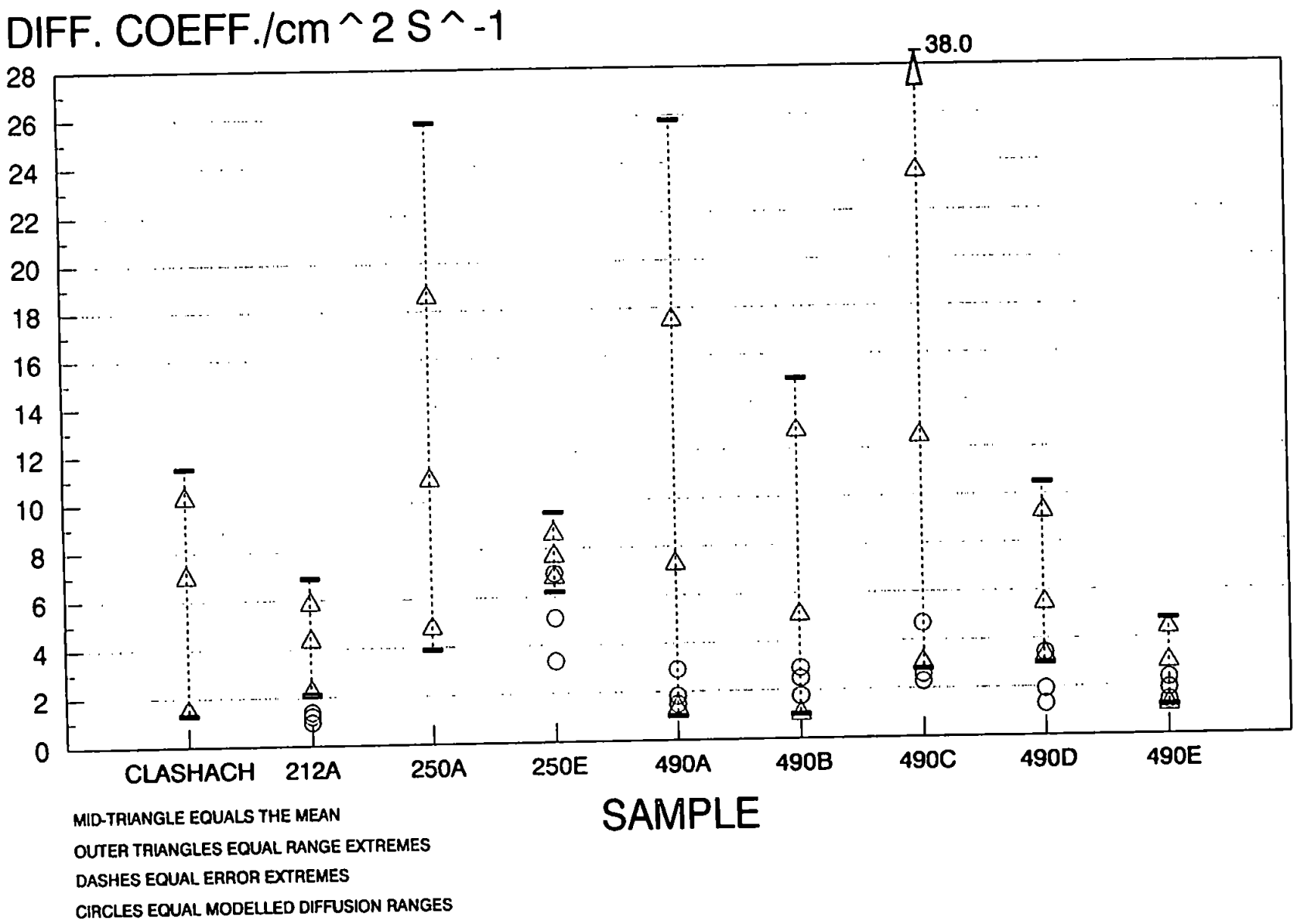

FIGURE 9.23: Simulated and Measured Iso-butane Diffusion Coefficient Ranges.

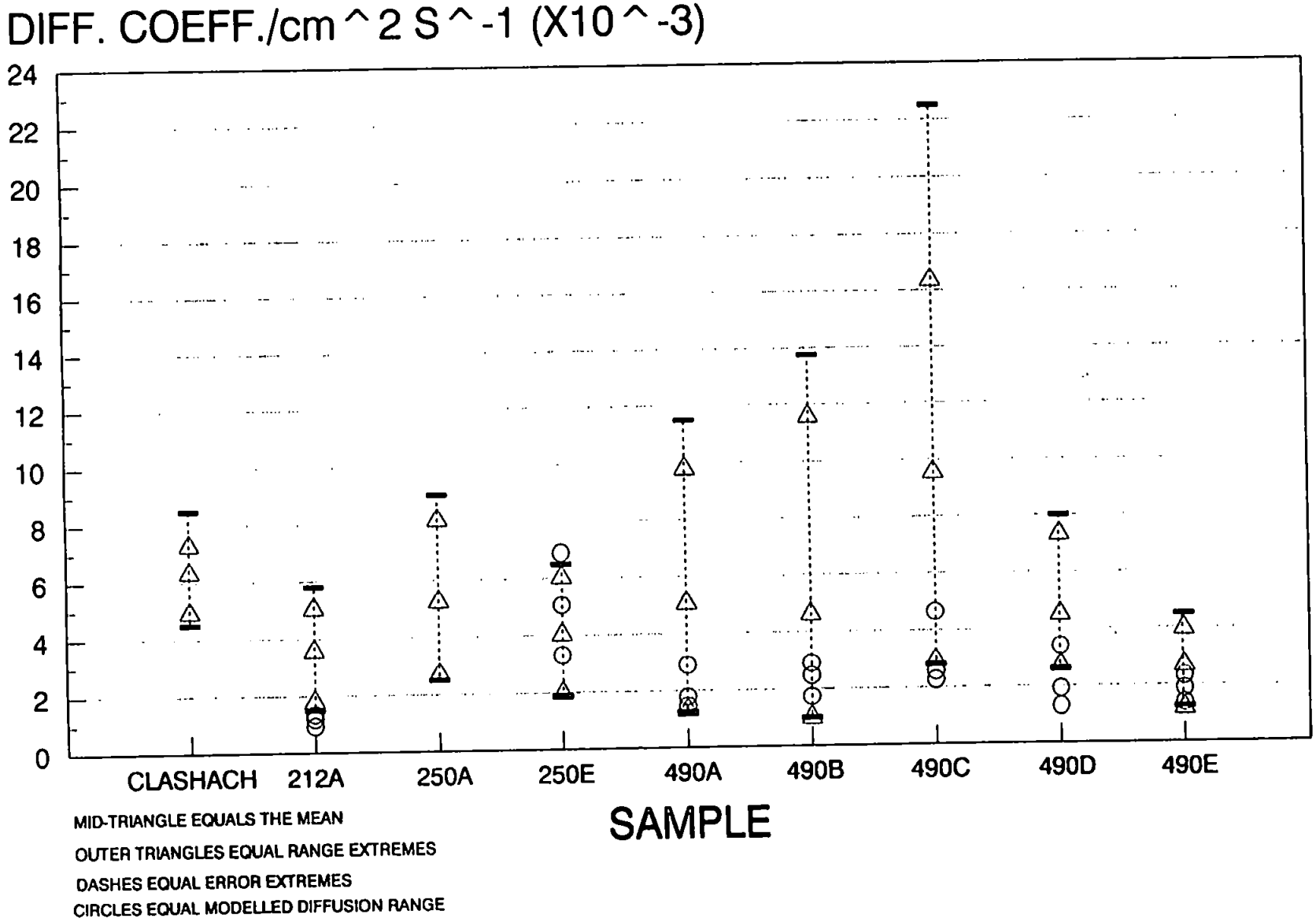

FIGURE 9.24: Simulated and Measured n-butane Diffusion Coefficient Ranges.

The mercury extrusion algorithm has been applied to the networks derived from the truncated curve fit procedure. The mercury extrusion curves for all the samples simulation are shown in Appendix 7. Experimental extrusion curves are truncated at the same diameter as the intrusion curves. The percentage of mercury trapped with the unit cell at the lowest simulated capillary pressure is significantly lower than that observed in the experiments. Unit cells with correlation have lower mercury residuals than random structures as mentioned earlier. Note that the simulated mercury intrusion curves always indicate less extrusion at small diameter than experiment curves. At large diameters, usually greater then 10μm, the simulated extrusion exceeds the experimental value.

9.3.2 Summary

i) The simulation of truncated mercury intrusion curves for samples with pore size correlation is successful. Random samples are less successful.

ii) Simulated porosity and permeability of correlated unit cells matched measured values closely. Porosity of random networks match the experimental values but the permeabilities of these simulations are much lower than experiment.

iii) The median tortuosity for each simulation is higher than the measured values. The first quartile of the tortuosity ranges show some correlation with experimental values. Diffusion coefficients calculated from simulation tortuosity also coincide with the measured ranges.

iv) Simulation of mercury extrusion follows an exaggerated path of very little extrusion followed by a sudden expulsion.

CHAPTER 10

MEASUREMENT AND SIMULATION OF COLLOIDAL FLOW FORMATION DAMAGE IN SANDSTONE

10.1 Introduction

In this chapter we discuss the flow of a colloidal suspension through sandstone void space. During such flow, colloid particles are forced out of suspension, adhere to the surface of the sandstone, and change its structure. The particular system we study is that of a flowing colloidal calcium carbonate suspension, similar to drilling mud infiltration - a common problem within hydrocarbon extraction. In this case the structure change is referred to as *formation damage*. However, the general approach we take is equally applicable to other porous solids and colloidal suspensions, and many of the observations and conclusions from the present study have wider implications.

Our experimental investigation has involved the study of the effects of flowing a colloidal calcium carbonate suspension, of known particle size distribution, through samples of Clashach outcrop sandstone and reservoir sandstone. Electron micrographs were used to confirm the distribution of precipitated colloidal particles within the samples. Porosity, mercury intrusion and extrusion permeability, tortuosity, gaseous diffusion coefficients were measured before and after colloid flooding.

The blocking of pores and throats by colloidal particles can be modelled, as can the consequent effect on the listed properties. The model has successfully simulated samples of outcrop sandstone and their subsequent induced formation damage. A simulation of the structure and alteration of a set of reservoir sandstones has also been performed, which is less precise but which gives a novel and powerful framework in which to discuss formation damage.

10.2. Formation Damage in Sandstone

Formation damage within oil and gas reservoirs has been a topic of research for over 40 years, and many papers have been published on the subject. The history of formation damage study has been outlined in a paper by K. E. Porter (1989). The reason for such intense interest is because of the great financial gains from increasing reservoir productivity. At present only 20-30% of reservoir oil is recovered at a cost of 80-90% of the reservoir energy (Porter 1989). The obvious way to increase productivity is to minimise damage, and thus a comprehensive understanding of the modes of formation damage is needed.

Formation damage due to particulate migration (the subject of this study) can be divided into two groups; migration of natural in-situ fines, and the introduction of foreign particles from drilling muds or other areas of the reservoir. In-situ fines can consist of varying quantities of clays, feldspars, small quartz crystals etc.

Most workers have concentrated on the role of clays in formation damage. Clays can be a problem component of reservoir sandstones because of the large aspect ratios and charged surfaces of the particles. Most clays have a net negative charge due to isomorphous substitution in the clay lattice (Lever and Dawe 1984). In aqueous conditions ions form a double layer around the clay particles. This double layer consists of the Stern layer of counter ions adsorbed to the clay surface. The second part of the double layer is called the Gouy-Chapman layer, an outer layer of diffuse ions. The degree of compression of the diffuse layer is dependent on the concentration and valence of the ions in solution. In a concentrated brine the diffuse layer is compressed. When a clay particle approaches a pore wall or another particle the diffuse layers interact and repulsion occurs. This repulsion is not the only force operating. Van der Waals attractions between single atom pairs are small and not very far reaching, but they are additive between atom pairs. The total van der Waals attractions between particles or particles and pore walls is large enough and far reaching enough to compete with the repulsion between the diffuse layers. Thus

in concentrated brines the diffuse layers are compressed and flocculation or particles adhering to the pore walls can occur (Van Olphen 1963).

These theoretical explanations have been supported by research into water-sensitivity of various sandstones. Khilar and Fogler (1981) found that clays were released from pore walls or 'conglomerate bundles' when the brine dropped below a critical salt concentration. Below this critical salt concentration clays moved within the pore space, blocking pore restrictions and causing a drastic permeability drop. Lever and Dawe (1984) found similar results with different brine compositions and concentrations. For Hopeman/Clashach sandstone, they found that no damage resulted for concentrations of 3% and above. However, a large permeability drop due to clay migration was noted when the concentration of KCl and NaCl brines was reduced to zero (fresh water). Calcium chloride brines showed no drop in permeability until a very low concentration was reached, but no further drop was experienced even at fresh water concentrations. This anomaly can be explained by the Schulze-Hardy Rule. The flocculation power of mono-, di- and trivalent ions is found to be in the ratio 1:50:700 respectively. Thus the di-valent calcium ions are much stronger flocculating agents than the mono-valent sodium and potassium ions. There may have been enough calcium ions left in solution to bind some of the clays to each other or the pore walls even at supposed fresh water concentrations.

If the composition of the brine within the pore space closely matches that of the formation brine, ie. the natural brine that has reached equilibrium with the sandstone, then the clays and other fines should be stable. However it has been noted that even flowing a formation brine through a sandstone can disturb the in-situ fines. Vinchon et al (1993) found that at low flow rates large kaolinite stacks were washed away, and ribbon-shaped illites migrated until they aggregated together. At higher flow rates some fines were removed from the cores studied thus increasing porosity, while other fines blocked the smallest pores decreasing permeability.

The other mode of particulate formation damage is by the invasion of foreign

particles. In the work by Vinchon et al they found that fines were removed from the studied core; obviously for an in-place sandstone these fines would migrate to another part of the formation causing damage.

In a study by Ochi and co-workers (1993), a sample of Vosgien sandstone experienced a 65% reduction in permeability, when a formation brine and calibrated particles were flowed through it. At the same flow rate the formation brine alone caused only a 50% permeability reduction. At higher concentrations of calibrated particles a 98% reduction in permeability occurred, corresponding to the formation of an internal filter cake at the cores input face. Rahman and Marx (1991) stated that the formation of a filter cake can be favourable as it filters fluids and stops damage deeper in the formation. Pore bridging by particles is found to be a good base for filter cake formation. Particles must be slightly smaller than the biggest pores down to about a third of that size. A bentonite and polymer suspension produced a very low permeability filter cake at low penetration depths. On the other hand a suspension of calcium carbonate (the particles used in this study) and polymer formed a more open filter cake, facilitated the invasion of fines to a greater depth, and thus caused more formation damage.

In direct observations of particle movement within a glass micromodel by Muecke (1979), particles were found to trap at pore bridges. A pore bridge forms when a large particle spans a pore. These pore bridges could be broken if the flow was reversed, whereupon permeability is temporarily restored until pore bridges form in the other direction. Similar conclusions have been reached by Khilar and Fogler, and Lever and Dawe, in sandstones. Ochi et al found that permeability could be temporarily restored by simply increasing brine flow rates to break up fines agglomerates at pore restrictions.

10.3 Modelling Colloidal Flow

In this work we are concerned not only with the measurement of colloidal flow, but

also with mathematical modelling of the effects. The model of colloidal flow which we use is simple, in that its only assumption is of physical blocking of pores and throats by particles which are bigger than the constriction, an effect which we term *simple pore blocking*. The experiments which we have carried out were deliberately designed to ensure that this was the dominant effect. Although the colloidal block modelling is straightforward in itself, it takes place within the three dimensional model of the sandstone void space which can also simulate the wide range of properties discussed earlier.

Other workers have developed models of colloidal flow effects which are more intricate in themselves, but based on simpler networks. Hampton et al (1993) employed a 2-dimensional network of size 40 by up to 200. They used a fixed coordination number of 4, reduced by random blocking of throats necessary to maintain a constant porosity. The constrictions were tubes only, i.e. there was no difference between pores and throats, and the tubes were given a log-normal size distribution. Permeability was calculated by a Hardy-Cross successive approximations method, and the particle deposition equations included a diffusion term. Rege and Fogler (1991) studied the effects of colloidal deposition in a radial situation, such as that found around a bore hole. Their two-dimensional radial model covered a 120° segment, and used a 20x30 radial matrix which was compared with a 20x30 linear matrix. Monodisperse and polydisperse colloid systems were studied. They found that particles have a greater blocking effect at the centre of the annulus than at the edge, but are less likely to deposit at the centre because of the higher flow velocities. Ohen and Civan (1990) have presented a phenomenological model, in which one dimensional horizontal flow is assumed through a porous medium containing pore bodies which are interconnected by pore throats whose sizes are log-normally distributed. The mechanisms for permeability alteration are pore blocking, particle deposition and bridging, and the swelling of clayey formations within the pores and throats.

10.4. Outcrop Sandstones

10.4.1 Clean and Damaged Samples

Our initial study into induced formation damage was performed on two samples of Clashach sandstone. The work was undertaken with the assistance of Gareth Powell an undergraduate at the university. Porosity and permeability were measured at the British Gas (LRS), Table 10.1. Scanning Electron Microscopy showed both samples to be almost clay free. The diffusion coefficients of methane, iso-butane and n-butane were measured for Sample 2, Table 10.1. This is the same Clashach sample discussed in Chapter 7. Tortuosity and the formation factor has been calculated from the mean diffusion coefficients.

The colloid suspension used to induce formation damage within the sample consisted of calcium carbonate particles suspended in a formation brine. The calcium carbonate was supplied by English China Clays International, St. Austell (ECCI). In its dried form it consisted of 97.1% by weight calcium carbonate and 1.9% by weight magnesium carbonate. The particle size distribution is given in Figure 10.1. The majority of the particles are of 5μm and below. These particles were chosen to be small enough to penetrate deep into the pore space of the samples.

The particles were suspended in a formation brine. The brine was the standard brine used for formation factor measurements in Chapter 4. However, the brine caused the calcium carbonate to flocculate so it was diluted tenfold and a dispersion polymer (dispex) was added. Even at this reduced brine concentration (3% NaCl) the brine was still of the strength which formation damage due to in situ fines migration is minimal, as discussed previously, (Lever and Dawe 1984).

The colloid suspension was introduced into the pore space of the dry samples by vacuum flooding. The sample was placed in a desiccator which was evacuated for two hours. The vacuum was broken by introduction of the colloid suspension. A mesh was

Sample No.	Condition	Porosity /%	Permeability /mD	Methane Diffusion Coeff.range/ cm^2s^{-1} $x10^{-3}$	Butane Diffusion Coeff.range/ cm^2s^{-1} $x10^{-3}$	Iso-butane Diffusion Coeff.range/ cm^2s^{-1} $x10^{-3}$	Tortuosity	Formation Factor
Sample 1	Clean	12.8	314.66	—	—	—	—	—
Sample 2	Clean	11.1	276.57	1.46-10.25 (5.415)	4.93-7.29 (6.325)	4.33-9.66 (6.978)	1.63	24.02
Sample 1	After colloid flood	11.8	197.43	—	—	—	—	—
Sample 2	After colloid flood	10.2 (Calc. value)	—	12.41-19.31 (16.57)	11.16-20.2 (14.18)	8.84-17.25 (11.63)	1.07	11.12

TABLE 10.1: PARAMETERS MEASURED FOR CLASHACH OUTCROP SANDSTONE
Extreme results excluded from ranges with 90% confidence. Bracketed diffusion coefficients are the mean of values included in the range.

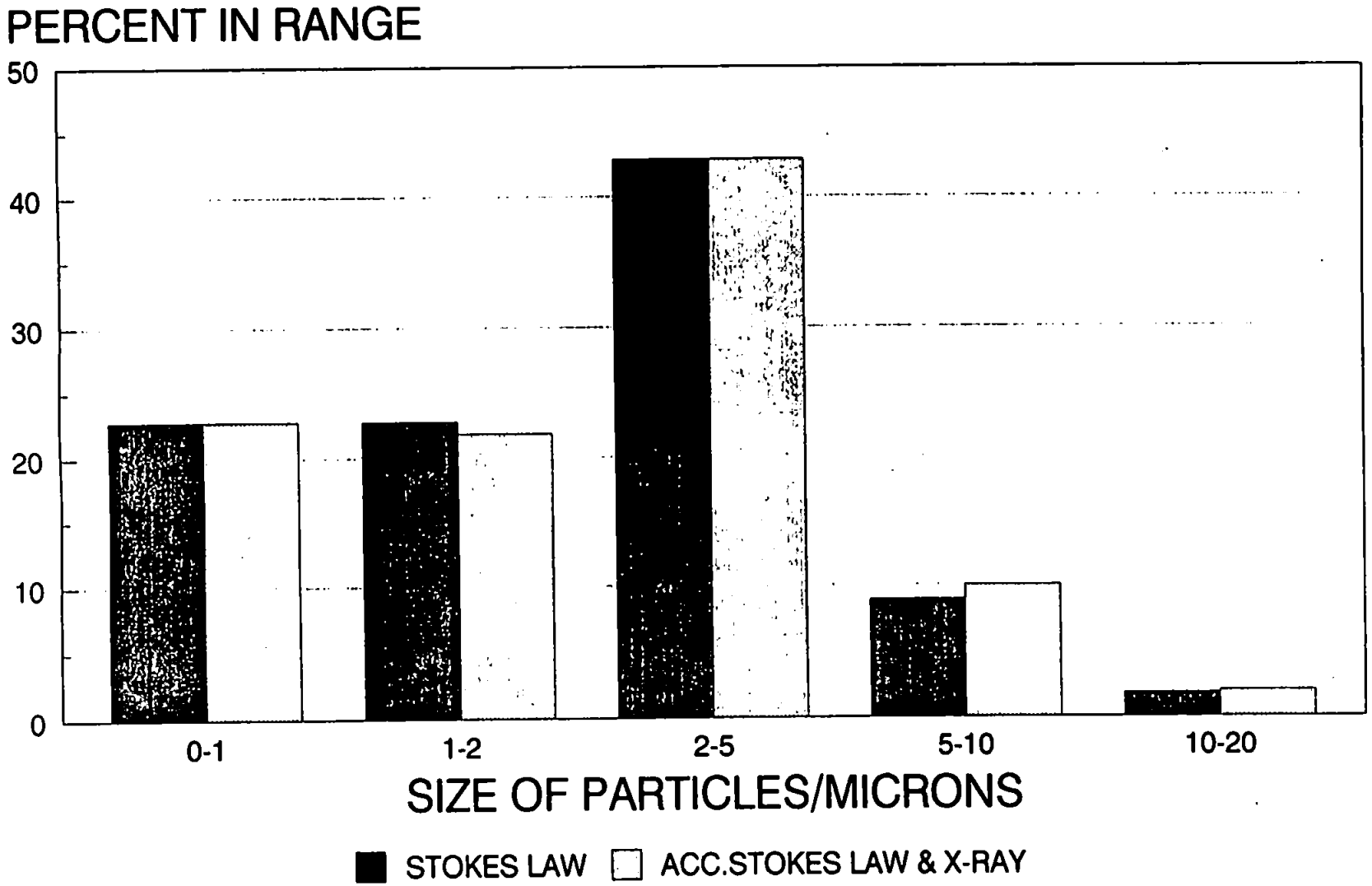

FIGURE 10.1: Size Distribution of Particles in the Colloidal Chalk Suspension Measured on a Micromeritics Sedigragh 2000.

placed over the sample to stop preferential dripping of the colloid in any one area of the sample. Confirmation of colloid penetration into the pore space was obtained by scanning electron microscopy. These observations are illustrated by Plate 10.1, which shows a random packed filter cake structure around an exposed pore at a depth of approximately 5mm from one of the sample faces. Most particles observed were less than 5μm in diameter, also supporting the assumption that these particles are the introduced colloidal particles, not the in-situ fines.

After colloid flooding the porosity of sample 1 was reduced from 12.8% to 11.8%, a relative decrease of 8%. The permeability dropped from 314.66 mD to 197.43 mD, a relative reduction of 37%. The porosity and permeability of sample 2 could not be measured after colloid flooding, because it was mounted in resin for diffusion coefficient measurement. Nevertheless, a porosity value is required for subsequent calculations, and it was therefore assumed that the porosity of sample 2 also experienced a relative drop of 8%, from 11.1% to 10.2%. Both the tortuosity and formation factor drop after colloidal flooding, corresponding to the rise in averaged diffusion coefficient.

10.5 Reservoir Sandstones

10.5.1 Clean and damaged samples

Five sandstone samples from a gas reservoir were supplied by British Gas, numbered 81, 82, 98, 107 and 108. The sandstones were tested by Toby Mathews as part of an undergraduate research project. Scanning electron microscope observations indicated similar mineralogy as the other reservoir samples, although these are all homogeneous ie. non-banded. A wide range of porosities, 9.5-16.2% and permeabilities, 29.17-431.47 mD were measured at the British Gas London Research Station, Table 10.2.

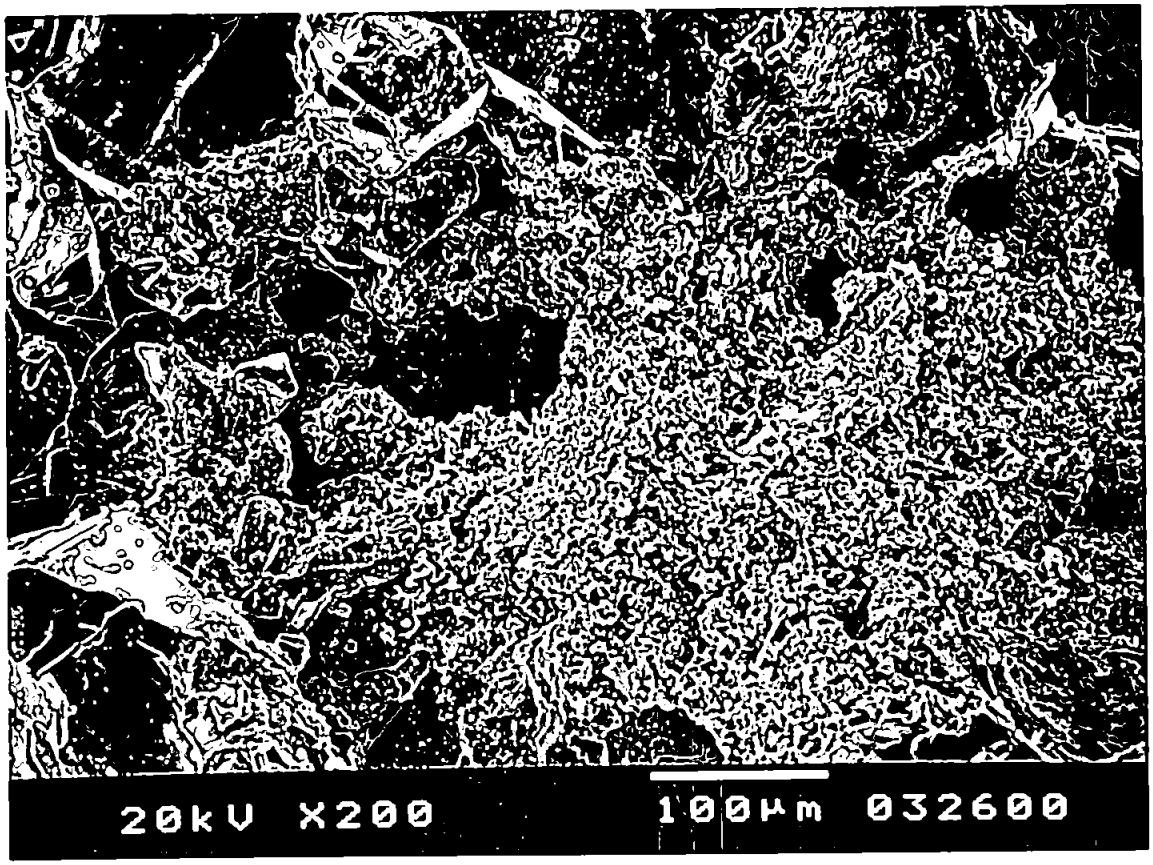

PLATE 10.1: Calcium Carbonate Particles Deposited With Clashach Pore Space.

INITIAL STATE						COLLOID FLOODED STATE				
Sample	Perm. /mD	Porosity /%	Mean Tortuos-ity	Range	Format-ion Factor	Perm. /mD	Porosity /%	Mean Tortuos-ity	Range	Format-ion factor
81	431.47	14.0	2.00	1.75-2.22	28.54	216.33	13.4	1.99	1.94-2.03	29.43
82	34.47	11.1	2.24	1.97-2.46	45.37	26.69	11.7	2.25	2.16-2.34	43.23
98	213.62	16.2	1.79	1.69-1.88	19.78	57.61	15.4	1.96	1.86-2.04	24.89
107	218.14	12.1	2.47	2.30-6.63	50.01	119.74	11.4	2.15	1.98-2.31	40.36
108	29.17	9.5	2.63	2.44-2.84	73.36	17.81	9.7	2.69	2.57-2.81	74.49

TABLE 10.2: Results of formation damage of reservoir sandstones. Tortuosity range is given by the 95% confidence interval around the mean.

10.5.2 Formation Factor/Tortuosity Measurements

The lefthand side of Table 10.2 shows formation factor and tortuosity results calculated from resistivity measurements for the five samples measured in their native state. The tortuosities of the samples are all higher than that of Clashach, Table 10.1, suggesting that the reservoir sandstones have a more complex pore network.

After completing the measurement on the reservoir sandstones in their native state, they were flooded with the colloidal suspension. To facilitate deep penetration of colloid into pore space, flooding was performed on brine saturated cores.

10.5.3. Mercury Porosimetry

Mercury intrusion and extrusion analysis was performed on the five dried reservoir sandstones before and after colloid flooding, using a Micromeritics Poresizer 9320 based at ECCI St.Austell. A section was removed from the clean core and analyzed, and after colloid flooding a similar size section was also cut and analyzed. Mercury extrusion on the micromeritics porosimeter is limited to a lowest pressure of 9 PSIA or a maximum void diameter of 20 μm.

Figures 10.2 to 10.6 show mercury intrusion and extrusion curves for each sample, before and after colloid flooding. All intrusion curves have the characteristic sigmoidal shape. Some of the curves have a discontinuity at an equivalent penetrated throat diameter of 20μm. This is caused by pressure fluctuations when the sample holder (penetrometer) is transferred from the low to high pressure port of the Micromeritics porosimeter. All samples experienced a drop in pore volume accessible to mercury, as shown in Table 10.3 and on Figures 10.2 to 10.6. Sample 81 for example (Figure 10.2) underwent a 25% drop. This is confirmation that the pore network has been damaged, either by the colloid or by the natural fines from within the pore space of the sandstone. It can be seen from Tables 10.2 and 10.3 that the permeabilities of all the samples were reduced, as might be

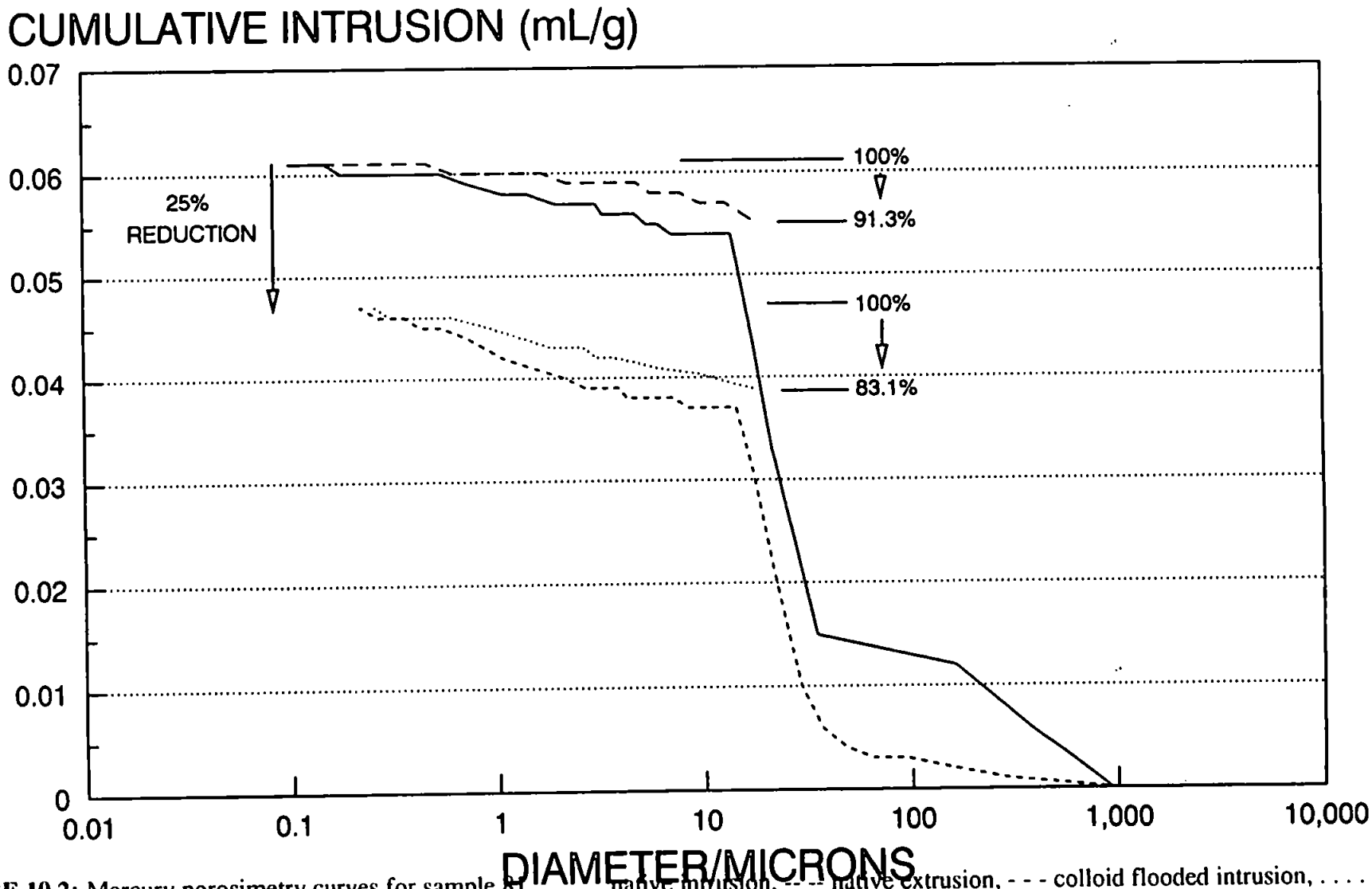

FIGURE 10.2: Mercury porosimetry curves for sample 81. ____ native intrusion, - - - native extrusion, - - - colloid flooded intrusion, ... colloid flooded extrusion.

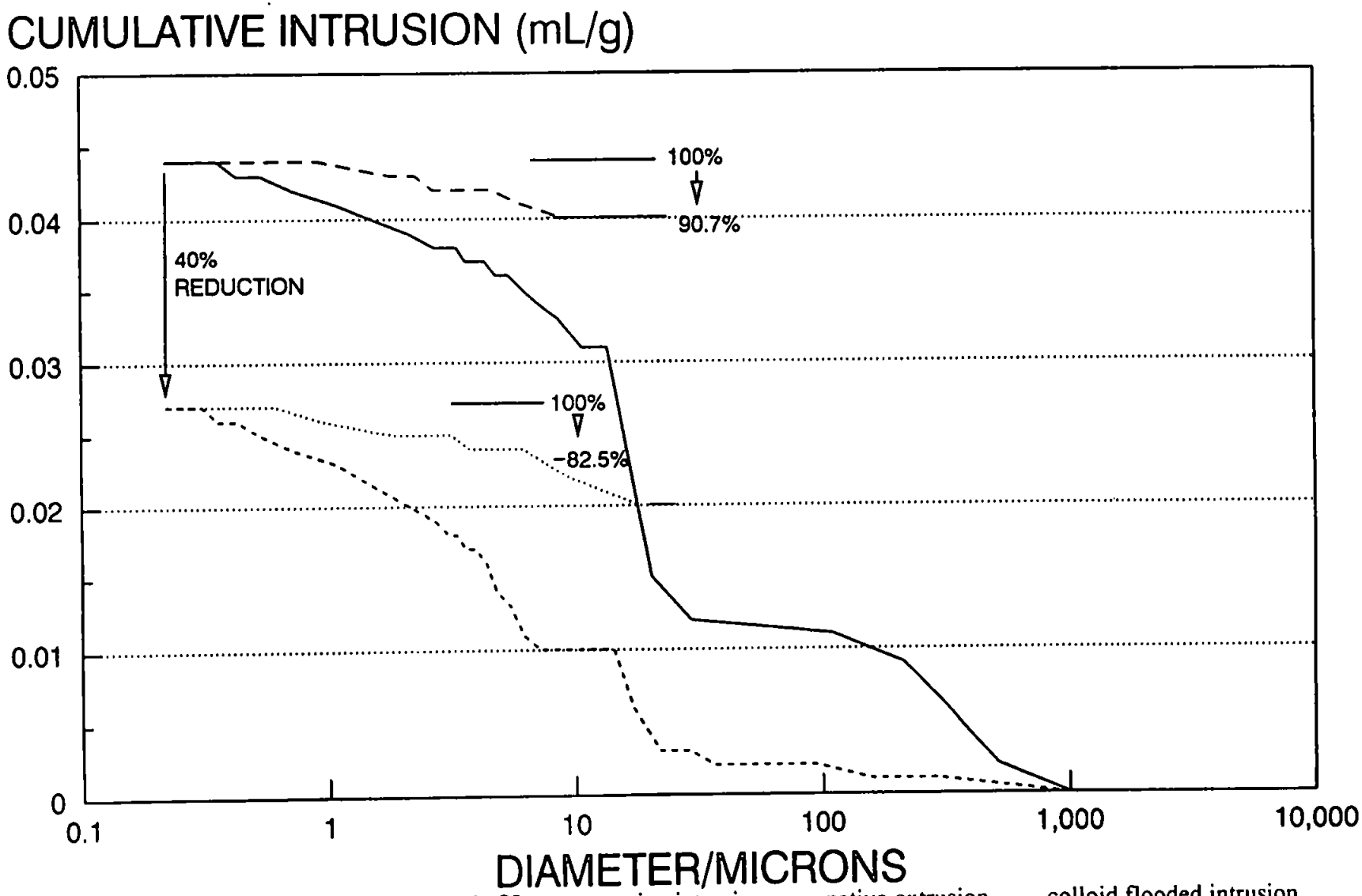

FIGURE 10.3: Mercury porosimetry curves for sample 82. _____ native intrusion, -- -- native extrusion, - - - colloid flooded intrusion, ... colloid flooded extrusion.

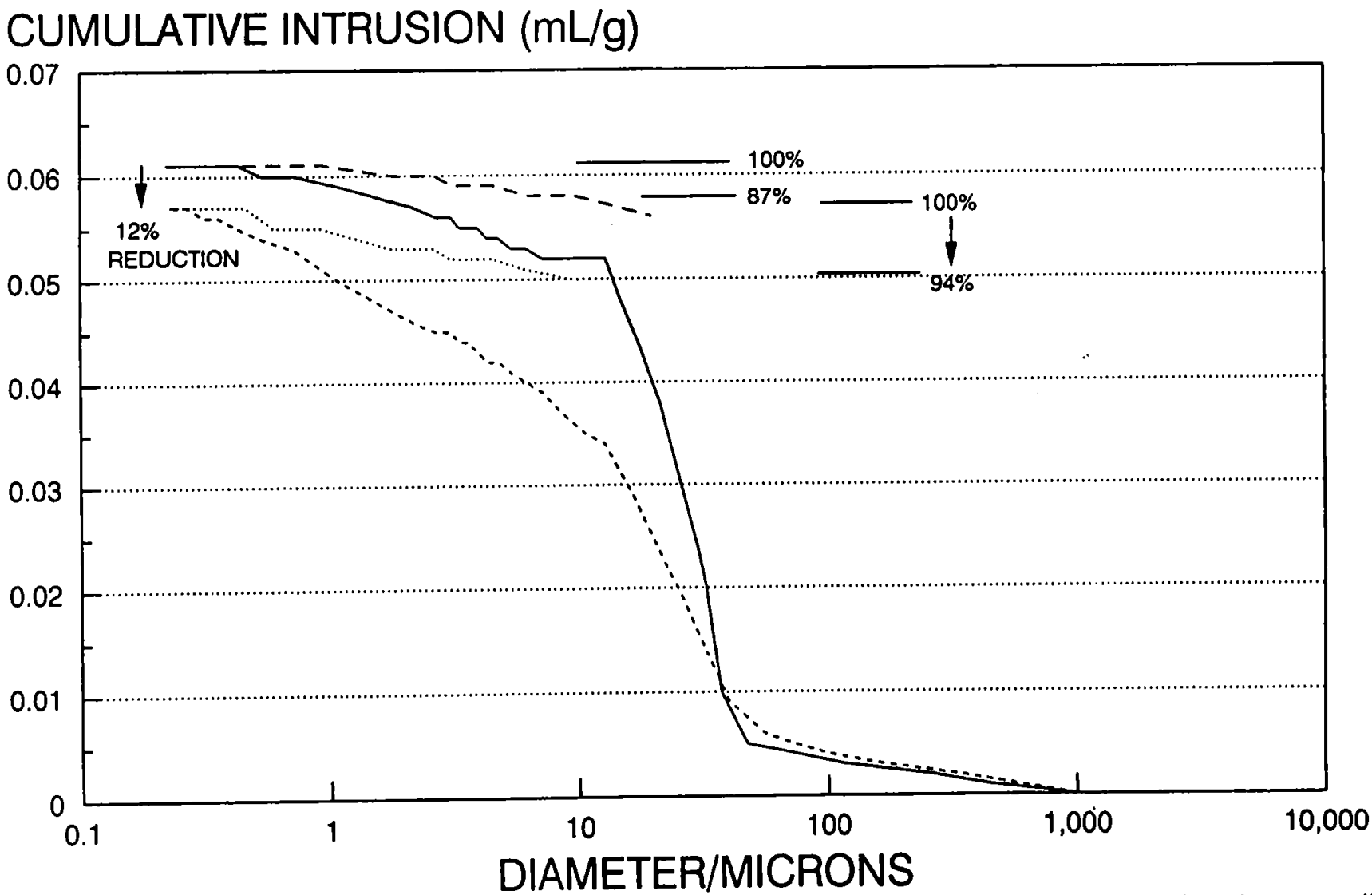

FIGURE 10.4: Mercury porosimetry curves for sample 98. _____ native intrusion, -- -- native extrusion, - - - colloid flooded intrusion, ... colloid flooded extrusion.

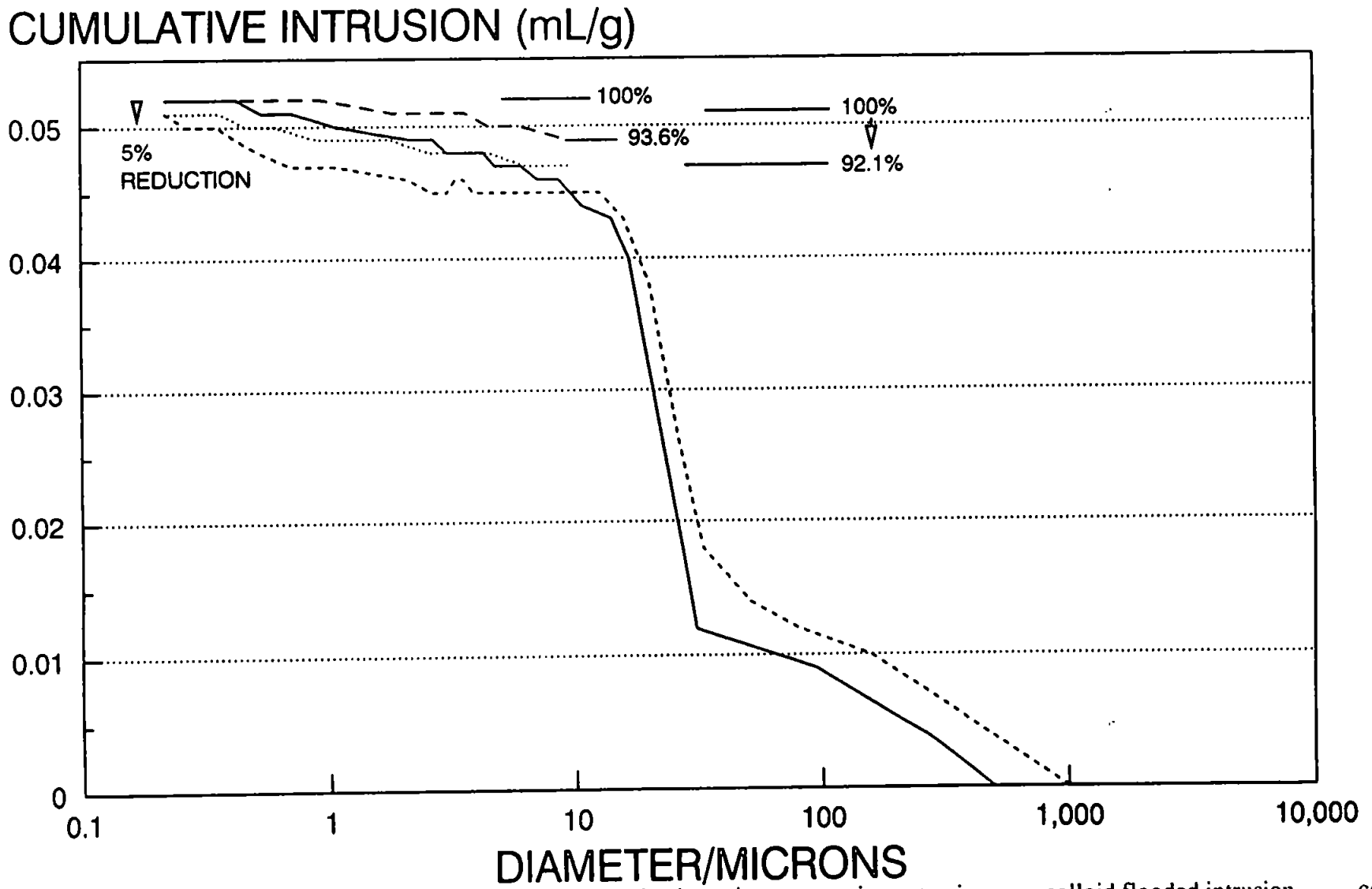

FIGURE 10.5: Mercury porosimetry curves for sample 107. _____ native intrusion, -- -- native extrusion, - - - colloid flooded intrusion, ... colloid flooded extrusion.

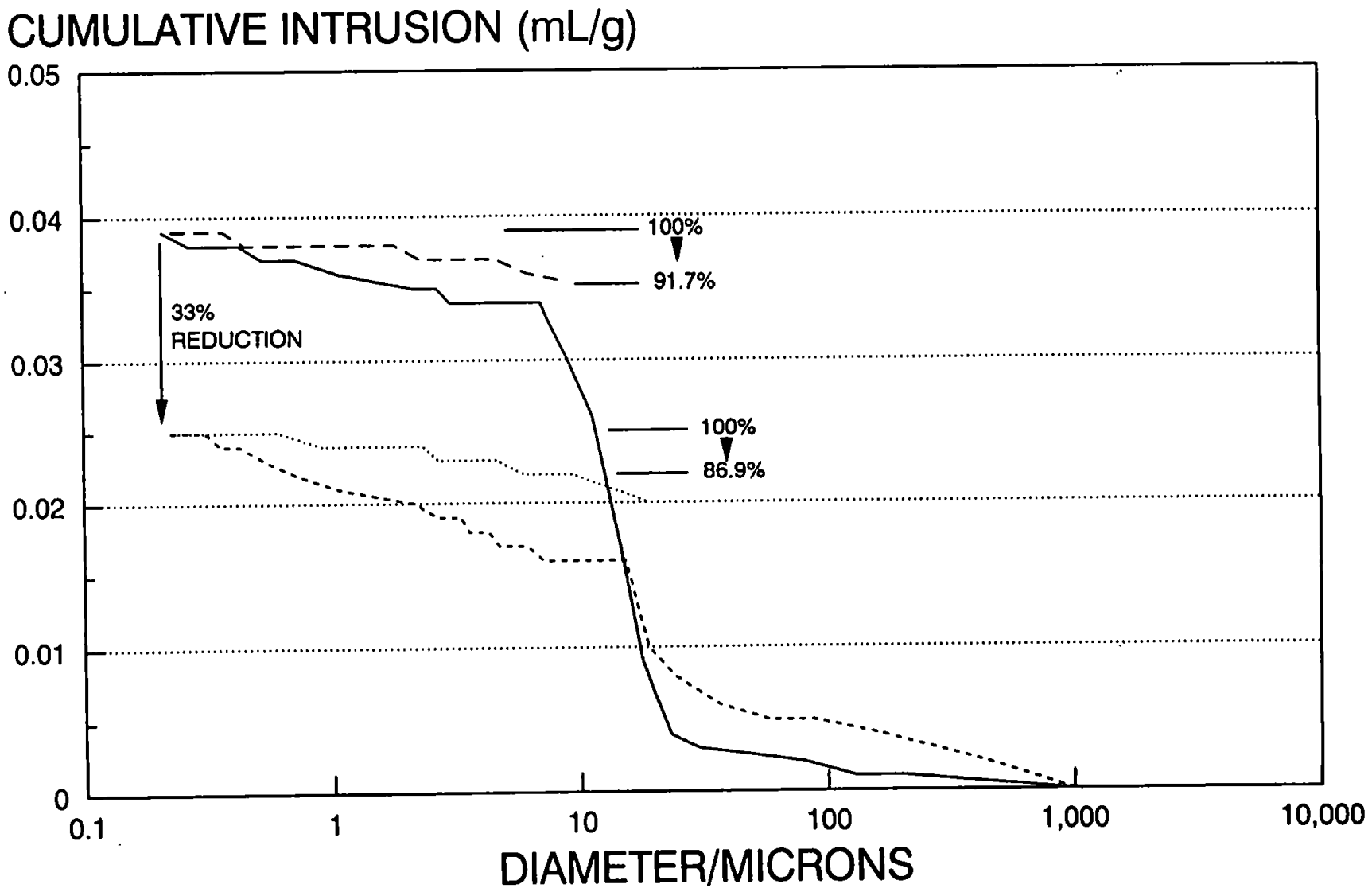

FIGURE 10.6: Mercury porosimetry curves for sample 108. _____ native intrusion, -- -- native extrusion, - - - colloid flooded intrusion, ... colloid flooded extrusion.

	Sample 81	Sample 82	Sample 98	Sample 107	Sample 108
Porosity: absolute damage / %	-0.6	+0.5	-0.8	-0.7	+0.2
Permeability: relative damage / %	-49.9	-22.6	-73.0	-45.1	-38.9
Relative decrease in pore volume accessible to mercury	Approx -25%	Approx -40%	Approx -12%	Approx -5%	Approx -33%
Point of inflection	23μm→21μm	17μm→5μm	26μm→17μm	24μm→26μm	14μm→13μm
Change in shape of intrusion curve	Loss large and some intermediate pores.	Loss of large and intermediate pores.	Wide spread blocking.	Similar curves.	Increase in big pores.
Change in relative amount of mercury trapped	91.31→83.05% at 18.1μm	90.70→82.5% at 9.3μm	87.0→94.2% at 9.4μm	93.6→92.1% at 9.2μm	91.7→86.9% at 9.2μm
Damage theory	Filter cake in large and same intermediate pores. Predominantly surface pores.	Blocking of large and intermediate pores.	Blocking over whole pore range.		Native fines move emptying large pores, but blocking intermediate

TABLE 10.3: Analysis of formation damage in reservoir sandstone samples

expected. Three of the samples exhibited an expected reduction in porosity, although two showed a marginal increase. It has been frequently stated that large permeability damage can be facilitated by a small amount of pore blocking material (Lever and Dawe, 1984), and therefore permeability is more sensitive to formation damage than porosity. The relative changes in porosity and permeability are shown in Table 10.3. Thus there is some broad similarity of the effects of colloid flooding on all the reservoir sandstone samples.

However, if the results for the samples are examined in more detail, various different colloidal flooding phenomena are revealed, as will now be discussed. The other changes to the samples induced by colloid flooding are also summarised in Table 10.3. There are two particular effects identifiable for sample 81. The first is the loss of large pores, as shown by the reduction in penetrated volume around 100 microns, Figure 10.2. A filter cake agglomeration could block large surface and near surface pore, and leave the remainder of the pore network unaffected. This process could be similar to that of filter cake formation proposed by Rahman and Marx (1991). The second effect is that the percentage of mercury contained within the pore space at a pressure corresponding to a throat diameter of 18.14μm during mercury drainage has reduced from 91.3% to 83.1%, as shown in Figure 10.2. This reduction indicates that the small pores empty of mercury slightly more efficiently after colloid flooding. This effect is probably related to the loss of large pores, but is difficult to interpret without the full hysteresis curve, which is inaccessible to the current apparatus.

Figure 10.3 shows that sample 82 has a much reduced mercury accessible pore volume after colloid flooding. The reduction is the highest of all the samples, at about 40%, as shown in Table 10.3. As with sample 81, the large pore region of the post colloidal flood intrusion curve (- - -) shows less intrusion for a particular pressure than the intrusion of the clean state (——), i.e the large pores are blocked. However, in sample 82, the blocking effect extends to those mid-range pores around the point of inflection. A

related feature in the intrusion curves is the less pronounced point of inflection of the colloid flooded sample (- - -) as compared to the clean sample (——). It is evident from the more gradual intrusion as pressure is increased that the number of routes available to the intruding mercury has been reduced - i.e. that there is a reduction in connectivity. This conclusion is supported by the computer modelling studies described later. As in sample 81, the percentage of trapped mercury during drainage drops after colloid flooding from 90.7% to 82.5% as shown in Figure 10.3 and Table 10.3.

In contrast to samples 81 and 82, in sample 98 there was negligible blocking of the large pores, Figure 10.4. Overall the sample experienced a slight drop in accessible pore volume after colloid flooding, showing that a small percentage of pores have been blocked. However, there is also a significant change in the shape of the intrusion curve. Thus the whole pore structure of this sample was altered by the colloid flooding, and the pores that were removed from the network must have been distributed throughout the sample. The less pronounced point of inflection shows that the connectivity has been reduced. Figure 10.4 also shows that the drainage efficiency is lower after colloid flooding (94% trapped) than before (87% trapped). This is again in contrast to samples 81 and 82. In sample 98, the large pores are not blocked, and the colloid flooding has presumably increased the shielding and snap-off effects. The large change in structure caused by the colloid flooding of this sample also results in the largest reduction in permeability from 213.6 mD to 57.6 mD and the largest increase in tortuosity from 1.79 to 1.96 (Table 10.2), a relative reduction of 73% and increase of 9.4% respectively (Table 10.3).

Very little damage appears to have been done to sample 107 during colloid flooding, although the porosity drops slightly and the permeability significantly, Table 10.3. The mercury porosimetry curves are very similar, and any small variations may be due to natural variations in the pore network which are encountered when any sample is halved and each half analyzed separately. Whereas the mercury is intruded from all

directions, the permeability is measured in the same direction as the colloid is intruded - hence it is not surprising to discover that the permeability measurements can be more sensitive to colloid flooding than the mercury porosimetry curves. Within this context, the significant reduction in tortuosity caused by the colloid flooding of the sample, Tables 10.2 and 10.3, is difficult to explain.

For sample 108, there is a large (33%) reduction in the pore volume accessible to mercury, Figure 10.6. There is also an increase in the percentage of large pores within the network after colloid flooding (- - -). An increase in the number of accessible large pores could be caused by micro-fractures opening during colloid flooding and drying. However, this is unlikely because there is a drop in the post colloidal flooding permeability from 29.17 to 17.md, Table 10.2, equivalent to a relative reduction of 39%, Table 10.3, whereas micro-fracturing is usually accompanied by a permeability increase. The other mechanism for an increase in large pore accessibility is by removal of natural in situ fines or the dissolving of grains or cement. Material could be removed from the large pores and deposited in smaller pores or be expelled completely from the sample. The porosity of sample 108 rose slightly after colloid-flooding, so it would appear that most of the damage was caused by natural in situ fines. The amount of mercury trapped at 9.25μm decreased from 91.7% for the clean sample to 86.9% for the damaged sandstone.

10.6 Modelling Outcrop Sandstone Clean and Damaged

We now describe the application of our Pore-Cor computer model to the simulation of colloidally induced formation damage. The simulations for both clean and colloid damaged sandstone void space are obtained from a manual curve fit procedure, since at the time of this study the automatic curve fit algorithms had not been developed. The manual simulations are of comparable quality to the later automatic simulations, but took much longer to compute. The experimental intrusion curves have not been truncated

because a large amount of the void blocking detected occurs in the surface voids.

Figure 10.7 shows the experimental mercury intrusion curve of a Clashach sample. This sample was originally adjacent to the samples used for the colloid flood investigation. Unlike reservoir sandstones Clashach is very homogeneous and it is reasonable to assume that the duplicate sample has a similar mercury porosimetry curve to that of sample 2. This assumption is supported by the almost identical porosity of the neighbouring samples.

The throat size distribution is manually skewed, so that the mercury intrusion curve agrees with experiment, Figure 10.7. The optimum skew gives 0.45% of throats of 1 micron diameter up to 1.55% of throats of 100 microns diameter (0.45% skew). The experimental porosity of 11.1% is achieved by a pore row spacing of 164.0 microns, giving a unit cell size of 1.64 mm (connectivity is 3.5).

The median simulated tortuosity is 2.4. This is higher than the Clashach experimental value of 1.58, Table 10.1 The interquartile ranges of the tortuosities of the random walks are Q(1)=1.9 and Q(3)=2.8, as with other simulations tortuosity is too low.

The pore block simulation has been applied to the Clashach colloid flood results. A 7μm radius pore block simulation on the optimized Clashach simulated pore and throat size distribution, causes a 37% drop in simulated permeability. This simulated permeability drop exactly matches the drop experienced by sample 1, after colloid flooding. A simulated tortuosity after pore blocking was unattainable due to no path being found through the unit cell.

10.7 Computer Modelling Of Reservoir Sandstones

The Pore-Cor package has been used to simulate the void space of the five reservoir sandstones in both clean and colloid flooded states. The model pore network of the clean sample 81 is used in the mercury intrusion simulation in Figure 10.8. The parameters for this simulation are listed in Table 10.4. When a simulated pore block of

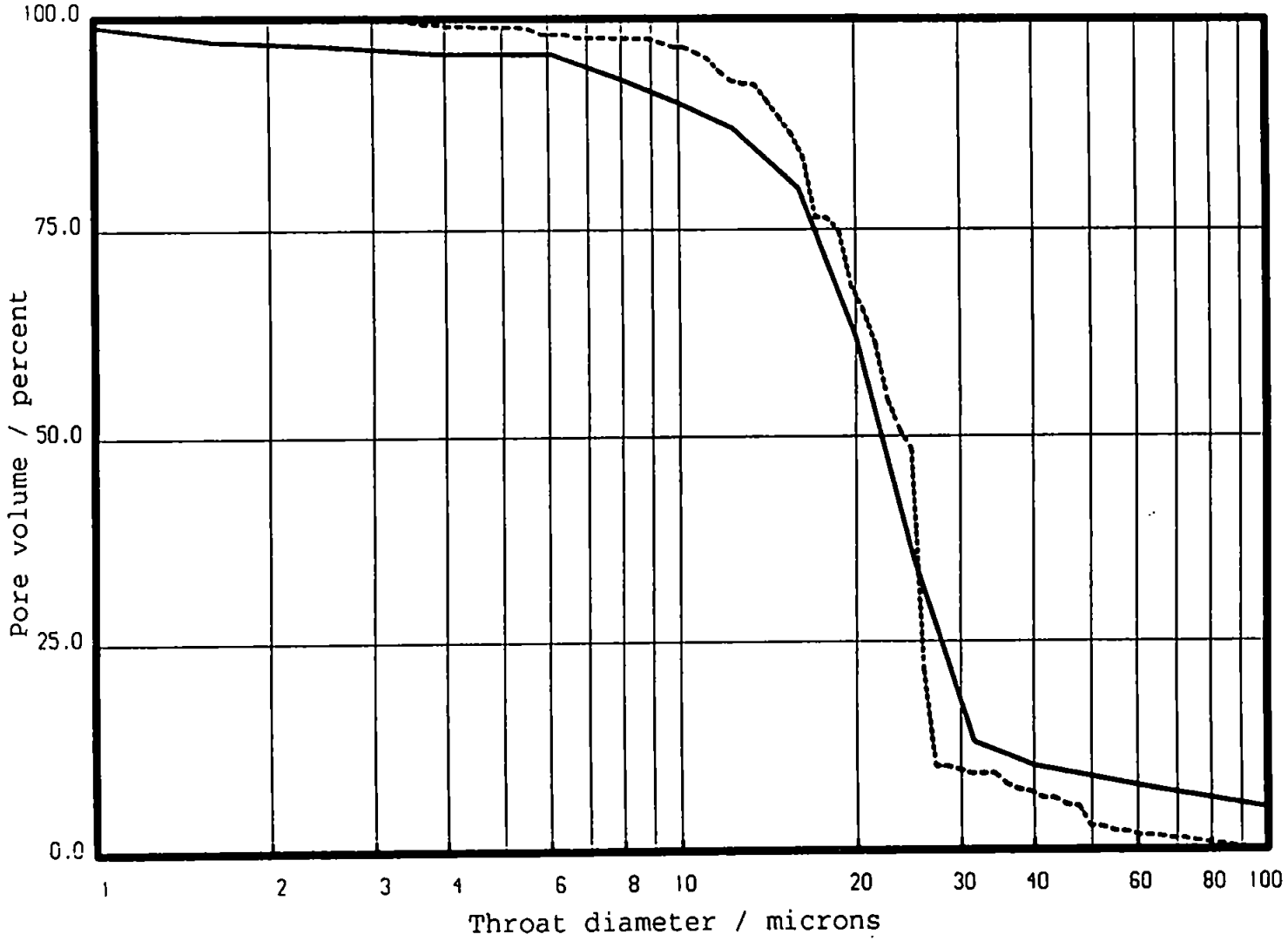

FIGURE 10.7: Mercury intrusion curves for Clashach sandstone: —— experimental, ----- optimum distribution

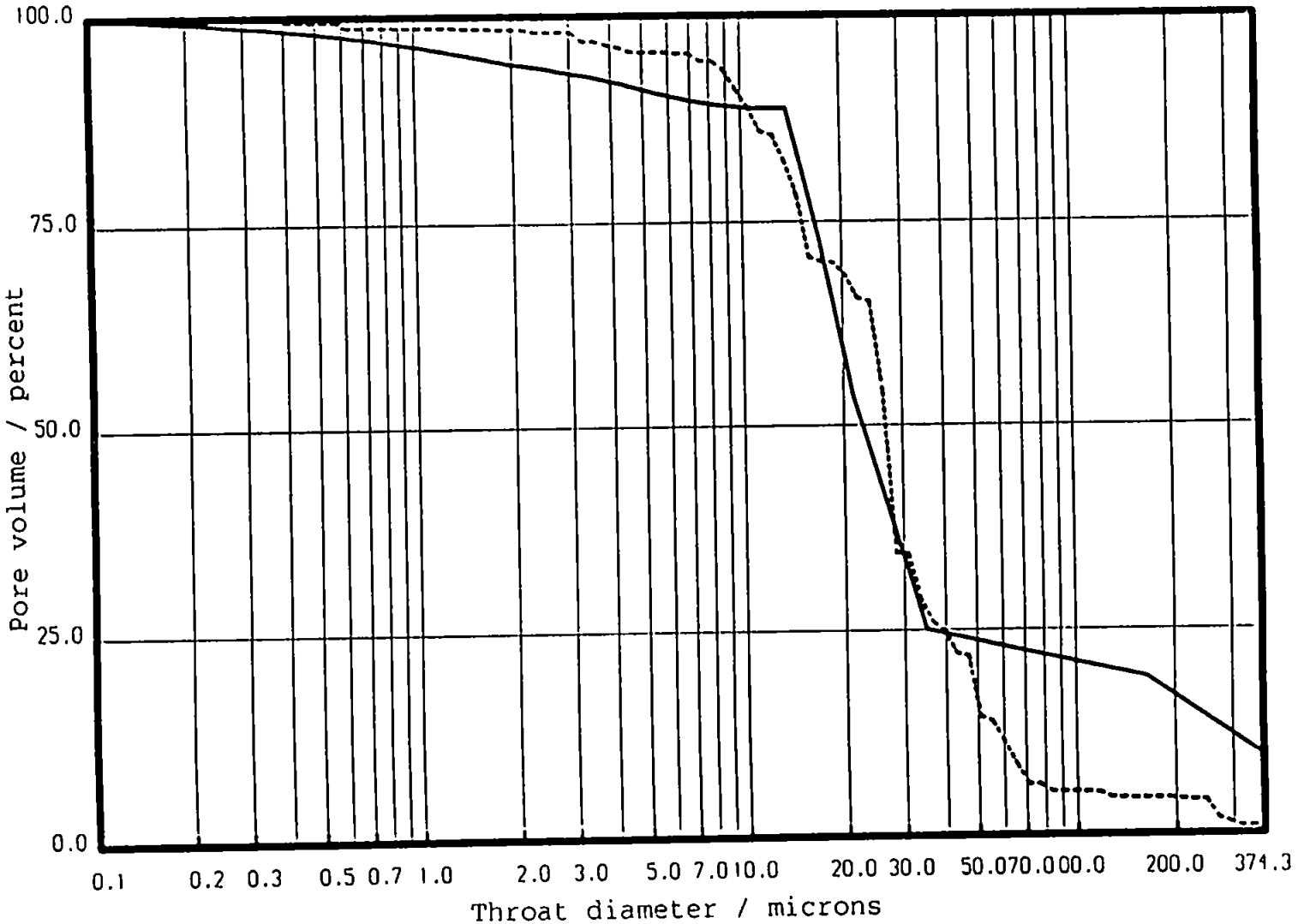

FIGURE 10.8: Mercury intrusion curves for clean sample 81: —— experimental, ----- optimum distribution

Sample no.	State	Simulation type	Porosity /%	Min. throat size/μm	Max. throat size/μm	% skew	Connectivity	Actual perm change	Simul. perm change	Actual tortuosity	Simulated tortuosity
81	Clean	Intrusion curve fit	14.00	0.10	374.32	0.70	3.90			2.00	4.40
81	Colloid flooded	Colloid block/7.3μm	(14.00)	0.10	374.32	0.70	3.90	-49.9%	-9.0%	1.99	3.40
81	Colloid flooded	Intrusion curve fit	13.40	0.22	294.93	0.70	3.45	-49.9%	-43.2%	1.99	2.70
82	Clean	Intrusion curve fit	11.10	0.36	517.30	0.85	3.00			2.24	4.9
82	Colloid flooded	Intrusion curve fit	11.70	0.31	294.90	1.20	2.80	-22.6%	-86.0%	2.25	N/A
98	Clean	Intrusion curve fit	16.20	0.30	258.00	0.60	3.50			1.79	1.90
98	Colloid flooded	Intrusion curve fit	15.40	0.30	258.00	0.60	2.80	-73.0%	-81.66%	1.96	2.90
107	Clean	Intrusion curve fit	12.10	0.22	265.00	0.50	3.40			2.47	2.10
107	Colloid flooded	Intrusion curve fit	11.40	0.31	750.00	0.75	3.20	-45.1%	-73.1%	2.15	2.40
108	Clean	Intrusion curve fit	9.50	0.22	203.70	0.95	3.90			2.63	4.40
108	Colloid flooded	Colloid block/6.5μm	(9.50)	0.22	203.70	0.95	3.90	-38.9%	-37.7%	2.69	N/A

TABLE 10.4: Computer simulation of colloid induced formation damage

radius 7.3μm is applied to the optimum simulated unit cell of sample 81, the simulated mercury-accessible pore volume decreases by the same degree as experiment, Table 10.3 and Figure 10.9. However, as can be seen in the figure, the shape of the simulated mercury intrusion curve after the simple pore blocking simulation is not very similar to the corresponding experimental curve.

Thus the simple removal of small pores from the simulated void space is not the correct approach to modelling the colloid damage in sample 81. As mentioned earlier, sample 81 underwent a loss of large pores during colloid flooding. To model the effect of the colloid on sample 81 the simulated pore and throat size distribution has to be totally altered, to obtain a good mercury intrusion curve fit (Figure 10.10). The remodelling (row 3, Table 10.4) gave a permeability 43.2% less than the initial clean sample model. This is in good agreement with the 49.9% permeability reduction measured in experiment for sample 81.

Table 10.4 shows that the simulated tortuosity is too high for this sample, both before and after colloid flooding. This is the same discrepancy as for all simulations, discussed earlier. However, the simulation does give the correct experimental trend of a reduction in tortuosity, although the simulation exaggerates the effect.

The simulated pore network for the clean sample 82 has a wide pore and throat size distribution, smallest pores and throats being 0.36μm and the largest 517.30μm (row 4, Table 10.4). Sample 82 underwent a reduction in the number of large and mid-range pores and throats (500 to 10μm) during colloid flooding. A simple pore block simulation would not be sophisticated enough to model the effects of colloid flooding on sample 82. Therefore the pore structure of the colloid flooded sample 82 is simulated by a total remodelling (row 5, Table 10.4). The new pore/throat size distribution has a smaller pore size range. The connectivity has reduced from 3.00 for the clean sample simulation to 2.80 for the colloid flooded. The results of the mercury porosimetry simulation on both clean and colloid flooded optimum pore/throat size distributions are shown in Figure 10.11. Experimental curves have been normalized so that

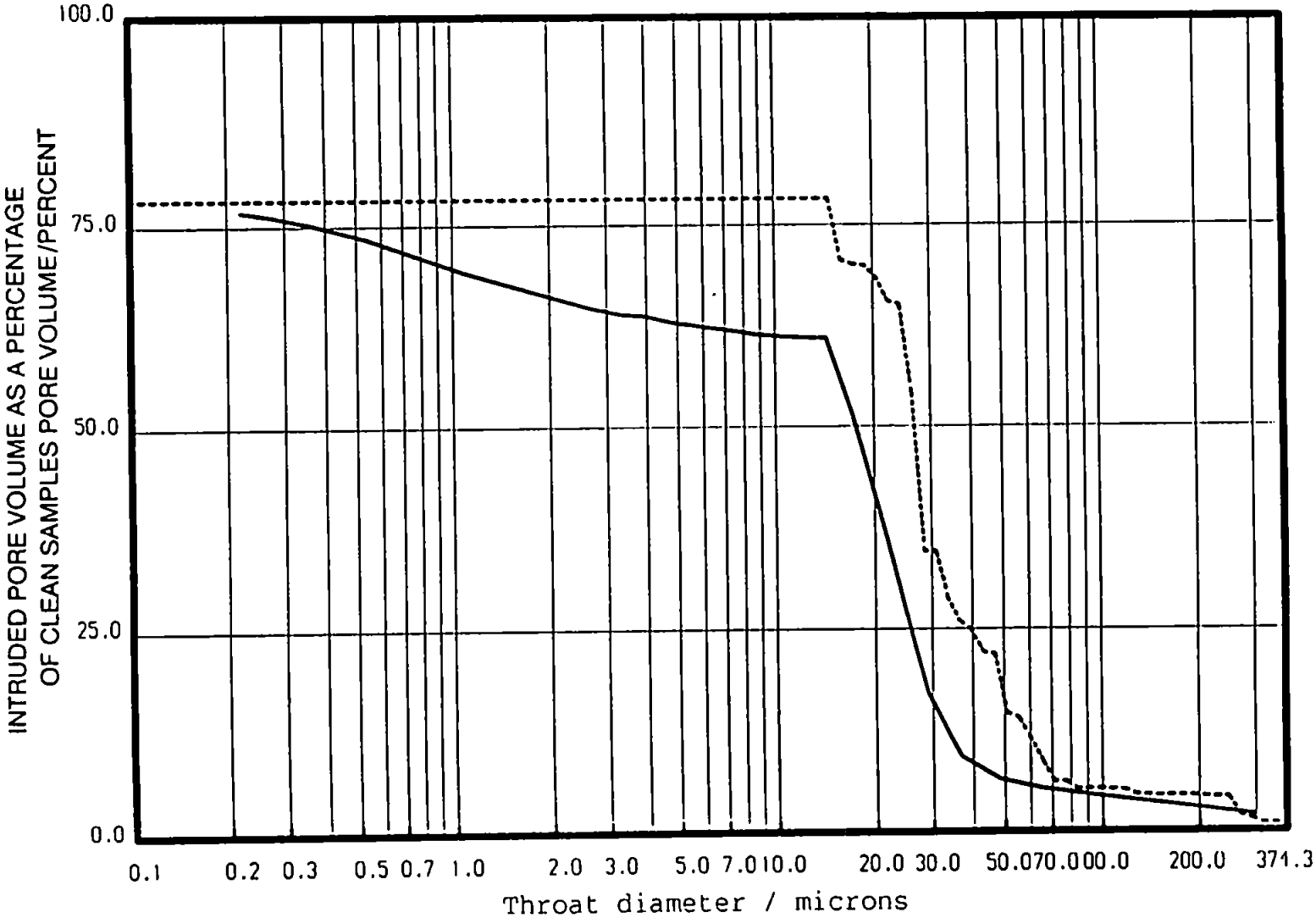

FIGURE 10.9: Mercury intrusion curves for colloid flooded sample 81, optimum distribution of clean sample 81 simulation with pore block of radius 7.3μm: ·—·— experimental, ----- optimum distribution

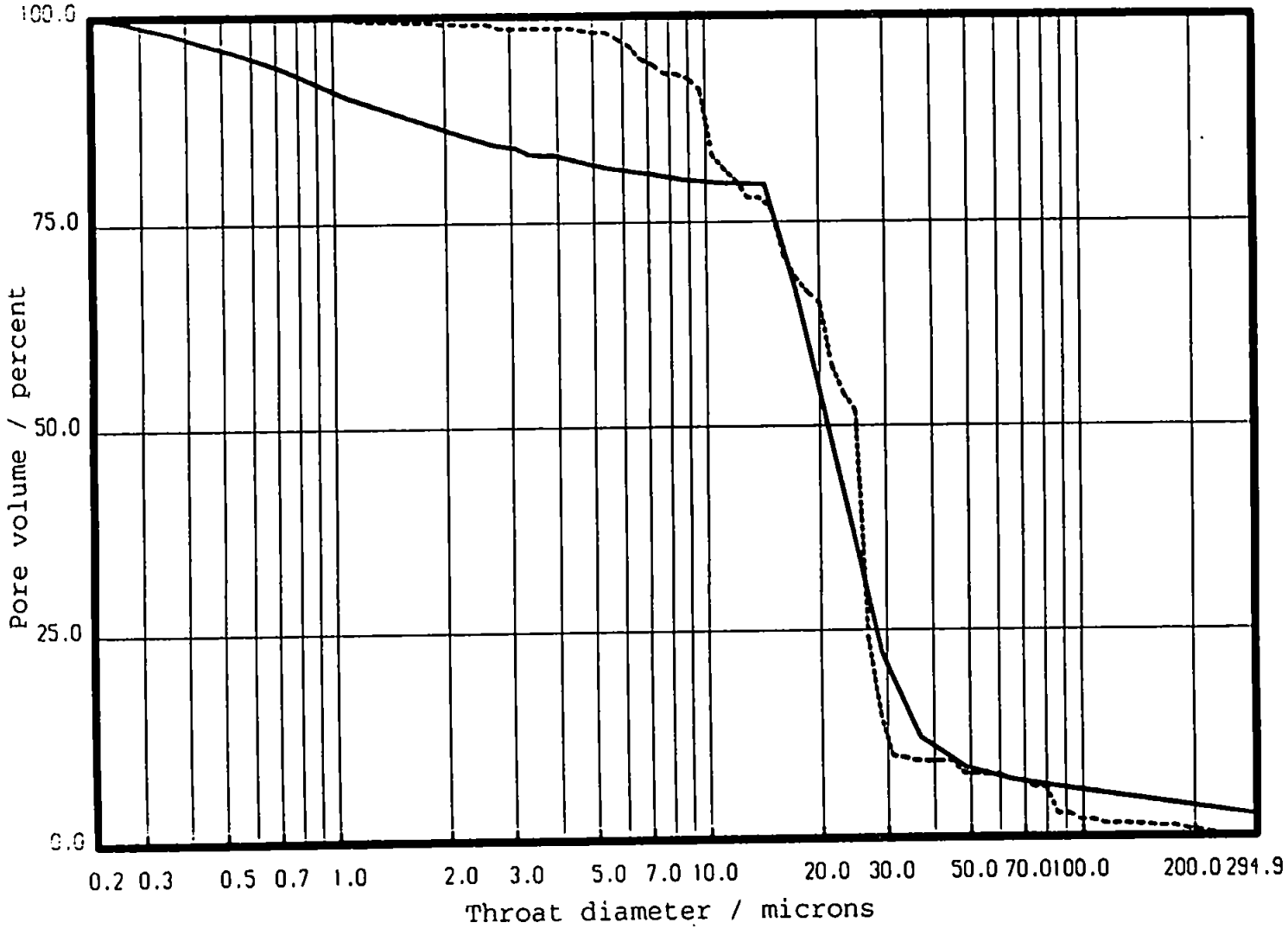

FIGURE 10.10: Mercury intrusion curves for colloid flooded sample 81: —— experimental, ----- optimum distribution

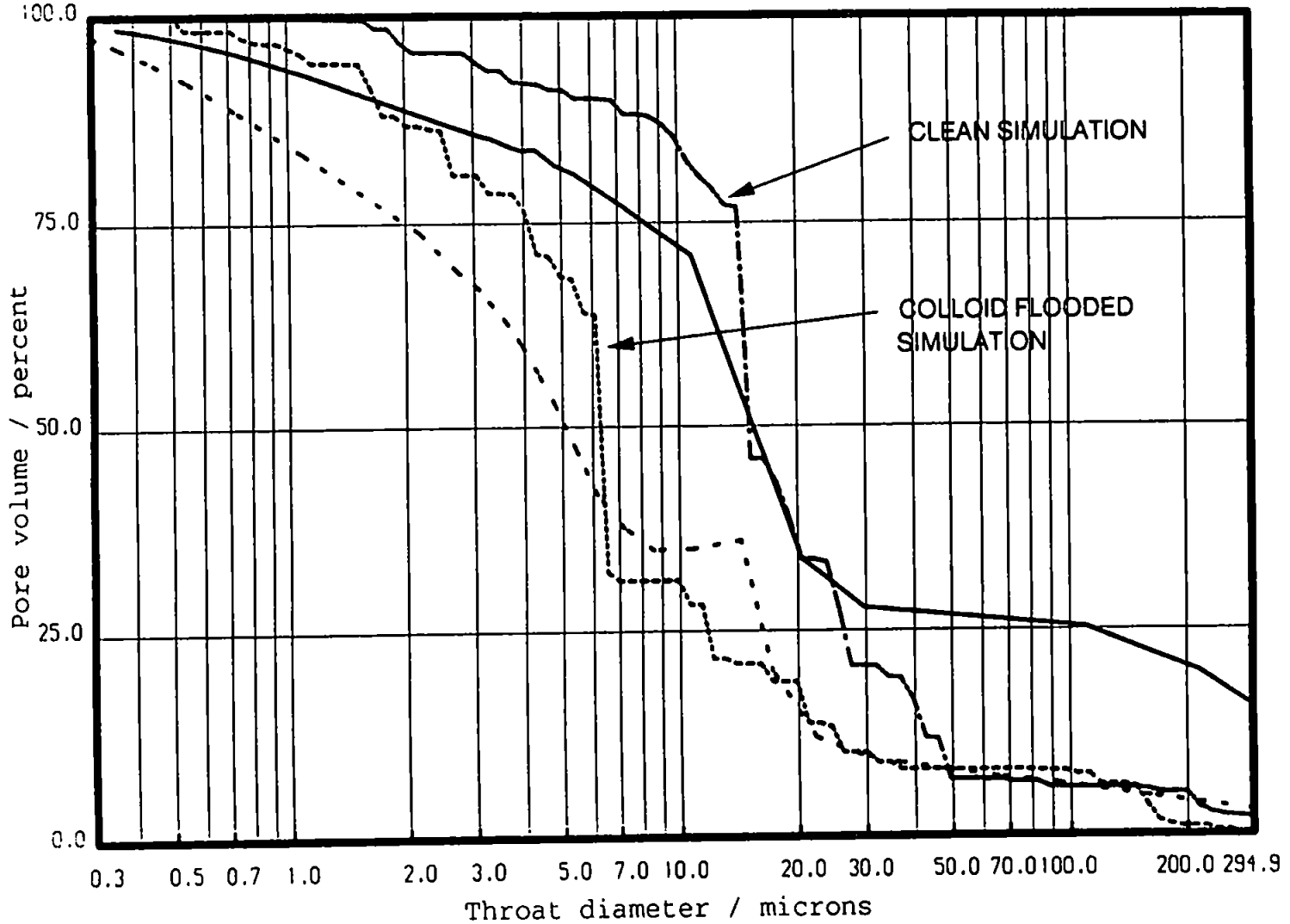

FIGURE 10.11: Mercury intrusion curves for sample 82: ····· experimental clean sample, ·-·-· clean optimum distribution, ----- experimental colloid flooded sample, ··· colloid flooded optimum distribution.

in both clean and colloid flooded experiments, the maximum volume of mercury intruded is equal to an intruded pore volume of one hundred percent. The experimental permeability reduced by 22.6% when sample 82 was flooded with colloid whereas the simulated pore networks produced an 86.0% reduction in permeability. Experimental measurements indicated a slight rise in tortuosity the simulations of the clean and colloid flooded pore networks show a change in tortuosity from a median value of 4.9 to no path through the unit cell respectively. Thus both simulated permeability and tortuosity show changes in the right direction but greatly exaggerated compared to the measured changes in these properties.

The widespread pore blocking experienced by sample 98 manifests itself in a reduction in the pore networks connectivity, discussed earlier. Thus to simulate the effect of colloid flooding, the pore and throat size distribution is unaltered from the clean to flooded simulation, but the connectivity used in the modelling changes from 3.50 to 2.80 (rows 6 and 7, Table 10.4). Figure 10.12 shows the mercury porosimetry curves for both clean and colloid flooded experiments and simulations. Simulated permeability reduction after colloid flooding is close to that measured experimentally for Sample 98. A comparison of experimental and simulated tortuosity changes shows that the trend of increase in tortuosity after colloid flooding is mirrored by the simulations, although again somewhat exaggerated.

Colloid flooding seems to have had little effect on the mercury intrusion for sample 107. The post colloidal flooding intrusion curve indicates a slight increase in the percentage of large pores intruded with mercury. This observation is evident in the post-colloidal simulated pore and throat size distribution which includes pores of 750μm, significantly larger than the largest pore size of 265μm used in the clean sample simulation (Table 10.4, row 8). Figure 10.13 shows both experimental and simulated mercury intrusion curves for the clean and colloid flooded sample 107. Both clean and colloid flooded simulated mercury intrusion curves appear similar in Figure 10.13, but the

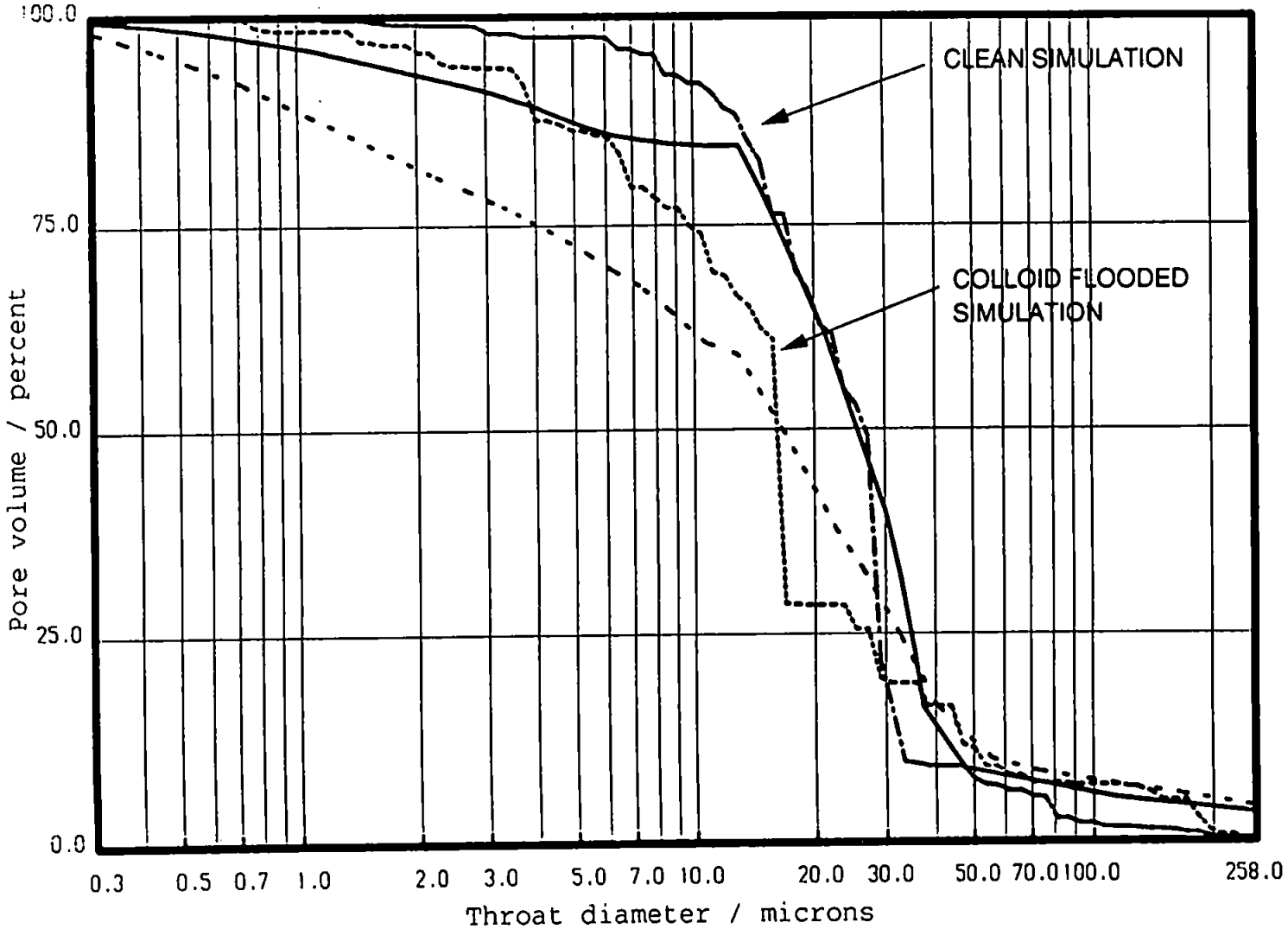

FIGURE 10.12: Mercury intrusion curves for sample 98: —— experimental clean sample, ·-·-· clean optimum distribution, ----- experimental colloid flooded sample, ····· colloid flooded optimum distribution.

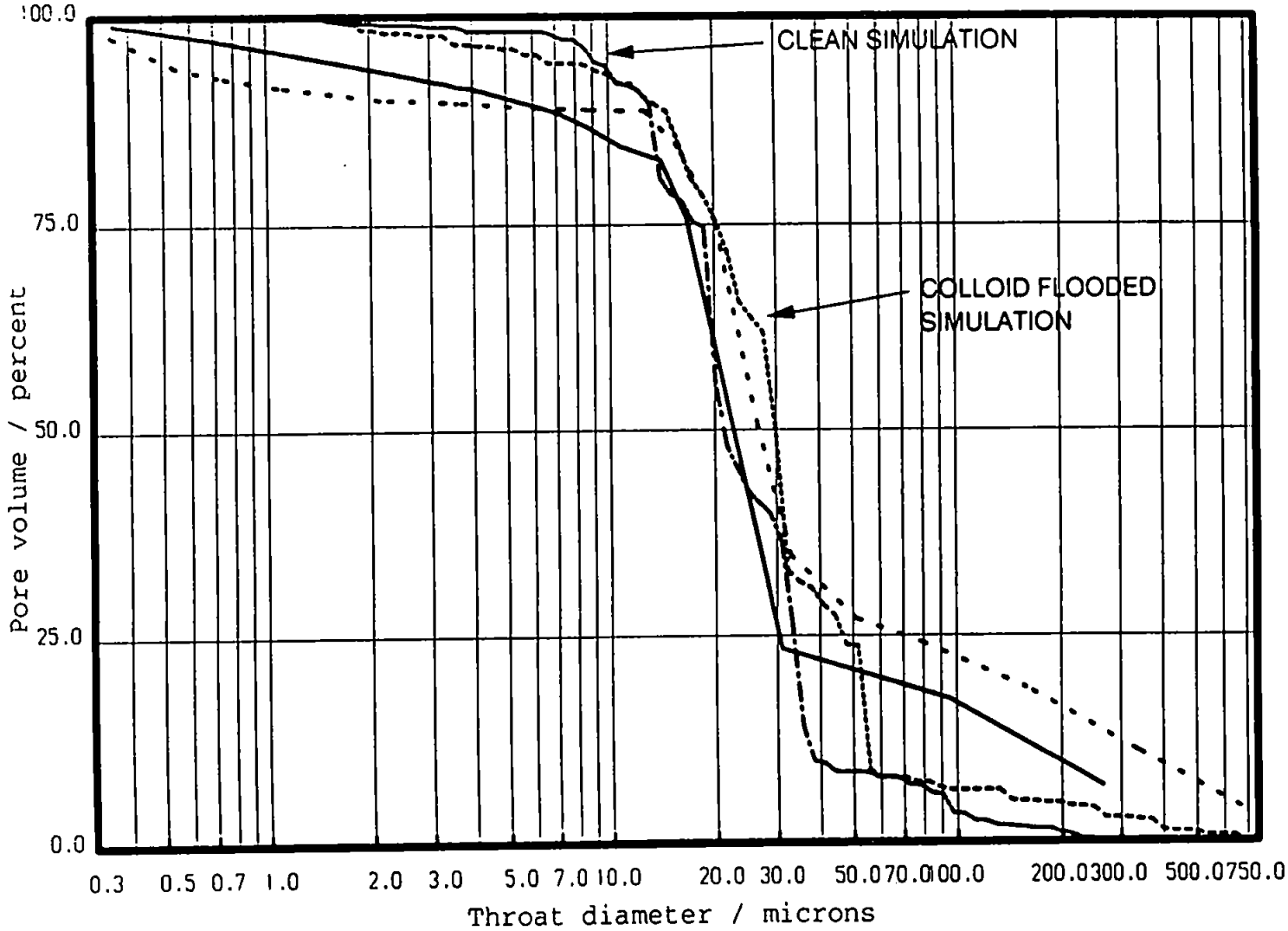

FIGURE 10.13: Mercury intrusion curves for sample 107: —— experimental clean sample, ·-·-· clean optimum distribution, ----- experimental colloid flooded sample, ···· colloid flooded optimum distribution.

simulated permeabilities for each pore network are very different. A drop in simulated permeability of 73.1% is obtained when comparing the clean simulation with the colloid flooded simulation. This change is larger than the 45.1% drop measured in experiment.Simulated tortuosity values also exaggerate the degree of blocking experienced by this sample. A rise in simulated tortuosity from 2.1 to 2.4 disagrees with a drop in measured tortuosity from 2.47 to 2.15 after colloid flooding.

The simulation data for the clean sample 108 are summarized in Table 10.4, row 10. A colloid block simulation of radius 6.5μm was applied to this simulated pore network. The resulting mercury intrusion curves are shown in Figure 10.14. Both curves are shown on the same axis, the y-axis now indicating percentage of pore volume intruded, as a percentage of the total pore volume of the clean sample. The pore block simulation of radius 6.5μm reduces the pore volume accessible to mercury, to the same volume as experiment. Simulated permeability is also reduced by the same degree as experiment when the 6.5μm pore block is applied, Table 10.4, row 11. Experimental tortuosity rose from 2.63 to 2.69 after colloid flooding. The simulated tortuosity also rose, but from 4.2 to infinity, ie. to no path through the cell.

10.8 Concluding Remarks

1) The invasion of pore space by colloidal particles causes the blocking of flow channels within the pore network. The six sandstone samples analyzed in this study all experienced large permeability drops after colloid flooding. The accessible pore space during mercury intrusion is also reduced, in all samples, after colloid flooding.

2) An accurate assessment of the manner of damage to the pore space can only be obtained by measuring many different properties of the sandstone samples. To study the effect of formation damage on one parameter, such as permeability, only reveals part of the picture.

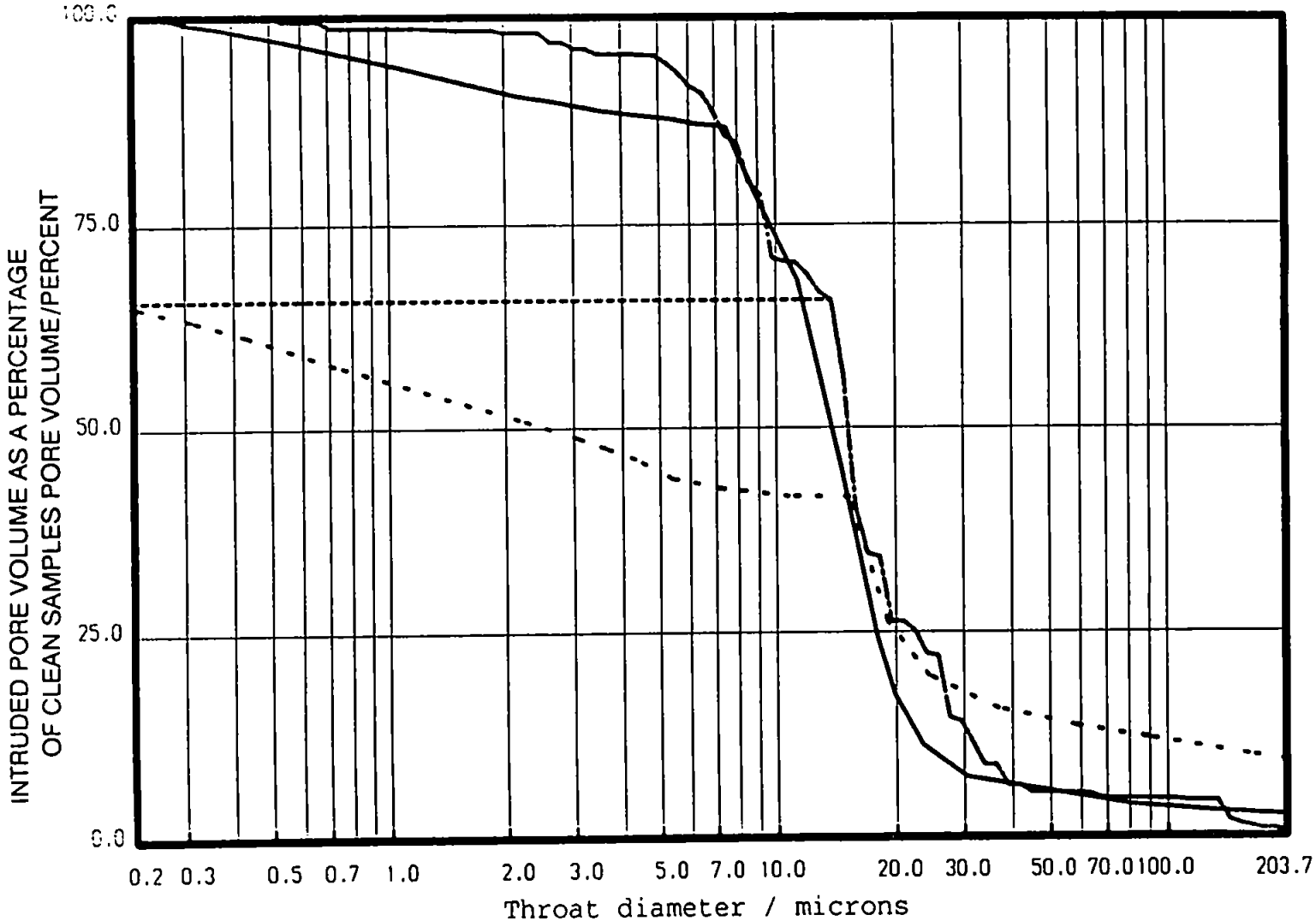

FIGURE 10.14: Mercury intrusion curves for sample 108: —— experimental clean sample, -·-·- clean optimum distribution, ----- experimental colloid flooded sample, ·· optimum distribution for clean sample 108 simulation with a pore block of radius 6.5μm.

A full investigation into the effects of formation damage should include mercury porosimetry data for both native and damaged state samples.

3) The six sandstone samples analyzed each experienced different modes of pore blocking during colloid flooding. Pore blocking was not confined to just filling of large pores with colloid - different samples underwent different blocking scenarios. The different behaviour of the colloid within the pore space is probably attributable to the different pore networks of each sample before colloid flooding.

4) To simulate formation damage the pore network of the undamaged sandstone must first be accurately modelled. We have presented a three dimensional pore network model which is capable of simulating the complexities of sandstone void space. To the primary void space geometry we applied a simple pore block simulation which was successful for the minority of cases where simple pore blocking was the dominant damage mechanism in the real sample pore networks. To model colloid flooding of the other samples the pore/throat size distribution and average pore connectivity of the primary void space model had to be altered.

5) An analysis of small samples of sandstone has revealed colloid flooding to be a complex mode of formation damage. The quantification and simulation of this type of formation damage is complex and requires careful use of a sophisticated 3-D pore space network even on a small scale, and underlines the problems of understanding and modelling formation damage on a reservoir scale.

CHAPTER 11

CONCLUSIONS

The void space of a number of reservoir sandstones has been simulated and characteristic phenomena such as porosity, permeability and mercury intrusion curves successfully modelled. Spearing's original model allowed a realistic modelling of clean homogeneous sandstone void space. The model has been refined to facilitate the simulation of inhomogeneous/banded sandstones. The degree of success attained within these simulations is related to the complexity and the sample's void space. Sandstones containing a high percentage of clay are far more complex than clean sandstones and simulation of their void space by the present model gives limited success. The next section outlines the level of success attained for each simulated parameter and possible routes to improvement.

11.1. Porosity

The application of intrusion curve truncation allows a wide range of porosities to be modelled. Prior to the truncation procedure the model overestimated the frequency of the large pores. The subsequent large pore row spacing needed to accommodate these large pores limited the range of simulated porosities attainable. A future refinement of the model would be to use a varying pore row spacing in networks with extreme pore:pore correlation. Thus regions of small pores could be compacted to mirror closely the pore arrangement in real banded sandstones.

11.2. Permeability

The simulated permeability of the correlated networks closely matched the measured values to within a factor of four or better. This level of success exceeds any

obtained by other modellers known to the author. The facility to reduce the pore row spacing in small pore areas would improve the simulated permeabilities even more. The failure of Pore-Cor to simulate the permeabilities of the clay-affected samples is due to the extreme complexity of the void space of these samples.

11.3. Tortuosity

The tortuosity simulation has been found to produce values that are too high. During the particle walk through the unit cell, the particle is allowed to 'wander' too far. This effect could be remedied by increasing the direction weighting from r^2/l to r^3/l, but this would be introducing a fitting parameter. A more realistic approach to modelling tortuosity would be to allow a large number of particles to walk through the unit cell at the same time. This is more analogous to ions migrating through the electrolyte filled pore space. If the simulation forbade particle grouping, the simulated tortuosity value should approach those measured experimentally.

11.4. The Unit Cell And Mercury Porosimetry

The truncation of mercury intrusion is a somewhat subjective procedure, the resulting curve being an approximation of that obtained if surface pores had a negligible effect. The best way to refine the model would be to increase its size to a 100 x 100 x 100 and intrusion/extrusion simulation could proceed through all faces of the unit cell. Surface pore effects could be modelled and a closer fit of extrusion curves would be obtained. A larger unit cell would allow simulation of clay affected pore space. A possible method of simulating the micro-porosity of clay filled pores could be to position a small unit cell within every big pore of the original unit cell. This would produce an extra degree of complexity within the model.

11.5 Formation Damage

The Simple pore block simulation was found to successfully model formation damage within only a minority of samples. In the majority of samples analyzed formation damage was found to be a complex process, and could only be simulated by altering the pore/throat size distribution and average pore connectivity of the void space model. Thus the model can successfully simulate sandstone void space before and after it has experienced formation damage due to a colloidal suspension.

GLOSSARY OF TERMS

Areosity: Ratio of effective cross-sectional area open to flow in a given direction to cross-sectional area normal to flow direction.

Authigenic: Formed or generated in place; specifically said of rock constituents and minerals that have not been transported or that were derived locally where they are found.

Capillary Pressure: The difference in pressure across a liquid meniscus in a capillary tube, ie. the amount of extra pressure required to force a non-wetting phase to displace a wetting phase in the capillary.

Cation Exchange Capacity: The sum of the exchangeable cations that a mineral can absorb at specific ph.

Clay: Fine-grained material, grain size less than 1/256mm, which becomes plastic when wetted.

Detritus: Rock or mineral particles derived from pre-existing rock by weathering and/or erosion.

Diagenesis: All the chemical, physical and biological changes, modifications or transformations undergone by a rock after formation.

Illite: Clay mineral with the general formula $K_{1\text{-}1.5}\ Al_4\ [Si_{7\text{-}6.5}\ Al_{1\text{-}1.5}\ O_{20}]\ (OH)_4$

Illite/Smectite Mixed Layer Clay: Clay particles with a mixed mineralogy of illite ($K_{1\text{-}1.5}\ Al_4\ [Si_{7\text{-}6.5}\ Al_{1\text{-}1.5}\ O_{20}]\ (OH)_4$) and the related clay mineral smectite ($(1/2Ca, Na)_{0.7}$ (Al. Mg, $Fe)_4\ [(Si, Al)_8\ O_{20}]\ .\ N\ H_2\ O$)

Kaolinite: Clay mineral with the formula $Al_4\ Si_4\ O_{10}\ (OH)_8$.

Node: A point in space.

Outcrop Sandstone:A sandstone unit which occurs at the surface.

Pixels: Unit cell component of a digitized image. An image being 512 pixels by 512 pixels.

Potassium Feldspar: Common rock-forming silicate with the formula K Al Si_3O_8.

Pressure Solution: Solution (in a rock) occurring preferentially at the contact surfaces of grains (crystals) where the external pressure exceeds the hydraulic pressure of the interstitial fluid.

Quartz: Common rock-forming silicate with the formula Si O_2.

Overgrowth: Secondary material deposited in crystallographic continuity around a crystal grain of the same composition.

Reservoir Sandstone: A sandstone unit which occurs in a hydrocarbon source area.

Sedimentary Basin: Area in which detritus is deposited.

Stratigraphic Unit: A distinct section of stratified rock in which age, formational environment and composition are known.

Type III Kerogen: Organic matter in hydrocarbon source rocks produces gas under appropriate conditions of pressure and temperature.

LIST OF SYMBOLS

A/m^2	=	Cross Sectional Area
a	=	Dimensionless 'Archie' Constant
a_i/m	=	Range
b/Pa	=	Slip Term
C_0/gm^{-3}	=	Initial Concentration
C_1/gm^{-3}	=	Concentration At Distance x = 0
C_2/gm^{-3}	=	Concentration At Distance x = l
C_c/Ω^{-1}	=	Clay Conductivity
C_k	=	Dimensionless Kozeny Constant
C_n	=	Capillary Number
C_s/Ω^{-1}	=	Sample Conductivity
$Cu/_m$	=	Diameter Of Cubic Pore
C_w/Ω^{-1}	=	Brine Conductivity
$C/molm^{-3}$	=	Concentration
c	=	Dimensionless Gas Slip Parameter
D/m^2s^{-1}	=	Diffusion Coefficient
D_{12}/m^2s^{-1}	=	Bulk Diffusion Coefficient
D_c/m	=	Pore Diameter
D_d/m	=	Extrapolated Displacement Diameter
D_n	=	Degrees Of Freedom
d_b/m	=	Throat Diameter At 'Break Through' On Mercury Intrusion Curve
$d_{exp(vi)}/m$	=	Experimentally Measured Throat Diameter At Pore Volume Point V_i
$d_{sim(vi)}/m$	=	Simulated Throat Diameter At Pore Volume Point V_i

E	=	Error
F	=	Formation Factor
F^*	=	Formation Factor Independent Of Clay Conductivity
G	=	Dimensionless Geometrical Factor
h	=	A Vector
$J/gs^{-1}m^{-2}$	=	Gas Flux Per Unit Area
K/m^2	=	Permeability
K_e/m^2	=	Measured Permeability
K_n	=	Knudsen Number
K_∞/m^2	=	True Permeability
L/m	=	Length Of Sample
L_e/m	=	Distance Through Pore Network
M	=	Viscosity of Injecting Fluid Over Viscosity of Static Fluid
m	=	Cementation Exponent
N	=	Number Of Molecules Per Unit Volume
n	=	Dimensionless Saturation Exponent
P/Pa	=	Pressure
P_c/Pa	=	Capillary Pressure
P_d/Pa	=	Extrapolated Mercury Displacement Pressure
P_m/Pa	=	Average Pressure
Q/gs^{-1}	=	Gas Flux
$R_o/\Omega m$	=	Resistivity Of 100% Brine Saturated Sample
$R_t/\Omega m$	=	Resistivity Of Partially Saturated Sample
$R_w/\Omega m$	=	Resistivity Of Saturating Brine
r/m	=	Pore Radius
S/m^{-1}	=	Total Externally Accessible Surface Area Per Unit Volume
S_w	=	Fraction Of Void Space Saturated With Brine

s	=	Dimensionless slip constant
T	=	Tortuosity
t/s	=	Time
t_o/s	=	Lag Time
V_{tot}/m^3	=	Maximum Intruded Volume
V_p/m^3	=	Pore Volume Point
$(V_b)_{pc}$	=	Fractional Bulk Volume Occupied By Mercury At Capillary Pressure P_c
$(V_b)_{p\infty}$	=	Fractional Bulk Volume Occupied By Mercury At Infinite Capillary Pressure
v/m^3	=	Volume
W	=	Dimensionless Statistical Weighting
X	=	Fraction Of Sample Cross-Sectional Area Made Up Of Voids
x_i	=	A Point In Space
x/m	=	Length
$Z(x_i)$	=	A Property At Point x_i
γ	=	Semi-Variance
Δ_{lin}	=	Sum Of Deviation Of $d_{exp(vi)}$ and $d_{sim(vi)}$
Δ_{log}	=	Sum Of Deviation Of Log $d_{exp(vi)}$ and Log $d_{sim(vi)}$
ε	=	Coefficient Of External Friction
θ	=	Contact Angle
κ/m	=	Knot Distance
ς/m	=	Collision Diameter
μ/cp	=	Viscosity
ξ	=	Areosity
σ/nm^{-1}	=	Surface Tension
Φ	=	Porosity

Ω	=	Averaging Operator
Υ/m	=	Mean Free Path

REFERENCES

Adler, P.M., Jacquin, C.G. and Quiblier, J.A., *Int. J. Multiphase Flow*, 1990, **16**, 691-712.

Adler, P.M., Jacquin, C.G. and Thovert, J-F., *Water Resources Research*, 1992, **28**, 1571-1576.

Archer, J.S. and Wall, C.G., *Petroleum Engineering Principles and Practice*, Graham and Trotman, London, 1986.

Archie, G.E., *Trans. AIME.*, 1942, **146**, 54-62.

Best, J.V., Stephen, W.J., and Wickham, A.J., *Progress In Nuclear Energy*, 1985, **16**, 127-178.

Blunt, M. and King, P., *Physical Review A*, 1990, **42**, 4780-4787.

Blunt, M. and King, P., *Transpore in Porous Media*, 1991, **6**, 407-433.

Bouabid, R., Nater, E.A., Barak, P., *Geoderma*, 1992, **53**, 309-328.

Bryant, S. and Cade, C., *3rd Euro. Conf. : Maths of Oil Recovery Delft.*, 1992, 209-224.

Cebeci, O.Z., *Journal of Colloid and Interface Science*, 1980, **78**, 381-388.

Chatzis, I. and Dullien, F.A.L., *International Chemical Engineering*, 1985, **25**, 47-66.

Chen, L.C., Ph.D thesis, Uni. Michigan, 1973.

Churcher, P.L., Shaw, J.C. and French, P.R., *Petroleum Society of CIM and Society of Petroleum Engineers*, **CIM/SPE 90-69.**

Conner, W.C. and Horowitz, J., *AIChE Symposium Series*, 1988, **266**, 29-34.

Cornell, D. and Katz, D.L., *Ind. and Eng. Chem.*, 1953, **45**, 2145-2152.

Crank, J *The Mathematics of Diffusion*, Oxford University Press, London, 1975.

Dawe, R.A., *Rev. Sci. Instrum.*, 1973, **44**, 1271.

Day, M., Parker, I.B., Bell, J., Thomas, M., Fletcher, R. and Duffie, J., *Characterization of Porous Solids II*, 1991, 75-84.

Daynes, H.A., *Proc. of Roy. Soc. London A.*, 1920, **97**, 286-307.

Dullien, F.A.L. and Batra, V.K., *Industrial and Engineering Chemistry*, 1970, **62**, 25-53.

Dullien, F.A.L. and Dhawan, G.K., *Journal of Colloid and Interface Science*, 1975, **52**, 129-135.

Finney, J.L., *Proc. Roy. Soc.*, 1970, **319A**, 479-494.

Garboczi, E.J., *Powder Technology*, 1991, **67**, 121-125.

Good, R.J. and Mikhail, R.S., *Powder Technology*, 1981, **29**, 53-62.

Gong, R.H., and Newton, A., *J. Text. Inst.*, 1992, **83**, 253-268.

Guven, N., Hower, W.F. and Davies, D.K., *Journal of Sedimentary Petrology*, 1980, **50**, 761-766.

Hampton, J.H.D., Savage, S.B., and Drew, R.A.L., *Chem. Eng. Sci.* 1993, **48**, 1601-11.

Ioannidis, M.A. and Chatzis, I., *Chemical Engineering Science*, 1993, **48**, 951-972.

Ioannidis, M.A., Chatzis, I., and Sudicky, E.A., *Water Resources Research*, 1993, **29**, 1777-1785.

Katz, A.J. and Thompson, A.H., *Physical Review B*, 1986, **34**, 8179-8181.

Katz, A.J. and Thompson, A.H., *Journal of Geophysical Research*, 1987, **92**, 599-607.

Keelan, D.K. and McGinley, D.C., Proceedings of the SPWLA Twentieth Annual Logging Symposium, 3rd-6th June, 1979.

Khilar, K.C. and Fogler, H.S. SPE 10103 presented at the 1981 SPE Fall Technical Conference, San Antonio, Oct 5-7.

Kloubek, J., *Powder Technology*, 1981, **29**, 63-73.

Koplik, J., Lin, C. and Vermette, M., *J. Appl. Phys.*, 1984, **56**, 3127-3131.

Krooss, B., *Erdöl und Kohle - Erdgas*, Petrochem.,1986, **39**, 300-402.

Krooss, B., *Advances in Organic Geochemistry*, 1987, **13**, 513-523.

Lenormand, R., Touboul, E. and Zarcone, C., *J. Fluid Mech.*, 1988, **189**, 165-187.

Lenormand, R., *Proc. R. Soc. Lond.*, 1989, **423**, 159-168.

Lever, A. and Dawe, R.A. *J. Pet. Geol.* (1984) **7**, 97-108

Leythaeuser, D., Schaefer, R.G. and Yukler, A., *Primary Mitigation*, 1982, **66**, 408-429.

Lin, C. and Cohen, M.H., *J. Applied Phys.*, 1982, **53**, 4152-4165.

Lymberopoulos, D.P. and Payatakes, A.C., *Journal of Colloid and Interface Science*, 1992, **150**, 61-79.

McPhee, C.A. and Arthur, K.G., Advances in Core Evaluation II : Proceeding of 2nd Soc. of Core Analysis, European Core Analysis Symposium, London, 20-22nd May 1991.

Macchi, L., Curtis, C.D., Levison, A., Woodward, K. and Hughes, C.R., *A.A.P.G. Bulletin*, 1990 **74**, 209-308

Mason, G. and Mellor, D.W., *Characterization of Porous Solids II*, 1991, 41-50.

Matthews, G.P., *Experimental Physical Chemistry*, Oxford University Press, 1985.

Matthews, G.P., Moss, A.K., Spearing, M.C., and Voland, F., *Powder Technology*, 1993, **76**, 95-107.

Matthews, G.P., Moss, A.K. and Ridgway, C.J., *Submitted to Powder Technology*, 1994.

Monicard, R.P., *Properties of Reservoir Rocks: Core Analysis*, Institut Francais du Petrole Publications, Paris, 1980.

Morrison, S.J. and Duggan, T.P., Advances in Core Evaluation II : Proceeding of 2nd Soc. of Core Analysis, European Core Analysis Symposium, London, May 20-22nd 1991.

Moscou, L. and Lub, S., *Powder Technology*, 1981, **29**, 45-52.

Muecke, T.W. *JPT* (Feb 1979) 144-150.

Neasham, J.W., *Society of Petroleum Engineers of AIME*, 1977, **SPE 6858.**

Ochi, J., Vernoux, J.F., Foucher, J.C. and Genter, A. "Experimental Percolation in Argillaceous Sandstones and Survey of Permeability and Porosity Changes: Application to the Reinjection of Cooled Brines into Geothermal Reserviors," presented at GEOFLUIDS '93, Torquay, May 4-7.

Ohen, H.A., and Civan, U., SPE 19420 presented at the 1990 SPE Symposium on Formation Damage Control, Lafayette, Lousiana, February 22-23.

Park, C-Y. and Ihm, S-K., *AIChE Journal*, 1990, **36**, 1641-1648.

Pittman, E.D., *Sedimentary Petrology*, 1972, **42**, 507-519.

Porter, K.E. *JPT* (Aug 1989) 780-786.

Postek, M.T., *Scanning Electron Microscopy - A Student's Handbook*, Burlington, Vermont, LADD Research Industries Inc., 1980

Rahman, S.S. and Marx, C. *J. Can. Pet. Tech.* (1991) **30**, 6, 40-46.

Rege, S.D., and Fogler H.S., *Chem. Eng. Comm.* (108, 1991) 67-83.

Ritter, H.L. and Drake L.C., *Ind. and Eng. Chem.*, 1945, **17**, 782.

Ruzyla, K., *S.P.E. Formation Evaluation*, 1986, 389-398.

Scheidegger, A.E., *Physics of Flow through Porous Media*, University of Toronto Press, 1970.

Schlicting, H., *Boundary Layer Theory*, McGraw and Hill, 1979, 613.

Shively, M.L., *Journal of Pharmaceutical Sciences*, 1991, **80**, 376-379.

Spearing, M.C., Ph.D Thesis, Polytechnic South West, 1991.

Smithwick, R.W., *Powder of Technology*, 1986, **48**, 233-238.

Suman, R. and Ruth, D., *Transport in Porous Media*, 1993, **12**, 185-206.

Templeton, C., *Petrol. Trans. A.I.M.E.*, 1954, **201**, 161.

Thomas, M.M., *A.A.P.G. Bulletin*, 1989, **73**, 787-791.

Thomeer, J.H.M., *Society of Petroleum Engineers*, 1960, 73-77.

Thompson, A.H., Katz, A.J. and Raschke, R.A., *Society of Petroleum Engineers*, 1987, **SPE 16794**, 475-481.

Thompson, M.L., Singh, P., Corak, S. and Strazheim, W.E., *Geoderma*, 1992, **53**, 399-415.

Thorstenson, D.C. and Pollock, D.W., *Reviews of Geophysics*, 1989, **27**, 61-68.

Tsakiroglou, C.D. and Payatakes, A.C., *Journal of Colloid and Interface Science*, 1990, **137(2)**, 315-339.

Tsakiroglou, C.D. and Payatakes, A.C., *Journal of Colloid and Interface Science*, 1991, **146(2)**, 479-494.

Tye, F.L., *Chemistry and Industry*, 15th May 1982, 322-326.

Van Brakel, J., *Powder Technology*, 1975, **11**, 205-236.

Van Brakel, J., Modry, S. and Svata, M., *Powder Technology*, 1981, **29**, 1-12.

Van Olphen, H.: *Clay Colloid Chemistry for Clay Technologists, Geologists and Soil Scientists*, J. Willey and Sons., London (1963).

Vavra, C.L., Kaldi, J.G. and Sneider, R.M., *The American Association of Petroleum Geologists Bulletin*, 1992, 840-850.

Vinchon, C., Matray, J.M. and Rojas, J.:"Textural and Mineralogical Changes in Argillaceous Sandstones, Induced by Experimental Fluid Percolation," presented at GEOFLUIDS '93, Torquay, May 4-7.

Wakeham, W.A. and Slater, D.H., *Journal. Phy. B. Atomic and Molecular Physics*, **6**, 886-896.

Wardlaw, N.C. and Cassan, J.P., *Bulletin of Canadian Petroleum Geology*, 1979, **27**, 117-138.

Wardlaw, N.C., Li, Y. and Forbes, D., *Transport in Porous Media* 2, 1987, 615-621.

Wardlaw, N.C. and McKellar, M., *Powder Technology*, 1981, **29**, 127-143.

Wardlaw, N.C. and Taylor, R.P., *Bulletin of Canadian Petroleum Geology*, 1976, **24**, 225-262

Waxman, M.H. and Smitts, L.J.M., *J. Soc. Pet. Eng.*, 1968, **243**, 107-122.

Wilson, M.D. and Pittman, E.D., *Journal of Sedimentary Petrology*, 1977, **47**, 3-31.

Worthington, A.E., Proceedings of the SPWLA Twentieth Annual Logging Symposium, 3rd-6th June, 1979.

Wyllie, M.R.J. and Rose, W.D., *Pet. Trans. AIME.*, 1950, **189**, 105-118.

Yanuka, M., Dullien, F.A.L. and Elrick, D.E., *Journal of Colloid and Interface Science*, 1986, **112**, 24-41.

APPENDIX 1

SCANNING ELECTRON MICROSCOPY

Scanning electron microscopes produce an image of the sample by interaction with an electron beam. The best possible resolution obtainable from light microscopes is 0.2μm, using an electron beam instead of light resolutions of 3nm are attainable. Thus scanning electron microscopes are ideally suited to analysis of sandstones.

The primary electron beam is produced by heating a fine tungsten filament (Figure A 1.1). The electron beam accelerates towards the sample under the influence of a voltage of 5-30 KV. The beam is demagnified and focused by a series of electromagnetic lenses, to produce a fine beam which interacts with the sample. The apparatus must be maintained at vacuum (approximately 2 x 10^{-6} Torr) to allow electron beam formation, this restricts samples to only dry non-volatile substances. Upon collision with the sample surface, the electron beam causes a number of emissions (Figure A1.2). Low energy electrons emitted from the sample surface are called Auger Electrons, this emission is not normally detected in S.E.M., the sample image is primarily formed by secondary electron emissions. Secondary electrons are emitted due to ionization when the electron beam collides inelastically with the sample surface. Secondary electrons have energies less than 50EV.

Backscattered electrons have energies greater than 50EV and normally produce signals of the same order as the primary electron beam 5-20KV (Postek 1980). Backscattered electrons are formed deep within the sample due to elastic collisions between the electron beam and the specimen nuclei or electrons. There is a correlation between backscattered electron production and atomic number of the sample. As atomic number increases, more backscattered electrons are emitted. Thus high atomic number elements produce a strong emission and appear brighter in a backscattered electron image. This facility is used in the imaging of the low atomic number epoxy resin filled pore space, which appears black compared to the sandstone grains.

If an electron is removed from an atomic shell of a sample atom by interactions with the primary electron beam, the "hole" is filled by an electron from an outer shell, Figure A1.3. This electron movement is accompanied by an emission of characteristic x-rays of the same energy as the difference in energy between the source and sink electron shells. Thus the x-ray emissions are characteristic of the sample elements. The detection and identification of these x-rays is known as energy dispersive x-ray analysis (E.D.X.) The characteristic x-rays overlay an x-ray continuum (Bremsträlung Radiation) which are of no diagnostic use.

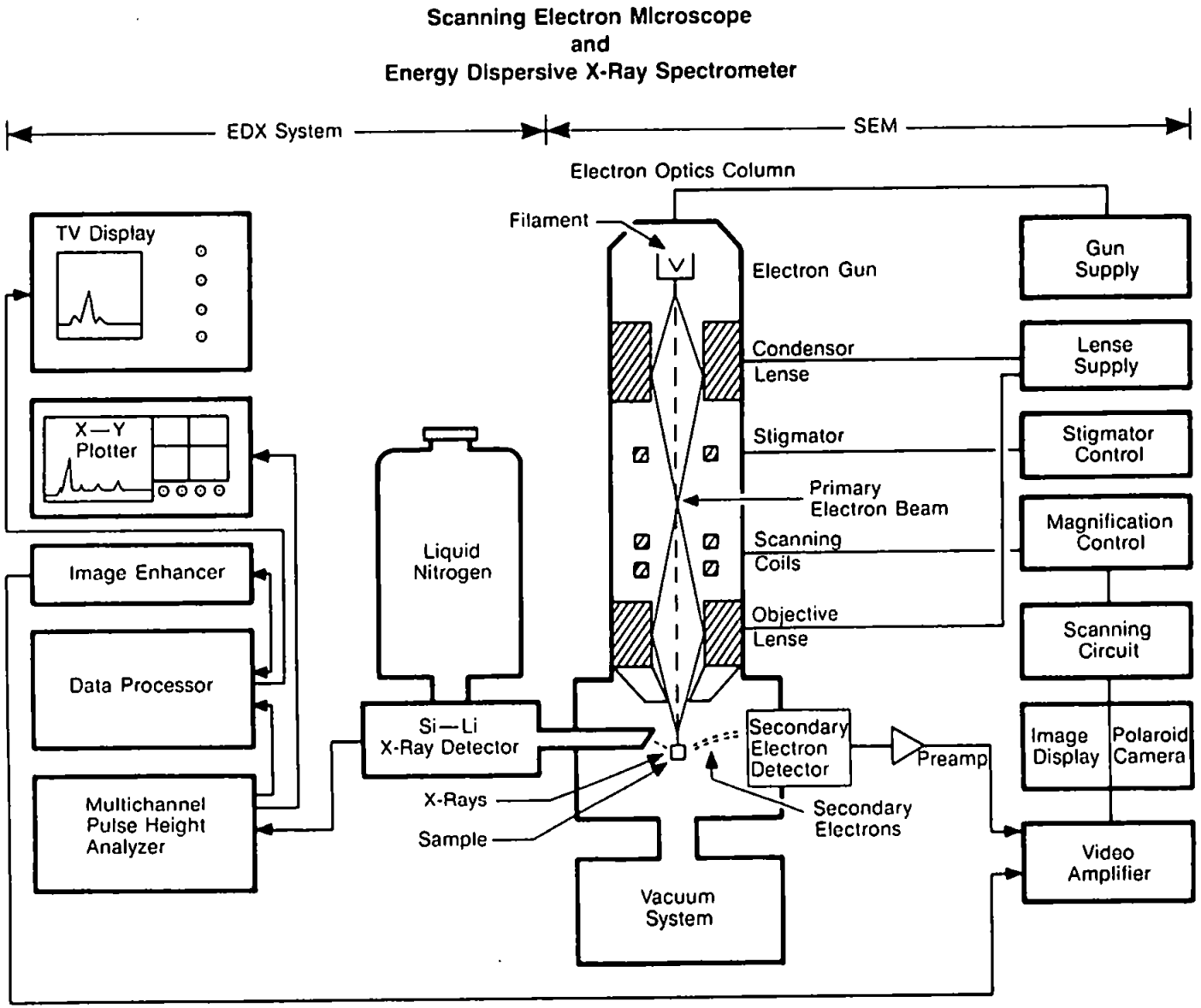

Figure A1.1: Schematic Showing SEM/EDX System (from Welton 1984).

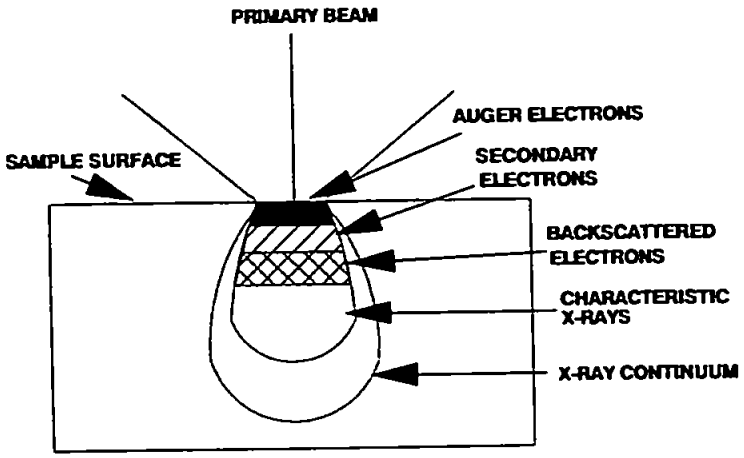

Figure A1.2: Interactions Between an Electron beam and sample.

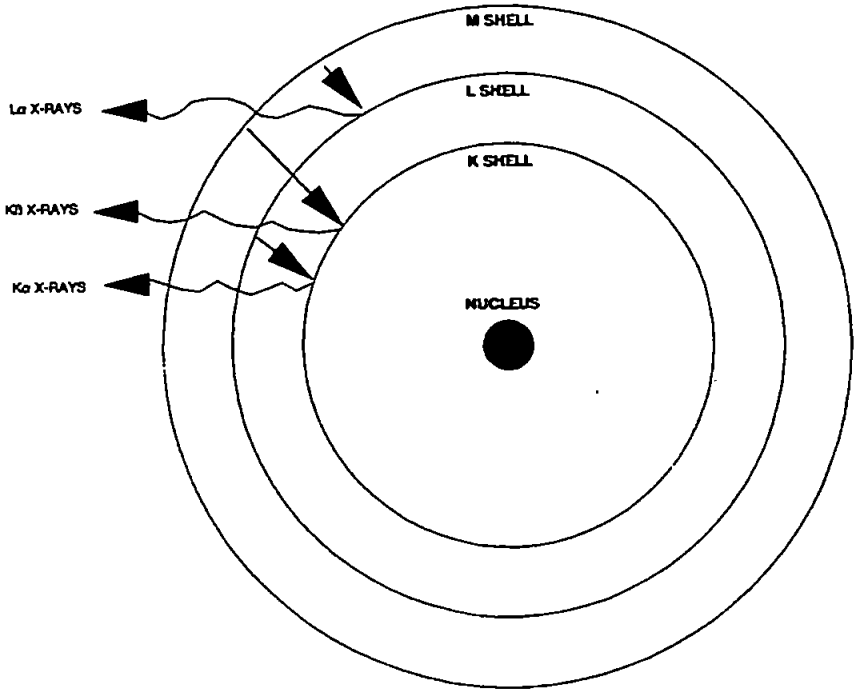

Figure A1.3: Electron Transactions in an Atom.

APPENDIX 2

BRINE COMPOSITION

sodium chloride 274.78 g/l

potassium chloride 1.18 g/l

calcium chloride (hydrated) 6.04 g/l

magnesium chloride 7.53 g/l

sodium sulphate 3.55 g/l

APPENDIX 3

MERCURY POROSIMETRY

A3.1 Apparatus

Mercury Intrusion/extrusion cycles were performed at the British Gas, London research station on a Ruska 1059 porosimeter. The apparatus is shown in Figure A3.1. The apparatus consists of a 100cc Ruska volumetric pump(1). The pump has a sliding vernier scale (2) for volume measurement. A high pressure sample chamber (3) (Penatrometer) is attached to the pump. The sample chamber can accommodate samples up to 2.5cm wide and 3.75cm long. The lid of the sample chamber is secured by a screw ring (4) which forms a pressure/vacuum tight seal. The lid has an observation window for viewing mercury level relative to a reference mark. The sample chamber lid is connected to the pressure regulator assembly by a high pressure hose (5). The assembly consists of three pressure gauges (6,7 & 8), covering 0-2000PSI, a vacuum gauge (9) and five pressure control valves (10-14). Pressure is varied by vacuum pump and nitrogen.

A3.2 Method

The pump piston is wound in so that the mercury is level with the reference mark. The vernier scale is zeroed, pump piston is wound back and sample chamber is evacuated down to pressures of 2×10^{-5}atm. The mercury is brought up to the reference mark (15), the reading on the vernier scale being the bulk volume of the sample, plus mercury expansion volume (See Calibration). The scale is re-zeroed, and pressure increased by venting the atmosphere control valve (14). The first intrusion point is usually at about 0.02atm, corresponding to a pore size of 200μm. The small amount of mercury which penetrates the pore space is allowed to reach equilibrium and its volume recorded by bringing the mercury level to the reference mark. Pressure is increased incrementally up to atmospheric pressure, at which point pressure is applied via a nitrogen cylinder up to

MERCURY - INJECTION CAPILLARY PRESSURE APPARATUS, MODIFIED RUSKA 1059

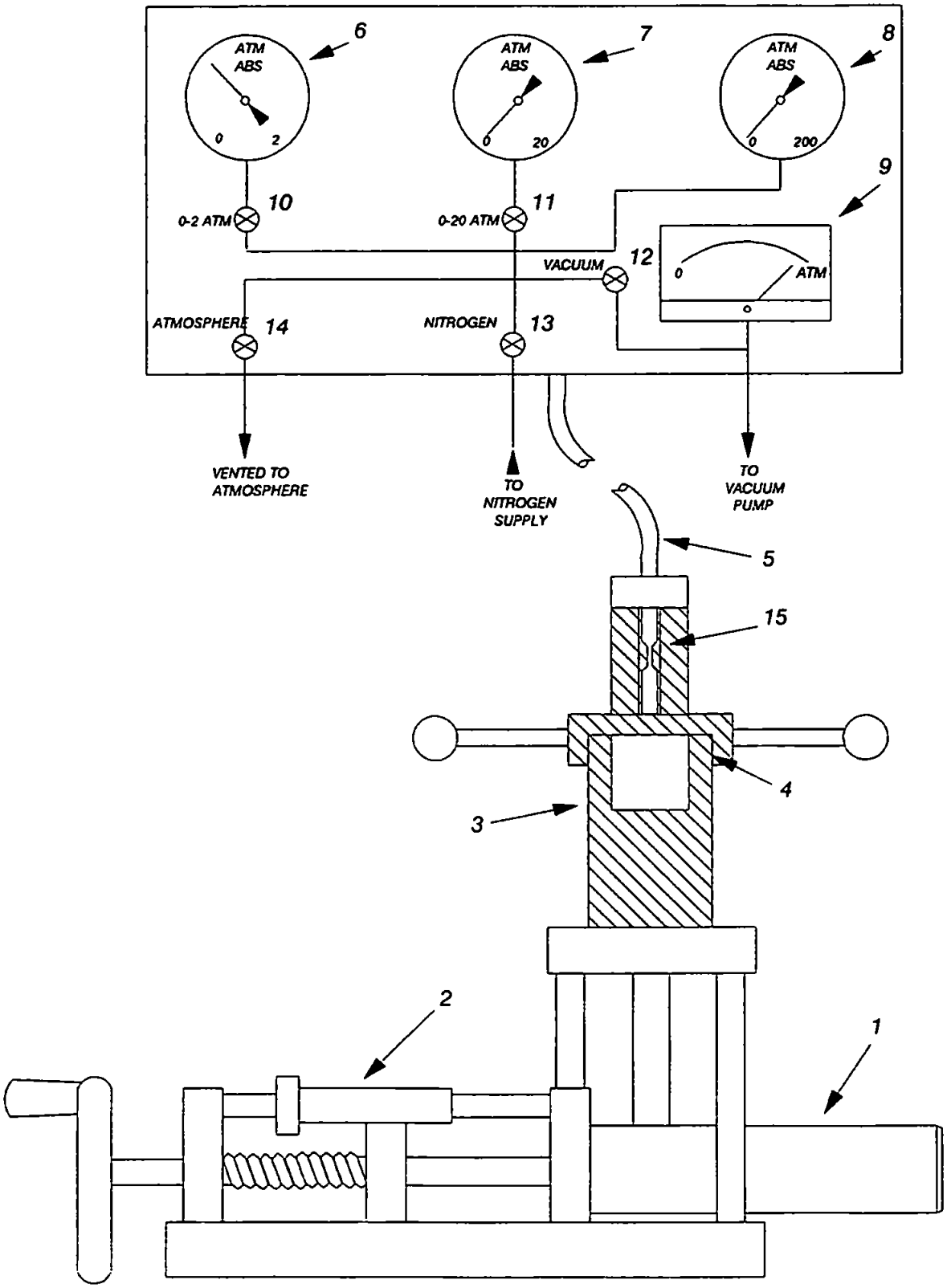

FIGURE A3.1: Mercury Injection Capillary Pressure Apparatus, a Modified Ruska 1059.

120 atm (0.12 μm by the Washburn Equation).

The mercury extrusion is measured by isolating the nitrogen at valve 13 and venting to atmosphere at valve 14. Extrusion at sub-atmospheric pressure is achieved by closing valve 14, opening vacuum valve 12 slowly whilst vacuum pump is on. Equilibrium at each increase or decrease in pressure is very important. Sometimes this may take up to half an hour, thus each full intrusion/extrusion cycle takes about one day to collect. Further extrusion of mercury during prolonged low pressure exposure indicates that equilibrium during extrusion can take a long time to attain.

A3.3 Calibration

The porosimeter must be calibrated prior to any experiment. A complete pressurization and depressurization of the mercury without a sample is performed. The column with each pressure change is noted as in a normal experiment. Thus the compression of mercury and expansion of the sample chamber with pressure increase can be accounted for. The calibration also indicates the volume of mercury forced into any "crevices" during pressurization. Figure A3.2 shows the calibration curves used for the fourteen mercury porosimetry experiments performed. The upper graph shows two calibration curves applied to the first three samples analyzed. The calibration curves are different because the sample chamber contained different volumes of mercury at each calibration. After the first three experiments the presence of a calibration hysteresis loop became evident (Bottom Graph : Figure A3.2).

Hysteresis occurs because small amounts of mercury become trapped within crevices in the sample chamber. The bulk of the mercury is trapped within the sample chamber screw thread. The calibration hysteresis does not form a closed loop, trapping is irreversible. The trapped mercury volume is very small ($0.017cm^3$), but it is important to know this volume so that accurate mercury residuals can be calculated for each sample.

PRESSURE-VOLUME CALIBRATION DATA

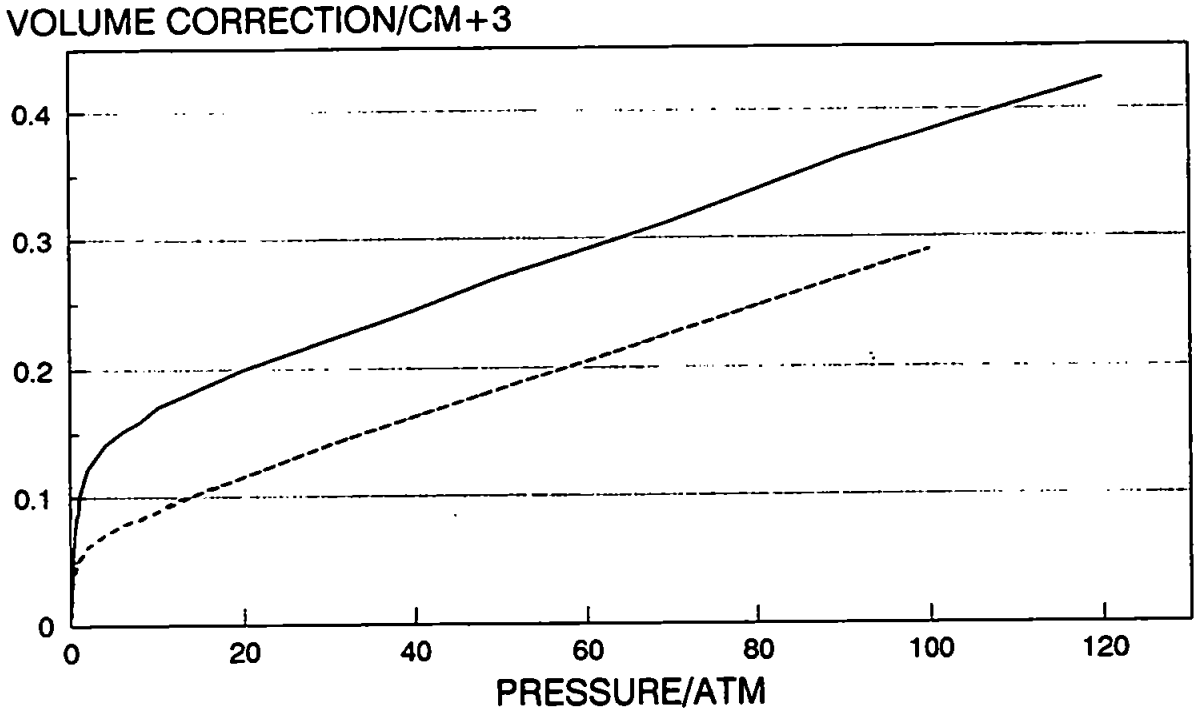

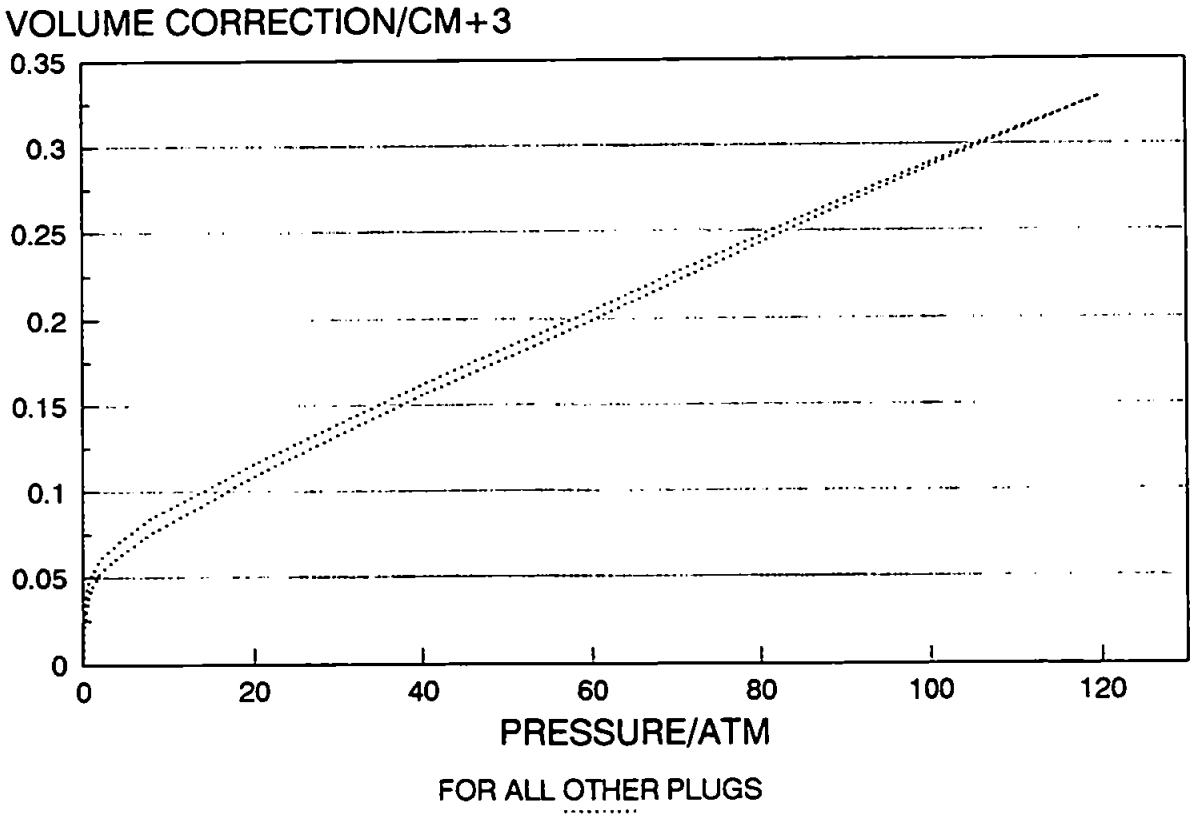

FIGURE A3.2: Pressure-Volume Calibration Data.

APPENDIX 4

GEO-EAS AVAILABILITY AND USAGE

The Geo-Eas software is entirely within the public domain and can be obtained from

Evan J. Englund (Geo-Eas)

USEPA EMSL-LV, EAD

P O Box 93478

Las Vegas

NV 89193-3478

U.S.A.

The source code is written in Fortran 77, and will run off any personal computer with a DOS facility. The program consists of two parts, Prevar and Vario. Prevar sorts the co-ordinates of the variable into paris. For this analysis Prevar uses the x and y co-ordinates of each feature centre of gravity to calculate the distances between every feature. The distances between each pair of features is saved in a pair comparison file. The Vario part of the programm uses the pair comparison file to calculate the estimate between every feature pair. The total analysis distance is divided into specified distances, termed Lag Distances.The estimate between all pairs of features within a specific Lag Distance group are calculated and the mean of these values is also calculated. The Geo-Eas programm quotes mean Lag Distance in each Lag Distance group and mean estimate, these are the two data points used to plot the variogram.

APPENDIX 5

PEAK AREA AGAINST TIME PLOTS FOR CLASHACH SAMPLE

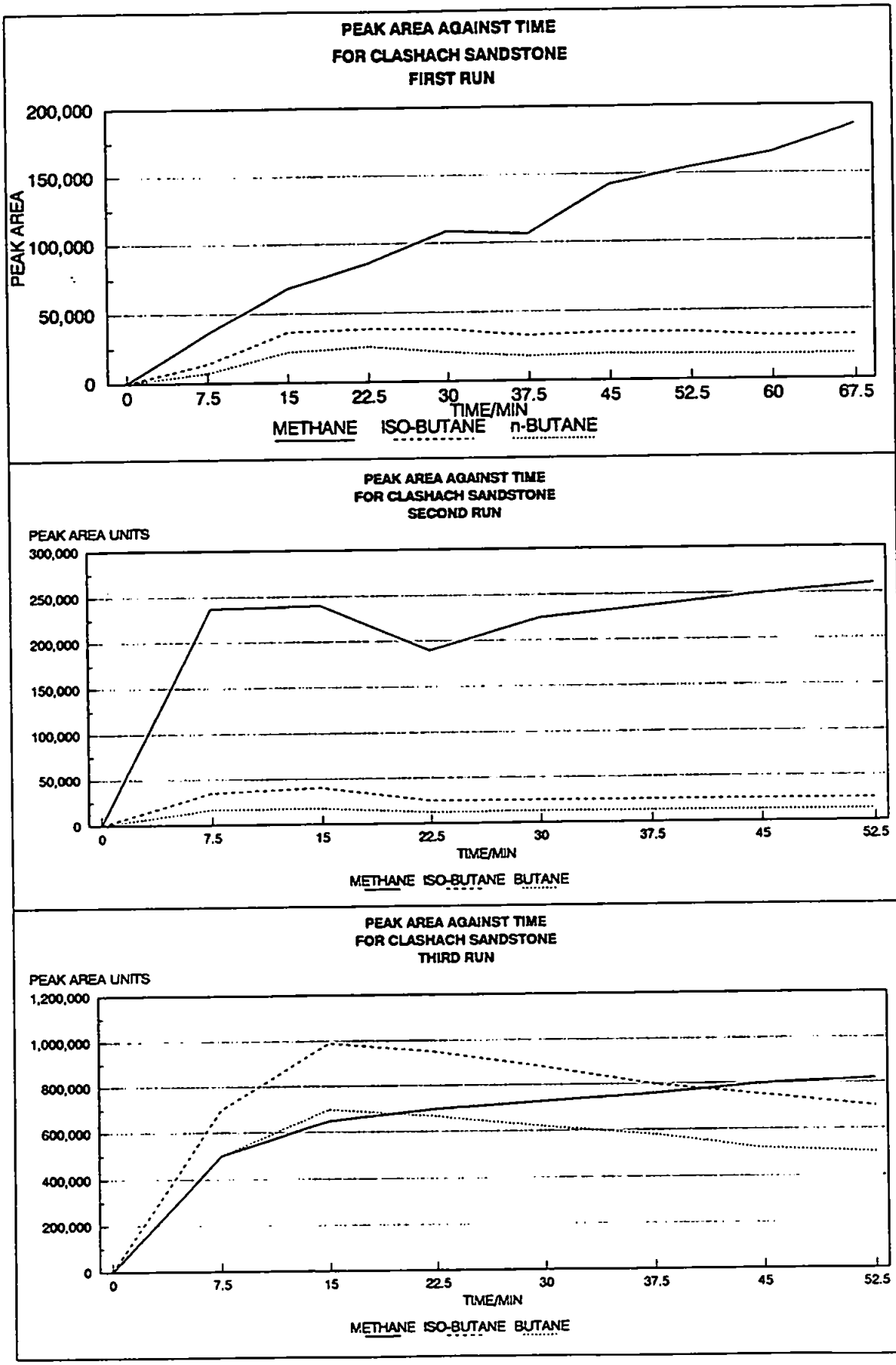

FIGURE A5.1: Peak Area Against Time Plots for Clashach.

PEAK AREA AGAINST TIME PLOTS FOR CLASHACH SAMPLE

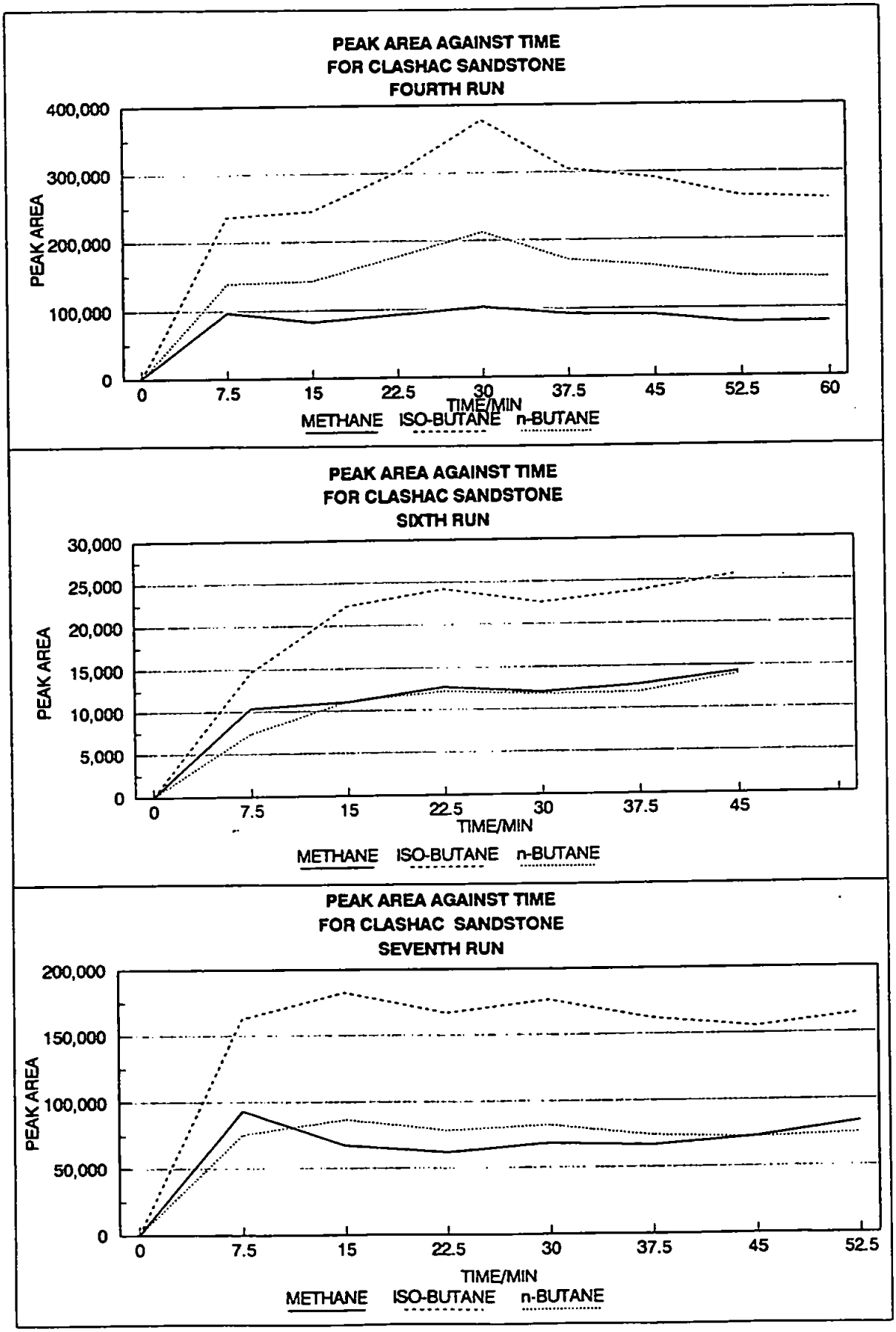

FIGURE A5.2: Peak Area Against Time Plots for Clashach.

PEAK AREA AGAINST TIME PLOTS FOR SAMPLE 212A

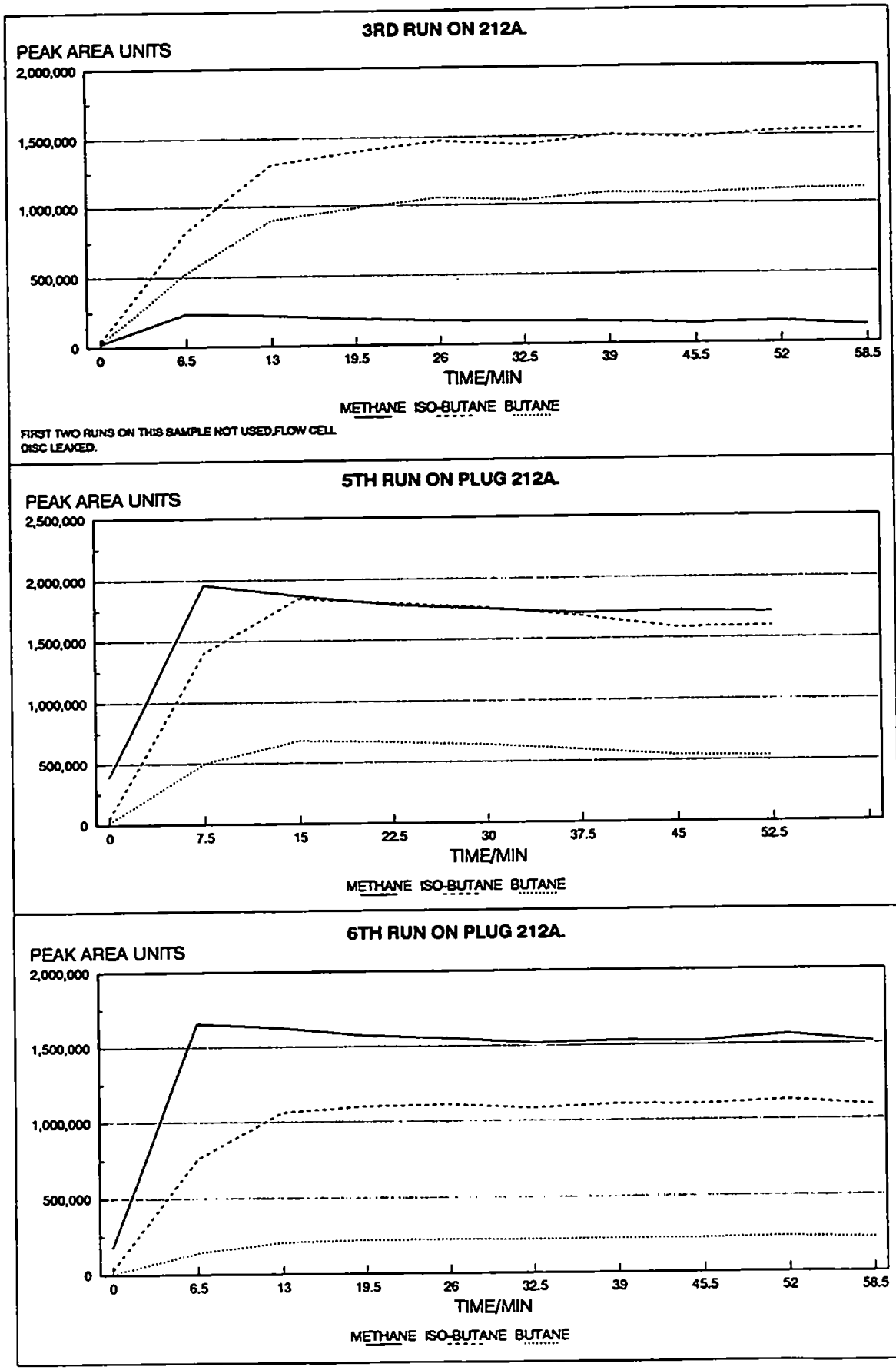

FIGURE A5.3: Peak Area Against Time Plots for Sample 212A.

PEAK AREA AGAINST TIME PLOTS FOR SAMPLE 212A

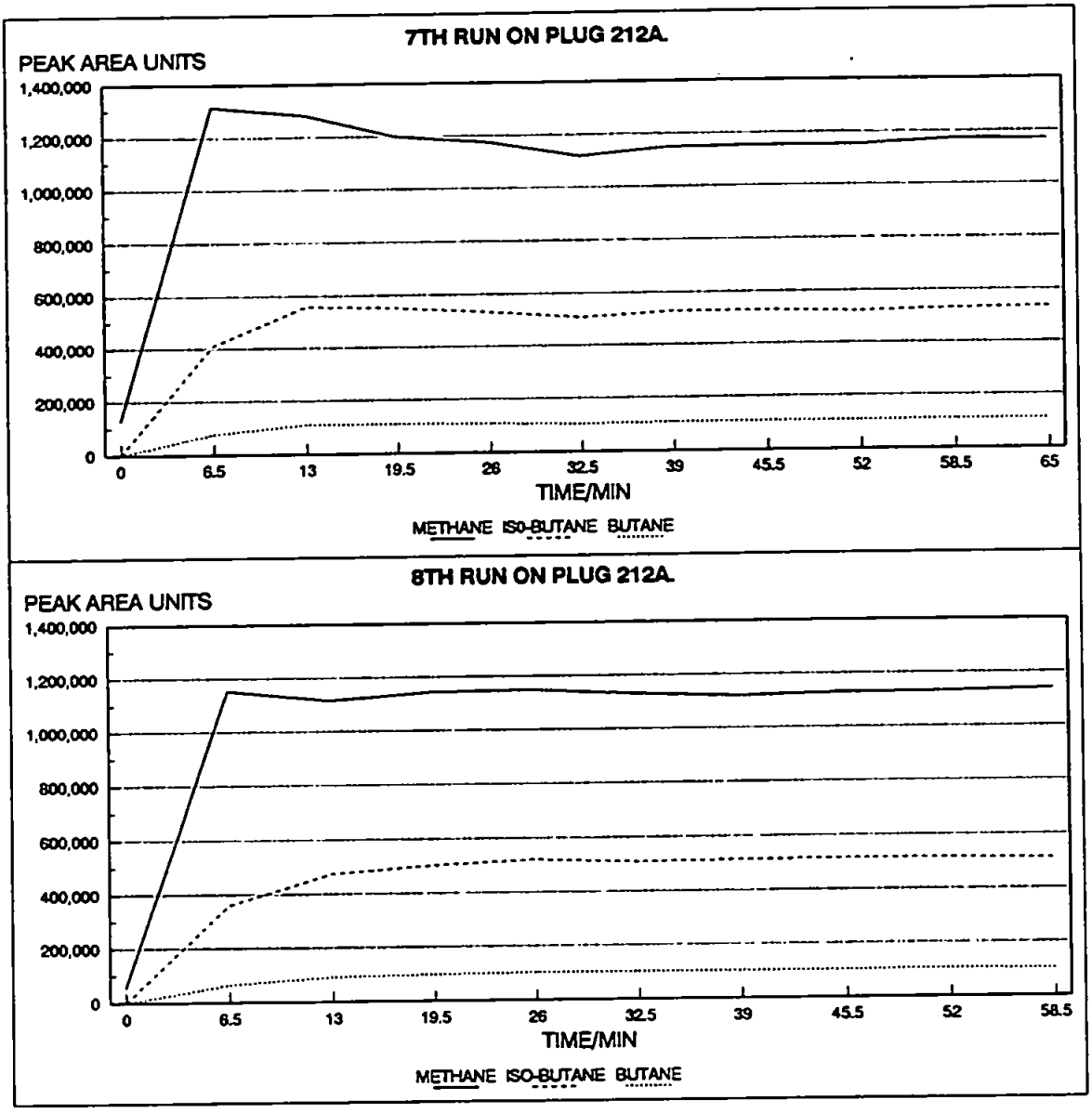

FIGURE A5.4: Peak Area Against Time Plots for Sample 212A.

PEAK AREA AGAINST TIME PLOTS FOR SAMPLE 250A

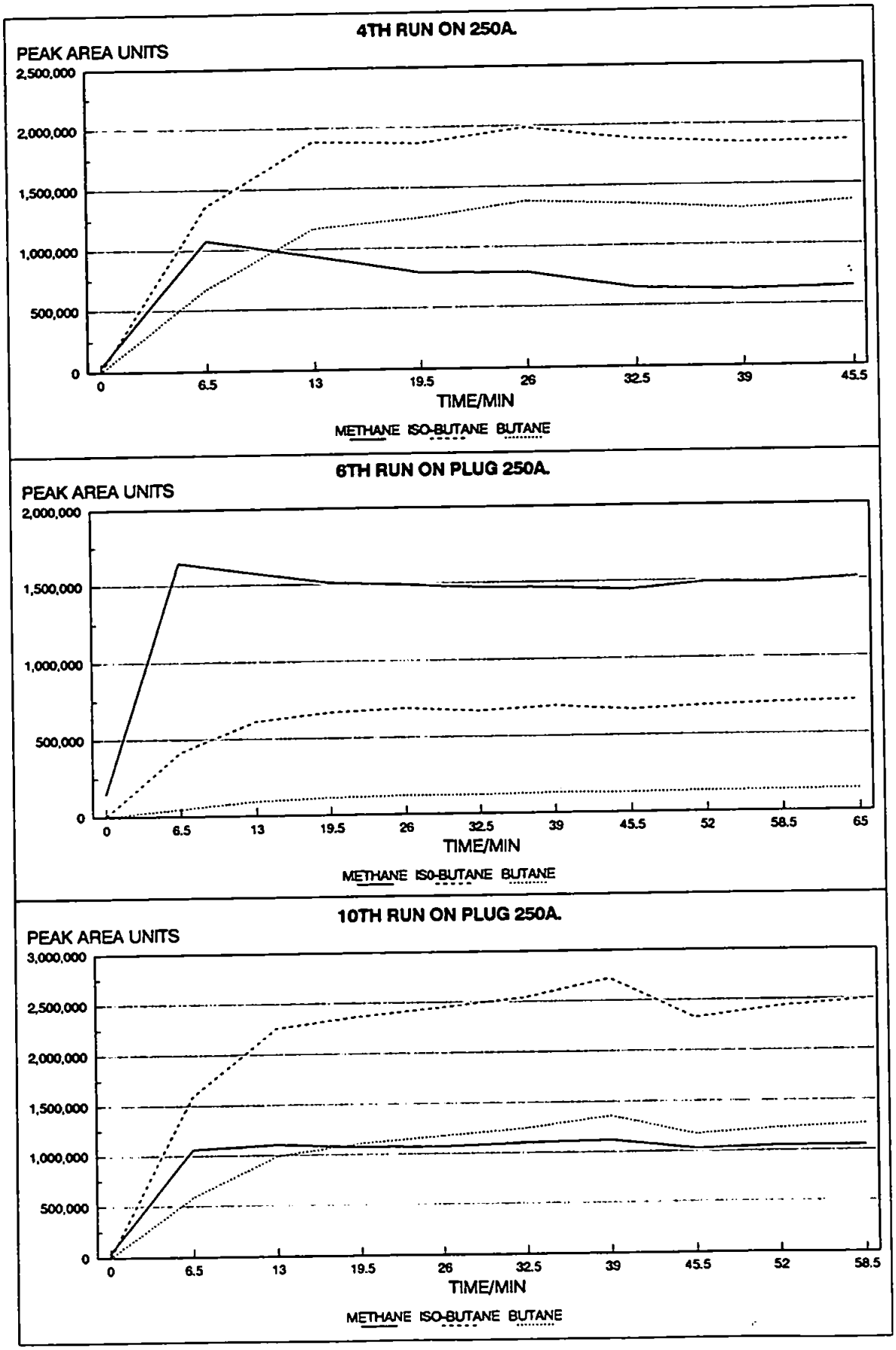

FIGURE A5.5: Peak Area Against Time Plots for Sample 250A.

PEAK AREA AGAINST TIME PLOTS FOR SAMPLE 250A

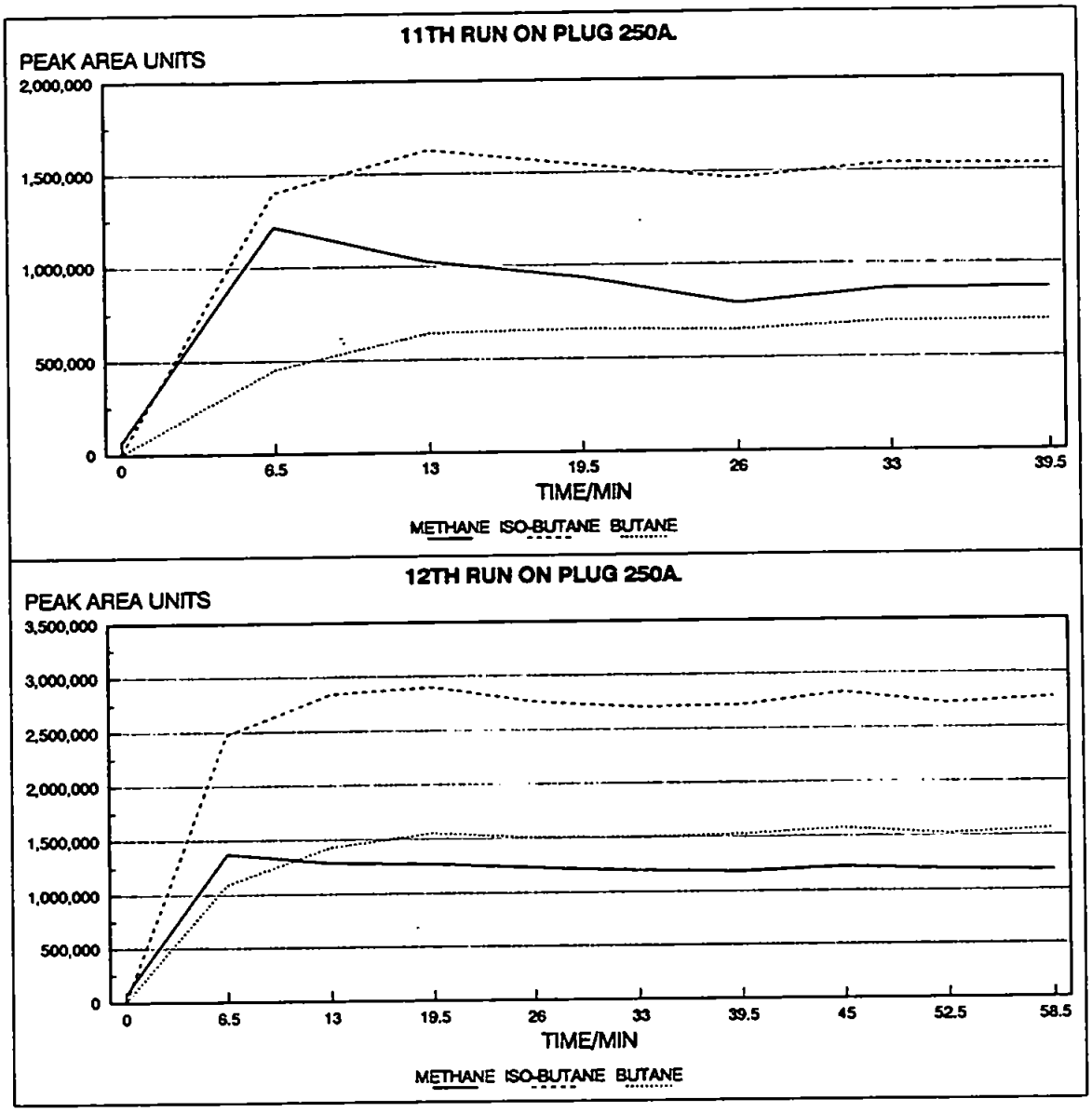

FIGURE A5.6: Peak Area Against Time Plots for Sample 250A.

PEAK AREA AGAINST TIME PLOTS FOR SAMPLE 250E

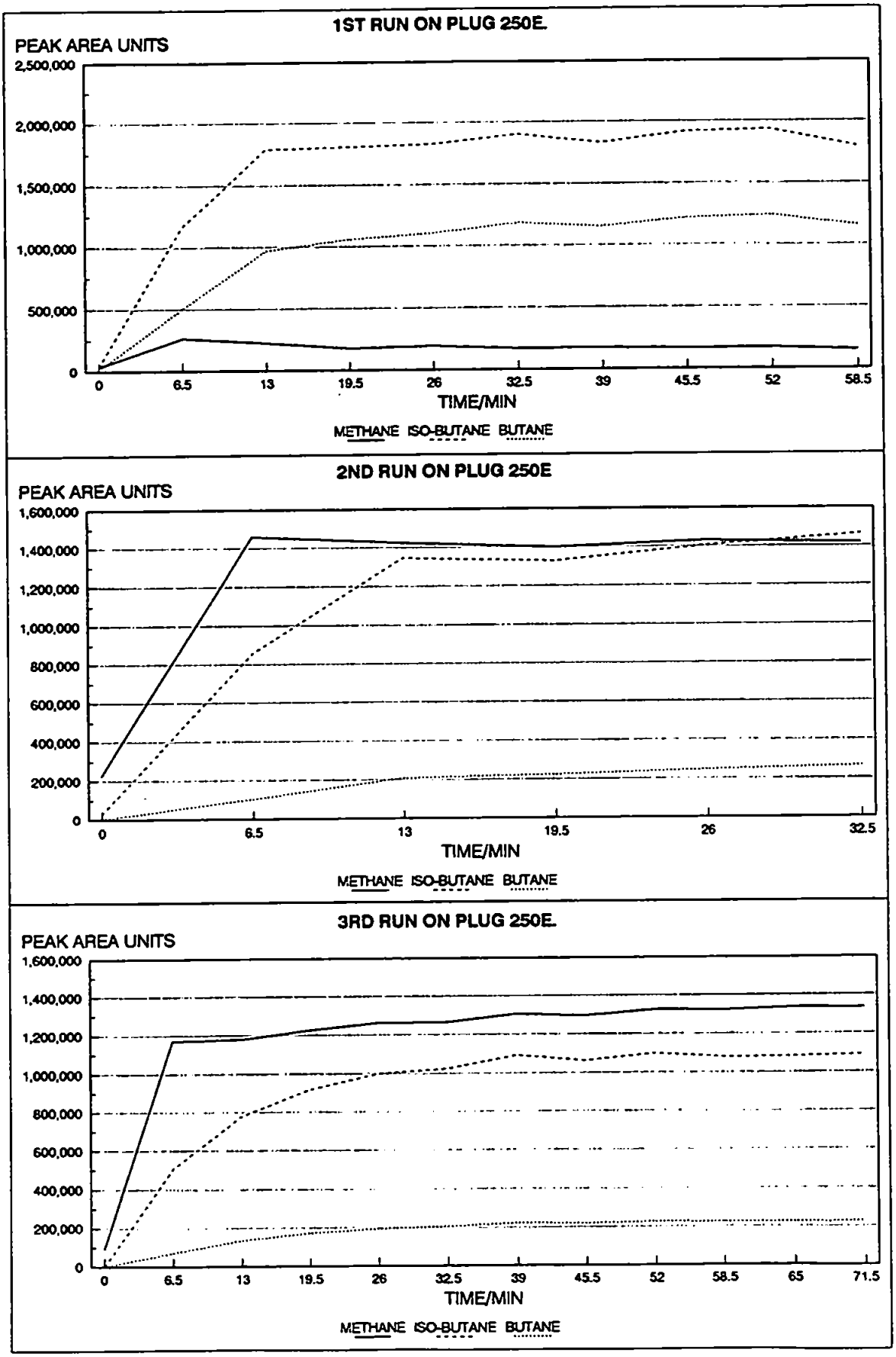

FIGURE A5.7: Peak Area Against Time Plots for Sample 250E.

PEAK AREA AGAINST TIME PLOTS FOR SAMPLE 250E

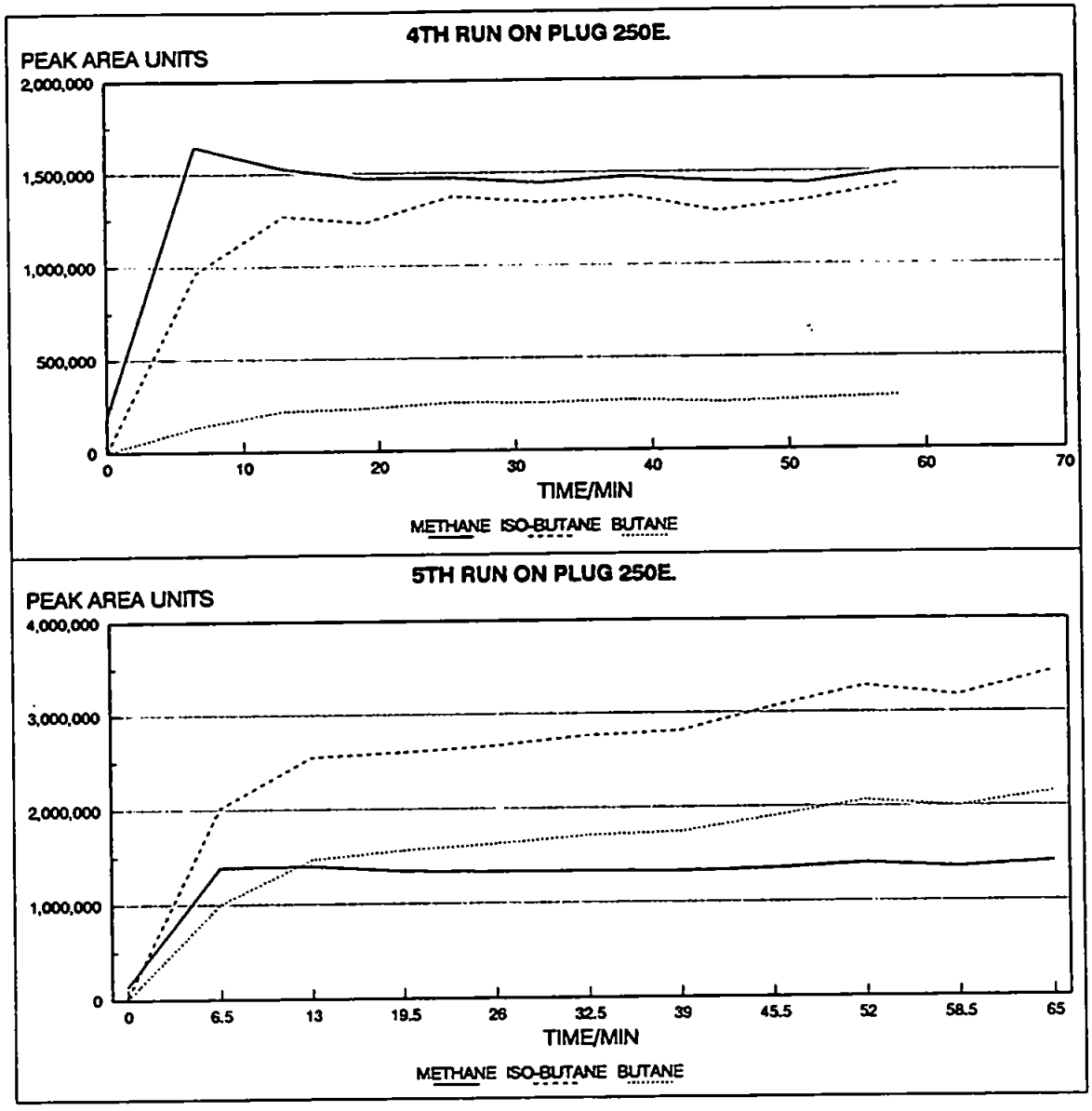

FIGURE A5.8: Peak Area Against Time Plots for Sample 250E.

PEAK AREA AGAINST TIME PLOTS FOR SAMPLE 490A

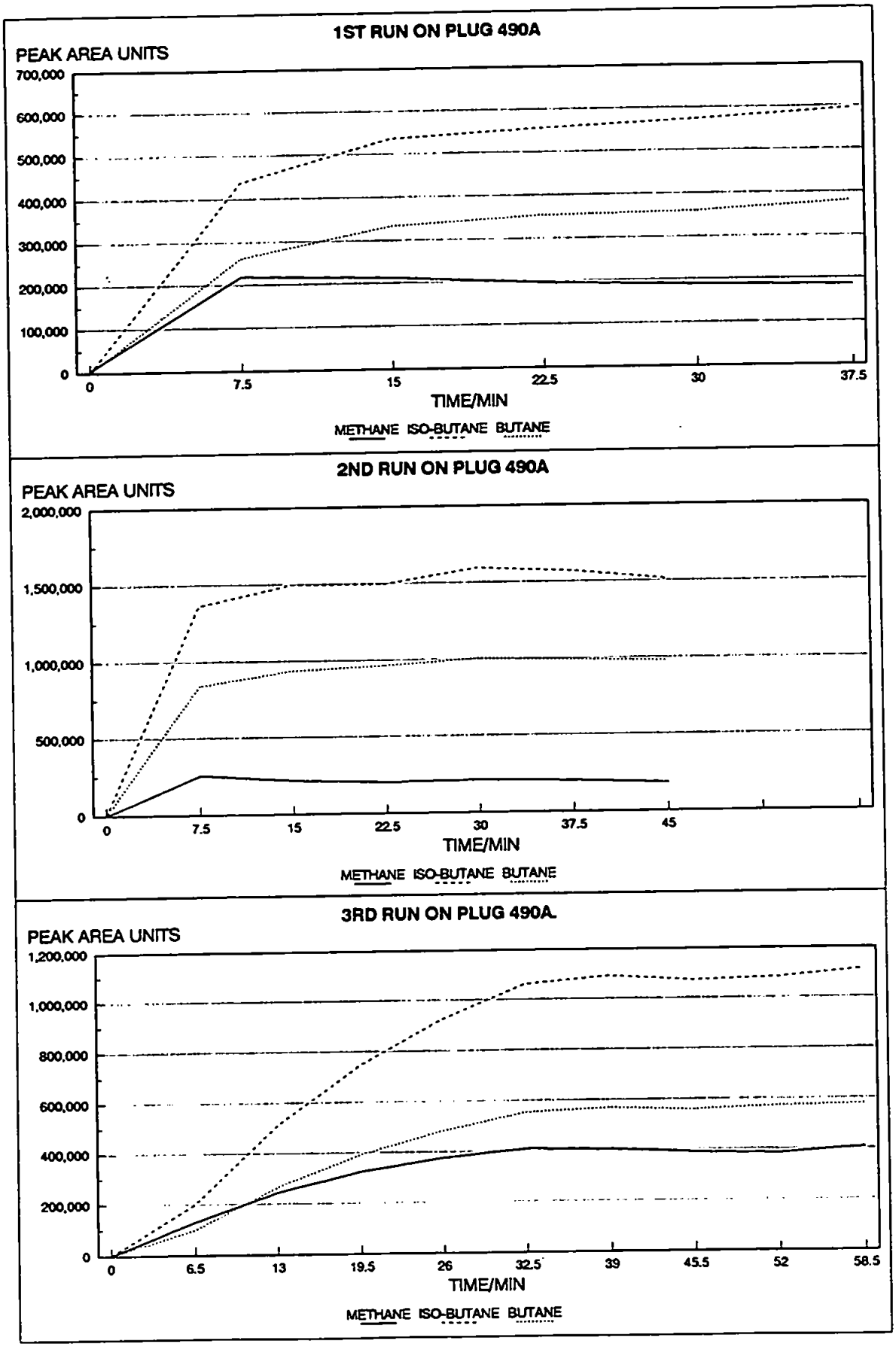

FIGURE A5.9: Peak Area Against Time Plots for Sample 490A.

PEAK AREA AGAINST TIME PLOTS FOR SAMPLE 490A

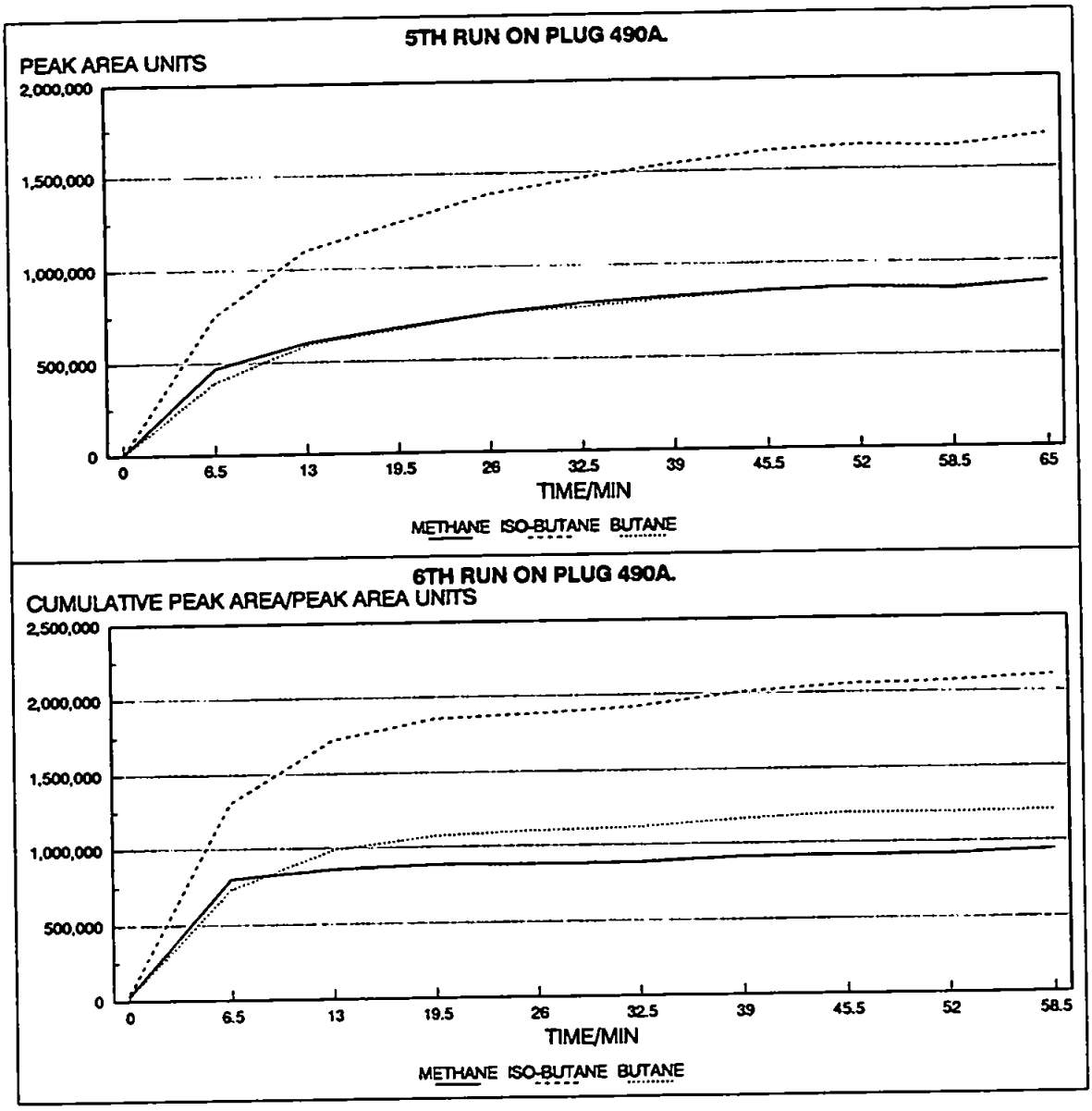

FIGURE A5.10: Peak Area Against Time Plots for Sample 490A.

PEAK AREA AGAINST TIME PLOTS FOR SAMPLE 490B

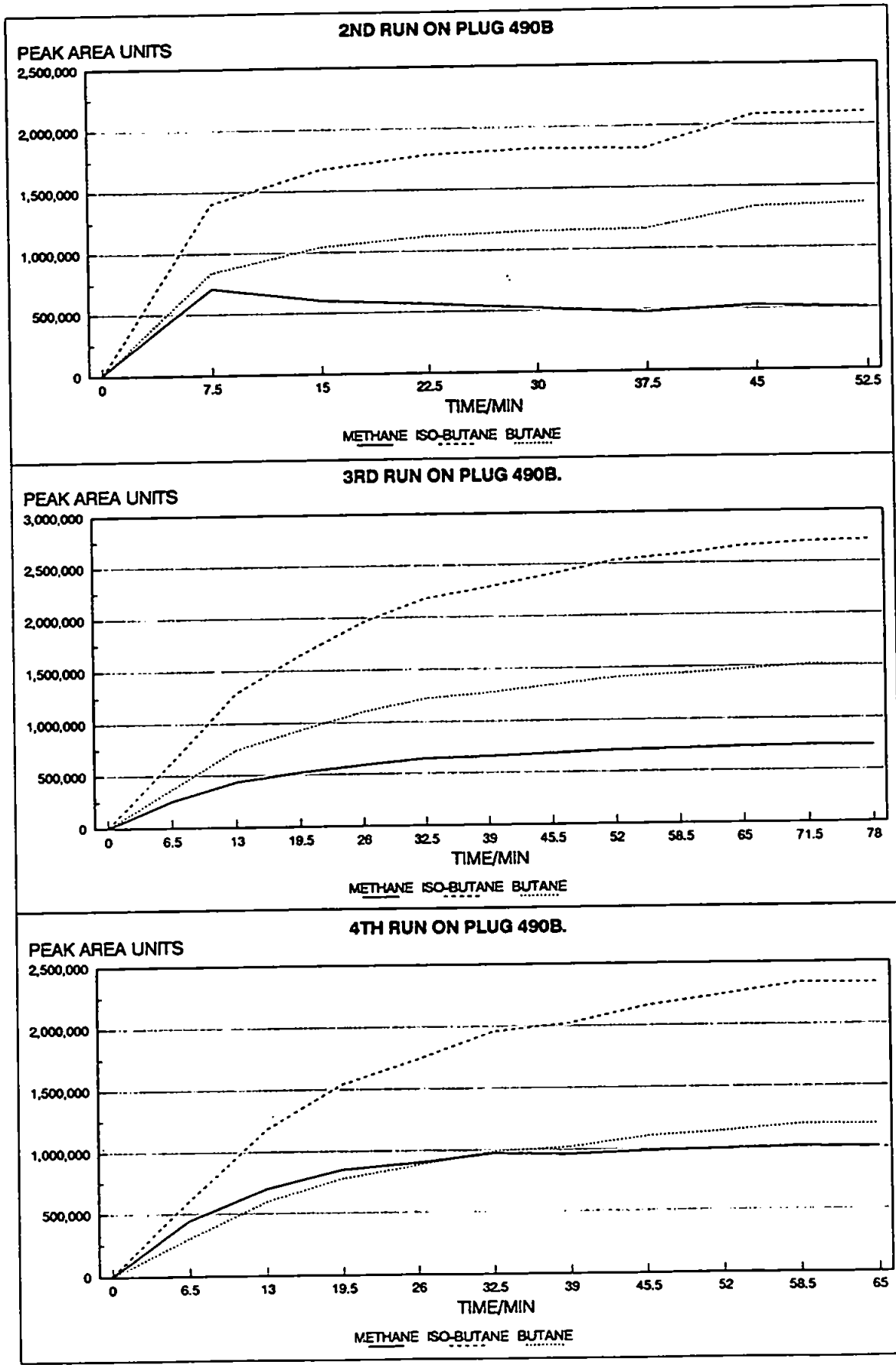

FIGURE A5.11: Peak Area Against Time Plots for Sample 490B.

PEAK AREA AGAINST TIME PLOTS FOR SAMPLE 490B

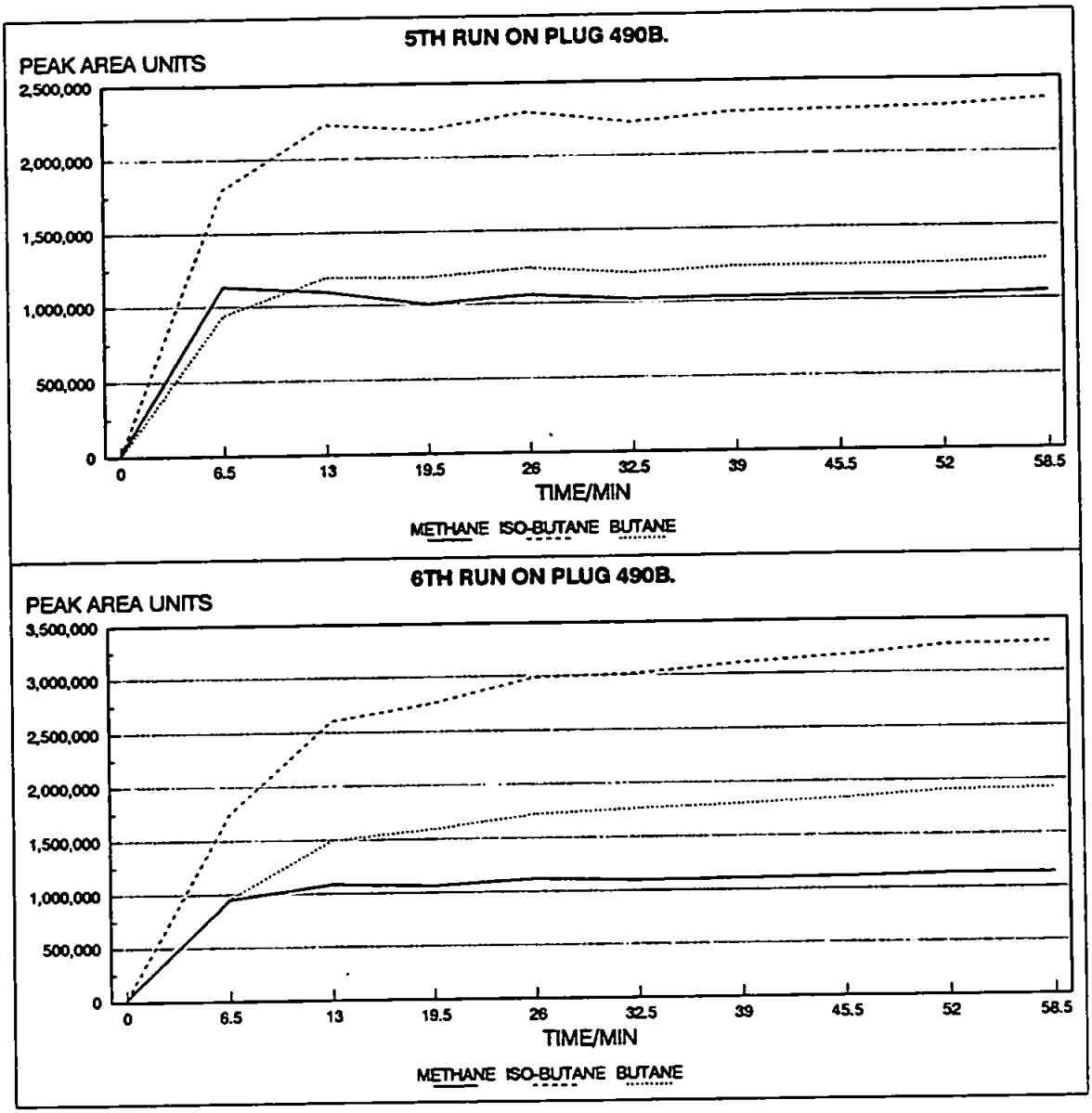

FIGURE A5.12: Peak Area Against Time Plots for Sample 490B.

PEAK AREA AGAINST TIME PLOTS FOR SAMPLE 490C

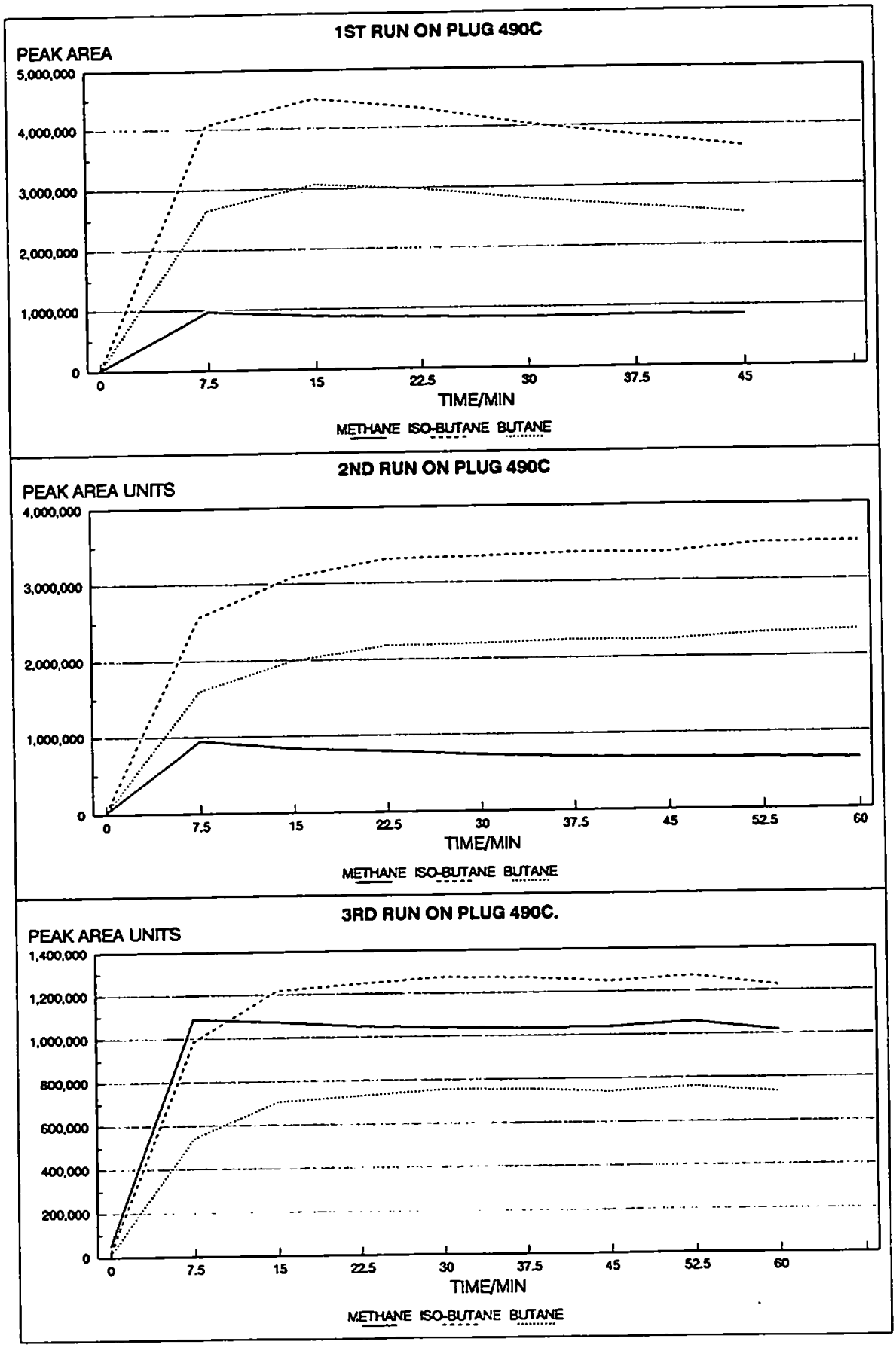

FIGURE A5.13: Peak Area Against Time Plots for Sample 490C.

PEAK AREA AGAINST TIME PLOTS FOR SAMPLE 490C

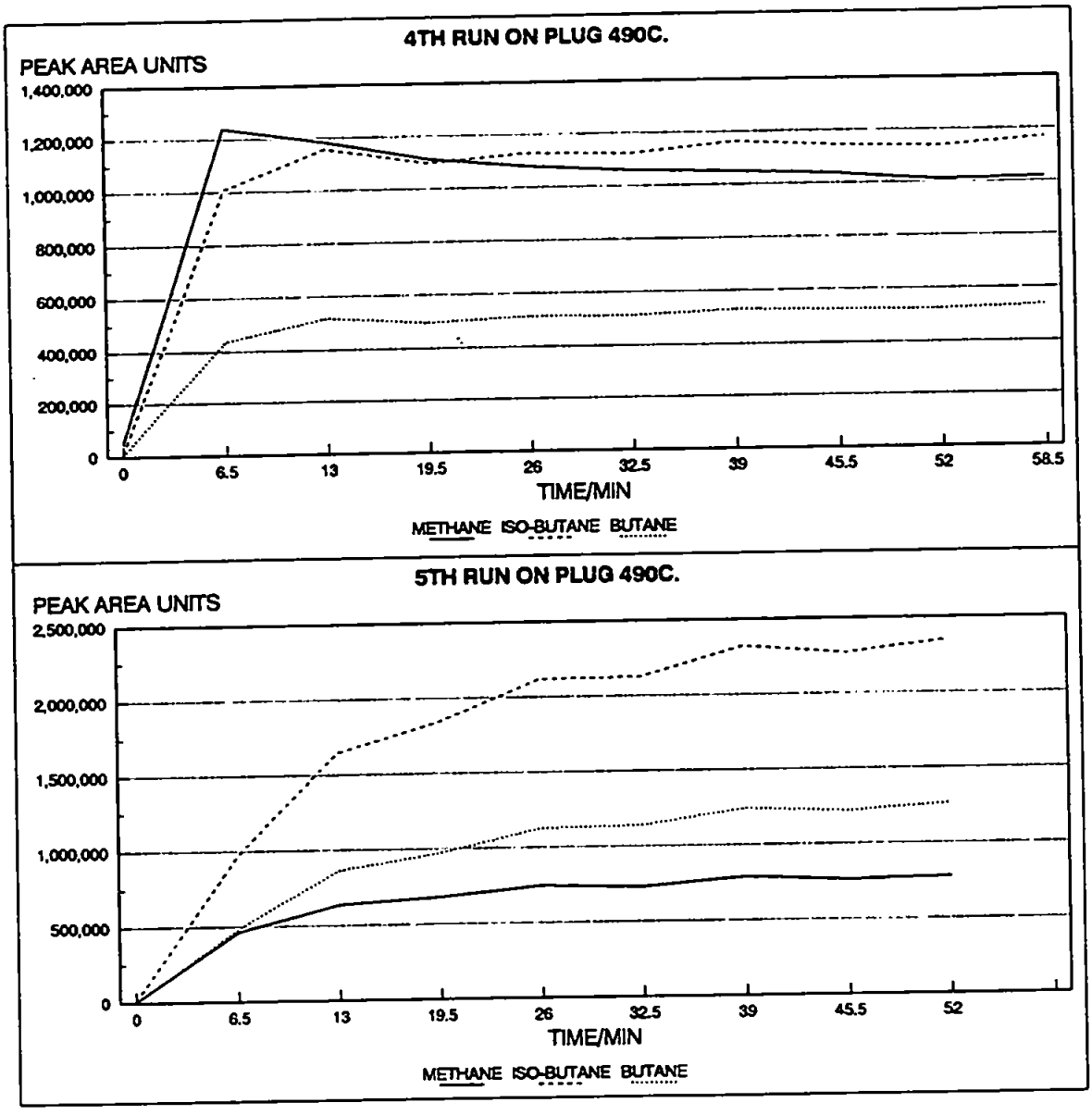

FIGURE A5.14: Peak Area Against Time Plots for Sample 490C.

PEAK AREA AGAINST TIME PLOTS FOR SAMPLE 490D

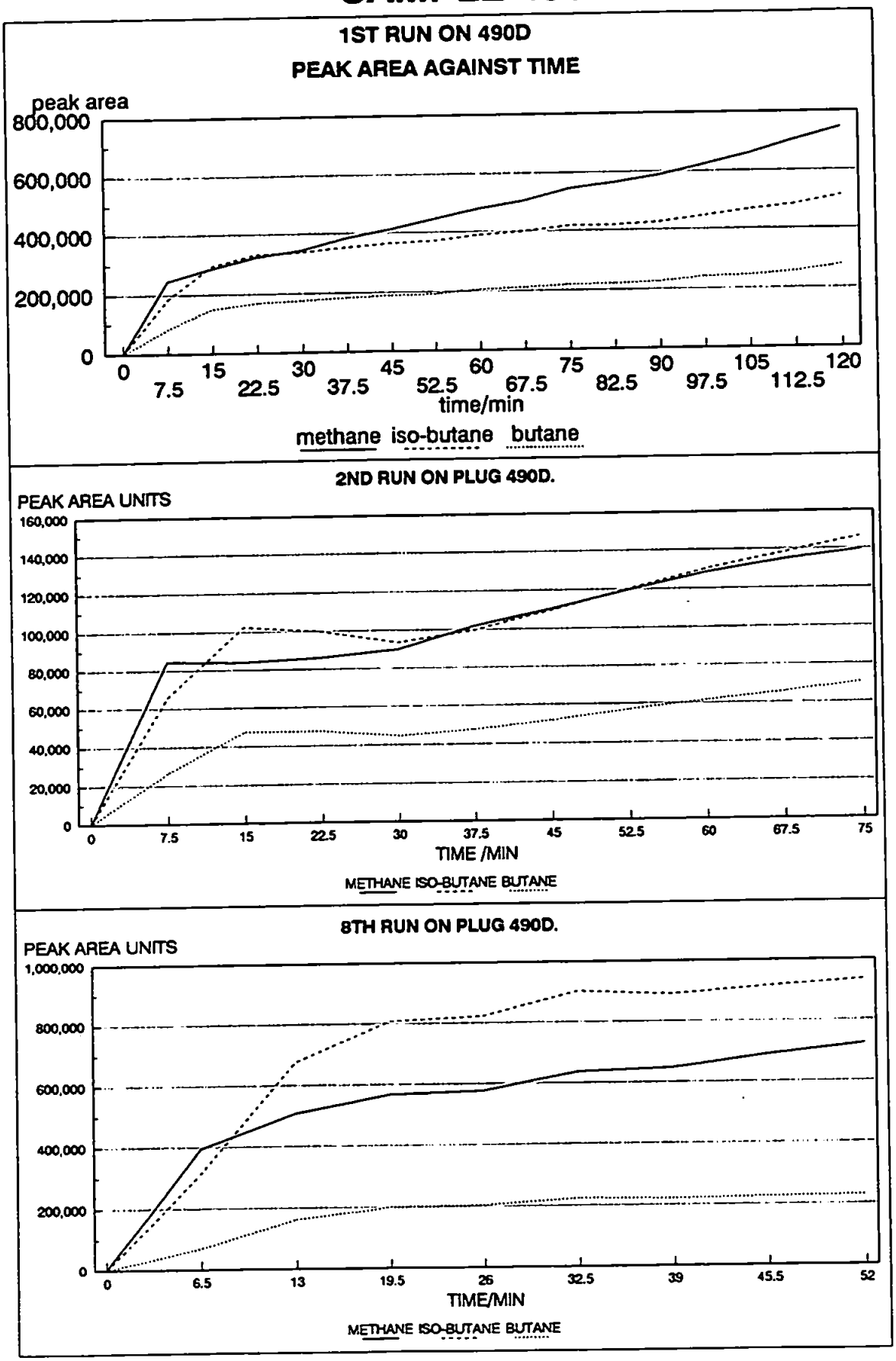

FIGURE A5.15: Peak Area Against Time Plots for Sample 490D.

PEAK AREA AGAINST TIME PLOTS FOR SAMPLE 490D

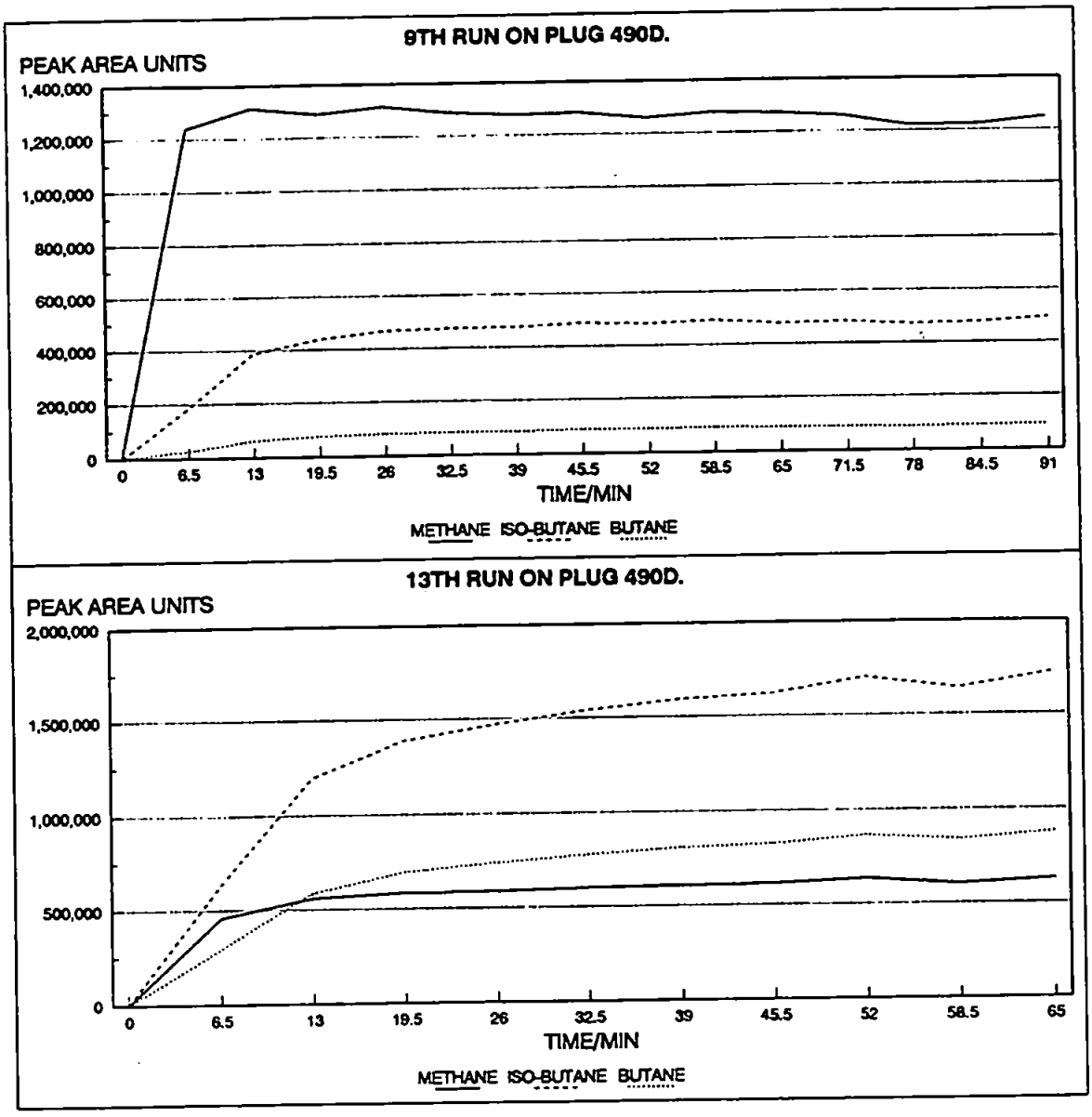

FIGURE A5.16: Peak Area Against Time Plots for Sample 490D.

PEAK AREA AGAINST TIME PLOTS FOR SAMPLE 490E

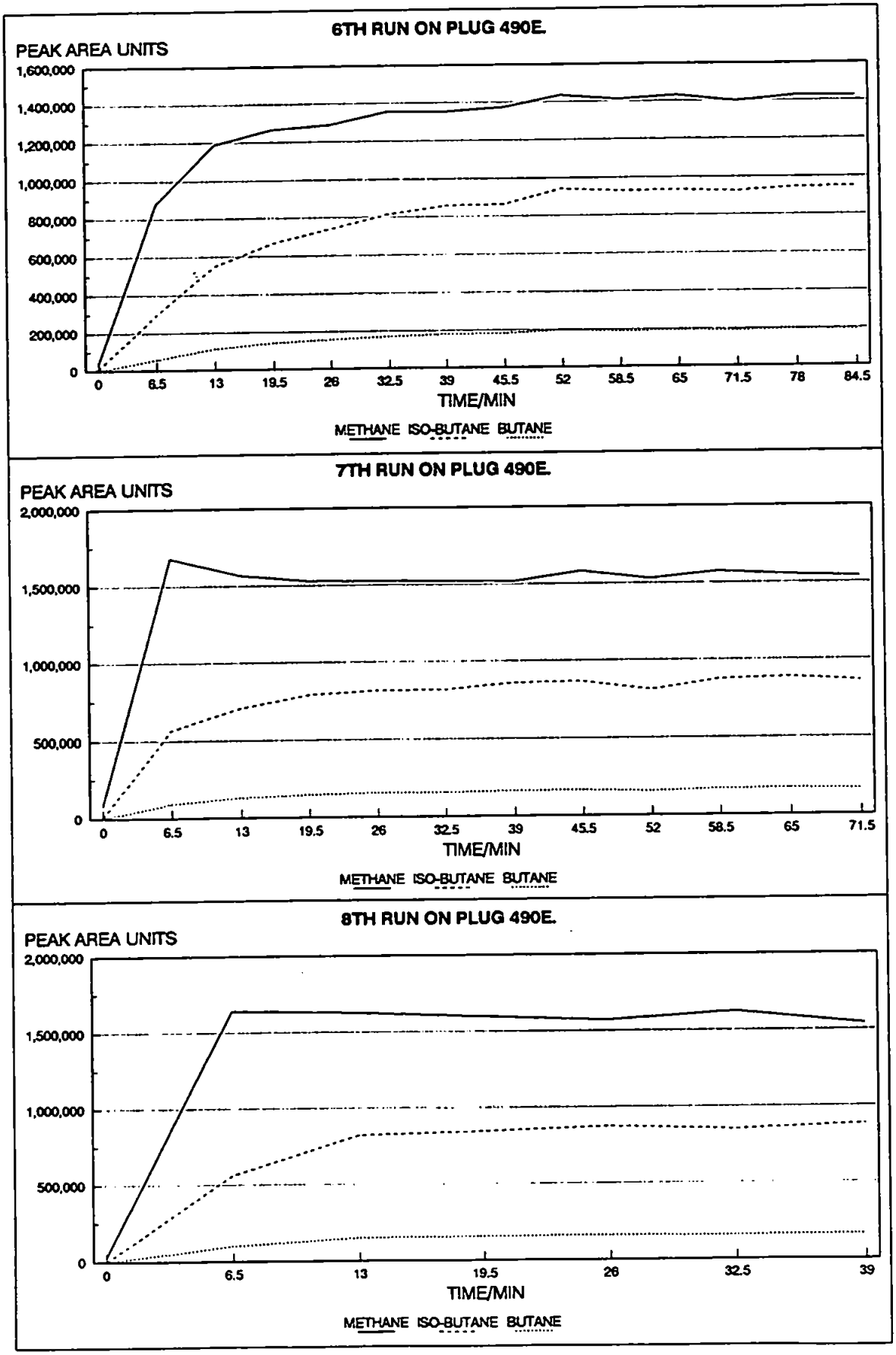

FIGURE A5.17: Peak Area Against Time Plots for Sample 490E.

PEAK AREA AGAINST TIME PLOTS FOR SAMPLE 490E

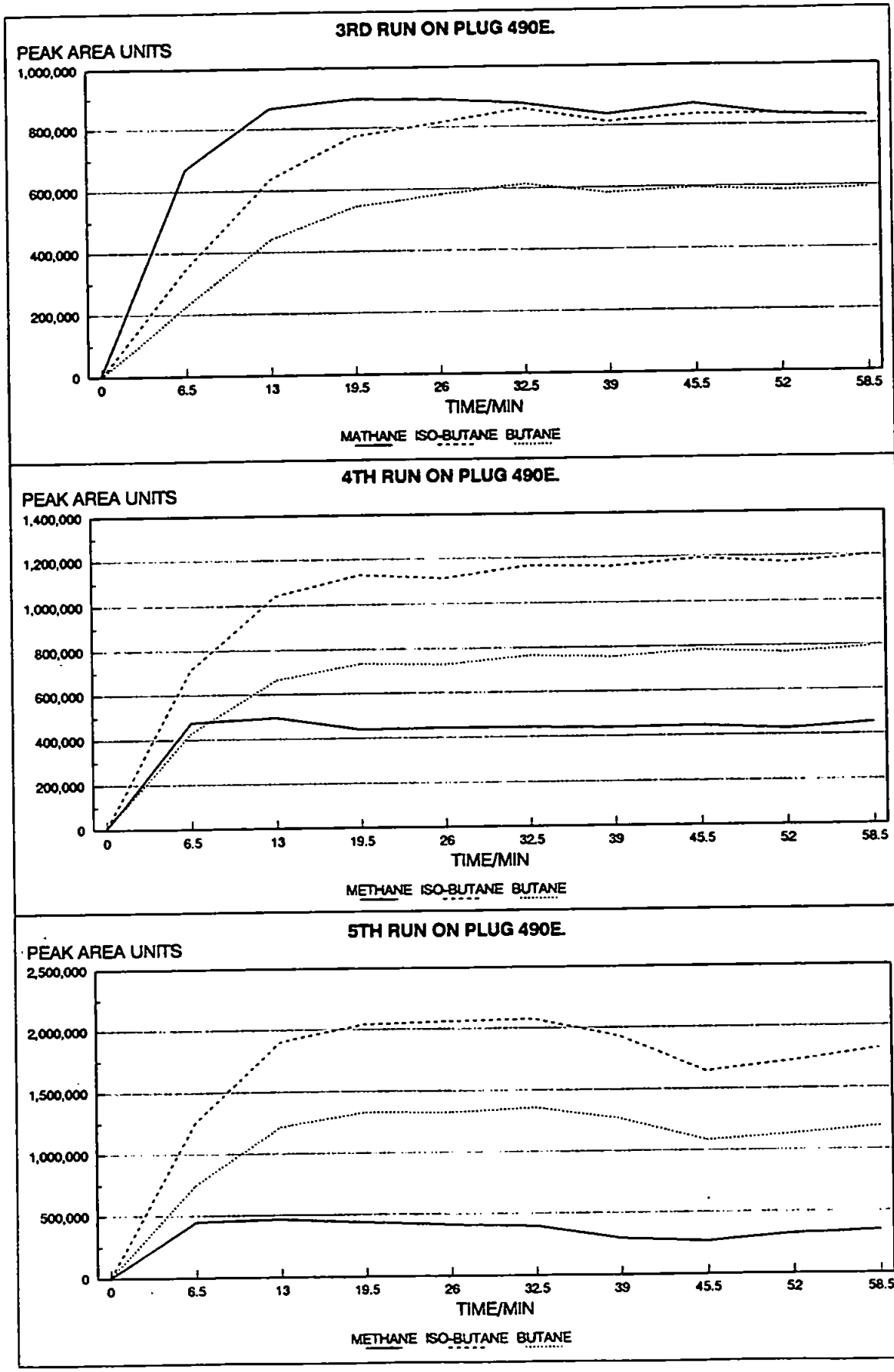

FIGURE A5.18: Peak Area Against Time Plots for Sample 490E.

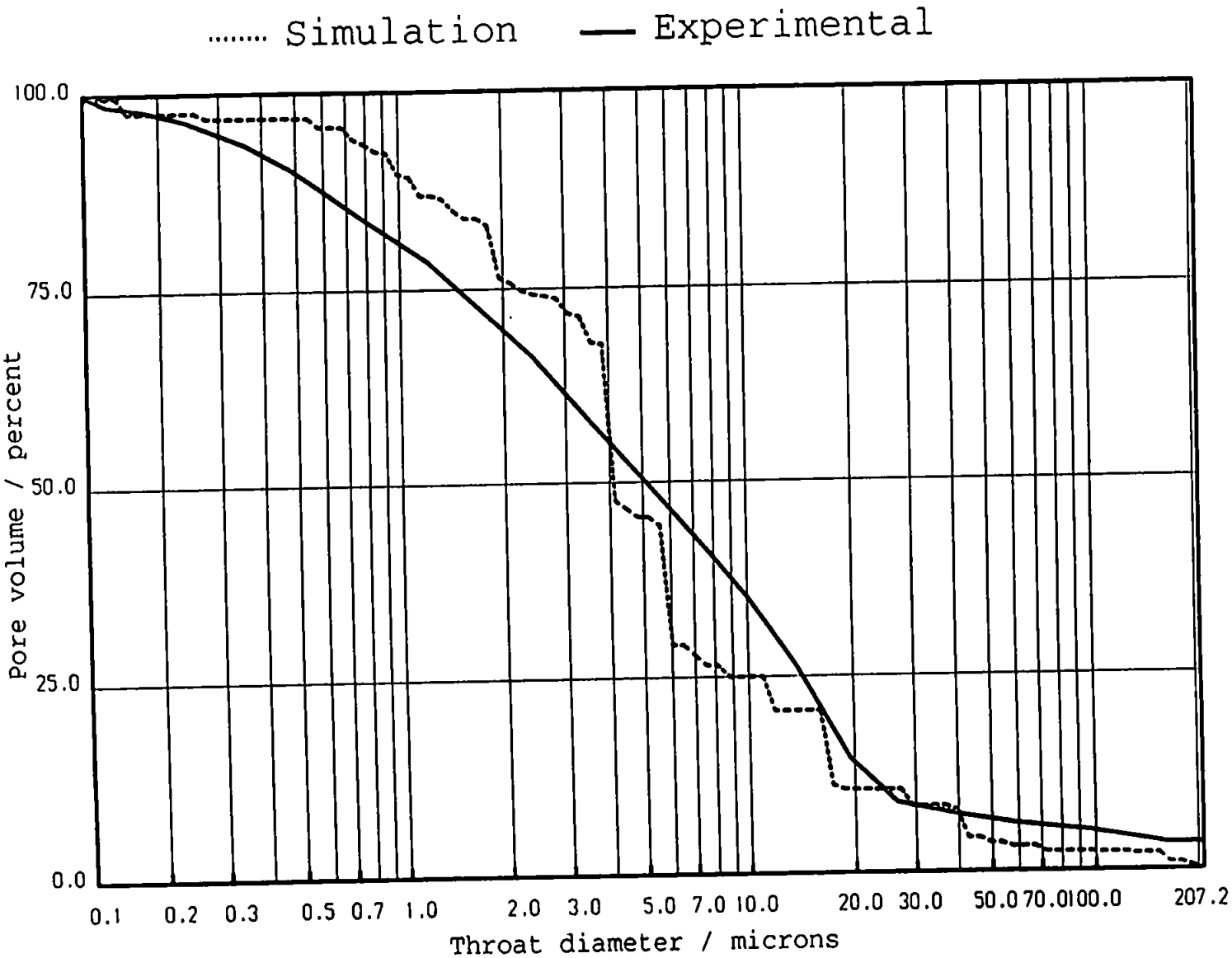

FIGURE A6.1: Experimental and Simulated Mercury Intrusion Curves for Sample 212A.

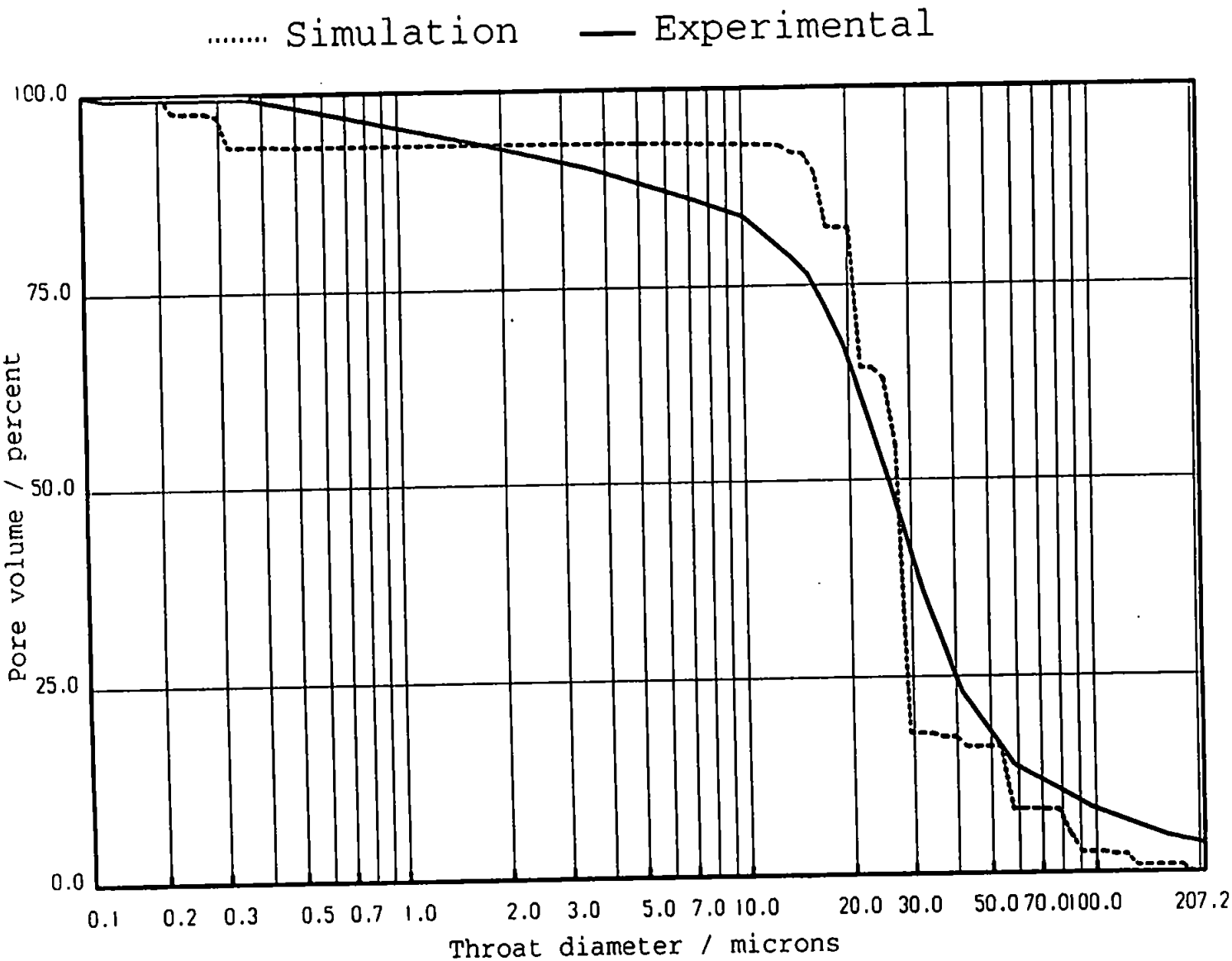

FIGURE A6.2: Experimental and Simulated Mercury Intrusion Curves for Sample 212B.

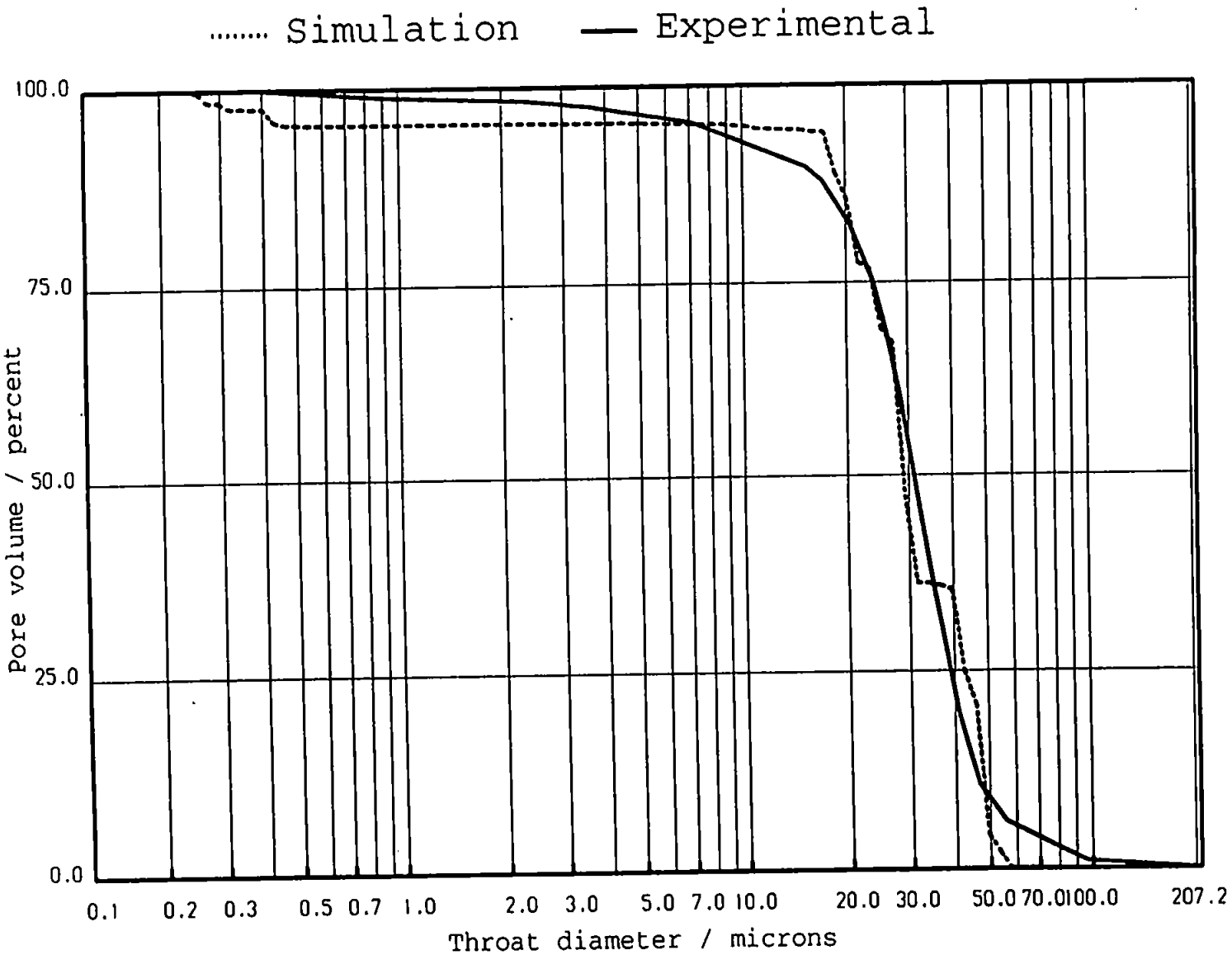

FIGURE A6.3: Experimental and Simulated Mercury Intrusion Curves for Sample 212C.

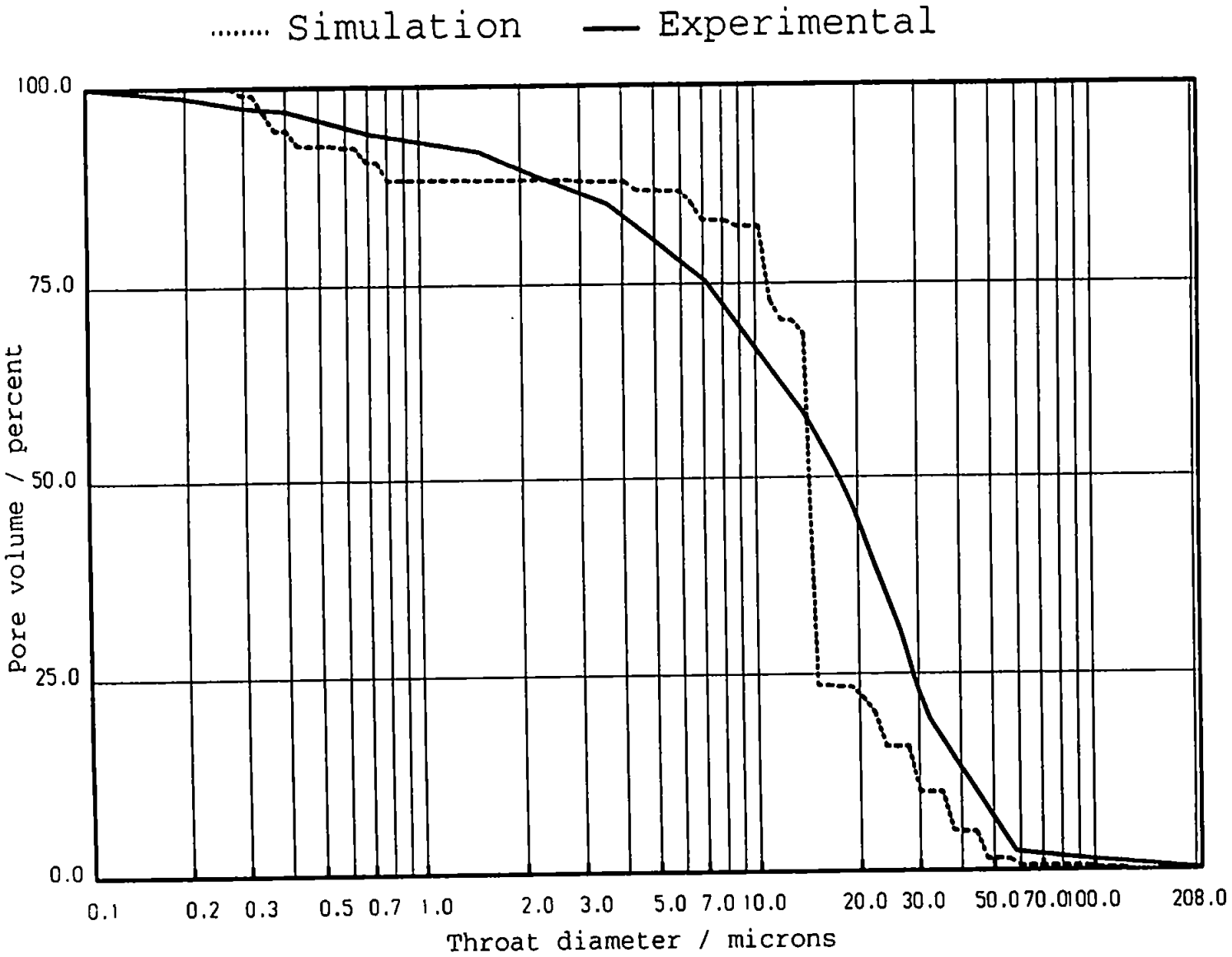

FIGURE A6.4: Experimental and Simulated Mercury Intrusion Curves for Sample 212D.

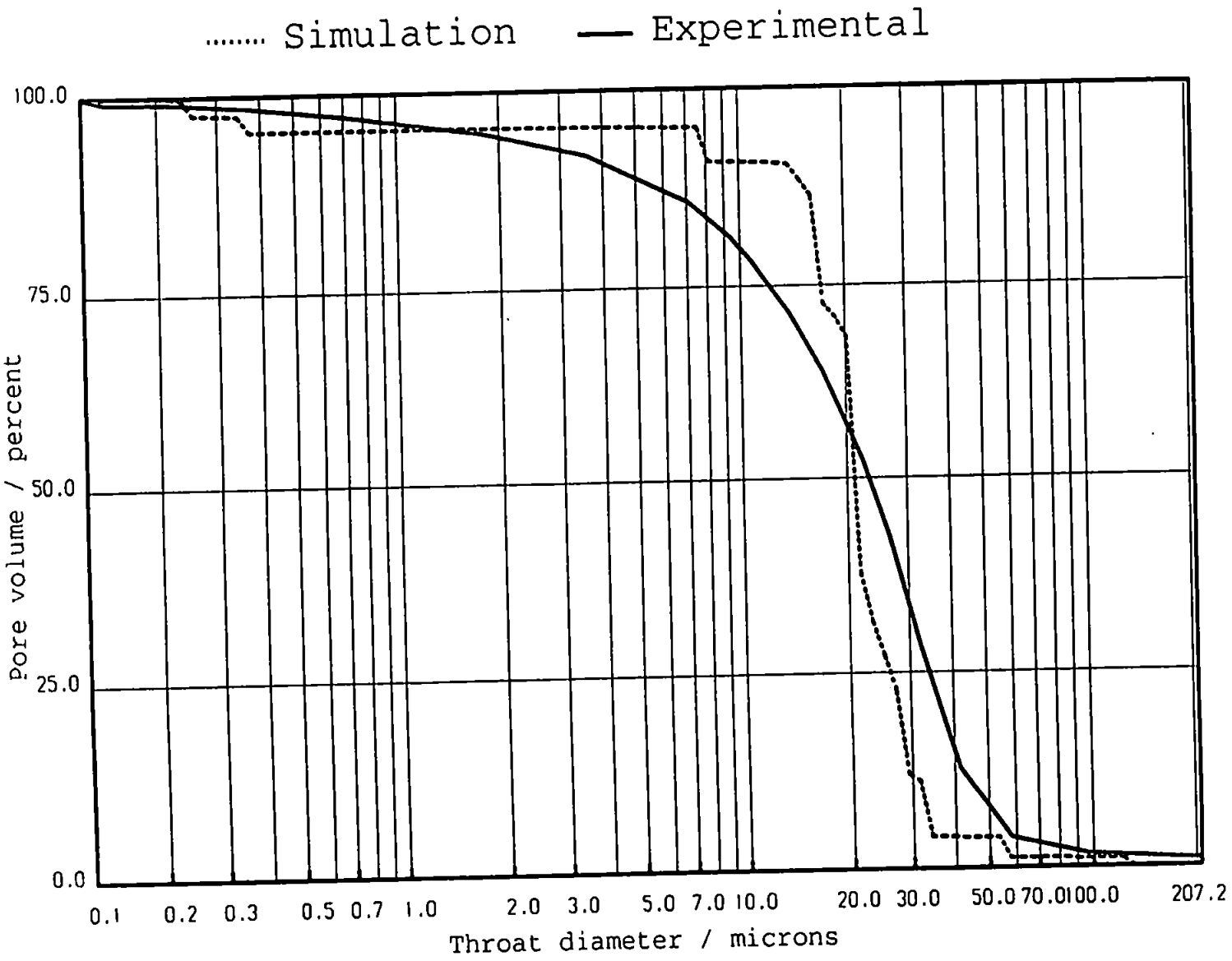

FIGURE A6.5: Experimental and Simulated Mercury Intrusion Curves for Sample 212E.

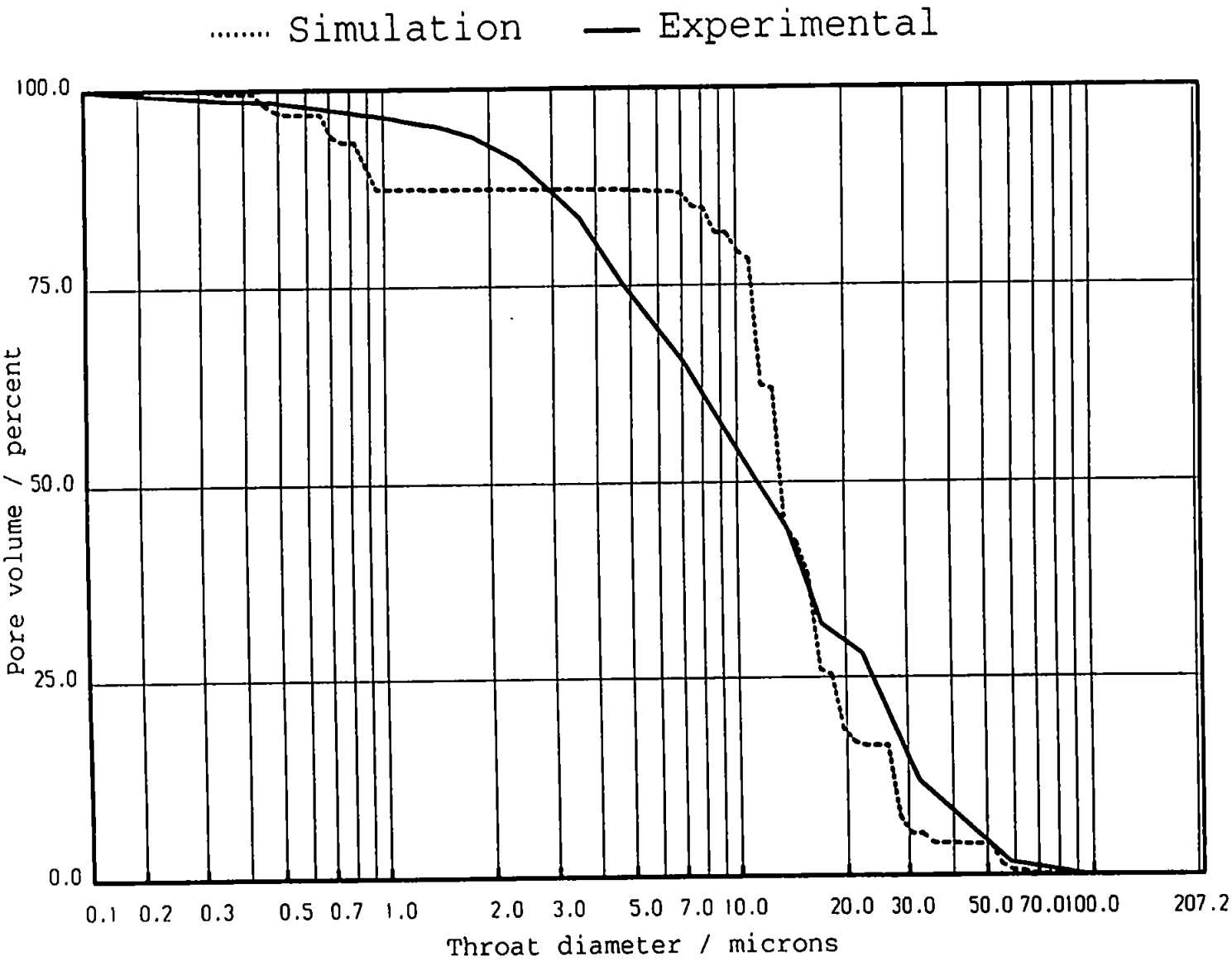

FIGURE A6.6: Experimental and Simulated Mercury Intrusion Curves for Sample 250A.

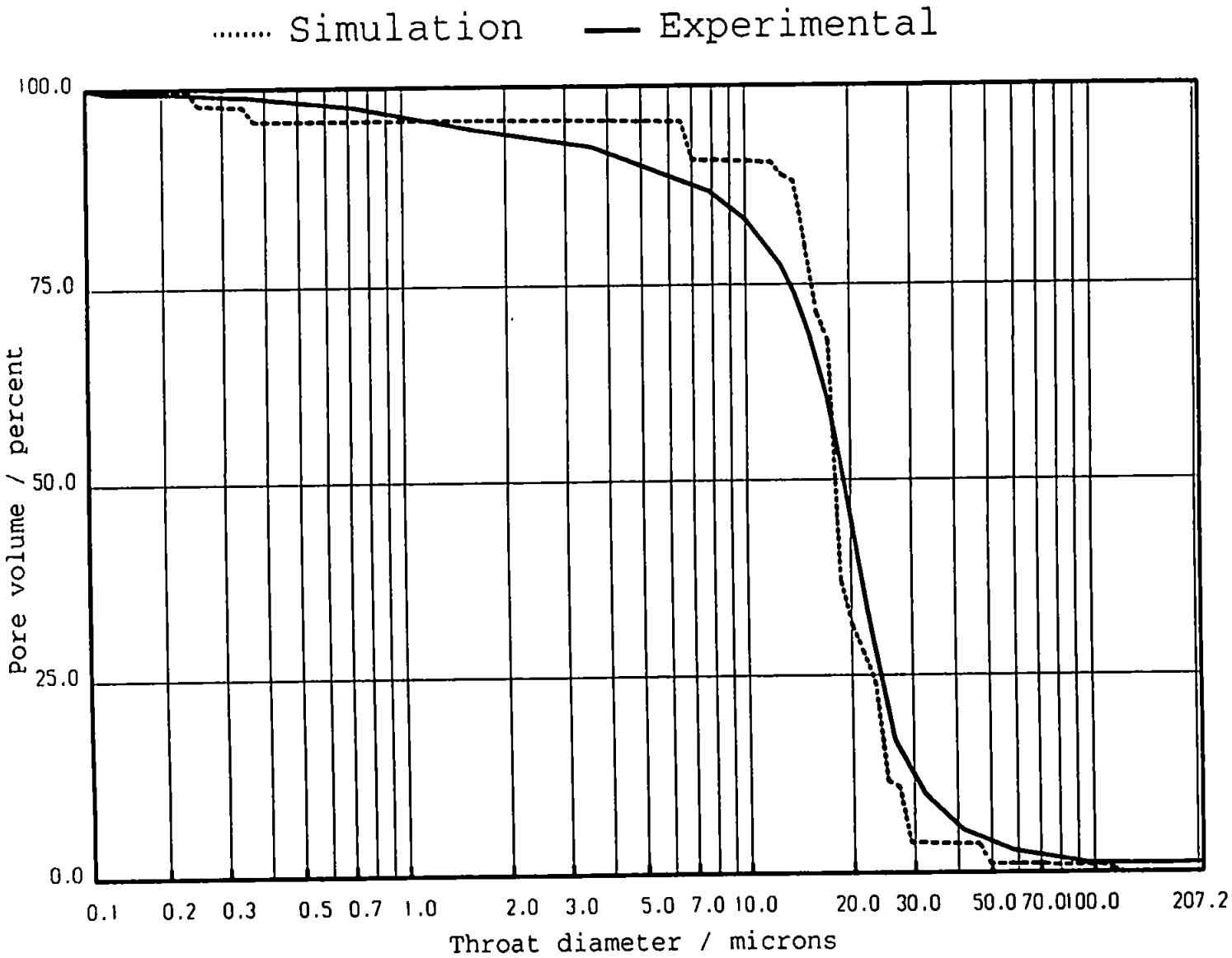

FIGURE A6.7: Experimental and Simulated Mercury Intrusion Curves for Sample 250E.

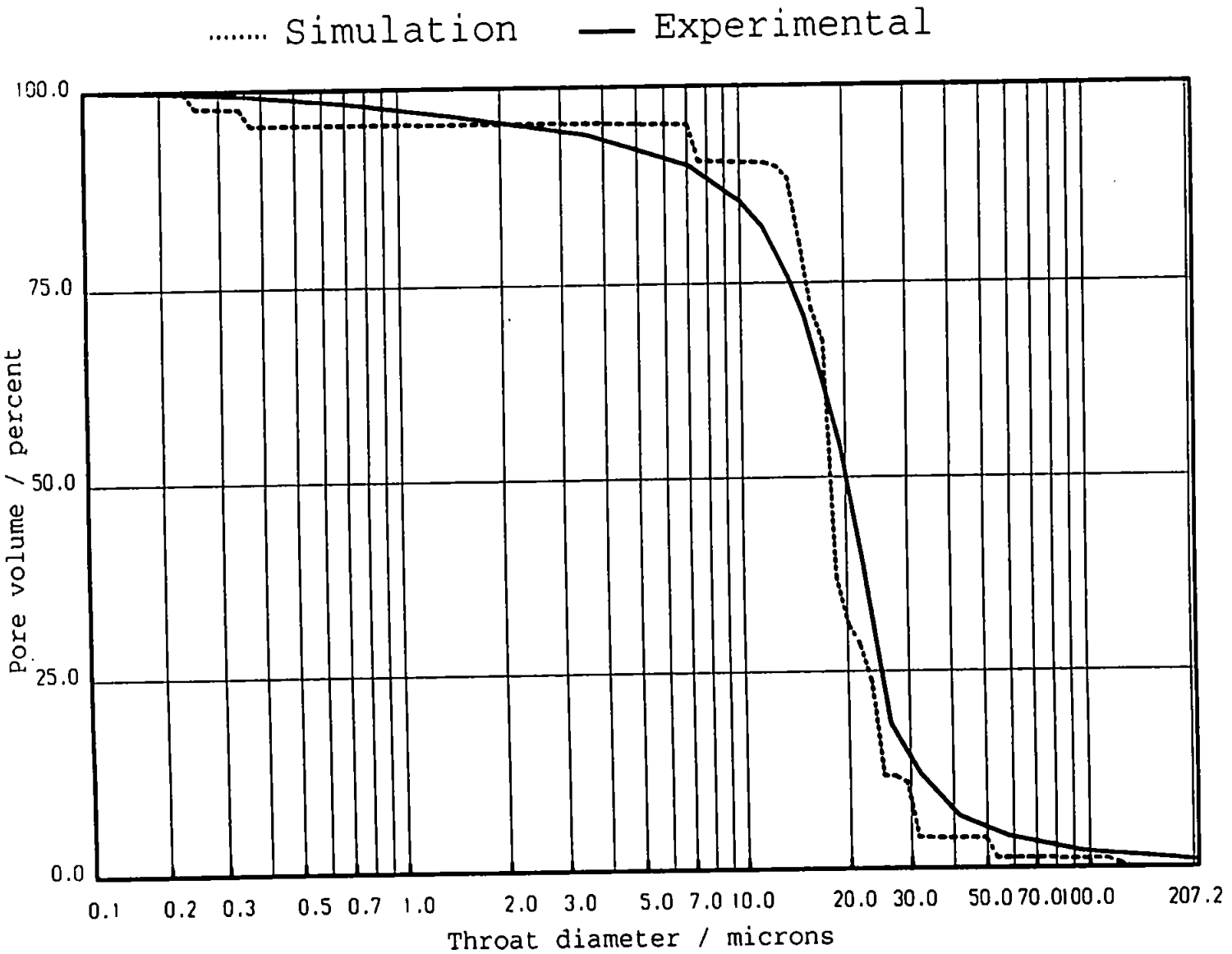

FIGURE A6.8: Experimental and Simulated Mercury Intrusion Curves for Sample 250E Repeat Run.

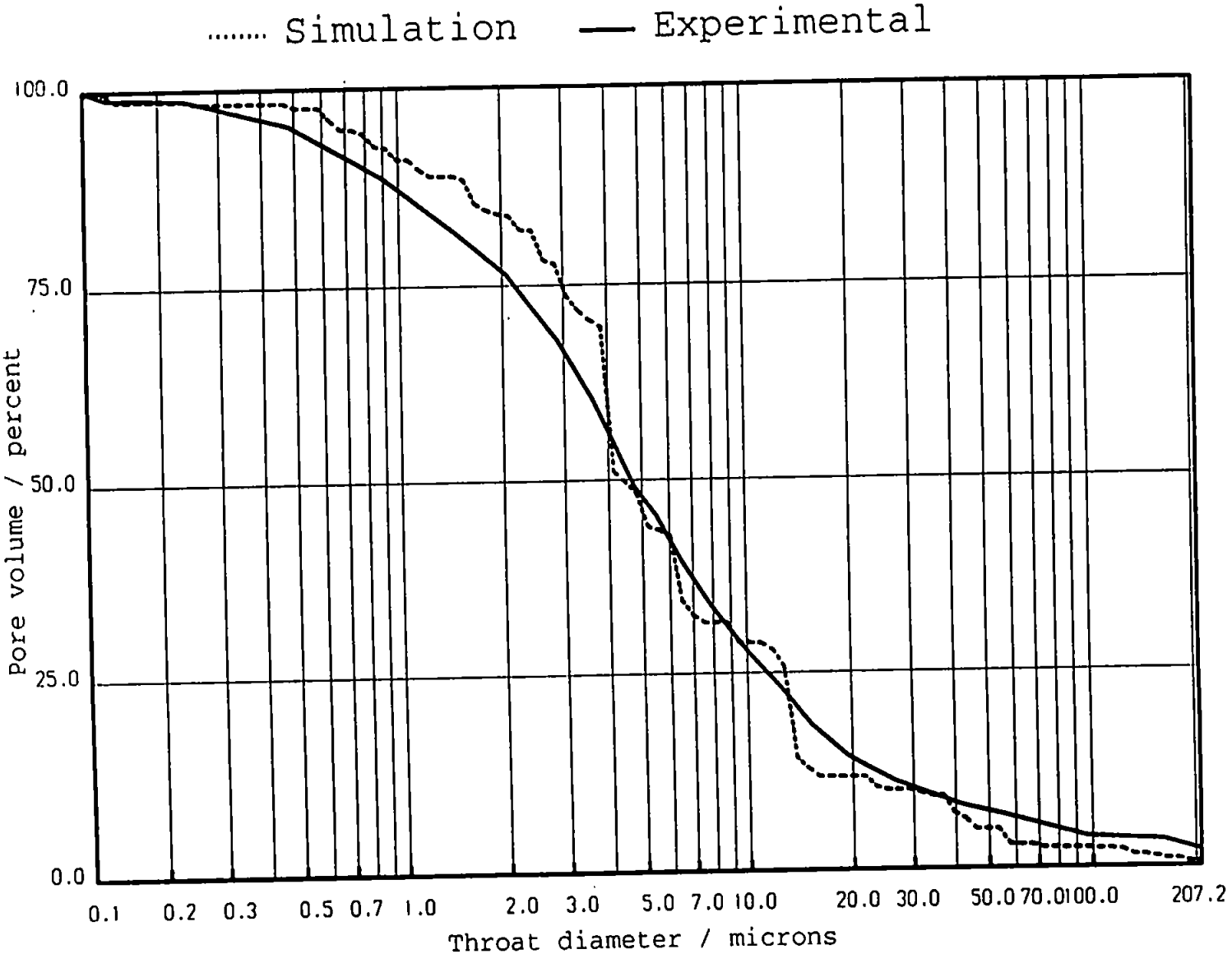

FIGURE A6.9: Experimental and Simulated Mercury Intrusion Curves for Sample 490A.

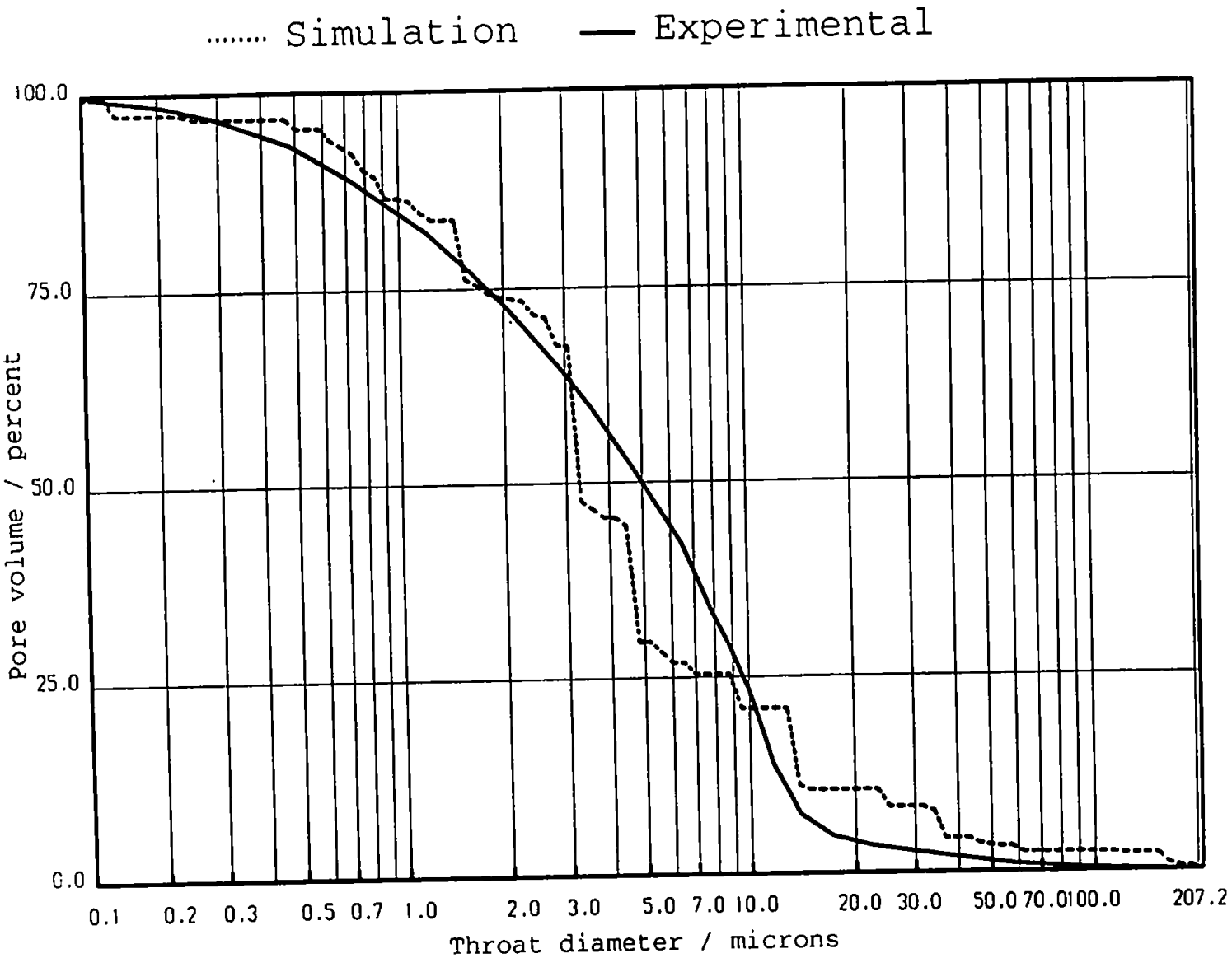

FIGURE A6.10: Experimental and Simulated Mercury Intrusion Curves for Sample 490B.

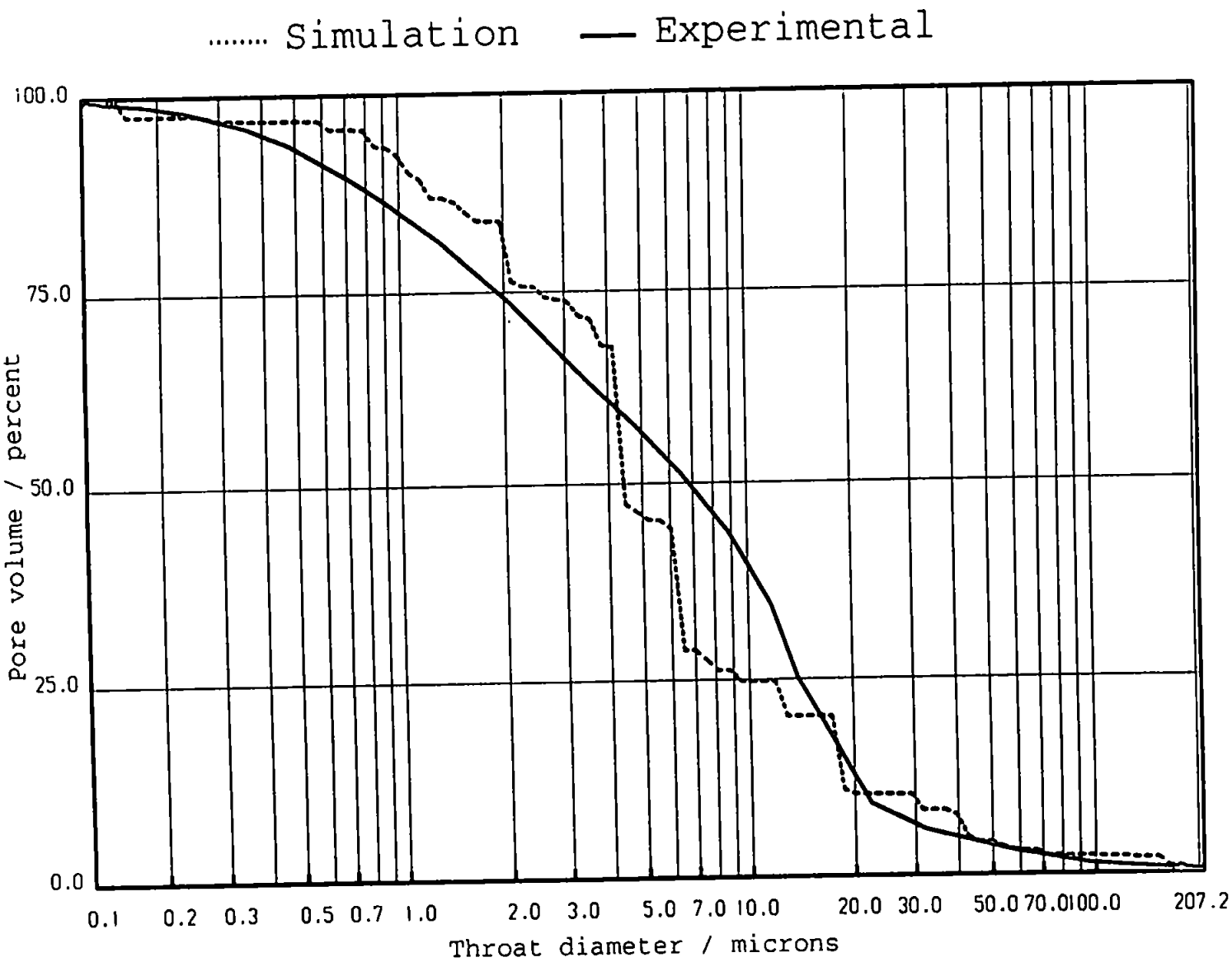

FIGURE A6.11: Experimental and Simulated Mercury Intrusion Curves for Sample 490C.

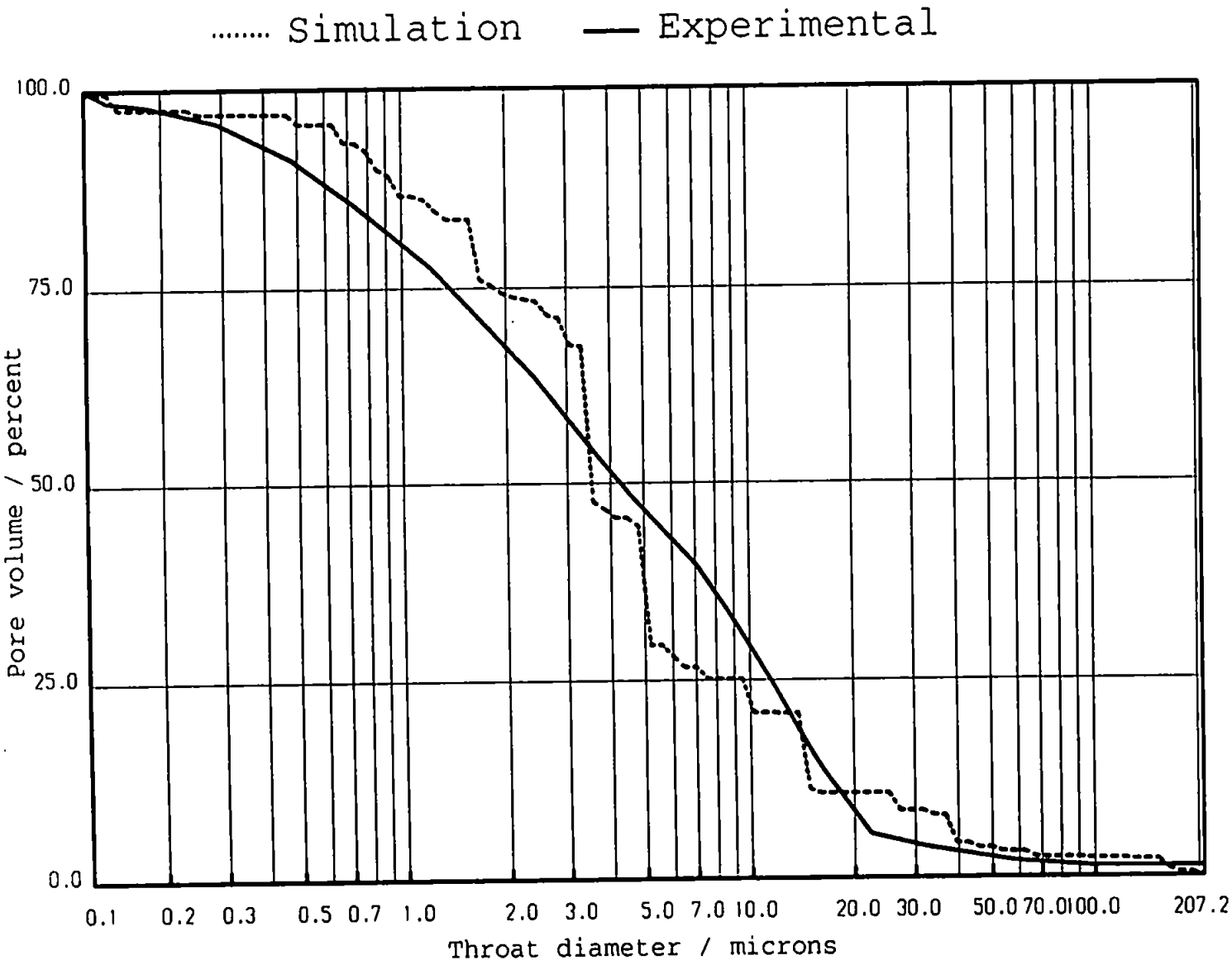

FIGURE A6.12: Experimental and Simulated Mercury Intrusion Curves for Sample 490D.

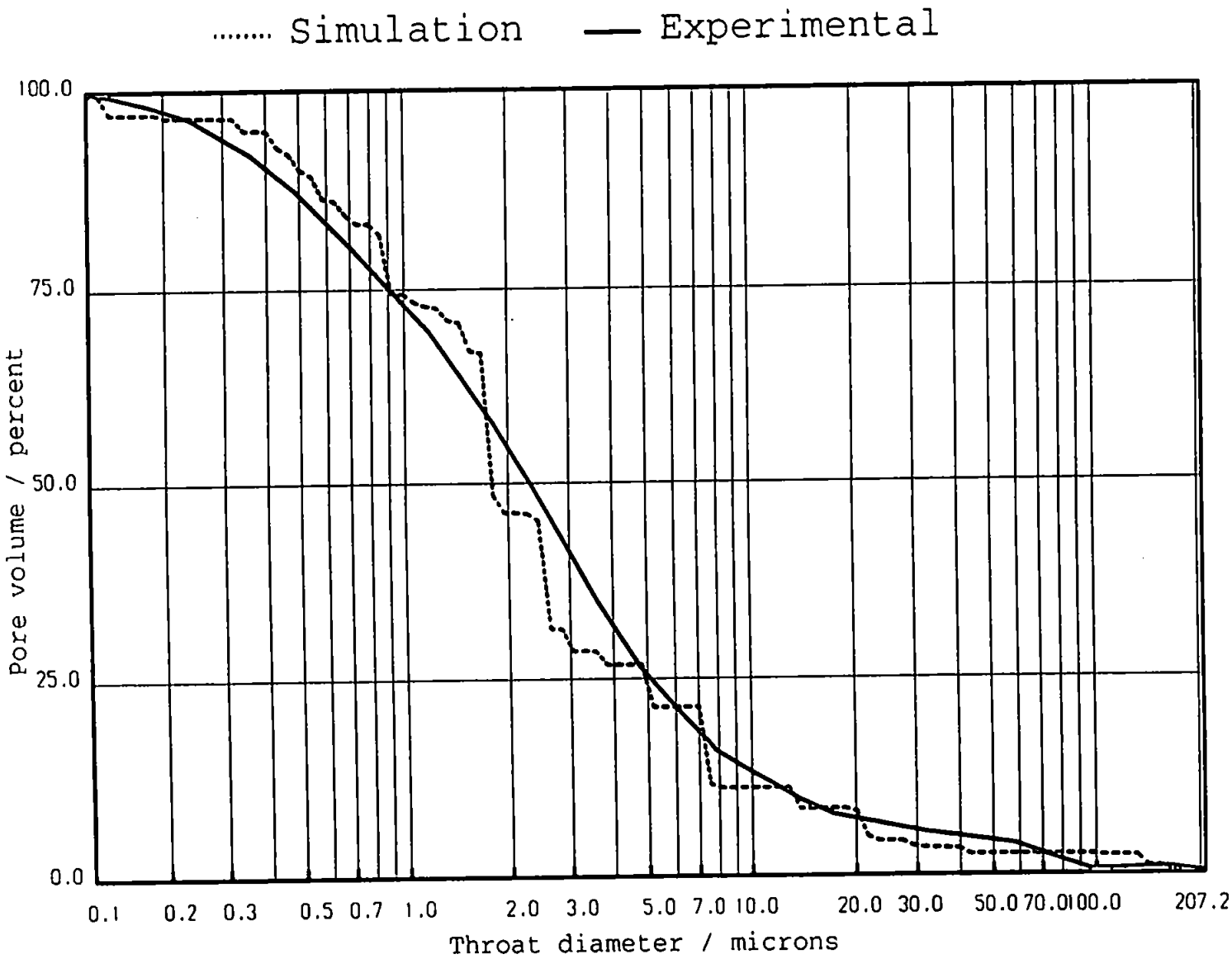

FIGURE A6.13: Experimental and Simulated Mercury Intrusion Curves for Sample 490D Repeat Run.

Axli

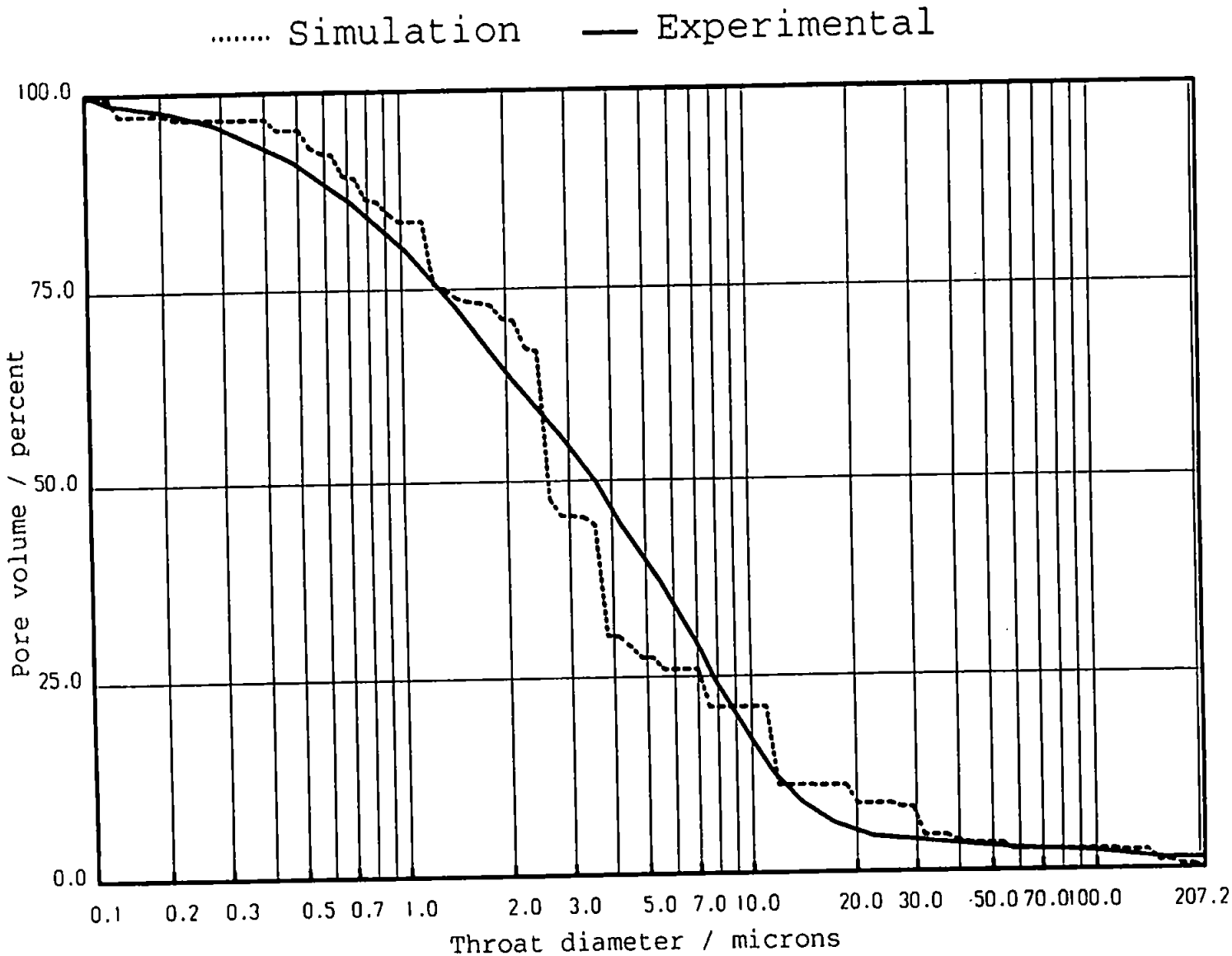

FIGURE A6.14: Experimental and Simulated Mercury Intrusion Curves for Sample 490E.

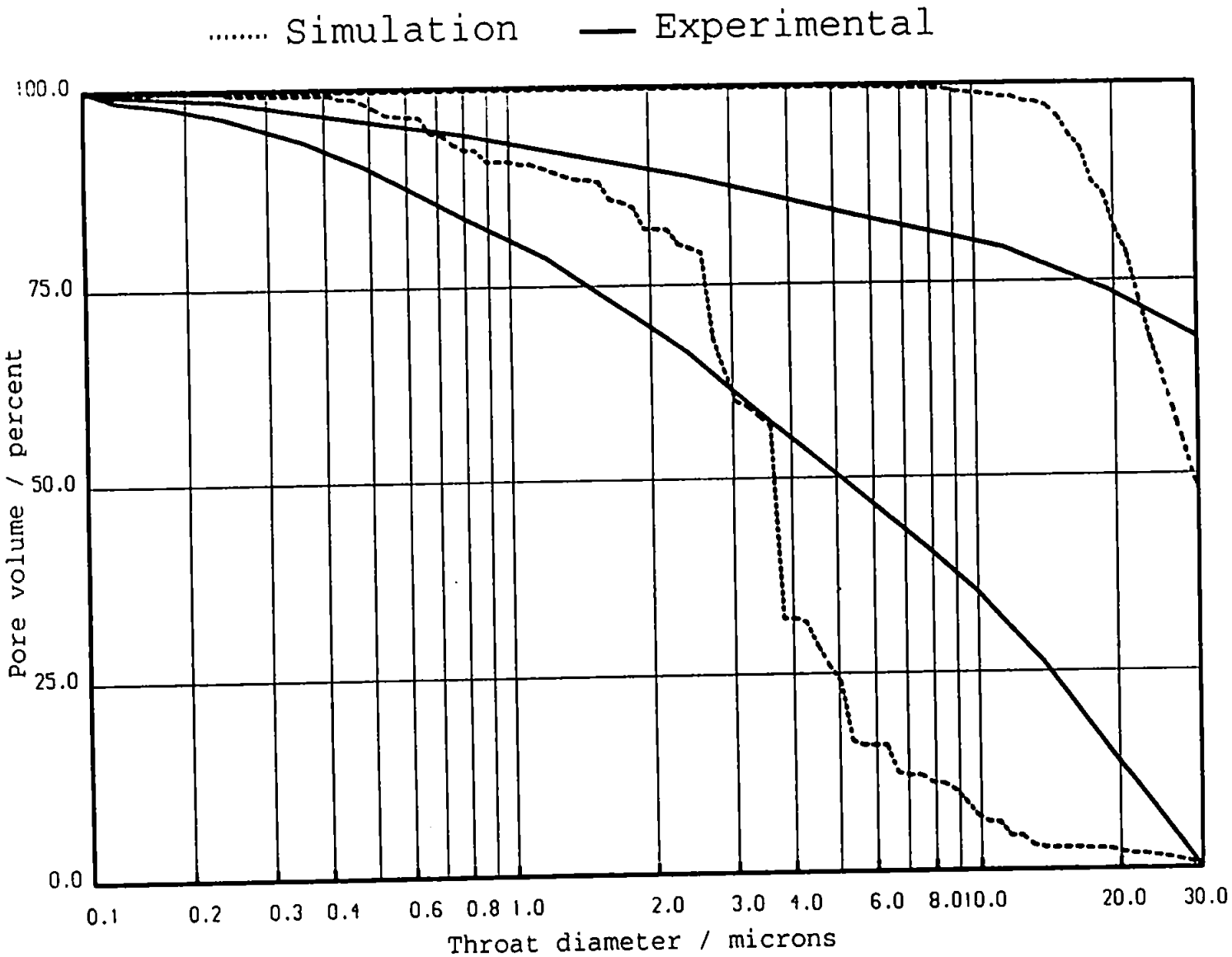

FIGURE A7.1: Simulated Mercury Intrusion and Extrusion Curve for Truncated Curve Fit for Sample 212A.

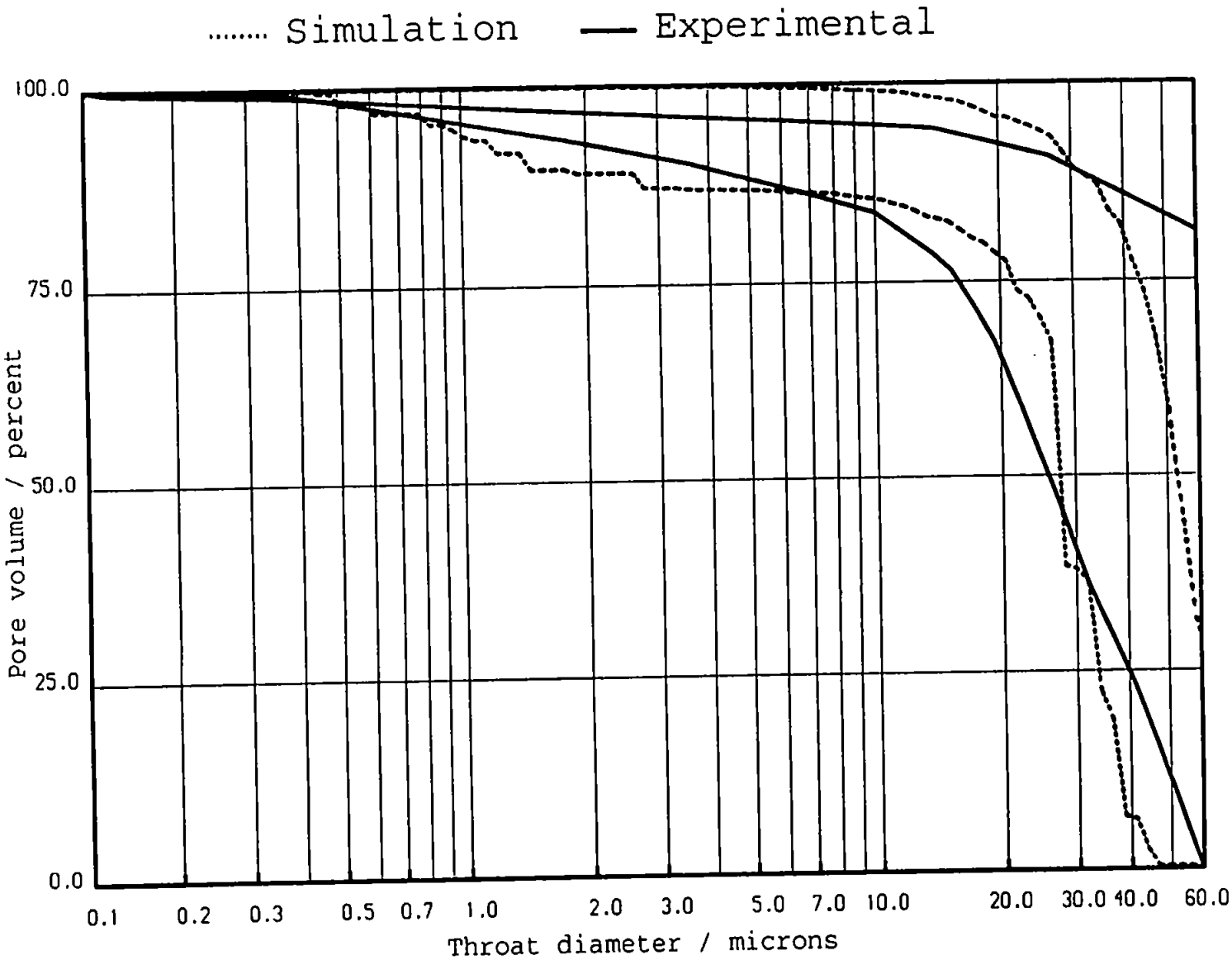

FIGURE A7.2: Simulated Mercury Intrusion and Extrusion Curve for Truncated Curve Fit for Sample 212B.

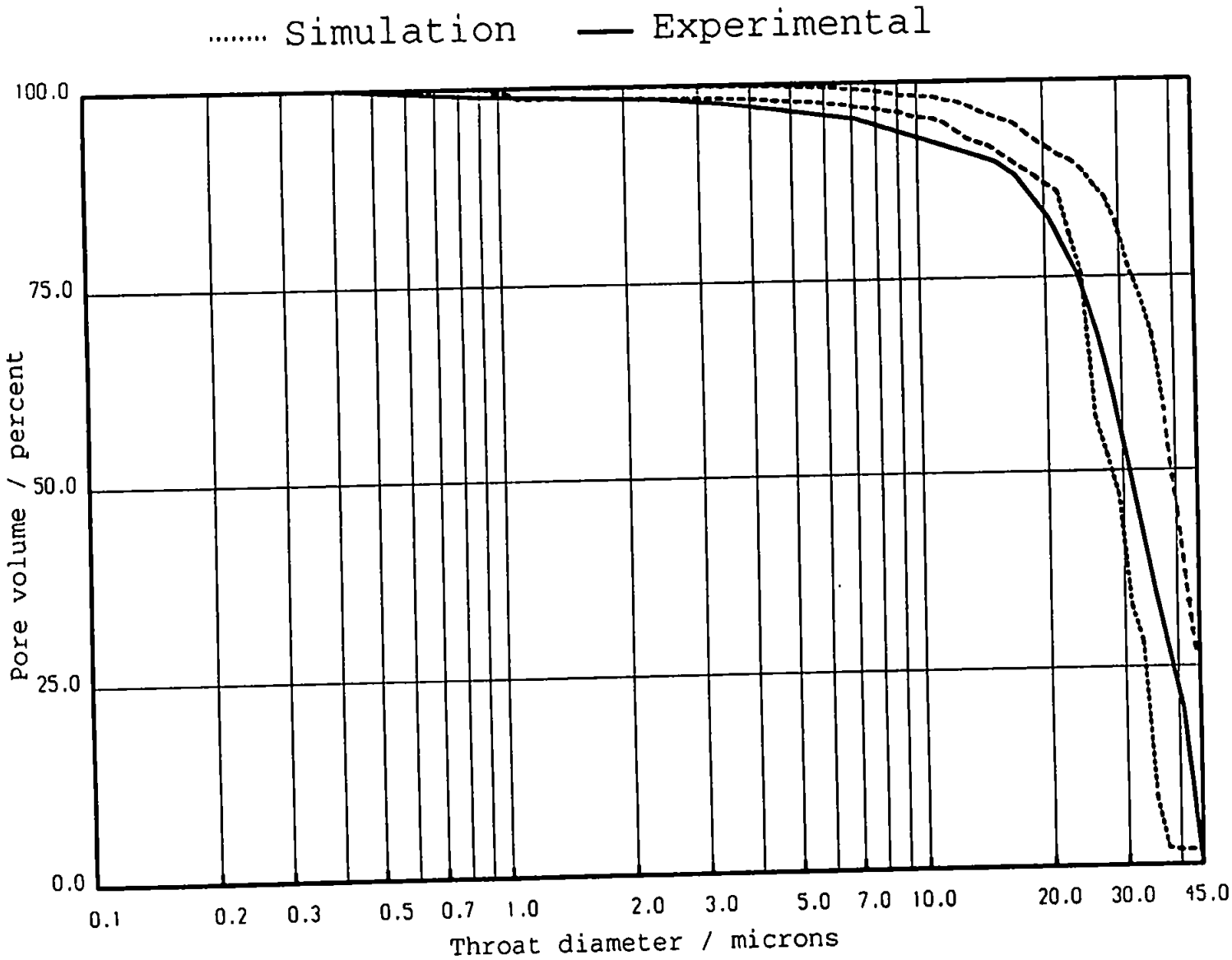

FIGURE A7.3: Simulated Mercury Intrusion and Extrusion Curve for Truncated Curve Fit for Sample 212C.

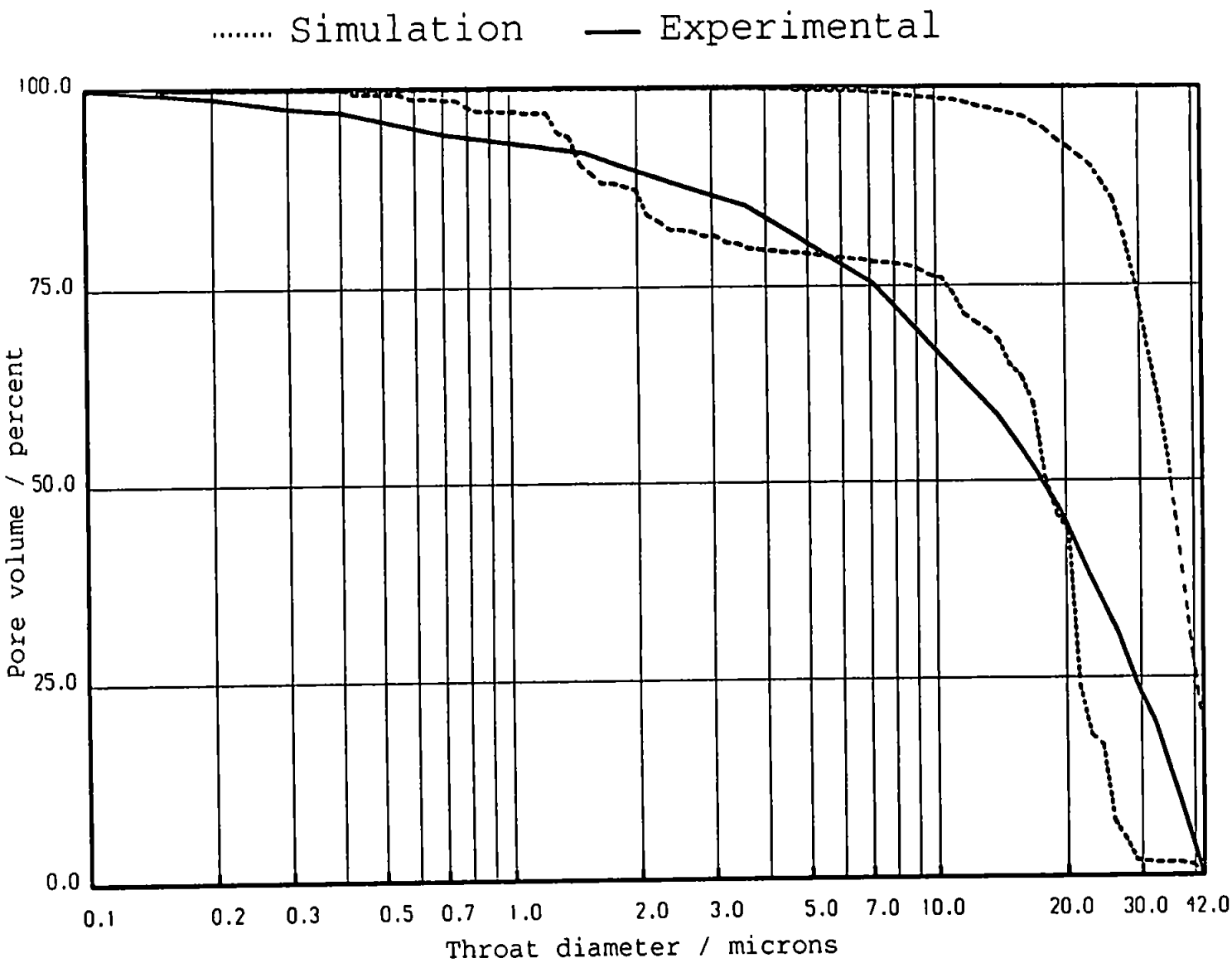

FIGURE A7.4: Simulated Mercury Intrusion and Extrusion Curve for Truncated Curve Fit for Sample 212D.

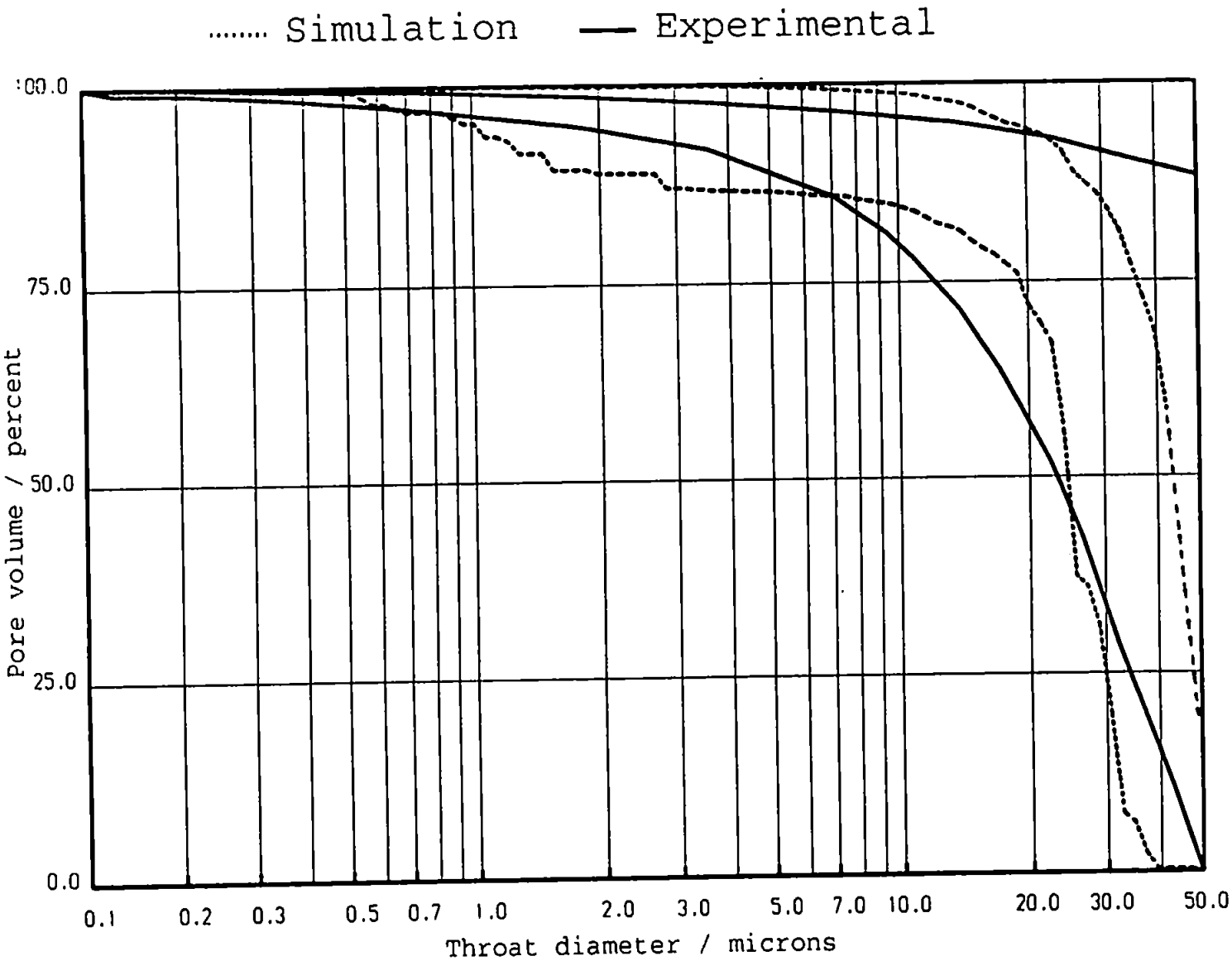

FIGURE A7.5: Simulated Mercury Intrusion and Extrusion Curve for Truncated Curve Fit for Sample 212E.

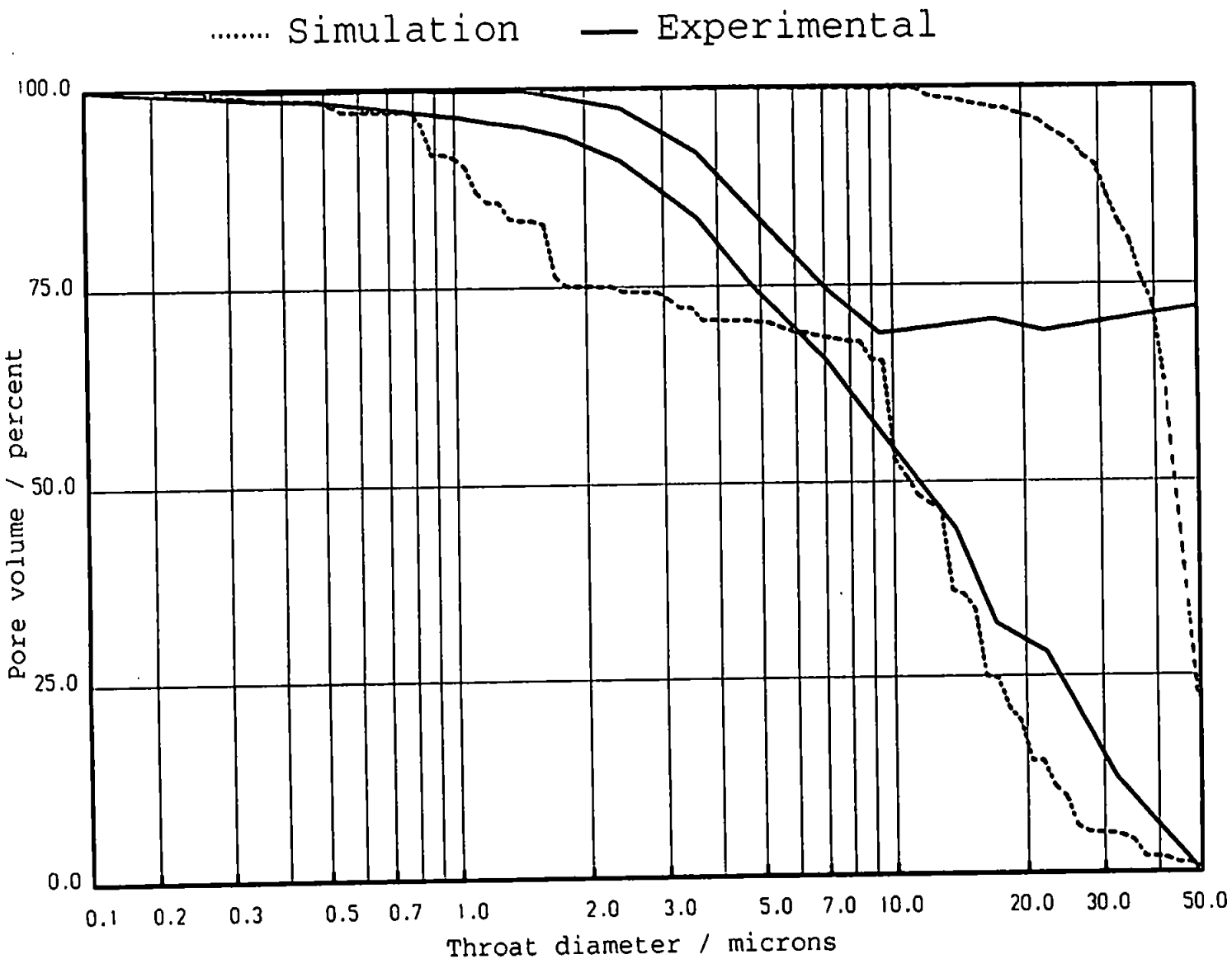

FIGURE A7.6: Simulated Mercury Intrusion and Extrusion Curve for Truncated Curve Fit for Sample 250A.

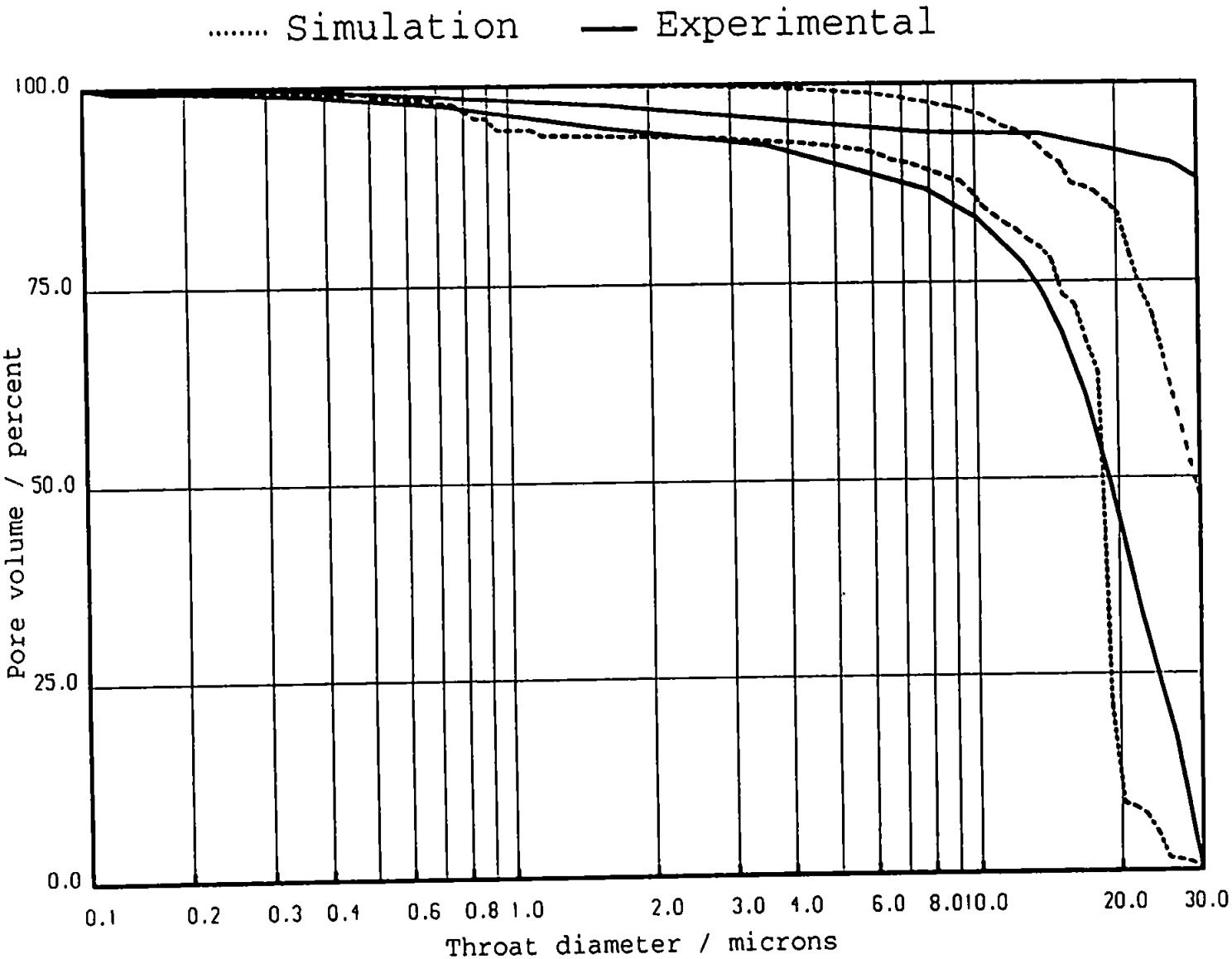

FIGURE A7.7: Simulated Mercury Intrusion and Extrusion Curve for Truncated Curve Fit for Sample 250E.

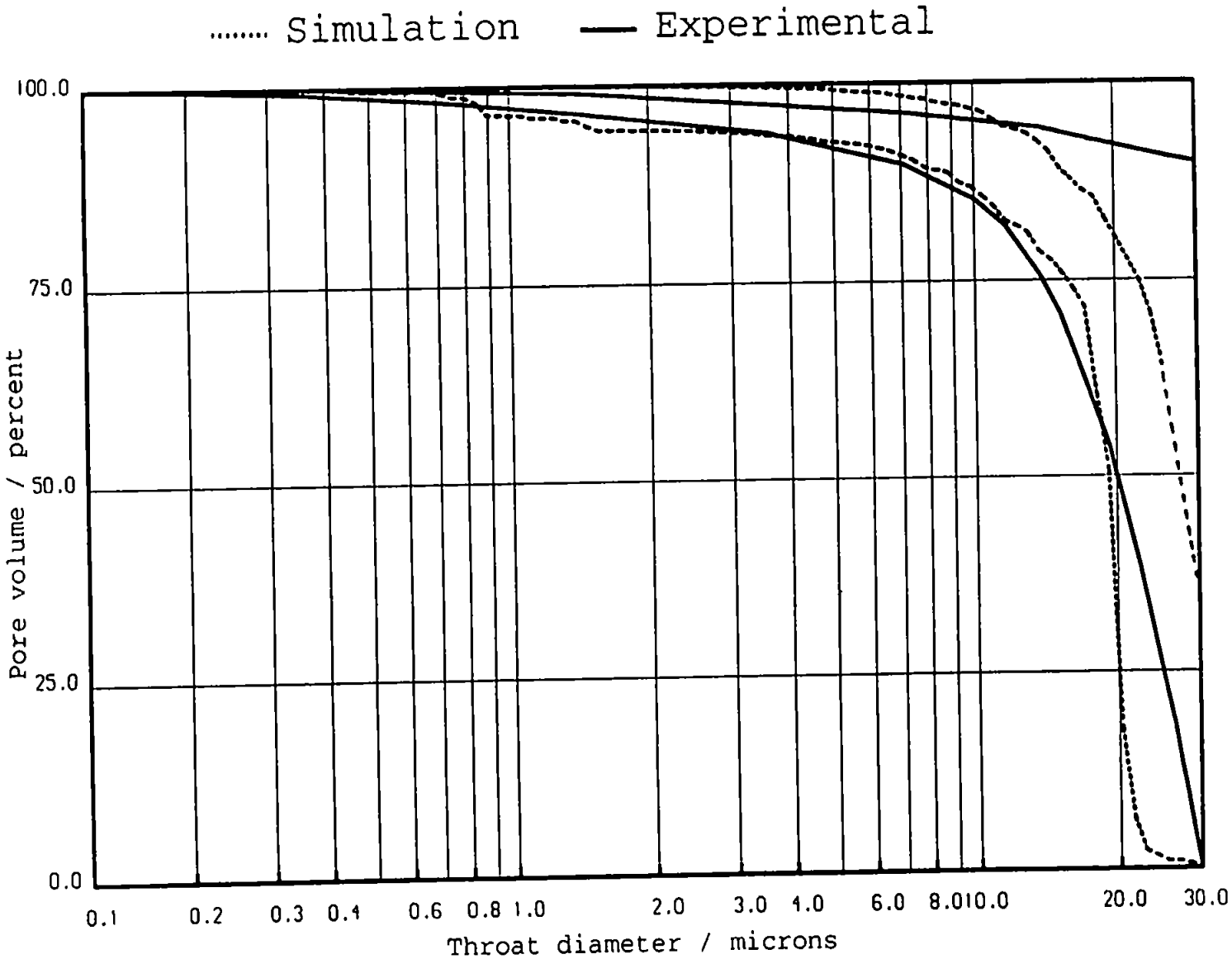

FIGURE A7.8: Simulated Mercury Intrusion and Extrusion Curve for Truncated Curve Fit for Sample 250E Repeat Run.

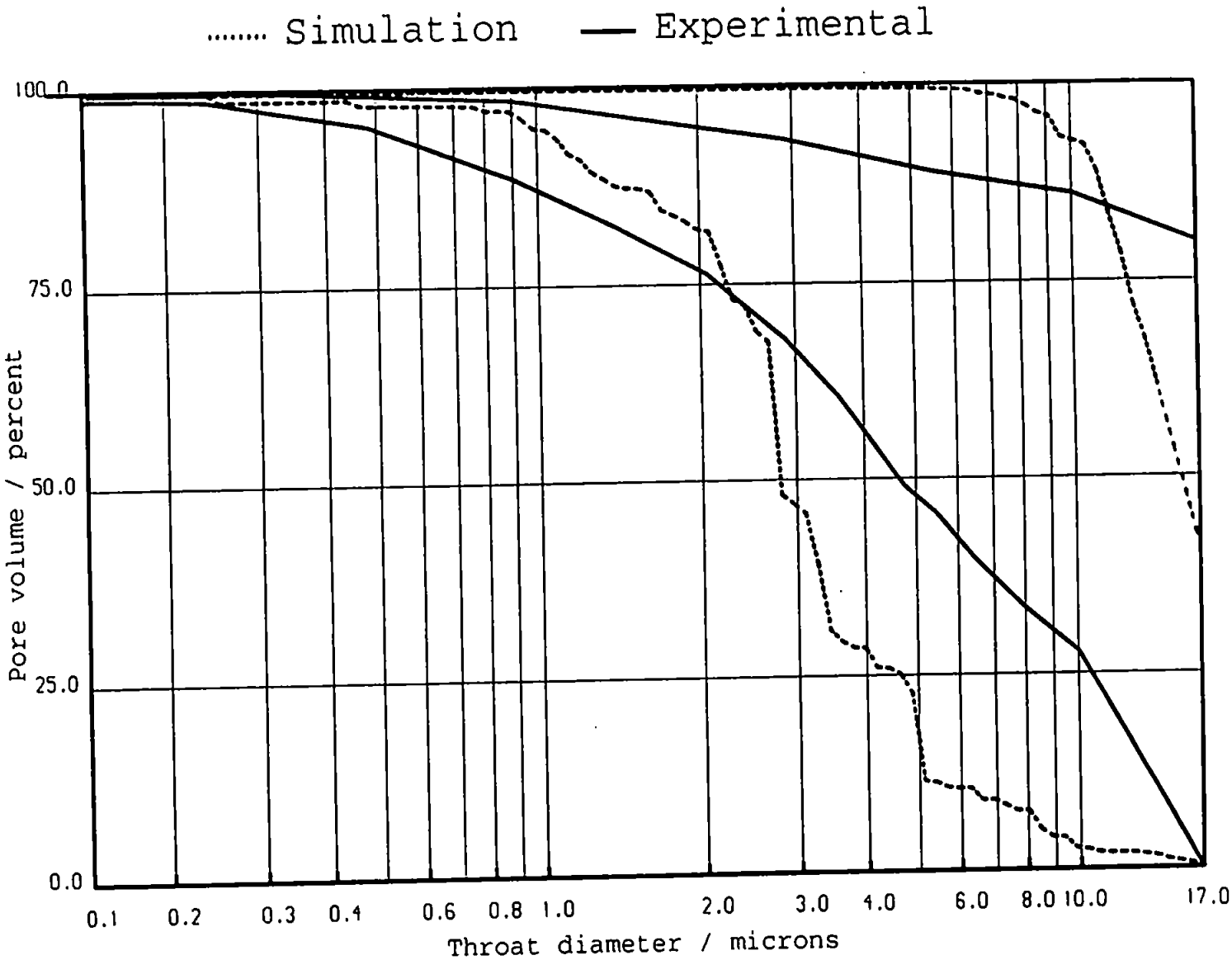

FIGURE A7.9: Simulated Mercury Intrusion and Extrusion Curve for Truncated Curve Fit for Sample 490A.

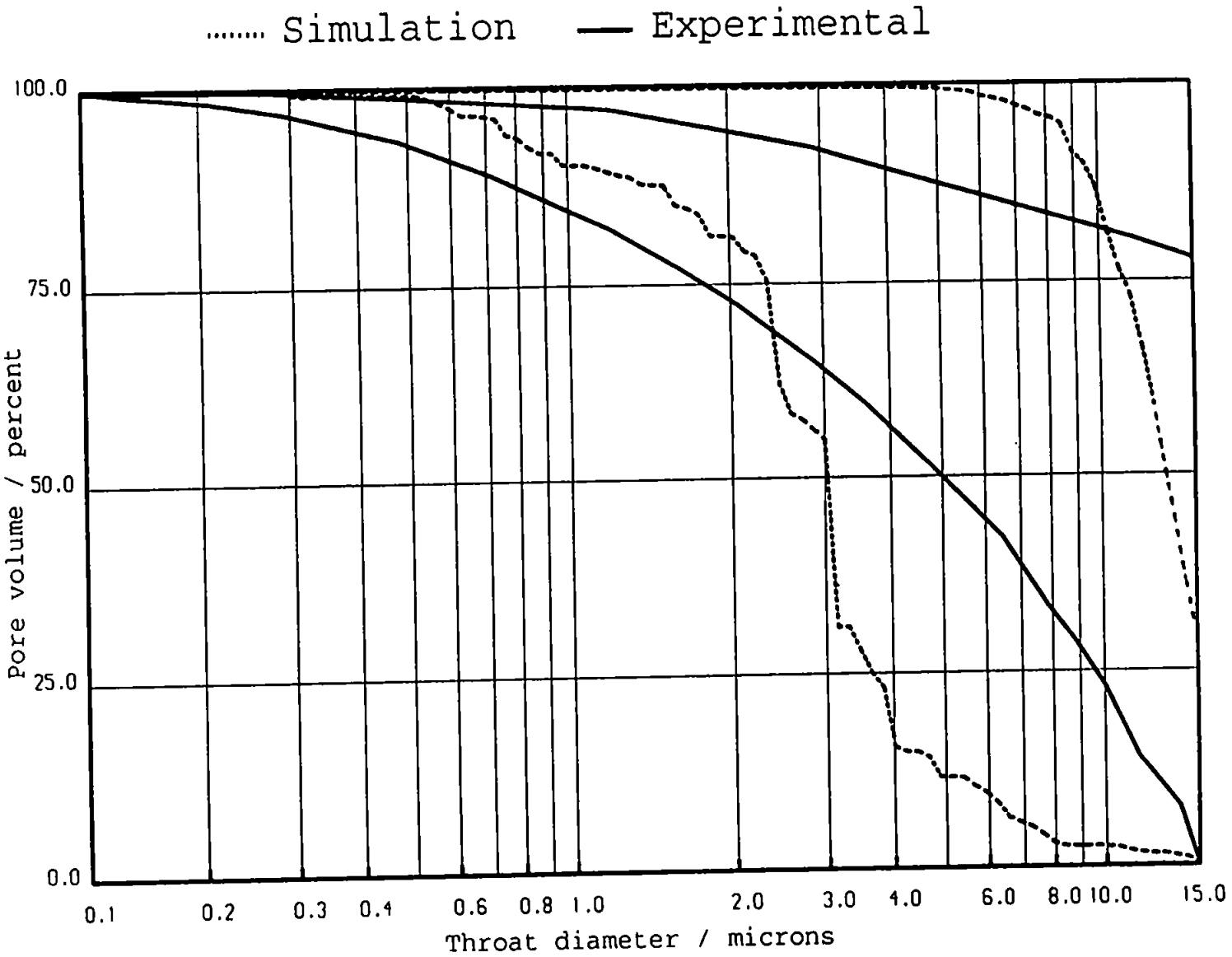

FIGURE A7.10: Simulated Mercury Intrusion and Extrusion Curve for Truncated Curve Fit for Sample 490B.

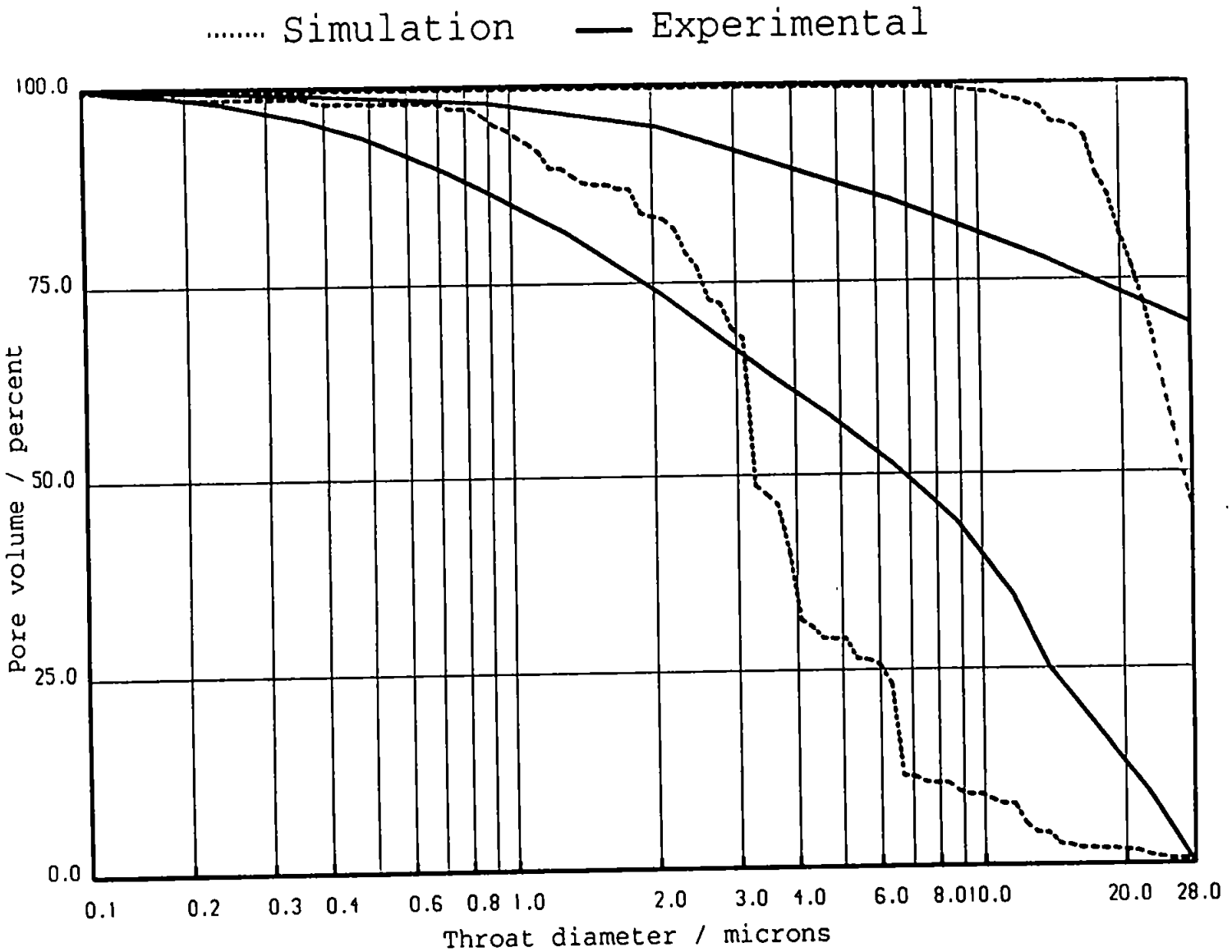

FIGURE A7.11: Simulated Mercury Intrusion and Extrusion Curve for Truncated Curve Fit for Sample 490C.

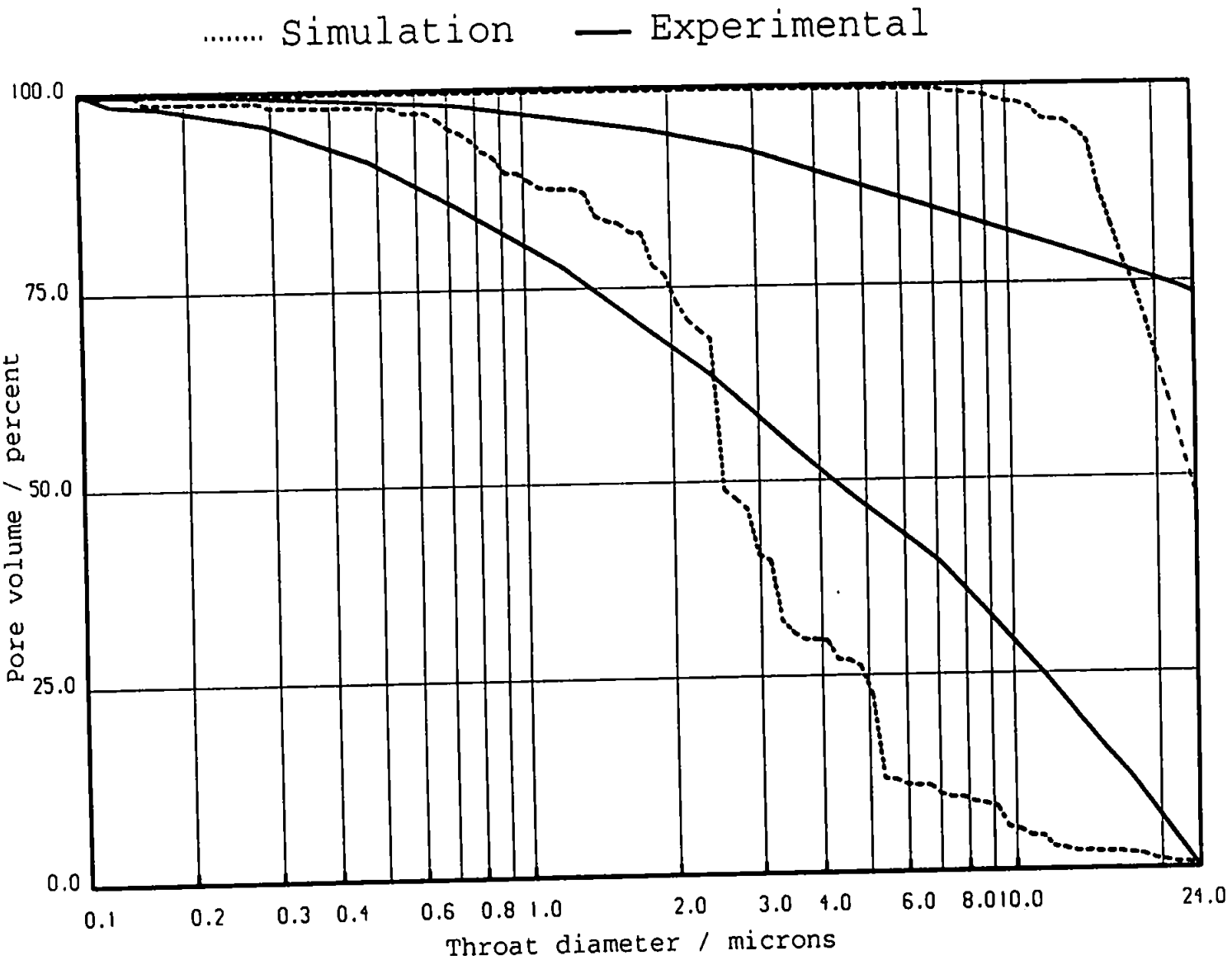

FIGURE A7.12: Simulated Mercury Intrusion and Extrusion Curve for Truncated Curve Fit for Sample 490D.

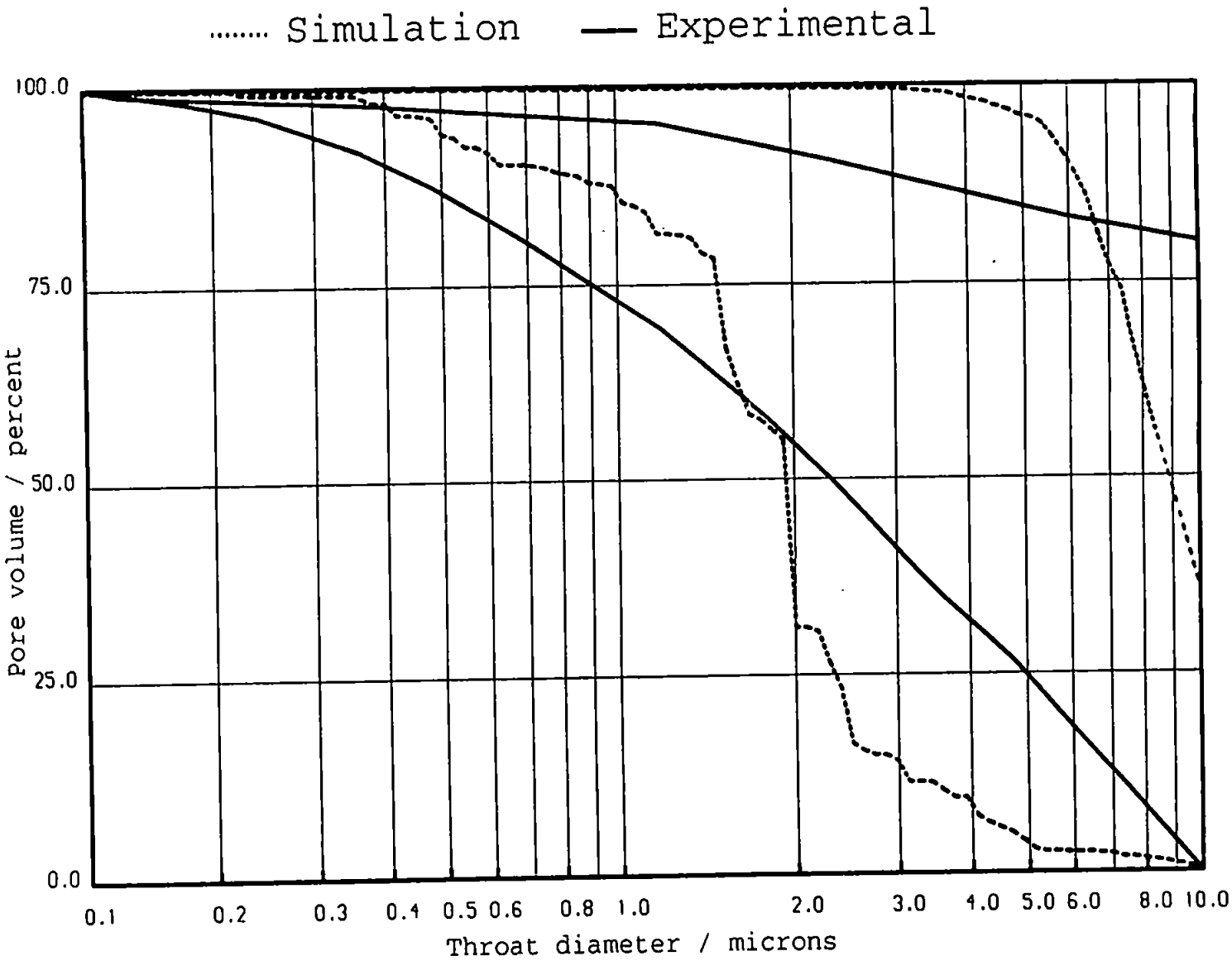

FIGURE A7.13: Simulated Mercury Intrusion and Extrusion Curve for Truncated Curve Fit for Sample 490D Repeat Run.

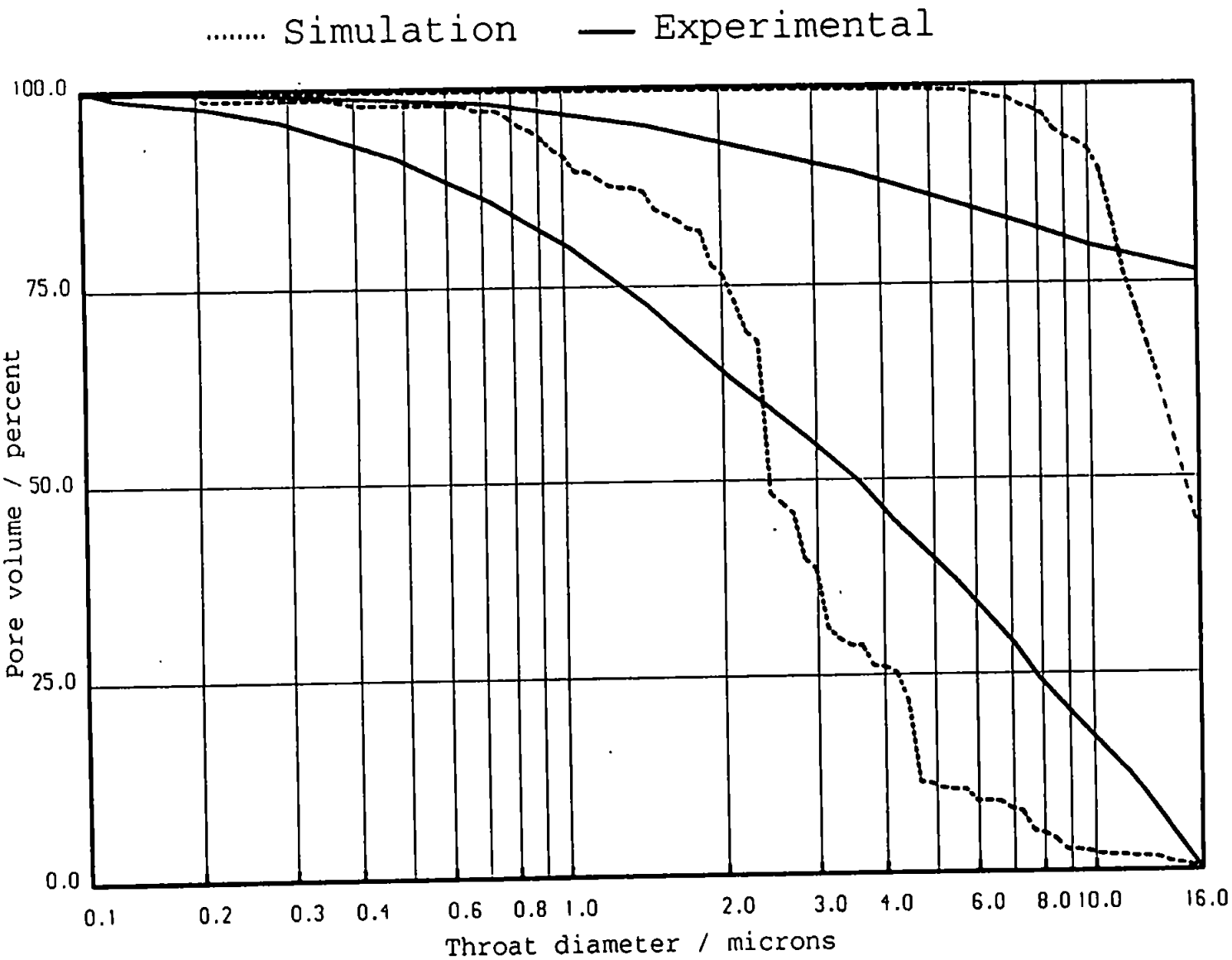

FIGURE A7.14: Simulated Mercury Intrusion and Extrusion Curve for Truncated Curve Fit for Sample 490E.